H24/3619

MONASH UNIVERSITY
THESIS ACCEPTED IN SATISFACTION OF THE
REQUIREMENTS FOR THE DEGREE OF
DOCTOR OF PHILOSOPHY

ON..... [redacted] 26 August 2003 .....

.....

Sec. Research Graduate School Committee

SHEAR STRENGTH OF REINFORCED CONCRETE T-BEAMS STRENGTHENED USING CARBON FIBRE REINFORCED POLYMER (CFRP) LAMINATES

by

LEE TUAN KUAN (BE (Hons))

MONASH UNIVERSITY

A thesis submitted in fulfilment of the requirements for the degree of Doctor of Philosophy

DEPARTMENT OF CIVIL ENGINEERING
MONASH UNIVERSITY

MAY 2003

STATEMENT

I hereby declare that this thesis contains no material accepted for any other degree or diploma in any university. To the best of my knowledge, this thesis contains no material previously written or published by another person, except where due acknowledgment is made in the text.

[redacted]

LEE TUAN KUAN

TO MY FAMILY

ACKNOWLEDGMENTS

I would like to take this opportunity to thank my supervisor, Dr. Riadh Al-Mahaidi for his invaluable guidance, expertise, encouragement and support throughout the course of this research. I would also like to thank my co-supervisor, Dr. Geoff Taplin for his support and guidance during the study.

Thanks are also due to the staff at the Noel Murray Strong Floor Laboratory. The completion of the experimental aspect would not be possible without the assistance of Jeffrey Doddrell, Len Doddrell, Michael Leach and Graeme Rundle. My gratitude also goes to Roger Doulis for his invaluable assistance with the instrumentation of the experimental works. I would also like to thank the Australian Research Council, DEETYA, Sika Australia Pty. Ltd. and Sika AG, Switzerland for providing partial funding and the materials required for this research.

Finally, I would like to thank my parents and brothers for their support and constant encouragement not only during the trying times of the research but throughout the course of this study and my life.

SUMMARY

The research undertaken herein investigated the short-term behaviour of T-beams shear strengthened with prefabricated L-shaped CFRP plates. The CFRP plates were bonded to the soffit and web of the beams extending into the flange. As part of the experimental programme, four large-scale reinforced concrete beams were fabricated and tested to failure. The effect on the beam behaviour of varying the spacing of the external reinforcement was investigated. The spacings considered were 0.75D, 0.60D and 0.50D where D is the overall depth of the beam. The control beam had no external reinforcement. To gain a better understanding of the bond behaviour between the CFRP and concrete and the mechanisms that occur in the T-beams under loading, thirteen CFRP-concrete bond specimens were fabricated and tested. Advanced photogrammetry measurement techniques were used to study the behaviour of the T-beams with and without shear strengthening. Numerical modelling of the T-beams and bond specimens using the non-linear finite element method was carried out to supplement the experimental results. The applicability of three existing beam shear strength prediction models were also investigated and compared against experimental results.

In the experiment, an increase in the ultimate shear capacity with reference to the control beam of 54%, 61% and 81% was achieved in beams '0.75D', '0.60D', and '0.50D'. The control beam failed due to the formation of two large shear cracks. Failure in the strengthened beams was characterised by formation of large shear cracks and the separation of the CFRP laps at the soffit of the beam tearing away concrete at the bend zone. The presence of the CFRP reinforcement did not impede or delay the initial formation and propagation of shear cracks. Shear cracks were observed to be smaller in the strengthened beams compared to the shear cracks in the control beam.

Results from the photogrammetry measurement show that the deformation mechanisms in the strengthened beams were similar to the control beam except that the width of the shear cracks was smaller. Therefore, existing equations used in the prediction of the shear capacity of reinforced concrete beams can be extended to

include the contributions from the CFRP reinforcement. The web shear crack widths were established quantitatively to be significantly smaller in the strengthened beams compared to the control beam. The smaller shear crack widths in the strengthened beams imply that the effect of aggregate interlock is more significant, therefore, the concrete contribution to the shear capacity of the beams increases.

Experimental testing of the CFRP-concrete bond specimens has established the effective bond length to be approximately 120 mm, which was based on a simple bilinear curve fit of the peak load versus bond length graph. The numerical results of the finite element models were in good agreement with the experimental results. Parametric studies were carried out to determine the effects of varying concrete strength, adhesive stiffness and CFRP stiffness. For the values investigated herein, it was found that the concrete strength had a significant effect on the peak load carried by the models. The effect on the slip behaviour and strain distribution profile of the CFRP plate was minor. Variations in the adhesive and CFRP plate stiffness did not have a significant effect on the peak load, slip behaviour and strain distribution profile of the CFRP plate.

A general methodology for the modelling of the reinforced concrete T-beams web-bonded with CFRP both in a 2D and 3D environment was presented. The finite element results of the bond specimens were used as the basis of the bond slip models between the CFRP and concrete elements in the T-beam models. The finite element models used to analyse the beams proved to be capable of modelling the general trends and behaviour reasonably well. Parametric studies were carried out to investigate the effects of varying the shear retention factor β of the concrete elements and bond slip behaviour between CFRP and concrete. The shear retention factor is an important factor. To a lesser extent, the bond slip behaviour is also important as the numerical results vary depending on the bond slip models adopted.

The three existing beam shear strength models investigated gave very conservative predictions of the FRP contribution to the shear strength. These prediction models can be used in the design of beams shear strengthened with the prefabricated L-shaped CFRP strengthening system used in the present study.

TABLE OF CONTENTS

LIST OF FIGURES

LIST OF TABLES

NOTATION

A_{frp}	-	FRP cross-sectional area
A_{st}	-	cross-sectional area of tension reinforcement
$A_{sv,min}$	-	cross-sectional area of minimum shear reinforcement
a_v	-	shear span
b_v	-	effective width of a web for shear
b_w	-	width of the web
D	-	overall depth of a cross section (= h)
D_{11}, D_{22}	-	normal and shear linear stiffness moduli
D_{frp}	-	stress distribution factor of FRP
d	-	effective depth of a cross-section
d_{frp}	-	effective depth of FRP (Khalifa et al. (1998), Khalifa and Nanni (2000) and Neale (2001))
	-	distance from the compression face to the lower edge of the FRP (Chen and Teng (2003a, b))
$d_{frp,t}$	-	distance from the compression face to the top edge of the FRP
d_{max}	-	maximum aggregate size
E_c	-	mean value of modulus of elasticity of concrete at 28 days
E_{frp}	-	modulus of elasticity of FRP reinforcement
E_s	-	modulus of elasticity of reinforcement
f'_c	-	characteristic compressive strength of concrete at 28 days
f_{cm}	-	mean value of compressive strength of concrete at the relevant age
f_{int}	-	internal forces (finite element context)
f_t, f'_{ct}	-	principal tensile strength of concrete
f_{frpe}	-	average shear stress in FRP intersected by shear crack at ultimate state
f_{frp}, f_{frpu}	-	tensile capacity of FRP
f_{sy}	-	yield strength of reinforcing steel
$f_{sy,f}$	-	yield strength of fitments
G	-	shear modulus of uncracked concrete

G^{cr}	-	shear modulus of cracked concrete
G_f^I	-	Mode-I fracture energy
G_{fo}	-	base value of fracture energy
g_i, g_j	-	strain gauge readings at location i and j
h	-	height of beam (= D)
	-	crack band width (finite element context)
h_{frp}	-	FRP bonded height
h_{frpe}	-	effective height of the FRP
k_1 & k_2	-	parameters accounting for shear strength of the concrete and FRP configuration
L_e	-	effective bond length of FRP
n_e	-	number of free ends of the FRP on one side of the beam
V_n	-	nominal shear strength of an reinforced concrete section
V_c	-	shear strength contribution provided by the concrete
V_{frp}	-	shear strength contribution provided by the FRP
V_s	-	shear strength contribution provided by the steel shear reinforcement
R	-	ratio of effective strain to ultimate strain ($\varepsilon_{frpe}/\varepsilon_{frpu}$)
s	-	spacing of steel shear reinforcement
s_{frp}	-	spacing of FRP shear reinforcement
t	-	a thickness
t_{frp}	-	FRP thickness
w_{frp}	-	width of FRP
w_{frpe}	-	effective width of FRP sheet
z_t & z_b	-	coordinates at the top and bottom ends of the effective FRP
α	-	reduction coefficient for the effective FRP strain ε_{frpe}
β	-	angle between FRP and longitudinal axis of member
	-	shear retention factor for concrete (finite element context)
Δ	-	a deflection
Δl_{i-j}	-	distance between two strain gauge positions
Δu_0	-	displacement increment (finite element context)
δu_i	-	i^{th} iterative displacement increment (finite element context)
ε_{cr}	-	critical strain level

ε_{frpe}	-	effective FRP strain
ε_{frpu}	-	ultimate tensile elongation of FRP
ε_{max}	-	maximum usable FRP strain
εv_{cu}	-	ultimate vertical tensile strain of concrete
γ_{frp}	-	partial safety factor for FRP
φ_{frp}	-	material resistance factor for FRP
λ	-	normalised maximum bond length
λ_1 & λ_2	-	parameters dependent on FRP material type
ν	-	Poisson's ratio
θ_c, θ	-	crack inclination angle
ρ	-	density of concrete
ρ_{frp}	-	FRP area fraction
$\sigma_{frp,max}$	-	maximum stress achievable in FRP intersected by shear crack
τ_{ave}	-	average shear stress
τ_{i-j}	-	average shear stress between two positions
τ_{ult}	-	interface shear strength
ζ	-	coefficient ($= z_t/z_b$)

CHAPTER 1 - INTRODUCTION

In Australia, the number of reinforced concrete T-beam bridges is estimated to be in excess of one thousand. Many of these bridges were designed and constructed prior to 1939, when existing bridge design specifications were less stringent and methods of analysis less precise than they are today. For example, the superseded design codes permitted the use of half the level of shear reinforcement allowable by current codes. In addition, design loads were much less than they are today. Based on current design codes, a reassessment has revealed many of these bridges to be deficient in shear and they require strengthening or replacement. To avoid the significant costs of replacement, emphasis has been placed on strengthening and rehabilitation. However, existing methods suffer from many problems.

Concrete bridges worldwide face a variety of problems. In Japan, numerous concrete bridges suffered extensive damage during the 1995 Kobe Earthquake or Hyogoken-Nanbu Earthquake. Subsequent investigation established that many of the bridges are deficient against seismic loading and they require immediate repair or retrofitting to reduce their vulnerability to future earthquakes. In Canada and the United States of America, many concrete highway bridges suffer from chloride-induced deterioration, which is the result of using de-icing salts during severe winter conditions. Bridge authorities worldwide have the common problem of an ageing bridge infrastructure subjected to increasing traffic volumes and loads with limited financial resources available for bridge rehabilitation. Other problems include poor design, errors during construction, change in design requirements, deterioration due to corrosive environment and damage due to accidents.

A range of methods exist for the strengthening of structurally deficient bridges such as section enlargement, external post-tensioning, deck widening, increasing deck overlay, use of additional props or steel plate bonding. Steel plate bonding is widely used in many strengthening applications including bridge retrofitting because such bonding is relatively simple, effective and efficient with minimum site disruption. The method involves the bonding of steel plates to the

surfaces of structurally deficient members by means of strong structural adhesives. Composite action between the steel and concrete element provided by the adhesive results in an increase in the overall structural stiffness and load carrying capacity. Changes in the dimensions of the retrofitted structures are only of the order of a few millimetres.

As with other strengthening techniques, however, the system has several negative aspects. In corrosive environments, deterioration of the bond between the plate and concrete substrate caused by the corrosion of steel renders the force transfer mechanism between the two components less effective. The long-term performance of the system then becomes questionable particularly in outdoor applications. Measures such as priming the steel surface impede the corrosion process but do not completely stop it. Macdonald and Calder (1982) reported that "slight signs" of corrosion were visible on unprimed as well as primed bonded steel plates after 2 years of natural exposure. Other shortcomings include high self-weight resulting in the need to use clamping devices and lifting equipment during operation and a restriction on the maximum length of the steel plate. For the latter, fabrication and handling issues arise when greater plate lengths are required which necessitates the use of joints, as otherwise the high welding temperatures would destroy the adhesive bond. These drawbacks have led to the search for an alternative material and the result is fibre-reinforced polymers (FRP) or composites.

Fibre-reinforced polymers (FRP) consist of a polymer matrix embedded with microscopic filaments, either short or continuous, unidirectional or multidirectional, woven or non-woven. The composite acquires its basic strength and other fundamental properties such as stiffness, corrosion resistance and thermal conductivity from the embedded fibres. The surrounding matrix binds the reinforcing fibres together acting as a load transfer medium between them. It also protects the fibres against mechanical and environmental damage.

Compared to conventional construction materials, FRP possess a superior combination of properties with respect to weight, strength, stiffness, durability, fatigue, impact and corrosion resistance. Its ease of handling and application, and its light weight eliminates the need for mechanical lifting or anchoring devices, hence

minimising disruption to services for the duration of the strengthening and maintenance process. Its use is particularly appealing in confined areas. The plate bonding operations are thus made even simpler, more cost effective and shorter in duration, and thus substantial savings can be realised when all of the project costs are considered. In the past, the use of FRP has been restricted to applications where the high cost is justified by strict requirements for high performance for example in the aviation and aerospace and automotive industries. Technological advancements in manufacturing and processing methods have only recently made it economically viable for FRP to be used in the construction industry.

Fibres commonly used in the manufacture of FRP materials are carbon, glass or aramid. Fibres used in limited quantities are boron, silicon carbide and aluminium oxide fibres. Meier (1997) carried out an assessment of the most suitable fibre composite materials for the post strengthening of structures. He evaluated 3 fibre types, carbon, glass and aramid, and concluded that carbon fibre-reinforced polymers (CFRP) are the best suited to the post strengthening of structures. Based on a set of criteria, carbon performed better than glass and aramid based FRP in almost every category. Hence, the focus of the investigation presented herein is on strengthening using CFRP.

Commercially available carbon fibres are manufactured using pitch or polyacrylonitrile (PAN) as the precursor material. The processes used on the two precursors are different although their essential features are similar. Fundamentally, the processes involve a stabilising phase in which the precursors are exposed to oxidised atmosphere to prevent melting or fusion of the fibre, a carbonising phase to remove non-carbon elements followed by a graphitizing phase to improve the mechanical properties of the final carbon fibre. Fibres to be used in composites undergo initial surface treatment to improve the bond between the fibres and the matrix. Thermoset resins, particularly epoxies, are commonly used as polymer matrices for carbon fibres. Pultrusion, hand lay-up and resin transfer moulding (RTM) are common methods used for fabricating CFRP.

There are numerous FRP strengthening systems available commercially. The ACI Committee 440 (1999) listed seven general categories of material forms suitable

for concrete strengthening. The cured laminate system is used in the present investigation. It comes in many forms, pre-manufactured to size and typically in plates or strips. The laminates are bonded to the concrete surface with an adhesive specified by the manufacturer. In the present research, pre-fabricated L-shaped CFRP plates developed by Sika AG (Switzerland) Pty. Ltd. are used. Prior testing carried out by EMPA, the Swiss Federal Laboratories for Materials Testing and Research, using L-shaped CFRP plates, has shown the strengthening system to be effective. It does not appear to suffer from peeling or end anchorage problems common in other systems.

Most previous studies of strengthening using advanced FRP materials have investigated flexure. Flexural strengthening is achieved by bonding the composite materials to the tension flange of the member in question. Numerous studies ranging from numerical models to experiments have been carried out in this area including studies by Saadatmanesh and Ehsani (1989), Triantafillou and Plevris (1992), Chajes et al. (1994), Ziraba et al. (1994), Arduini et al. (1996), Spadea et al. (1998). The technique has been shown to be effective with experimental results in satisfactory agreement with theoretical predictions.

There has not been as much research done in the field of shear strengthening of reinforced concrete beams. This is partly because the mechanisms of shear are not well understood and, unlike those of flexure, are complex. Nevertheless, significant improvements have been made in understanding shear mechanisms in beams. To strengthen concrete beams in shear, the advanced FRP materials are bonded to the web of the beams. The shear loads are distributed between the internal shear reinforcement (stirrups) and the externally bonded FRP resulting in an increase in shear capacity. Much of the research in shear strengthening has been done using FRP sheets or fabrics. Little work has been done in investigating the behaviour of reinforced concrete beams strengthened using pre-manufactured cured laminate strips or plates. Investigation carried out on shear strengthening using L-shaped cured laminate plates has only been reported by EMPA (1998a), EMPA (1998b) and Czaderski (2002). The experimental programs reported in the studies did not focus on the effects of varying CFRP spacing or the difference in the deformation mechanisms compared to the state of the beam without strengthening.

The aim of this research is, therefore, to study the short-term behaviour of shear deficient reinforced concrete T-beams strengthened using external bonding of prefabricated L-shaped CFRP plates, in particular the failure modes of the strengthening system. Four T-beams were fabricated and tested in the experimental investigation. To gain a better understanding of the bond behaviour between the CFRP and concrete and the mechanisms that occur in the T-beams under loading, thirteen CFRP-concrete bond specimens were fabricated and tested. Advanced photogrammetry measurement techniques were used to study the behaviour of the T-beams with and without shear strengthening. Numerical modelling of the T-beams and bond specimens using the non-linear finite element method was carried out and compared against the experimental and photogrammetry results. The results of existing shear strength prediction models compared to the experimental results of the current study were also investigated.

The work presented herein is organised into different chapters. Previous studies relevant to the shear strengthening of reinforced concrete beams are summarised in Chapter 2. Chapter 3 describes the background, experimental program and results of the CFRP-concrete bond specimens. The development, analyses and results of the finite element models of the bond specimens are presented in Chapter 4. Chapter 5 outlines the experimental program of the T-beams and the results are presented and interpreted in Chapter 6. The advanced photogrammetry measurement techniques used in the experimental program of the T-beams and its results are reported in Chapter 7. The methodology and results of the finite element analyses of the T-beams are reported in Chapter 8. Predictions of strengths of the beams using existing models compared to the experimental results are reported in Chapter 9. Concluding remarks and recommendations for further studies are presented in the chapter Conclusions.

CHAPTER 2 - LITERATURE REVIEW

2.1 Introduction

The existing shear capacity of reinforced concrete beams can be enhanced by bonding FRP materials to the web, typically with the dominant fibre direction perpendicular to the length of the member. There are a variety of FRP systems and arrangements reported in the literature. The type of arrangement used strongly influences the contribution of the externally bonded FRP to the shear load capacity. A review of the different arrangements and their performance is presented, followed by common factors that influence the effectiveness of the various layouts. The remainder of the chapter focuses on existing prediction models of the external FRP's contribution to the beam's shear capacity. A review of past studies on FRP-concrete bond is presented separately in Chapter 3.

Authors have used different terminologies to describe the various layouts. For consistency, the terms used in this thesis are based on those used in the study carried out by Al-Sulaimani et al. (1994), which provide accurate descriptions of the schemes used. In the literature, the terms plates, sheets and strips have been used loosely to describe the various forms of FRP. In the current study, plates are taken to mean pre-cured FRP systems typically with two or more layers of fibres. The pre-cured FRP are bonded to the concrete surface with an adhesive specified by the manufacturer. Sheets are taken to mean FRP fashioned using either the dry or wet lay-up technique. Single or multiple layers of dry or uncured fabric or sheet are bonded to the concrete surface to form the FRP. Strips refer to narrow pieces of either the plates or sheets having a length to width ratio of more than two. The strips are placed at regular intervals along the beam's length. Plates are typically in strip form whereas sheets can be cut to obtain individual strips.

2.2 Review of shear strengthening schemes

2.2.1 Side bonded sheets/plates

In side bonded sheets or plates, the FRP is bonded only to the web of the reinforced concrete member. The two main arrangements are the side strips and the

wings. In the side strip layout, strips of cured laminate plates or sheets pre-cut to a fixed width are placed along regions of the spans that are critical in shear. Typically, the strips are bonded so that the dominant fibre direction is perpendicular to the longitudinal axis of the beam. They may be spaced at equal distances throughout the shear span or at decreasing spacing towards the support. Figure 2.1 illustrates the use of side strips on a rectangular beam and T-beam. Unidirectional FRP plates or sheets are normally used. Since small loads are transferred in the width direction due to the relatively small strip width, using bi-directional plates or strips is inefficient. The main advantage of this arrangement lies in the efficient use of the FRP material, which is quite expensive. In most cases, it represents the bulk of the total strengthening cost.

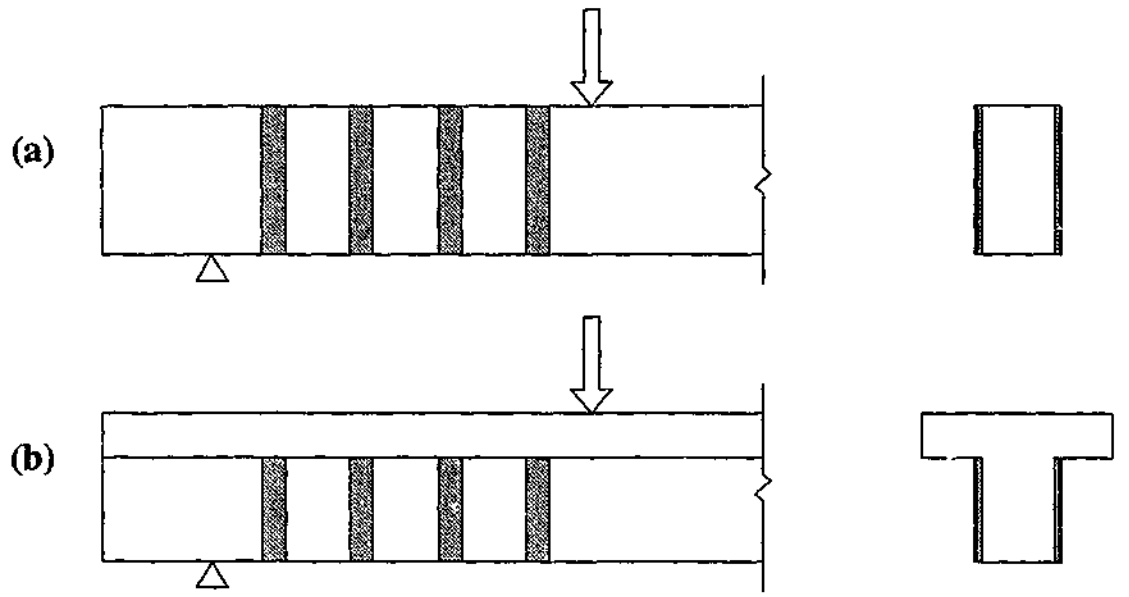

Figure 2.1 - Vertical side strips in (a) rectangular beam and (b) T-beam

The effectiveness of the arrangement depends greatly on the spacing of the FRP strips along the shear span regions and the amount of FRP used. Similar to internal steel shear reinforcement or stirrups, a maximum allowable spacing requirement must be satisfied. For reinforced concrete beams, this spacing equates to the minimum of 0.75D or 500 mm, based on the assumption that the concrete compression strut forms conservatively at 45° to the longitudinal axis (Standards Australia International, SAI (2001)). This requirement ensures that any diagonal shear crack will be intercepted by at least one stirrup, hence on the same basis, this requirement should also apply to externally bonded FRP side strips. Studies by Al-Sulaimani et al. (1994), Sharif et al. (1995), Sato et al. (1996), Triantafillou (1998),

Chaallal et al. (1998a) and Kamiharako et al. (1997) reported improvements in shear capacity over that of non-strengthened control beams.

A variation of the above arrangement is to bond the side strip at an angle as shown in Figure 2.2. Shear cracks typically form at an inclination of 30° to 45° from the horizontal axis, therefore by placing side strips perpendicular to the shear crack, an increase in the shear capacity can be expected since the FRP is loaded along the fibre direction. This increase may be possible only if other failure modes do not occur beforehand. With the inclination angle set between 45° to 60° and the maximum strip spacing requirement satisfied, it is likely that a shear crack will be intercepted by at least two strips. Studies carried out by Chaallal et al. (1998a) and Triantafillou (1998) on rectangular beams revealed that using side strips results in noticeable enhancements in shear capacity compared to that of non-strengthened beams. When the shear capacity of side strips positioned at an angle is compared to that of side strips positioned vertically, Chaallal et al. (1998a) reported increases in the shear strength of beams with diagonal side strips compared to beams with vertical side strips. The study reported increase in the stiffness of the strengthened beams compared to the control beams due to the reduction of shear cracking. Two failure modes were reported in the strengthened beams with vertical side strips. One beam failed due to shear cracking, which caused delamination of the strips. Another identical beam and all the beams with diagonal side strips failed due to excessive longitudinal and transverse cracking that had peculiarly developed at the bottom of the beams along the reinforcing steel bars. These beams failed at a higher load compared to the beam that failed due to shear cracking. It was concluded that the diagonal side strips outperformed vertical side strips in terms of crack propagation, stiffness and shear strength but may produce premature failure as a result of concrete peel-off at strip curtailment in tension stressed zones. In Triantafillou's study, however, the shear strengths of beams with diagonal and vertical side strips were similar, which implied little or no benefit in using the diagonal as compared to the vertical side strips. All the strengthened beams failed by debonding through the concrete near the concrete-FRP interface, which had offset the benefit of diagonal side strips. Chaallal et al. (1998a) reported the use of cured unidirectional CFRP laminate strips whereas Triantafillou (1998) reported the use of the lay-up method

with CFRP sheets. In the former case, the amount of FRP used was significantly higher, which may have contributed to the difference in the observed failures between the two studies. There seems to be an added advantage in using inclined side strips but further research is required to confirm this. Since debonding was reported in both studies, it is most likely to be the dominant failure mode.

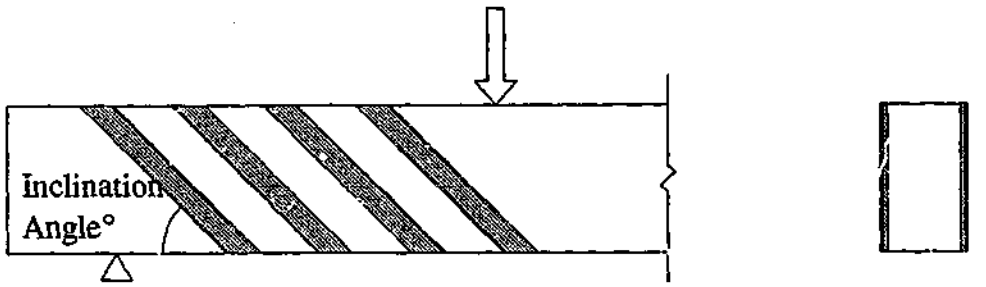

Figure 2.2 - Inclined side strips

The second arrangement for side bonded FRP is the layout with wings. Unlike the side strip layout, the entire shear span is covered using a single FRP material as shown in Figure 2.3. Typically, unidirectional or bi-directional FRP sheets are used in the wings layout, as the cost of cured laminate plates is prohibitively high. Unidirectional sheets may be positioned such that the fibre direction is perpendicular or inclined at 45° to the length of the beam. In the case of bi-directional sheets, the positioning may be based on the dominant fibre direction. Unless flexural strengthening is required, unidirectional sheets should be used to minimise material costs. For flexural strengthening, bi-directional sheets should be positioned such that the fibre directions are parallel and perpendicular to the length of the beam. This practice is not recommended, as it is more efficient to bond unidirectional plates or sheets to the bottom of the beam across the entire span.

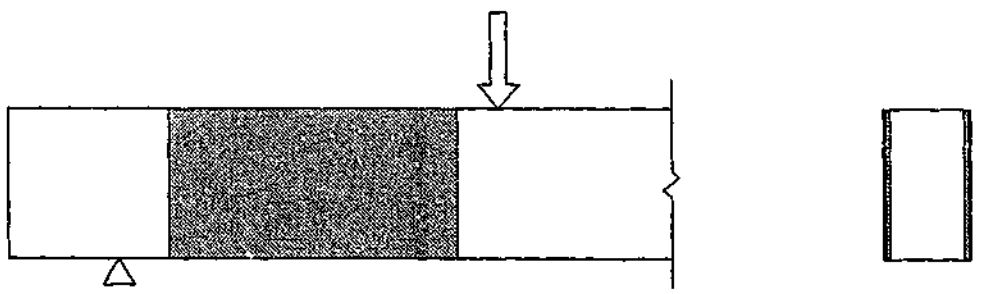

Figure 2.3 - Wings

The benefit of the wings arrangement lies in the FRP material intercepting any diagonal shear crack along most of its length. With a significant increase in the bonded area of FRP, beams strengthened using the wings arrangement can be expected to have higher ultimate load capacities compared to beams strengthened using the side strips layout. The study carried out by Al-Sulaimani et al. (1994) on rectangular concrete beams, however, has shown only slight increase in shear capacity of beams strengthened with the wings arrangement compared to beams strengthened using the side strip. The results indicated shear failure due to debonding. Fibreglass plates were used to strengthen beams that had been preloaded to a predetermined level. Sato et al. (1996) conducted a similar study but used unidirectional carbon fibre sheet (CFS) as the strengthening material. As the beams' steel reinforcement configurations were different, it is difficult to establish from the study the additional load capacity gained by using the wings arrangement compared to the side strip arrangement.

The failure modes of beams strengthened using either the side strip or wings arrangement depend on the beam configuration and FRP material used. Beams sufficiently shear strengthened may exhibit flexural failure through yielding of the main steel reinforcement or concrete crushing, but when shear failure occur, FRP material typically peels away from the concrete substrate. The study by Sato et al. (1996) provided an insight into the peeling process of vertically placed side strips on rectangular beams. Through the use of strain gauges, results indicated that debonding of the unidirectional strips initiated from the portion where the strips intercept the shear crack. The formation of the shear crack creates a localised region of high shear stress that easily exceeds the interface shear strength, hence peeling of CFRP. Debonding may also have occurred as a result of surface cracking offsets. As the shear load was gradually increased, areas of roughly similar sizes directly above and below the shear crack began to debond. The bonded area progressively decreased as debonding of CFRP proceeded outwards away from the shear crack location towards both ends of the strip. The strip ceased to carry load when debonding of CFRP had occurred all the way to either end of the strip. As no load was transferred to the CFRP, further debonding stopped as well. The study revealed that strips intercepting the shear crack close to the end have small areas of debonding. Those intercepting the shear crack close to mid-height show greater area of debonding. In the former case,

the distance between the strip end and location of the shear crack is short hence the smaller area of debonding. None of the strips was reported to have debonded across the full height. In the study, the debonding failure of the wings configuration has not been described, as the beam failed in flexure. A similar but improved configuration to the wings layout was used whereby the bonded FRP was extended to the soffit of the beam. However, the failure mode reported was similar to the side strip arrangements. Studies by many investigators have revealed that peeling of the FRP is indeed the dominant form of failure for both the side strips and wings configuration. This combined with the fact that the shear capacity of wings is only slightly higher than the side strips arrangement indicate that the cause of failure may be similar to that of the side strips described above.

Due to lack of end anchorage, both wings and side strips strengthened beams typically fail by peeling or debonding of the FRP material from the concrete substrate. Hence, from the viewpoint of material efficiency, the wing arrangement is unfavourable and not recommended. Uji (1992) carried out an investigation into the strength of rectangular beams retrofitted in this manner. He reported shear failure as a result of debonding of the carbon fibre sheet in beams with no internal shear reinforcement. Sharif et al. (1995) carried out a similar study with steel plates instead of FRP. A similar trend was reported where the failure mode was by debonding of the plates with some concrete attached. Uji (1992) also carried out an investigation into the effect on the shear strength of a beam with the fibre direction of the external sheet inclined at 45° to the beam's longitudinal axis or right angles to the diagonal crack. The rectangular beam with the carbon fibre sheet direction bonded diagonally failed at a higher shear load than beams with the sheet fibre direction bonded vertically. Failure in the beam was still through debonding of the carbon fibre sheet.

Figure 2.4 illustrates a hypothetical shear crack on an example T-beam with vertical side strips. There is a length of FRP where the bond becomes fully developed. This length is defined as the effective bond length. Beyond this length there is no further transfer of load to the FRP. The effective bond length is dependent on the concrete strength, modulus of elasticity, geometry and thickness of the composite (Chajes et al. (1996), Chen and Teng (2001)). In certain cases, by providing the effective bond length, it is possible to fracture the FRP. Referring to the

example beam, the first FRP strip from the support does not have sufficient length to develop full bond as the shear crack has crossed the strip close to the bottom of the beam. This can result in the bottom portion of the FRP strip debonding or peeling prematurely causing the entire strip to be ineffective. The situation is similar for the second FRP strip from the support. The shear crack has crossed the strip close to the web-flange junction and this can result in the upper portion of the FRP strip debonding prematurely also. Due to the flange, the bonded area of the FRP is even smaller on the T-beam than on a rectangular beam of the same overall depth. The third FRP strip from the support is ineffective also as the shear crack has propagated along the web-flange junction. By using the wings arrangement, the problem would still remain, particularly at locations where the shear crack is near the web-flange junction or the bottom of the beam. In both the side strips and wings arrangement, the FRP cannot intercept the shear crack that forms in the flange.

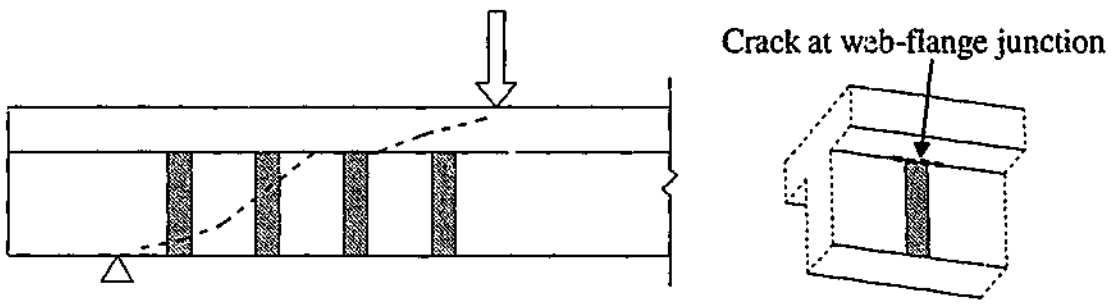

Figure 2.4 - Hypothetical shear crack in T-beam with FRP side strips

Both the side strips and wings arrangements lack end anchorage. End anchorage can eliminate the premature peeling of the FRP near the ends. Therefore, the side strips and wings arrangements were not investigated in the present study. The FRP materials are not utilised efficiently.

2.2.2 Sheets/plates wrapping

The premature peeling failure of side bonded FRP may be eliminated by providing some form of anchorage at the FRP ends. An effective and simple way of providing this anchorage is by extending and bonding the FRP material to the underside or soffit of the beam. Significant increase in shear carrying capacity can be achieved, in some cases promoting rupture in the FRP or flexural failure through yielding of the main steel reinforcement. The wrapping of the FRP provides a

confining effect delaying the peeling process. As with the side bonded FRP, there are several arrangements but most are extensions of the side bonded FRP layouts. The literature review has shown that there are three main arrangements, which are the U and L-strips, U-jackets and full wrapping.

The U & L strips layout is an improvement of the side strips arrangement outlined in the previous section. In addition to being bonded to the sides, the FRP extends past the web and is bonded to the soffit across the full width. Similar to the side strips arrangement, flexible FRP sheets as well as cured laminate plates may be used. For the latter, innovative moulding techniques are used to manufacture U or L-shaped FRP plates for bonding to the sides and bottom of the beam as illustrated in Figure 2.5.

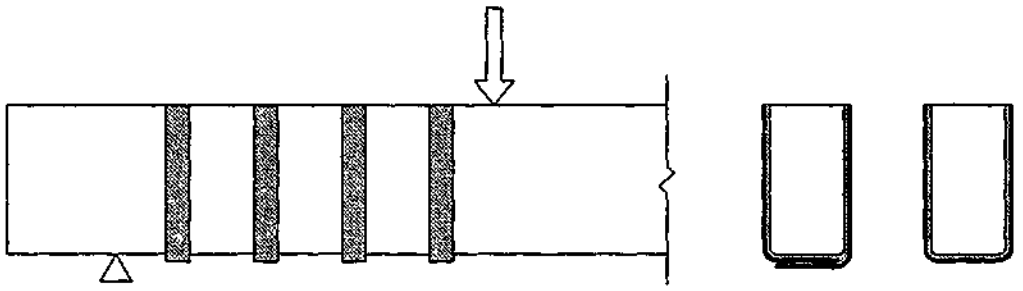

Figure 2.5 - U and L shaped FRP strips

Studies carried out by Sharif et al. (1995), Sato et al. (1996) and Taerwe et al. (1997) reported a significant increase in the shear capacity of beams strengthened in this manner compared to beams without strengthening. When comparing the shear capacity of U strips and side strips, Sharif et al. (1995) reported slightly higher shear strength in beams with U-strips. Sato et al. (1996) reported a significant increase in the shear strength of beams with U-strips compared to beams with side strips. Although the materials and beam configuration used were different, the studies demonstrate the importance and benefit of providing effective anchorage. The failure mode reported is similar to the side strips. Sharif et al. (1995) observed the debonding of steel U-strips from the sides of rectangular beams partially exposing the internal reinforcement. Sato et al. (1996) reported peeling of CFRP sheet from the web in the vicinity of where the diagonal crack intercepted the strips. Taerwe et al. (1997) reported fracture of CFRP sheet resulting from the peeling failure of crucial

strips. The debonding of the strips closest to the applied load led to an instantaneous increase in the force carried by strips further away. The result was the immediate and successive fracture of these strips. The fracture occurred at the position where the strips intercepted the crack. In this case, peeling failure had initiated fracturing of the CFRP sheet. In the study by Sato et al. (1996), the debonding process was similar to that described for the side strip layout. However, the anchorage provided at the bottom of the beam allowed a greater area of CFRP to be debonded. Strips located at where the shear crack had formed close to the bottom of the beam debonded across the full height. Even though the portion of the strip beneath the shear crack had completed debonded, the CFRP bonded to the soffit of the beam provided the anchorage necessary for the debonding to continue to the top of the beam. For strips intercepting the shear crack close to the top of the beam, the debonded area is smaller. As no anchorage exists at the top end, debonding ceases once the top portion has completely peeled off.

Figure 2.5 shows the strips placed perpendicular to the beam's length. Similar to the side strip layout, the U-strips may be inclined at an angle as well. The material system that can be used, however, would be restricted to FRP sheet or fabric only. It would be quite complex to fabricate cured laminate plates to fit the angled profile at the bottom of the beam. Studies to gauge the efficiency of diagonally placed U or L-shaped strips against vertically positioned strips are limited. The study by Hutchinson et al. (1997) reported an increase in the shear capacity over vertically placed CFRP strips when inclined strips are used.

Bleibler et al. (1998), Khalifa and Nanni (2000), Deniaud and Cheng (2001) and Czaderski (2002) carried out studies on T-beams shear strengthened using U or L-shape strips. Bleibler et al. (1998) tested three full-scale T-beams with different geometry strengthened using L-shaped cured laminate plates shaped by a special pressing method. In addition to being strengthened in shear, one of the T-beams was strengthened in flexure as well by bonding unidirectional CFRP laminate plate to the soffit. A simple way of anchoring the L-shape strip at the compression zone is employed. The T-beams strengthened in shear only failed in flexure by yielding of the reinforcing steel in mid-span. The study revealed how effective and simple the L-shape plate-strengthening system is with the use of this unique anchoring system. The

beam that failed by shear, which had also been strengthened in flexure, occurred due to the separation of the CFRP overlap at the soffit. At roughly the same time as the present investigation, Czaderski (2002) carried out a similar study using the same strengthening system and anchoring technique. The researcher reported a similar failure mode in the beam that failed in shear. Both studies investigated the shear strength of T-beams with constant L-strip spacing. The strengthening programme of the present study utilises this innovative system with the aim of increasing the limited data in literature regarding shear strengthening, in particular the effects of FRP spacing. Khalifa and Nanni (2000) reported the use of another anchoring system that was innovative and unique. Details of the anchorage systems used in both studies are reported in Section 2.3.2. The researchers investigated the shear strength of T-beams with U-strips, side strips and U-jackets with and without anchorage.

The U-jacket retains a similar layout to the wing configuration (Figure 2.6). The only modification is that of the FRP being bonded to the soffit as well, providing anchorage at the beam soffit lacking in the previous configuration (Figure 2.3). Unidirectional or bi-directional fabrics are normally used in this scheme. The high cost of material and manufacturing would exclude the use of cured laminate plates. The U-jacket may be used to cover the entire span of the beam. This approach is considered to be conservative with no attempt to optimise the amount of material used. Studies carried out using this scheme are numerous. Dolan et al. (1992), Chajes et al. (1995), Izumo et al. (1997) and Shahawy and Beitelman (1999) utilised this scheme in strengthening T-beams where the FRP reinforcement is bonded up to the web-flange junction. Norris et al. (1997) employed this scheme in the strengthening of rectangular beams with FRP bonded across the full depth. The use of FRP covering the entire span opens up the possibility of strengthening the beam in flexure as well. Instead of using unidirectional sheets or fabrics, woven composite fabric with fibres orientated at 0 and 90° can be used. The fabric is placed such that the weave directions are orientated along and perpendicular to the beam's longitudinal axis. Chajes et al. (1995), Izumo et al. (1997) and Shahawy and Beitelman (1999) have employed this scheme in their research work. If the strengthening required is that of shear only, the arrangement where the FRP is applied to just the shear span should be utilised to minimise material cost. There seems to be no apparent benefit to be gained in applying the FRP across the full span.

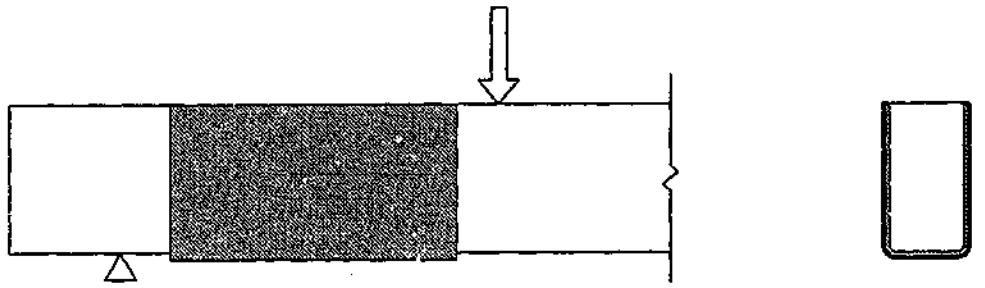

Figure 2.6 - U jackets covering shear span only

Research carried out by Al-Sulaimani et al. (1994) has demonstrated the effectiveness of the U-jacket shear strengthening arrangement. Rectangular beams strengthened in this manner had failed in flexure by yielding of the steel reinforcement as opposed to the premature peeling failure observed in beams strengthened using the wings configuration. Increase in load capacity of about 19% over the wing strengthened beams and 45% over the non-strengthened control beams were reported. Taerwe et al. (1997) carried out a similar investigation using the U-strip and U-jacket repair category. The U-jacket strengthened beam failed in flexure despite a shear crack forming underneath the jacket. Sharif et al. (1995) reported a flexural failure mode as well. In all studies, the enhanced shear capacity exceeded the flexural capacity. In the study by Sato et al. (1996), the beam strengthened using the U-jacket arrangement failed by peeling of the CFRP sheet. The shear capacity reported, however, was approximately the same as the beam with U-strip with the peeling mode being similar as well. No explanation was given. One possible reason was that the FRP strips were not anchored at the compression zone and the interface bond strength that had developed was still insufficient to resist premature peeling of the FRP sheet. Despite having larger area of FRP bonded to the web, premature peeling rendered the FRP sheet ineffective in carrying any additional loads over the U-strip. In the current study, the bond strength is defined as the maximum force that can by carried by the FRP-concrete joint. Sato et al. (1997) carried out a study of T-beams strengthened using U-jackets. The reported failure mode was also the peeling of the carbon fibre sheet. The peeling failure was due to the inadequate bond length provided, as the bonded area is only the depth of the beam web.

As with the side strip and wing arrangements, the FRP may be orientated with the principal fibre direction at 90° or inclined at an angle to the beams

longitudinal axis. For the latter, studies have been carried out where this angle was set at 45° or 135°. Chajes et al. (1995) investigated T-beams strengthened along the entire span with woven graphite fabrics having equal fibre distribution at both 0 and 90°. The study reported that beams strengthened with the weave directions orientated at 45/135° to the beams' longitudinal axis failed at noticeably higher shear loads than beams strengthened with the weave directions orientated at 0 and 90°. Norris et al. (1997) carried out a similar investigation but on rectangular beams. A similar trend was reported.

In the full wrap layout, the FRP material is wrapped around and bonded to all sides of the beam as shown in Figure 2.7. This strengthening arrangement provides the most effective form of anchorage apart from mechanical ones when compared to the previous FRP layouts. The FRP material behaves as a hoop to continue to carry the shear force even after it has debonded from the concrete. The FRP may be bonded in the form of individual strips or jackets covering only the shear span or entire beam span.

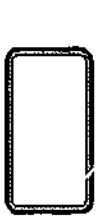

Figure 2.7 - Full wrap

In the study by Uji (1992), comparisons of rectangular beams strengthened with the wing and full wrap arrangement were carried out. The fully wrapped beam failed at a higher shear load compared to the beams with wings. Rupture of the carbon fibre sheet near the corner resulted in shear failure of the fully wrapped beam. Miyauchi et al. (1997) completed a similar investigation but full wrap strips were used to strengthen the rectangular beams. Three different failure modes were reported across the range of beams - flexural compression, flexural tension and diagonal tension. For the strengthened beams that failed in shear, the failure occurred immediately after the carbon fibre sheet ruptured at the intersection with diagonal cracks. Umezu et al. (1997) carried out strengthening of rectangular beams using aramid and carbon fibre sheet. They reported shear failure followed by sheet rupture

in several of the beams. In the studies above, full wrapping of the FRP eliminated the peeling failure inherent in the other arrangements. The sudden formation of a diagonal crack causes an abrupt load transfer to a localised region of the FRP intersecting the diagonal crack. This combined with the confining effect and adequate anchorage available allows fracturing or tearing of the FRP along this highly stressed region. In reality, however, the full wrap arrangement would only have limited area of application in strengthening structures. The complete wrapping of the FRP around a structural member such as a beam is hardly a feasible or practical approach. Most beams are integrated or cast with concrete slabs or wall partitions. Wrapping of the FRP would mean the removal of portions of the obstacle. Hence, the strengthening arrangement can only be applied to open structural members such as bridge piers or columns. In addition, the bend in the FRP at the bottom edge of the beam represents a region of high stress concentration. In cured laminate L-shaped plates, the bend is manufactured to a specific radial profile to minimise this stress concentration. Hence the bottom edges of the beam must be rounded to conform to the radius of the bend. Regardless of the material system used, cured laminate plates or sheets, rounding of the edges is necessary to prevent premature rupture of the FRP.

Depending on beam configurations, the U and L-strips and U-jackets can potentially offer significant increase in strength compared to the side strips and wings arrangement. The lack of anchorage at the compression zone, however, can still result in premature debonding of the FRP at this end. In T-beams, the presence of the flange reduces the bonded area even further hence less bond length is available to develop the required interface shear resistance.

2.3 Factors influencing effectiveness of applications

2.3.1 Concrete surface preparation

The most crucial part of any strengthening application is the bond between the FRP and the surface to which the FRP is bonded. Proper bond ensures that the force carried by the structural member is transferred effectively to the FRP. Poor bond resulting from unsatisfactory surface preparation can render the strengthening application completely ineffective. The effectiveness of the bond mostly depends on the quality of the surface preparation and the concrete itself (Bizindavyi and Neale

(1999)). The quality of the surface preparation is related to the surface texture, which varies depending on the methods used. The quality of the concrete is related to its strength, composition and general condition.

There are several methods to prepare the concrete surface (Aldinger and Fultz (1989)). The typical methods are wet or dry abrasive blasting, scarifying, or high pressure water jetting. In the present study, the wet or dry abrasive blasting were not considered as it required fairly extensive equipment set up to contain the blast material. Scarifying by sanding and grinding were also not considered as it was time consuming and laborious and the finished surface had a smooth texture. A portable high-pressure water jet machine was utilised as it was effective and economical. The water jet effectively removed a thin concrete layer to expose the aggregates without causing much damage to the aggregates. The resulting concrete surface had the desired rough texture, which enhanced the mechanical bond between the FRP and concrete.

2.3.2 Anchorage

The effectiveness of the FRP end anchorage varies depending on the strengthening schemes employed. It has been reported that side bonded FRP typically failed by debonding whereas U or L-wrap failing by FRP fracture has been reported. For U or L-wrap strengthened beams that have failed by debonding, it is the result of anchorage provided only at one end of the FRP. The absence of anchorage at the top end allows local debonding to propagate towards this end. The level of anchorage and bond strength achievable also depends on the geometry of the beam, particularly the depth available for bonding the FRP material. There exists a critical length allowing the development of sufficient bond strength to either resist or delay debonding of the FRP reinforcement. For T-beams, the bond length available is less than rectangular beams due to the presence of the flange. Shear cracks developing near the compression zone will mean that the FRP have minimal bonded length near the web-flange junction and hence are susceptible to debonding here. By providing anchorage at both ends, even if the FRP has debonded along most of its length, it can still contribute to carrying shear load by acting as tension ties. There are several options available to improve the anchorage for the various strengthening schemes.

The following describes the different types used by various investigators in attempts to delay the premature peeling failure of FRP retrofitted beams.

Steel plates or bolts are typically used as mechanical anchorage to delay debonding of FRP ends. The steel plates are placed at the FRP end, held in place by bolting the plate into the concrete. Figure 2.8 shows the different variation of mechanical anchorage used by Aridome et al. (1998) in their investigation into the shear strengthening of T-beams. Steel plate strip and angled profiles were used and fixed to the beam by means of anchor bolts. Strengthened beams without any anchorage in the compression zone were not tested but the researchers reported yielding of the main flexural reinforcement in all the strengthened beams with steel anchorages. Sato et al. (1997) carried out a similar study using U-wrap carbon fibre sheet in both T- and rectangular beams. They studied the effectiveness of anchoring the ends of the carbon fibre sheets with steel plates and bolts. The strengthened beam with anchorage provided failed at a higher load compared to the beam with no anchorage. The presence of the anchorage has delayed the premature debonding failure of the sheet.

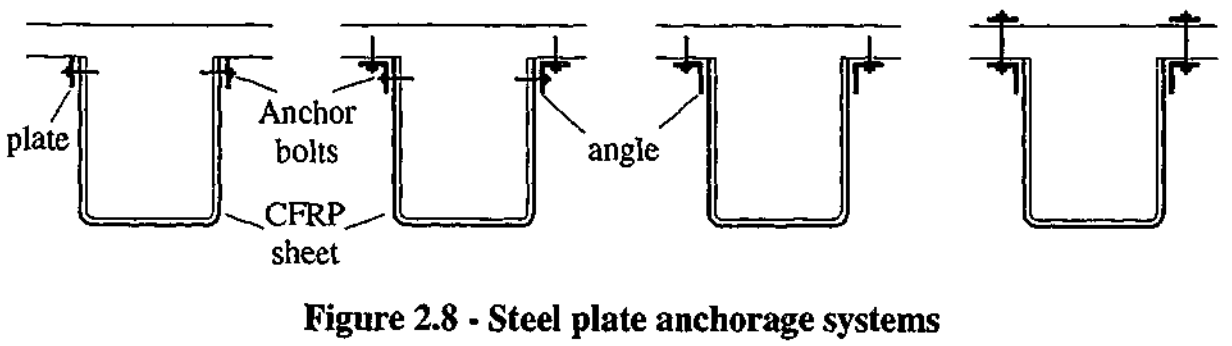

Figure 2.8 - Steel plate anchorage systems

Caution however should be exercised when using mechanical anchors made of steel. Stress concentration exists at locations where bolts are used. Corrosion of the steel may be of concern due to the galvanic coupling with the carbon fibre sheet. The performance of the anchorage remains questionable in the long term.

Khalifa et al. (1999) investigated the shear strengthening of full-scale T-beams using a novel anchoring system. Developed at the University of Missouri-Rolla, the anchorage system utilises only FRP materials, eliminating issues with corrosion. The patented system called the U-anchor involved embedding a bent

portion of the FRP end into grooves made at the flange (Figure 2.9), which were secured in place by a glass FRP rod along the entire length of the strengthened portion. Failure in the strengthened T-beam with no end anchorage was initiated by debonding of CFRP sheets over the main shear crack after which shear compression failure followed. The strengthened beam with the U-anchor failed at a significantly higher shear load with the failure mode changed to that of flexure. The researchers reported that no debonding was observed in the beam at ultimate capacity. The anchorage at the CFRP ends allowed the development of sufficient bond strength to resist the premature debonding of the sheet. The cutting of the groove will require specialised machinery that can potentially increase installation cost.

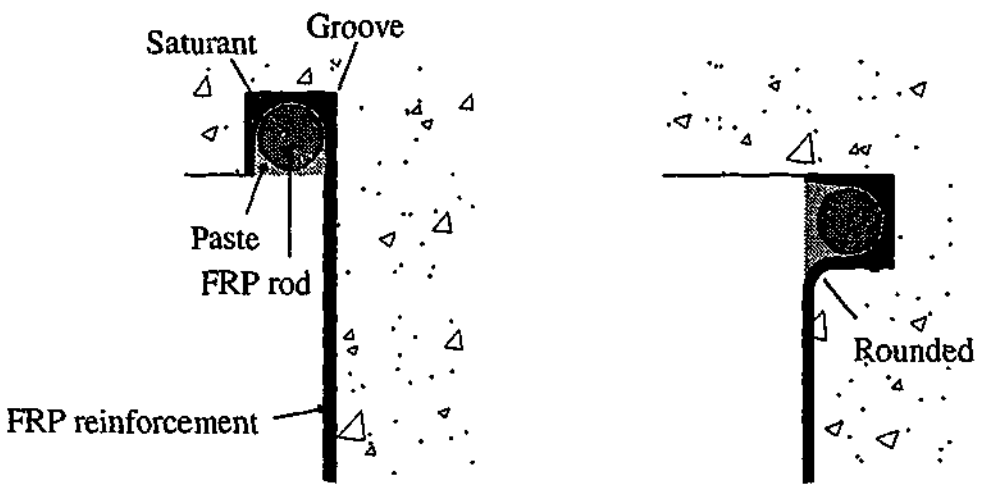

Figure 2.9 - U-anchor systems

A more simple and cost-effective way of anchoring the FRP at the web-flange junction is to bond the FRP to the underside of the flange as illustrated in Figure 2.10. This approach, however, is less effective compared to the two anchorage types reported earlier. When the FRP bonded on the web has debonded, the forces now act out of plane to the FRP bonded on the flange. Typically, the force required to debond the FRP is significantly smaller in the out-of-plane direction than in the in-plane direction. Deniaud and Cheng (2001) investigated the shear behaviour of full-scale T-beams with U-strips and jacket anchored in the manner. All the beams failed in shear with the failure mode of the strengthened beams characterised by the debonding of the FRP.

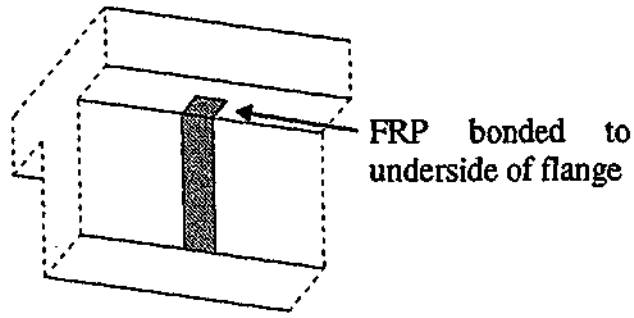

Figure 2.10 - FRP bonded to the underside of flange

In any strengthening applications, providing bond lengths less than the effective bond length means that the full bond development of the FRP system will not be achieved. As a result, the FRP may debond prematurely. In T-beam bridges, this length is often lacking as the concrete deck is normally integrated with the beam. Sika AG, a materials firm in Zurich, Switzerland in collaboration with EMPA, the Swiss Federal Laboratories for Materials Testing and Research developed an innovative way of increasing the bond length as well as providing the required end anchorage in T-beams. The additional bond length and required end anchorage would be gained by coring away part of the beam's flange and bonding the FRP reinforcement in its place. The core holes are filled with epoxy anchoring the FRP in place. The FRP are anchored at the bottom as well using cured L-shaped laminate plates. Details of this anchorage scheme are illustrated in Figure 2.11. The effectiveness of this scheme has been reported by Bleibler et al. (1998) referred from EMPA (1998a). EMPA (1998a) and EMPA (1998b) reported the testing to failure of three T-beams, two of which failed in flexure by yielding of the main flexural reinforcement and one by shear failure. Two possible reasons were cited for the beam that failed in shear, which had also been strengthened in flexure. The first reason was that the L-shaped CFRP shear strips had separated at the overlap in the soffit of the beam. The second reason was the anchorage failure of the internal flexural reinforcement. The length of the flexural reinforcement into the concrete overhang was believed to be insufficient.

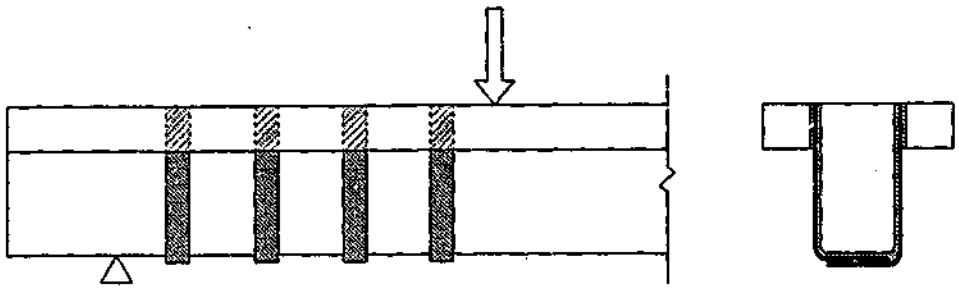

Figure 2.11 - Details of flange anchorage

Apart from the opening of the CFRP L-shaped plate at the overlap, it is also possible for the L-shaped CFRP shear strips to pull out from the flange slot. Pull out tests reported by EMPA (1998a) have revealed that a 20cm embedded length is sufficient to develop the full tensile strength of the CFRP. With 10cm anchorage length, CFRP can be pulled out with the failure load at 60-65% of the tensile capacity of the CFRP. This failure load level is still quite high and the probability of exceeding it is small under field conditions. The pull out tests, however, do not represent the true loading condition in the T-beams. In the flange, the CFRP plates are subjected to high compressive forces in the direction of the beam's length. The forces will vary depending on the loading level and location and it is difficult to determine the effect it has on the strength of the anchorage.

Using an identical strengthening system to that reported by EMPA (1998a) and EMPA (1998b), Czaderski (2002) expanded further on the studies by testing five T-beams with and without internal steel stirrups. The T-beams have a flange and web width of 900 and 150 mm respectively. The overall depth was 500 mm and the flange depth was 120 mm. Three of the beams were strengthened with the CFRP L-shaped plates at the spacing of 300 mm (0.60D). One of the strengthened beams had no internal steel stirrups and another had been preloaded prior to strengthening. Significant increase in the shear strength was achieved in the strengthened beams compared to the beams without strengthening. The strengthened beams with internal steel stirrups were reported to have failed due to yielding of the internal flexural reinforcement. The strengthened beam without internal steel stirrups was reported to have failed due to the opening of the overlap at the underside of the beam. EMPA (1998a) carried out tensile tests on the CFRP L-shaped plates with the 90° bend overlap lengths of 150, 225 and 300 mm. It was shown that the ultimate load reached

in all of the tests was about 70 kN, which was 55% of the tensile capacity of the CFRP plate. The failure reported was the debonding of the entire CFRP. Similar to the pull out tests, however, it does not represent the loading condition in the T-beams. In the shear span, the CFRP plates are subjected to both shear and bending forces.

In the present study, this unique anchorage system with the specially pressed L-shaped laminate plates was used in the experimental programme with the aim of increasing the limited data in literature regarding shear strengthening. The effects of varying the CFRP spacing on the shear strength were investigated. The spacing investigated was set at 0.75D, 0.60D and 0.50D. There is very limited data in the literature regarding the deformation behaviour between beams with and without strengthening. Hence, advanced photogrammetry measurement techniques were used to study and quantify the difference in deformation behaviour of the T-beams with and without shear strengthening.

2.4 Existing shear strength models

2.4.1 Introduction

In the literature, various failure modes have been observed in experiments on reinforced concrete beams shear strengthened with bonded FRPs. Several researchers have reported a shift from shear to flexural failure in the strengthened beams due to yielding of the main flexural reinforcement or concrete crushing in the compression zone. For the typical reinforced concrete beams without shear strengthening, the shear failure modes may be flexural shear, diagonal tension or diagonal compression. As for beams that have failed in shear, FRP rupture, FRP debonding and localised failures were reported. Rupturing of the FRP typically occurs with the formation of diagonal tension cracks. As the diagonal crack widens, the strain in the FRP increases, eventually reaching its ultimate strain and the FRP ruptures along the shear crack. Within the vicinity of the shear crack, partial debonding of the FRP may occur. At or near the shear cracks are regions of localised shear stress concentration. Debonding occurs when the tensile capacity of the concrete is exceeded. As more load is applied, the debonded area extends towards the bonded portion. Typically, critical portions of the FRP will debond completely first before other modes of failures. The sudden loss of force transfer to the FRP leads to the total failure of the

beam in a brittle manner. Failure by FRP debonding can be deferred by providing effective anchorages at the FRP ends, which allows the FRP to act as tension ties even though the entire length has debonded.

Several prediction models have been developed to calculate the shear strength of a strengthened beam accounting for failure by either FRP rupture or debonding. For a typical reinforced concrete beam without strengthening, the mechanisms of shear are complex and much research has been dedicated to its understanding and the development of predictive strength models suitable for practical design. The shear strength depends on numerous factors such as loading condition and type, material properties, beam size and geometry, internal shear and flexural reinforcement and loading span. The use of FRP for shear strengthening adds to the complexity of the problem.

The general expression used to calculate the shear strength of a strengthened reinforced concrete beam is given by Equation 2.1 (Al-Sulaimani et al. (1994), Chaallal et al. (1998b), Khalifa et al. (1998), Khalifa and Nanni (2000), Neale (2001)), where V_c, V_s and V_{frp} are the contributions from the concrete, steel stirrups and bonded FRP respectively. V_c and V_s may be calculated according to the guidelines of existing design codes.

$$V_n = V_c + V_s + V_{frp} \tag{2.1}$$

The sections to follow outline existing prediction models of the contribution of the FRP, V_{frp}, that have been developed and reported by various researchers. The results of only three prediction models based on the beam configuration of the present study are reported and compared in Chapter 9. The three models are refined models based on earlier work carried out many researchers. The predictive models reported and compared are by Triantafillou and Antonopoulos (2000), Neale (2001) and Chen and Teng (2003a, c).

2.4.2 Al-Sulaimani et al. (1994)

Al-Sulaimani et al. (1994) proposed the following equations to calculate the contribution of the FRP depending on the strengthening schemes employed:

$$V_{frp,side\ strip} = \frac{2\left[\tau_{ave}\left(\frac{t_s h_s}{2}\right)\right]d}{s_{frp}} \tag{2.2}$$

$$V_{frp,wing} = 2\left[\tau_{ave}\left(\frac{dh_w}{2}\right)\right] \tag{2.3}$$

$$V_{frp,U-jacket} = 2\left[\tau_{ult}\left(\frac{dh_j}{2}\right)\right] \tag{2.4}$$

where

t_s = width of each strip

s_{frp} = spacing between FRP

h_s = depth of each strip

h_w = depth of wing

h_j = depth of jacket

d = distance from extreme compression fibre to centroid of steel reinforcement

τ_{ave} = average shear stress

τ_{ult} = interface shear strength

The major drawback of the models is the predetermination of the shear stresses, τ_{ave} and τ_{ult}, which are dependent on the FRP type and concrete strength. In the study, τ_{ave} was estimated by assuming a shear stress distribution along the FRP and using experimental results from the beam tests. It is impractical to determine τ_{ave} and τ_{ult} for every FRP type as the numbers and variations available commercially are immense. In addition, slightly different shear stress distributions exist for different FRP types and variations.

2.4.3 Chajes et al. (1995)

Chajes et al. (1995) proposed Equation 2.5, which was based on the formula used to compute the contribution of the shear capacity of stirrups based on the truss analogy. The expression is superior to those proposed by Al-Sulaimani et al. (1994) as it takes into account the properties of the FRP used. The contribution of the FRP is determined by the strain in the FRP taken as the ultimate tensile strain of concrete because failure of the beam was initiated by failure of the concrete.

$$V_{frp,\,U\text{-}jacket} = A_{frp}\, E_{frp}\, \varepsilon v_{cu}\, (\sin\beta + \cos\beta)\, d \qquad (2.5)$$

where

A_{frp} = cross sectional area per length of beam length

E_{frp} = FRP modulus of elasticity

β = angle between FRP and longitudinal axis of member

εv_{cu} = ultimate vertical tensile strain of concrete

The equation assumes that perfect bond exists between the FRP and concrete prior to failure. It is apparent that the equation cannot be used in cases where failure is initiated by debonding of FRP as the strain in the FRP will be significantly smaller. In addition, the researchers themselves noted that taking the ultimate strain at failure of concrete does not account for the different FRPs or wrapping orientations they have used in their study.

2.4.4 Malek and Saadatmanesh (1998b)

Malek and Saadatmanesh (1998b) reported that the shear crack inclination angle is changed as a result of bonding of the FRP. This has an effect on the contribution of the FRP to the shear strength of the beams, which had lead the researchers to propose Equation 2.6. The crack inclination angle is determined using an iterative approach that satisfies both equilibrium and compatibility requirements.

$$V_{frp,U-jacket} = \frac{h_{frp}}{\tan\theta_c} f_{frpu}\, t_{frp} \qquad (2.6)$$

where

h_{frp} = FRP bonded height

θ_c = crack inclination angle

f_{frpu} = tensile capacity of FRP

t_{frp} = FRP thickness

The determination of the crack inclination angle is slightly more involved compared to models developed by other researchers and may be unsuitable for use as a design tool. Similar to the model developed by Chajes et al. (1995), the model is not appropriate when failure occurs due to the debonding of FRP. In the case where failure is initiated by debonding, it is difficult to establish that the shear crack inclination angle will change. In the present investigation, it has been reported in Section 6.2.6 that the shear inclination angles were slightly steeper in the strengthened beams compared to the beam without strengthening. It is difficult to confirm this fact conclusively as even identical beams can give different results.

2.4.5 Chaallal et al. (1998b)

Chaallal et al. (1998b) proposed the general expression on the basic assumption that the externally bonded FRP behaves in a similar manner to internal steel shear reinforcement. The FRP intersected by the shear crack is assumed to reach its full tensile capacity at beam failure unless otherwise limited by debonding. The prediction models for FRP contribution limited by debonding are similar to the ones proposed by Al-Sulaimani et al. (1994).

$$V_{frp} = \varphi_{frp} A_{frp} f_{frpu} \frac{d}{s_{frp}} (\sin\beta + \cos\beta) \qquad (2.7)$$

where

φ_{frp} = material resistance factor for FRP

The bond strength model to determine the contribution of the FRP is flawed as it does not take into account the effective bond length and the effect of concrete strength.

2.4.6 Triantafillou (1998) and Triantafillou and Antonopoulos (2000)

Triantafillou (1998) used a semi-quantitative approach and derived an expression that relates the FRP effective strain $\varepsilon_{frp,e}$ to the axial rigidity of the externally bonded reinforcement expressed as $\rho_{frp}E_{frp}$. He proposed the following expression:

$$V_{frp} = \frac{0.9}{\gamma_{frp}} \rho_{frp} E_{frp} \varepsilon_{frpe} b_w d(1+\cot\beta)\sin\beta \qquad (2.8)$$

where

γ_{frp} = partial safety factor for FRP

ρ_{frp} = FRP area fraction ($2t_{frp}/b_w$)

ε_{frpe} = effective FRP strain

b_w = minimum width of cross section over the effective depth

The relationship between the FRP effective strain and axial rigidity was obtained from the curve-fitting of experimental data of beam tests and is given by:

$0 \le \rho_{frp}E_{frp} \le 1$:

$$\varepsilon_{frpe} = 0.0119 - 0.0205\,(\rho_{frp}E_{frp}) + 0.0104\,(\rho_{frp}E_{frp})^2 \qquad (2.9a)$$

$\rho_{frp}E_{frp} > 1$:

$$\varepsilon_{frpe} = 0.000655\,(\rho_{frp}E_{frp}) + 0.00245 \qquad (2.9b)$$

Triantafillou and Antonopoulos (2000) reported that the modelling approach above had three shortcomings. Firstly, FRP fracture was assumed to occur simultaneously with shear failure. Secondly, there is no distinction between failure by FRP fracture and debonding. Lastly, concrete strength was not introduced as a design variable. In addition, the model does not differentiate between the different strengthening schemes, for example, wrapping and side bonding. Based on a larger database, Triantafillou and Antonopoulos (2000) improved upon the previous model by proposing different effective strain expressions for the two failure modes. Different expressions were developed for two FRP types (CFRP and AFRP) based on the fully wrap, side bonded and U-wrap strengthening scheme. However, there is still no distinction between side-bonded and U-wrapped strengthening schemes. Also, Chen and Teng (2003b) showed that the model is statistically unsatisfactory for safe

practical design. Nevertheless, based on the beam configuration of the present study, the results of the predictive model by Triantafillou and Antonopoulos (2000) are reported and compared in Chapter 9.

2.4.7 Khalifa et al. (1998) and Khalifa and Nanni (2000)

Khalifa et al. (1998) extended on the effective strain model by Triantafillou (1998) by introducing two different expressions to account for the FRP rupture and debonding failure mode. However, instead of using expressions relating the effective strain to the axial rigidity, the researchers expressed R, defined as the ratio of effective strain to ultimate strain $\varepsilon_{frpe}/\varepsilon_{frpu}$, to the axial rigidity, eliminating the effects of various types of FRP. The following expressions were developed:

Fracture of FRP

$$R = 0.5622 (\rho_{frp}E_{frp})^2 - 1.2188 (\rho_{frp}E_{frp}) + 0.788 \leq 0.50 \qquad (2.10a)$$

Debonding

$$R = \frac{0.0042(f'_c)^{2/3} w_{frpe}}{(E_{frp}t_{frp})^{0.58}\varepsilon_{frpu}d_{frp}} \leq 0.50 \qquad (2.10b)$$

Teng et al. (2002) pointed out that the model has two shortcomings. Firstly, the upper limit of 0.50 meant that at best, no more than half the tensile capacity of the FRP can be utilised at failure. No satisfactory explanation was given and since the expressions were obtained from the curve fitting of test data, it lacks a rational theoretical basis. Chen and Teng (2001) reported that the bond model adopted, which was developed by Maeda et al. (1997), is invalid as it cannot correctly predict the effective bond length.

Khalifa and Nanni (2000) proposed a new expression for R for failure by FRP debonding:

$$R = \frac{(f'_c)^{2/3} w_{frpe}}{\varepsilon_{frpu}d_{frp}} [738.93 - 4.06(E_{frp}t_{frp})]\times 10^{-6} \leq 0.50 \qquad (2.11)$$

where

w_{frpe} = effective width of FRP sheet

d_{frp} = effective depth of the FRP

Similar to the previous model, the upper limit is still set at 0.50. In order to determine R, the effective bond length, L_e, has to be determined but no expression was reported. Instead, the researchers suggested a conservative value of 75 mm. The equation above is only valid for CFRP stiffness that ranged from 20 to 90 mmGPa. Expressions for other FRP types were not reported. In the present study, the elastic modulus E_{frp} of the FRP used was determined to be 137,345 MPa and a thickness of 1.31 mm. The axial rigidity $E_{frp}t_{frp}$ (180 GPa) is beyond the range specified.

2.4.8 Neale (2001)

Based on past studies of and reviews by researchers, Neale (2001) proposed the following expression for the FRP contribution to the shear strength of a beam. The expression is applicable to the side strip and U-strip arrangement only where $A_{frp} = 2t_{frp}w_{frp}$.

$$V_{frp} = \frac{\varphi_{frp} E_{frp} \varepsilon_{frpe} A_{frp} d_{frp} (\sin\beta + \cos\beta)}{s_{frp}} \tag{2.12}$$

The effective strain ε_{frpe} is determined by the following expression (Equation 2.13a) that accounts for failure by FRP fracture or debonding. The equation for determining the effective strain governed by FRP fracture is based on the expression proposed by Triantafillou and Antonopoulos (2000). For failure governed by FRP debonding, the effective strain is a function of the concrete strength, FRP end anchorage configuration and the effective bond length. The equation for determining the effective bond length (Equation 2.13c) is based on the experimental data proposed by Maeda et al. (1997). The effective strain is limited to a value of 0.004 to ensure the integrity of the concrete and engage aggregate interlock mechanism.

$$\varepsilon_{frpe} = \min\left[\alpha\lambda_1 \left(\frac{f'^{\,2/3}_c}{\rho_{frp} E_{frp}} \right)^{\lambda_2} \varepsilon_{frpu}\ (\text{Fracture}),\ \frac{\alpha\varphi_{frp} k_1 k_2 L_e}{9525}\ (\text{Debonding}),\ 0.004 \right] \tag{2.13a}$$

$$\rho_{frp} = \frac{2t_{frp} w_{frp}}{b_w s_{frp}} \tag{2.13b}$$

$$L_e = \frac{25350}{(t_{frp}E_{frp})^{0.58}} \tag{2.13c}$$

$$k_1 = \left(\frac{f'_c}{27.65}\right)^{2/3} \tag{2.13d}$$

$$k_2 = \frac{d_{frp} - n_e L_e}{d_{frp}} \tag{2.13e}$$

where

α = reduction coefficient (= 0.8)

λ_1 & λ_2 = parameters dependent on FRP material type

k_1 & k_2 = parameters accounting for shear strength of the concrete and FRP configuration

n_e = number of free ends of the FRP on one side of the beam

Equation 2.13c expresses that the effective bond length decreases as $t_{frp}E_{frp}$ increases, which contradicts the trend reported by Chen and Teng (2001). In fact, the researchers reported that the effective bond length L_e increases linearly with $\sqrt{E_{frp}t_{frp}}$. Nevertheless, the results of the predictive model by Neale (2001) using the T-beam configurations of the present study are reported and compared in Chapter 9.

2.4.9 Chen and Teng (2003 a, b)

Chen and Teng (2003a, b) proposed the following expression that is applicable to side bonded and wrapped FRP arrangement either in discrete strips or in continuous form. In the case of beams strengthened with continuous FRP, s_{frp} is given as Equation 2.15a, which cancels out the term w_{frp} in Equation 2.14. It should be noted that the expressions present hereafter are not design equations, which the researchers have also proposed through the introduction of safety and reduction factors. In the present study, design values are not required as we are comparing against actual experimental results.

$$V_{frp} = 2f_{frpe}t_{frp}w_{frp}\frac{h_{frpe}(\cot\theta + \cot\beta)\sin\beta}{s_{frp}} \tag{2.14}$$

$$s_{frp} = \frac{w_{frp}}{\sin\beta} \text{ (For continuous FRP plates/sheets only)} \tag{2.15a}$$

$$h_{frpe} = z_b - z_t \tag{2.15b}$$

$$z_t = d_{frp,t} \tag{2.15c}$$

$$z_b = d_{frp} - h + 0.9d \tag{2.15d}$$

where

d_{frp} = distance from the compression face to the lower edge of the FRP

$d_{frp,t}$ = distance from the compression face to the top edge of the FRP

f_{frpe} = average shear stress in FRP intersected by shear crack at ultimate state

h = height of the beam

h_{frpe} = effective height of the FRP

z_t & z_b = coordinates at the top and bottom ends of the effective FRP

The average stress in the FRP intersected by the shear crack at the ultimate state f_{frpe} is given as

$$f_{frpe} = D_{frp}\sigma_{frp,max} \tag{2.16}$$

where

$\sigma_{frp,max}$ = maximum stress achievable in FRP intersected by shear crack

D_{frp} = stress distribution factor

The values of $\sigma_{frp,max}$ and D_{frp} depend on whether failure is governed by FRP rupture or debonding, determined by the following set of expressions

FRP Fracture

$$D_{frp} = \frac{1+\zeta}{2} \tag{2.17a}$$

$$\zeta = \frac{z_t}{z_b} \tag{2.17b}$$

$$\sigma_{frp,max} = \min\begin{cases} f_{frp} & \text{if } f_{frp}/E_{frp} \le \varepsilon_{max} \\ \varepsilon_{max}E_{frp} & \text{if } f_{frp}/E_{frp} > \varepsilon_{max} \end{cases} \tag{2.18}$$

where f_{frp} = tensile strength of FRP, ε_{max} = maximum usable FRP strain

FRP Debonding

$$\sigma_{frp,max} = \min\begin{cases} f_{frp} \\ 0.427\beta_w\beta_L\sqrt{\dfrac{E_{frp}\sqrt{f'_c}}{t_{frp}}} \end{cases} \tag{2.19a}$$

$$\beta_L = \begin{cases} 1 & \text{if } \lambda \geq 1 \\ \sin(\pi\lambda/2) & \text{if } \lambda < 1 \end{cases} \tag{2.19b}$$

$$\beta_w = \sqrt{\frac{2 - w_{frp}/(s_{frp}\sin\beta)}{1 + w_{frp}/(s_{frp}\sin\beta)}} \tag{2.19c}$$

$$\beta_w = \frac{\sqrt{2}}{2} \text{ for continuous sheets / plates} \tag{2.19d}$$

$$\lambda = \frac{L_{max}}{L_e} \tag{2.19e}$$

$$L_{max} = \begin{cases} h_{frpe}/\sin\beta & \text{for U jackets} \\ h_{frpe}/(2\sin\beta) & \text{for side plates / wings} \end{cases} \tag{2.19f}$$

$$L_e = \sqrt{\frac{E_{frp}t_{frp}}{\sqrt{f'_c}}} \tag{2.19g}$$

$$D_{frp} = \begin{cases} \dfrac{2}{\pi\lambda}\dfrac{1-\cos(\pi/2)\lambda}{\sin(\pi/2)\lambda} & \text{if } \lambda \leq 1 \\ 1 - \dfrac{\pi - 2}{\pi\lambda} & \text{if } \lambda > 1 \end{cases} \tag{2.20a}$$

According to Equation 2.19g, the effective bond length increases linearly with $\sqrt{E_{frp}t_{frp}}$. The predicted values agree well with the limited experimental observations in studies carried out by Bizindavyi and Neale (1999) and Täljsten (1997). Since the proposed model is an empirical model, further research will be required to increase confidence in and verify the robustness for predicting the effective bond length. The predicted values based on the beam shear strength model presented here are reported and compared in Chapter 9.

2.5 Summary

The past studies reported in the literature have established clearly that the two most common modes of shear failure of strengthened beams are the tensile

rupture of the FRP and the debonding of the FRP. In both cases, failure of the beam is abrupt and typically without warning. Complete debonding of the FRP can be delayed and in some cases eliminated by providing end anchorages, which can be achieved by wrapping the FRP around the top and bottom face of the beam. In T-beams, however, the presence of the flange makes it difficult to anchor the FRP properly in the compression zone. EMPA (1998a) and EMPA (1998b) reported the use of prefabricated CFRP L-shaped plates on three T-beams whereby anchorage in the compression zone is achieved by bonding the FRP into the flange. This was achieved by coring away part of the beam's flange and bonding the FRP reinforcement in its place. Only one beam, which had also been strengthened in flexure, was observed to fail in shear. It was not the tensile rupture or debonding of the FRP but the separation of the overlap at the soffit. At the same time of the present investigation, Czaderski (2002) reported a similar failure mode in only one beam, which had no internal shear reinforcement. Therefore, the experimental results on this particular strengthening system are very limited. Currently, no study has been carried out to investigate the effect of varying the spacing of the L-shaped CFRP strengthening system on the shear strength of T-beams. The strengthening programme of the present study utilises this innovative system with the aim of increasing the limited data in literature regarding shear strengthening, in particular the effects of FRP spacing. Advanced photogrammetry measurement techniques were used to study and quantify the difference in deformation behaviour of the T-beams with and without shear strengthening.

A review of the existing prediction models on the external FRP's contribution to the beam's shear capacity has shown that earlier models were too simplistic in that key parameters such as concrete strength, FRP failure mode and strengthening configurations were not considered all together. The more recent prediction models proposed by Triantafillou and Antonopoulos (2000), Neale (2001) and Chen and Teng (2003a, c) are more sophisticated addressing all the key parameters at once. The applicability of these three models in the case of shear strengthening with prefabricated L-shaped CFRP is determined by comparing predicted values against experimental results.

CHAPTER 3 - BOND BEHAVIOUR OF CFRP BONDED TO CONCRETE

3.1 Introduction

The most crucial aspect of any strengthening application using externally bonded FRP is the bond between the FRP and the concrete. In general, the effectiveness of the bond depends mainly on the quality of the surface preparation and the concrete itself. The purposes of surface preparation are to remove any bond inhibiting materials and improve the chemical and mechanical bond of the concrete surface. Typical methods to prepare the concrete surface include wet or dry abrasive blasting, scarifying or high pressure water jetting. In the present study, high pressure water jetting was used. The water jet effectively removed a thin concrete layer to expose the aggregates without causing much damage to the aggregates. The resulting concrete surface had a rough texture.

The bond behaviour is dependent on numerous factors including but not limited to FRP type, adhesive type and thickness, concrete surface preparation, concrete strength and the FRP bonded area. The bonded area relates to the width and length of the FRP in contact with the concrete surface. In the present study, the parameter investigated was the bonded length of the FRP. All other parameters were fixed. There does not appear to be any study on bond behaviour in the literature between concrete and the L-shaped CFRP plate system used in the present study. Bond specimen tests were carried out to gain a better understanding of the bond behaviour of the system and the mechanisms that occur in the actual T-beams under loading. Finite element modelling was carried out to supplement the experimental results.

Previous studies relevant to the present chapter are presented first followed by presentation of the experimental program and results of the bond specimen tests. The finite element modelling methodologies and results are reported in subsequent sections. Results from the numerical models and experiments are then compared and discussed.

3.2 Literature review

The focus of the literature review is on the specimen test configurations and factors affecting the bond behaviour reported by previous researchers. Theoretical models developed to predict bond stress and strength are mentioned in brief only as they are beyond the scope of the present study. The various test configurations used by previous researchers formed the basis of the test configurations used in the present study. The shortcomings and advantages of the test configurations are highlighted and discussed. The bond behaviour reported by past researchers do not vary significantly from each other. Despite the range of materials and configurations used, a general trend exists in terms of the force transfer behaviour and failure mechanisms of a composite-concrete joint. Therefore a background of the bond behaviour is presented first.

Consider a concrete block bonded with FRP for the length L as illustrated in Figure 3.1. The concrete block is held fixed while load is applied at the free end of the FRP. The tensile force in the FRP is transferred to the concrete as shear force through the adhesive layer. A schematic diagram showing the general strain distribution along the bonded length in the FRP is illustrated in Figure 3.1 (b).

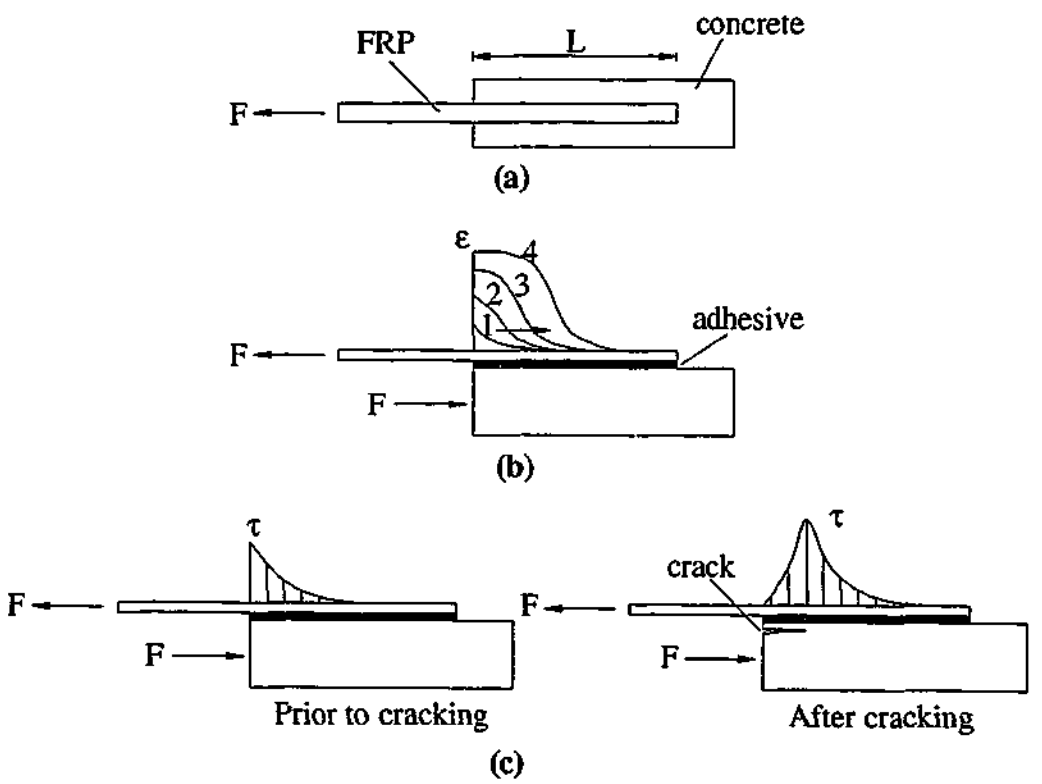

Figure 3.1 - FRP-concrete bond specimen (a) top view (b) strain distribution along FRP and (c) shear stress distribution along FRP

The strain distribution indicates the rate at which the applied tensile load is transferred from the FRP to the concrete. It is a function of the mechanical properties of the adherends and adhesive. The relative stiffness of the materials influence how the load is transferred. At the early stage of loading, the strain in the FRP is highest near the loaded edge gradually decreasing along the length indicated by the strain distribution curve '1'. There is a length of FRP where the bond becomes fully developed. Bizindavyi and Neale (1999) defined this length as the initial transfer length. Beyond this length, there is no further transfer of load to the concrete. The researchers have shown that this value is constant for load levels below the initial cracking load. The initial transfer length is a function of the properties and geometry of the test specimens and also surface preparation. As more load is applied, the strain distribution shifts upwards accordingly with the highest strain value at the loaded edge gradually decreasing to zero as indicated by the curve '2'. As more load is applied, the strain at the loaded end will eventually exceed the shear strain capacity of the concrete. At this point, cracking due to shearing of concrete under the adhesive layer will initiate at the loaded end. This is characterised by a flattening strain curve near the loaded end of the FRP shown in curve '3'. The corresponding shear stress distribution prior to and after cracking is illustrated in (c). Initially, shear stress is highest at the loaded end. When cracking occurs, the maximum shear stress shifts away from the loaded end and attains higher value. This is due to the concrete portion not being confined at the loaded end and therefore has a lower shear capacity. Further increase in load will extend the crack and gradually shift the area for active bonding towards the unloaded end until the whole FRP is debonded. Maximum shear stress will occur near the vicinity of the crack front. Bizindavyi and Neale (1999) have shown that the transfer length increases with crack propagation beyond the cracking load. The transfer lengths at the post cracking load levels were determined in a similar manner to the initial transfer length, that is, by measuring the distance from the loaded end to the point on the FRP where the strain reaches zero. The cracked concrete may contribute to carrying part of the load through tension softening. However, this does not mean a joint with longer bonded length will carry higher loads. The contributions of tension softening are limited and insignificant particularly in short joints. The transfer length will reach a maximum value beyond which no further increase in failure load can be achieved. Provided that the FRP did not fail by tensile rupture, this maximum transfer length is known as the critical anchor length or

the effective bond length. Beyond this length, no further transfer of load from the FRP to the concrete takes place. These observations were reported in studies conducted by Chajes et al. (1996) and Izumo et al. (1998). Further increase in load will result in the sudden concrete shearing failure of the whole joint. It should be noted that the effective bond length is different to the development length. There are situations where the full tensile strain develops in the FRP causing it to fracture before debonding or failure in the adhesive layer. The length required to achieve the full tensile capacity of the FRP is referred to commonly as the development length. For certain types of FRP, it is not uncommon for the development length to be the effective bond length. Bizindavyi and Neale (1999) reported failure by FRP rupturing and concrete shearing beneath the glue line in their study. In the experimental program carried out in the present study, failure by CFRP rupturing did not occur. Rupturing of the CFRP was impossible given the extremely high tensile strength of the composite. Failure will always be in the concrete layer. The strain level of the CFRP and adhesive remained within the elastic capacities.

The effective bond length of a joint is dependent on the concrete strength, the maximum tensile strain, modulus of elasticity and thickness of the composite. Using experimental results from past studies and their own, Maeda et al. (1997) reported that the effective bond length decreases as the stiffness of CFRP increases, where the stiffness is expressed as the product of the elastic modulus and thickness of the CFRP material. The researchers also showed that the ultimate load carried by the CFRP bonded joint increases with higher stiffness of FRP. The study carried out by Nakaba et al. (2001) and Chen and Teng (2001), however, disproved the trend that the effective bond length decreases with increase in the FRP stiffness. Chen and Teng (2001) reported that the effective bond length, L_e, increases linearly with the square root of the stiffness, $\sqrt{E_{frp}t_{frp}}$. Täljsten (1997) reported that there is a critical strain level, ε_{cr}, at which concrete begins to fracture and therefore a governing factor for failure. It follows that for a given strain level, the higher the FRP stiffness, the higher the load it is possible to transfer. In the present author's view, the critical strain level is a function of the bond strength of the concrete layer. In the study by Izumo et al. (1998), CFRP-concrete and AFRP-concrete joints were investigated. The variables studied were concrete compressive strength and bond length. The researchers

reported that the effective bond length was the same for all the specimens, which was 100 mm. The implication of this is that difference in stiffness of FRP has no influence on the effective bond length, thus contradicting the findings of Nakaba et al. (2001) and Chen and Teng (2001). However, it should be noted that the range of stiffness investigated by Izumo et al. (1998) was limited and there was some scatter in the experimental results. Expressing the stiffness in the terms reported by Chen and Teng (2001), the calculated stiffness values were small (12 and 27 mmGPa). It is likely that the low range of the FRP stiffness combined with experimental scatter gave the impression that stiffness has an insignificant influence on the effective bond length.

The test configurations that have been used by past researchers for investigating bond behaviour between FRP and concrete are shown in Figure 3.2. The test configurations (a) and (b) are the most commonly used. In test configuration (a), two blocks of concrete placed end to end are held together by FRP bonded on opposing sides of the specimen. The concrete blocks are separated by a small gap. Force is applied by means of pulling on the reinforcement bar that has been cast in with each concrete block. The reinforcement is centrally located in the concrete blocks terminating at the gap. This test set-up is referred to as the double lap shear bond test. The main advantage of this test set-up is that specimens can be tested in tensile testing machines for steel bar reinforcement. The test simulates closely the actual behaviour of FRP used in shear and flexural strengthening of beams. Maeda et al. (1997), Horiguchi and Saeki (1997), Izumo et al. (1998) and Nakaba et al. (2001) reported the use of test configuration type (a). In test configuration (b) or the single lap shear bond test, FRP is bonded to only one side of a concrete block. Load is applied to the FRP at the free end. The concrete block is held in place using end plate supports bearing against the concrete surface near the loaded end. The main advantage of this test configuration is the reduced use of FRP materials. In the first test configuration, the bonded length of the FRP has to be longer on one end to ensure failure occurs at the other end, particularly when measurements are required. Investigations into longer bond lengths can be costly. However, the second test configuration requires the use of special grips to hold the FRP in place. Typically, servo-hydraulics grips are used where the bearing pressure can be controlled without crushing the FRP. Even with the use of such grips, slippages and premature failure of

the FRP within the grips are not uncommon in such systems. The second test configuration also does not simulate correctly the actual behaviour of FRP used in shear or flexural strengthening of beams. Assume that the loaded edge of the bond specimen represents a crack that had formed within the FRP in an actual beam. In the bond specimen, the region of concrete close to the end support plate is subjected to compressive forces. This force simply does not exist in the case of the actual beam. Chajes et al. (1996), Täljsten (1997) and Bizindavyi and Neale (1999) reported the use of test configuration type (b). The remaining test configurations work on the same principle as the first two. In test configuration (c), the specimen is pulled apart through steel plates bonded to the sides. Additional surface preparation will be required on the specimen. Van Gemert (1980), Brosens and Van Gemert (1997) reported the use of test configuration type (c). Van Gemert (1980) investigated the bond behaviour of steel to concrete joints. In test configuration (d), a hydraulic actuator is place in between the concrete blocks, which are seated on rollers. Dolan et al. (1998) reported the use of test configuration type (d). Test configuration (e) is a combination of test configurations (a) and (b). The concrete block is secured using brackets located a certain distance away from the FRP. Sakai et al. (1997) reported the use of test configuration type (e).

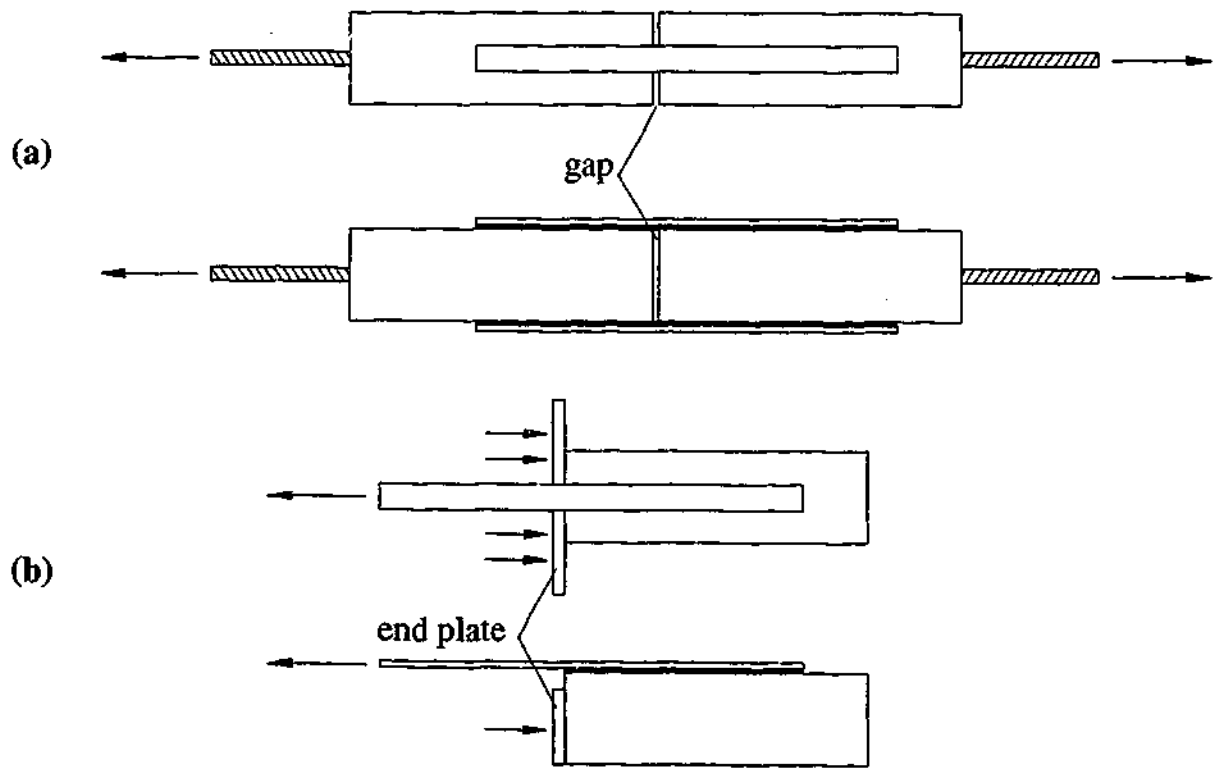

Figure 3.2 - Test configurations for determining bond behaviour

(c)

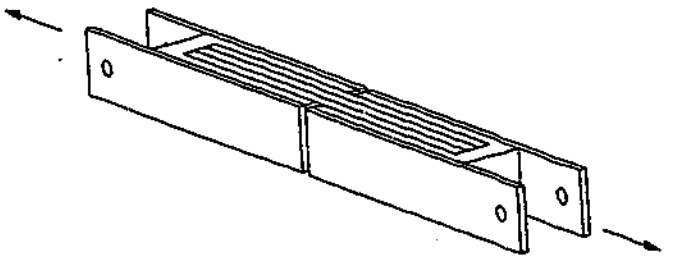

(d)

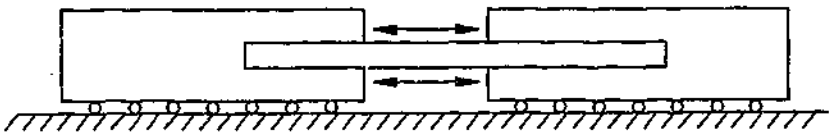

(e)

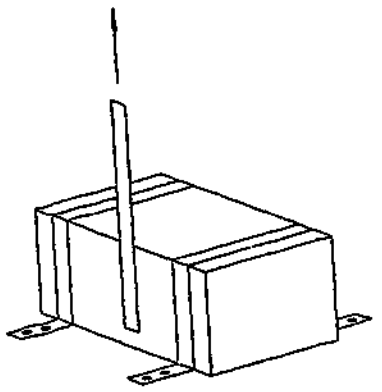

Figure 3.2 (continued) - Test configurations for determining bond behaviour

Chajes et al. (1996) investigated the effects of concrete surface preparation, adhesive type and concrete strength on the bond strength of the composite-concrete joint. The surface preparations investigated were no surface preparation, grinding with a stone that gave a smooth finish and mechanically abrading with a wire wheel that left the aggregate slightly exposed. The researchers reported that the concrete surface should be mechanically abraded or sandblasted to achieve the best possible bond. Toutanji and Ortiz (2001) conducted a similar study but compared two types of surface preparation, which were water jet blasting and sanding. The investigators reported that surface treatment by water jet produced higher bonding strength than surface treatment by sander. The conclusions drawn from these two studies were similar. Surface treatments that leave a rough concrete surface produce a better bond compared to surface treatments that leave a smooth concrete finish. The surface area available for bonding is more in rough surfaces compared to smooth surfaces. The

bond strength is enhanced only if the surface treatments employed do not damage the concrete surface. Pneumatic hammer produces a rough texture but the high impact force damages the concrete surface layer and creates a zone of weakness below the surface. The resulting bond strength may be lower than the bond strength of specimens with smooth surface finishes.

Chajes et al. (1996) also investigated the effect of concrete strength on the ultimate bond strength of the joint. For failure mode due to shearing of concrete directly beneath the bond, the ultimate bond strength is proportional to $\sqrt{f'_c}$. The researchers arrived at this conclusion based on the knowledge that the bonded joints failed by shearing of concrete and the ultimate shear stress in concrete at failure is typically taken to be proportional to $\sqrt{f'_c}$. The researchers developed a simple equation for determining the ultimate capacity of a joint based on two parameters, the average bond resistance and bonded length. The drawbacks of the equation are that the bond resistance and effective bond length have to be determined for other FRP types. Izumo et al. (1998) conducted a similar study and developed the relationship, $a.f_c^{2/3} + b$, to determine the bond strength for a given concrete strength and bonded length, where a and b are material constants. The term $f_c^{2/3}$ is related to the tensile strength of concrete reported in JSCE (1996) as $f_t = 0.23 f_c^{2/3}$. Similar to the equation developed by Chajes et al. (1996), the material constants and effective bond length would have to be determined for different FRP types with failure by shearing of concrete beneath the bond. Brosens and Van Gemert (1997) also reported the use of the tensile strength of concrete as a parameter in determining the load capacity of a bonded joint. The method is a conservative approach ignoring the reserve of strength available after first cracking in concrete. However, the shear stress distribution of the joint must be determined for the type of FRP used. Horiguchi and Saeki (1997) carried out a similar study and reported an increase in bond strength with increase in concrete compressive strength. An estimation of the bond strength based on the relationship $0.09 f_c^{2/3}$ was developed. Maeda et al. (1997) developed an equation for determining the ultimate load of a bonded joint based on the effective bond length and the average bond strength. Using experimental results carried out by previous researchers and their own, Maeda et al. (1997) developed an empirical equation

relating the effective bond length with the stiffness of the CFRP, which was expressed as the product of the elastic modulus and thickness of the CFRP material. The average bond strength was a function of the FRP stiffness and the rate of force transfer, which was assumed to be a constant. Carbon fibre sheet was used in these past studies. The expression does not account for the effect of concrete strength. Based on regression of data available from literature, Chen and Teng (2001) proposed a more rational model where the effective bond length is a function of $\sqrt{E_{frp}t_{frp}}$ and the concrete strength. Brosens and Van Gemert (1997) reported on the expression developed by Täljsten (1994), that was based on non linear fracture mechanics, for determining the ultimate load capacity of steel-concrete joints with brittle adhesive. The expression is a function of the material properties and mode II (pure shear) fracture energy. Determination and definition of the fracture energy is complicated.

Täljsten (1997) investigated the effect of varying the width of a steel-concrete bonded joint on the ultimate load capacity. The results indicated that the ultimate load capacity of the specimens increases with width of the steel plates. This is because a larger force is required to initiate and propagate fracture along the concrete layer of a wider joint. Studies reporting the effect of width of an FRP-concrete bonded joint were not available from the literature. Nevertheless, the trend can be expected to be similar to that of a steel-concrete joint. Täljsten (1997) did not report the effect of varying the bonded joint width on the effective bond length. In the present study, the effect of varying the bond width was not investigated because the composite system used is pre-manufactured to a particular width only.

It was mentioned in brief earlier that the strain distribution of a bonded joint depends on the mechanical properties of the adherends and adhesive. In the study by Chajes et al. (1996), the strain distribution showed an exponential curve at early stages of loading becoming somewhat linear near the ultimate load. The result of the specimen with a bonded length of eight inches (200 mm) has been reproduced in Figure 3.3. In the study by Maeda et al. (1997), the strain distribution was described as being quadratic at the early stage of loading and bi-linear near the ultimate load. The strain distribution curves at various load levels of the 300 mm bond length specimen have been reproduced in Figure 3.4. The specimen had a bonded length of

300 mm. Täljsten (1997) developed a theoretical model for determining the strain distribution on a bonded joint. Analytical results were reported to be in good agreement with the experimental data within the elastic region. Bizindavyi and Neale (1999) reported a similar theoretical model based on shear lag theory, valid only within the elastic region. As pointed out by the investigators themselves, the applicability of the model for bonded joints that involve stiffer composite laminates and other materials needs to be validated.

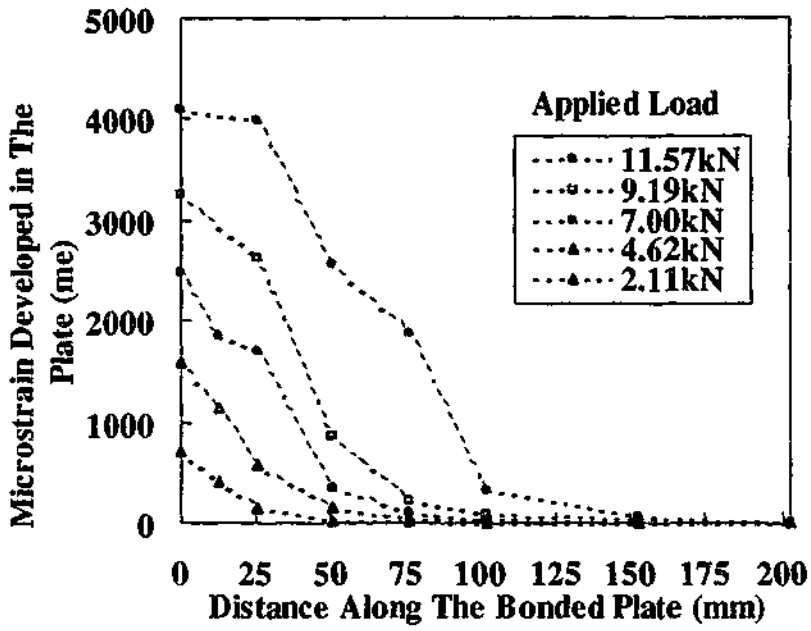

Figure 3.3 - Strain distribution profile of 8-inch (200 mm) bond length (Chajes et al. (1996))

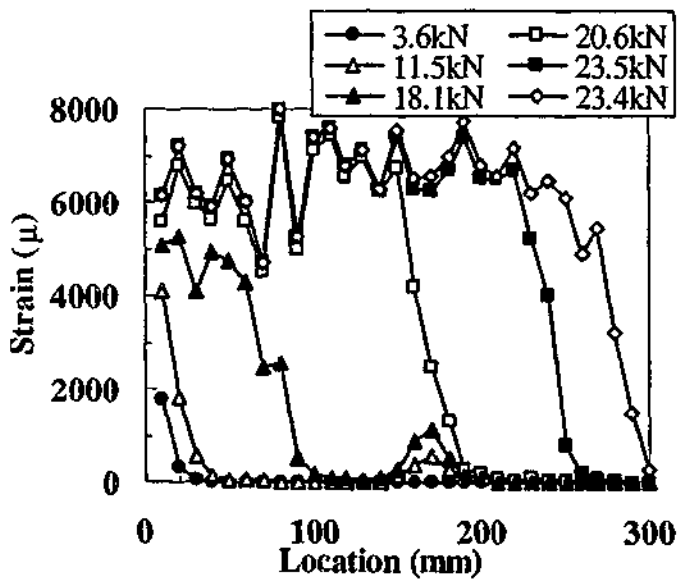

Figure 3.4 - Strain distribution profile of 300 mm bond length (Maeda et al. (1997))

In the experimental works carried out by Täljsten (1997), slip between the plate and concrete was measured. Measurements were taken at the top of the plate near the loaded end relative to a point on the concrete surface at which the plate was bonded. The relationships between the applied load and slip were reported and it can be observed that the stiffness of the specimens of the same plate width and type were similar for different bond lengths. The results also indicated that the specimens were stiffer in specimens bonded with wider steel plate. Lee et al. (1999) carried out an investigation into the effect of the adhesive thickness on the slip modulus at the concrete-FRP interface. The researchers reported that the slip modulus hence specimen stiffness increases with decreasing thickness of the adhesive layer. The researchers also measured and quantified the slip modulus using moiré interferometry measurements.

Nakaba et al. (2001) investigated the effect of FRP stiffness ($E_{frp}t_{frp}$), concrete strength and putty thickness. The putty is a thickened epoxy paste used to fill voids and smooth surface discontinuities. The maximum load was reported to increase as the stiffness of FRP increases. Putty stiffness was reported to have no effect on the bond behaviour. It was also reported that the maximum local bond stress is not influenced by the FRP type, but increases as concrete compressive strength increases. In addition, they proposed a model representing the local bond stress-slip relationship of the FRP-concrete bond. The applicability of the model for bonded joints that involve stiffer composite laminates such as the one adopted in the presented study needs to be validated. In the model, the proposed model requires the determination of the maximum local bond stress. The proposed equation for determining the maximum local bond stress for a given concrete strength is based on limited experimental results. Therefore, the bond stress-slip model has not been adopted in the T-beam finite element models reported in Chapter 8. In the T-beam finite element models, several simple linear bond stress-slip models were investigated.

These past studies highlight the numerous factors affecting the bond behaviour and strength of a concrete-composite joint. Further experimental and analytical work will be required to develop a relationship for modelling of the bond behaviour that can accommodate the combined effects of varying concrete strength, composite geometries and properties and specimen configurations.

3.3 Scope and aims of the CFRP-concrete bond tests

CFRP-concrete bond tests using Sika CarboShear L Plates type "4/20/50" were carried out in the experimental program. The variable selected for investigation was the bonded length. The main aim of the tests was to study the short-term bond behaviour of the CFRP-concrete joint. Other aims of the experimental program were to determine the effective bond length, the bond strength of the concrete and the strain in the CFRP at which concrete began to crack for the configuration adopted.

3.4 Specimen details

The details of the CFRP-concrete bond specimens are illustrated in Figure 3.5. The test configuration illustrated in Figure 3.2 (a) had been adopted based on its aforementioned merits. The bond lengths L of 50, 75, 95, 150 and 200 mm were investigated. Slip between the concrete and the steel bars was minimised by welding steel nuts at the bar ends and using deformed bars. The specimens are designated using the example notation, 'B100II', where the prefix 'B' identifies that the test specimens are bond specimens, the number '100' indicates the bond length in mm and the suffix 'II' indicates the number of the specimens.

Figure 3.6 illustrates the locations of the strain gauges that were bonded to the CFRP plates to measure the strain distribution along the bonded length. For each specimen, strain gauges were bonded to both CFRP plates at the concrete block bonded with a shorter CFRP length. Slip between the concrete and CFRP plates was measured using two linear variable displacement transducers (LVDTs) secured in position using steel brackets. The locations where slip was measured are illustrated in Figure 3.7. Small flat steel plates were spot welded to the underside of the steel brackets. The brackets were adhered to the concrete surface and CFRP plates through these small plates. The purpose of these small plates was to minimise the area at which slip measurements were taken whilst bearing the weight of the LVDTs and brackets. The LVDTs were secured in perspex brackets with shielded magnetic bases for direct mounting onto the steel brackets. This configuration allows the LVDT cores to be positioned appropriately by sliding the perspex brackets along the steel brackets. Two specimens were not instrumented with strain gauges or LVDTs for the

purpose of confirming the ultimate load capacity of a given bond length. Table 3.1 summarises the number of specimens investigated and their designations.

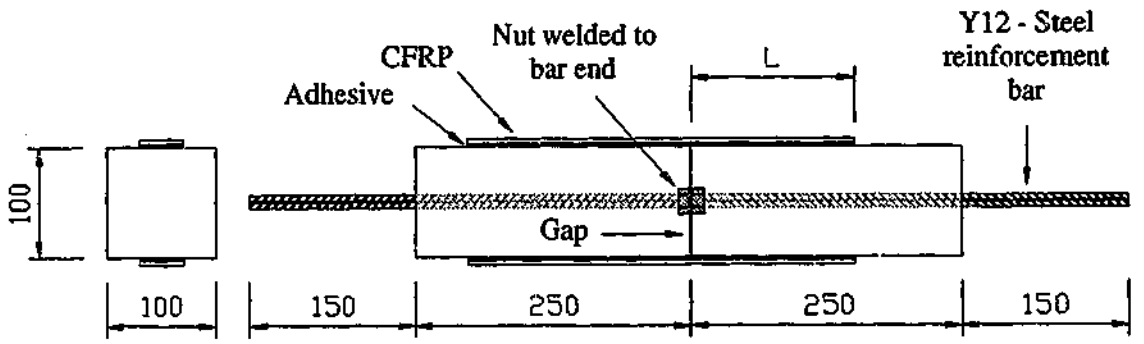

Figure 3.5 - Details of bond specimens

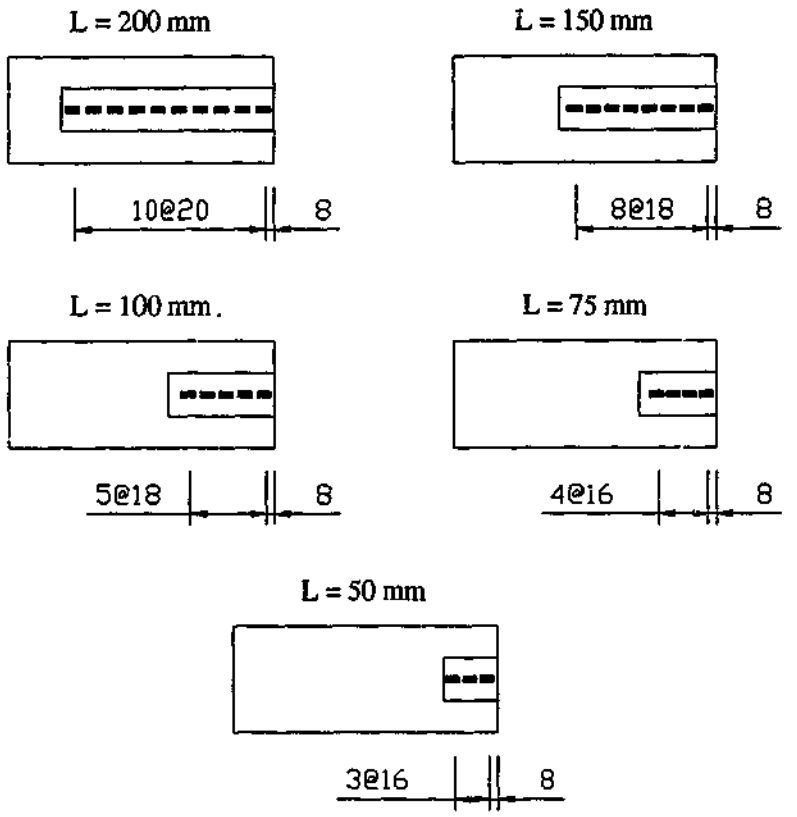

Figure 3.6 - Locations of strain gauges on CFRP-concrete bond specimen

Table 3.1 - Bond specimen lengths and designations

Bond length (mm)	No. of specimens	Designation
50	2	B50I, B50II
75	3	B75I, B75II, B75III
93	2	B93I*, B93II
95	1	B95I
97	1	B97I*
150	2	B150I, B150II
200	2	B200I, B200II

* Specimen not instrumented with strain gauges or LVDTs

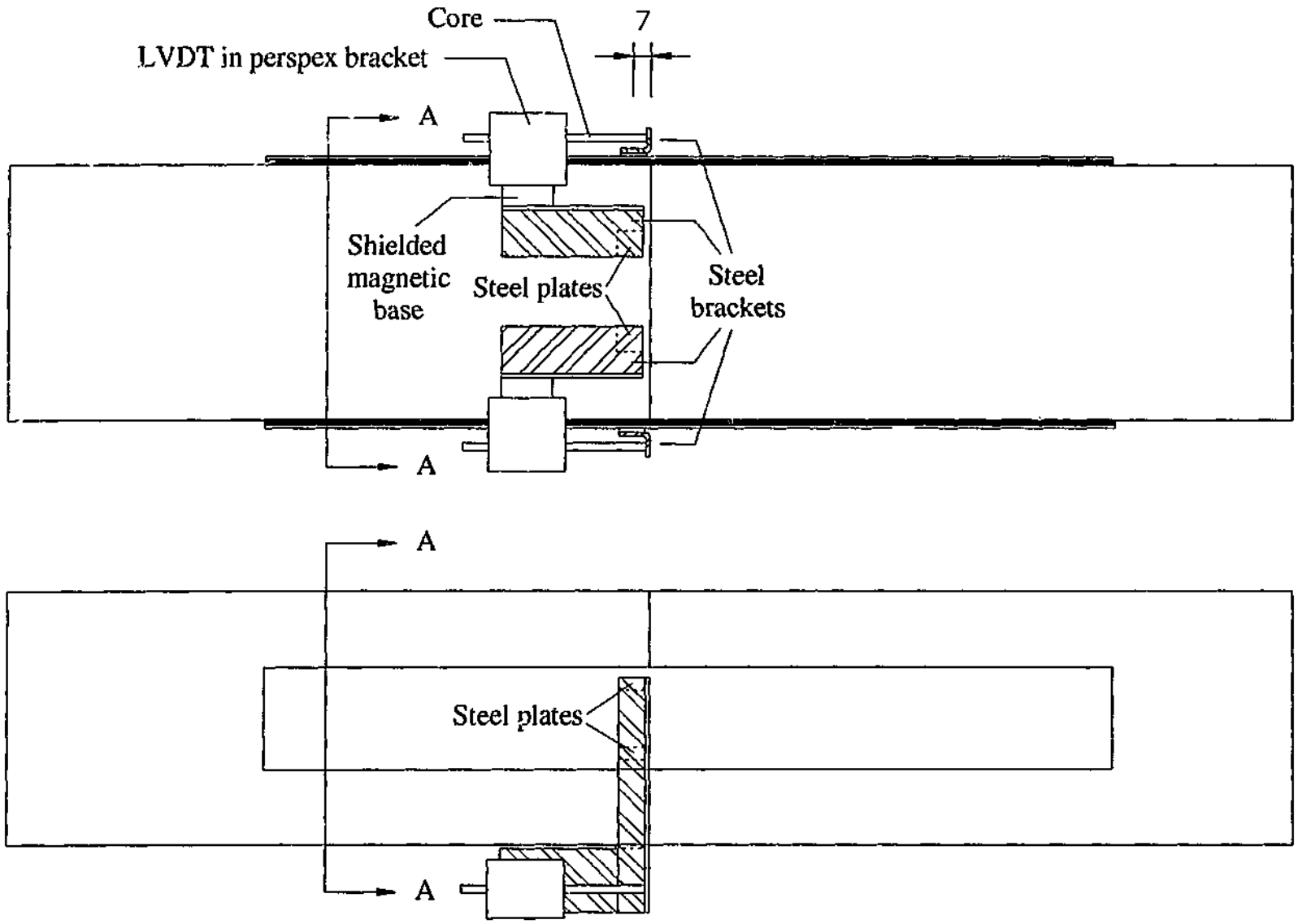

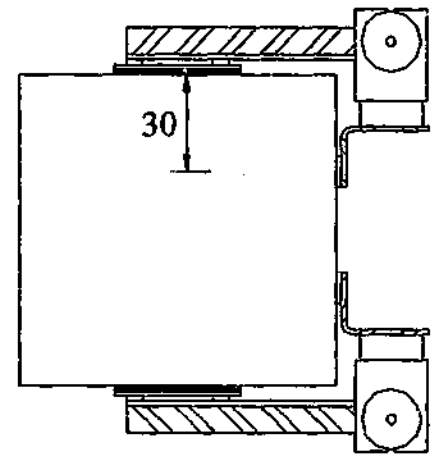

Section A-A

Figure 3.7 - Slip measurement set-up for bond specimen

3.5 Material properties

3.5.1 Concrete

The concrete for the bond specimens was designed to have a 28-day mean compressive strength of 25 MPa with a design slump of 80 mm. The maximum aggregate size of the concrete mix was 14 mm. The specimens were cast under laboratory conditions and cured under plastic cover in steel formwork for one week before removal. The specimens were then allowed to cure in air under indoor laboratory conditions for at least three weeks before testing. Concrete cylinders 100 mm diameter by 200 mm high were cast concurrently for determination of the compressive strength of the bond specimens at the time of testing. The cylinders were stripped after 24 hours and cured in a water bath for one week. The cylinders were then removed from the water bath and cured in air under indoor laboratory conditions until the time of testing.

3.5.2 Steel reinforcement

Twelve millimetre diameter deformed steel bars with minimum yield strength of 400 MPa (Y12) were used to ensure that the reinforcement bars do not yield or slip from the concrete during testing. The expected maximum stress in the bars was 380 MPa, which corresponded to approximately 43 kN. The specimen was gripped along the full length of the 150 mm overhanging bars to prevent any slippages from the test grip.

3.5.3 Sika CarboShear L Plates strengthening system

The Sika CarboShear L Plates strengthening system used in the study was developed by Sika AG (Switzerland) Pty. Ltd, a global company specialising in the fields of chemicals for construction and industry. The material system consists of 2 components, pre-fabricated CFRP L-shaped plates and structural adhesive.

The CFRP L-shaped plates consisted of ten layers of carbon fibres aligned longitudinally held together in a durable epoxy-based thermoset matrix. The nominal width of the plates is 40 mm with a thickness of 1.2 mm. The plates have a 90° bend with an internal radius of 25 mm. Both sides of the plates have a peel-ply layer with no release agent designed to protect the surfaces from chemical contamination. This

system removes the need for abrading the plate to prepare the surface or using solvents on site for cleaning the surface. In this study, the L-shaped plate type "4/20/50" was used with the numbers "20/50" representing the leg lengths of 200 mm and 500 mm respectively (Figure 3.8). In the bond specimens, flat CFRP plates of the required length were cut from the L-shaped plates using a guillotine.

The structural adhesive, SikaDur 30 Normal, is a solvent free, two component epoxy resin based adhesive. It is made of bisphenol A resin with a polyamine based hardener and inert fillers. In the present study, the material properties of the adhesive system have not been determined experimentally.

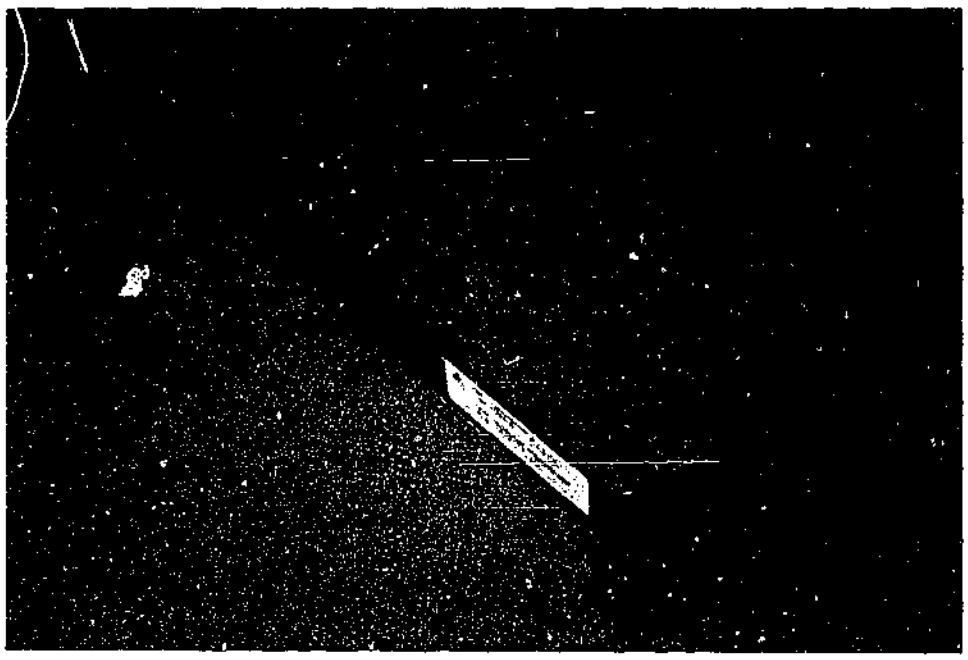

Figure 3.8 - Sika CarboShear L Type 4/20/50

3.6 Specimen fabrication

The bond specimens were fabricated using 500(L) x 100(H) x 100(B) mm steel moulds. A steel plate was secured at mid length of the mould to create two separate concrete blocks. The steel plate also served to hold the deformed bars in position during casting of concrete. Surface preparations were carried out on the concrete specimens approximately two weeks after casting. High-pressure water jet was used to remove a thin layer of concrete to expose the aggregates. The operating pressure was 4000 psi (28 MPa). The specimens were then left to air-dry under laboratory conditions for at least one week. Prior to application of the CFRP plate, loose particles and dust were removed from the concrete surface with pressurised air

and an industrial vacuum cleaner. The specimens were laid on a flat surface and the faces where the blocks meet up were coated with a thin layer of grease. This prevents the adhesive from bonding the two blocks together. Adhesive was applied to both the concrete surface and CFRP plates. The CFRP plate was then pressed lightly against the concrete surface. The CFRP plates were positioned centrally along the width of the specimens with the aid of a ruler. To ensure failure occurred at one side of the specimen, the length of the CFRP plate to be bonded to the other side was longer. Using a roller, light pressure was exerted until excess adhesive was pressed out on both sides of the plate. Two circular steel guides welded to both sides of the roller ensured that the thickness of the adhesive layer was maintained at 3.5 mm throughout. Excess adhesive was then removed using a spatula. The adhesive was left to cure under laboratory conditions for at least seven days before testing was carried out on the specimens.

3.7 Experimental set-up and testing

The specimens were tested in a 120000 lbs (534 kN) Baldwin universal testing machine. The specimens were secured in position by means of wedge grips that 'bite' into the deformed bars at the top and bottom crossheads. Figure 3.9 ilustrates the test configuration for the bond specimens. Loading was applied by means of a fixed displacement rate of 0.5 mm per minute until failure occurs. During testing, readings were recorded once every second.

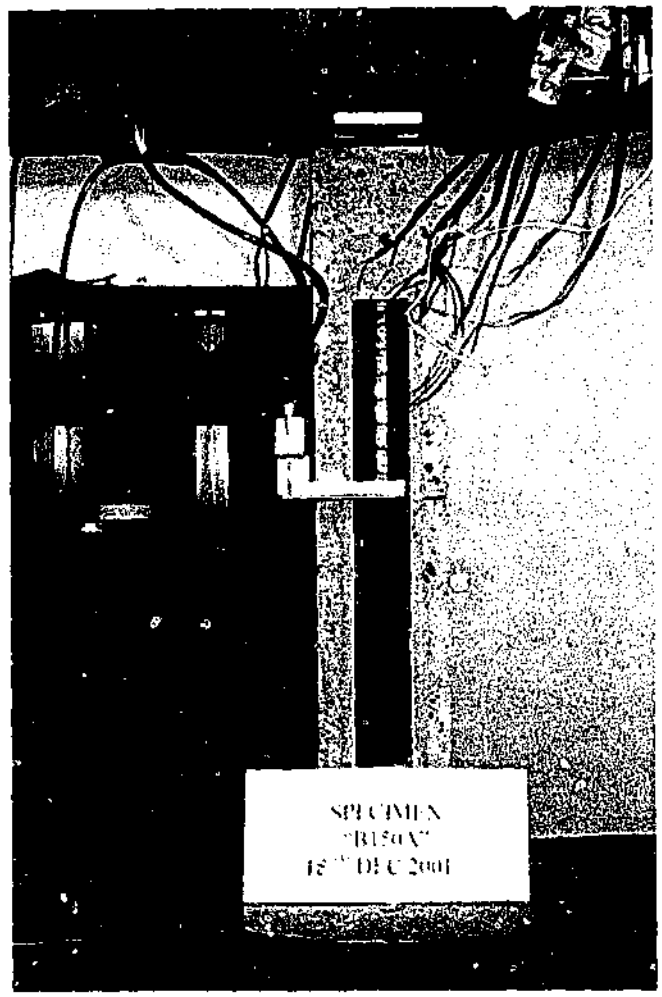

Figure 3.9 - Set-up of bond specimen

3.8 Experimental results

3.8.1 Concrete strength

Compressive tests were carried out on the concrete cylinders for the bond specimens in accordance to Standards Australia, SAA (1999). The average compressive strength of the cylinders at the time of the bond specimen tests are given in Table 3.3. Slight variations in the compressive strength were reported despite the fact that the same concrete mix design had been used. Nevertheless, the compressive strengths across the cylinders were comparable to each other. The average concrete compressive strength was approximately 30 MPa. The strength of the actual bond specimens may vary slightly from the results reported here due to difference in size and curing conditions. In the numerical models of the bond specimens, a range of compressive strength was investigated.

3.8.2 Sika CarboShear L Plates strengthening system

Tension coupons were prepared from the L-shaped CFRP plates to determine the tensile elastic modulus along the longitudinal direction. The tests were carried out in accordance to ASTM (1995). Table 3.2 sets out the results from the tests. The values obtained herein were consistent with the value reported by EMPA (1998a). They reported a tensile elastic modulus of 139900 MPa. Measurements taken prior to each test indicated that the average width and thickness of the CFRP L-shaped plates were 41.71 and 1.31 mm. Independent tests to determine the properties of the adhesive were not performed. According to the technical data provided by the manufacturer, the pot life is approximately one hour at 25°C with the epoxy reaching its design strength after 7 days. The specified tensile strength and flexural modulus are approximately 30 MPa and 12800 MPa respectively. Further information on preparation of the coupons and the tensile tests is contained in Appendix A.5.

Table 3.2 - Tensile Modulus of L-shaped CFRP plates

Sample No.	Tensile elastic modulus (MPa)
1	135667
2	138714
3	136714
4	138286
Average	137345

3.8.3 Failure mode

All of the specimens failed due to the three-dimensional fracturing of concrete at the loaded end. The failures were sudden and brittle due to the separation of a triangular prism from the main block. Figure 3.10 (c) and (d) illustrates the specimens B95I and B150II after failure has occurred. It can be observed from the figure that the concrete edge had fractured at one edge and the joint completely debonded along the entire length. A layer of concrete attached to the CFRP plate had debonded from the main block. All of the specimens except for B50I, B50II, B75I and B93I failed in a similar manner. For the latter, the concrete fractured at the inside end of the joint as illustrated in Figure 3.10 (a) and (b). The CFRP plates were observed to be undamaged in all of the specimens.

In every specimen except for B93II, B150I and B200II, the concrete fractured at the block with the shorter bond joint. In specimen B93II, the bond length on one block of the specimen was only slightly longer that the bond length on the block where failure should occur. Therefore the ultimate load bearing capacities of both blocks were similar. In the case of specimens B150I and B200II, the bond lengths on one block were significantly longer than the bond lengths of the other block. However, the joint lengths on both blocks were longer than the effective bond length for the configuration used in the present investigation. The implication of this was that the ultimate load bearing capacities of both blocks of each specimen were similar. Since failure in the specimens was due to concrete fracturing, the failure path was dependent on the weakest portion in the concrete block. For these specimens, it was at the concrete block with the longer bond joint.

The shape of the fractured concrete prism was similar across all the specimens but the size varied considerably, even in specimens with the same bond length. Observation of the crack pattern indicated a lack of trend between the size and bond length. The arrangement of aggregates in the concrete matrix varied significantly from specimens to specimens. As a result, the fracture path was different due to its dependency on the arrangement of the aggregates. The average dimension of the fractured concrete at the loaded edge is 42(L) by 37(B) mm. Measurements were taken at the side of the specimen without the CFRP as illustrated in Figure 3.10 (d).

(a)

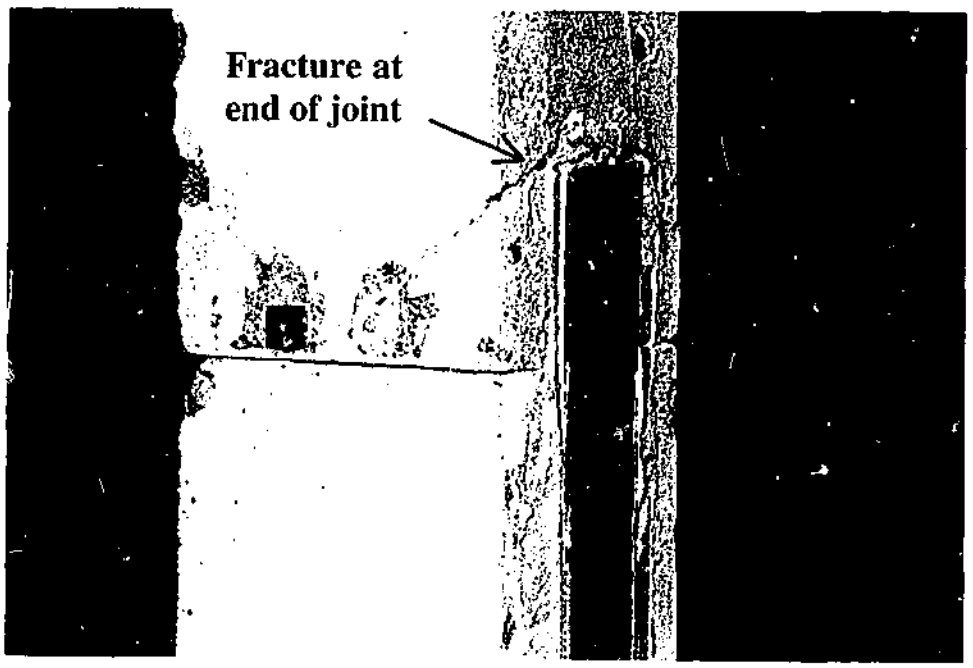

(b)

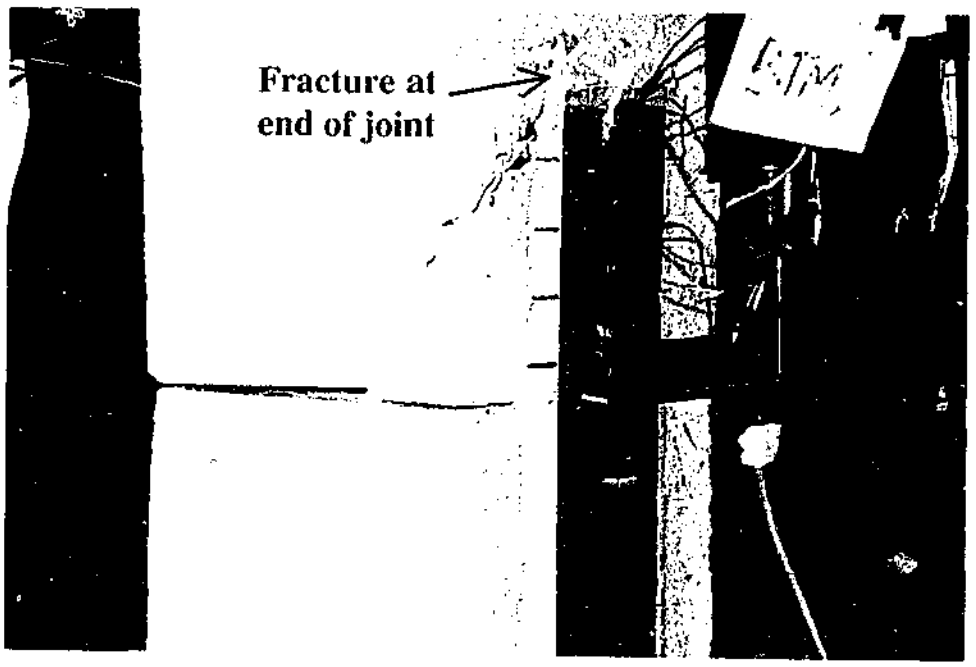

(c)

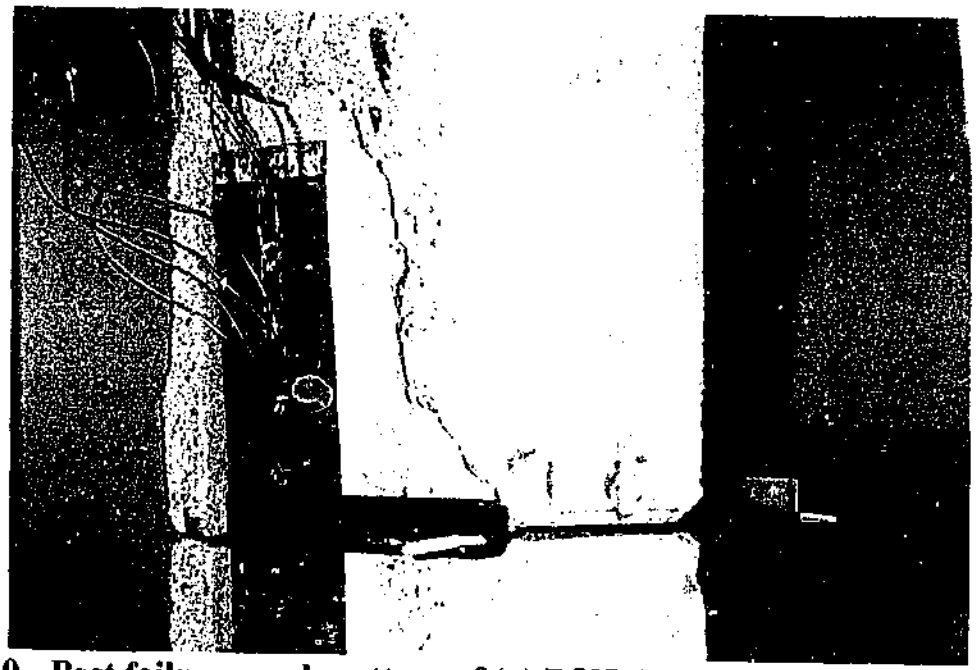

Figure 3.10 - Post failure crack pattern of (a) B50I (b) B75I (c) B95I (d) B150II

(d)

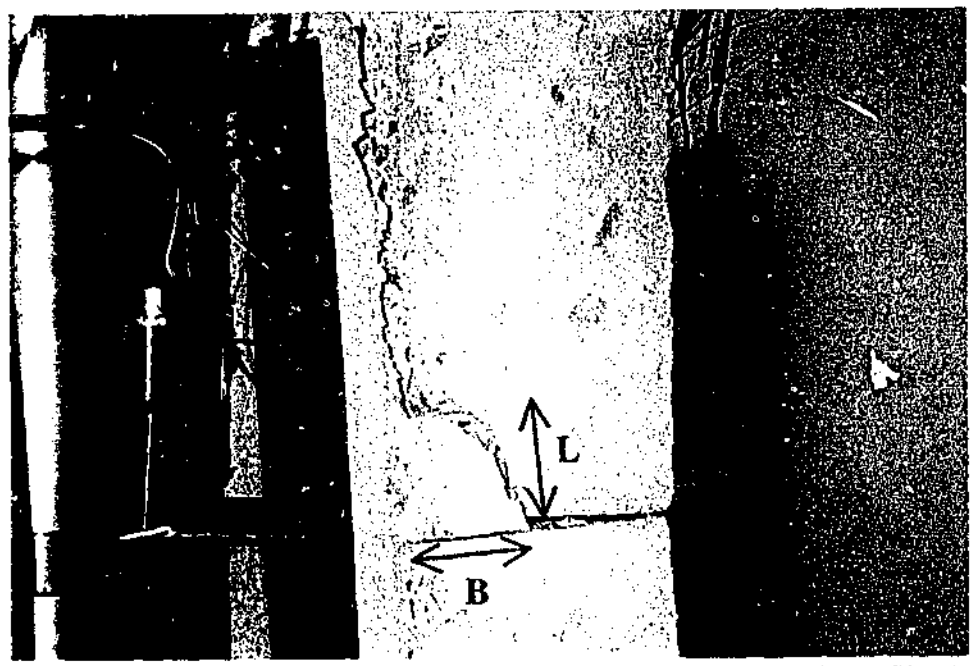

Figure 3.10 (continued) - Post failure crack pattern of (a) B50I (b) B75I (c) B95I (d) B150II

3.8.4 Bond strength of joints

The failure load and average bond stress at failure of the specimens are tabulated in Table 3.3 and summarised graphically in Figure 3.11 and Figure 3.13. Although failure had occurred in the longer joint in some specimens, the shorter joint lengths had been adopted in the figures for all the specimens. Referring to Table 3.3, it can be observed for some specimens that the failure loads of specimens with a lower concrete strength were slightly higher than the failure loads of specimens with a higher concrete strength. The differences in concrete strengths are insignificant and the differences in failure loads were simply experimental scatter.

It can be observed from Figure 3.11 that the failure load increased almost linearly from the 50 to 95 mm bond lengths. Beyond 95 mm, the failure load began to level off with no increase observed for the longer bond lengths of 150 and 200 mm. Therefore, the effective bond length lies between 95 and 150 mm. Using a simple bilinear fit to the experimental results, the effective bond length was approximated to be 120 mm for the particular CFRP-concrete joint studied herein. The experimental results of Chajes et al. (1996) have been reproduced in Figure 3.12 for comparison with the present study. The experimental results obtained herein exhibited a similar trend to those obtained by Chajes et al. (1996). In their study, Chajes et al. (1996) used one inch (25.4 mm) wide CFRP plate with elastic modulus of 15.73 x 10^6 psi

(108400 MPa) with concrete strength of 5283 psi (36.4 MPa). The effective length was reported to be approximately 3.75 in (95 mm).

The average bond stresses at failure of the specimens are illustrated and compared in Figure 3.13. The average bond stress was calculated using the total bond area of the joint. It can be seen that the average bond stress at failure decreases fairly linearly with increases in the bonded length. This is due to the fact that the entire bond is not utilised for longer bond lengths while the failure load remained the same. This trend is consistent with the trend reported by Chajes et al. (1996). The result reported by Chajes et al. (1996) is illustrated in Figure 3.14. The values of average bond stresses at failure were lower compared to the values of average bond stresses reported in the present study. The CFRP plate used in the present investigation had a higher stiffness, thickness and width.

Table 3.3 - Failure load and average bond stress of bond specimens

Specimen	Cylinder compressive strength (MPa)	Failure load (kN)	Average bond stress at failure (MPa)	Location of failure
B50I	33.1	18.5	8.9	S
B50II	28.9	21.2	10.2	S
B75I	28.9	25.9	8.3	S
B75II	33.1	25.7	8.2	S
B75III	28.9	27.0	8.6	S
B93I*	28.9	28.1	7.2	S
B93II	29.3	28.4	7.3	L
B95I	28.4	34.3	8.7	S
B97I*	33.1	33.9	8.4	S
B150I	28.4	40.1	6.4	L
B150II	28.4	40.8	6.5	S
B200I	28.4	41.4	5.0	S
B200II	28.4	40.7	4.9	L

* Specimen not instrumented with strain gauges or LVDTs, S - short bond joint, L - long bond joint

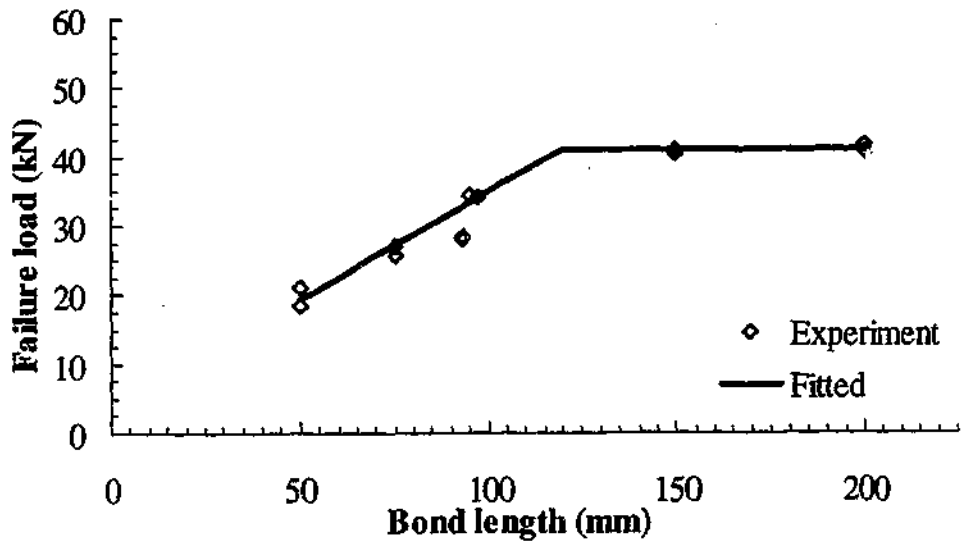

Figure 3.11 - Failure load with different bond lengths

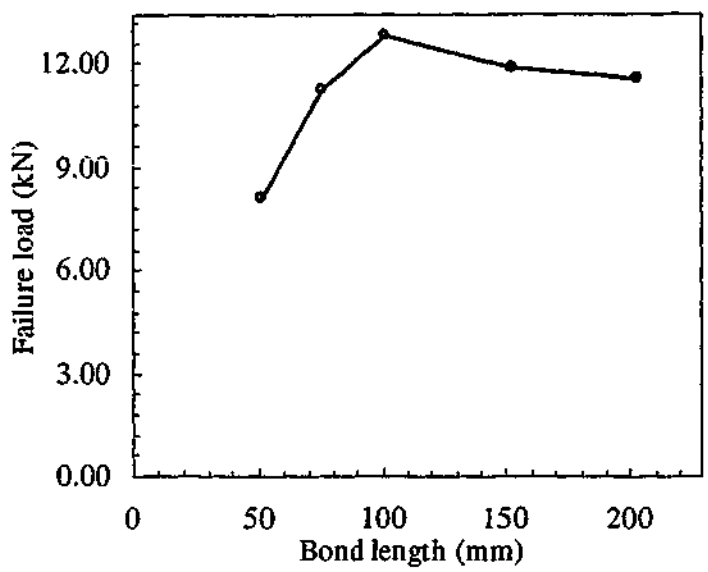

Figure 3.12 - Failure load versus bond length (Chajes et al. (1996))

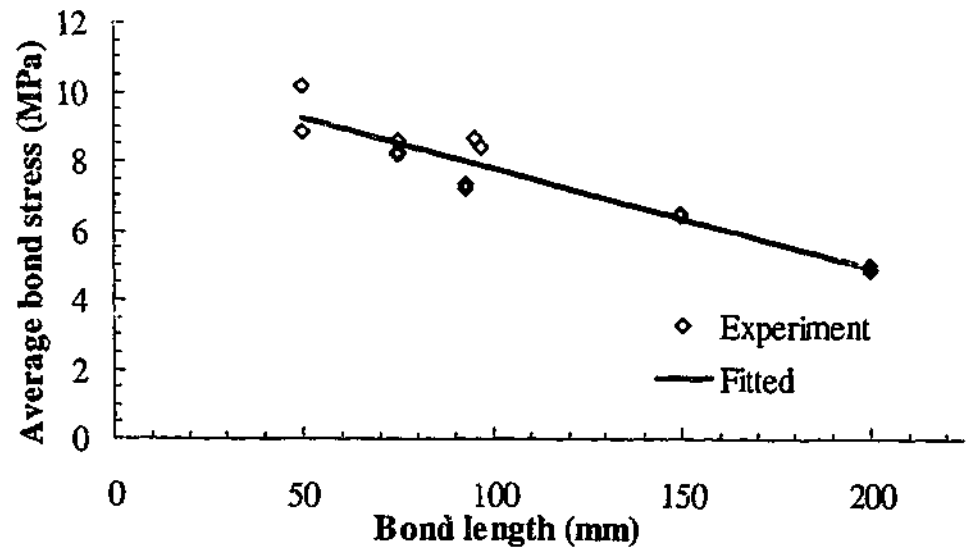

Figure 3.13 - Average bond stress at failure with different bond lengths

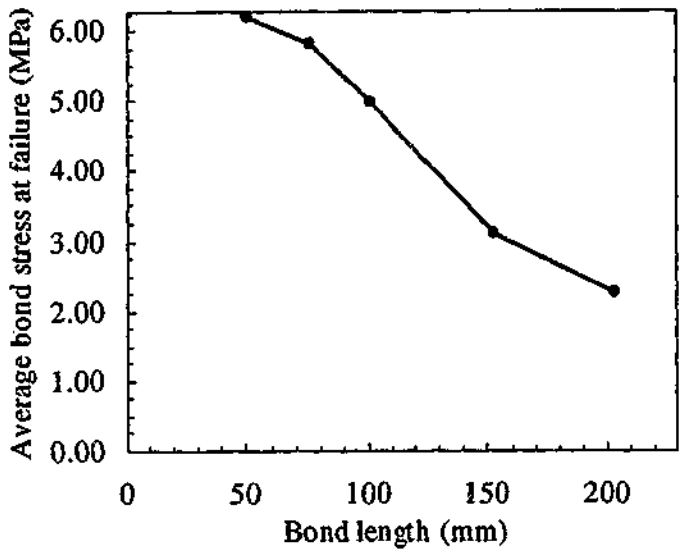

Figure 3.14 - Average bond stress versus bond length (Chajes et al. (1996))

3.8.5 Strain and shear stress distributions along bonded joints

The strain distributions along the length of the bonded joints measured at the CFRP plates are illustrated in Figure 3.15 to Figure 3.17. The strain distributions at different load levels are presented for each plot with each discrete data point representing the strain in the plate at the location of a strain gauge. It should be noted that the strain values obtained were average strains measured along the gauge length of the strain gauges, which was six millimetres. In the plots, the load corresponds to the total load carried by the specimen. The distance was measured in the direction from the edge where the concrete blocks meet, taken as zero, towards the end of the block. Only the results of the specimens where failure had occurred on the block with the shorter bond lengths are presented. The strain distributions shown in the figure correspond to readings measured at the CFRP plate on the side where failure had occurred.

At loads below or at service load levels, as expected, the strain in the CFRP plate is highest at the edge of the bond gradually decreasing with distance along the joint. In all of the bond lengths except for 50 mm, the strain distributions show an exponential curve at the early stages of loading. Due to the length of the joint, there were insufficient data points on the 50 mm bond lengths to determine the shape of the strain distribution curve. Beyond the service load levels, the curve gradually becomes horizontal at the beginning of the joint with increasing loads, which indicates the initiation of cracking in the concrete layer. The CFRP plate had begun to debond

from the main block and there is no load transfer from the CFRP plate to the concrete layer at this portion of the bond. This observation is evident for all of the bond lengths except for 50 mm at the failure load. In the 50, 75 and 95 mm bond lengths, the strain distribution curves shift upwards with increasing load levels with the curves becoming steeper (decreasing slope) at locations where the bond is still intact. Although not obvious from the plots, the curves are shifted gradually to the right, which indicates the shifting of the area for active bonding towards the unloaded end. For the 150 and 200 mm bond lengths, the shift in the curves with increasing load levels can be seen clearly. The debonded lengths were significant indicating a more progressive failure compared to the shorter bond lengths. At the ultimate load, the strain distribution shows combination of a linear and exponential curve. The trends observed herein were similar to the trends reported in past studies.

The effective bond length of the CFRP-concrete joint can be approximated from the strain distribution plots of the 150 and 200 mm bond lengths. The maximum strain in the composite plate when shearing failure of the concrete occurred was similar for both specimens at approximately 2370 ¡με. Therefore, the effective bond length must be equal to or less than 150 mm. It was observed that the strain distribution curves were similar for both specimens at different load levels. At the ultimate load, the length of the exponential portion of the curve where load from the CFRP is still transferred to the concrete is similar for both specimens. It has not increased despite the fact that a longer bond length has been used. This length is the effective bond length. From the two plots, the average effective bond length was measured to be approximately 120 mm.

(a)

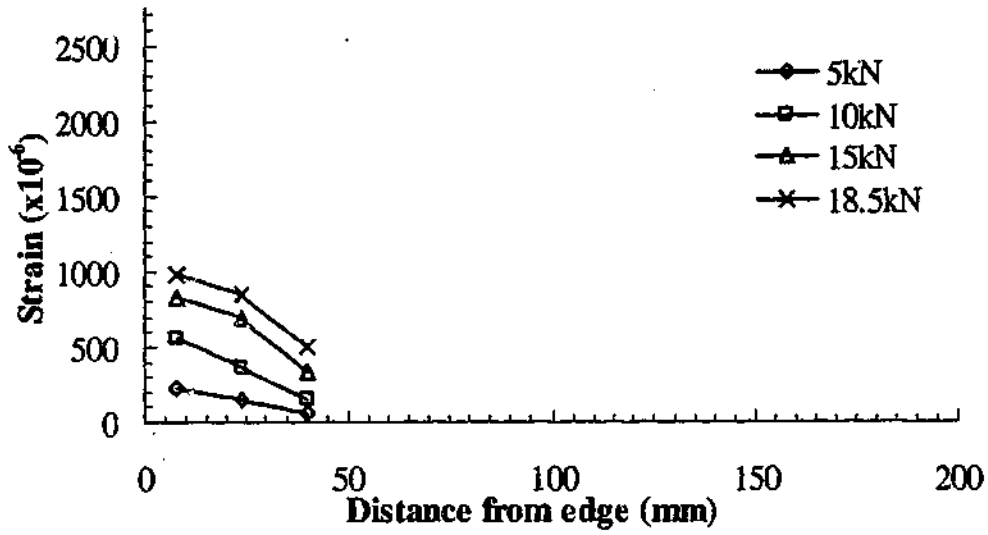

(b)

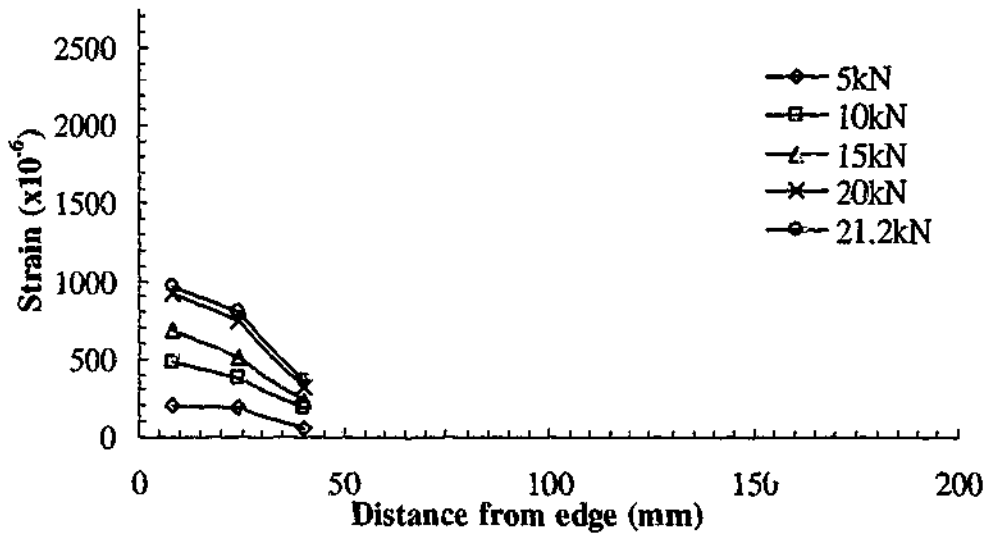

(c)

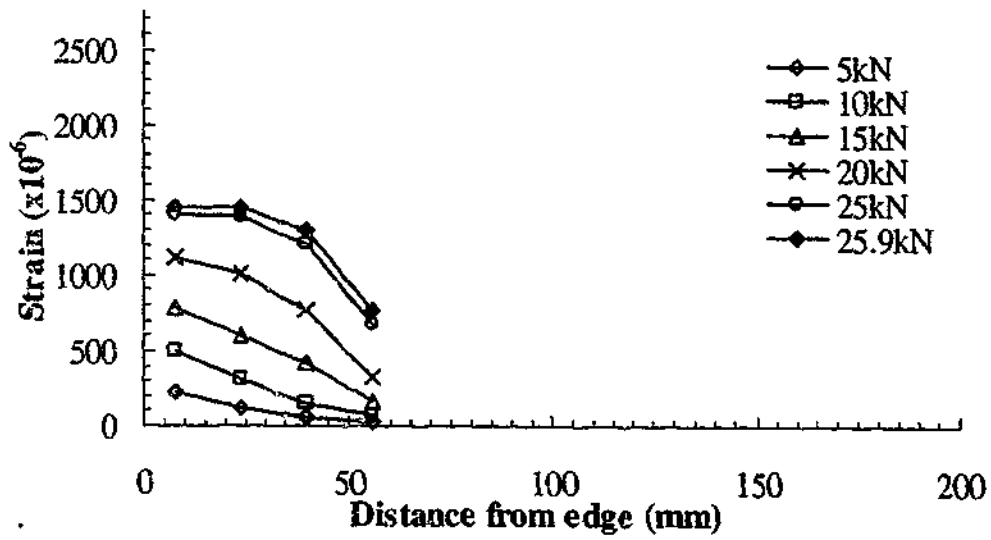

Figure 3.15 - Strain distribution along bonded length for (a) B50I (b) B50II and (c) B75I

(a)

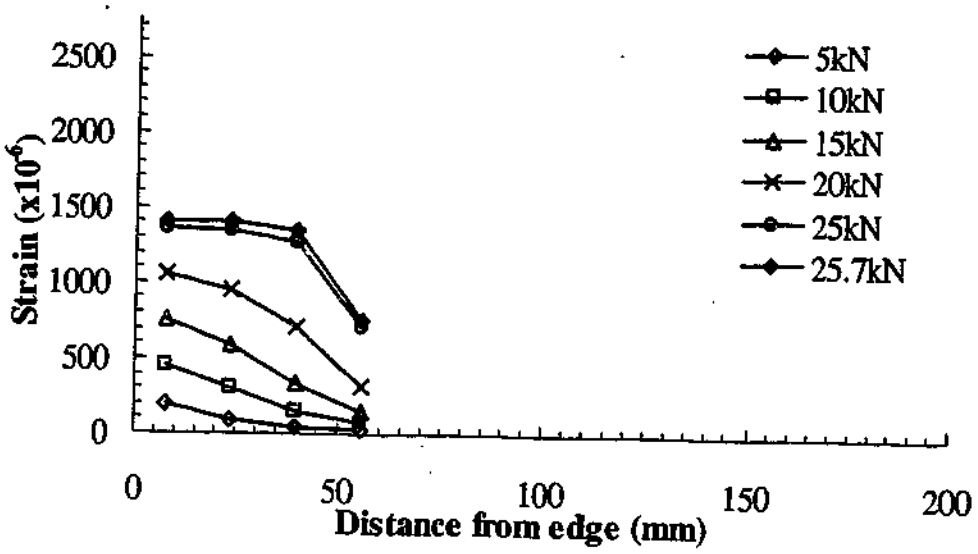

(b)

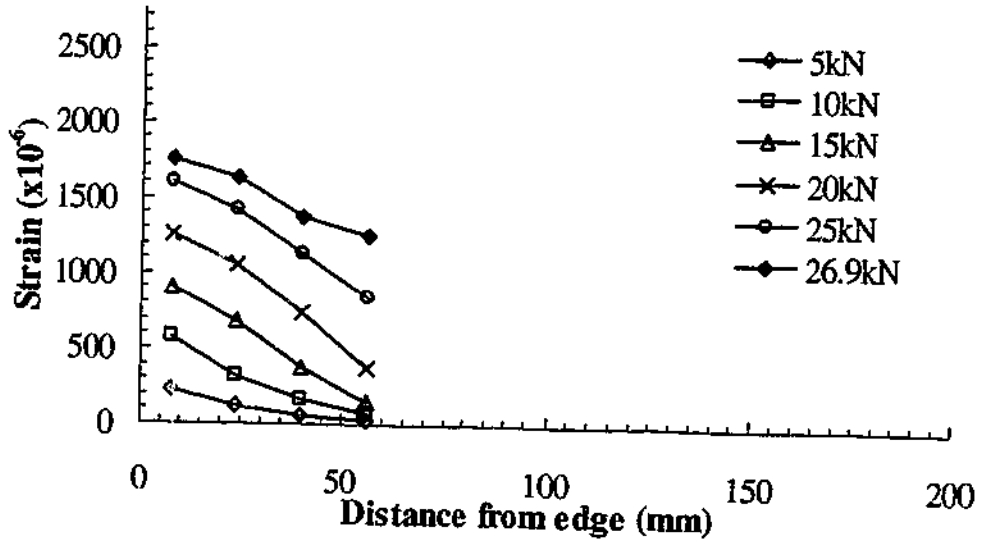

(c)

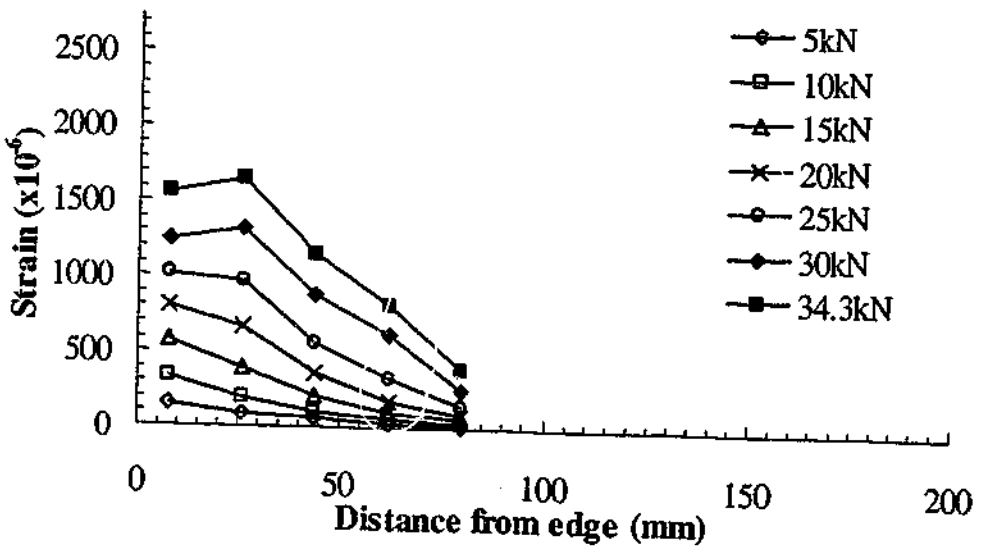

Figure 3.16 - Strain distribution along bonded length for (a) B75II (b) B75III and (c) B95I

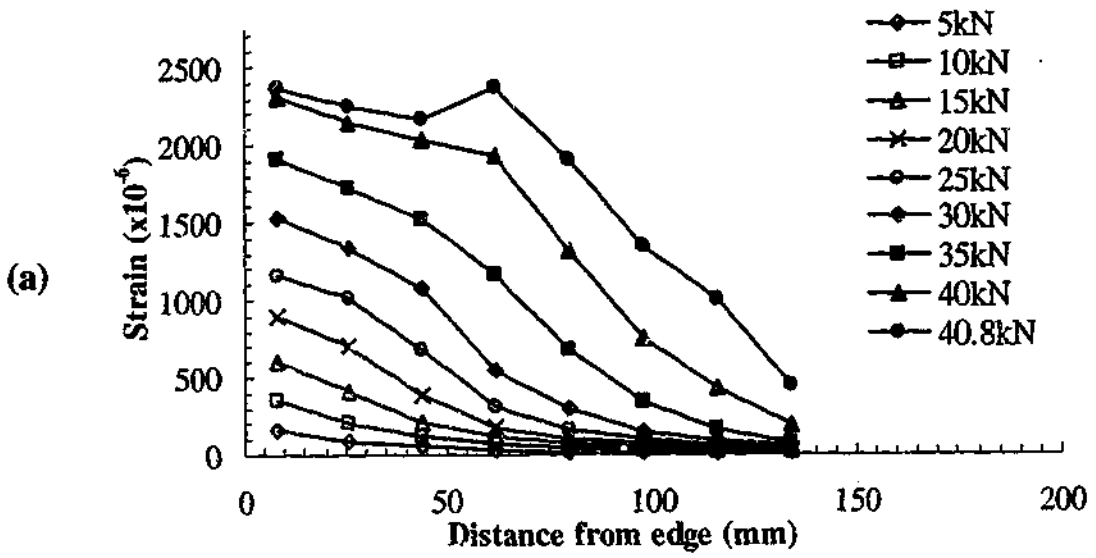

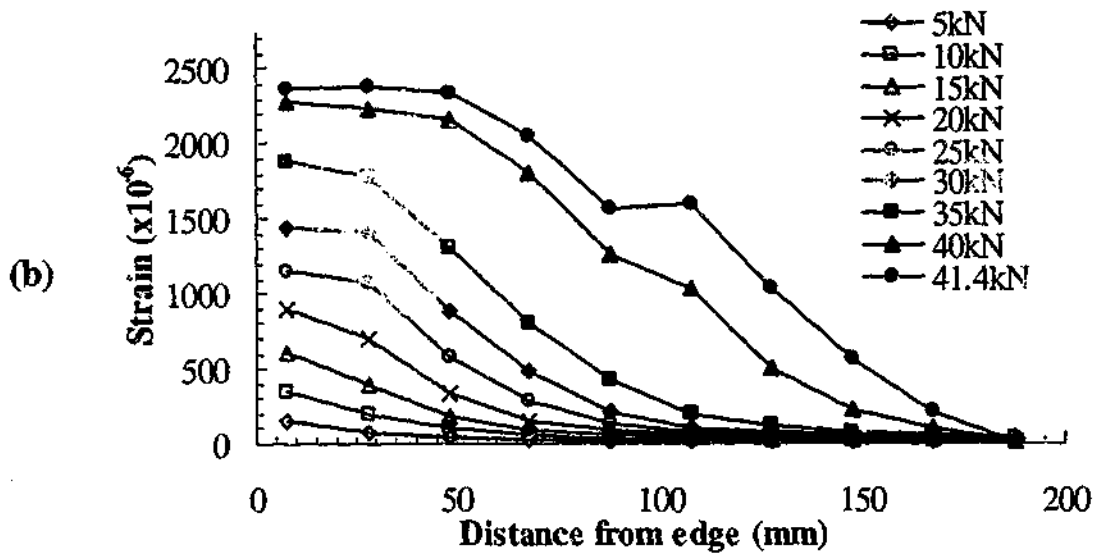

Figure 3.17 - Strain distribution along bonded length for (a) B150II (b) B200I

The mean shear stress between two consecutive strain gauge positions can be computed from the measured strain values. Therefore, the shear stress distribution can be determined from the measured strain profiles along the joint. Assume two strain gauges at positions i and j with the strain readings g_i and g_j at a given time. The distance between the two gauge positions is Δl_{i-j}. The composite plate has an elastic modulus E_{frp} and thickness t_{frp}. Given these properties, the average shear stress τ_{i-j} between the two consecutive gauge positions is calculated using the relationship outlined in Equation 3.1. Proceeding in this way for all the gauge positions, the trend for the shear stress distribution along the bonded joint is obtained.

$$\tau_{i-j} = \frac{E_{frp}(g_i - g_j)t_{frp}}{\Delta l_{i-j}} \qquad (3.1)$$

Figure 3.18 illustrates the shear stress distributions computed from the strain profiles of specimens B150II and B200I shown earlier in Figure 3.17. The average shear stresses computed are plotted as discrete data points at the midpoints between two consecutive gauges. The shear stress distributions for the shorter bond lengths have not been presented because the plots do not illustrate clearly trends immediately evident in the longer bond lengths. Due to the shortness of the joint, the shear stress distributions computed from the strain profiles were distorted. Referring to Figure 3.18, it can be observed from both plots that for loads below the service load levels, the trend is exponential, as expected from the corresponding strain distribution profiles. Beyond the service load levels, when the shear stress at the most highly stressed end exceeds the shear capacity, concrete cracking occurs. At that end, less shear stress is transferred and the maximum shear stress is displaced toward the unloaded end of the specimen as the area for active bonding is shifted.

(a)

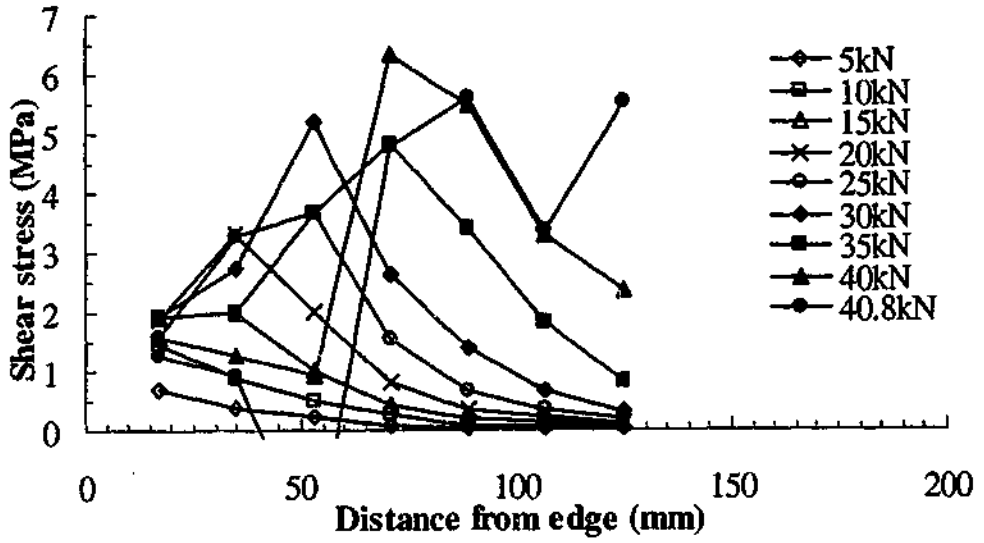

(b)

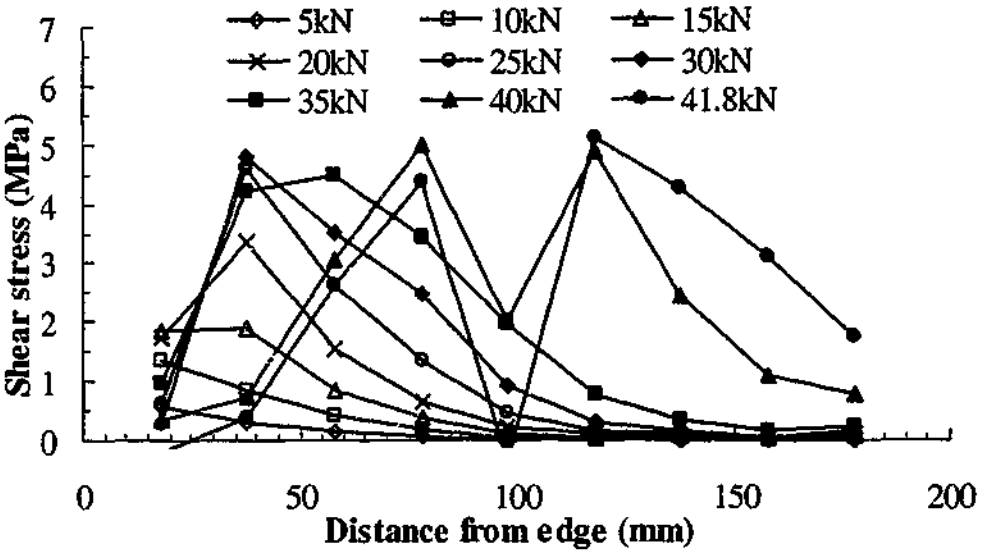

Figure 3.18 - Shear stress distribution along joint at different load levels for (a) B150II (b) B200I

Figure 3.19 to Figure 3.21 shows the development of the shear stresses at various regions of the bond specimens as a function of the relative load level, expressed as F/F_{max}. The term F refers to the current applied load level and F_{max} is the measured ultimate load capacity of the joint. For each region between two consecutive strain gauges, the average shear stresses were computed at various load levels using the corresponding strain values giving the complete shear stress development in that region. In both the 50 mm bond length specimens, the data recorded during testing were 'noisy'. The curves shown in Figure 3.19 correspond to a fourth order polynomial curve fit of the experimental results. In the region near the loaded edge, the plots show that the shear stress reaches a peak and then decreases. At the same time, the shear stress in the adjacent region increases. The decrease of

the shear stress indicates concrete cracking in that region while the increase of shear stress in the adjacent region denotes the transfer of load there. The phenomenon continues from one region to another until the entire length debonds resulting in total failure. It can be observed that the shear stress attained was higher in the region away from the loaded edge compared to the region at or near the loaded edge. As mentioned earlier, this is due to the fact that the concrete is not confined at the loaded edge and therefore, has a lower shear capacity.

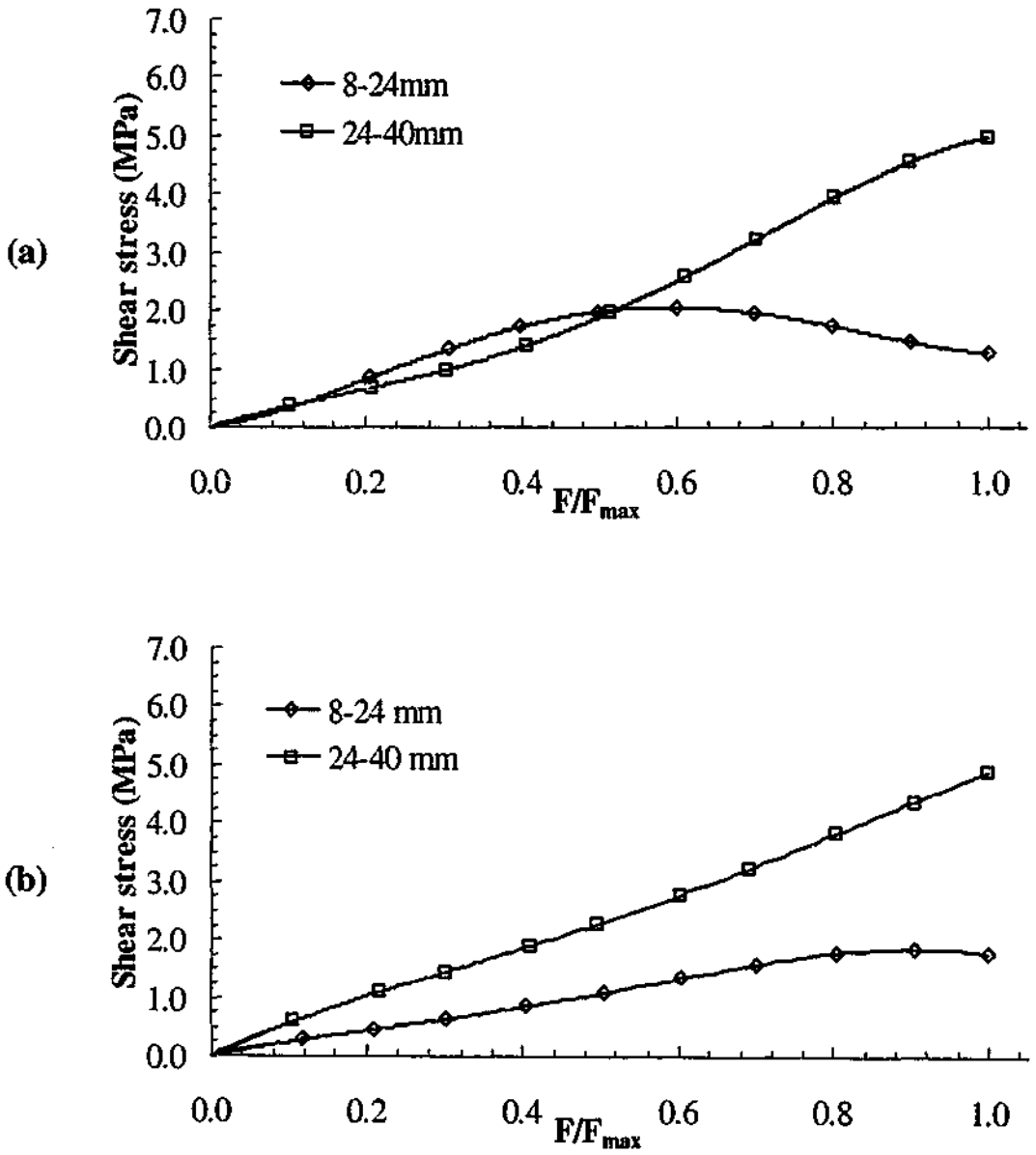

Figure 3.19 - Development of shear stress at different locations along joint as function of relative load level for (a) B50I and (b) B50II

(a)

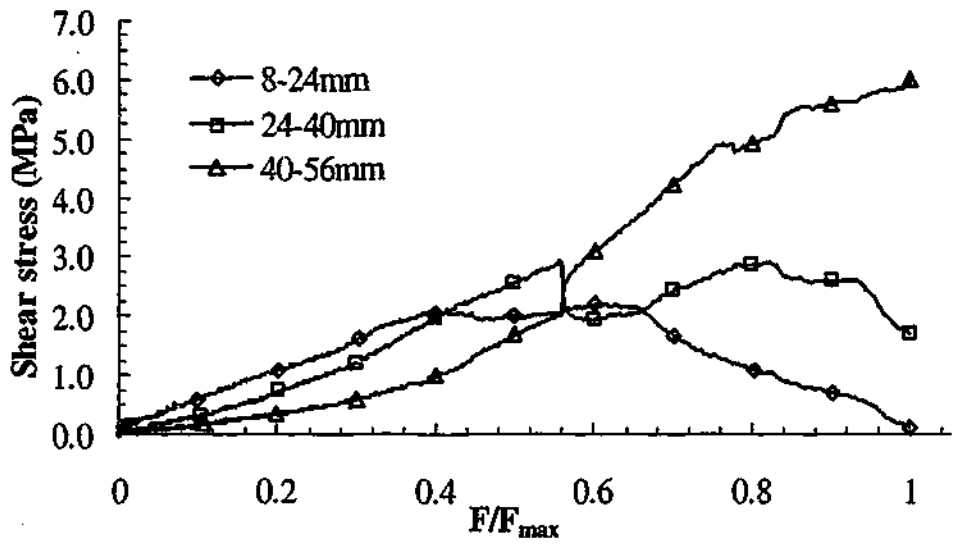

(b)

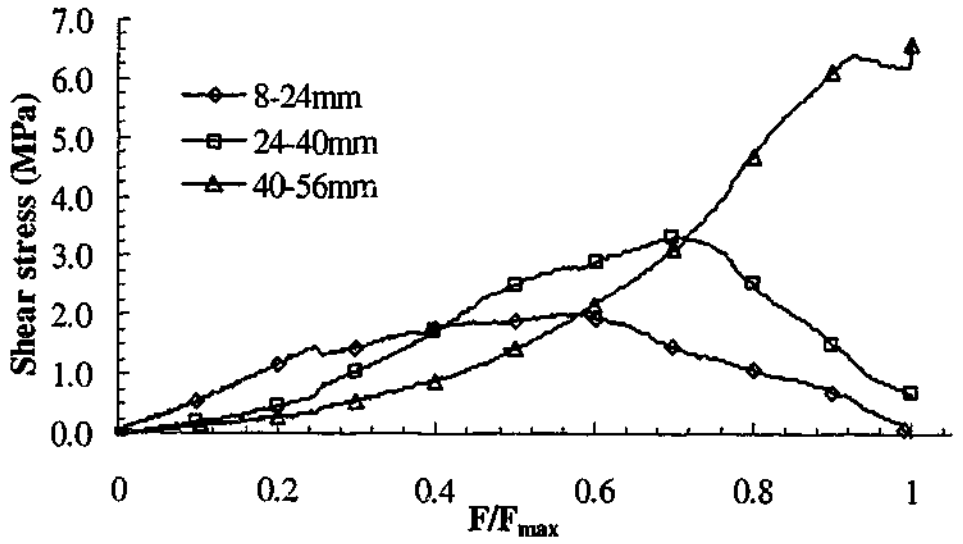

(c)

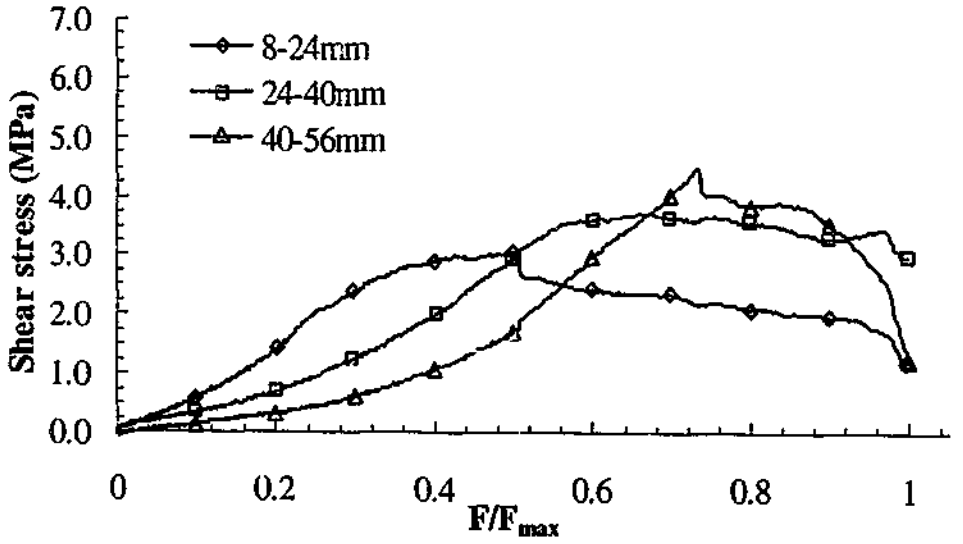

Figure 3.20 - Development of shear stress at different locations along joint as function of relative load level for (a) B75I (b) B75II and (c) B75III

(a)

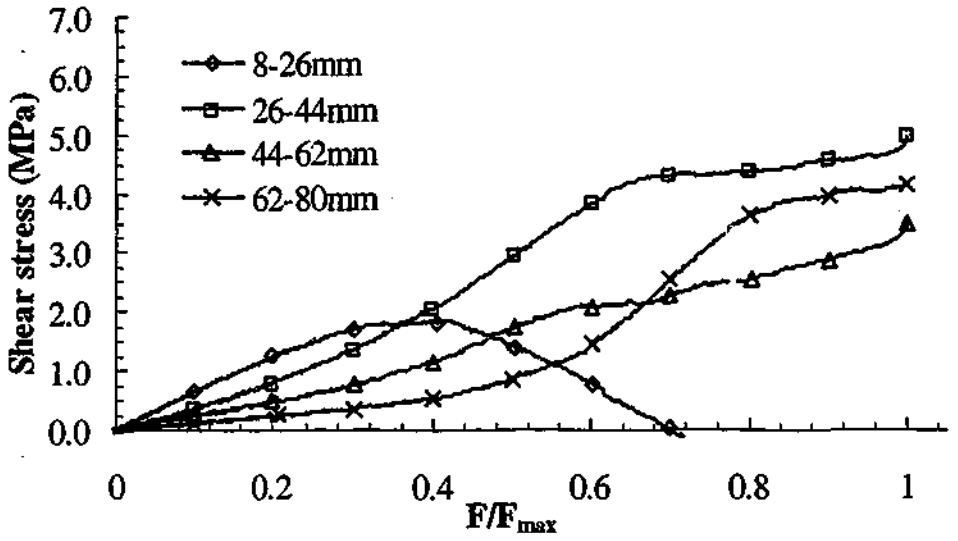

(b)

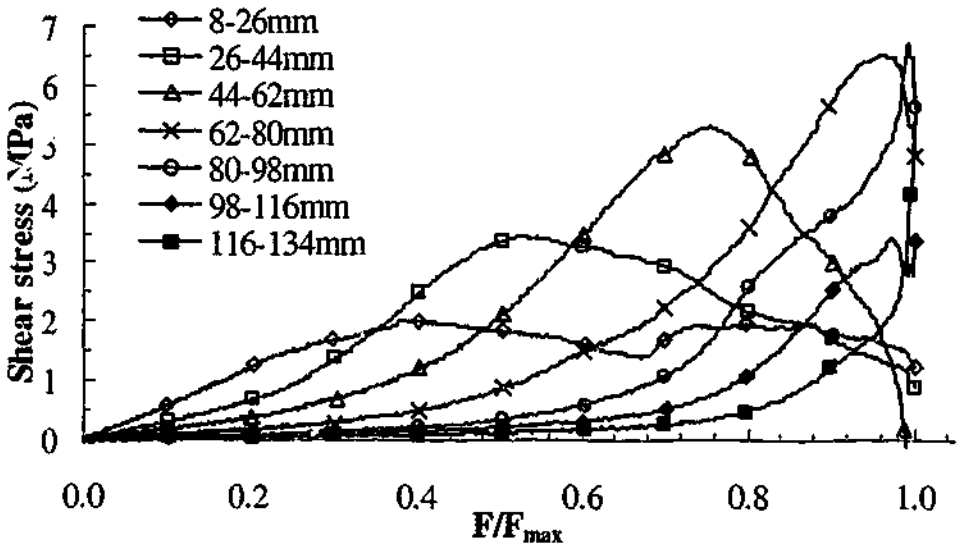

(c)

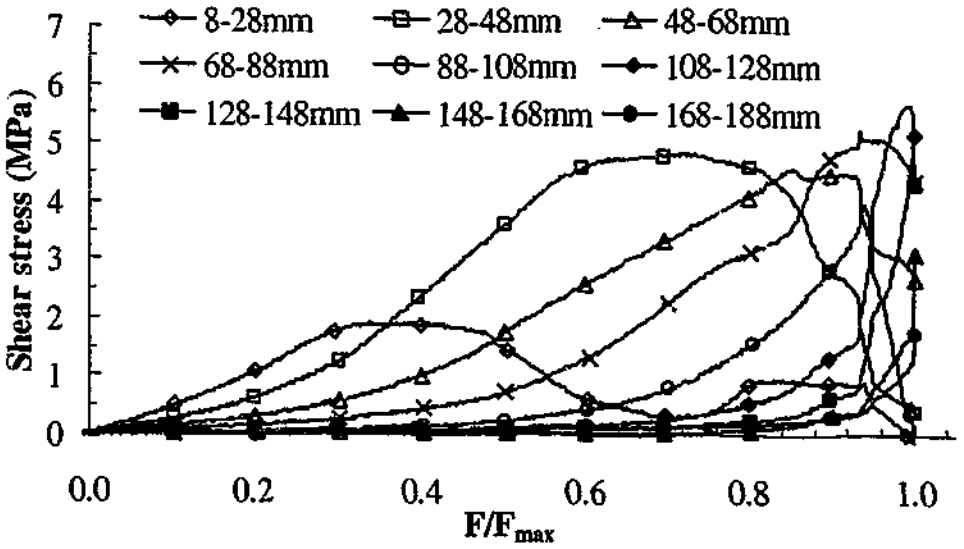

Figure 3.21 - Development of shear stress at different locations along joint as function of relative load level for (a) B95I (b) B150II and (c) B200I

Referring back to Figure 3.15 to Figure 3.17, at the beginning of the bond, there exists a strain level in the bonded plate at which concrete starts to fracture. Täljsten (1997) termed this strain level as the critical strain level, ε_{cr}. The load level at which the concrete begins to fracture is difficult to determine from the experiment since the cracks were too minute to be identified visually before failure. However, it is possible to locate changes in the slope of the strain distribution curve near the loaded end. An increase in the slope of the strain distribution curve near the loaded end indicates the beginning of the formation of a horizontal crack. The critical strain level is, therefore, the strain on the vertical axis of the strain distribution plots at which this change first occurs. An increase in the slope corresponds to a decrease in the shear stress transferred and vice versa. Figure 3.22 illustrates the average shear stress development at the region closest to the loaded edge as a function of the relative load level. In both the 50 mm bond length specimens, the data recorded during testing were 'noisy' and the curves shown in Figure 3.22 correspond to a fourth order polynomial curve fit of the experimental results for these specimens. For each specimen, the relative load level at which the shear stress begins to decrease after reaching the peak can be determined directly from the figure. The strain in the CFRP plate corresponding to this load level is then acquired giving the critical strain level of the specimen. The peak average shear stress near the loaded edge and critical strain level of the specimens are summarised in Table 3.4. The computed peak shear stresses were similar in all of the specimens except for B75III, which gave a higher value. It is most likely experimental scatter. The average peak shear stress near the loaded end is approximately 2.1 MPa. The results show that the critical strain levels were similar in all of the specimens. It ranges from 633 to 872 με with an average of 719 με. In the actual T-beam tests, this value gives an indication of whether the CFRP has begun to debond or not. It should be noted that the shear stress obtained from the readings of the two strain gauges near the loaded end is only an average and not the actual peak of the joint investigated herein. In practice, it is difficult to measure accurately the peak shear stress and the location where it occurs. The gauge length of and spacing between the strain gauges bonded on the FRP should be as small as possible, which increases the instrumentation cost significantly. This may not yield a more accurate result as experimental scatter exists even in identical specimens.

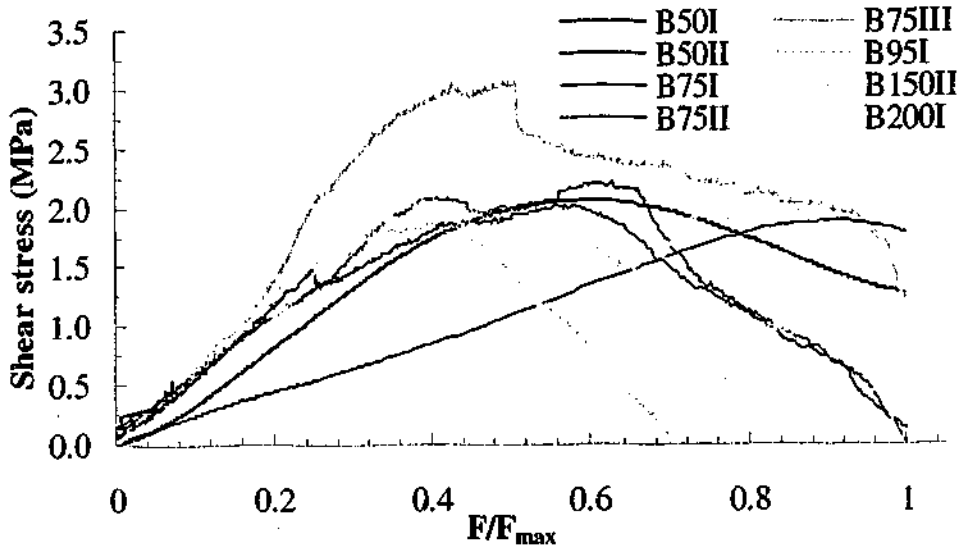

Figure 3.22 - Development of shear stress near the loaded edge for bond lengths of 50, 75, 95, 150 and 200 mm

Table 3.4 - Peak average shear stress near loaded edge and critical strain level of bond specimens

Specimen	Peak average shear stress (MPa)	Critical strain level (με)
B50I	2.1*	633
B50II	1.9*	729
B75I	2.2	872
B75II	2.0	717
B75III	3.0	808
B95I	1.9	667
B150II	2.0	668
B200I	1.9	660
Average	2.1	719

* 4th order polynomial fit of experimental results

3.8.6 Load slip behaviour

The relationship between the applied load and slip of the CFRP plate near the start of the bond is illustrated in Figure 3.23. Here, slip is defined as the relative movement between the CFRP plate and the concrete surface at a particular point. The location where the slip is measured has been shown in Figure 3.7. Similar to the previous plots, only the result of the LVDT mounted at the location where failure occurred is presented. The load in the plots corresponds to the total load applied to the specimen. It can be observed that the stiffness varies between the specimens at the initial stage of loading. However, there is no noticeable trend between bond length and stiffness. In theory, the initial stiffness of specimens with different bond

lengths should be identical, assuming Hooke's law holds true and all of the variables are identical. This is difficult to achieve in the actual specimen due to the variability that exists in the concrete, adhesive and CFRP plate. In general, it can be observed that the longer the bond joint, the higher the slip at failure. Failure was more ductile in the long bond lengths compared to the short bond lengths. The values of slip attained at the peak load in this study were fairly similar to the values reported by Täljsten (1997).

Figure 3.24 illustrates the relationship between the average shear stress near the loaded end and the slip. Although the stiffness varies between the specimens, the general trend was similar. It can be observed that the slip value at which the peak shear stress is reached varies significantly between the specimens. Nonetheless, the peak shear stress is reached when the slip value is between 0.016 and 0.05. Although less precise compared to the critical strain level, this slip range can also be used as an indication of when the CFRP begins to debond in the actual T-beam.

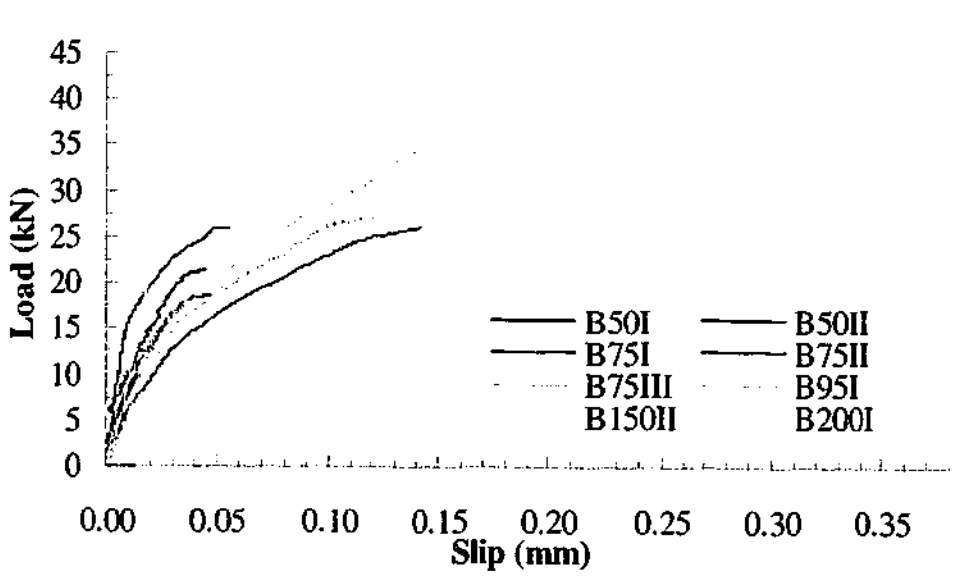

Figure 3.23 - Load slip behaviour of experimental bond specimens

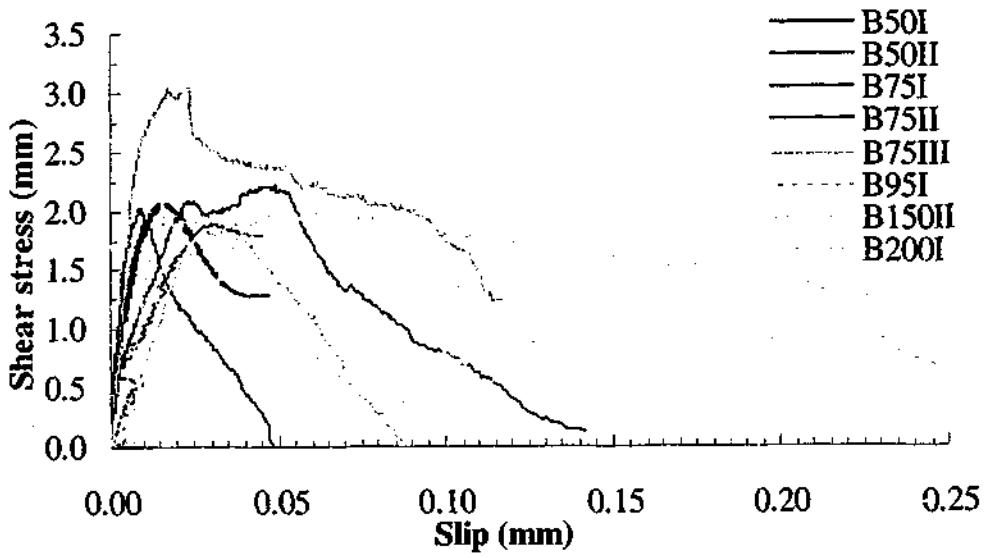

Figure 3.24 - Shear stress development versus slip for bond lengths of 50, 75, 95, 150 and 200 mm

3.9 Summary of findings

Thirteen CFRP-concrete joint tensile specimens of varying bonded lengths were fabricated and tested to failure in the experimental program. The average concrete cylinder compressive strength of the specimens at the time of testing was approximately 30 MPa. Bonded lengths of 50, 75, 95, 150 and 200 mm were investigated. In all of the specimens with bond length of 50 mm and one of the specimens with bond length of 75 mm, failure occurred by fracturing of an entire concrete block at the inside end of the joint. For all the other specimens, failure occurred by fracturing of a concrete block at the start of the bond and complete debonding of the CFRP plate from the main specimen with a layer of concrete still attached to the CFRP plate. The average dimension of the fractured concrete at the loaded edge was 42(L) by 37(B) mm as illustrated in Figure 3.10 (d).

Using simple bilinear curve fitting, the effective bond length of the CFRP-concrete joint is approximated to be 120 mm. In all of the specimens, the strain profile in the CFRP plate along the joint shows an exponential curve at the early stages of loading. Beyond the service load levels, the curve gradually becomes horizontal at the beginning of the joint with increasing loads. At the ultimate load, the strain distribution shows combination of a linear and exponential curve. Near the start of the bond, the computed peak average shear stress was similar in all of the specimens, which was approximately 2.1 MPa. The critical strain levels were similar

in all of the specimens, ranging from 633 to 872 με with an average of 719 με. This value can be used as an indication of whether the CFRP plate has begun to debond or not in the T-beams.

Slip between the CFRP plate and concrete near the start of the bond was measured in selected specimens. It was observed that the longer the bonded length of the specimen, the larger the slip at failure. Failure was more ductile in the long bond lengths compared to the short bond lengths. The slip range at which the CFRP plate begins to debond from the concrete was between 0.016 to 0.05 mm. This range can be used also as an indication of when the CFRP plate begins to debond in the actual T-beam.

CHAPTER 4 - NON-LINEAR FINITE ELEMENT MODELLING OF BOND SPECIMENS

4.1 Introduction and scope

The finite element method (FEM) has become an indispensable tool used in virtually every field of engineering analysis. It provides a powerful and general analytical tool for studying the behaviour of systems in a cost-effective manner. Stresses, strains and displacements at any location on the structure can be obtained at any stage of the loading. From experiments, a general insight into the behaviour of structures can be gained but the amount of information that can be acquired is limited. To measure the stresses and strains of the various components would not be impossible but the instrumentation required would be very costly. Experimental results are still necessary, however, for comparison against the results of the finite element analysis. The finite element method allows important parameters to be varied systematically and conveniently, which greatly reduces the number of costly large-scale tests whilst gaining new insights to the behaviour. In the past, the majority of analyses have been restricted or carried out only in the linear elastic range. In concrete, its non-linear behaviour is due primarily to cracking and time dependent effects such as creep, shrinkage, temperature and loading history. Linear elastic analysis is simply inadequate in describing the complete behaviour of concrete and hence non-linear analysis is required. The trend towards the use of non-linear modelling is increasing as many researchers realise the importance of non-linear analysis particularly in ultimate limit state analyses. An increase in its use has been accelerated with the advent of high-speed and affordable computers.

In the present study, non-linear finite element analyses are used to study the short term bond behaviour of the CFRP-concrete joint outlined earlier. The numerical results are used to supplement the experimental results. Two sets of studies were carried out. In the first set, models with a given set of material properties were generated and analysed to verify whether or not the models are simulating the behaviour of the bond specimens properly. In the second set, selected material properties of the models of the first study were varied and the effects investigated.

The aim was to determine qualitatively the sensitivity of the results with respect to slight variations in the material properties adopted in the first set of analyses. The effect of varying the concrete strength, adhesive stiffness and CFRP stiffness on the peak load, effective bond length, load slip behaviour and strain distribution profiles were investigated. The main aim of the investigation is to use the results and findings of the numerical analyses in the development and understanding of the finite element models of the actual T-beams strengthened in shear. The commercially available non-linear finite element code, DIsplacement method ANAlyser or DIANA (version 7.2), developed by TNO Building and Construction Research in the Netherlands (de Witte and Jansen (2000)), was used to model and analyse the CFRP-concrete bond joint specimen. An in-depth review of the mathematical basis of the finite element method, material model theories and formulations will not be presented.

4.2 Finite element idealisation

The finite element method involves the analytical modelling of a continuous structure that is idealised as an assemblage of smaller discrete elements, interconnected at joints called nodes or nodal points. In its entirety, the elements simulate the behaviour of the real structure but like any other numerical method, it is an approximation with a certain margin of error that is inherent in the method itself. It allows variables to be varied conveniently and systematically greatly reducing the number of costly experimental tests over the full range of variables. Nevertheless, it is necessary to have some test results against which the results of the finite element analysis may be compared.

The first step of finite element modelling is to define the analysis type. Referring to Figure 3.5 where the specimen is illustrated along its full length, loading and deformation occurs mainly within the plane of the specimen and out-of-plane forces are negligible. For simplicity, the specimen is idealised as a plane stress problem. The next step would be to discretize the specimen into the appropriate number and size of elements. Figure 4.1 illustrates the finite element model of the CFRP-concrete bond specimens with bonded length L. Only one quarter of the whole specimen is modelled with the axes of symmetry taken at mid length and height of the specimen. The concrete and CFRP plate are modelled using eight-node quadrilateral

isoparametric plane stress element (CQ16M) shown in Figure 4.2. Each element has sixteen degrees of freedom (dof) with two displacements, u_x and u_y, at each node. A 2 x 2 Gaussian integration scheme is used. The adhesive layer is modelled using the structural interface element (CL12I) shown in Figure 4.3. The element describes a relation between the tractions (a stress), t, and the relative displacements, Δu, across the interface, based on quadratic interpolation and the 4-point Newton-Cotes integration scheme. The Y12 steel reinforcement bar is omitted from the model for simplicity. The thickness of the adhesive layer and CFRP plate in the model is 3 and 1.31 mm respectively. The width of both the CFRP plate and adhesive layer is set at 41.71 mm and the concrete layer at 100 mm. The element size is maintained at or close to 6.5 mm x 6.25 mm for the concrete elements, 6.5 mm x 3 mm for the adhesive layer elements and 6.5 mm x 1.31 mmfor the CFRP plate elements. The aspect ratios (length over height) are kept as close as possible to 1 with a maximum of approximately 5. As illustrated in Figure 4.1, the entire model is supported vertically at the base and horizontally at the edge of the CFRP plate with roller supports. Load is applied by means of a prescribed horizontal displacement. The entire row of nodes at the bottom of the model is displaced horizontally to simulate the loading of the specimen through the steel reinforcement bar. In the model, concrete cracking is based on the smeared model approach.

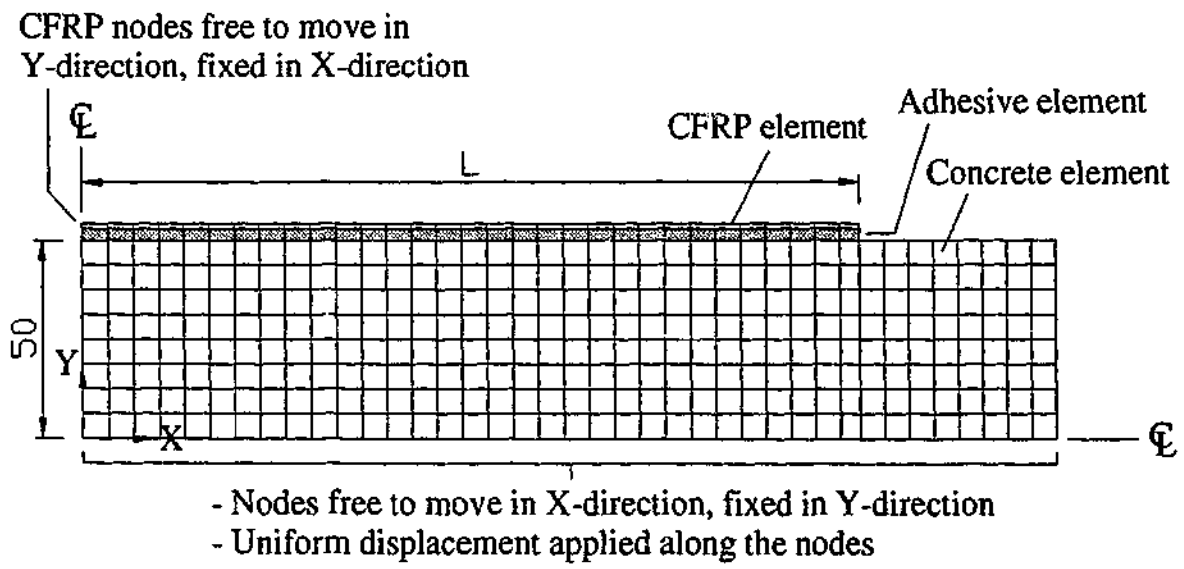

Figure 4.1 - Plane stress finite element mesh of bond specimen

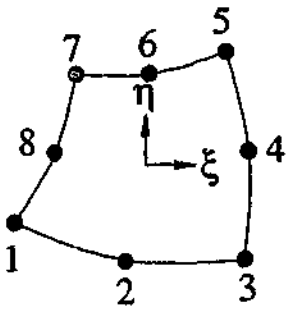

Figure 4.2 - Eight-node quadrilateral isoparametric plane stress element (CQ16M) for concrete and CFRP plate

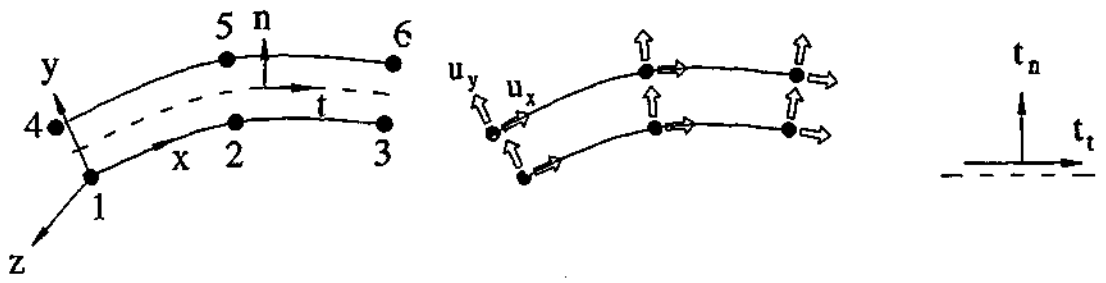

(a) **(b)** **(c)**

Figure 4.3 - 3+3 nodes structural interface element (CL12I) for the adhesive layer (a) topology (b) displacements and (c) tractions

4.3 Material models

4.3.1 Concrete

For the concrete, the constitutive model based on the total strain concept was used to describe the tensile and compressive behaviour with one stress-strain relationship. According to de Witte and Kikstra (2000), the model is developed along the lines of the Modified Compression Field Theory, initially proposed by Vecchio and Collins (1986). In the model, the theoretical description by Selby and Vecchio (1993) was implemented to account for lateral expansion effects in three-dimensional modelling. The models are well suited for serviceability and ultimate limit state analyses that are predominantly governed by cracking or crushing of the material. In the present study, the fixed stress-strain concept was adopted in the analyses in which the stress-strain relationships are evaluated in a fixed co-ordinate system, which is fixed upon cracking. The finite element analyses results were in good agreement with the experimental results. An in-depth review of the formulation of the theory will not be presented.

In the analyses, the input for the model comprises of two parts, the basic properties and the definition of the behaviour in tension, shear and compression. The basic properties consist of the Young's modulus, Poisson's ratio, tensile and compressive strength. The Young's modulus was determined in accordance to SAI (2001) reproduced herein as Equation 4.1. The density of concrete, ρ, was assumed as 2400 kg/m^3. The Poisson's ratio, ν, was taken as equal to 0.2. The tensile strength of the concrete was determined using Equation 4.2, which is essentially a modification of the equation reported in SAI (2001). The concrete compressive strengths of 20, 30 and 40 MPa were investigated.

$$E_c = (\rho)^{1.5} \times \left(0.043\sqrt{f_{cm}}\right) \tag{4.1}$$

$$f'_{ct} = 0.4\sqrt{f_{cm}} \tag{4.2}$$

The behaviour of the concrete in compression is described by the function of Thorenfeldt et al. (1987), the general shape of which is illustrated in Figure 4.4(a). The function models both the hardening and softening behaviour of concrete. The effect of lateral cracking and confinement is disregarded in plane stress analysis.

In tension, the behaviour is based on a bilinear stress-strain relationship illustrated in Figure 4.4 (b). The stress is assumed to increase linearly with strain until the peak, beyond which the stress decreases linearly with strain until zero stress. The area under the descending branch of the stress-strain curve is given by G_f^I / h, where G_f^I is the Mode-I fracture energy and h is the crack band width of the element. The crack band width is related to the area or volume of the element, which is determined automatically in DIANA. The fracture energy is estimated using the relationship reported in CEB-FIP (1993), outlined herein as Equation 4.3. The fracture energy is related to the compressive strength, f_{cm}, and the base value of fracture energy, G_{fo}. The latter depends on the maximum aggregate size, d_{max}, as given in Table 4.1. The term f_{cmo} is given as 10 MPa. In the present study, G_{fo} is calculated as 0.02875 for d_{max} of 14 mm using linear interpolation. According to the model code, Equation 4.3 does not take into account size effects and other concrete properties, resulting in deviations of the computed values of up to ±30%. No

modification was made to the fracture energy value computed using Equation 4.3. The concept of fracture energy is not addressed nor reported in SAI (2001).

$$G_f = G_{fo}(f_{cm}/f_{cmo})^{0.7} \tag{4.3}$$

Table 4.1 - Base values of fracture energy G_{fo}

d_{max} (mm)	G_{fo} (Nmm/mm^2)
8	0.025
16	0.030
32	0.058

In smeared crack models, it is common to represent the shear stiffness of cracked concrete by means of a shear retention factor, β, which indicates the percentage of elastic shear capacity that remains after cracking. This factor is used to account for the effect of aggregate interlock in the concrete. In the current implementation in DIANA, only the constant stiffness reduction model is available, which is given by Equation 4.4 and illustrated in Figure 4.4 (c). In reality, the shear stiffness that remains after cracking is a function of the strain normal to the crack. In the present study, the loading and deformation mechanism of the bond specimens is such that the effect of aggregate interlock is minor. For numerical stability of the finite element models, β is assumed to be 0.05 or 5%.

$$G^{cr} = \beta G \tag{4.4}$$

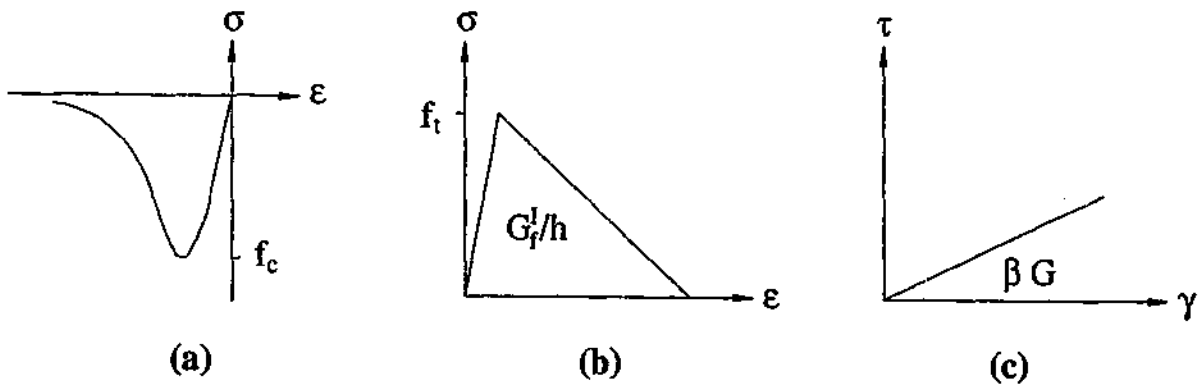

Figure 4.4 - Concrete models in (a) compression (Thorenfeldt et al. (1987)) (b) tension and (c) shear after cracking

4.3.2 Adhesive layer

For simplicity, the adhesive is assumed to be an isotropic material. A linear elastic model is used to describe the relationship between the traction and the relative displacements. This assumption is reasonable since failure occurred by fracturing of the concrete layer. In the finite element model, the input of the linear stiffness moduli, D_{11} and D_{22}, are required. D_{11} sets the relation between the normal traction, t_n, and the normal relative displacement, u_n, and D_{22} sets the relation between the shear traction, t_t, and the shear relative displacement, u_t. The dimension of the stiffness moduli is force per area per length (N/mm^3). D_{11} and D_{22} were approximated using Equations 4.5 and 4.6, where t is the thickness of the adhesive layer. The Poisson ratio of the adhesive is assumed to be 0.37.

$$D_{11} = E/t \tag{4.5}$$

$$D_{22} = G/t$$

$$\text{where } G = \frac{E}{2(1+v)} \tag{4.6}$$

4.3.3 CFRP plate

The CFRP plate is assumed to be an isotropic material and modelled using a linear elastic model. The assumption is valid since failure is governed by the fracturing of the concrete layer and the thickness of the plate is very small compared to its length or width. The Poisson ratio of the CFRP plate is assumed to be 0.35.

4.4 Solution procedure

There are several numerical methods that can be used to solve non-linear problems. In general, the numerical methods can be classified into three categories, which are the incremental, iterative and combined incremental-iterative methods. In the present study, the combined incremental-iterative method is used. In all of the models, load was 'applied' in steps or increments of 0.005 mm initially and then at smaller increments, which were selected subjectively on a case by case basis. At each load step, the modified Newton-Raphson iterative scheme was used to bring the internal forces to an acceptable level of equilibrium. The convergence criterion

adopted is based on the energy norm composed of internal forces and relative displacements indicated by Equation 4.7. A new reference norm was determined at the start of each step. In all of the models, the tolerance for convergence was set to 0.0001 to ensure accurate and good results. The maximum number of iterations for each load step or increment was set to 500.

$$\text{Energy Norm Ratio} = \frac{\left|\delta u_i^T (f_{int,i+1} + f_{int,i})\right|}{\left|\Delta u_0^T (f_{int,1} + f_{int,0})\right|} \tag{4.7}$$

where

δu_i = i^{th} iterative displacement increment

Δu_0 = displacement increment

f_{int} = internal forces

In the finite element models, cracking of concrete is modelled by the smeared cracking method. Consequently, the failure mode observed in the experiment cannot be replicated exactly in the finite element models, making the failure and hence peak load difficult to determine. In all of the models, the criterion for 'failure' of the specimen is initially assumed as the non-convergence of the solution at the step after the structure begins to 'soften'. Here, softening is defined as the decrease in the total load carried by a structure after the peak load has been reached. In the case where non-convergence of the solution occurs at the step where softening occurs, the step size is reduced accordingly and the model analysed again. This process is repeated until the criterion outlined earlier is satisfied. The criterion used in the analyses is based on observations from the experiment where the specimens failed in a brittle manner and exhibited limited softening behaviour (Figure 3.23). In non-linear finite element analyses, non-convergence of solutions indicates either the formation of cracks, steel yielding, concrete crushing or a combination of these effects that can lead to the failure of the structure. In the current investigation, the non-convergence of the solutions is caused by the formation of cracks. For each model, crack patterns at selected load steps leading up to and after the peak load were produced, examined and compared against experimentally observed cracks. If the crack patterns prior to or at the peak load showed similar failure patterns to the experiment, it is a good indication that the peak load has been reached. In the

experiment, failure is characterized by the fracturing of a concrete block at the start of the bond. Referring to Figure 3.10 (d), the dimension L varied from 14 to 93 mm with an average of 42 mm. In the finite element models, the average corresponded to the sixth or seventh element from the start of the bond. The model is considered to have 'failed' when the cracks formed at the sixth or seventh element and the criterion specified earlier is satisfied.

In addition to the previous criterion, irregularities in the load-displacement curves of the models such as sudden drop in load, flattening of the curve and sudden change in the stiffness were examined as well. These irregularities typically indicate the formation of cracks that may or may not cause failure although the solutions show convergence at or beyond this step. In these cases, crack patterns and solutions at the step where the irregularities occurred were logically assessed to determine whether failure has occurred or not.

4.5 Results of non-linear finite element analyses

4.5.1 Verification of finite element models

4.5.1.1 Introduction

To verify the finite element models are simulating the behaviour of the bond specimens properly, four items are compared between the experimental and numerical results. They are the peak load attained, crack patterns at failure, the slip behaviour and the strain distribution along the length of the CFRP plate. Five finite element models, each with similar bond lengths as the experiment, were generated and analysed. The bond lengths of the models were 50, 75, 95, 150 and 200 mm. In Figure 3.11, the effective bond length of the CFRP-concrete joint was approximated using a bilinear fit to the experimental results. In order to determine more accurately the effective bond length, three additional models with bond lengths of 130, 175 and 220 mm were generated and analysed. The concrete strength reported in the experiment varies from 28.4 to 33.1 MPa. For simplicity, a concrete strength of 30 MPa was adopted for the models. The corresponding Young's modulus, tensile strength and fracture energy values are 27691 MPa, 2.19 MPa and 0.0620 Nmm/mm^2. For the CFRP plate, the modulus used was 137345 MPa. For the adhesive layer, the

normal and shear stiffness moduli were 4266 and 1557 N/mm^2/mm calculated using the flexural modulus of 12800 MPa.

4.5.1.2 Peak loads and effective bond length

The peak loads obtained from the experiment and numerical models are summarised in Table 4.2. For the experiment, the peak loads shown in the table are the total loads measured. For the numerical model, the peak loads are multiplied by a factor of two since only half of the specimen was modelled. The numerical models underestimated slightly the peak loads of the 50 and 75 mm bond lengths. Nevertheless, using the material properties and values outlined earlier, the numerical peak loads were in good agreement with the experimental peak loads. The relationships between the peak loads and bonded lengths are compared in Figure 4.5. It can be observed that the trends are similar for the experimental and numerical results. Using a bilinear fit to the numerical results, the effective bond length given by the numerical models is approximately 145 mm, which is comparable to the experimental value of 120 mm.

Table 4.2 - Comparison of ultimate loads from experiments and finite element analyses

Bond length	Experiment failure load (kN)	Finite element model failure load (kN)
50	18.5, 21.2	15.2
75	25.9, 25.7, 27.0	22.8
95	28.9, 29.3, 28.4, 33.1	29.4
130	-	37.8
150	40.1, 40.8	42.7
175	-	42.8
200	41.4, 40.7	40.4
220	-	40.8

- No experimental result

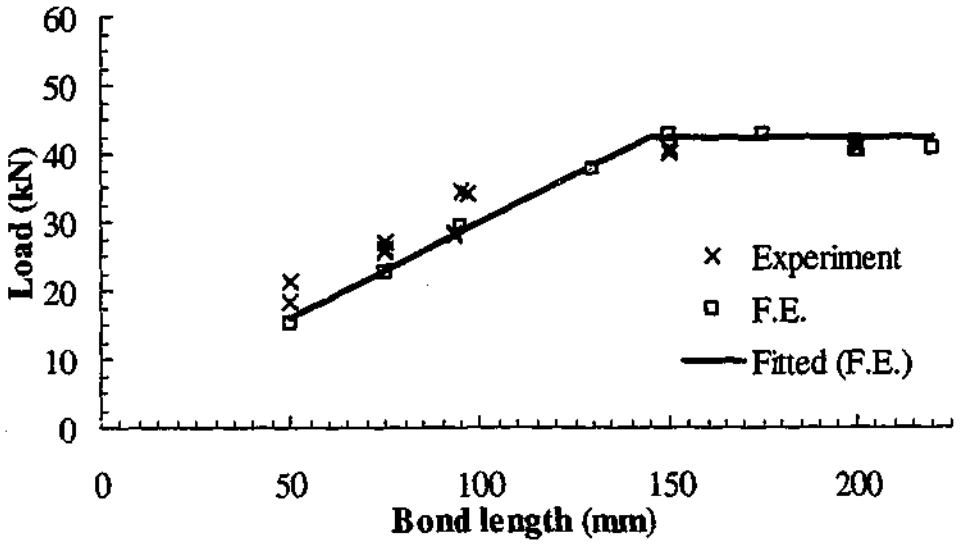

Figure 4.5 - Comparison of failure loads between finite element and experiment

4.5.1.3 Crack pattern

From the non-linear finite element analyses, 'open' crack patterns were produced as illustrated in Figure 4.6. The crack type corresponds to strain that has exceeded the softening branch of the tension model illustrated in Figure 4.4 (b). In all of the bond lengths except for 50 and 75 mm, the crack patterns at or after the peak load step are shown. For the latter, open cracks did not form prior to or at the peak load. The crack patterns shown were produced at the step when open cracks first formed, which occurred when the specimen had begun to soften considerably. It can be observed that for bond lengths of 50 and 75 mm, the cracks formed at the edge of the joint at the inside end of the specimen. For the remaining bond lengths, cracks initially formed approximately four elements away (26 mm) from the loaded end at the concrete layer directly under the adhesive layer. Near the peak load, a second set of cracks formed further along the joint at the location of the seventh element, which matched the experimental average dimension, L, of 42 mm described earlier. The similarity in the experimental and finite element crack patterns and the load at which it occurs justifies the assumption that 'failure' had occurred in the model and peak load had been reached in the models.

In the experiment, only one set of cracks was observed to form in the specimens. The concrete had fractured at the average distance L of 42 mm from the start of the joint, which correspond to the location of the second set of cracks in the finite element models. In the experiment, the formation of the first set of cracks may

not be visible to the naked eye. In theory, vertical cracks in the concrete layer directly beneath the adhesive formed at the location of highest shear stress. As the load is progressively increased, the joint debonds at the concrete layer and the area for active bonding is shifted towards the unloaded end. As a result, the location at which the shear stress is highest is shifted as well. Another set of vertical cracks will form at this location and the process is repeated until the whole joint is debonded. Therefore, vertical cracks will form at regular intervals along the joint before failure of the specimen. In the finite element models, two sets of vertical cracks had formed approximately four and six elements away from the start of the bond. For bond lengths of 130 mm and longer, cracks can be observed to have formed further along the joint. This is an indication of the formation of further vertical cracks as expected in theory but the models have been calibrated to fit experimental results. In the experiment, fracture is a brittle process and the dynamic effects from the sudden release of energy caused the entire joint to debond. The formation of cracks further along the joint is, therefore, unlikely. In the present study, it is physically not possible to reduce the speed at which the specimens were loaded to obtain the progressive formation of the vertical cracks at regular intervals in the specimen.

Based on the failure criterion described earlier, the crack patterns produced from the finite element models were similar to the crack patterns observed in the experiments. The fracture of concrete at the inside end of the joint as observed in specimens B50 and B75I had been simulated by the finite element models.

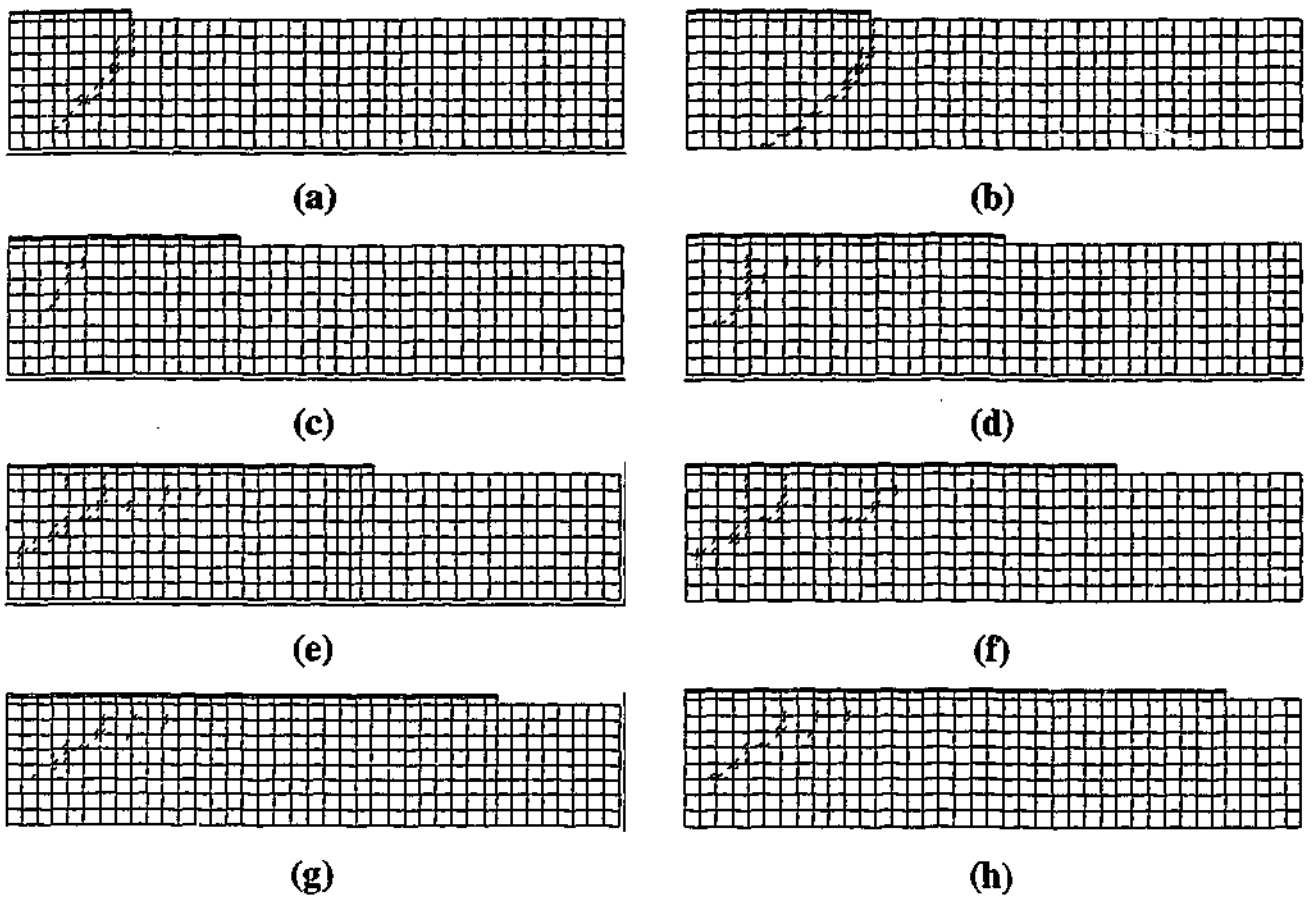

Figure 4.6 - Open crack patterns for bond lengths of (a) 50 (b) 75 (c) 95 (d) 130 (e) 150 (f) 175 (g) 200 and (h) 220 mm (30 MPa concrete strength)

4.5.1.4 Load slip behaviour

The load slip behaviour obtained from the experiment and finite element models are compared in Figure 4.8 and Figure 4.9. In the models, slip is taken at nodes at similar locations to the experiment, illustrated in Figure 4.7. Slip is taken as the difference in the average horizontal movement between the selected nodes on the CFRP elements and the concrete elements. The loads obtained from the models are increased by a factor of two for direct comparison with the experimental results shown in Figure 3.23. The curves for the models are plotted up to the step before non-convergence of the solution.

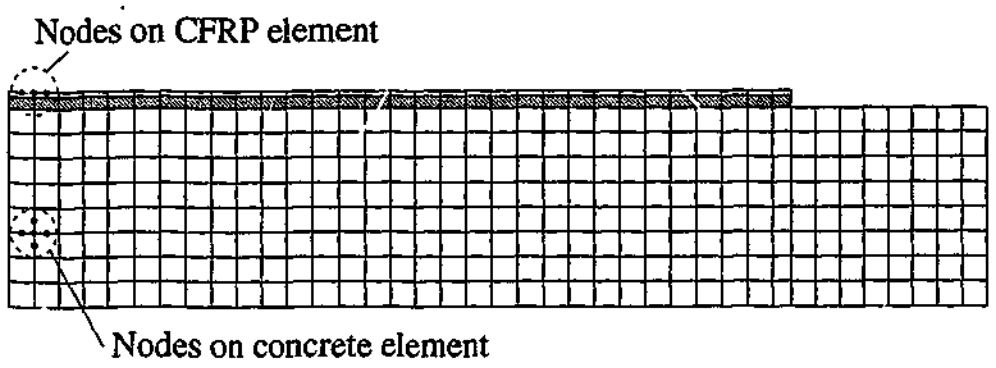

Figure 4.7 - Locations of nodes for slip measurement

In all of the cases except for the 150 mm bond length, it can be observed that the load slip behaviour of the experiment and numerical models were similar. In the latter, the experimental results exhibited a higher stiffness between 10 to 25 kN. Nevertheless, at the initial stages of loading, the stiffness was similar for the experiment and numerical models for all bond lengths. Based on the material models and properties outlined earlier, the analyses gave a reasonably accurate prediction of the load-slip behaviour to the experiment.

Figure 4.10 compares the load slip curves of the finite element models with various bond lengths. As expected, the initial stiffness of the specimens is identical across the different bond lengths. The load slip curves are also identical as the longer bond lengths traced the load slip behaviour of the shorter lengths up to 75% of the ultimate load. Similar to the load slip curves for the experiment, in general, the slip is higher in the longer bond lengths due to the higher load carrying capacity.

(a)

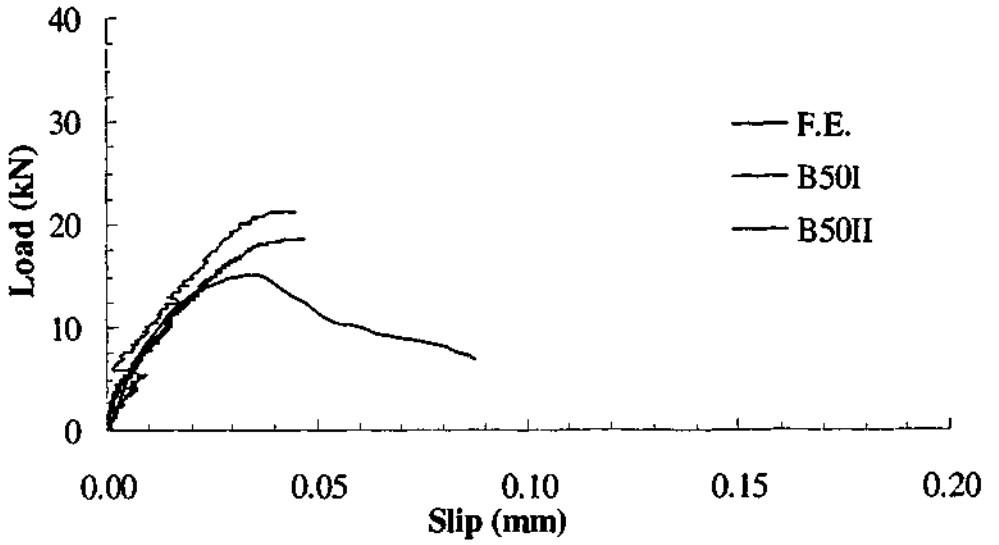

(b)

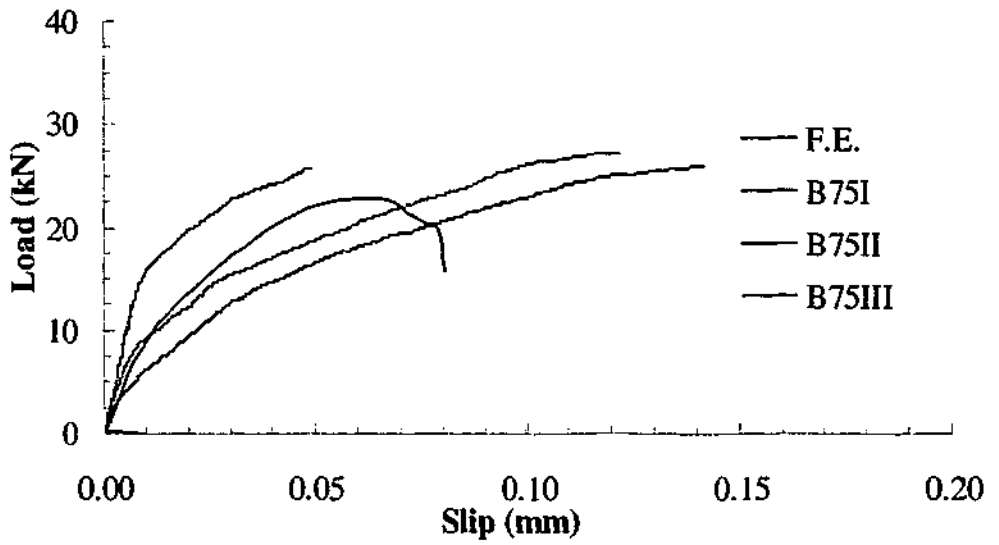

(c)

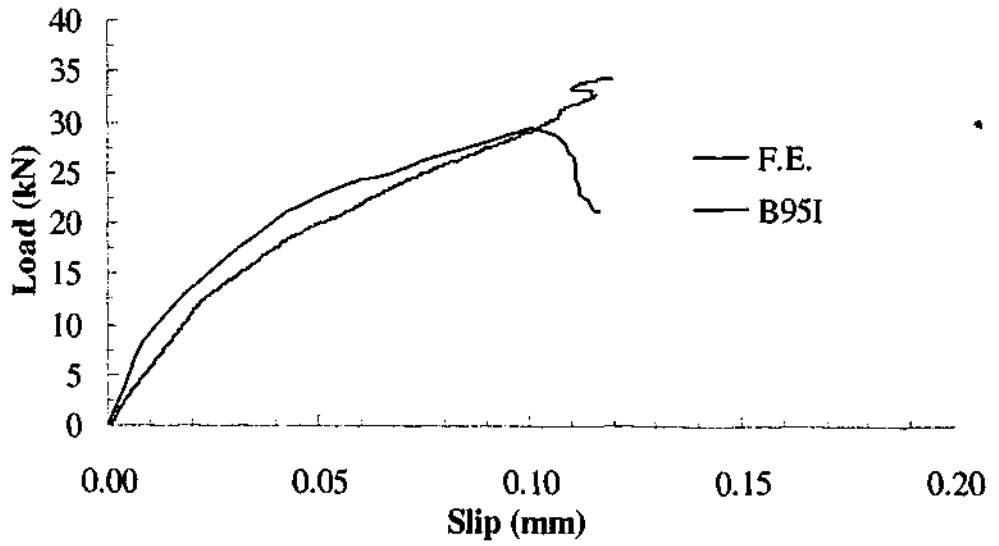

Figure 4.8 - Comparison of load slip behaviour between experiment and finite element analyses for bond lengths of (a) 50 (b) 75 and (c) 95 mm

(a)

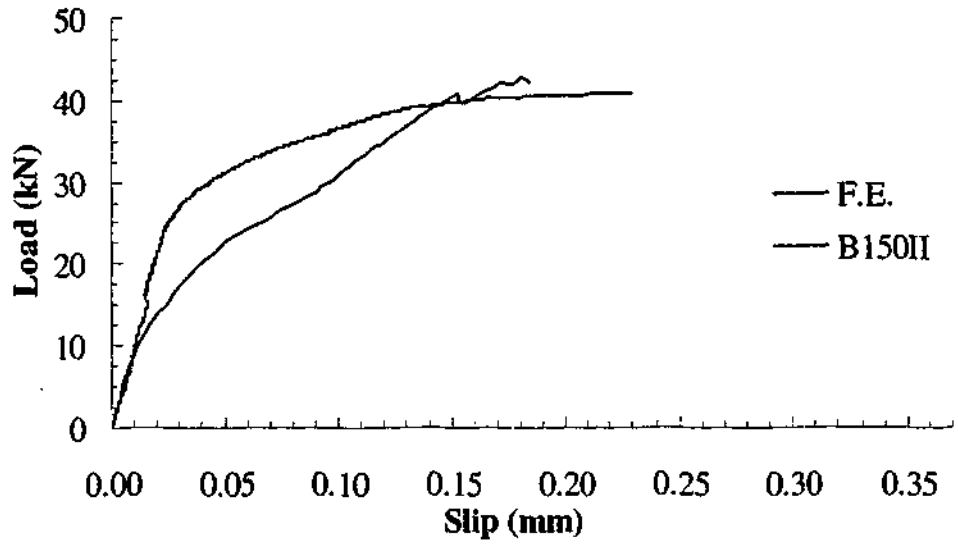

(b)

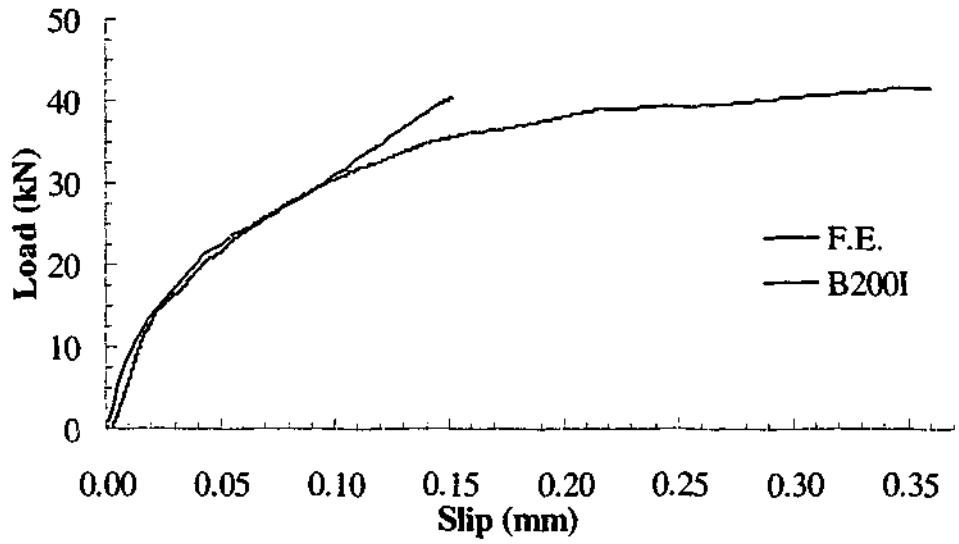

Figure 4.9 - Comparison of load slip behaviours between experiment and finite element analyses for bond lengths of (a) 150 and (b) 200 mm

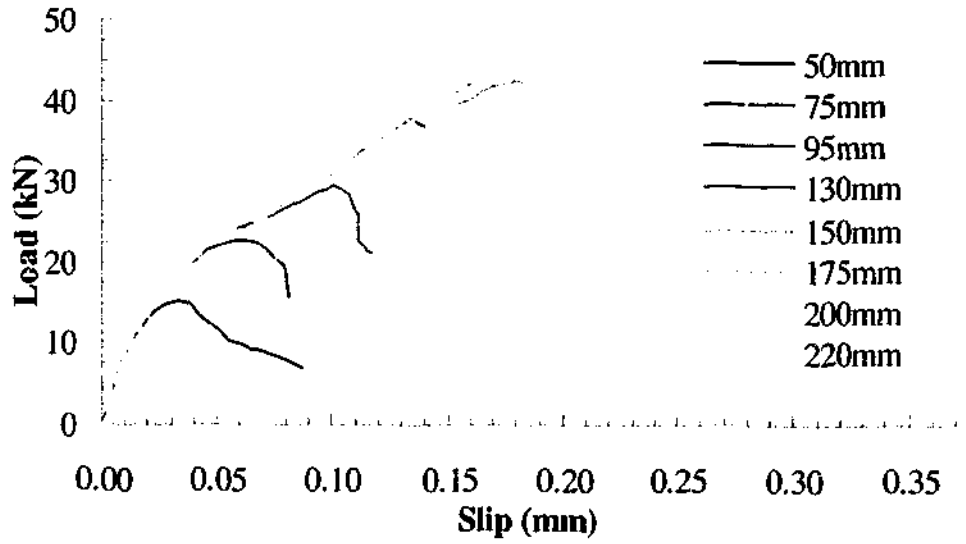

Figure 4.10 - Load slip behaviour of finite element bond specimens

4.5.1.5 Strain distributions along bonded joints

The experimental and numerical strain distributions along the bonded joint at selected load levels are compared in Figure 4.11 to Figure 4.13. At each load level, the experimental and numerical load levels were selected to be as close as possible to each other. The numerical models with bond lengths of 130, 175 and 220 mm have been included. For the numerical results, each discrete data point corresponds to the average strain calculated at the location of the nodes at the top of the CFRP plates. At low load levels, the numerical strain distribution agrees well with the experimental results in all cases with a fairly smooth curve along the joint. Beyond the service load level, however, the computed strain is larger than the experimental strain, particularly near the start of the bond. For the bond lengths of 95, 150 and 200 mm, the strain distribution curves appear distorted with strain values varying considerably from one node to another. In the finite element formulation, cracking results in a localised strain concentration at the Gauss points of the elements, the values of which are extrapolated to the nodes. The absence of cracks in the neighbouring elements will mean a significantly lower strain values at the nodes for those elements and hence the considerable variation in the strain values from one node to the other. Unlike the finite element models, the experimental strain is an average measured across the gauge length of the strain gauge. The result is a smoother strain distribution curve. In the finite element models, the strain at the start of the bond (0 mm) is lower than the strain a few millimetres further along the joint. The nodes at the start of the bond are restrained and represent a region of high stress concentration. Nevertheless, the numerical strain distribution showed comparable trend to the experimental results. In general, the numerical models have simulated the strain distribution profiles quite accurately.

Examining the numerical results more closely, for load levels below or at the service load level, it can be observed that the strain distribution exhibited an exponential trend. Beyond the service load level, the strain distribution curve becomes distorted near the start of the bond, displacing the exponential curve further along the joint with increasing load. Similar to the experimental results, the effective bond length can be approximated as the length of the exponential portion of the strain distribution curve. It is, however, more difficult as there is no distinct flat portion as in the case of the experimental strain distributions shown in Figure 3.15 to Figure

3.17. The value determined would be subjective and therefore has not been determined in this manner. Figure 4.5 gives a good approximation of the effective bond length as determined from the finite element models.

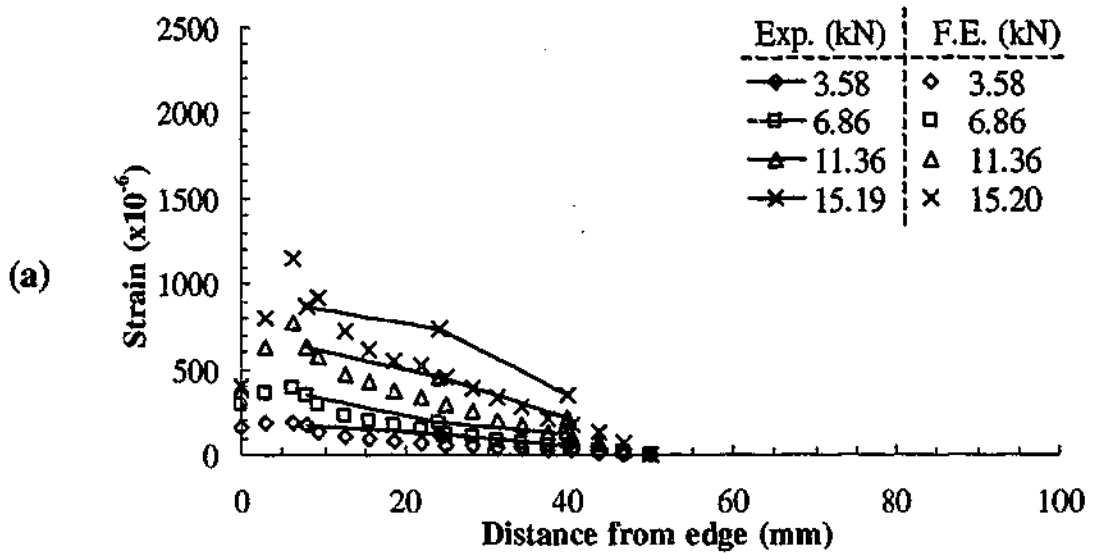

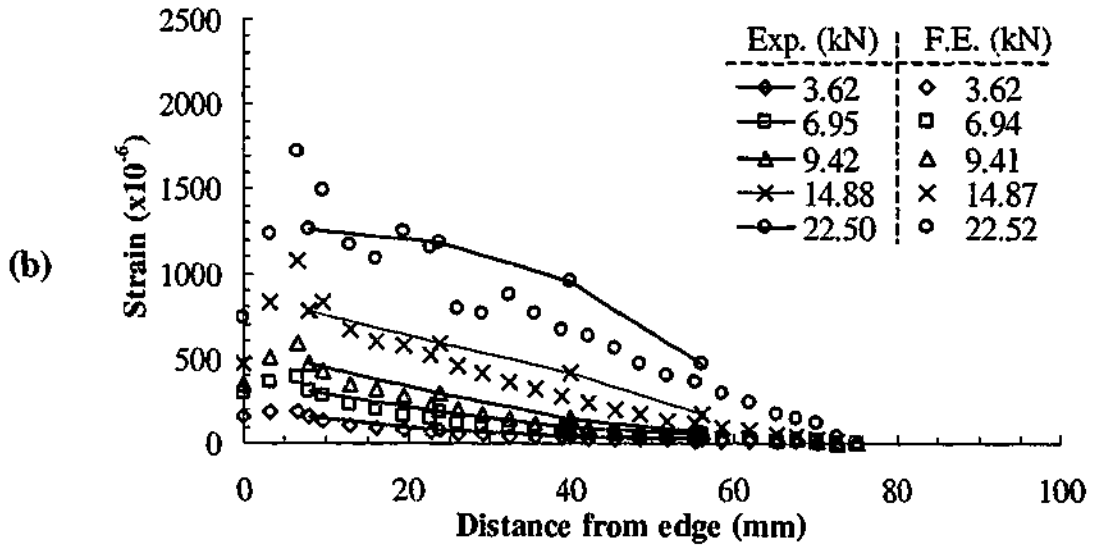

Figure 4.11 - Comparison of CFRP strain distributions along length for bond lengths of (a) 50 and (b) 75 mm

(a)

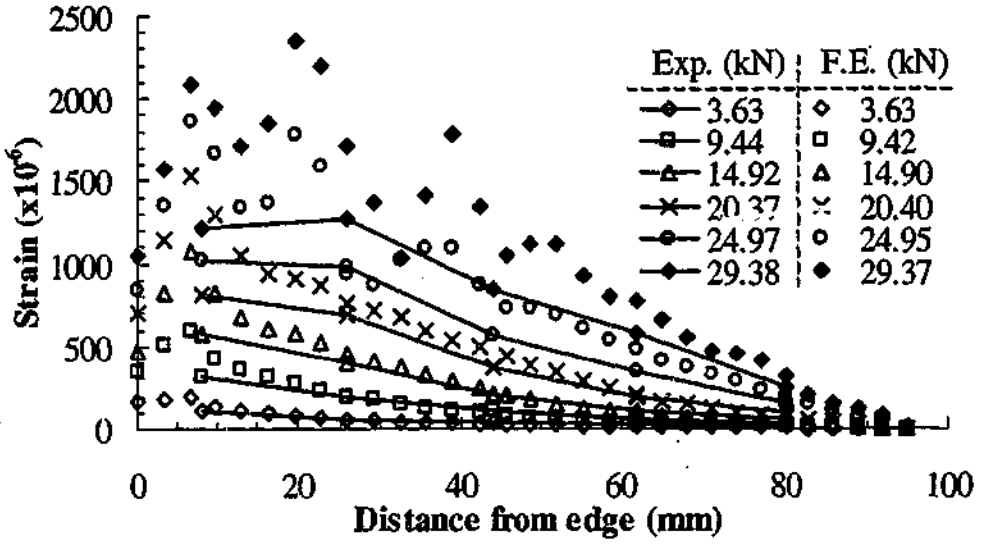

(b)

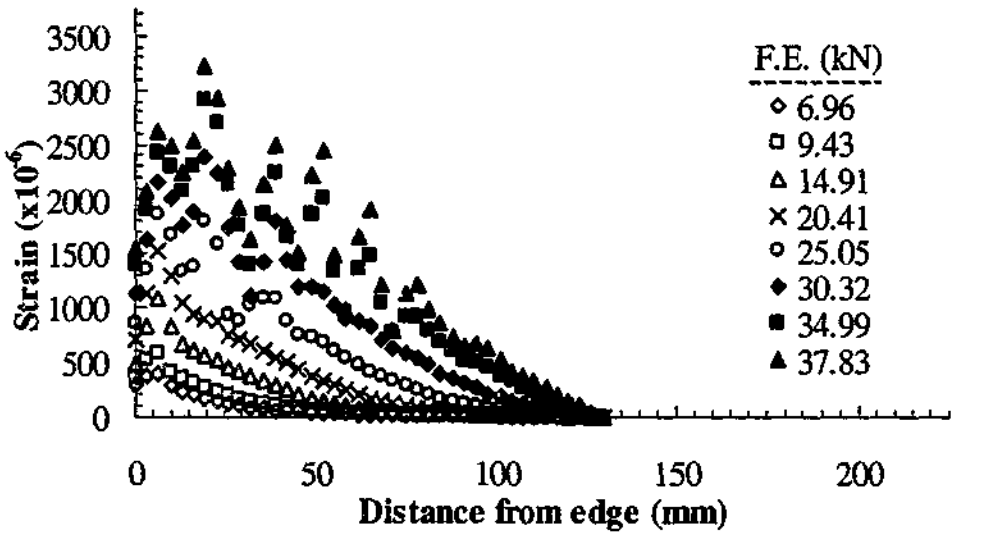

(c)

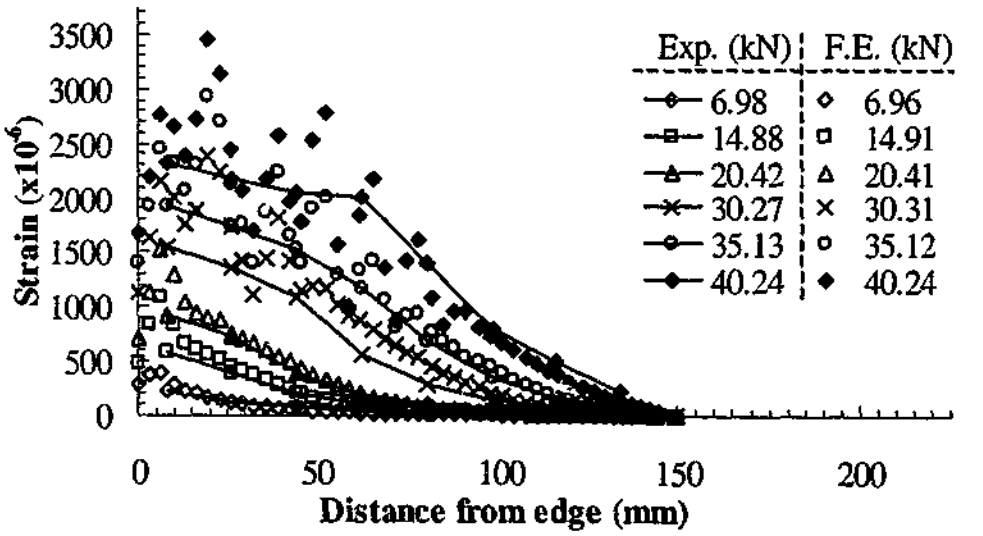

Figure 4.12 - Comparison of CFRP strain distributions along length for bond lengths of (a) 95 (b) 130 and (c) 150 mm

(a)

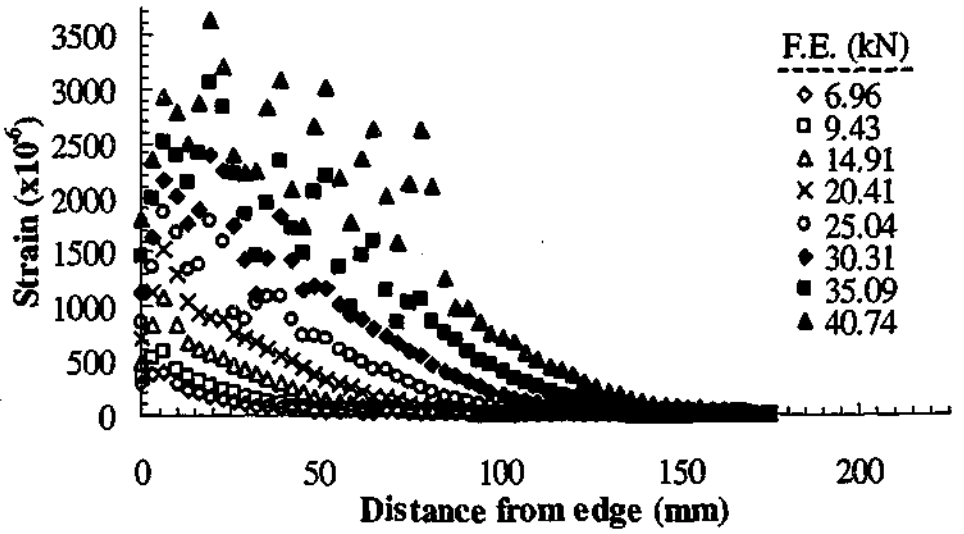

(b)

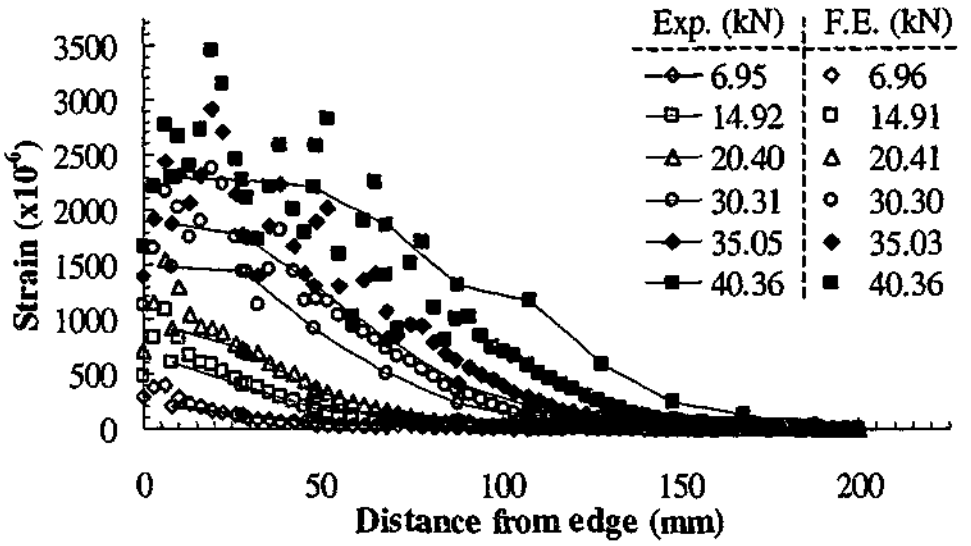

(c)

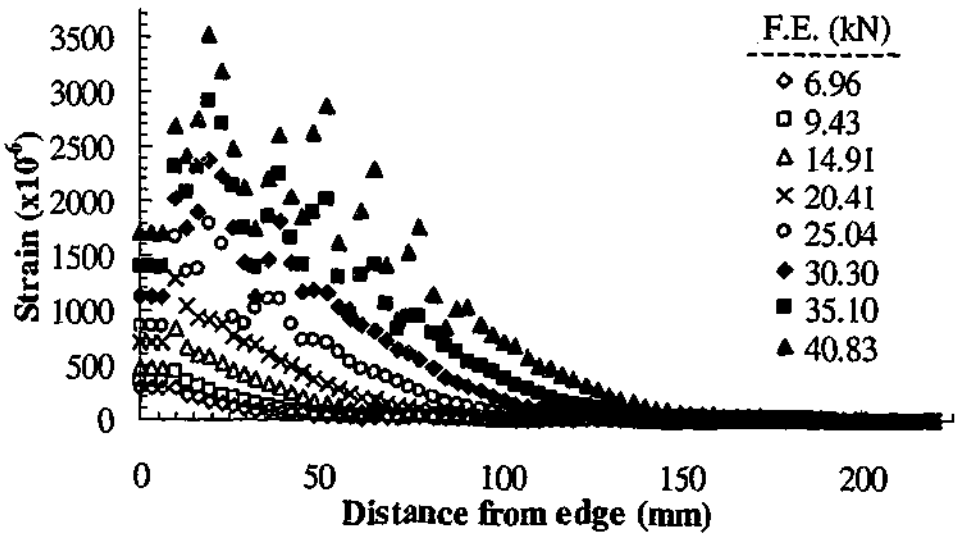

Figure 4.13 - Comparison of CFRP strain distributions along length for bond lengths of (a) 175 (b) 200 and (c) 220 mm

4.5.1.6 Validity of model

The finite element models with the material models and properties adopted produced comparable results to the experiments. The numerical peak loads were in good agreement with the experimental peak loads. The crack patterns, load-slip behaviour and strain distribution profiles of the numerical models were similar to the experimental results, with the trends simulated adequately. Therefore, the results of the finite element models are valid. In the sections to follow, a parametric study is carried out using the models with material properties outlined earlier as the basis for comparison.

4.5.2 Effect of varying concrete strength

4.5.2.1 Introduction

In this section, the effects of varying the concrete strength on the peak load, load-slip behaviour and strain distribution profiles were investigated. Numerical models with concrete strengths of 20 and 40 MPa were analysed and compared against the base model of 30 MPa presented earlier. The material properties are summarised in Table 4.3. All other material properties have remained the same as the base model. The determination of 'failure' of the models is based on the criterion used for the base models described earlier. In the base models, 'failure' is assumed to have occurred when two sets of cracks formed in the concrete element under the adhesive layer. Since experimental results of varying concrete strength are not available, it is assumed that 'failure' in the finite element models occur after the formation of two sets of cracks in the concrete elements under the adhesive layer similar in pattern to the base models. The assumption is reasonable based on the fact that concrete fracture governs the failure.

Table 4.3 - Material properties according to concrete strength

Concrete strength (MPa)	Young's Modulus (MPa)	Tensile strength (MPa)	G_f^1 (Nmm/mm^2)
20	22610	1.79	0.0467
30*	27691	2.19	0.0620
40	31975	2.53	0.0759

* Base model

4.5.2.2 Peak loads and effective bond length

Figure 4.14 compares the computed peak loads of the various models with different concrete strengths. For all the concrete strengths, it can be observed that the computed peak load increases with increases in the bond lengths until a certain length, beyond which the peak load remains constant. Using simple bilinear fits to the numerical results, the figure suggests that the effective bond length is the same for all concrete strengths. The effective bond length is approximately 145 mm. According to Equation 2.19g, the effective bond length should decrease with an increase in the compressive strength. Figure 4.15 expresses the peak load as a function of concrete strength for the different bond lengths. For all the bond lengths, it can be observed that the peak load increases slightly with the concrete strength. This is due to the fact that the tensile strength of concrete is only a fraction of its compressive strength. An increase in compressive strength would only result in a relatively small increase in its tensile strength.

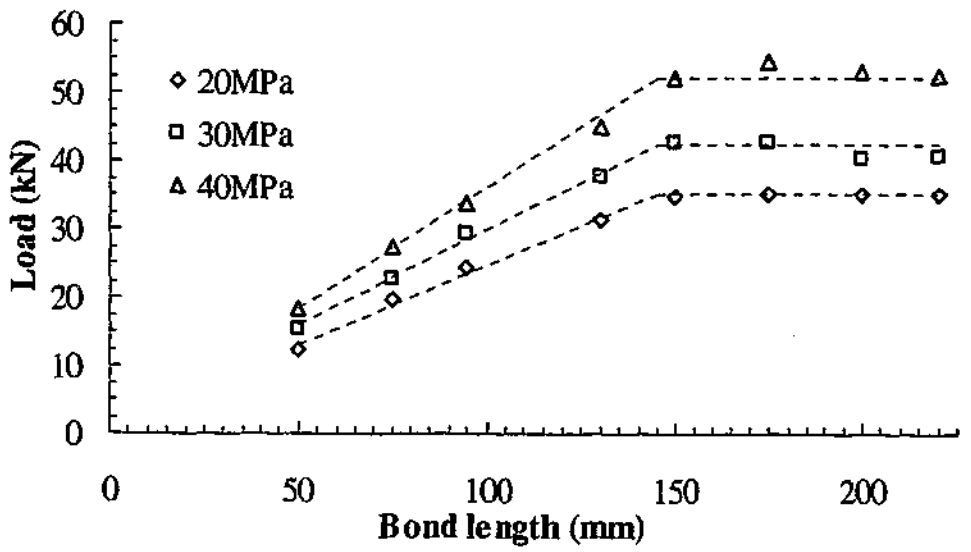

Figure 4.14 - Computed peak load with varying bond lengths of different concrete strengths

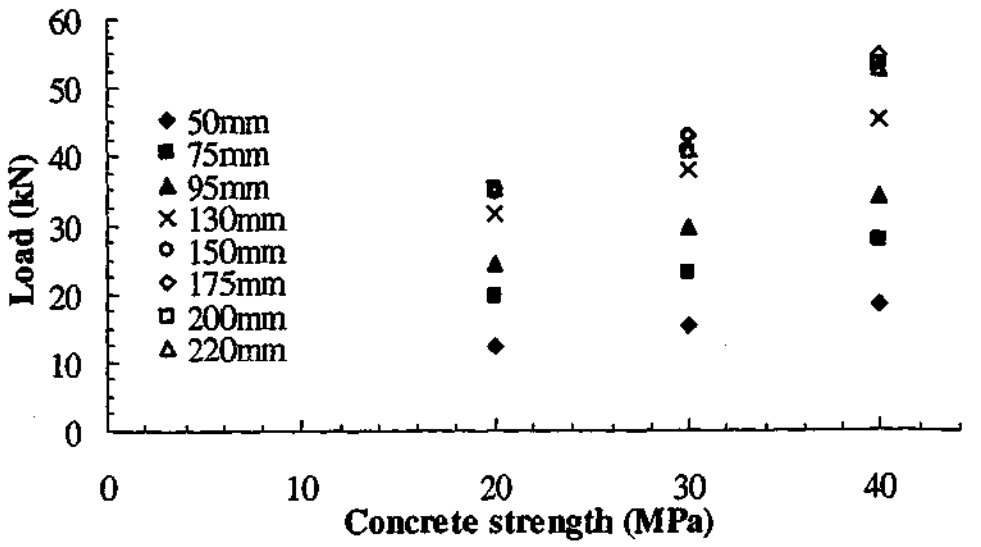

Figure 4.15 - Computed peak load with varying concrete strength of different bond lengths

4.5.2.3 Crack pattern

The 'open' crack patterns of the finite element models with concrete strengths of 20 and 40 MPa are illustrated in Figure 4.16 and Figure 4.17. In most of the models, the crack patterns shown were produced at steps near the peak load. For the models having bond lengths of 50 and 75 mm with 20 MPa concrete strength and bond length of 50 mm with 40 MPa concrete strength, open cracks did not form prior to or at the peak load. The crack patterns shown were produced at the step when open cracks first formed, which occurred when the specimen had begun to soften.

For the concrete strength of 20 MPa, it can be observed that for bond lengths of 50 and 75 mm, the cracks formed at the edge of the joint at the inside end of the specimen. For the remaining bond lengths, cracks initially formed approximately two elements away (13 mm) from the loaded end at the concrete layer directly underneath the adhesive. As load is progressively increased, the cracks closed up and a second set of cracks formed further along the joint at the location of the fourth element (26 mm). Near the peak load, a third set of cracks formed approximately at the location of the eleventh element. In the base models, failure occurred when two sets of cracks formed, which was at the fourth and seventh element from the start of the joint. Therefore, for the models with 20 MPa concrete strength, it is reasonable to consider that failure occurs when the second and third set of cracks formed. The peak load had been reached in the models.

For the concrete strength of 40 MPa, cracks formed at the inside end of the joint for the bond lengths of 50 and 75 mm. For the remaining bond lengths, cracks initially formed approximately three elements away (19.5 mm) from the loaded end. As load is progressively increased, the cracks closed up and a second set of cracks formed further along the joint at the location of the sixth element. At the peak load, cracks can be observed to form further behind the second set of cracks. The locations of the two sets of cracks of the 40 MPa concrete strength models are within the vicinity of the two sets of cracks observed in the base models. For the former, it is reasonable to consider that failure had occurred and the peak load had been reached. The peak loads illustrated in Figure 4.14 are therefore valid.

Near the peak load, the crack patterns of the 20 and 40 MPa concrete strength models are similar to the base models. Variations in concrete strength do not have a significant effect on the crack patterns.

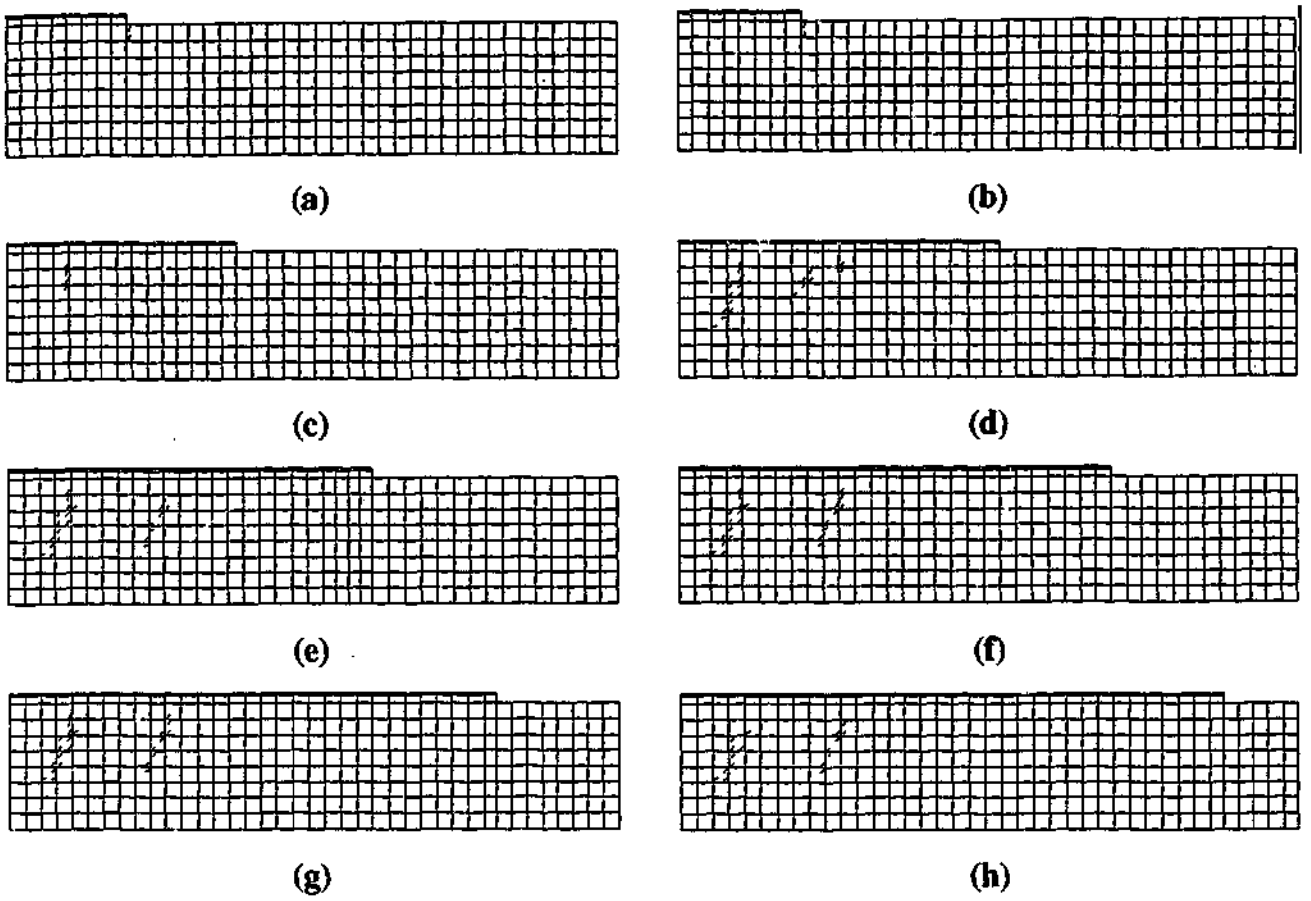

Figure 4.16 - Open crack patterns for bond lengths of (a) 50 (b) 75 (c) 95 (d) 130 (e) 150 (f) 175 (g) 200 and (h) 220 mm (20 MPa concrete strength)

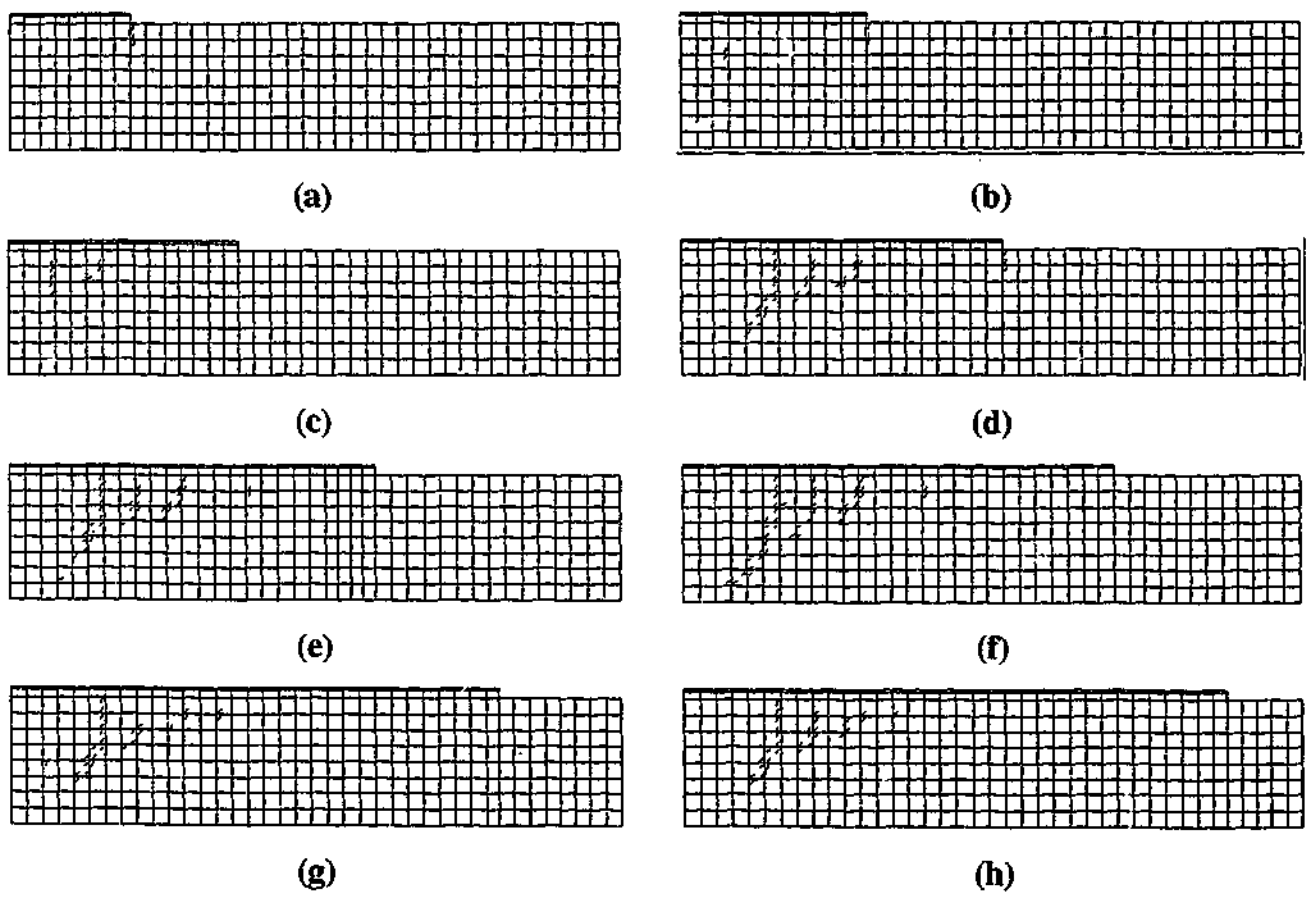

Figure 4.17 - Open crack patterns for bond lengths of (a) 50 (b) 75 (c) 95 (d) 130 (e) 150 (f) 175 (g) 200 and (h) 220 mm (40 MPa concrete strength)

4.5.2.4 Load slip behaviour

Figure 4.18 to Figure 4.20 illustrate the load-slip relationship produced from the models. The location where the slip is measured is shown in Figure 4.7. In all of the bond lengths, it can be seen from the figures that the stiffness increases with concrete strength. It should be noted that this is the result of the corresponding increase in the modulus of the concrete. Slip between the CFRP and concrete was measured between two locations with approximately 30 mm layer of concrete in between. The stiffer the concrete, the smaller the deformation in the concrete layer hence slip between the two locations. From the graphs, the slip value at the peak load increases with concrete strength. As illustrated in Figure 4.21 and Figure 4.22, the stiffness was identical in all the bond lengths of the same concrete strength. The load slip curves were similar as well with the longer bond lengths tracing the path of the shorter bond lengths until 75% of the peak load.

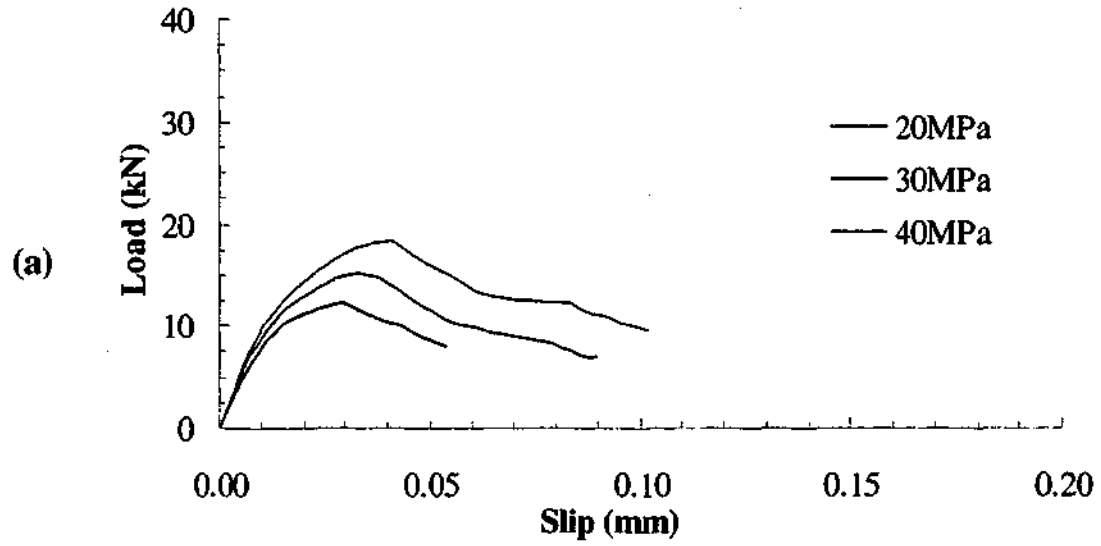

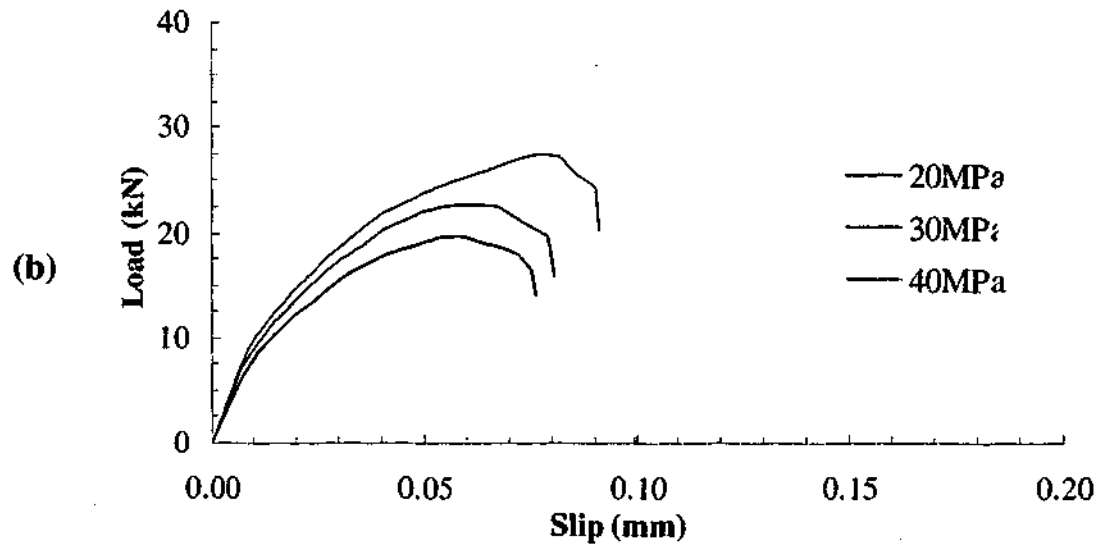

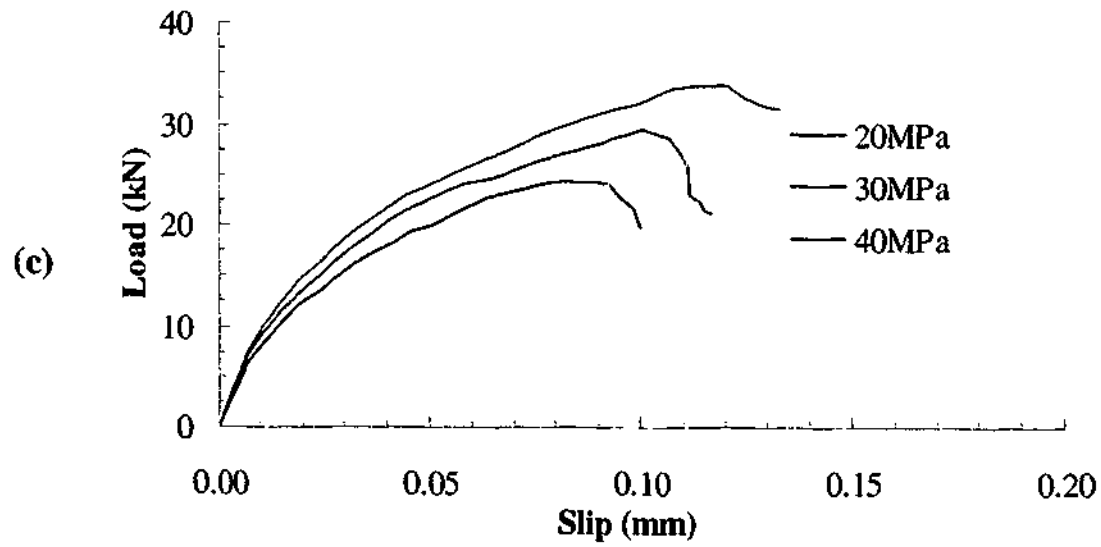

Figure 4.18 - Load slip behaviour of varying concrete strengths for bond lengths of (a) 50 (b) 75 and (c) 95 mm

(a)

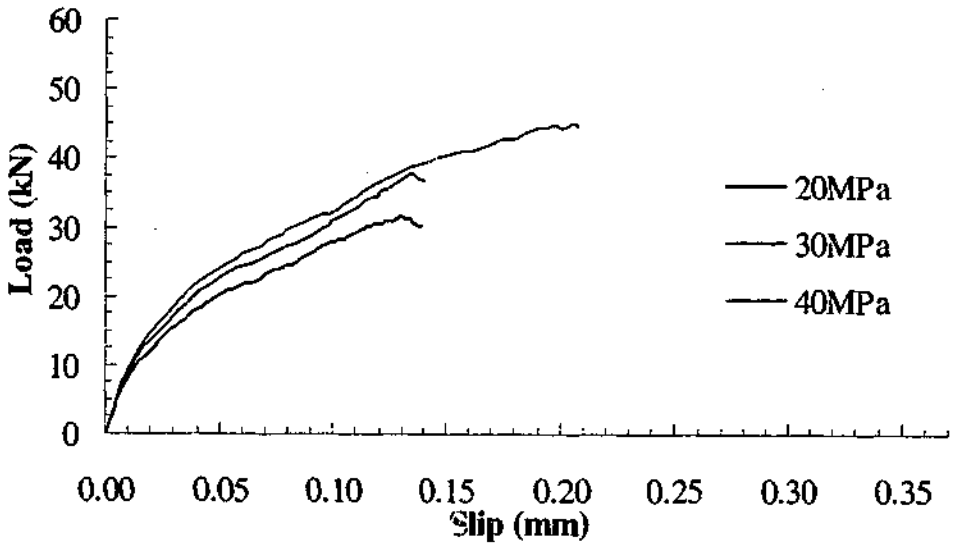

(b)

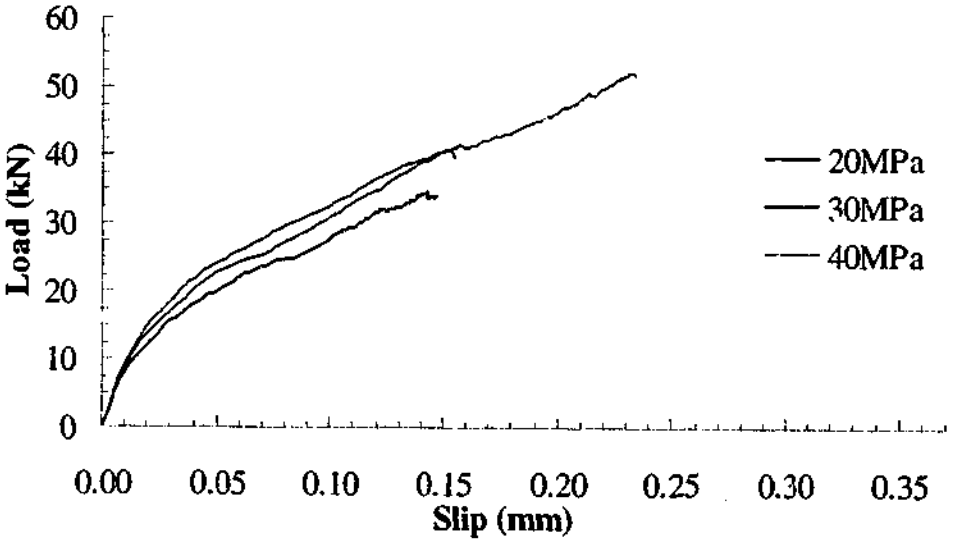

(c)

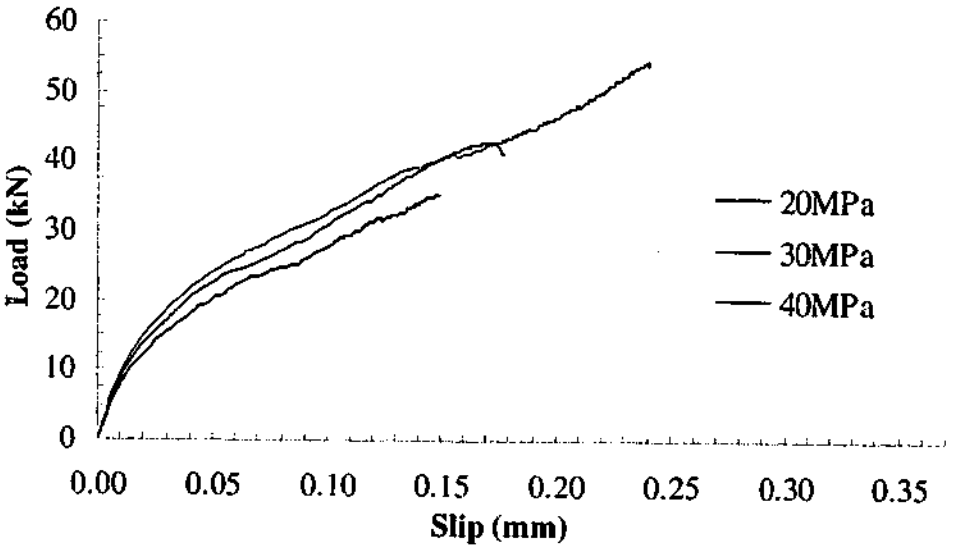

Figure 4.19 - Load slip behaviour of varying concrete strengths for bond lengths of (a) 130 (b) 150 and (c) 175 mm

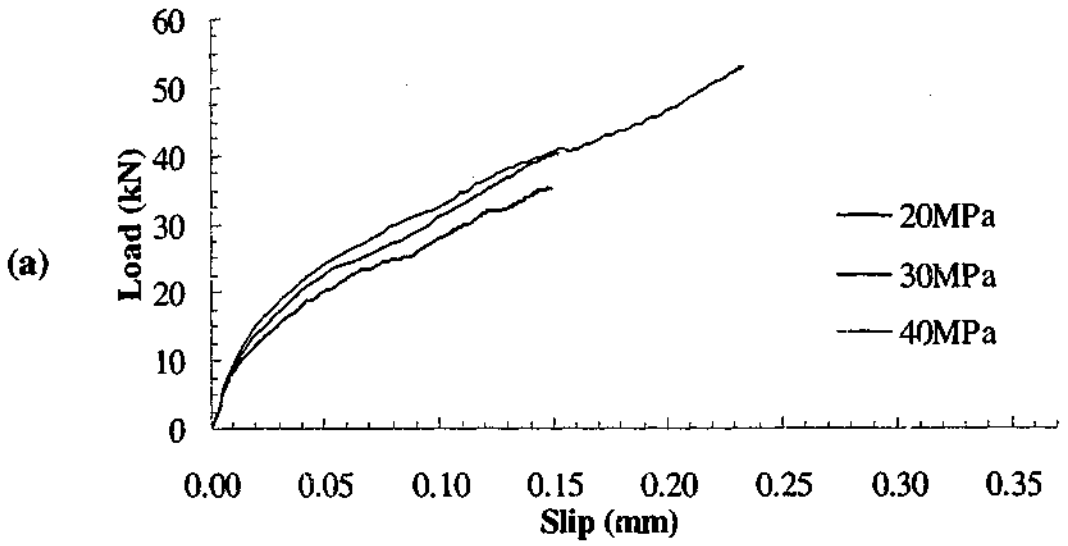

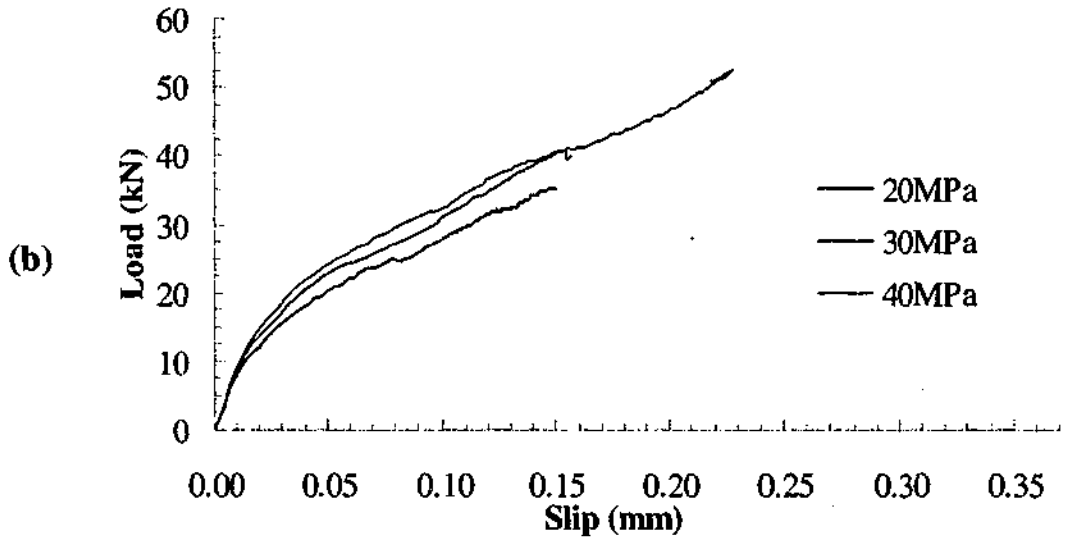

Figure 4.20 - Load slip behaviour of varying concrete strengths for bond lengths of (a) 200 and (b) 220 mm

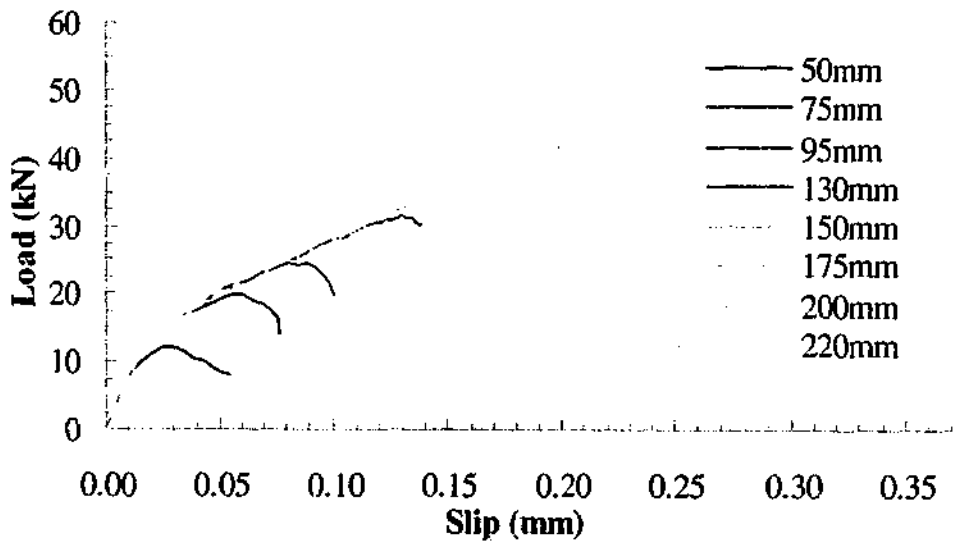

Figure 4.21 - Load slip behaviour for concrete strength of 20 MPa

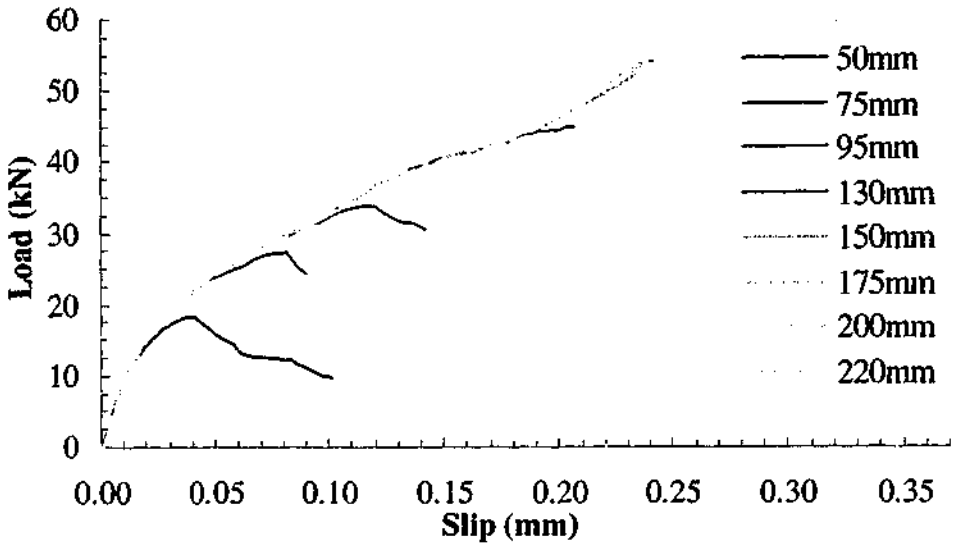

Figure 4.22 - Load slip behaviour for concrete strength of 40 MPa

4.5.2.5 Strain distributions along bonded joints

A direct comparison of the strain distribution profiles such as those illustrated in Figure 4.11 to Figure 4.13 for different concrete strengths has not been carried out. It is difficult to determine any difference since the computed loads do not coincide and the changes are too minute to be established visually. Instead, the strain development with load at selected node locations along the joint is plotted to determine the effect of concrete strength on the strain distribution profile. Figure 4.23 and Figure 4.24 illustrate the strain development at the surface of the CFRP plate at three node locations along the joint for the bond lengths of 50, 95, 150 and 200 mm. The first node location is at least five nodes away from the start of the bond where the model is restrained. The remaining two nodes are selected to be near the mid-length and the end of the joint. For a given load level, particularly at or below the service load level, it can be observed that the strain in the CFRP decreases as concrete strength increases. This was observed for intermediate node locations as well as at node locations near the end of the joint. At the node location at the start of the bond (0 mm), the strain levels in the CFRP plate were higher in the models with higher concrete strength. This is the result of the increase in the modulus or stiffness of the concrete, which increases the load transferred to or carried by the concrete layer near the start of the bond. The behaviour described here was observed in all of the bond lengths.

In view of the fact that the strain level decreases as the concrete strength increases, it is possible that the CFRP strain distribution profile reaches zero within a shorter distance in specimens with higher concrete strength. This implies that the effective bond length decreases with increases in concrete strength. It was difficult, however, to establish this conclusively from the finite element models. The change in the strain level due to change in the concrete strength is minor, particularly near the unloaded end of the joint.

(a)

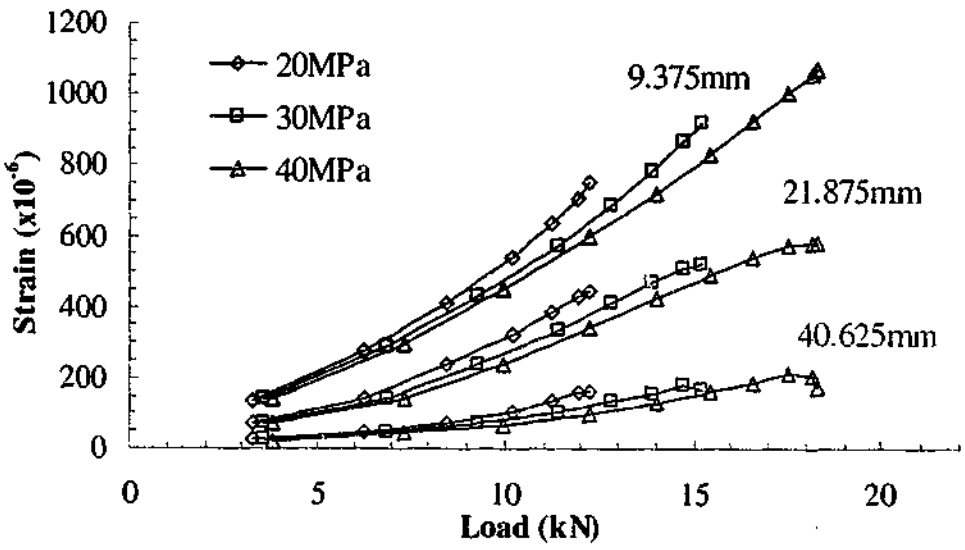

(b)

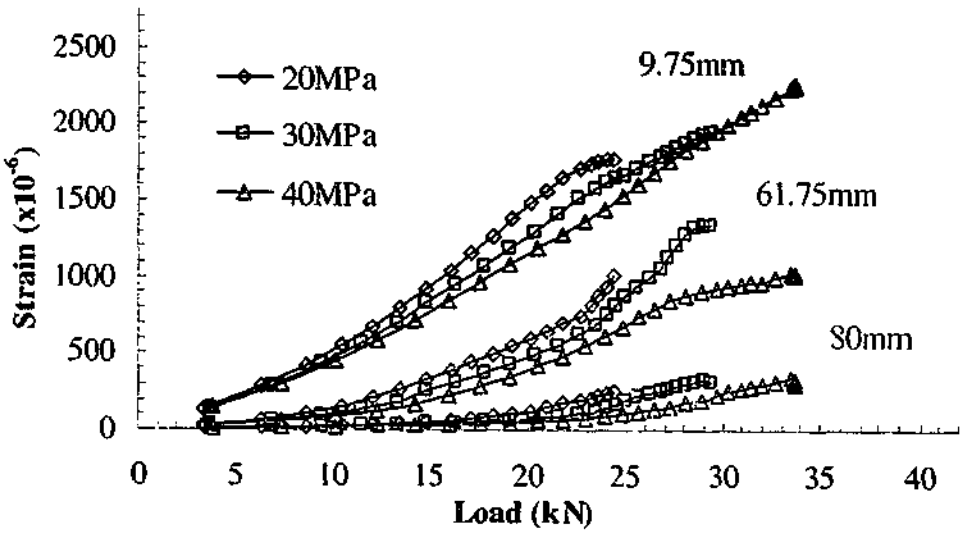

Figure 4.23 - Strain development in CFRP plate of varying concrete strengths for bond lengths of (a) 50 and (b) 95 mm

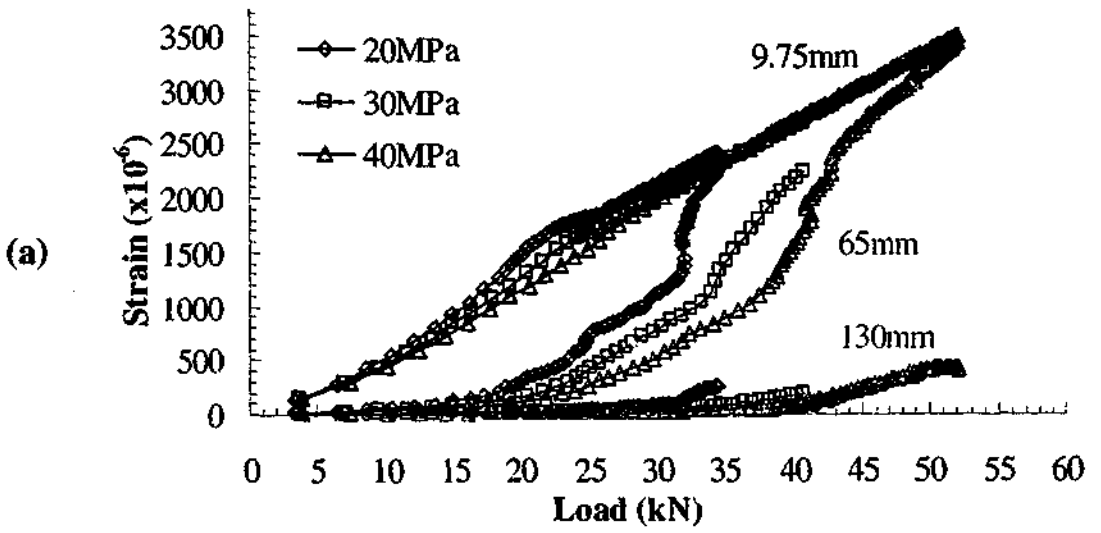

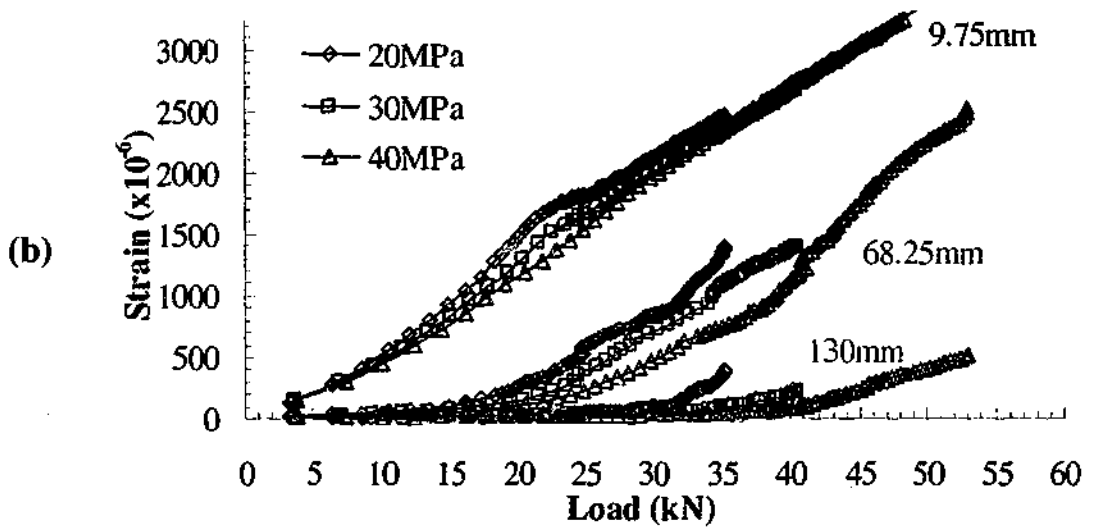

Figure 4.24 - Strain development in CFRP plate of varying concrete strengths for bond lengths of (a) 150 and (b) 200 mm

The main finding of the present section is that a large variation in the concrete strength results in a significant change in the peak load but a minor change in the load-slip behaviour and strain distribution. Based on the material properties used herein, the numerical analyses suggest that the effective bond length decreases as the concrete strength increases. In the finite element model, adopting identical concrete strength to the actual experiment is, therefore, not crucial. Although a large variation in the concrete strength results in a significant change in the peak load achieved in the bond specimens, this factor is not critical for the T-beams. The variation of the concrete strength in the different T-beams is minor.

4.5.3 Effect of varying adhesive stiffness

4.5.3.1 Introduction

In this section, the effects of varying the adhesive stiffness on the peak load, load-slip behaviour and strain distribution profiles were investigated. Two sets of models with different adhesive stiffness were analysed and compared against the base model outlined earlier. The stiffness was determined using Equations 4.5 and 4.6, where E = 12800 MPa with the assumed adhesive thickness, t, of 2 and 4 mm. In the base models, the adhesive thickness was set as 3 mm. Table 4.4 summarises the adhesive stiffness used in the models. All other material properties have remained the same as the base model. It should be noted that the same mesh as the base model has been used and the thickness of the adhesive layer has not changed. The thickness of the adhesive layer set in the mesh is not taken into account in the computation of the numerical solutions. The properties and geometry of the adhesive layers are specified in terms of stiffness, which minimises the combinations of variables to be investigated. The determination of 'failure' of the models is based on the criterion used for the base models described earlier and in the previous section.

Table 4.4 - Normal and shear stiffness of adhesive layer used in models

Model	D_{11} (N/mm^3)	D_{22} (N/mm^3)
1*	4266	1557
2	3200	1167
3	6400	2335

* - Base model

4.5.3.2 Peak loads and effective bond length

Figure 4.25 compares the computed peak loads of the models with different adhesive stiffness. For all of the bond lengths, it can be observed that the peak loads differ slightly with varying adhesive stiffness. For the values adopted herein, the difference in the adhesive stiffness has an insignificant effect on the effective bond length. The effective bond length is similar for models 1 to 3, which is approximately 145 mm. Figure 4.26 expresses the peak load as a function of the adhesive shear stiffness for the different bond lengths. It can be observed that the peak load does not

vary significantly with adhesive stiffness. For a given bond length, the trend between the peak load and adhesive stiffness can be observed to be linear.

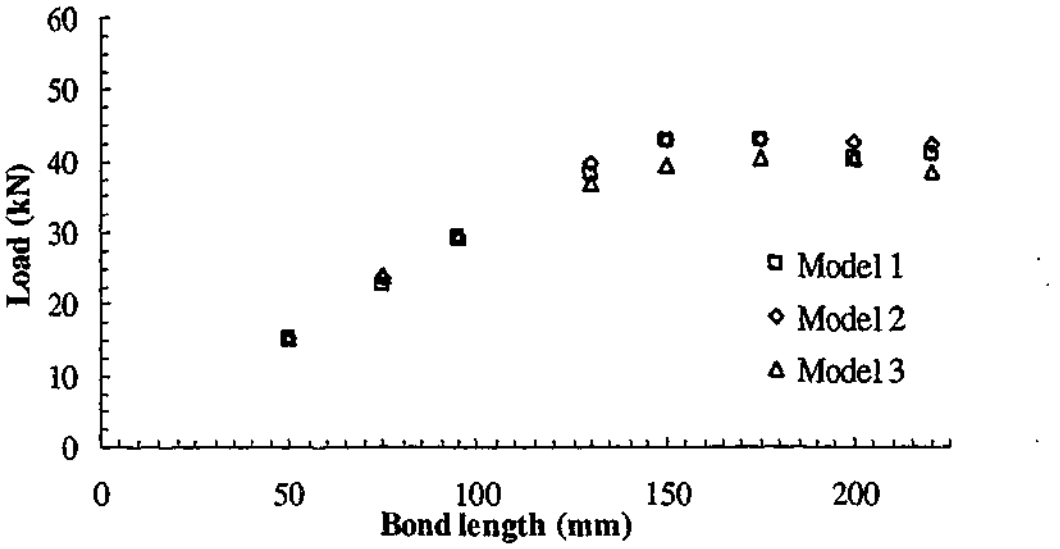

Figure 4.25 - Computed peak load with varying bond lengths of different adhesive stiffness

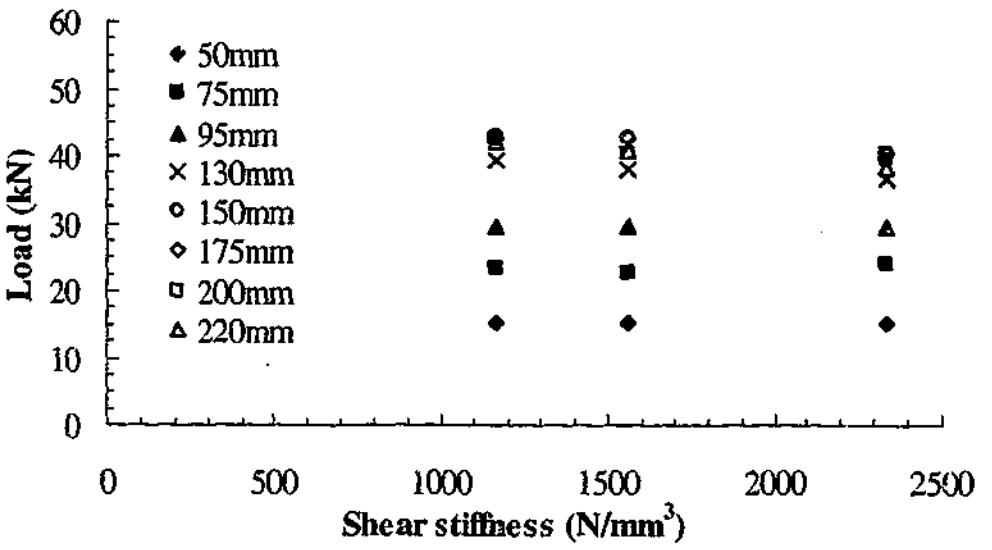

Figure 4.26 - Computed peak load with varying adhesive stiffness of different bond lengths

4.5.3.3 Crack pattern

The 'open' crack patterns of models 2 and 3 are illustrated in Figure 4.27 and Figure 4.28. In most of the models, the crack patterns shown were produced at steps prior to or at the peak load. In model 2 for the bond length of 50 mm and in model 3 for the bond lengths of 50 and 75 mm, open cracks did not form prior to or at the peak

load. The crack patterns shown were produced at the step when open cracks first formed.

In model 2, for the bond lengths of 50 mm, cracks formed at the inside edge of the joint. For all the other bond lengths, cracks initially formed approximately three elements away (19.5 mm) from the start of the joint in the concrete layer under the adhesive. As load is progressively increased, a second set of cracks formed further along the joint within the vicinity of the sixth element. Near the peak load, more cracks can be observed to form further behind the second set of cracks, as illustrated in Figure 4.27. In some of the bond lengths, the second set of cracks closed up. The locations and patterns of the two sets of cracks of model 2 are similar to the two sets of cracks observed in the base models.

In model 3, for the bond lengths of 50 and 75 mm, cracks formed at the inside edge of the joint. For all the other bond lengths, cracks initially formed approximately four elements away (26 mm) from the start of the joint in the concrete layer under the adhesive. As load is progressively increased, for the bond length of 95 mm, a second set of cracks formed further along the joint within the vicinity of the fifth element. For bond lengths of 130 mm and longer, the second set of cracks formed within the vicinity of the tenth element from the start of the joint. Near the peak load, more cracks can be observed to form further behind the second set of cracks, as illustrated in Figure 4.28. In the base models, failure occurred when two sets of cracks formed, which was at the fourth and seventh element from the start of the joint. For model 3, it is reasonable to consider that failure occurs when two sets of cracks formed. The peak loads illustrated in Figure 4.25 are therefore valid.

The crack patterns of models 2 and 3 are similar to the base model. Variations in adhesive strength do not have a significant effect on the crack patterns.

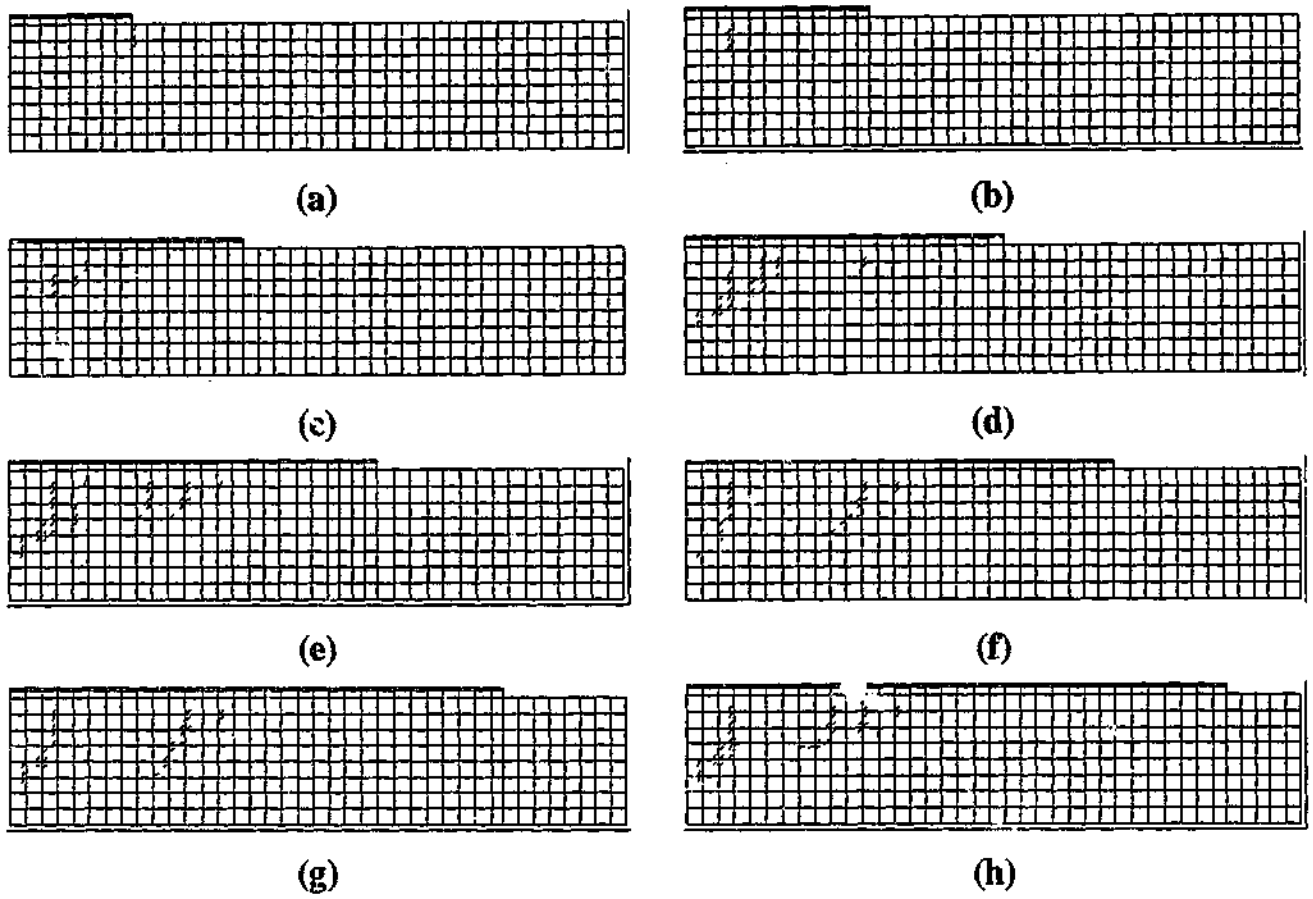

Figure 4.27 - Open crack patterns for bond lengths of (a) 50 (b) 75 (c) 95 (d) 130 (e) 150 (f) 175 (g) 200 and (h) 220 mm (Model 2)

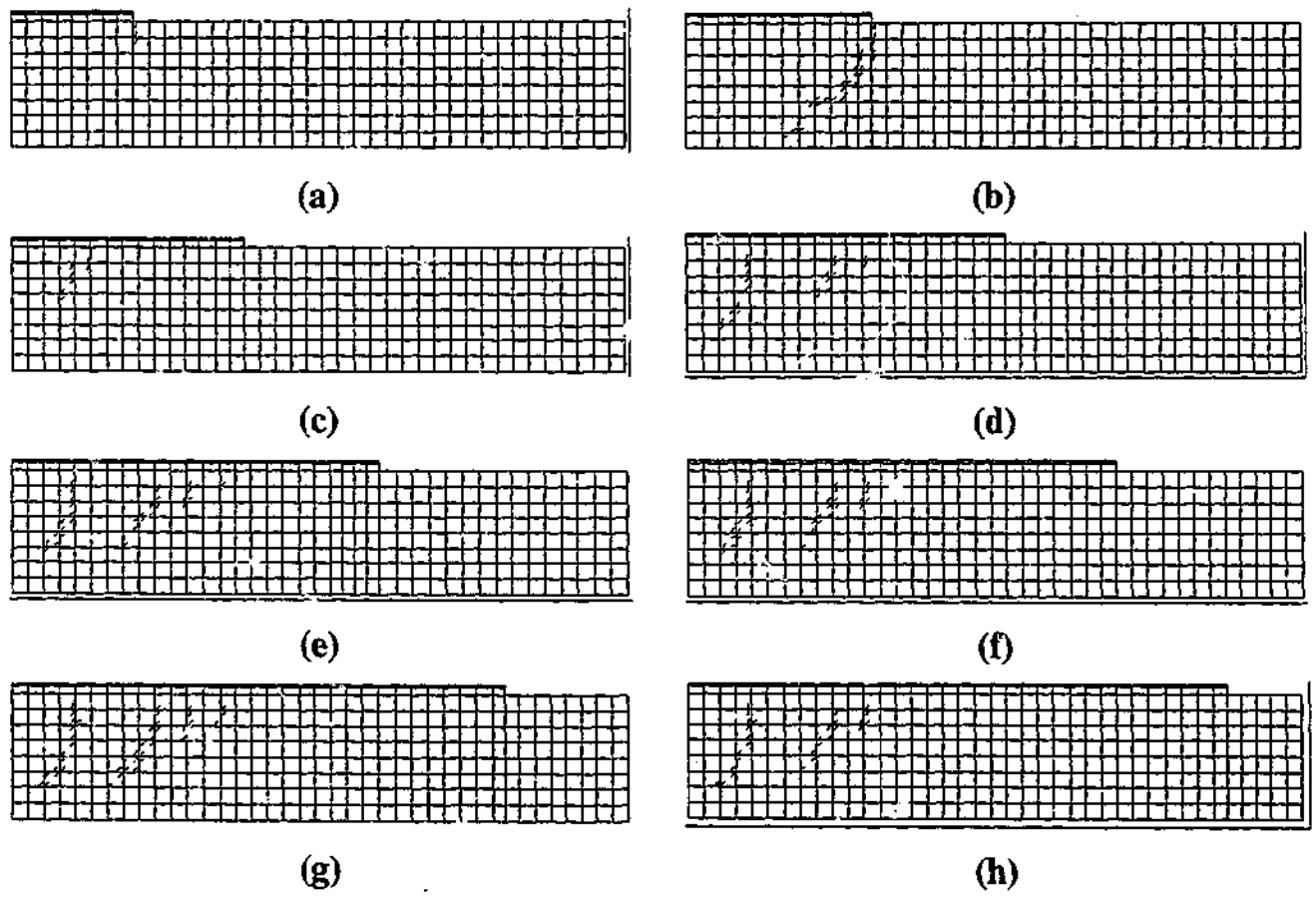

Figure 4.28 - Open crack patterns for bond lengths of (a) 50 (b) 75 (c) 95 (d) 130 (e) 150 (f) 175 (g) 200 and (h) 220 mm (Model 3)

4.5.3.4 Load slip behaviour

Figure 4.29 to Figure 4.32 illustrate the load-slip relationship produced from the models. The location where the slip is measured is shown in Figure 4.7. From Figure 4.29 to Figure 4.31, for all of the bond lengths, it can be seen that the stiffness of the load slip curve increases with adhesive stiffness. However, a significant change in the adhesive stiffness results only in a minute change in the stiffness of the load slip curve. From Figure 4.32, the stiffness of the load slip curve was identical in all the bond lengths of the same adhesive stiffness. The load slip curves of the longer bond lengths trace the path of the shorter bond lengths for most of the loading

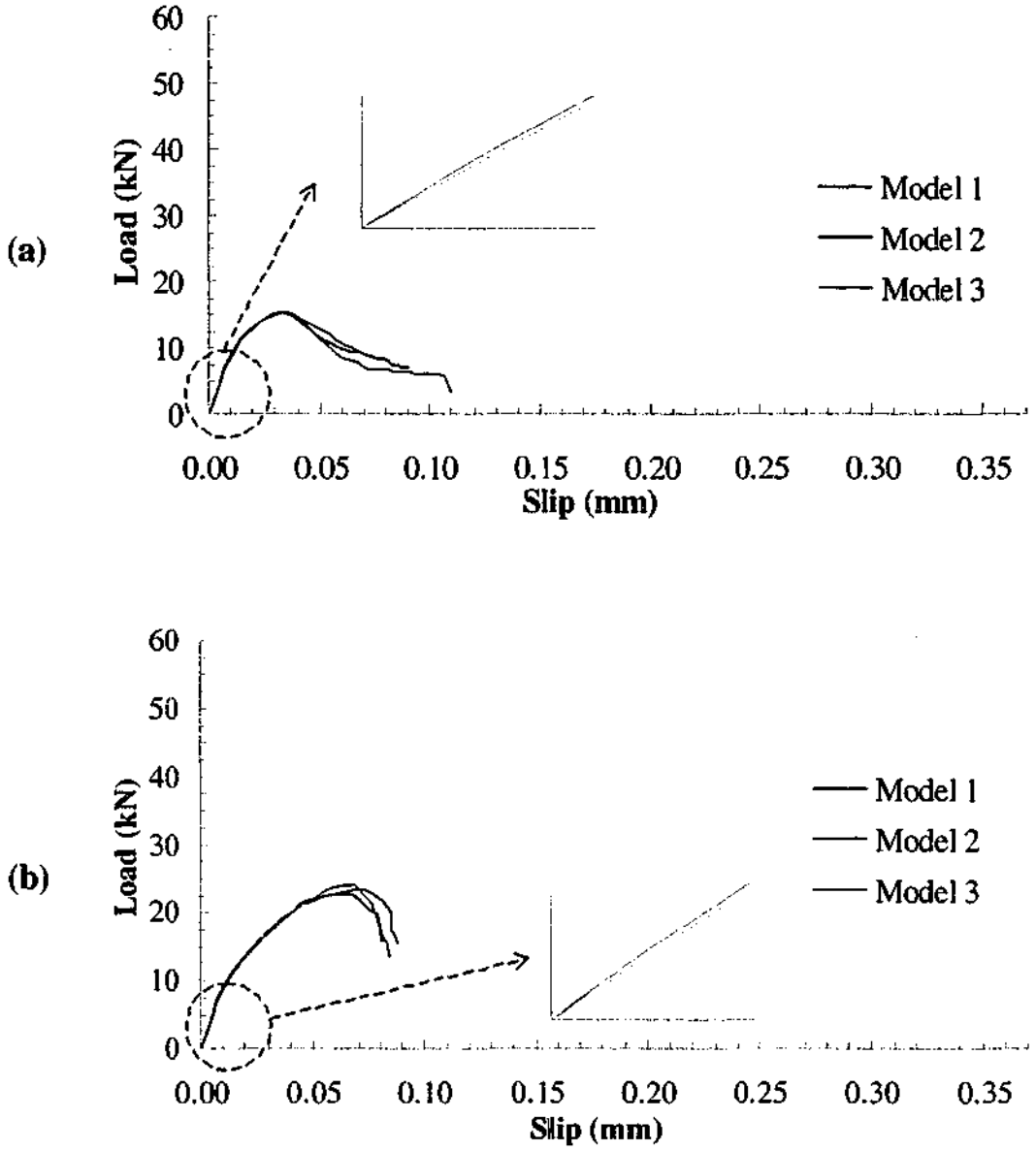

Figure 4.29 - Load slip behaviour of varying adhesive stiffness for bond lengths of (a) 50 and (b) 75 mm

(a)

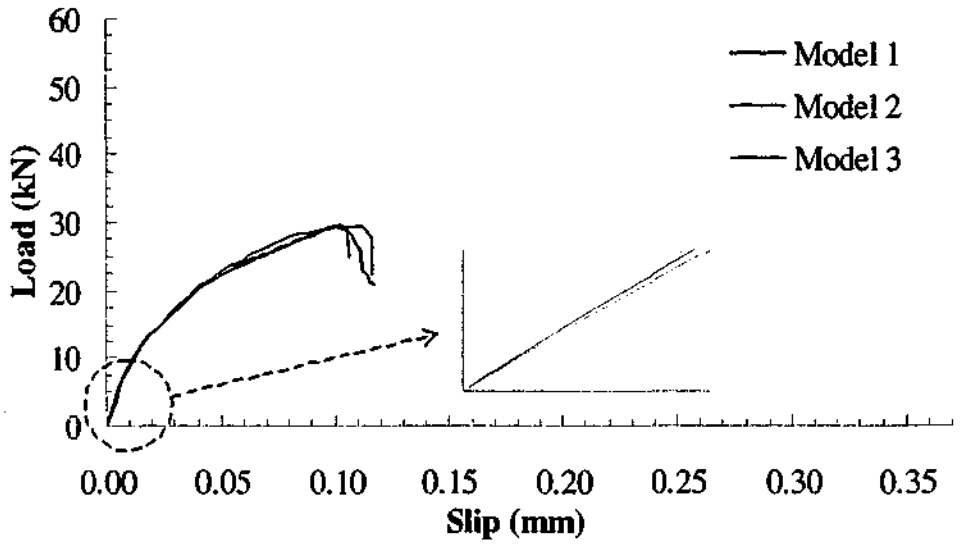

(b)

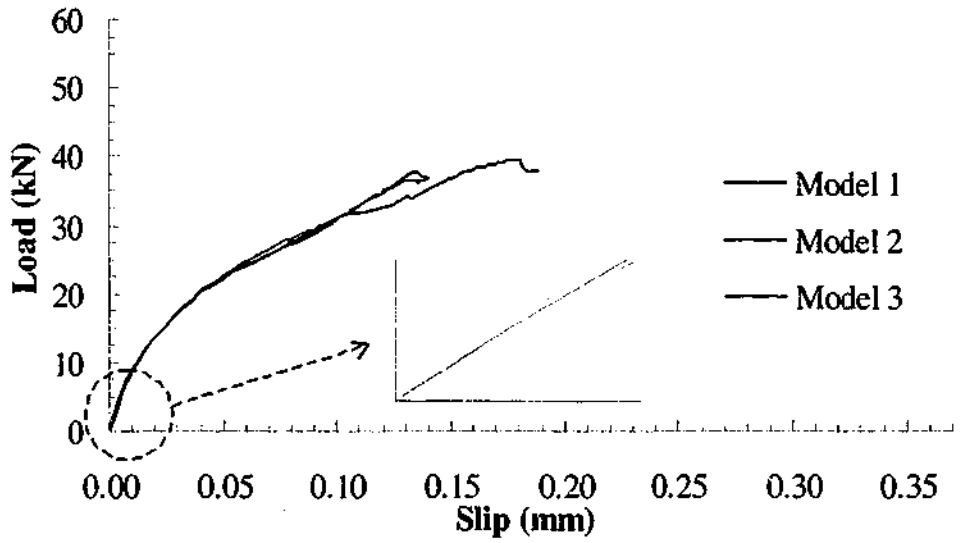

(c)

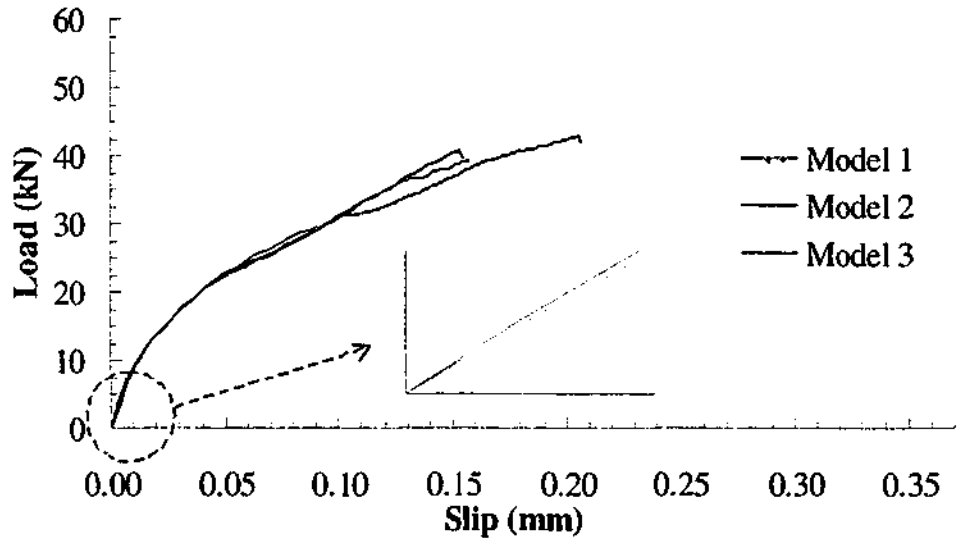

Figure 4.30 - Load slip behaviour of varying adhesive stiffness for bond lengths of (a) 95 (b) 130 and (c) 150 mm

(a)

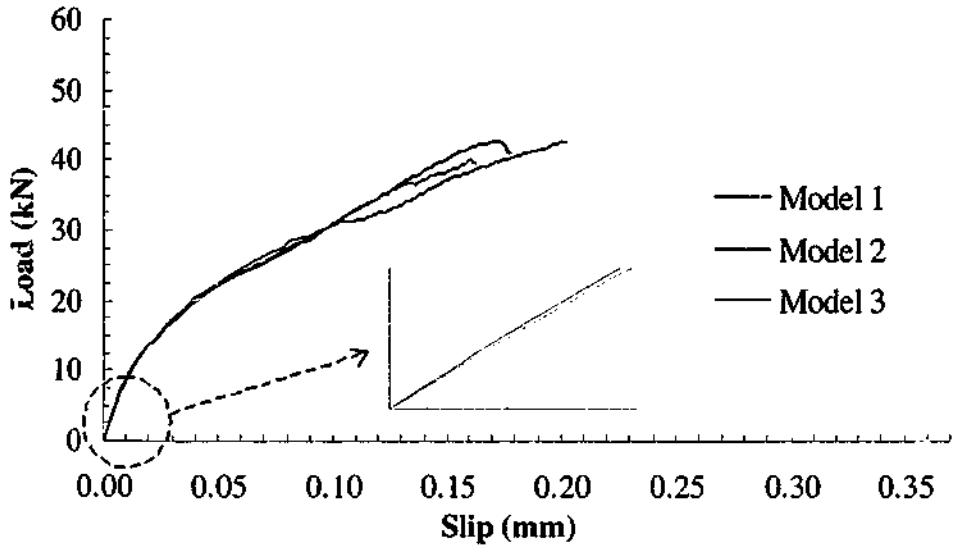

(b)

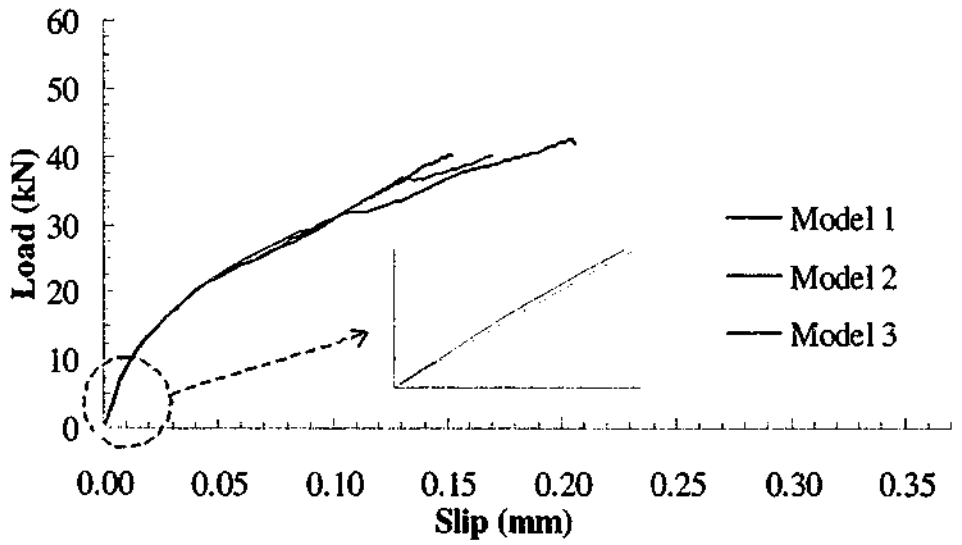

(c)

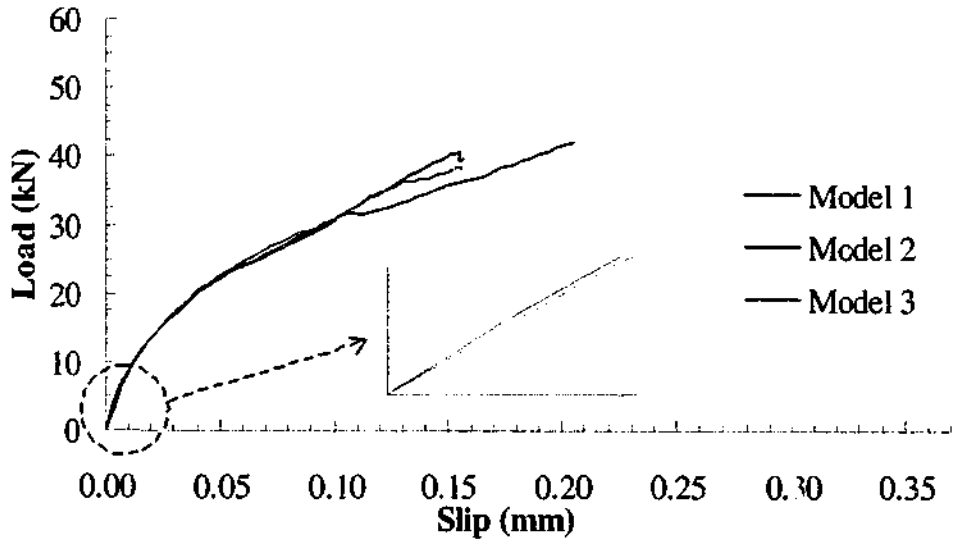

Figure 4.31 - Load slip behaviour of varying adhesive stiffness for bond lengths of (a) 175 (b) 200 and (c) 220 mm

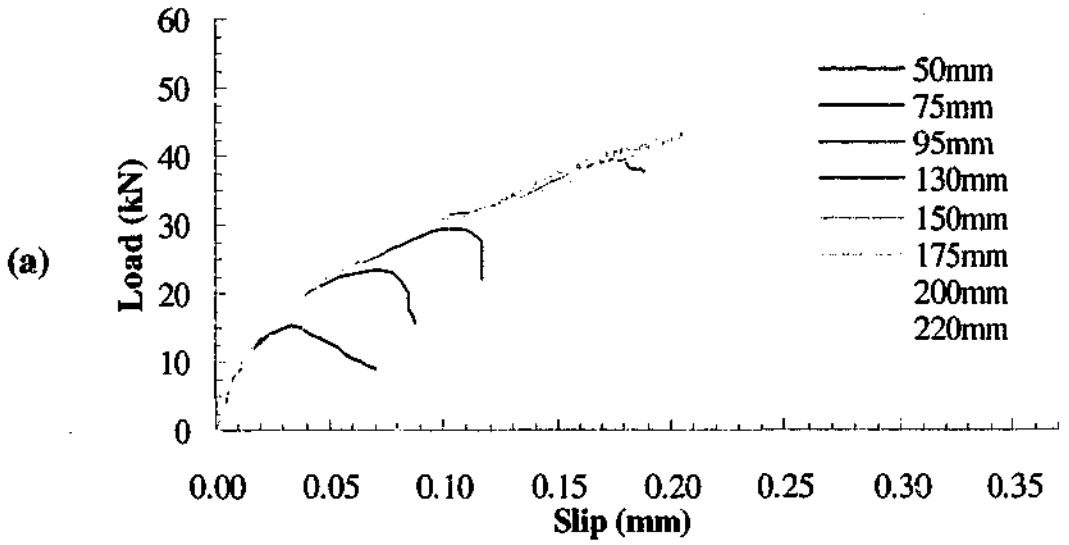

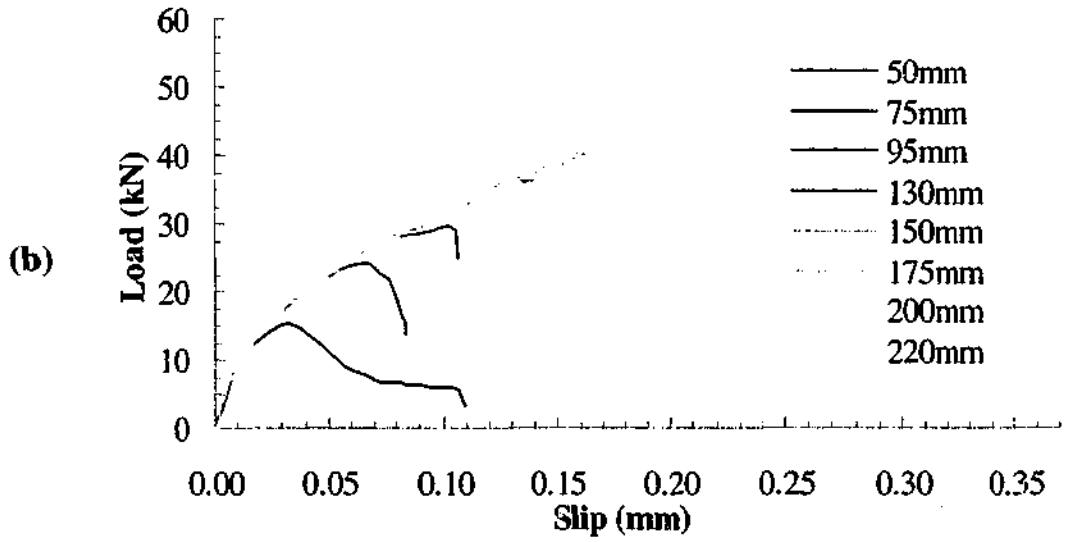

Figure 4.32 - Load slip behaviour for adhesive stiffness D_{11}/D_{22} (N/mm^3) of (a) 3200/1167 and (b) 6400/2335

4.5.3.5 Strain distributions along bonded joints

For the bond lengths of 50, 95, 150 and 200 mm, the strain developments in the CFRP plate with load at selected node locations along the joint are illustrated in Figure 4.33 and Figure 4.34. The locations of the nodes at which the strain readings were extracted are indicated in the figure. For a given load level, particularly at or below the service load level, it can be observed that the strains in the CFRP were fairly similar for the different adhesive stiffness. Closer examination of the results showed a trend whereby the strain in the CFRP plate decreases as the adhesive stiffness increases and vice versa. This is due to the fact that a stiffer adhesive is able to transfer more load from the CFRP plate to the concrete layer, which results in a lower CFRP plate strain. Based on the values investigated herein, variations in the

adhesive stiffness do not have a significant effect on the strain distribution profile of the CFRP plate at or below the service load levels.

It has been shown that variations in the adhesive stiffness results in an insignificant change in the peak load, load-slip behaviour and strain distribution of the CFRP plate. The use of adhesive properties similar to the experiment is, therefore, not crucial. The effects of the adhesive stiffness are less pronounced compared to the effects of concrete strength.

(a)

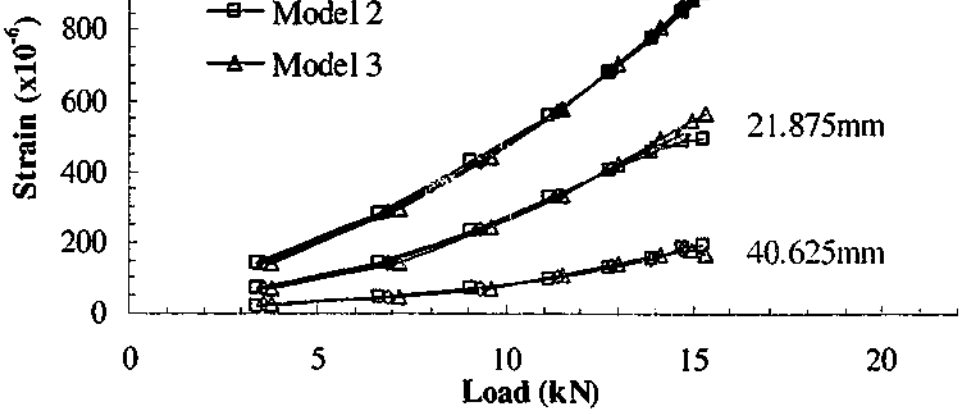

(b)

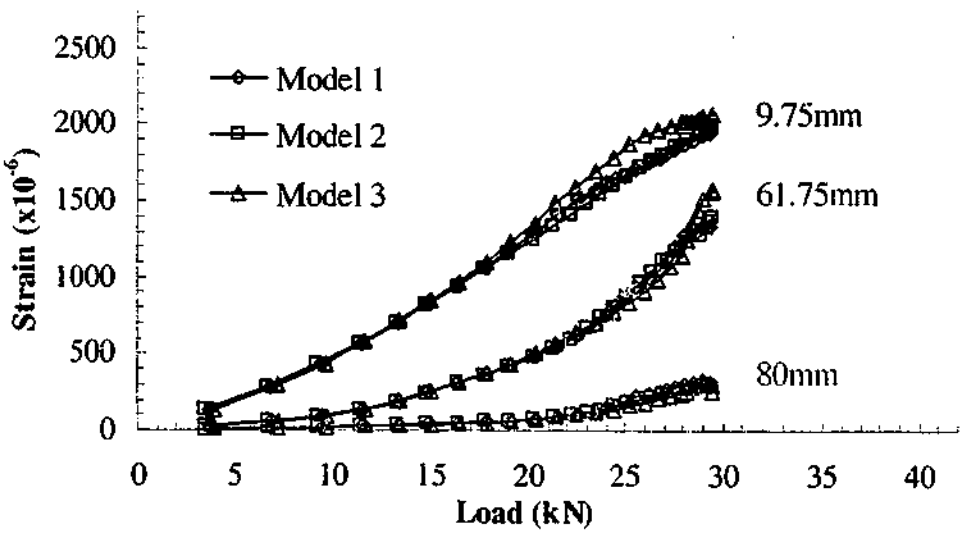

Figure 4.33 - Strain development in CFRP plate of varying adhesive stiffness for bond lengths of (a) 50 and (b) 95 mm

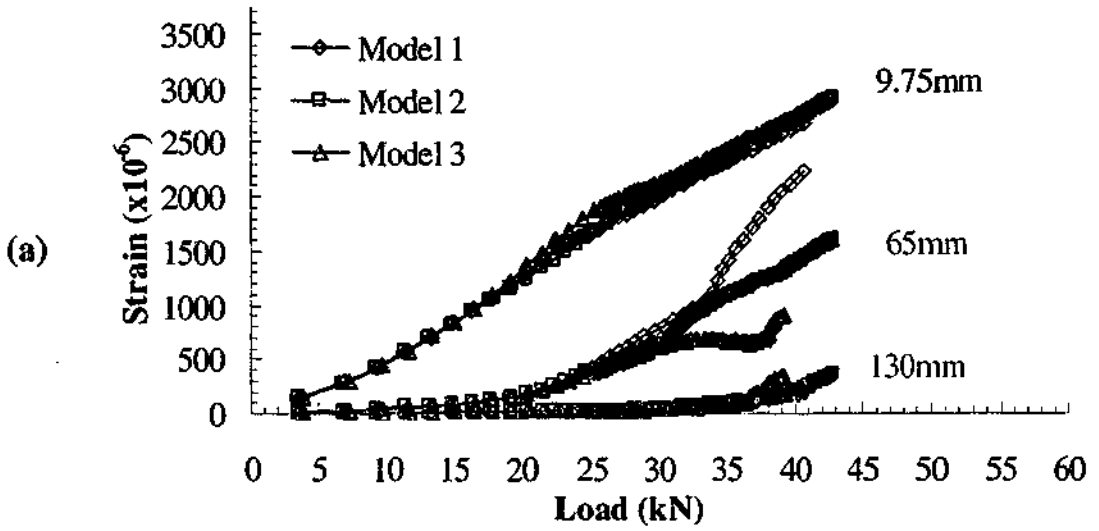

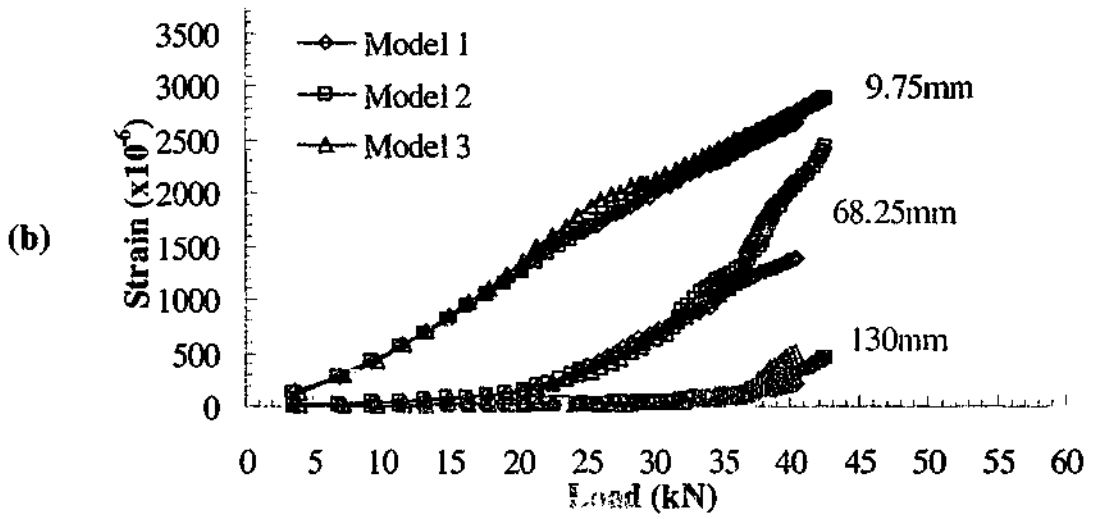

Figure 4.34 - Strain development in CFRP plate of varying adhesive stiffness for bond lengths of (a) 150 and (b) 200 mm

4.5.4 Effect of varying CFRP plate stiffness

4.5.4.1 Introduction

The effects of varying the CFRP plate stiffness on the peak load, load-slip behaviour and strain distribution profiles were investigated in this section. Two sets of models with different CFRP plate stiffness were analysed and compared against the base model outlined earlier. The CFRP stiffness used in the model was assumed arbitrarily and is summarised in Table 4.5. The thickness of the CFRP plate remained the same at 1.31 mm. All other material properties have remained the same as the base model. Due to the lack of experimental results, the determination of 'failure' of the models is based on the criterion used for the base models described earlier.

Table 4.5 - CFRP plate stiffness used in models

Model	Modulus (MPa)
1*	137345
2	125000
3	155000

* - Base model

4.5.4.2 Peak loads and effective bond length

Figure 4.35 compares the computed peak loads of the models with different CFRP plate stiffness. From Figure 4.36, it can be observed that for bond lengths of 95 mm and less, the peak loads obtained were quite similar for a given bond length even though the CFRP plate stiffness was different. For bond lengths of 130 mm and longer, the peak loads obtained do not differ significantly between the CFRP plate stiffness of 137345 and 155000 MPa. The difference in the peak loads was more pronounced between the CFRP plate stiffness of 125000 and 137345 MPa. The results imply that the peak loads decrease as the CFRP plate stiffness decreases. In addition, the peak load would not increase if a certain CFRP plate stiffness limit has been exceeded. Without experimental results for the CFRP-concrete joint type used herein, it is difficult to determine conclusively the hypothesis. Nevertheless, the main aim of the analyses is to determine the sensitivity of the solutions to variations in the material properties adopted. The attainment of the correct peak loads in the models is not important in the current investigation. The change in the overall response of the model due to variations in material properties is more important in the modelling of the CFRP-concrete joint in the T-beams. In the T-beams, the fracturing of a concrete block as observed in the bond specimens is unlikely to occur. For the values adopted herein, it can be observed from the two figures that the computed peak load is not significantly affected by the CFRP plate stiffness. The difference in the peak loads of the models to the base models obtained is less than 20%. The effective bond length across the three different CFRP plate stiffness is similar, which is approximately 145 mm.

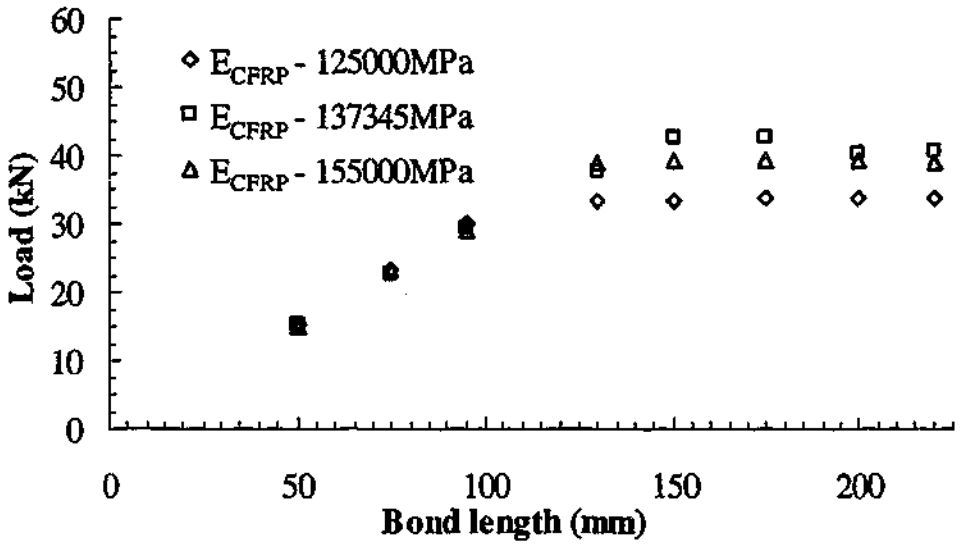

Figure 4.35 - Computed peak load with varying bond lengths of different CFRP plate stiffness

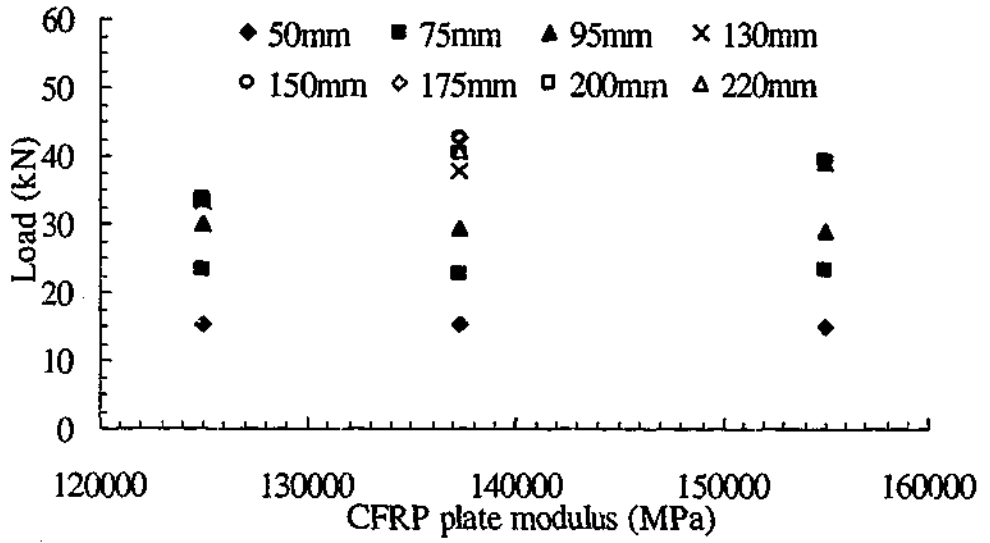

Figure 4.36 - Computed peak load with varying CFRP plate stiffness of different bond lengths

4.5.4.3 Crack pattern

The 'open' crack patterns of the finite element models with CFRP plate stiffness of 125000 and 155000 MPa are illustrated in Figure 4.37 and Figure 4.38. In most of the models, the crack patterns shown were produced at steps near the peak load. For the bond lengths of 50 with CFRP plate stiffness of 125000 MPa and bond length of 50 and 75 mm with CFRP plate stiffness of 155000 MPa, open cracks did not form prior to or at the peak load. The crack patterns shown were produced at the step when open cracks first formed.

For the CFRP plate stiffness of 125000 MPa, it can be observed for the bond length of 50 mm, cracks formed at the inside edge of the joint. For all the other bond lengths, cracks initially formed approximately four elements away (26 mm) from the start of the joint in the concrete layer under the adhesive. Near the peak load, more cracks can be observed to have formed further along the joint for the bond lengths of 130 mm and longer (Figure 4.37). The crack patterns were similar to the crack patterns of the base models.

For the CFRP plate stiffness of 155000 MPa, cracks formed at the inside edge of the joint for the bond length of 50 mm. For the remaining bond lengths, cracks initially formed approximately four elements away (26 mm) from the start of the joint in the concrete layer. Near the peak load, for the bond lengths of 130 mm and longer, a second set of cracks formed further along the joint within the vicinity of the seventh element from the start of the bond. In some of the models, more cracks can be observed to formed further along the joint at the ninth element from the joint.

The crack patterns of the models with CFRP plate stiffness of 125000 and 155000 MPa are similar to the base models. The peak loads illustrated in Figure 4.35 are, therefore, considered to be acceptable.

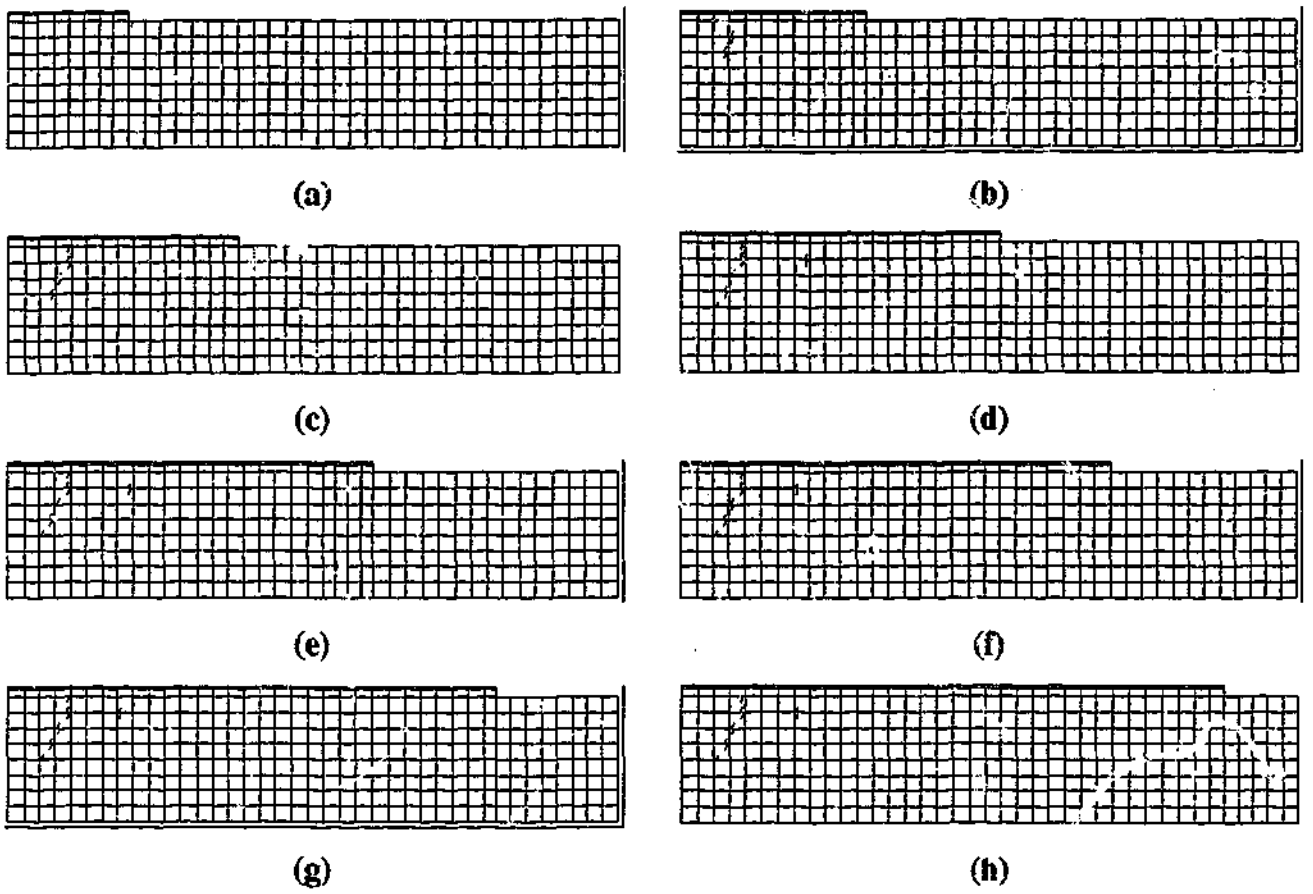

Figure 4.37 - Open crack patterns for bond lengths of (a) 50 (b) 75 (c) 95 (d) 130 (e) 150 (f) 175 (g) 200 and (h) 220 mm with CFRP plate modulus of 125000 MPa

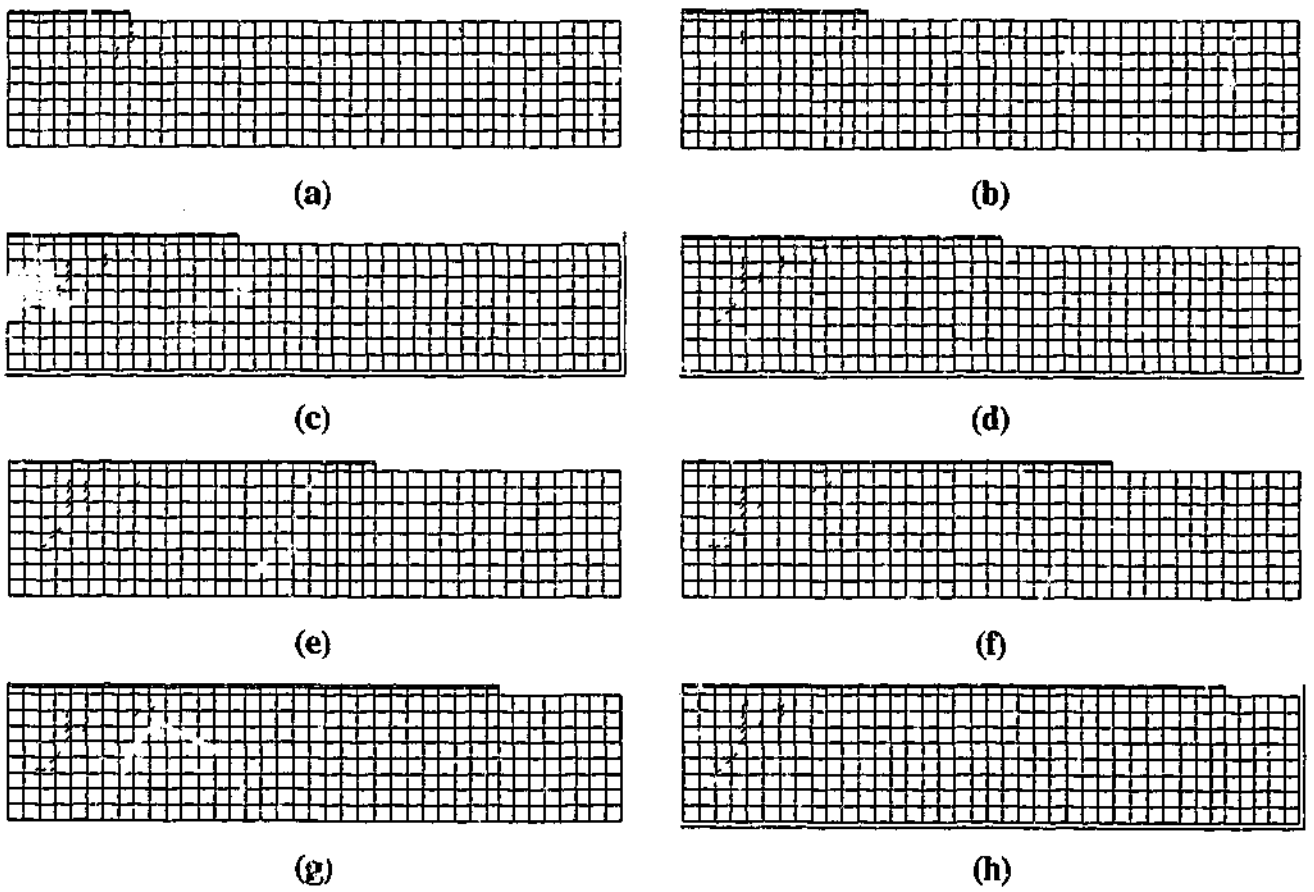

Figure 4.38 - Open crack patterns for bond lengths of (a) 50 (b) 75 (c) 95 (d) 130 (e) 150 (f) 175 (g) 200 and (h) 220 mm with CFRP plate modulus of 155000 MPa

4.5.4.4 Load slip behaviour

Figure 4.39 to Figure 4.42 compare the load-slip relationship produced from the models with CFRP stiffness of 125000 and 155000 MPa. The location where the slip is measured is shown in Figure 4.7. It can be observed from the figures that the stiffness as indicated by the slope of the load slip curve increases with CFRP plate stiffness. Variations in the CFRP plate stiffness result in only an insignificant increase in the stiffness of the specimen. In Figure 4.42, it can be seen that the stiffness of the load slip curve was identical in all the bond lengths of the same CFRP plate stiffness.

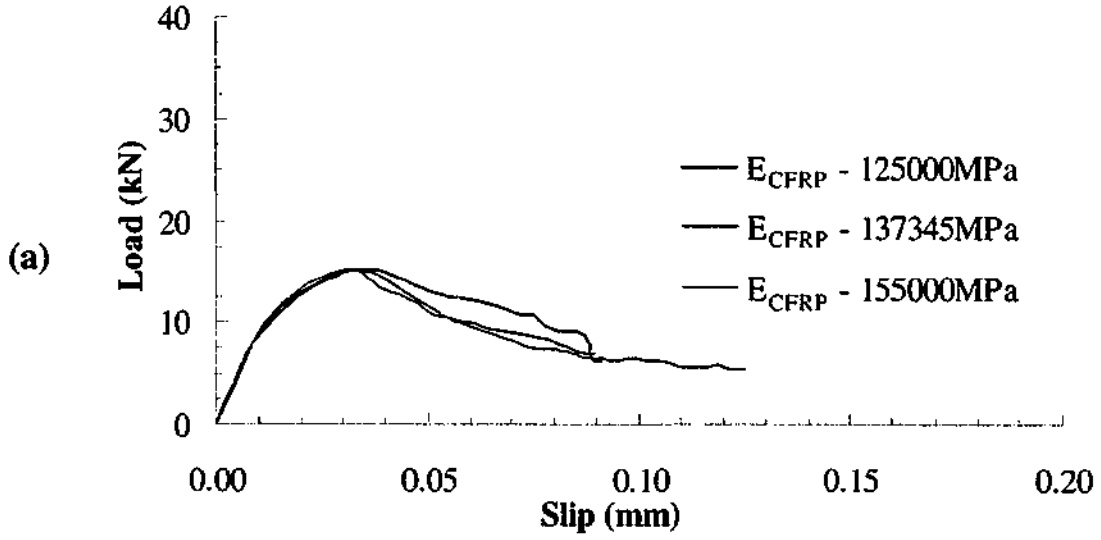

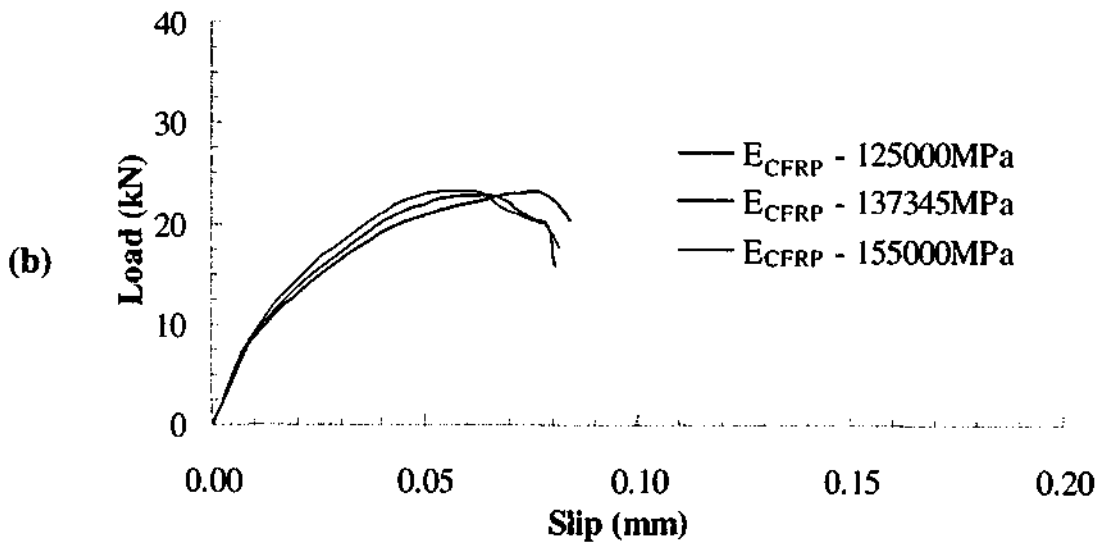

Figure 4.39 - Load slip behaviour of varying CFRP plate moduli for bond lengths of (a) 50 and (b) 75 mm

(a)

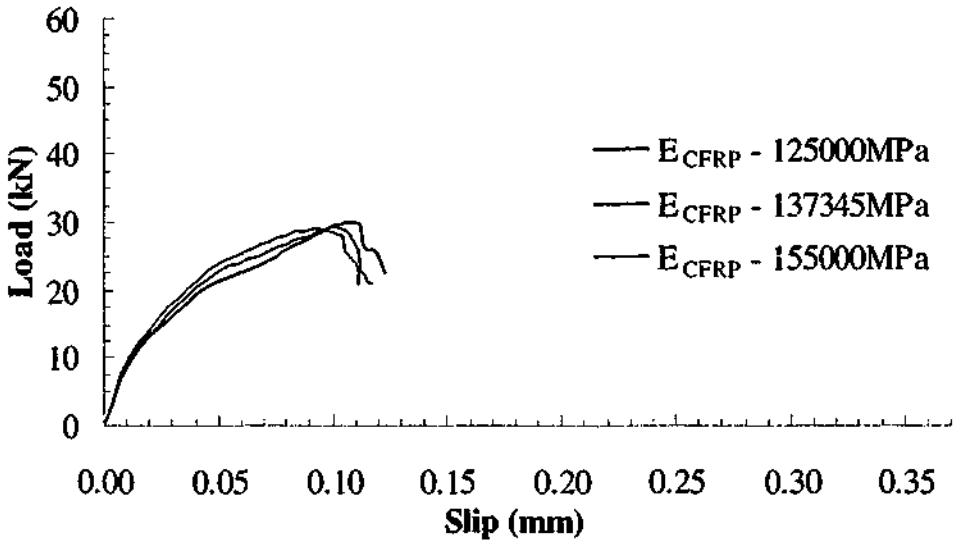

(b)

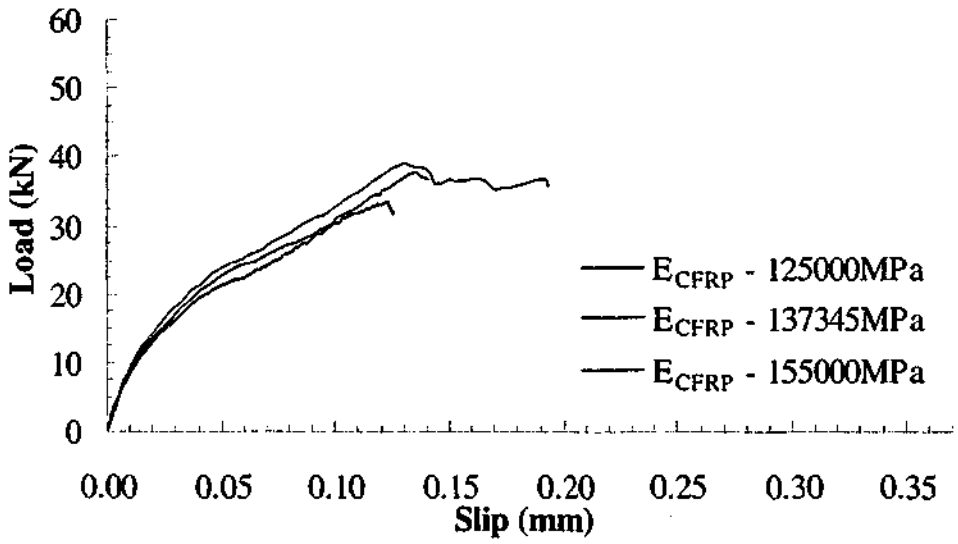

(c)

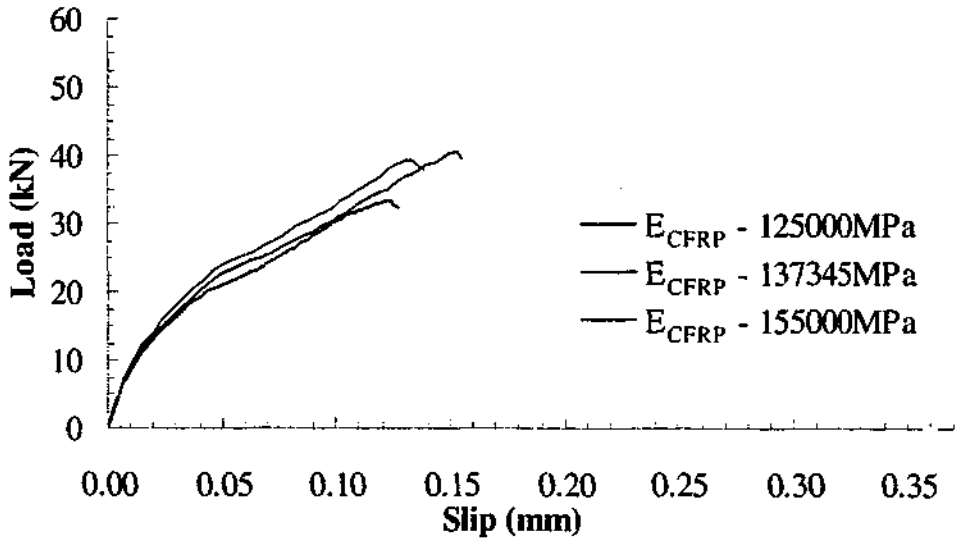

Figure 4.40 - Load slip behaviour of varying CFRP plate moduli for bond lengths of (a) 95 (b) 130 and (c) 150 mm

(a)

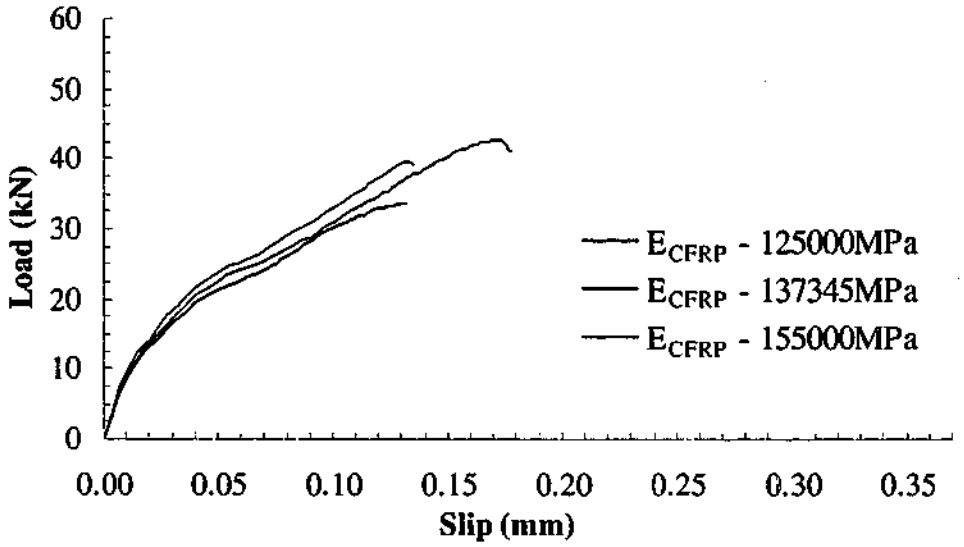

(b)

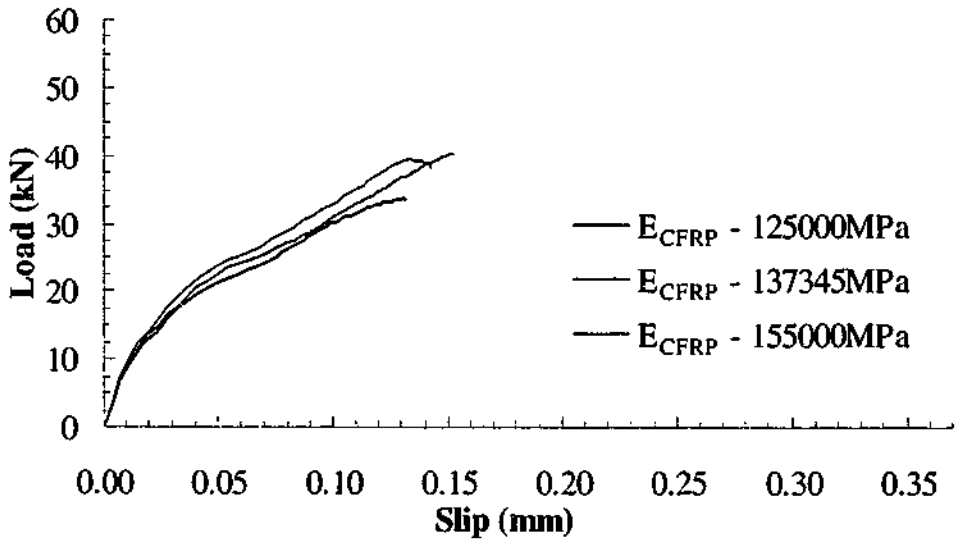

(c)

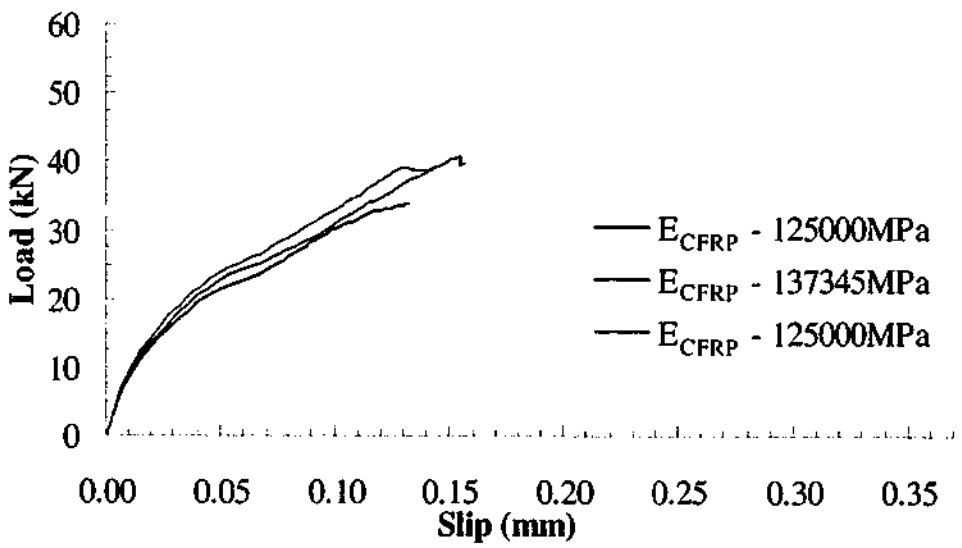

Figure 4.41 - Load slip behaviour of varying CFRP plate moduli for bond lengths of (a) 175 (b) 200 and (c) 220 mm

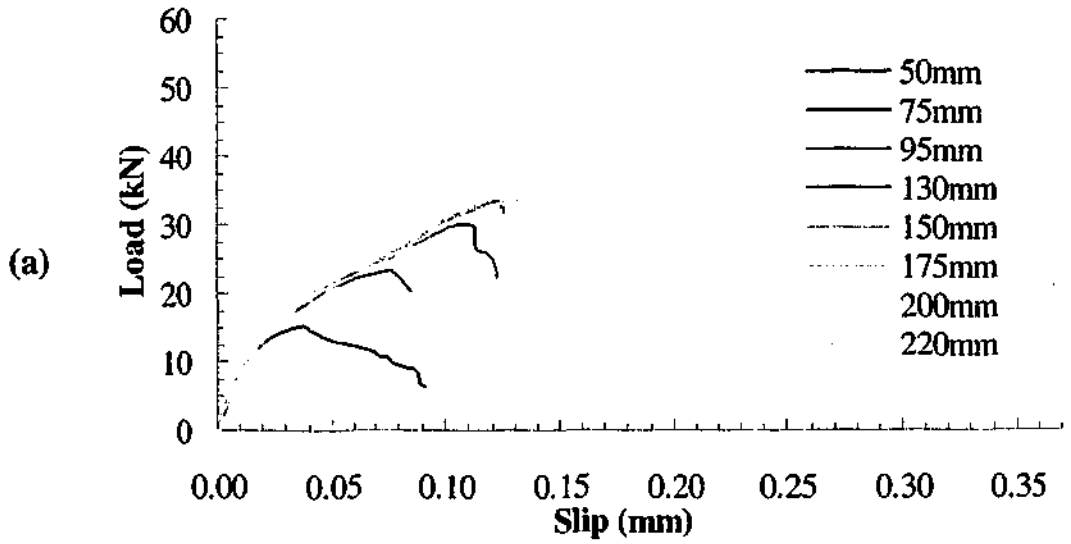

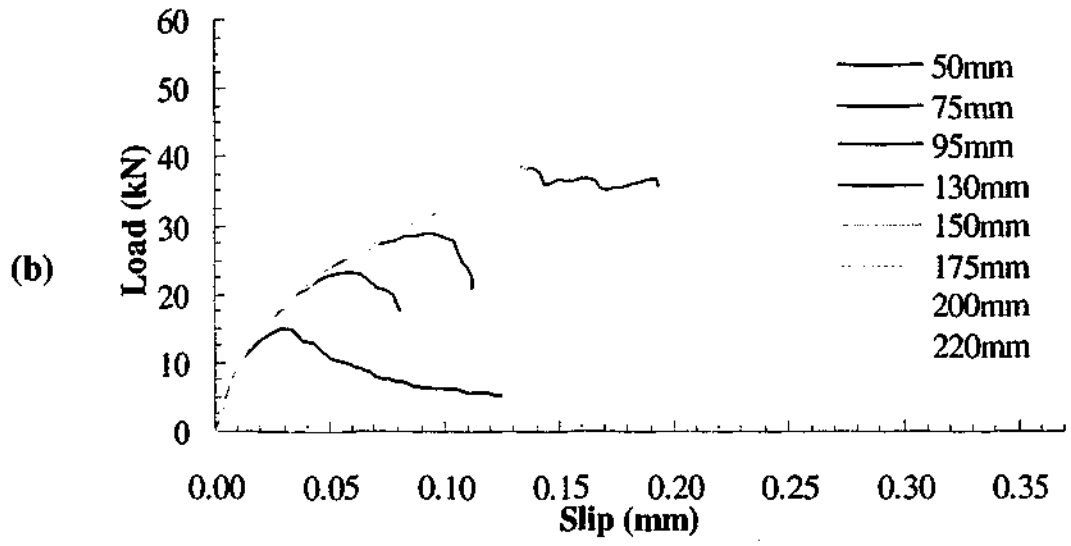

Figure 4.42 - Load slip behaviour for CFRP plate moduli of (a) 125000 and (b) 155000 MPa

4.5.4.5 Strain distributions along bonded joints

For the bond lengths of 50, 95, 150 and 200 mm, the strain development in the CFRP plate with load at selected node locations along the joint are illustrated in Figure 4.43 and Figure 4.44. The node locations at which the strain readings were extracted are indicated in the figure. For a given load level, particularly at or below the service load level, it can be observed that the strain in the CFRP plate decreases as the CFRP plate stiffness increases. This is due to the fact that for a given load, a CFRP plate with low stiffness will strain more compared to a CFRP plate with higher stiffness. The strain distribution profiles suggest that the strain level may reach zero within a shorter distance in specimens with higher CFRP plate stiffness. Therefore, there is a possibility that the effective bond length decreases with increases in the CFRP plate stiffness. However, the trend reported by Nakaba et al. (2001) and Chen

and Teng (2001) stated that the effective bond length should increase with increases in the FRP stiffness. It was difficult to establish this conclusively from the finite element models as the change in the strain values is minor near the unloaded end of the joint.

The main finding of the present section is that variations in the CFRP plate stiffness do not have a significant effect on the peak load, load-slip behaviour and strain distribution of the CFRP plate. Based on the material properties used herein, the numerical analyses suggest that the effective bond length decreases as the concrete strength increases. In the finite element model, adopting identical CFRP plate stiffness to the actual experiment is, therefore, not crucial. The numerical solutions do not change significantly or are sensitive to changes in the CFRP plate properties.

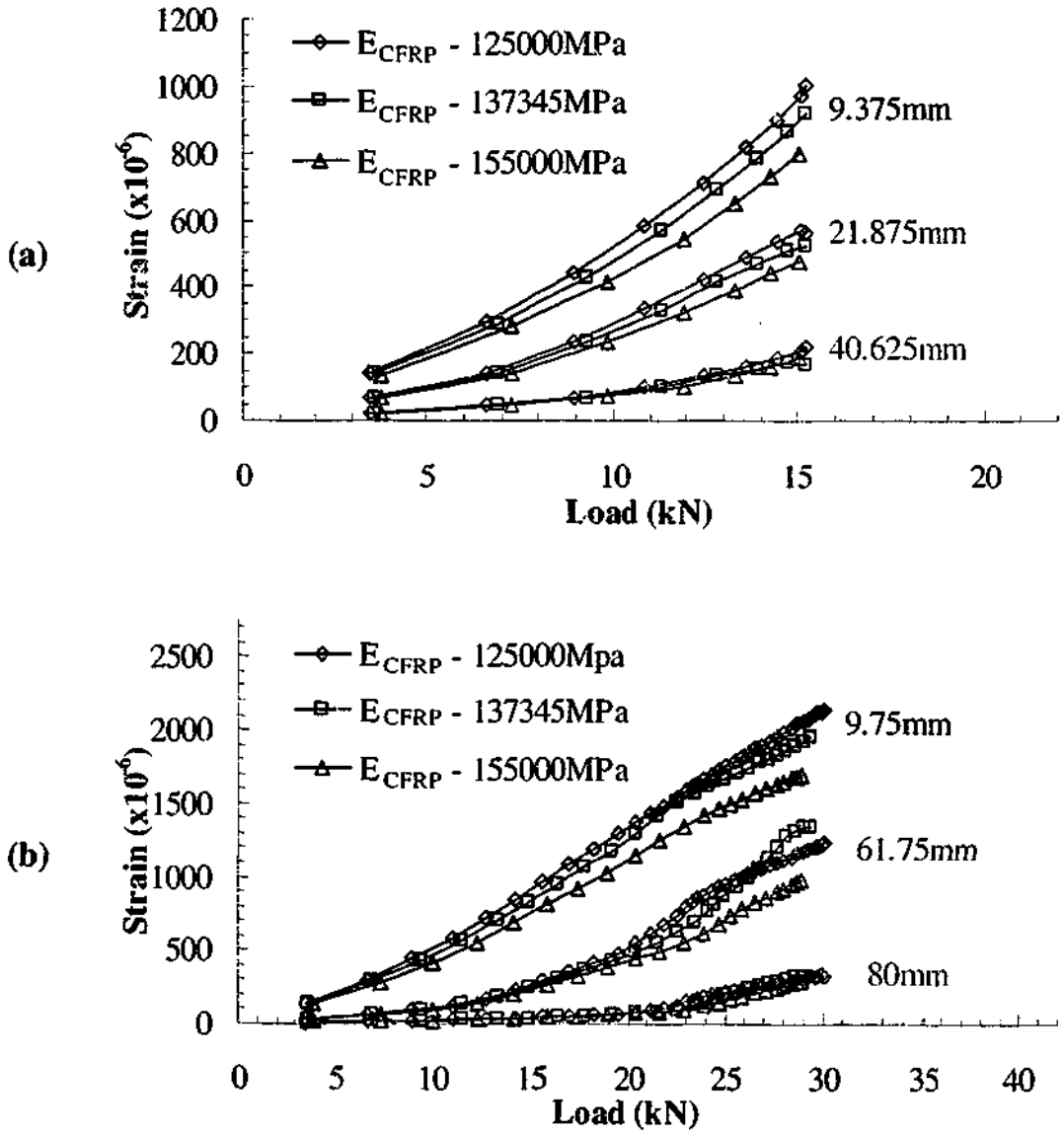

Figure 4.43 - Strain development in CFRP plate of varying CFRP plate stiffness for bond lengths of (a) 50 and (b) 95 mm

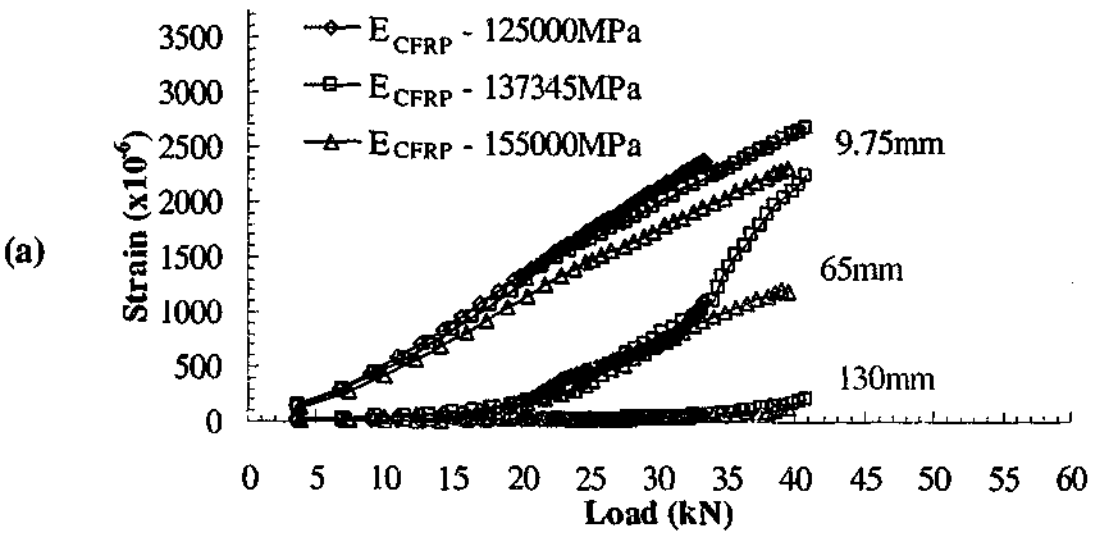

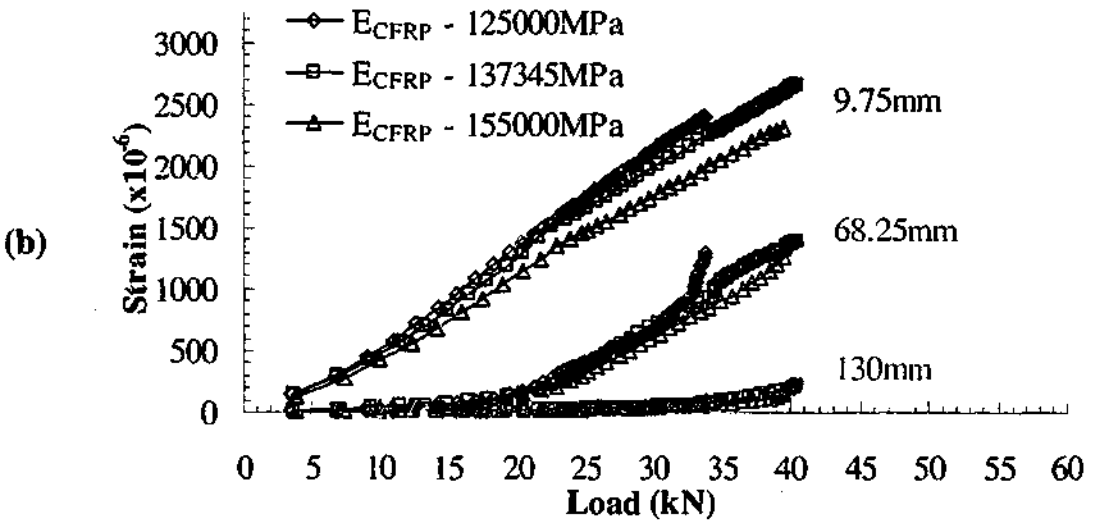

Figure 4.44 - Strain development in CFRP plate of varying CFRP plate stiffness for bond lengths of (a) 150 and (d) 200 mm

4.6 Summary of findings

Two sets of non-linear finite element analyses were carried out to supplement the experimental results of the bond specimens. The first set of analyses was carried out to verify the feasibility of using the finite element method to model the behaviour of the bond specimens. The second set of analyses was carried out to determine qualitatively the sensitivity of the numerical results with respect to slight variations in the material properties adopted in the first set of analyses. The main aim was to use the results and findings of the numerical analyses in the development and understanding of the finite element models of the actual T-beams strengthened in shear.

In the first set of analyses, the numerical peak loads were in good agreement with the experimental peak loads. The effective bond length given by the numerical models was approximately 145 mm. The numerically obtained crack patterns were similar to the crack patterns observed in the experiment. Load slip behaviour was predicted reasonably accurately by the numerical models. For the strain distribution profile in the CFRP plate, the numerical results agree well with the experimental results at or below the service load levels. Beyond the service load level, however, the computed strain becomes larger than the experimental strain, particularly near the start of the bond. Nevertheless, the experimental trend has been simulated adequately. Overall, the material models and properties adopted produced comparable results to the experiment.

In the second set of analyses, it was found that a large variation in the concrete strength results in a significant change in the peak load but minor change in the slip-behaviour and strain distribution profile of the CFRP plate. For the values investigated herein, the effective bond length remained virtually the same for all concrete strengths. The peak load increases with concrete strength. The stiffness of the model as indicated by the slope of the load slip curve increases slightly with concrete strength. The strain in the CFRP plate decreases slightly as concrete strength increases indicating an increase in the load carried by the concrete layer. Adopting identical concrete strength to the actual experiment is not crucial.

In the models, the effect of varying adhesive stiffness is less pronounced compared to the effects of varying the concrete strength and CFRP plate stiffness. For the values investigated herein, variations in the adhesive stiffness results in an insignificant change in the peak load, load-slip behaviour and strain distribution profile of the CFRP plate. A significant change in the adhesive stiffness results only in a minute change in the stiffness of the load slip curve. The stiffness of the load slip curve increases with adhesive stiffness. At the initial stages of loading, the CFRP plate strain distribution profiles of models with different adhesive stiffness were virtually identical. The results showed a trend whereby the strain in the CFRP plate decreases as the adhesive stiffness increases and vice versa.

Variations in the longitudinal stiffness of the CFRP plate between 125000 and 155000 MPa do not have a significant effect on the peak load, load slip behaviour and strain distribution profile of the CFRP plate. For the values investigated herein, compared to the effects of concrete strength, the effects of varying CFRP stiffness are less pronounced. The effective bond length remained similar. The stiffness of the load slip curve increases only slightly with CFRP plate stiffness. For a given load, the strain in the CFRP plate decreases as the CFRP plate increases.

The material properties and models adopted in the first set of analyses gave similar results to the experimental results. It has been shown that the numerical solutions do not change significantly or are sensitive to variations in the material properties. Therefore, for the finite element modelling of the T-beams shear strengthened using the L-shaped CFRP plate, the material properties of the numerical results in this section will be used to simulate the bond behaviour between the concrete and CFRP plate.

CHAPTER 5 - EXPERIMENTAL TESTING OF CFRP SHEAR STRENGTHENED T-BEAMS

5.1 Introduction

Studies of T-beams strengthened using pre-cured L-shaped laminates are limited. There are only two studies reported in the literature regarding the failure modes of this particular strengthening system. Most studies focused on the use of lay-up fabrics or sheets strengthening system.

In this study, four T-beams were tested to investigate the failure modes of the CFRP L-shaped plate strengthening system. The effect on the failure mechanism and ultimate strength of varying the spacing of the external reinforcement was investigated. The spacings considered were 0.75D, 0.60D and 0.50D where D is the overall depth of the beam. The beams were designated accordingly as '0.75D', '0.60D' and '0.50D'. The control beam had no external reinforcement. As part of the experimental program, photogrammetry measurements were conducted to supplement experimental results. Details of the measurement technique and results are presented separately in Chapter 7.

5.2 Design methodology

The primary aim of the experimental program was to study the failure modes of the CFRP strengthening system. With this in mind, the test beams were designed to have significantly higher flexural capacity than the shear capacity. The dimensions of the T-beams were based on the Kiewa Valley Highway Bridge located in the north-east of Victoria, Australia. The bridge, designed in 1916, is a good representative example of bridges constructed in periods when the design provisions were less severe than current design requirements. The bridge has an average span of 7.213 metres.

Different scales of the actual bridge beam were considered before the final beam design was adopted. The aim was to minimise cost and ensure that laboratory testing was physically viable while still achieving the experimental objective. Several reinforcement configurations were investigated for beam scales from 50% to 100%.

The shear reinforcement spacing was set to the maximum allowable by AS3600 (1995), which was 0.75D where D is the overall depth of the member. The area of shear reinforcement was then determined using Equation 5.1, which is the minimum allowable by SAI (2001). The calculated stirrup diameter was set to match the nearest available sizes. The bar type considered was limited to plain round bars with yield stresses ($f_{sy.f}$) of 250 and 350 MPa. For the flexural reinforcement, the bar sizes considered varied from 16 to 36 mm with the smaller sizes used for smaller scale beams and larger sizes for larger scale beams. The bar type investigated was limited to deformed bars with yield stresses (f_{sy}) of 450 and 500 MPa. The concrete strengths considered were 25 and 30 MPa, which were the typical strength of old bridges. For each beam, the margin between shear failure and flexural failure was calculated. This margin was expressed as the ratio between the load corresponding to the ultimate moment capacity and the shear failure load. The flexural strength was calculated using bending theory whereas the shear strength was calculated using a computer program that utilised the modified compression field theory (MCFT) developed by Vecchio and Collins (1986). Details of the program are outlined in the studies by Al-Mahaidi and Taplin (1998) and Al-Mahaidi et al. (2000). The contribution of the L-shaped CFRP plates was calculated independently. It was assumed that shear cracks would intersect two CFRP plates on each side. Based on the study carried out by EMPA (1998a), it was assumed that each strip would contribute up to 55% of its ultimate load capacity before failing by concrete debonding. The ultimate tensile capacity of each CFRP plate was assumed to be 126 kN. The shear strength of the beam was calculated to be the total of the load contributed by the CFRP plates and the load obtained using the MCFT.

$$A_{sv.min} = 0.35 b_v s / f_{sy.f} \tag{5.1}$$

Based on the investigation, an 80% beam scale was selected for the experimental program. Further information of the geometries and reinforcement configurations considered is contained in Appendix A.1.

5.3 T- beams details

The dimensions and reinforcing details of the T-beams are shown in Figure 5.2 to Figure 5.4. Each beam had a total length of 6 metres with an effective depth of 418 mm. The concrete cover to the shear reinforcement was 20 mm. The main reinforcement was arranged in four bundles consisting of two bars each. In the shear span, the spacing of the shear reinforcement was 365 mm. Closed stirrups were used. To facilitate the placement of the L-shaped CFRP plates, polystyrene blocks were cast into the flange of the beams, except for the control beam. The positions of the L-shaped CFRP plates are detailed in Figure 5.5. Figure 5.6 illustrates how the polystyrene blocks were secured to the formwork. Once the formwork was removed, the blocks were drilled out.

5.4 Material properties

5.4.1 Concrete

The concrete for each of the four T-beams was supplied separately, pre-mixed from a local supplier. The concrete mixes had a specified 28-day mean compressive strength of 25 MPa with a maximum aggregate size of 14 mm. The specified slump was 80 mm. Water reducing and air entraining admixtures were used to improve workability and freeze-thaw resistance. The beams were cast in an outdoor environment and cured under plastic cover in timber formwork for one week before removal. Twelve 100 mm diameter by 200 mm high cylinders were cast concurrently with each pour. The cylinders were stripped after 24 hours and cured in a water bath for one week. The cylinders were then removed and left to cure in air under indoor laboratory conditions until the time of testing. Further information on the concrete mix design is contained in Appendix A.3.

5.4.2 Steel reinforcement

The main flexural reinforcement used in the study consisted of grade 400 deformed bars with a nominal diameter of 28 mm (Y28). The top transverse and longitudinal reinforcement consisted of grade 250 plain bars with a nominal diameter of 10 mm (R10). For the shear reinforcement, the same R10 bar type was used.

5.4.3 Sika CarboShear L Plates strengthening system

The Sika CarboShear L Plates strengthening system used in the study has been described under Sections 3.5.3 and 3.8.2.

5.5 Strengthening methodology

Surface preparation is critical in ensuring satisfactory bond between concrete and FRP. The concrete surface must be free from any bond inhibiting materials with roughened surfaces exhibiting improved mechanical bonding. In this study, similar surface preparation treatment to the bond specimens was used. A high-pressure water jet was used to remove a thin layer of concrete to expose the aggregates (Figure 5.1). The slots for anchoring the CFRP plates were cleaned to remove any remaining polystyrene. The T-beams were left to air-dry under laboratory conditions for 14 days. Prior to application of the CFRP plate, loose particles and dust were removed from the concrete surface and flange slots with pressurised air and an industrial vacuum cleaner. Adhesive was applied to both the concrete surface and CFRP plates. Using a guide bracket, the adhesive thickness on the concrete surface was maintained evenly throughout at 4 mm on the web and soffit. Using a spatula, a considerable amount of adhesive was then applied at the chamfer and to fill the slots completely. As for the CFRP plate, the adhesive was applied and shaped to have a domed profile with a thickness of 3 mm in the centre gradually decreasing to 1 mm at the sides. This was achieved by pulling the CFRP plate along a steel bracket with a dome-shaped opening at one end. Adhesive was also applied on the other side of the plate at the portion to be inserted into the flange. The CFRP plate was inserted first into the flange slot and then pressed lightly against the web and soffit of the beam. Using a roller with circular steel guides welded to both sides, light pressure was exerted until excess adhesive was pressed out on both sides of the plate while maintaining an even adhesive layer of 3.5 mm throughout. The excess adhesive was removed using a spatula. The adhesive was left to cure under laboratory conditions for at least seven days before testing was carried out.

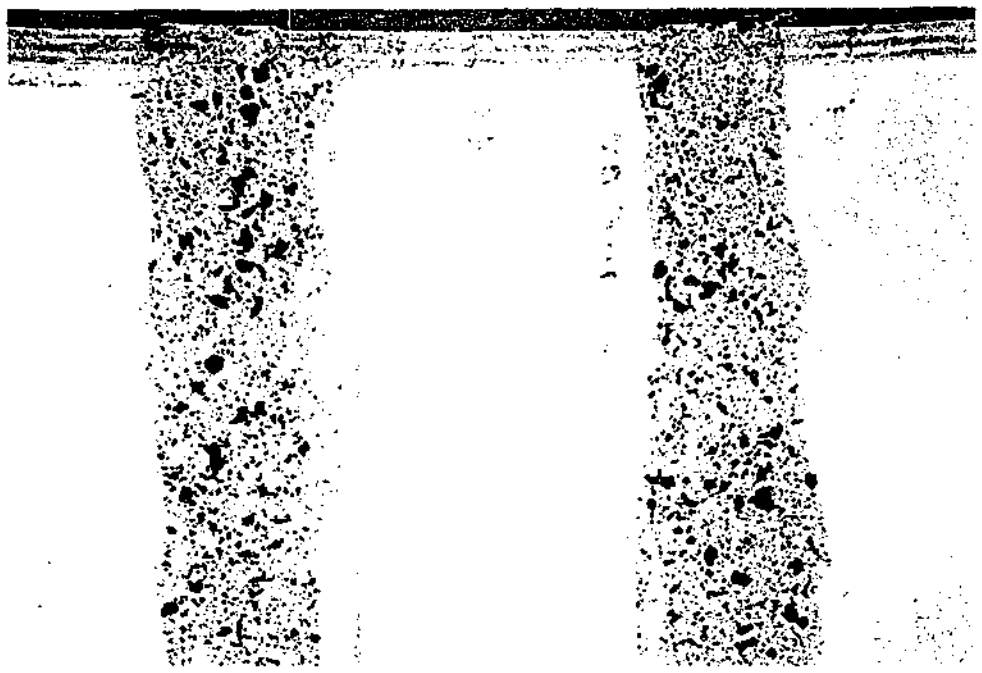

Figure 5.1 - Exposed aggregate on web

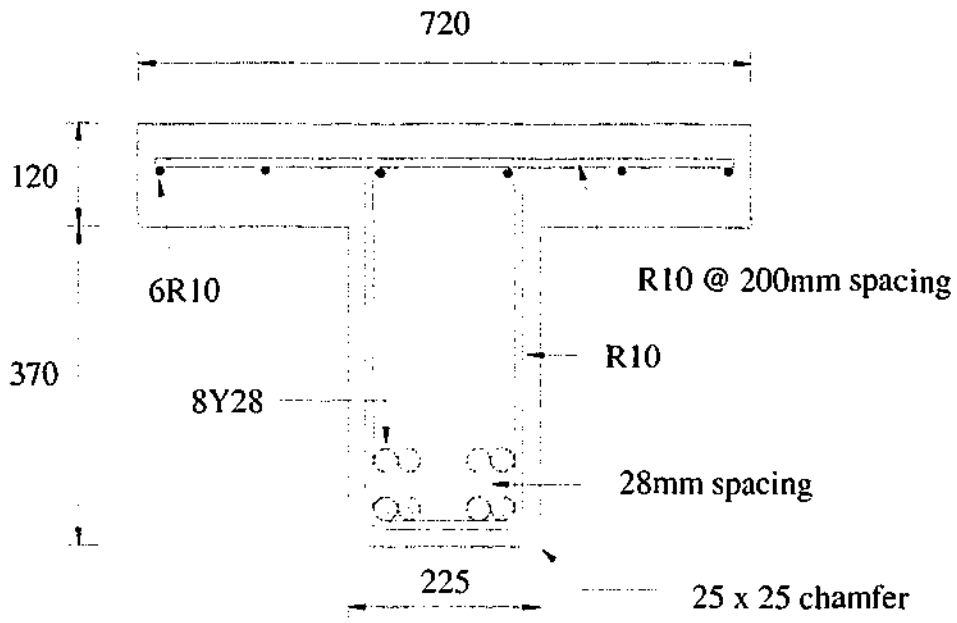

Figure 5.2 - T-beam cross-sectional detail

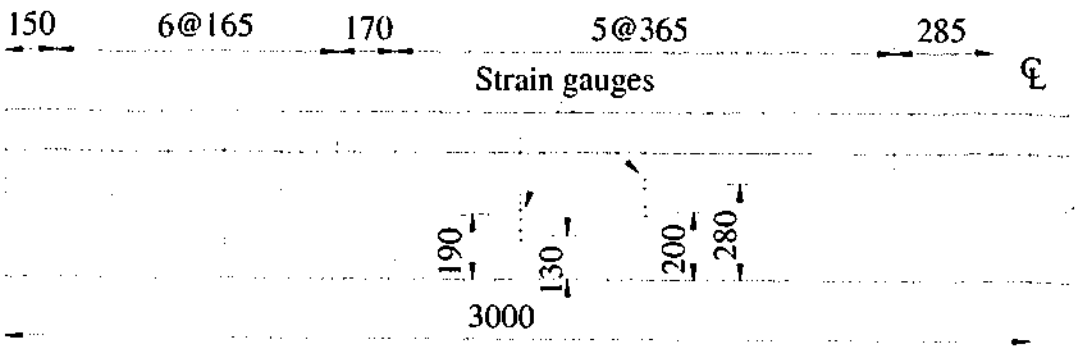

Figure 5.3 - Shear reinforcement details

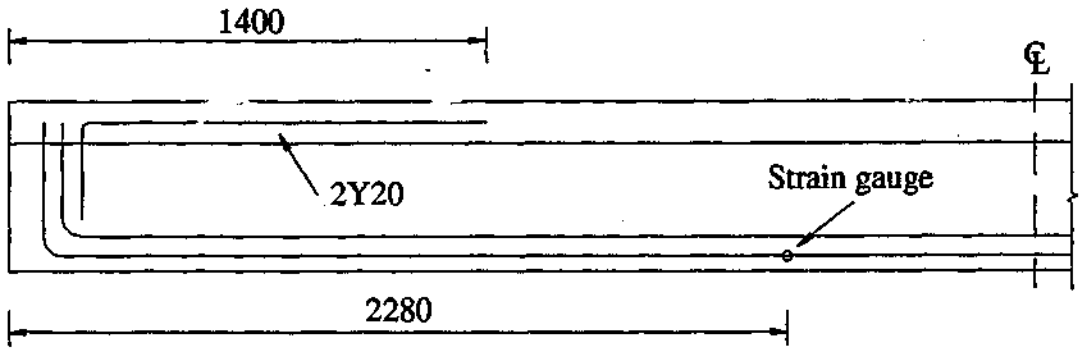

Figure 5.4 - Longitudinal reinforcement details

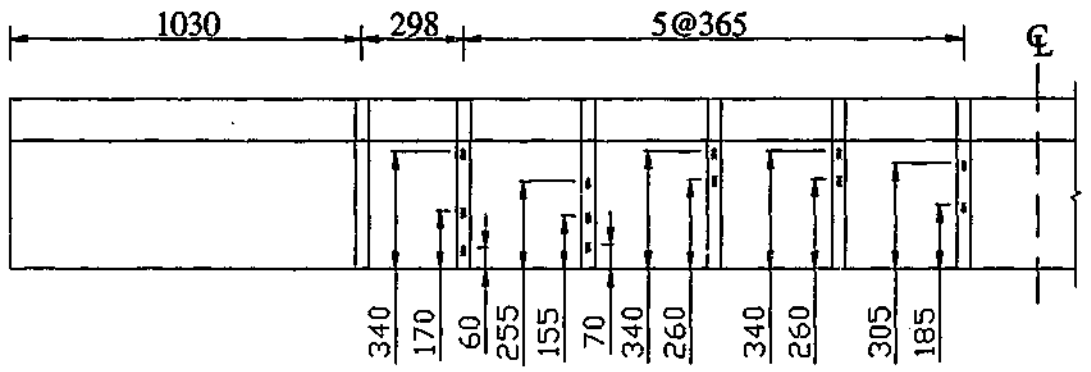

Beam '0.75D'

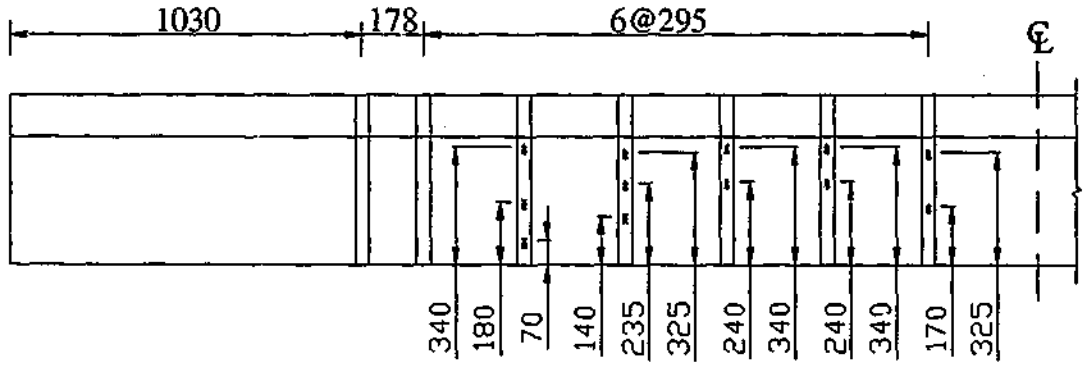

Beam '0.60D'

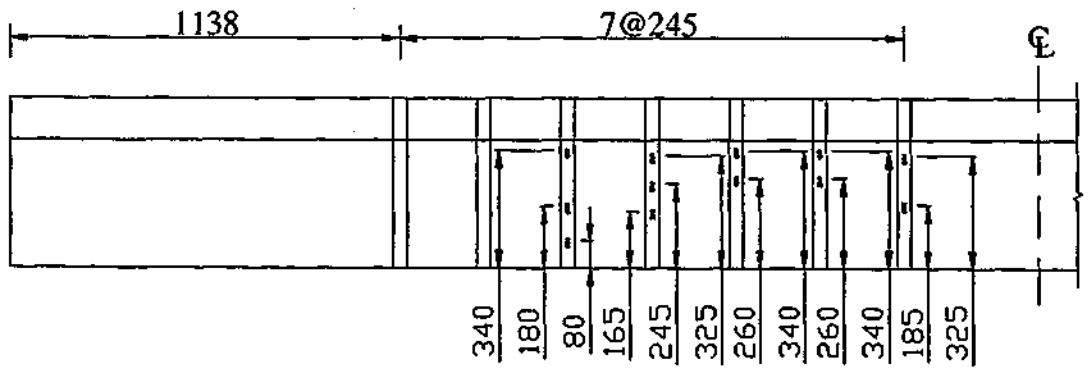

Beam '0.50D'

Figure 5.5 - Locations of L-shaped CFRP plates and strain gauges

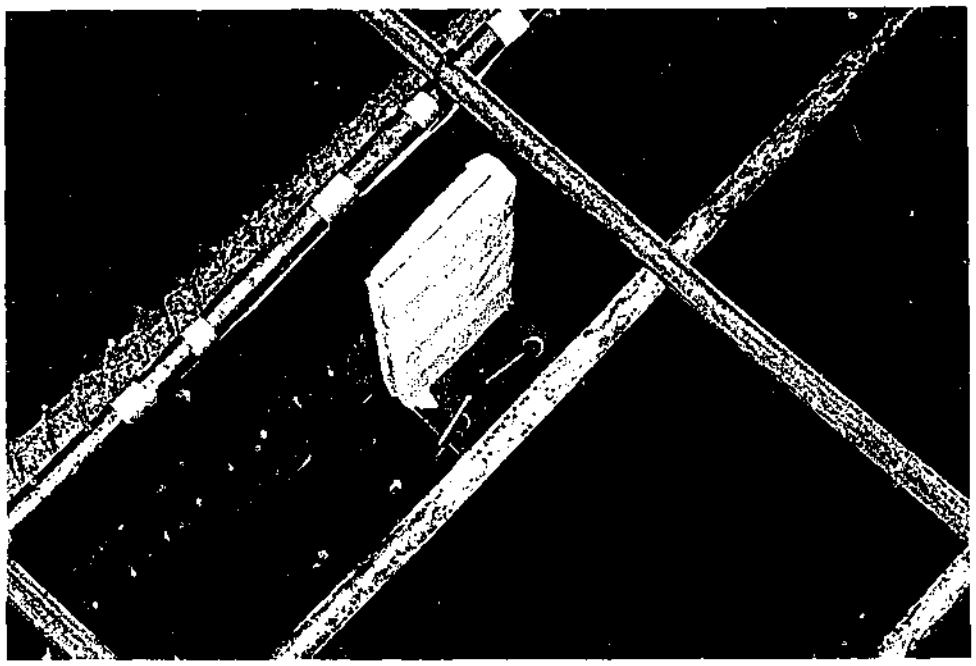

Figure 5.6 - Securing of polystyrene block to formwork

5.6 Instrumentation

The T-beams were instrumented extensively to record strain, load and deflection readings. Strain gauges were used to measure strain levels in the steel stirrups, main flexural reinforcement and the L-shaped CFRP plates. Figure 5.3 illustrates the positions of the strain gauges on the stirrups. At both shear spans, strain gauges were bonded to both legs of each stirrup. On the main flexural reinforcement, only one strain gauge was used at each shear span (Figure 5.4). The strain gauges were bonded to the bottom and outermost bars at opposing sides. For each gauge, waterproofing followed by wax coating was applied. On each strengthened beam, forty-eight strain gauges were bonded on the L-shaped CFRP plates, twelve each side per shear span. The positions of the strain gauges are detailed in Figure 5.5. For both the stirrups and CFRP plates, the strain gauges were positioned at locations where shear cracks were most likely to form. Based on the investigation carried out by Taplin and Al-Mahaidi (1999) and Taplin and Al-Mahaidi (2000), shear crack patterns of T-beams were compiled and scaled accordingly to correspond to the dimensions used in the present study. The beam details and test set up are similar to the present investigation. A drawing outlining the locations of stirrups and CFRP plates was placed on top of the shear crack patterns to identify where to bond the strain gauges. Further information on the shear crack patterns can be found in Appendix A.2.

The strain gauges were labelled using the notation illustrated in Figure 5.7. Pictorial descriptions of the labelling convention used are shown in Figure 5.8 and Figure 5.9.

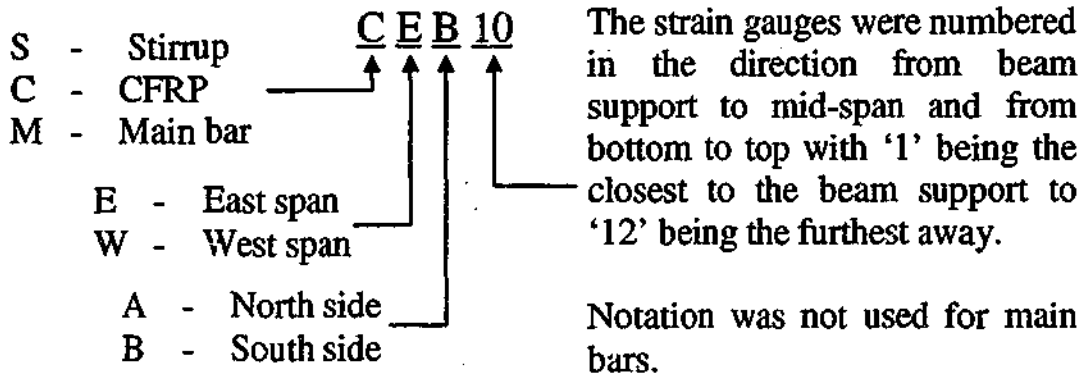

Figure 5.7 - Strain gauge notations

Deflections of the beam at mid-span and the load points were measured using a stringpot located under the beams. Load cells at the actuators and supports measured the applied loads and reaction forces.

The slip between certain CFRP plates and the concrete surface at particular points was measured using linear variable displacement transducers (LVDTs). The LVDTs were used on the north side of the beams and were positioned at locations where shear cracks were anticipated to form. Two LVDTs were used for beam '0.75D', one at each shear span. For beams '0.60D' and '0.50D', four LVDTs were used, two at each shear span. Each LVDT was mounted close to one end of a flat steel plate approximately 30 mm wide by 70 mm long. At the other end of the steel plate, a smaller steel plate 17x17 mm in size was spot-welded on the other side. The aim was to minimise the bonded area to the concrete surface and at the same time carry the weight of the LVDT and its fixtures. The steel fixtures on the CFRP are similar to the ones fashioned for the bond specimens reported in Section 3.4 and illustrated in Figure 3.7. Two small flat steel plates spot welded to the underside of a steel bracket were adhered to the CFRP plates, minimising the area at which slip measurements were taken. The locations of the LVDTs are illustrated in Figure 5.10. The LVDTs are identified by its location on the span of the beam and the CFRP plate, for example 'E2' or 'W1'. The letters 'E' and 'W' refer to the east and west span and

the numbers '1' and '2' refer to the location of the CFRP plate as illustrated in Figure 5.10.

The data acquisition equipment made by dataTaker, 'DT500' and 'CEM', were used in the experimental program. During testing, readings were recorded once every two seconds using the computer software 'HP VEE Version 5.01'.

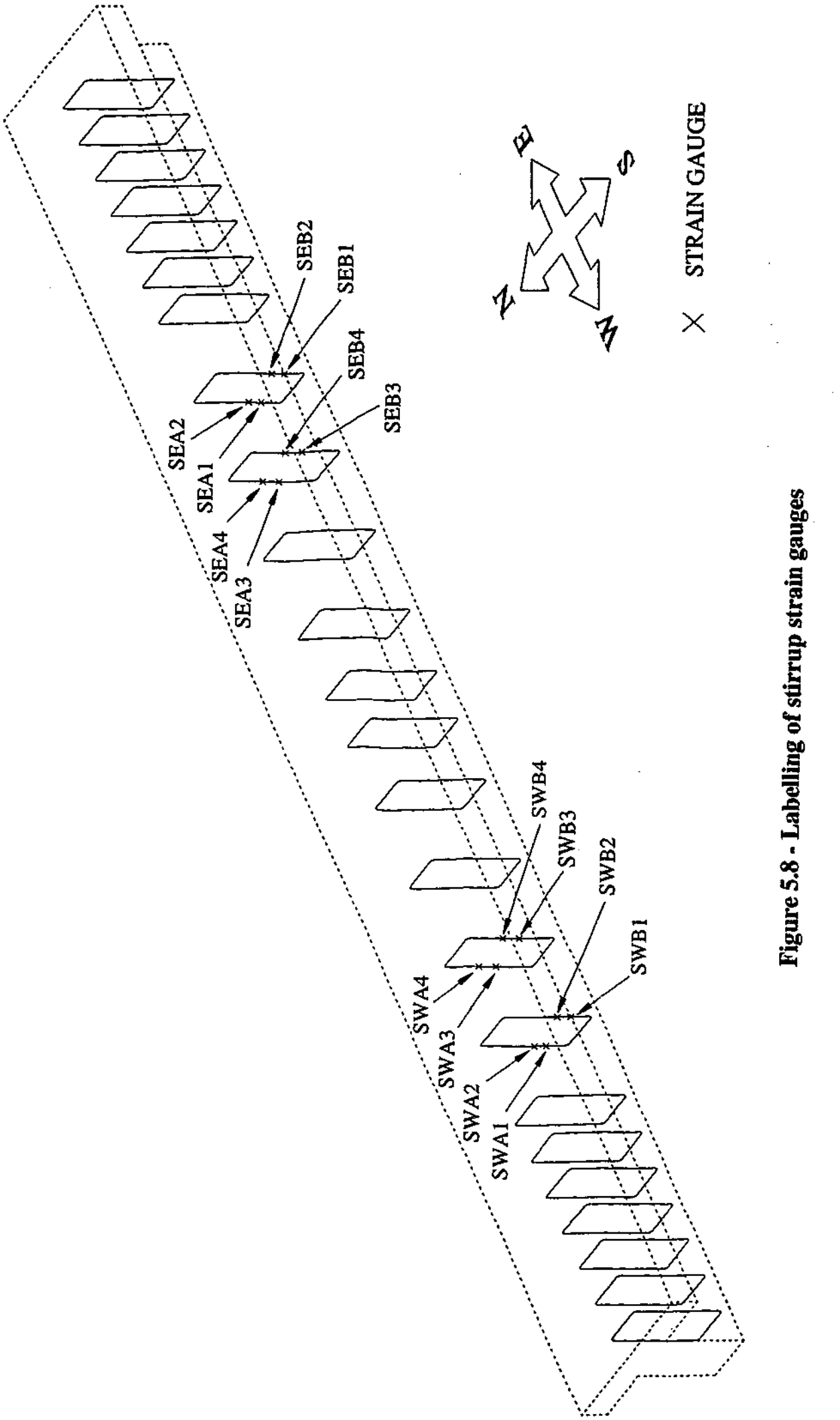

Figure 5.8 - Labelling of stirrup strain gauges

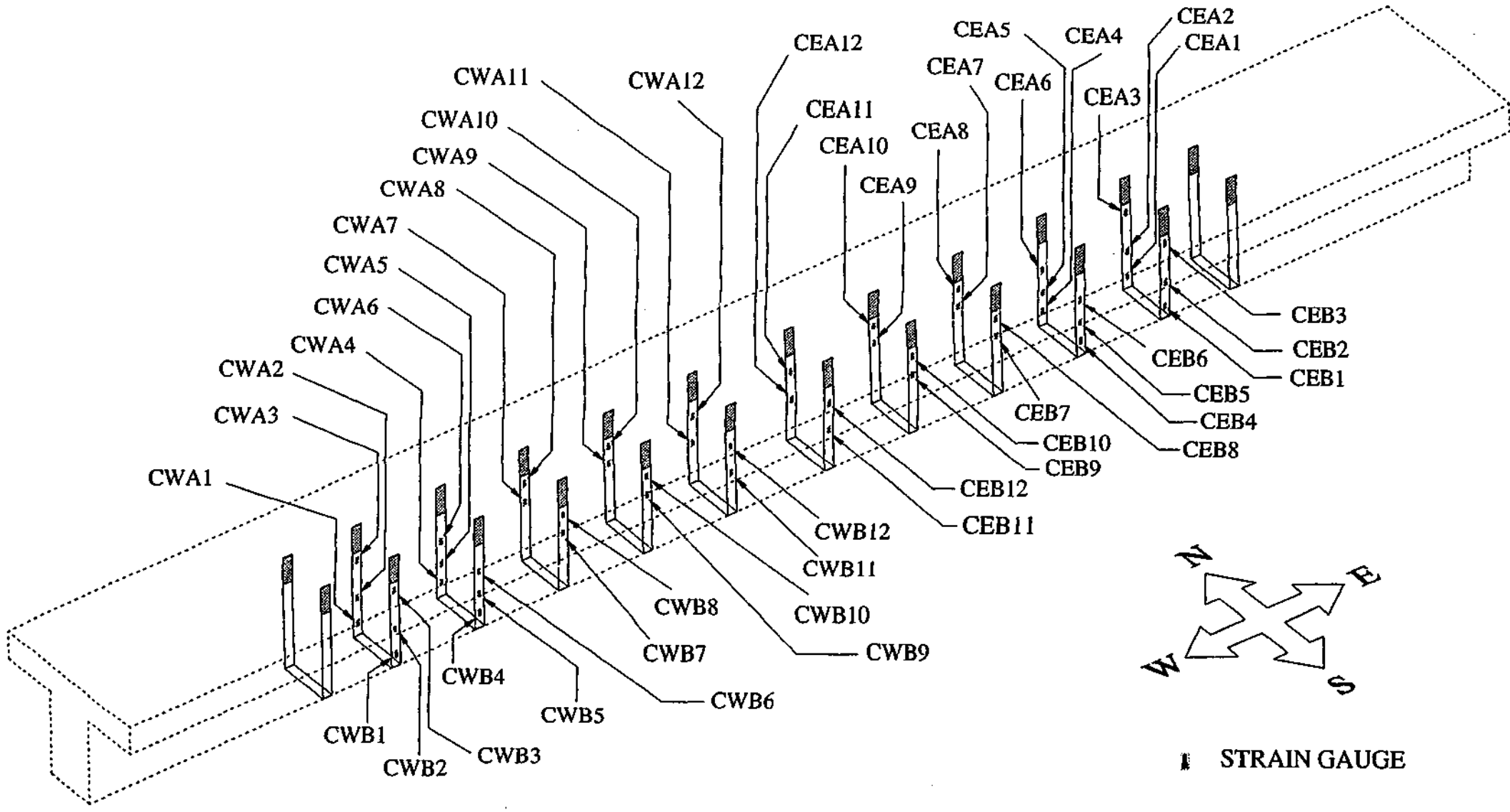

Figure 5.9 - Labelling of CFRP strain gauges for beam '0.75D'

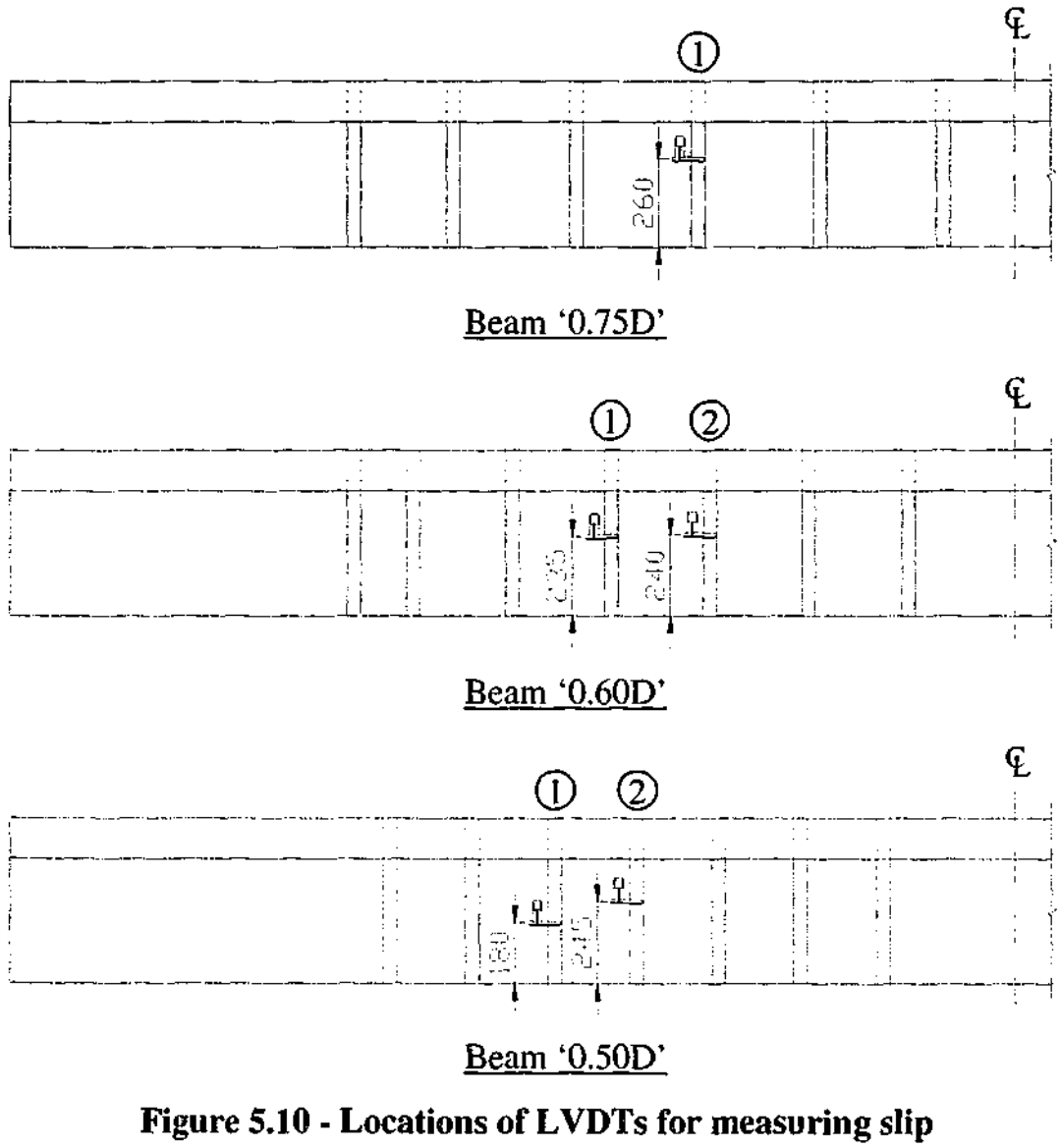

Figure 5.10 - Locations of LVDTs for measuring slip

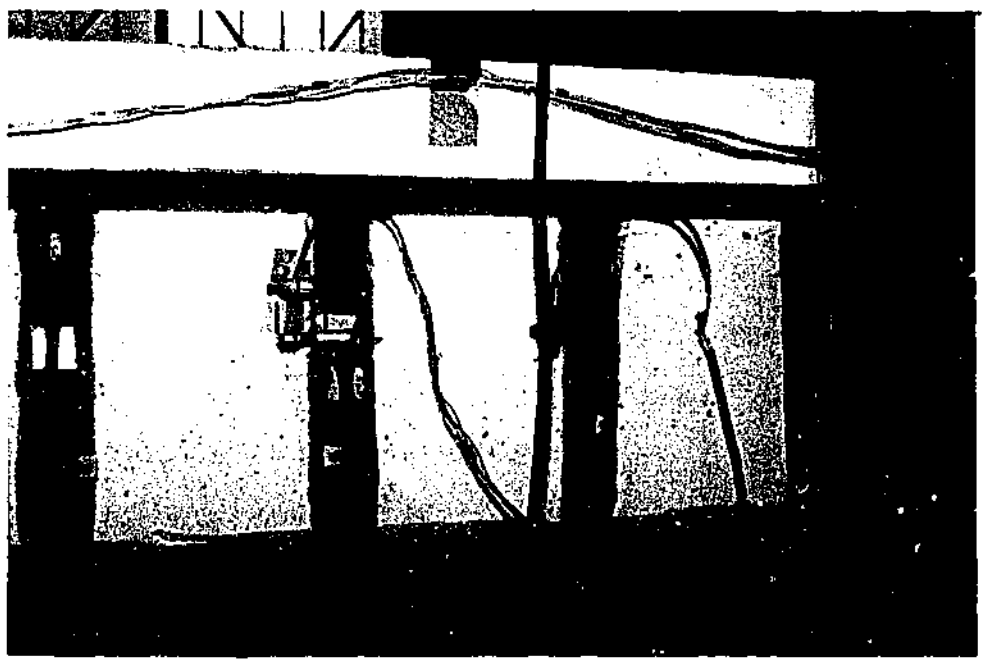

Figure 5.11 - LVDTs for slip measurement for beam '0.60D'

5.7 Testing setup and procedure

The T-beams were subjected to four-point loading using two 220000 lbs (979 kN) Mohr & Federhaff hydraulic actuators with a piston stroke of 10 inches (254 mm). The shear span was set to 1265 mm giving a shear span to depth ratio (a_v/d) of approximately 3.0. A schematic of the experimental set up is shown in Figure 5.12.

Each actuator has a flat circular loading plate located at the end of the piston. The plate was attached by springs that allowed it to rotate freely about the piston. The load applied was measured using 100 kN load cells positioned directly underneath each actuator. The actuators were secured to the crossbeams of the loading frames using clamps. A spreader beam with a loading area of 720 mm by 80 mm was placed under each actuator to prevent localised punching failure. Rubber bearings seated underneath the spreader beams were used to ensure that the loads were evenly distributed. The spreader beam had been stiffened significantly ensuring that the load applied across the beam flange was uniform. A Moog servo-hydraulic distributor system was used to power both actuators. Loading was in displacement control achieved using a string pot attached to each actuator that provided constant feedback to a computer program, which controlled the hydraulic distributor system. Based on the readings of the string pots, the computer program constantly adjusted the pressure output to the actuators accordingly to maintain the required displacement rate. Further adjustments required could also be entered manually into the program during testing.

Each loading frame consisted of two crossbeams bolted to two 4.5m high steel columns. Each column was secured in place using two anchor bolts pre-tensioned to 50 kN against the strong floor as illustrated in Figure 5.13. The reinforced concrete strong floor has an overall thickness of 1200 mm. The centre to centre distance of the loading frames was 1520 mm.

The supports used in the tests were roller systems (Figure 5.14). The low friction bearing strips seated underneath the support blocks allowed horizontal movements. Guide blocks were bolted to each side of the support to ensure that the

support blocks slide in one direction only. A 100 kN load cell was seated underneath the steel roller to measure the load carried by each support.

At the start of each test, an initial loading rate of 0.3 mm per minute was applied to the specimens. As the test progressed further, cracks began to form causing the applied loads to differ between the actuators. With the exception of the control beam, the outputs of the actuators were adjusted accordingly such that the applied loads were as close as possible to each other. For the control beam, the output of the actuators were adjusted such that the total piston displacements in each actuator were as close as possible to each other.

During testing, loading of the specimens was paused intermittently to allow photogrammetry measurements to be taken. The load levels at which photogrammetry measurements were taken are indicated in Table 7.1. Further information regarding the photogrammetry measurements used is presented in Chapter 7.

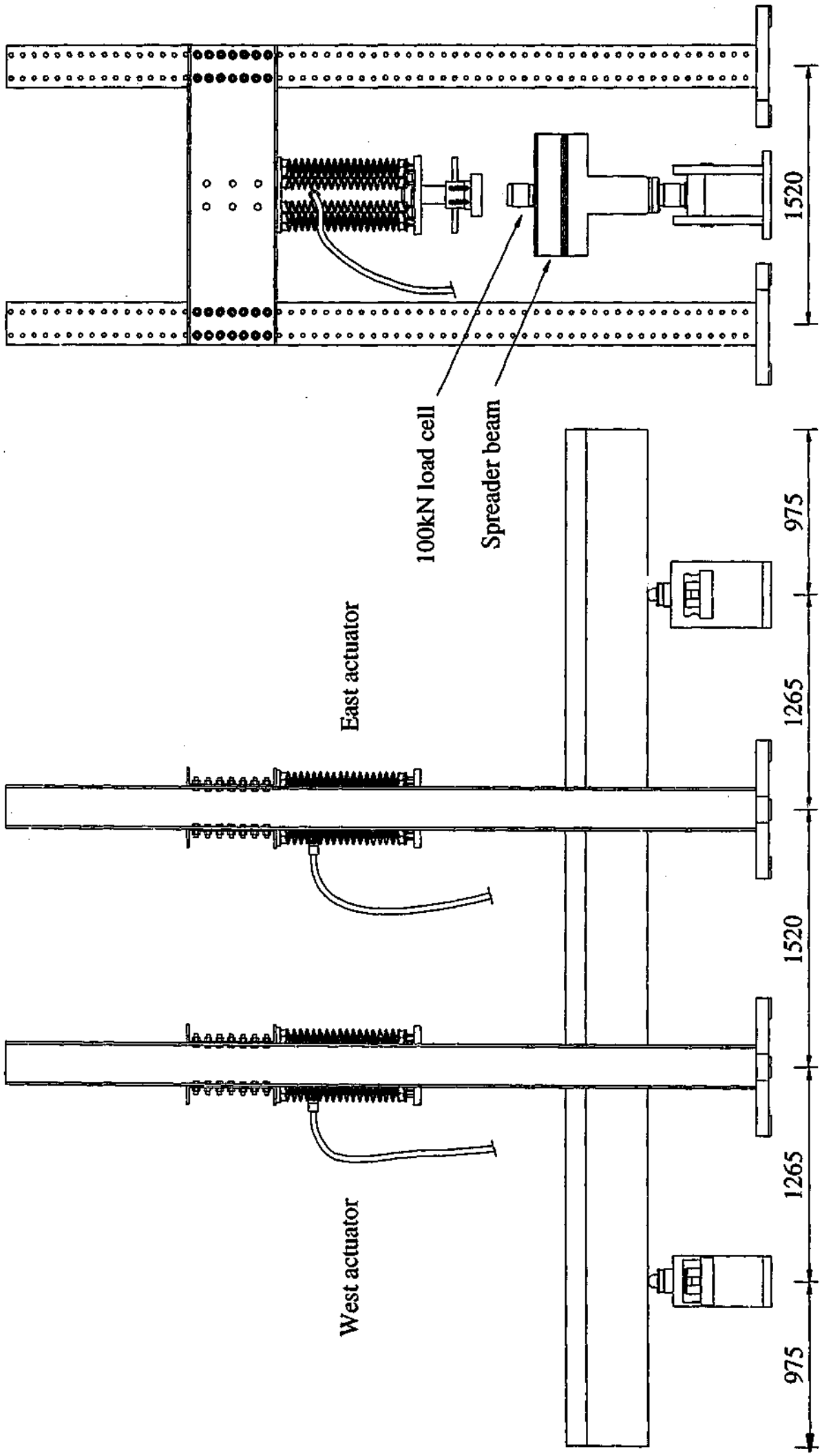

Figure 5.12 - T-beam set up

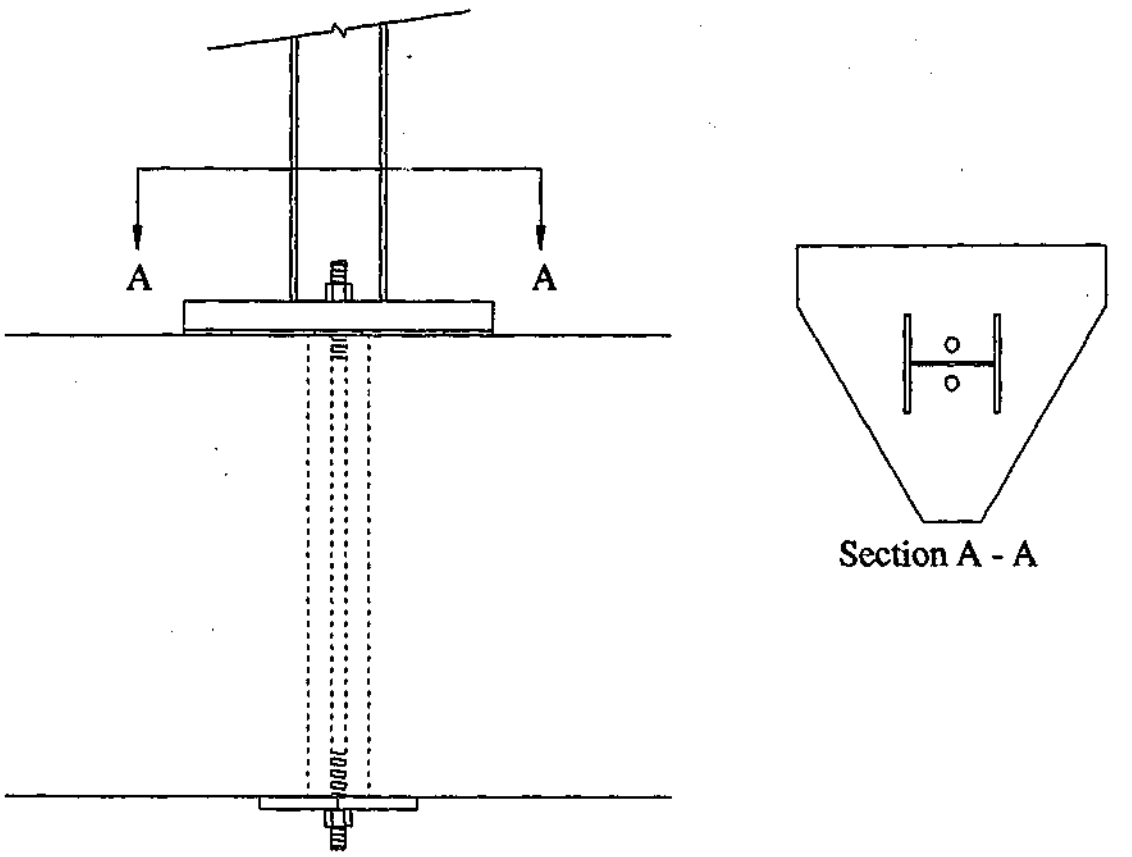

Figure 5.13 - Column secured to strong floor with pre-tensioned anchor bolts

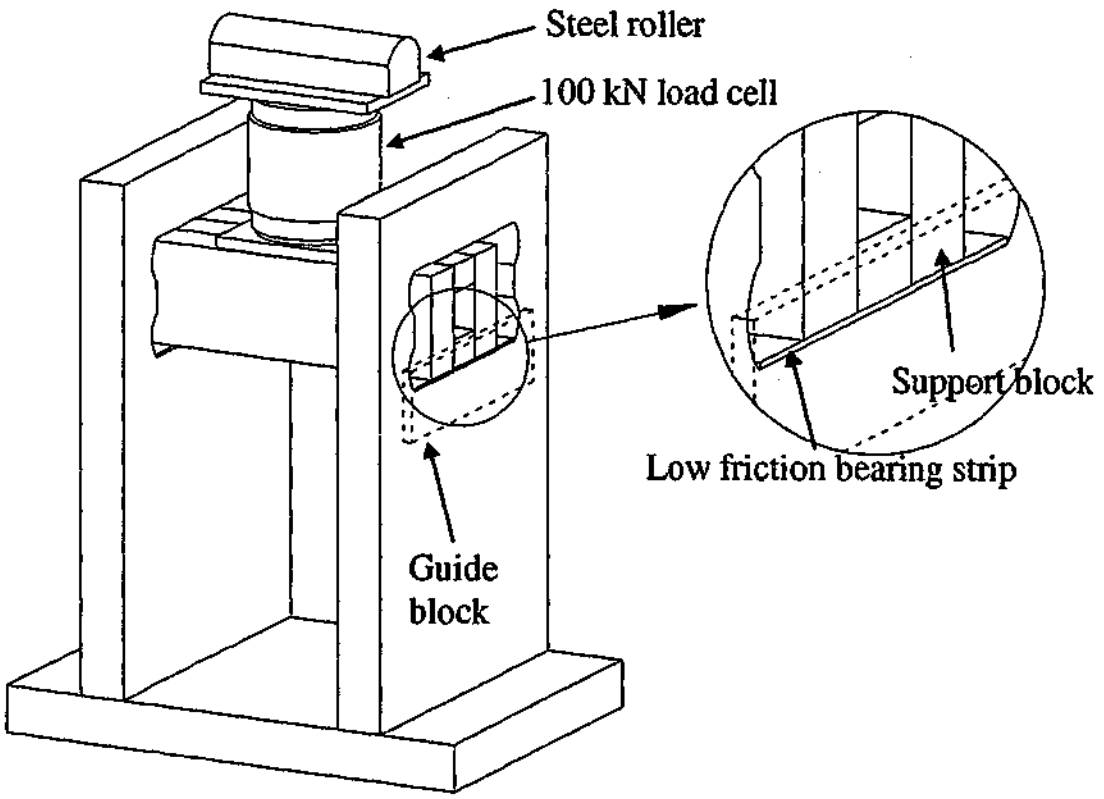

Figure 5.14 - Support system

CHAPTER 6 - PRESENTATION AND INTERPRETATION OF T-BEAM TEST RESULTS

6.1 Material properties

6.1.1 Concrete

Compressive tests were carried out on concrete cylinders for each beam at selected periods in accordance to SAA (1999). In addition, three core samples were taken from each beam after testing for comparison with the concrete cylinders. The concrete strengths at the time of the beams and core samples tests are given in Table 6.1. Due to different curing conditions, there is a noticeable difference in strengths between the cylinders and core samples. The cylinders were continuously hydrated in a constant temperature water bath whereas the T-beams were left to cure in an outdoor environment under plastic cover. Nevertheless, the concrete strength of the core samples across all the beams is similar.

In the theoretical models, the compressive strengths of the core samples were adopted since the cylinders show little difference in strength between the times of the beam tests and the core samples tests. The average compressive strength of the core samples for all the T-beams is approximately 31.9 MPa. Further information on the concrete strength development with time is contained in Appendix A.3.

Table 6.1 - Average concrete strength at the time of beams and core samples tests

Beam Designation	At beam test date	At core sample test date	
	Cylinder (MPa)	Cylinder (MPa)	Core Samples (MPa)
Control	45.9	46.0	34.2
'0.75D'	38.1	36.7	31.1
'0.60D'	38.9	38.3	30.9
'0.50D'	34.3	35.6	31.6

6.1.2 Steel Reinforcement

Tensile tests in accordance to SAA (1991) were carried out to determine the properties of the steel reinforcement used in the T-beams. Table 6.2 shows the results obtained for the main flexural (Y28) and shear (R10) reinforcement. The yield strains for the Y28 and R10 bar types are 2363 and 1718 microstrains respectively. These values are used to determine the yield status of the steel reinforcement in the T-beams after testing. Typical stress-strain profiles of the reinforcement are contained in Appendix A.4.

Table 6.2 - Yield strength of steel reinforcement

Main flexural reinforcement (Y28)		Shear reinforcement (R10)	
Yield stress (MPa)	**Young's modulus (MPa)**	**0.2% proof stress (MPa)**	**Young's modulus (MPa)**
442	187823	350	204018
450	189299	351	204425
444	188384	352	205281
		351	203922
AVERAGE		**AVERAGE**	
445	188502	351	204411

6.1.3 Sika CarboShear L Plates strengthening system

The results of tensile tests performed on the Sika CarboShear L-plates strengthening system are presented under Section 3.8.2.

6.2 Beams test results

6.2.1 T-beams shear capacities

The shear capacities of the four T-beams are tabulated in Table 6.3. It corresponds to the maximum load recorded by the support load cell at the shear span that total structural failure occurred in. In the experimental program, failure was deemed to occur when there was a significant decrease in the total load carried by the beam after the peak load had been reached. Failure was characterised by formation of large shear cracks and the separation of the CFRP laps at the soffit of the beam tearing away concrete at the bend zone. With the exception of beam '0.50D', failure occurred

at the west span in all of the beams. For the shear strengthened beams, the shear capacity was at least 50% more compared to the control beam with a maximum of 81% observed in beam '0.50D'.

Table 6.3 - Shear capacity of T-beams

Beam type	Shear capacity (kN)	Failure location	$V_{n,ctrp} / V_{n,control}$
Control	247.1	West span	1.00
'0.75D'	381.0	West span	1.54
'0.60D'	398.3	West span	1.61
'0.50D'	446.2	East span	1.81

6.2.2 Load deflection behaviour

The load versus mid-span displacement behaviour of each T-beam is illustrated and compared in Figure 6.1. The load shown in the diagrams corresponds to the measured support loads at the span where failure occurred. At the early stages of loading, it can be observed that the stiffness of all the beams were almost similar to each other. The dips in the curves represented the load levels at which photogrammetry measurements were taken. Figure 6.2 illustrates the approximate load level at which the stiffnesses of the beams were observed to vary significantly. There is very little difference in the responses between both spans of the beams except for the control beam. As discussed earlier in Section 5.7, the loading manner was different. The discussion that follows refers primarily to the responses of the beam spans at which failure occurred and Figure 6.1.

At first loading, the control beam exhibited an almost linear elastic behaviour until about 140 kN, beyond which the stiffness began to decrease. Flexural cracks near the mid-span became visible at approximately 130 kN. At the 140 kN load level, shear cracks became visible at both shear spans. As the load level increased further, the shear cracks began to propagate and widen causing the beam to deflect significantly as observed in the load-displacement curve. The control beam ultimately failed in shear. Since loading was carried out under displacement control, the failure was ductile as indicated by the extended post-peak response.

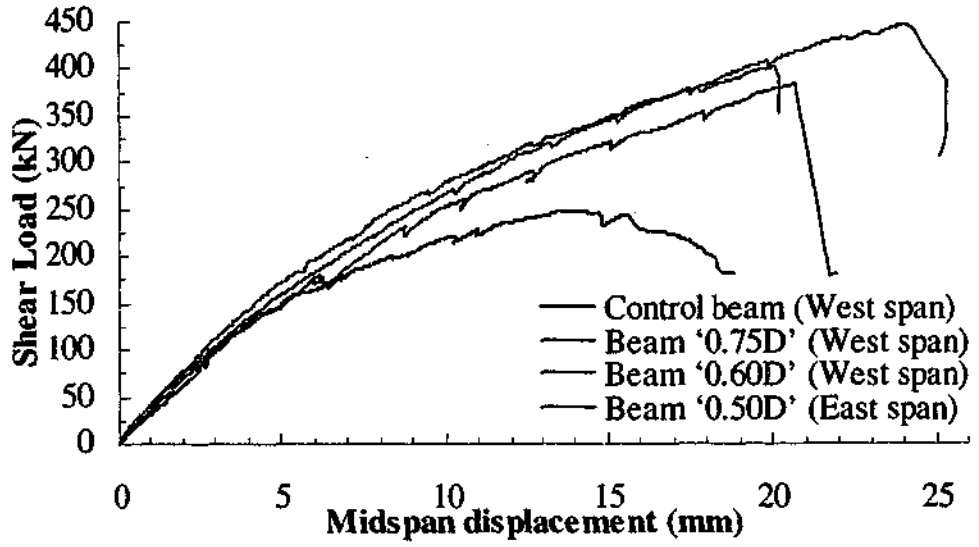

Figure 6.1 - Load versus displacement behaviour of the T-beams

For beam '0.75D', the load displacement behaviour is similar to the control beam until about 175 kN. Flexural cracks were first observed when the shear load level reached approximately 125 kN. The first visible shear crack was observed at about 170 kN. Compared to the control beam, the shear cracks propagated very slowly as the applied loads increased. At a given load level, the crack width in beam '0.75D' was relatively smaller than the crack width in the control beam. The presence of the external shear reinforcement had impeded the growth of the shear cracks. As a result, beam '0.75D' exhibited a stiffer response compared to the control beam beyond the 170 kN load level. Due to the increase in shear strength, the beam could carry increased shear load and undergo larger deflection. Failure was brittle with a significant drop in load level almost immediately after peak load was reached.

Beam '0.60D' exhibited similar load displacement response to the control beam at the initial stages of loading. The initial stiffness was maintained until 165 kN beyond which it decreased slightly. From this load level until failure, the stiffness of the beam was similar to beam '0.75D'. Between 80 to 170 kN, beam '0.60D' exhibited a slightly higher stiffness compared to all the other beams. This resulted in the beam carrying more shear load. It is very likely that this might be experimental scatter as beam '0.50D' exhibited similar response to beam '0.75D' at low load levels despite having closer spaced CFRP reinforcement. Shear cracks were first observed at approximately 100 kN and flexural cracks around 130 kN. The shear failure load of beam '0.60D' was 17.3 kN higher than beam '0.75D'. Both beams failed in a

similar manner. The maximum displacement measured was slightly less compared to the maximum displacement in beam '0.75D'.

From the load level of 0 to 150 kN, beam '0.50D' exhibited an almost identical load displacement response to the control beam and beam '0.75D'. The stiffness remained similar to beams '0.75D' and '0.60D' at various stages of loading except between 280 and 360 kN, where the stiffness was slightly higher. At the shear load of 150 kN, shear cracks became visible at the west span. Flexural cracks were observed to form at approximately 130 kN. It was observed that at very high shear load, the shear crack width was smaller compared to beams '0.75D' and '0.60D' at the same load level. Similar to both beams, beam '0.50D' failed in a brittle manner.

In all of the beams except for beam '0.60D', the change in structural stiffness occurred at approximately 135 kN. For the strengthened beams, the second change in stiffness occurred at approximately similar load levels, which was at 270 kN. The initial change in stiffness was caused by the formation of shear and flexural cracks. For beam '0.75D', the second change in stiffness was the result of debonding of concrete at the location of the CFRP L-shaped plates, yielding of the internal steel shear reinforcement and further shear crack propagation. Debonding is defined as direct concrete shearing beneath the concrete surface. The layer of concrete is still attached to the CFRP reinforcement. In Sections 6.2.4 and 6.2.5, results of the strain level of the internal steel shear reinforcement and the external L-shaped CFRP plate indicate that the second change in overall stiffness of the beam is due primarily to the debonding of the L-shaped CFRP plates. Results of the slip behaviour between concrete and CFRP presented in Section 6.2.8 give a similar observation.

Compared to the shear capacity increase between beams '0.75D' and '0.60D', the shear capacity increase was significantly higher between beams '0.60D' and '0.50D'. The CFRP reinforcement spacing of 0.60D was not as effective as the CFRP reinforcement spacing of 0.50D in distributing the shear loads carried amongst the CFRP reinforcement. Failure of beam '0.60D' occurred through the separation of the laps of two CFRP plates as most of the shear load was concentrated at that location.

In summary, the presence of the external shear reinforcement did not affect significantly the initial stiffness of the strengthened beams compared to the control beam at first loading. The CFRP reinforcement impeded shear crack propagation and growth. It was observed that for beams with closely spaced CFRP reinforcement, the shear cracks widths and propagation were smaller and more limited at a given load.

(a)

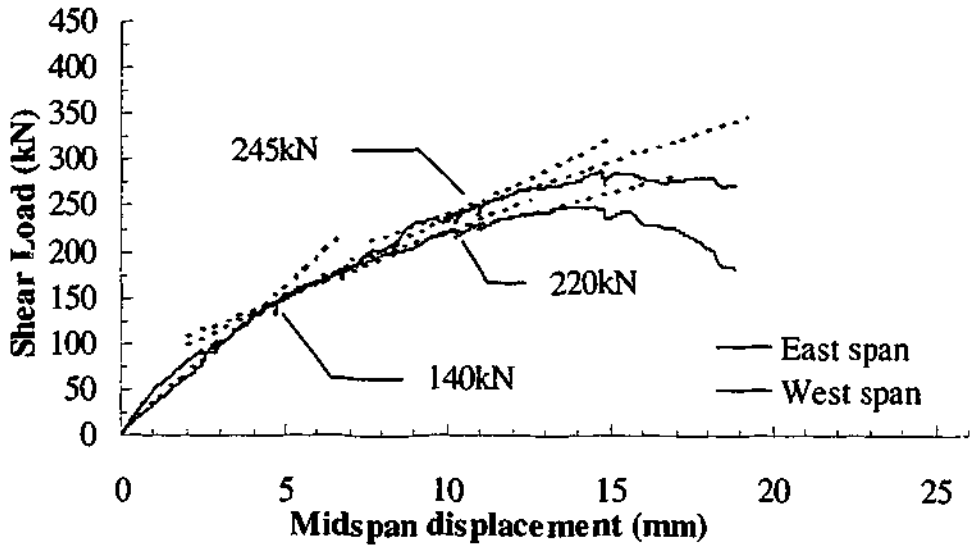

(b)

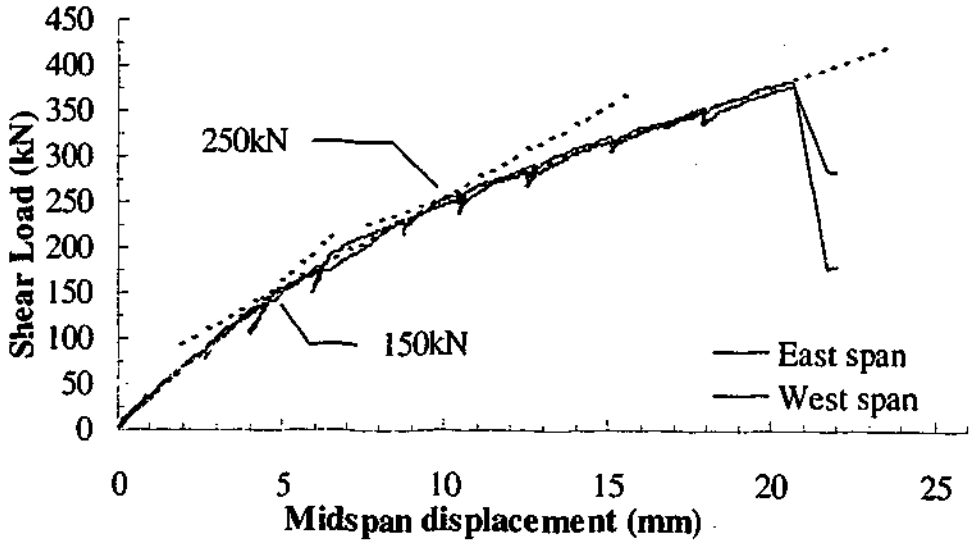

Figure 6.2 - Approximate load levels at which stiffness varied for (a) control beam (b) beam '0.75D' (c) beam '0.60D' and (d) beam '0.50D'

(c)

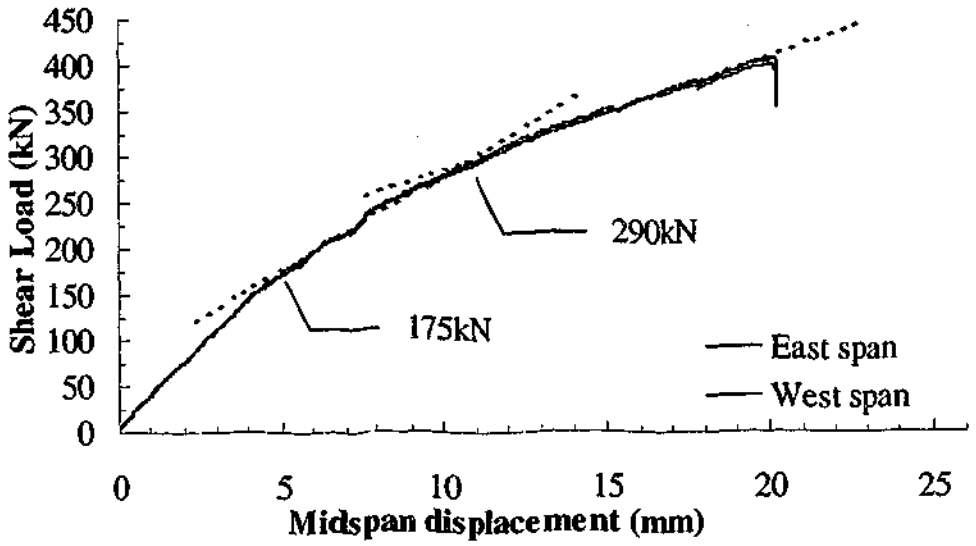

(d)

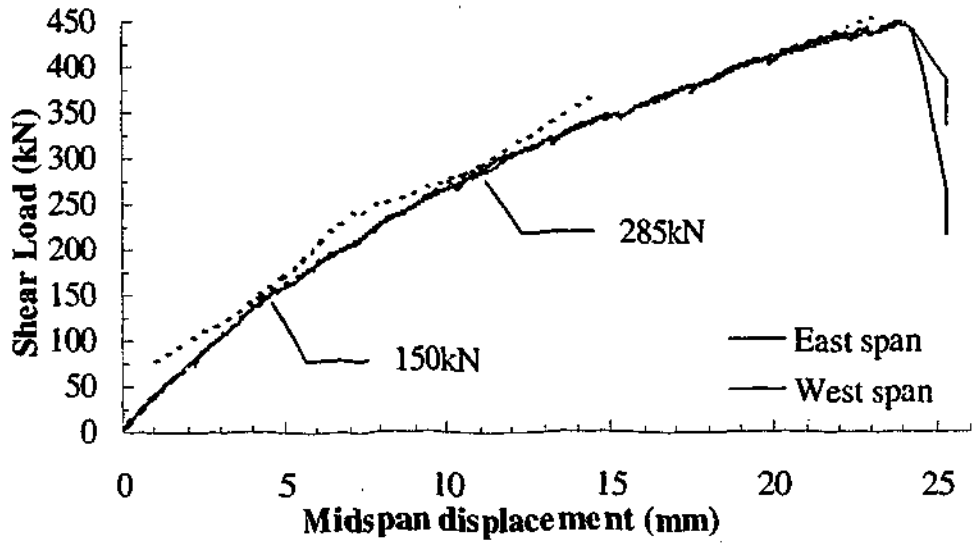

Figure 6.2 (continued) - Approximate load levels at which stiffness varied for (a) control beam (b) beam '0.75D' (c) beam '0.60D' and (d) beam '0.50D'

6.2.3 Behaviour of main flexural reinforcement

The load strain behaviour of the main flexural reinforcement of the T-beams is compared in Figure 6.3. With the exception of beam '0.60D', the strain values corresponded to readings of strain gauges located at the span at which failure occurred. The load corresponded to the measured support loads at the span where the strain gauges were bonded. For beam '0.60D', the strain gauge at the failure span was damaged during concrete casting. The locations of the strain gauges are indicated in the figure.

The reinforcement in the different T-beams exhibited almost identical load strain responses. The reinforcement strained linearly with load until structural failure.

In all of the beams, the main reinforcement did not yield indicating that flexural tensile failure did not occur. Each beam had sufficient flexural capacity remaining after shear failure.

The load strain responses of the main flexural reinforcement measured at opposing spans and sides of beam '0.75D' are illustrated in Figure 6.4. The figure indicates that the responses recorded were similar until failure of the beam. For the other beams, similar trends were observed. Further information on the load strain responses of main flexural reinforcement is contained in Appendix B.1. The use of the external shear reinforcement did not increase the flexural stiffness of the beams but had made possible the additional utilisation of the beams' flexural capacity.

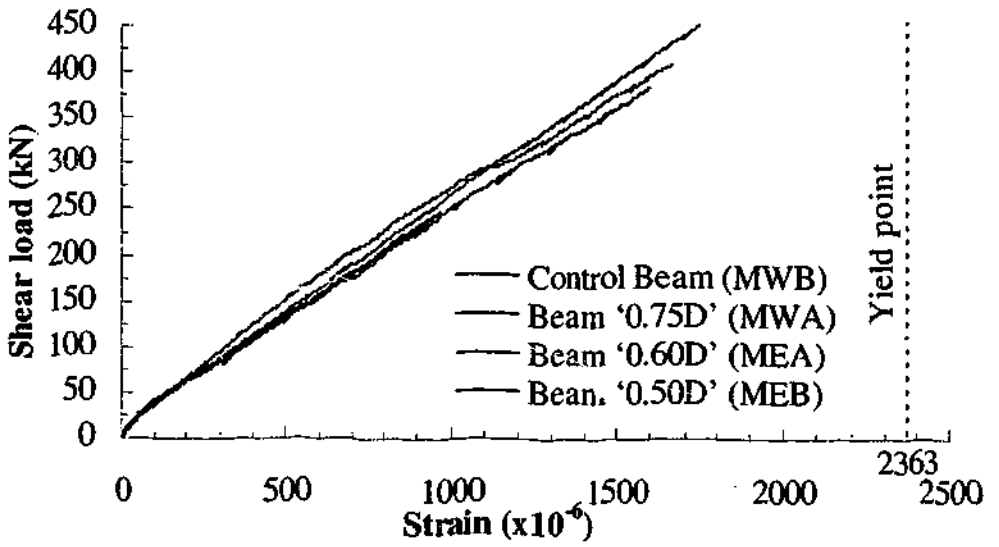

Figure 6.3 - Comparison of load strain behaviour of main flexural reinforcement

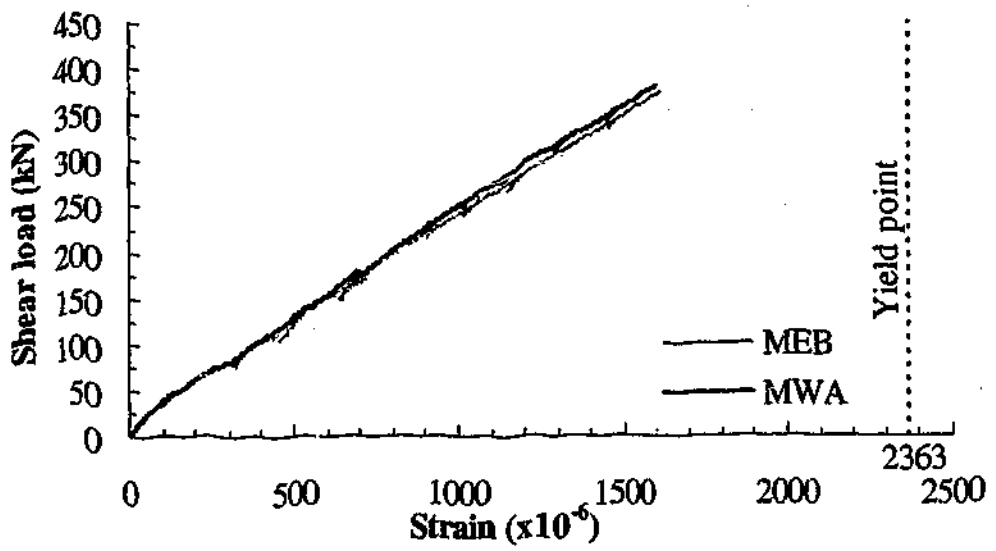

Figure 6.4 - Load strain behaviour of main flexural reinforcement in beam '0.75D'

6.2.4 Behaviour of shear reinforcement

The shear reinforcement responses of the T-beams are presented and compared in this section. The responses are first examined and discussed individually for each beam followed by comparisons across all the beams. For the load strain plots contained in this section, the shear load corresponded to the measured support load at the span where the strain gauges were bonded. The locations of the strain gauges are illustrated in Figures 5.3 and 5.8. For each beam, a total of four stirrups were instrumented with strain gauges.

The typical load strain response of each stirrup in the control beam is illustrated in Figure 6.5 (a). At the initial stages of loading, the strain readings were small indicating that the stirrups were carrying very little load. From the strain readings, the first shear crack formed at approximately 60 kN. At approximately 140 kN, the load carried by the stirrups increased significantly as the shear cracks began to widen and propagate further. As noted earlier in Section 6.2.2, the beam stiffness decreased as a result and shear cracks were first observed on both spans of the beam. The two stirrups closest to the supports SEB1 and SWA1 exhibited comparable response. Both stirrups yielded before the peak shear loads were reached at approximately 230 kN. This load level coincided with the second change in the overall beam stiffness as observed in Figure 6.2 (a). The two stirrups closest to the load points SEB4 and SWB3 did not yield when failure occurred. Both stirrups

exhibited comparable response until 150 kN beyond which SWB3 underwent significantly more strain at the same load. This is due to a major shear crack that had crossed the stirrup. The results from the strain readings indicated that the control beam failed in shear at the west span.

For beam '0.75D', the typical load strain responses of the stirrups are shown in Figure 6.5 (b). Similar to the control beam, the strain readings were small at the initial stages of loading. According to the strain readings, shear cracks started to form at approximately 55 kN. Until the 150 kN load levels, the stirrups carried increasing but relatively small loads. The load carried by the stirrups began to increase significantly due to widening and propagation of shear cracks. This resulted in the first observed decrease in stiffness shown in Figure 6.2 (b). Before the peak shear loads were reached, the stirrups nearest to the supports SEB2 and SWA1 yielded. By taking into consideration the readings of the strain gauges bonded on these two stirrups, the average load level at which yielding occurred was 260 kN. This value coincided with the load level shown in Figure 6.2 (b) where the second change in overall stiffness was observed. The two stirrups closest to the load points SEB3 and SWA4 did not yield and exhibited comparable response until failure. From observation and results of the strain readings, beam '0.75D' failed in shear at the west span.

At the initial stages of loading, the load strain responses of the stirrups in beam '0.60D' exhibited a similar trend to the load strain responses of the stirrups in the control beam (Figure 6.5 (a)). The average shear load level at which shear cracks formed was 50 kN. The load carried by the stirrups in beam '0.60D' increased significantly at 175 kN which was consistent with the observed decrease in beam stiffness shown in Figure 6.2 (c). The stirrups nearest to the supports SEB1 and SWB2 yielded before the peak loads were reached at the average shear load level of 350 kN. This value is significantly higher compared to the shear load level of 290 kN at which the second change in overall stiffness occurred as observed in Figure 6.2 (c). Examination of the strain readings of SEA3 and SWA4 indicated that the two stirrups nearest to the load points did not yield when failure occurred. From observation and results of the strain readings, beam '0.60D' failed in shear at the west span.

For beam '0.50D', the load strain responses of the stirrups are illustrated in Figure 6.5(d). At low shear load levels, the stirrups supported small loads as indicated by the low strain readings, a trend observed in all the other beams. The strain readings indicated that shear cracks first formed at an average shear load of 50 kN. According to Figure 6.2 (d), the first change in overall beam stiffness occurred at approximately 150 kN. The load carried by the stirrups had begun to increase significantly before this load level, as shown in Figure 6.5 (d). This response was due to widening and propagation of shear cracks. The stirrups nearest to the supports SEA1 and SWA2 yielded at the average shear load level of 360 kN before the beam reached its peak shear loads. This value did not coincide with the shear load level at which the second change in overall stiffness occurred as observed in Figure 6.2 (d). However, all the gauges indicated that the stirrup located closest to the support in the west span yielded at approximately 280 kN shear load. This load level coincided with the shear load level at which the stiffness changed. The stirrup in the east span did not yield despite failure having occurred in that span. From observation and results of the strain readings, beam '0.50D' failed in shear at the east span.

The load strain responses of the stirrups for the four T-beams at the failure spans are compared in Figure 6.6 and Figure 6.7. Figure 6.6 compares the responses of the stirrups closest to the supports and Figure 6.7 compares the responses of the stirrups closest to the load points. At low shear load level, there was very little difference in the responses between the T-beams. In all of the beams, the stirrups were carrying very small loads. As the shear cracks began to widen and propagate considerably, the strains in the stirrups of the strengthened beams were less at a given shear load compared to the strains in the stirrups of the control beam. The external CFRP reinforcement contributed to carrying part of the total shear load. There is a general trend that the smaller the spacing of the external reinforcement, the lesser the strain hence load carried by the stirrups at a given shear load. In all the beams, shear cracks formed at approximately the same shear load level. In addition, the stirrups began to sustain more loads at approximately the same shear load.

In summary, the presence of the external CFRP reinforcement had an insignificant influence on the initial formation of shear cracks. For the strengthened beams, shear cracks formed at approximately the same load level as in the control

beam. The shear load at which the stirrups began to carry significantly more loads was similar for all the beams. This load level corresponded to the load at which the shear cracks widened and propagated sufficiently causing the initial decrease in stiffness. The CFRP reinforcement had little influence on the shear crack propagation when the crack widths were still minute. Beyond this load level, as the cracks started to widen sufficiently, the external CFRP reinforcement contributed to carrying part of the total shear load. This was characterised by the smaller stirrup strain readings at a given shear load in the strengthened beams compared to the strain readings in the control beam. The strain readings of the stirrups were generally smaller in beams with more closely spaced CFRP reinforcement. It was shown in all the beams that the stirrups closest to the supports at the failure spans yielded before the beams reached their respective peak shear loads. The stirrups closest to the point loads at the failure spans did not yield when failure occurred. Further information on the strain readings of the stirrups is contained in Appendix B.2.

(a)

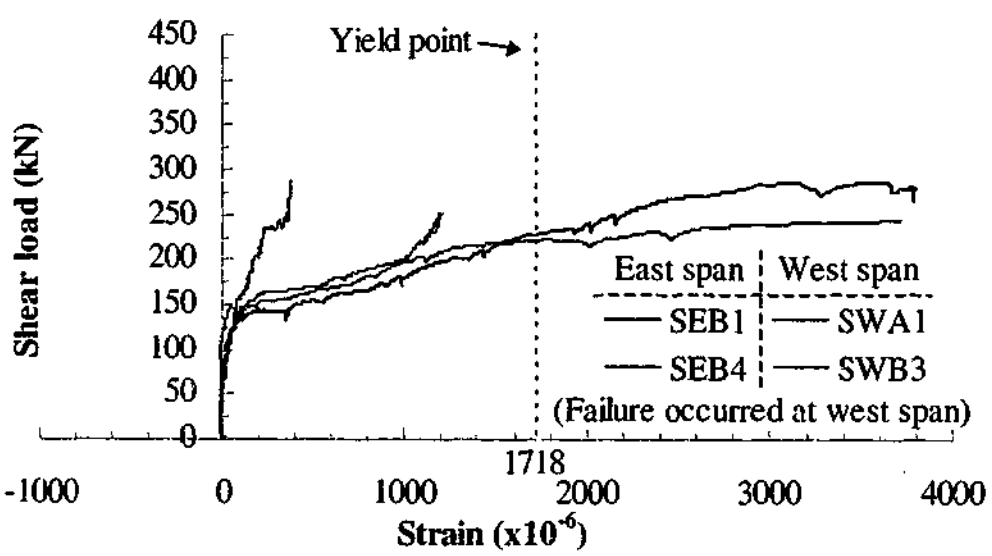

Figure 6.5 - Typical load strain behaviour of stirrups in (a) control beam (b) beam '0.75D' (c) beam '0.60D' and (d) beam '0.50D'

(b)

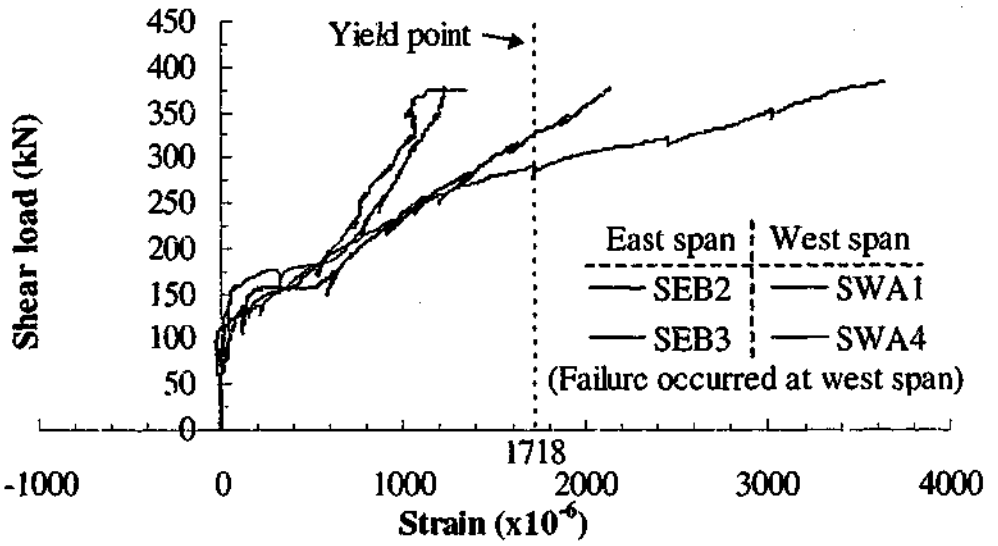

(c)

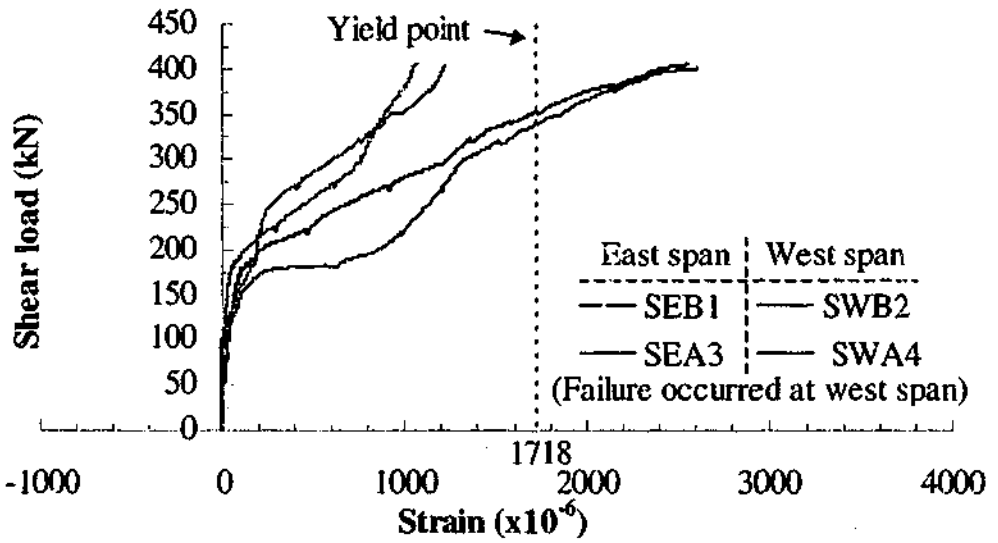

(d)

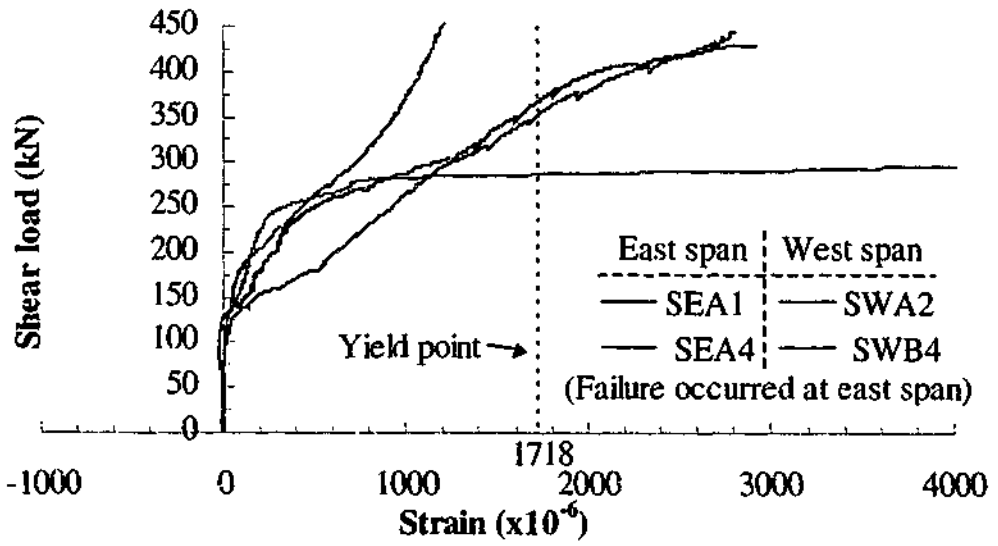

Figure 6.5 (continued) - Typical load strain behaviour of stirrups in (a) control beam (b) beam '0.75D' (c) beam '0.60D' and (d) beam '0.50D'

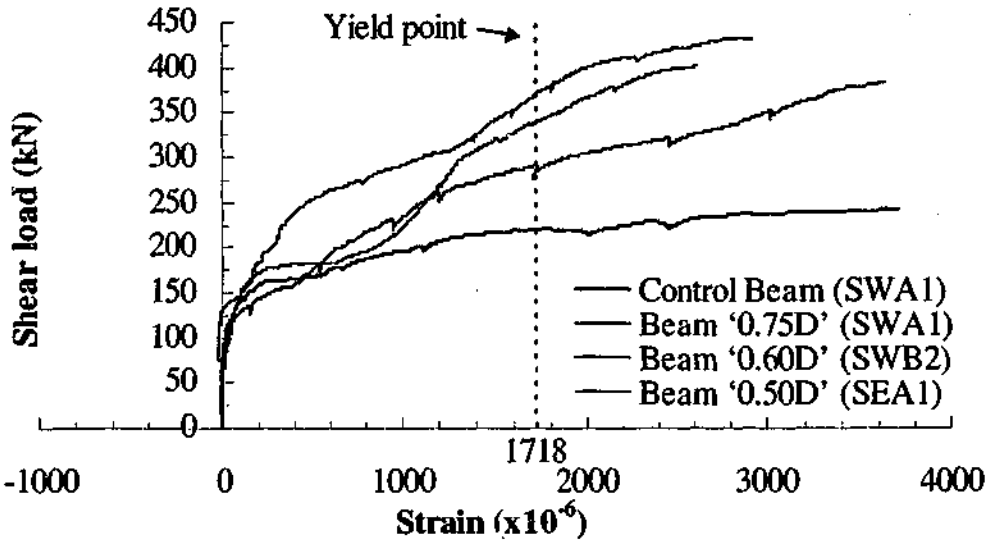

Figure 6.6 - Comparison of load strain behaviour of stirrups closest to supports at failure span

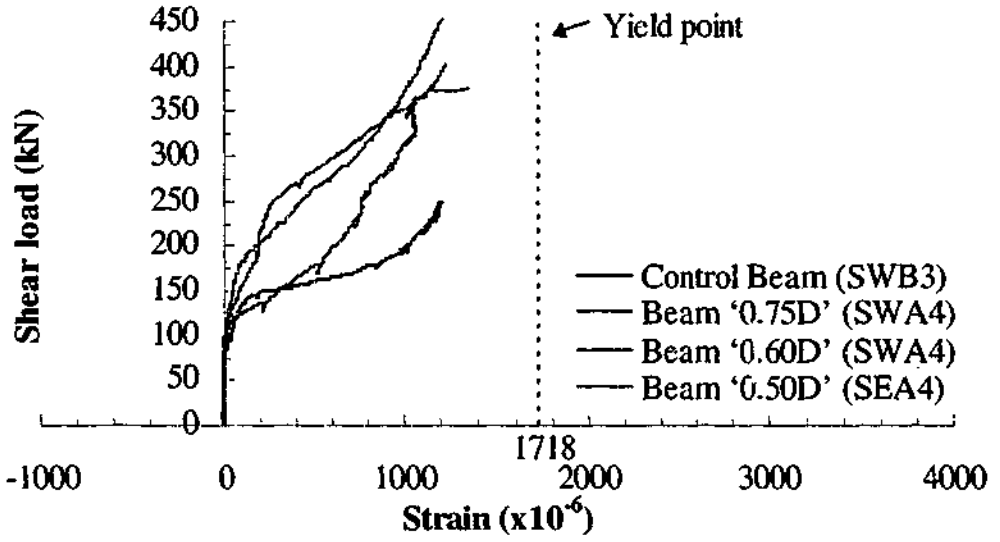

Figure 6.7 - Comparison of load strain behaviour of stirrups closest to point loads at failure span

6.2.5 Behaviour of L-shaped CFRP plate

The load strain responses of the L-shaped CFRP plates are presented in this section. The results are examined and discussed for each beam followed by comparisons across all the beams. On each beam, a total of 48 strain gauges were bonded to the CFRP reinforcement with twelve per shear span per side. The locations and notations of these strain gauges are illustrated in Figures 5.5 and 5.9. For the load-strain plots presented in this section, the load shown corresponds to the measured support load at the span where the strain gauges were bonded.

The load strain responses of the L-shaped CFRP plates at the failure span of beam '0.75D' are illustrated in Figure 6.8. The responses recorded by the strain gauges at a given web height at opposing sides of the beam were comparable. This indicated that the beam was loaded uniformly across the section. Figure 6.9 compares the responses of the CFRP reinforcement with gauges 1, 2 and 3 at both shear spans. The strain gauges gave similar responses indicating that the beam was loaded uniformly at both shear spans. This similarity was observed for all of the CFRP reinforcement on the beam. The load-strain responses of the CFRP reinforcement on the east span of beam '0.75D' are contained in Appendix B.3. The discussions to follow focus mainly on the CFRP reinforcement located at the west span.

At the early stages of loading, similar to the internal shear reinforcement at the shear span, the CFRP reinforcement carried small load. In addition, both the CFRP reinforcement and internal shear reinforcement began to carry more shear load at similar shear load level. This meant that the CFRP reinforcement barely contributed to carrying the load until shear cracks had formed and propagated. The adhesive used had relatively low stiffness compared to concrete therefore the CFRP reinforcement would sustain load only when shear cracks had formed and propagated sufficiently. The CFRP reinforcement outside of the shear spans carried very low shear loads as expected. The reinforcement underwent compression near the web-flange junction as indicated by gauges 10 and 12.

Unlike the internal shear reinforcement, the CFRP reinforcement did not strain uniformly along the length. For the former, slip between the concrete and round bars allowed the bars to extend uniformly along the entire length. For the latter, the portion of the CFRP where shear cracks had intersected would result in a localised stress concentration. Referring to Figure 6.8, it can be interpreted from the strain readings that shear cracks began to propagate and cross the CFRP reinforcement within the vicinity of gauge 2, gauges 4 and 5, gauge 6, and gauge 8. This was because significant increases in strain of the CFRP reinforcement were noticed to have occurred first at these locations. A shear crack later formed within the vicinity of gauge 3 at higher shear loads. This observation is illustrated more clearly in Figure 6.10. The figure shows plots of the strain profiles along the length of the L-shaped CFRP reinforcement at different load levels. At higher shear loads, the strain

values of all the gauges on any particular reinforcement became approximately equal. This indicated that the CFRP reinforcement had begun to debond from the web between the portions where the strain gauges were bonded. The debonding initiated from the location of the shear cracks and propagated along the length of the CFRP reinforcement. The post failure crack patterns illustrated in Figure 6.22 confirmed that shear cracks had indeed crossed the CFRP reinforcement at these locations.

In Section 3.8.5, the critical strain level ε_{cr} was established to range from 633 to 872 με with an average of 719 με. The critical strain level refers to the strain level in the CFRP plate at which concrete starts to fracture and debonding initiates. It is a function of the bond strength of the concrete layer. The bond specimens were reported to have an average compressive strength of 30 MPa. In beam '0.75D', the average compressive strength of the concrete core samples was 31.1 MPa. To determine the critical strain level for this particular concrete strength, it is assumed that the bond strength of the concrete is proportional to $\sqrt{f'_c}$, the square root of the compressive strength. Assuming a linear relationship between the critical strain level and the bond strength, the corresponding critical strain level for a different concrete strength can be approximated using Equation 6.1, where the subscript i refers to the reference value and j the new value to be determined.

$$\varepsilon_{crj} = \sqrt{\frac{f'_{cj}}{f'_{ci}}} \times \varepsilon_{cri} \qquad (6.1)$$

For beam '0.75D' with a concrete strength of 31.1 MPa, the critical strain level as approximated by Equation 6.1 ranges from 645 to 888 με with an average of 732 με. From Figure 6.8, the shear load level that corresponds to this strain level in the strain gauges near the vicinity of the shear crack varies from one CFRP plate location to another. The values range from 200 to 265 kN with an average of 227 kN. Referring back to Figure 6.2 (b), the load level range at which debonding of the CFRP plates initiated is within the load level at which the second change in the overall beam stiffness occurs. It has been reported that the internal steel shear reinforcement had begun to yield at approximately similar load level. The combined effects of steel

yielding and CFRP plate debonding resulted in the second change of overall beam stiffness observed in Figure 6.2 (b).

Examination of the actual beam after failure revealed that the debonded area varied from plate to plate. At the failure span, the debonded areas were from the web-flange junction to approximately mid depth of the web for the CFRP reinforcement closest to the load points. The CFRP reinforcement closest to the supports and outside of the shear spans did not exhibit any sign of debonding. For the remaining CFRP reinforcement in the failure shear span, the debonded areas were across the entire length along the web terminating a few millimetres from the web flange junction. At the beam soffit, the CFRP overlaps separated and concrete was torn off at the chamfer exposing the main flexural reinforcement as shown in Figure 6.23. The strain levels reached at peak load varied across the CFRP reinforcement. The reinforcement bonded with gauges 4 to 6 gave the highest average strain value. This was observed for the CFRP reinforcement on the east span as well. This indicated that a significant proportion of the shear load was transferred through this section of the shear span. At the failure shear span, the maximum strain values and the corresponding stress levels of the CFRP reinforcement recorded prior to beam failure are summarised in Table 6.4. It should be noted that the maximum strain recorded did not always occur at the peak load. The stress values were calculated using Hooke's law $\sigma = E\varepsilon$ based on the assumption that the strain across the width of the CFRP was constant and E equalled to 137345 MPa. The maximum strain recorded from the strain gauges was 8884 με corresponding to a stress value of 1220 MPa, which was almost 3.5 times more than the yield stress of the internal shear reinforcement. There is a distinct difference in the stress level between the CFRP reinforcement at different locations. This can be seen clearly in Figure 6.11 where the responses of the three CFRP reinforcement in the shear span given by strain gauges 2, 6 and 8 are compared. The strain gauges corresponded to locations where shear cracks had crossed the CFRP reinforcement.

Beam '0.75D' failed in an abrupt manner as a result of CFRP anchorage failure at the soffit. There are two possible failure modes. The first failure mode was the sudden separation of the CFRP laps at the beam soffit that resulted in concrete

being torn away at the bend zone. The second failure mode was the cracking of concrete block at the chamfer. Near the peak load, the CFRP reinforcement had debonded from the web along most of its length and was therefore effectively anchored only at the flange and bottom of the beam. At the soffit, a small area of concrete near the bend zone was subjected to both compressive forces and forces pointing into the direction of the bend zone. The resultant forces caused cracks to occur a few centimetres from the chamfer that initiated separation of a block of concrete. The CFRP laps separated as a result followed by total structural failure.

Table 6.4 - Maximum strain and stress levels recorded for the L-shaped CFRP reinforcement in beam '0.75D'

CFRP reinforcement	Side A		Side B	
	Strain ($x10^{-6}$)	Stress (MPa)	Strain ($x10^{-6}$)	Stress (MPa)
1, 2 and 3	6617	909	6940	953
4, 5 and 6	8884	1220	8297	1140
7 and 8	5033	691	5249	721

(a)

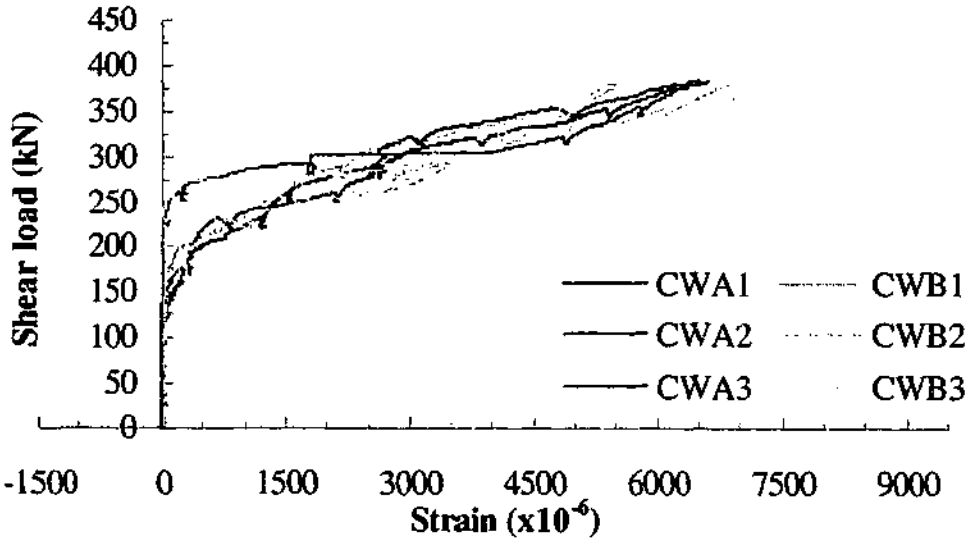

Figure 6.8 - Load strain responses of L-shaped CFRP reinforcement with strain gauges (a) 1, 2 and 3 (b) 4, 5 and 6 (c) 7 and 8 (d) 9 and 10 and (e) 11, 12 for beam '0.75D'

(b)

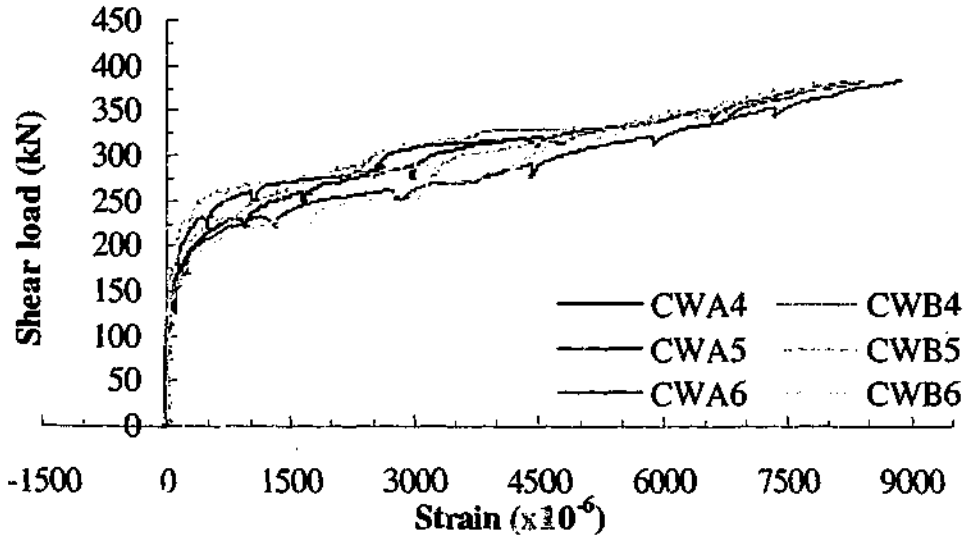

(c)

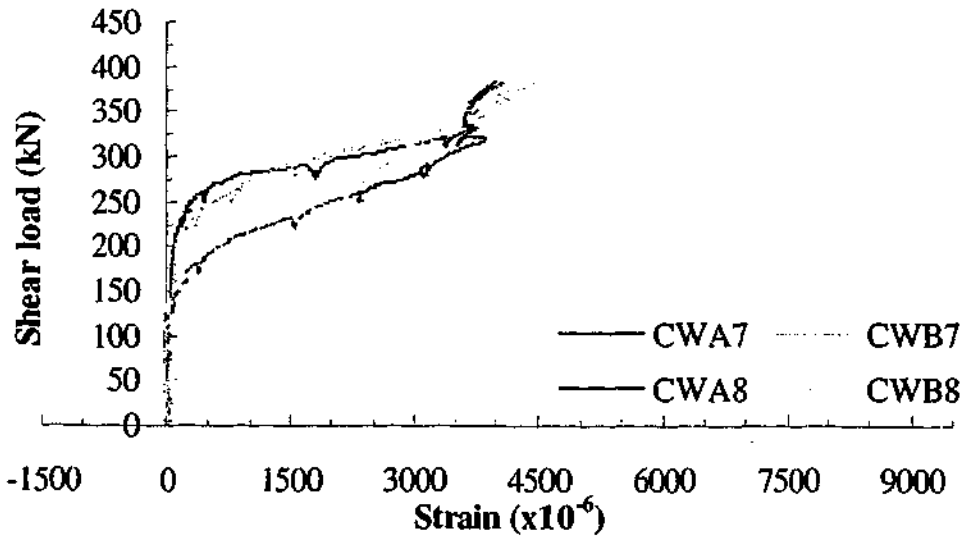

(d)

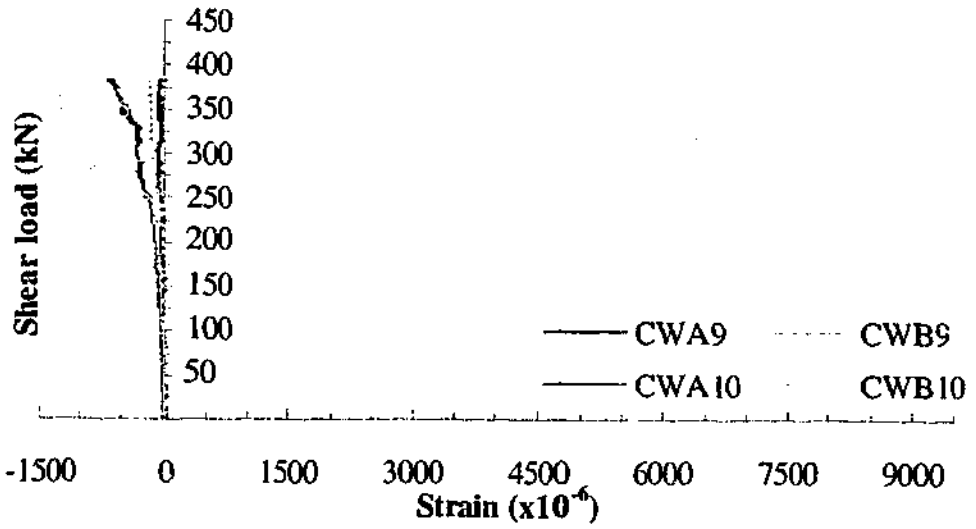

Figure 6.8 (continued) - Load strain responses of L-shaped CFRP reinforcement with strain gauges (a) 1, 2 and 3 (b) 4, 5 and 6 (c) 7 and 8 (d) 9 and 10 and (e) 11 and 12 for beam '0.75D'

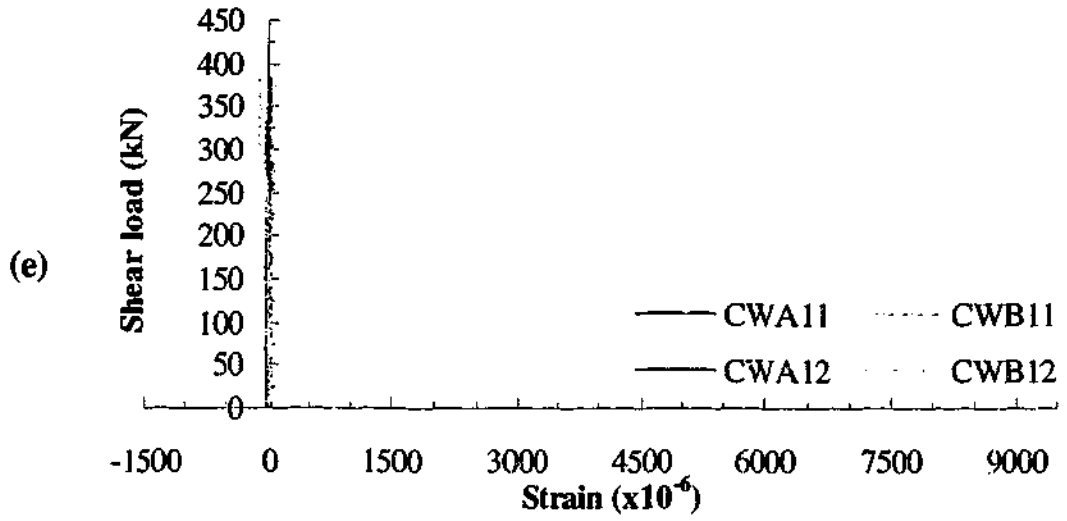

Figure 6.8 (continued) - Load strain responses of L-shaped CFRP reinforcement with strain gauges (a) 1, 2 and 3 (b) 4, 5 and 6 (c) 7 and 8 (d) 9 and 10 and (e) 11 and 12 for beam '0.75D'

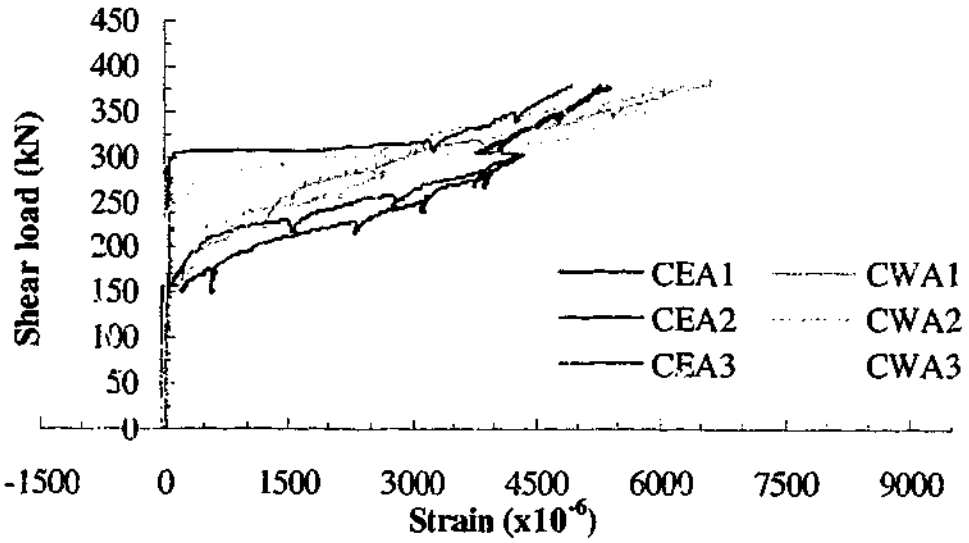

Figure 6.9 - Comparison of load strain responses of L-shaped CFRP reinforcement with gauges 1, 2 and 3 at east and west spans for beam '0.75D'

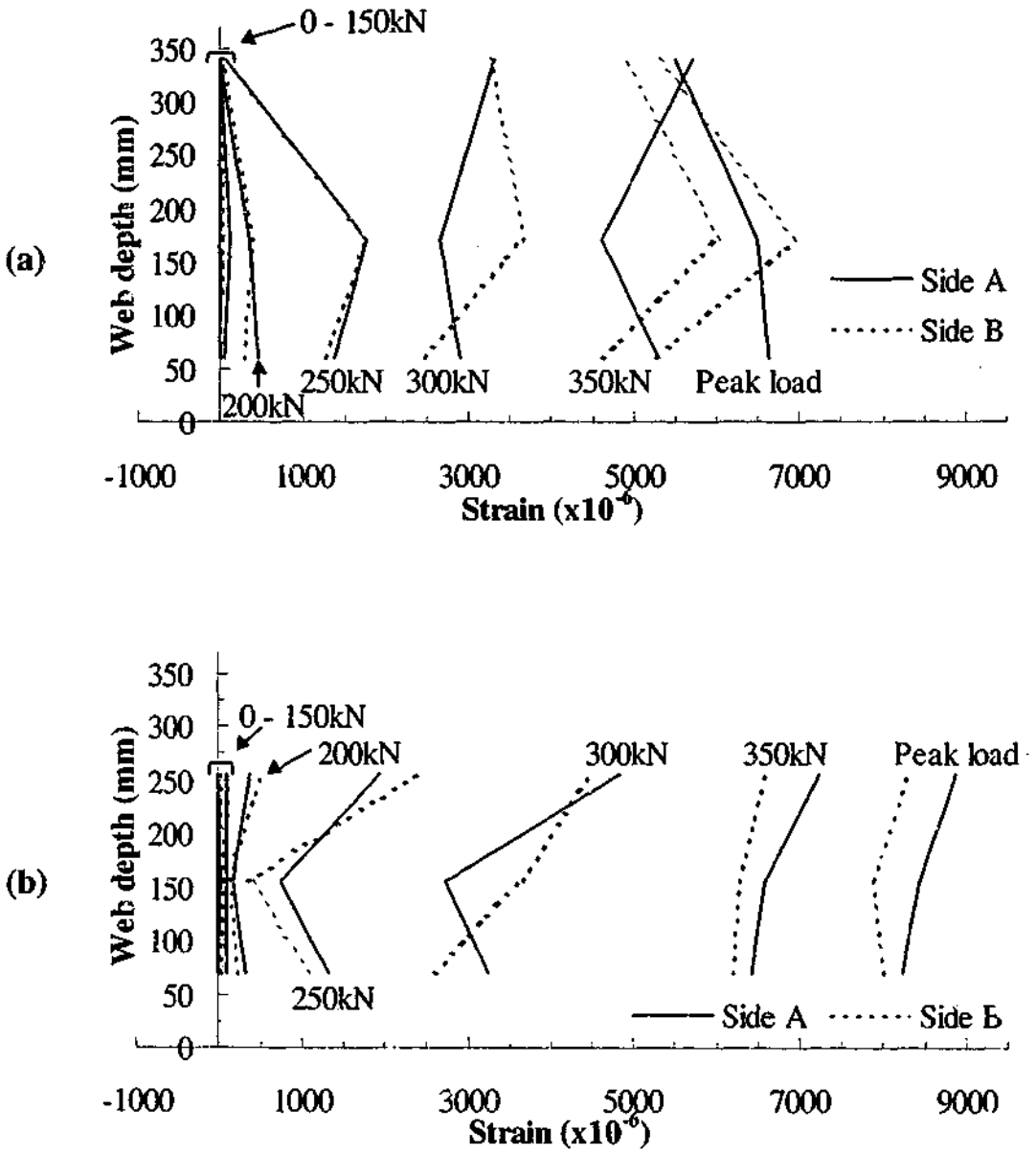

Figure 6.10 - Strain profile along length of L-shaped CFRP reinforcement with strain gauges (a) 1, 2 and 3 and (b) 4, 5 and 6 for beam '0.75D'

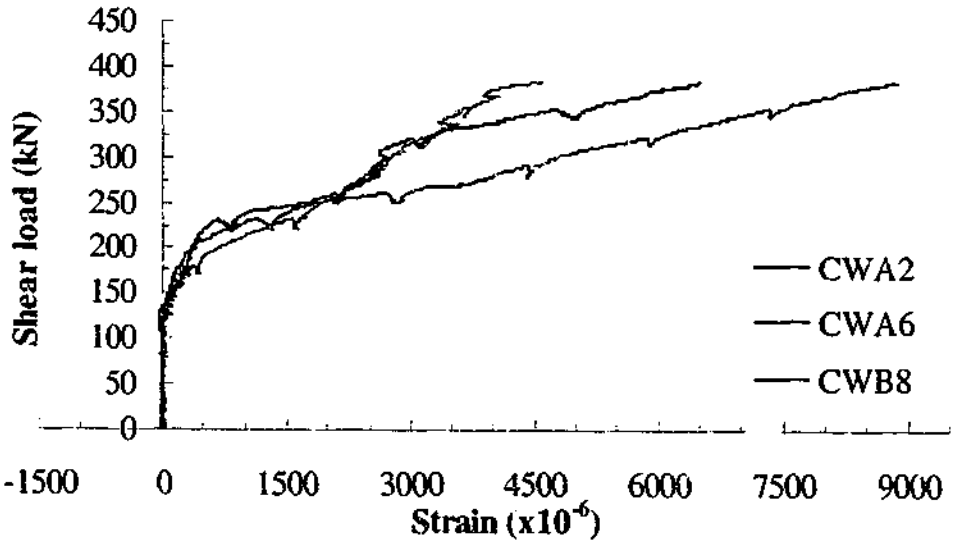

Figure 6.11 - Comparison of load strain responses of L-shaped CFRP reinforcement for beam '0.75D'

The load strain responses of the CFRP reinforcement at the failure span (west span) of beam '0.60D' are shown in Figure 6.12. The load strain responses given by the strain gauges at the same web height were comparable at opposing sides of the beam. Figure 6.13 compares the responses of the CFRP reinforcement with gauges 1, 2 and 3 at opposing shear spans. The load strain responses of gauge 2 were different between the two shear spans. It was very likely that shear cracks had formed at one span first. In general, the trends in the responses were similar for all of the gauges. This similarity was observed for all of the CFRP reinforcement on the beam. The load strain responses of the CFRP reinforcement on the east span is contained in Appendix B.3. The discussion that follows applies mainly to the CFRP reinforcement located at the west (failure) span.

For the CFRP reinforcement within the shear span, the strain values were small at the early stages of loading. At approximately 150 kN, the strain in the reinforcement began to increase more rapidly. For the CFRP reinforcement outside of the shear span, as expected, the strain values remained relatively small throughout the loading process. Similar to the CFRP reinforcement outside of the shear span in beam '0.75D', the same reinforcement in beam '0.60D' underwent compression near the web-flange junction.

The strain readings indicated that the first shear cracks propagated and crossed the CFRP reinforcement near the vicinity of gauges 2 and 3, gauge 6 and gauge 7. The post failure crack pattern illustrated in Figure 6.24 confirms the formation of shear cracks at these locations. The average compressive strength of the core samples of beam '0.60D' was 30.9 MPa. Using Equation 6.1, the corresponding critical strain value ranges from 642 to 885 με with an average of 730 με. From Figure 6.12, the shear load level that corresponds to this strain level varies significantly from one CFRP plate location to another. The values range from 165 to 260 kN with an average of 204 kN. Referring back to Figure 6.2 (c), the load level range at which debonding of the CFRP plates initiated is within the load level at which the second change in the overall beam stiffness occurs, which was at 290 kN. Unlike beam '0.75D', however, the internal steel shear reinforcement started to yield only when the load level is approximately 350 kN. Further shear crack propagation

and the debonding of the CFRP plate resulted in the second decrease in the overall stiffness of beam '0.60D'.

Figure 6.14 shows plots of the strain profiles along the length of the CFRP reinforcement bonded with gauges 1 to 3 and 4 to 6 at different load levels. Similar to the CFRP reinforcement at the shear span of beam '0.75D', the CFRP reinforcement in beam '0.60D' began to debond from the web commencing from the location where the shear cracks intersected the reinforcement. The extent of the debonded area can be seen in Figure 6.24. The two CFRP reinforcement with gauges 1 to 3 and 4 to 6 debonded along most of the length. For the reinforcement with gauges 4 to 6, the debonded area terminated a few millimetres from the chamfer and the web-flange junction. For the reinforcement with gauges 1 to 3, the CFRP overlaps separated with concrete torn off at the chamfer at one side (Figure 6.25). The strain gauges on these reinforcement gave the highest average strain value but only slightly more compared to the CFRP reinforcement with the gauges 1, 2 and 3. On the east span, the CFRP reinforcement with the gauges 4, 5 and 6 gave the highest average strain value. The maximum strain values and the corresponding stress levels of the CFRP reinforcement at the west span prior to beam failure are summarised in Table 6.5. There is only a slight difference in stress level between the CFRP reinforcement with gauges 1 to 3 and gauges 4 to 6. Figure 6.15 compares the responses of the CFRP reinforcement given by strain gauges 2, 6 and 7. The responses were comparable between gauges 6 and 7. Beam '0.60D' failed in a similar fashion as beam '0.75D'.

Table 6.5 - Maximum strain and stress levels recorded for the L-shaped CFRP reinforcement in beam '0.60D'

CFRP reinforcement	Side A		Side B	
	Strain ($x10^{-6}$)	Stress (MPa)	Strain ($x10^{-6}$)	Stress (MPa)
1, 2 and 3	7298	1002	6673	916
4, 5 and 6	6777	931	6365	874
7 and 8	2564	352	2881	396

(a)

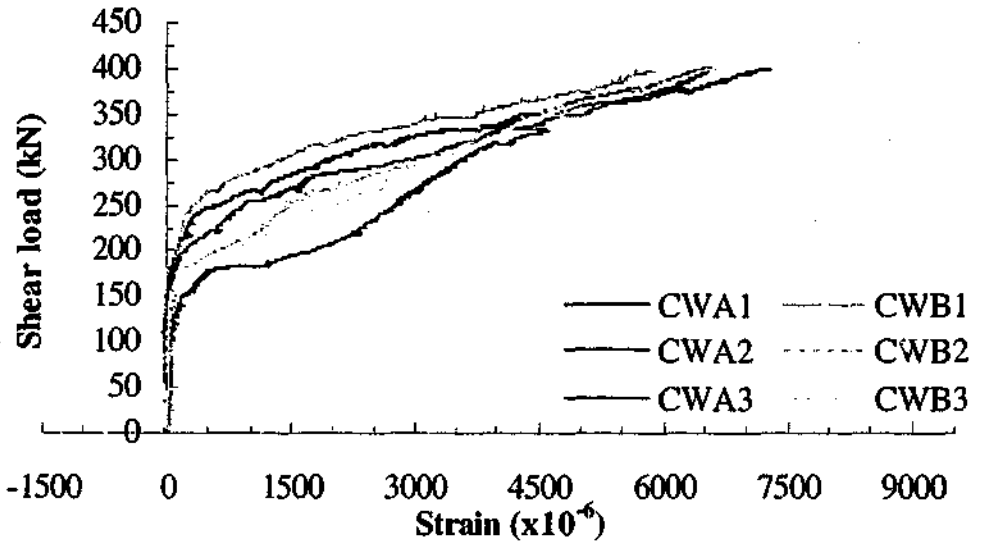

(b)

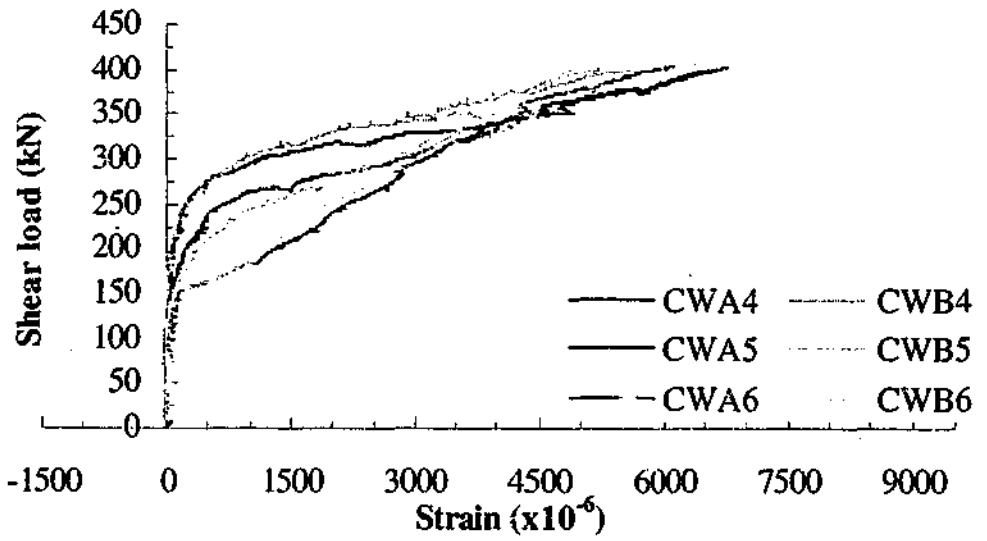

(c)

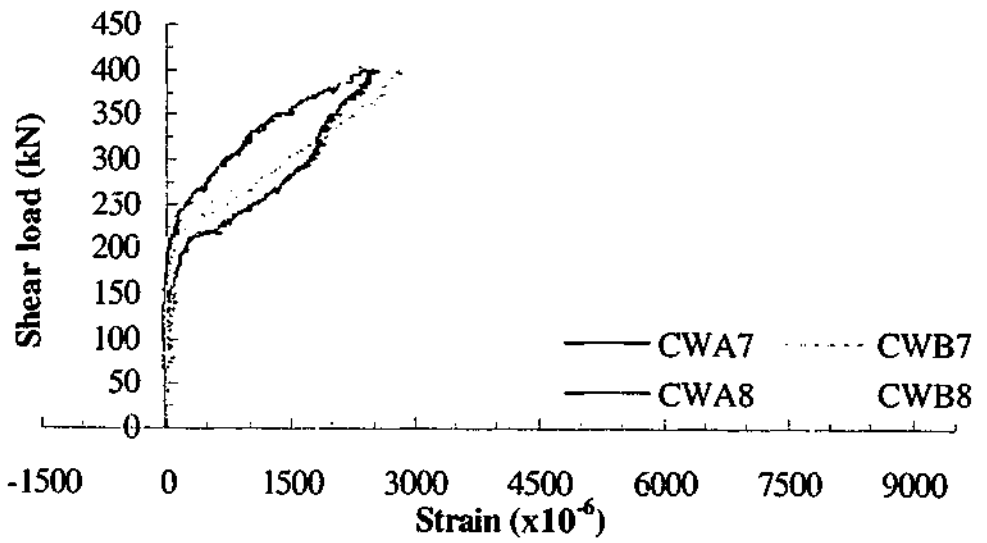

Figure 6.12 - Load strain responses of L-shaped CFRP reinforcement with strain gauges (a) 1, 2 and 3 (b) 4, 5 and 6 (c) 7 and 8 (d) 9 and 10 and (e) 11 and 12 for beam '0.60D'

(d)

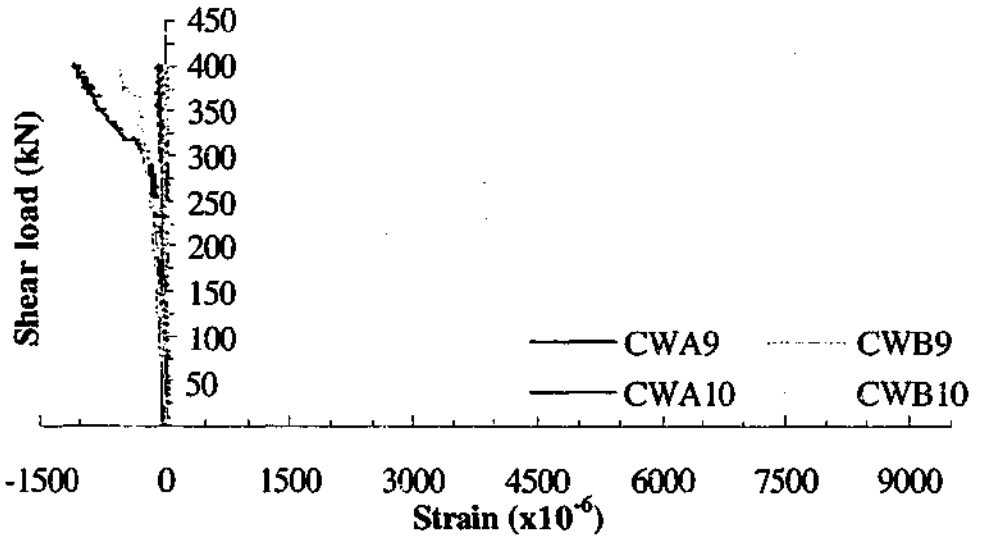

(e)

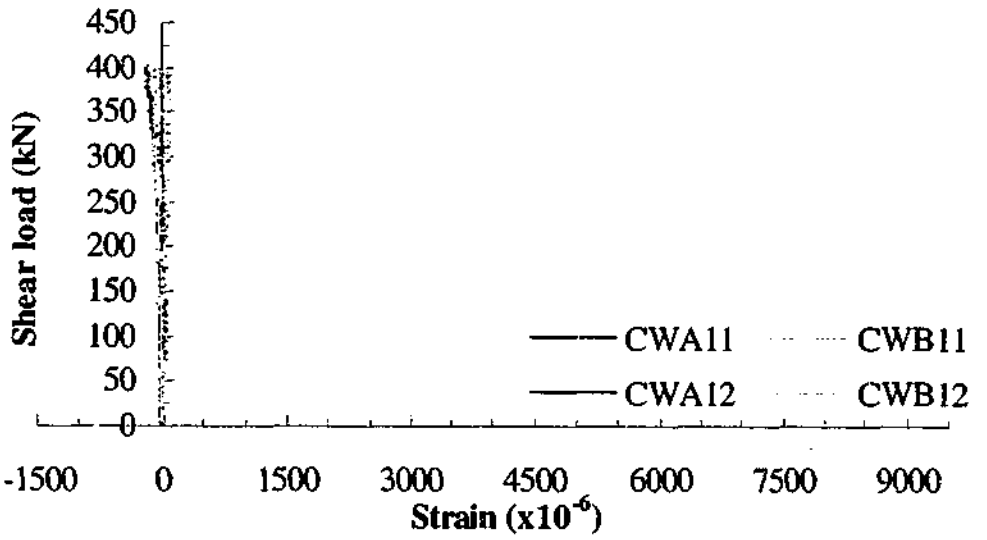

Figure 6.12 (continued) - Load strain responses of L-shaped CFRP reinforcement with strain gauges (a) 1, 2 and 3 (b) 4, 5 and 6 (c) 7 and 8 (d) 9 and 10 and (e) 11 and 12 for beam '0.60D'

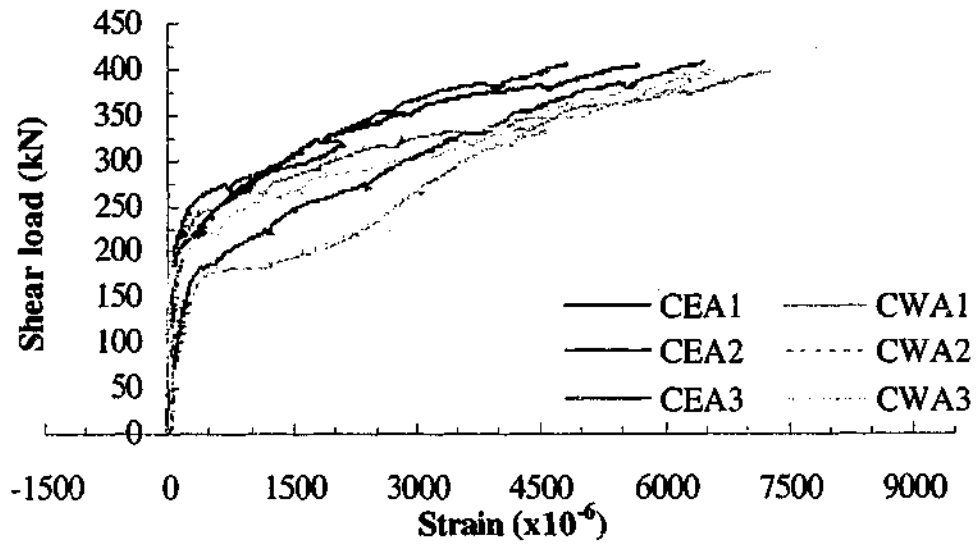

Figure 6.13 - Comparison of load strain responses of CFRP L-shaped reinforcement with gauges 1, 2 and 3 at east and west spans for beam '0.60D'

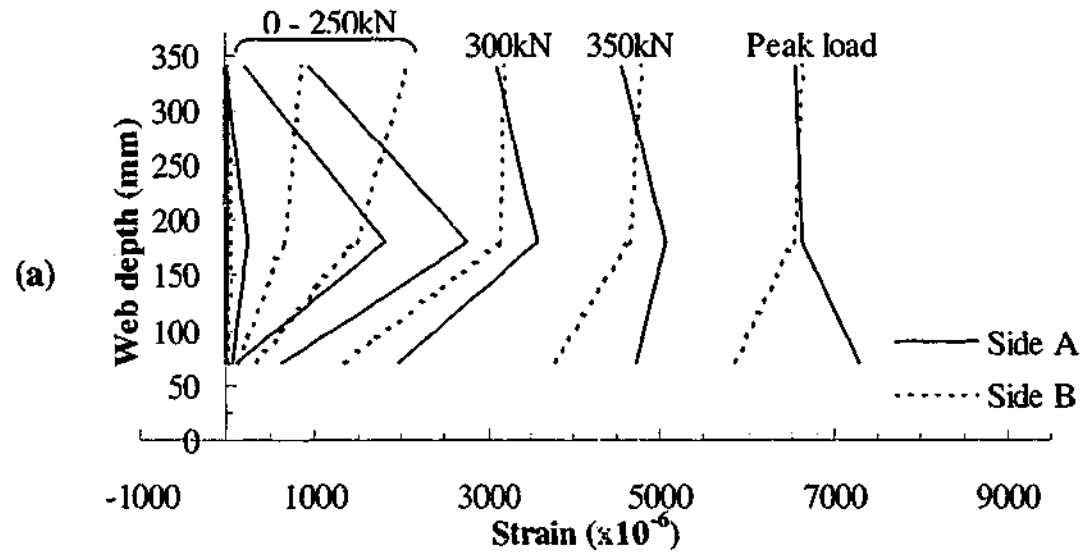

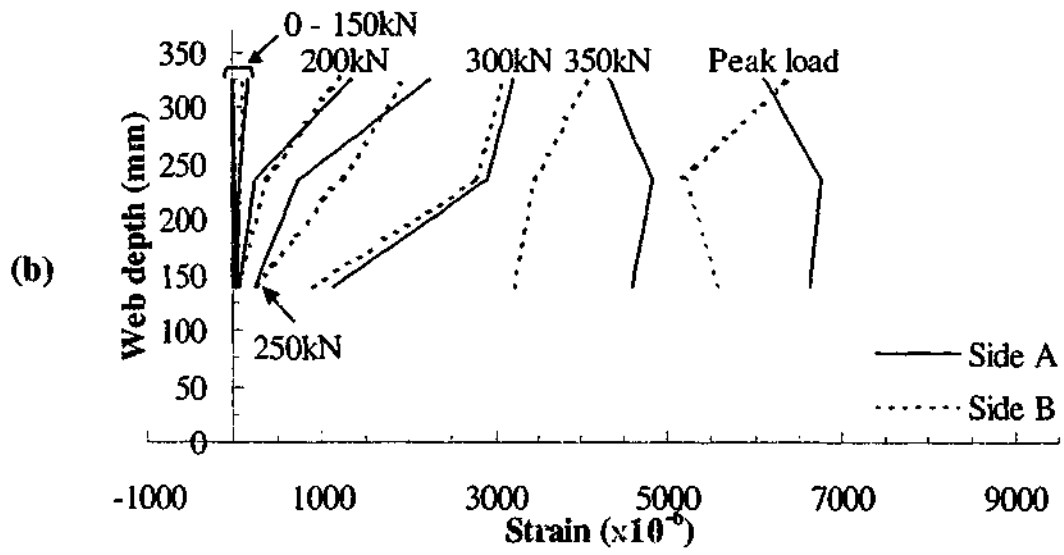

Figure 6.14 - Strain profile along length of L-shaped CFRP reinforcement with strain gauges (a) 1, 2 and 3 and (b) 4, 5 and 6 for beam '0.60D'

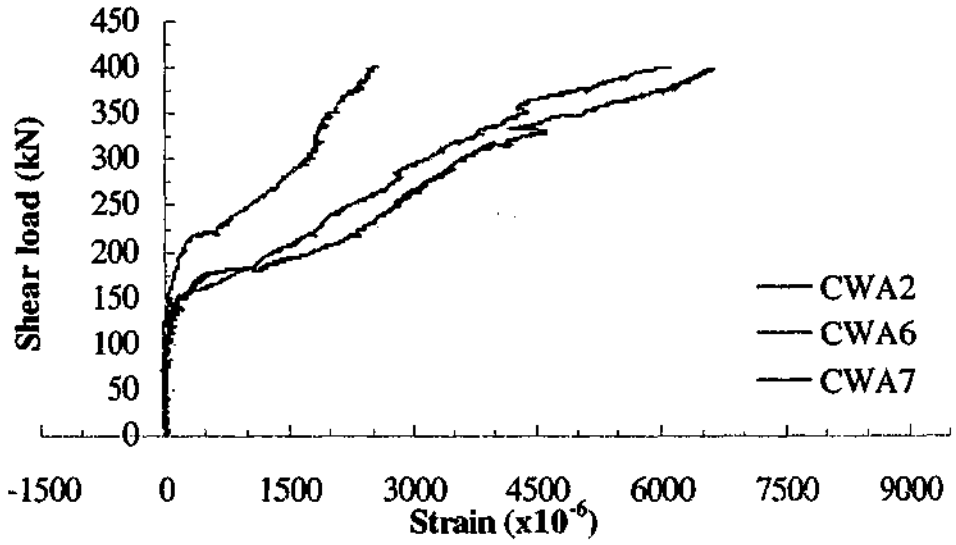

Figure 6.15 - Comparison of load strain responses of L-shaped CFRP reinforcement for beam '0.60D'

The load strain responses of the CFRP reinforcement at the failure span of beam '0.50D' are illustrated in Figure 6.16. The strain gauges located at the same web height and CFRP location but on opposing sides of the beam gave comparable load strain responses. Figure 6.17 compares the responses of the CFRP reinforcement with gauges 1, 2 and 3 at opposing shear spans. Only the load strain responses of gauges 1 and 3 were different between the two shear spans. In general, the trends in the responses were similar for all of the gauges. Further information on the load-strain responses of the CFRP reinforcement on the west span of beam '0.50D' is contained in Appendix B.3. It can be seen from Figure 6.16 that the CFRP reinforcement carried negligible shear load until approximately 150 kN. For the CFRP reinforcement with gauges 1 to 3 and 4 to 6, the strains along the length were almost similar near the peak load. The CFRP reinforcement outside of the shear span underwent compression near the web-flange junction.

Readings from the strain gauges indicated that the first shear cracks propagated and crossed the CFRP reinforcement near the vicinity of gauge 6 and gauge 8. For the CFRP reinforcement with gauges 1, 2 and 3, shear cracks appeared to have formed simultaneously near the vicinity of all the gauges. This can be seen more clearly in Figure 6.18, where the strain values at three locations along the CFRP reinforcement are almost similar. The average compressive strength of the core samples of beam '0.50D' was 31.6 MPa. Using Equation 6.1, the corresponding

critical strain value ranges from 650 to 895 με with an average of 738 με. From Figure 6.16, the shear load level that corresponds to this strain level varies from one CFRP location to another. The shear load level ranges from 190 to 300 kN with an average of 218 kN. Referring back to Figure 6.2 (d), the shear load level range is within the load level at which the second change in the overall beam stiffness occurs, which was at 285 kN. The internal steel shear reinforcement yielded at the shear load level of approximately 360 kN. Therefore, the decrease in the overall beam stiffness is the result of further shear crack propagation and debonding of the CFRP plate.

The extent of the debonded areas of the CFRP reinforcement is illustrated in Figure 6.26. Three of the CFRP reinforcement in the failure shear span on each side had debonded along most of their lengths. Photographs of the post failure crack pattern at the failure span are shown in Figure 6.27. In the web, two major shear cracks had formed and the CFRP overlaps separated at two locations. Prior to failure, extensive cracking in the flange caused the concrete surrounding the anchorage zone of the second and third CFRP reinforcement from the load point to fail abruptly. The instantaneous separation of the web and flange within the vicinity of these reinforcement caused a sudden force transfer to the adjacent CFRP reinforcement. As a result, the overlaps separated abruptly. On side B of the beam, the magnitude of the force caused one of the CFRP reinforcement to debond completely and fracture at the web-flange junction. The shear force carried by the CFRP reinforcement with gauges 1 to 3 was the highest. This was observed for the CFRP reinforcement on the west span as well. Table 6.6 summarises the maximum strain values and the corresponding stress levels of the CFRP reinforcement at the east span prior to beam failure. There is a distinct difference in the stress level between the CFRP reinforcement at different locations. Figure 6.19 illustrates clearly the differences in responses of the CFRP reinforcement at different locations.

Table 6.6 - Maximum strain and stress levels recorded for the L-shaped CFRP reinforcement in beam '0.50D'

CFRP reinforcement	Side A		Side B	
	Strain ($x10^{-6}$)	Stress (MPa)	Strain ($x10^{-6}$)	Stress (MPa)
1, 2 and 3	7515	1032	8145	1119
4, 5 and 6	5810	798	5682	780
7 and 8	2204	303	2080	286

(a)

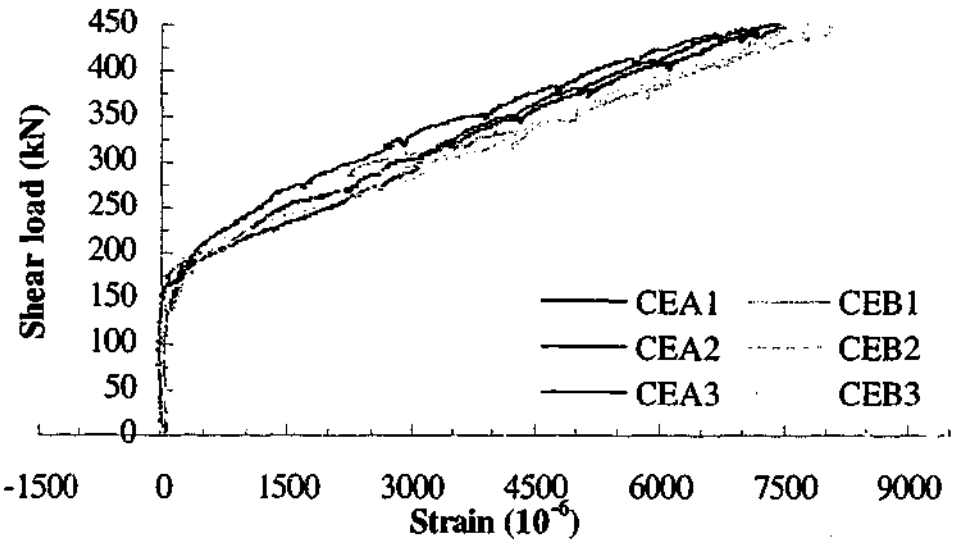

(b)

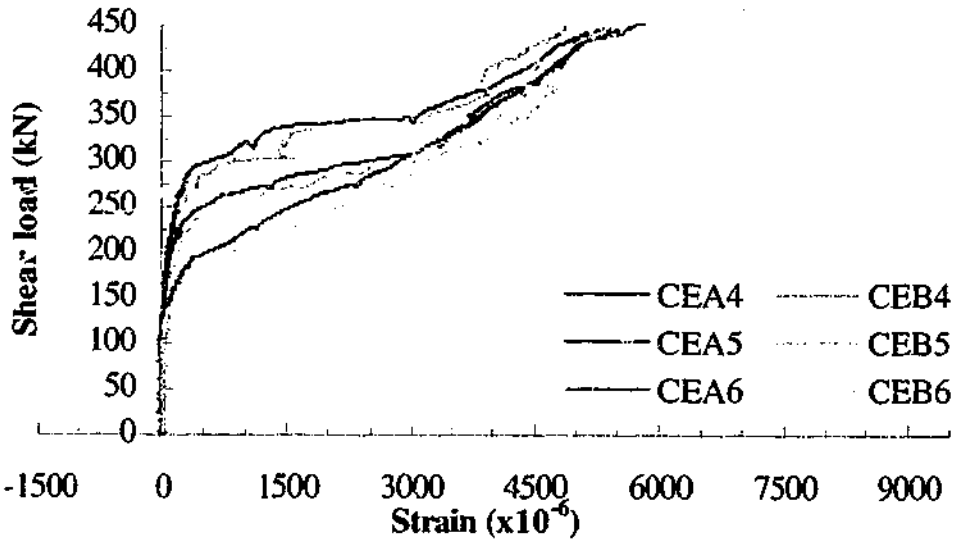

Figure 6.16 - Load strain responses of L-shaped CFRP reinforcement with strain gauges (a) 1, 2 and 3 (b) 4, 5 and 6 (c) 7 and 8 (d) 9 and 10 and (e) 11 and 12 for beam '0.50D'

(c)

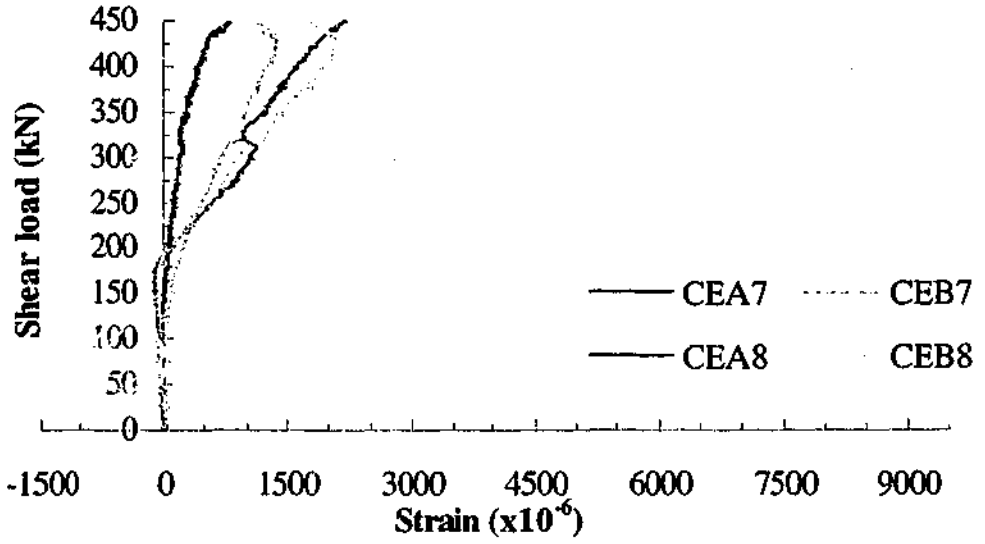

(d)

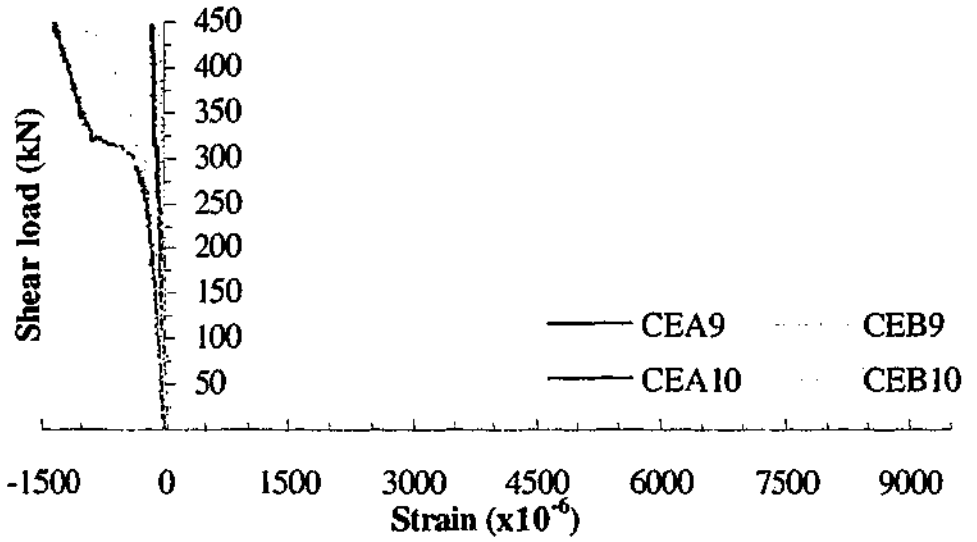

(e)

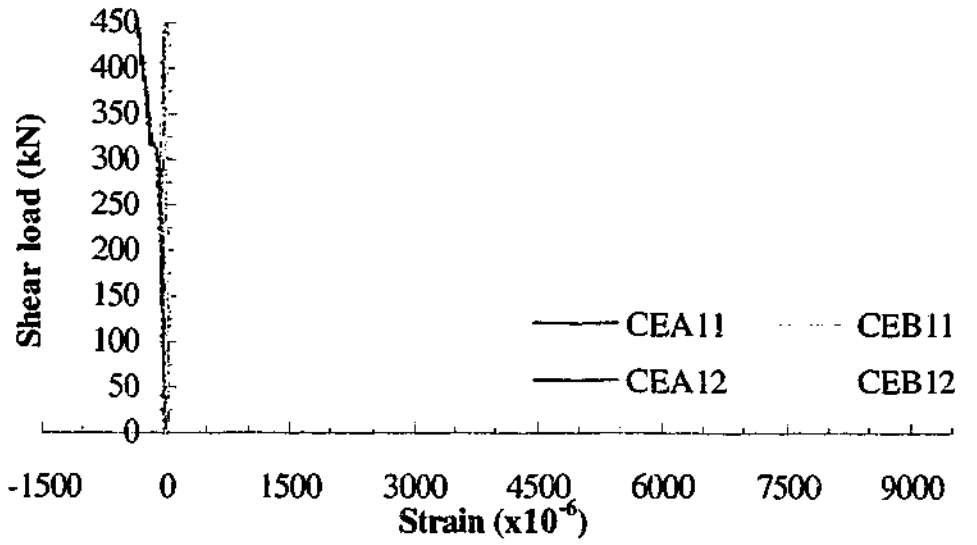

Figure 6.16 (continued) - Load strain responses of L-shaped CFRP reinforcement with strain gauges (a) 1, 2 and 3 (b) 4, 5 and 6 (c) 7 and 8 (d) 9 and 10 and (e) 11 and 12 for beam '0.50D'

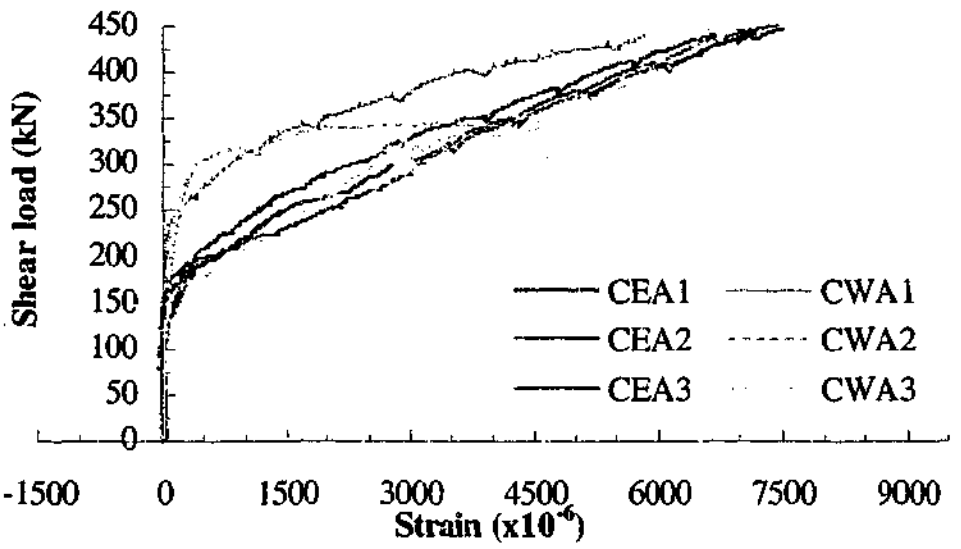

Figure 6.17 - Comparison of load strain responses of CFRP L-shaped reinforcement with gauges 1, 2 and 3 at east and west spans for beam '0.50D'

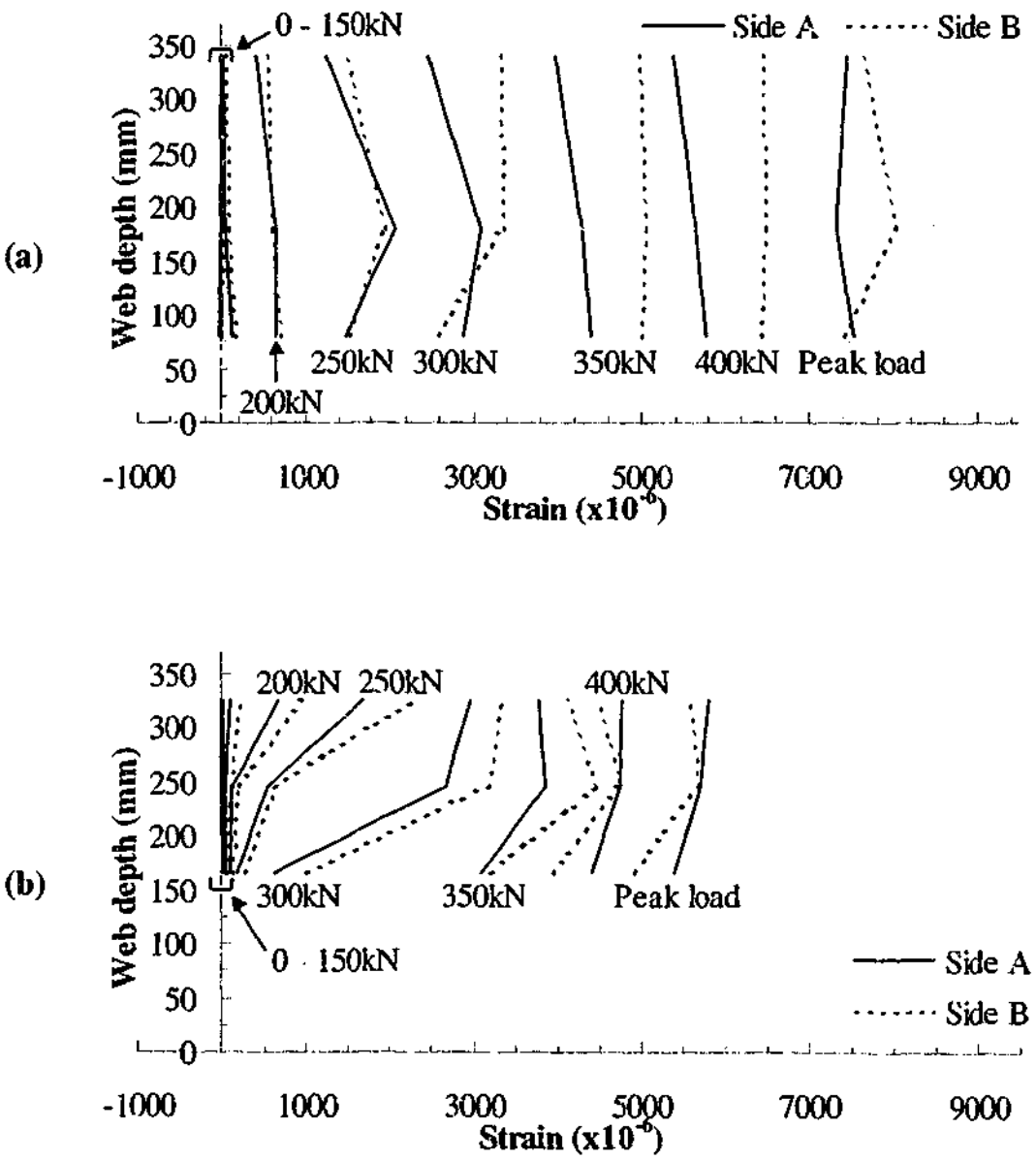

Figure 6.18 - Strain profile along length of L-shaped CFRP reinforcement with strain gauges (a) 1, 2 and 3 and (b) 4, 5 and 6 for beam '0.50D'

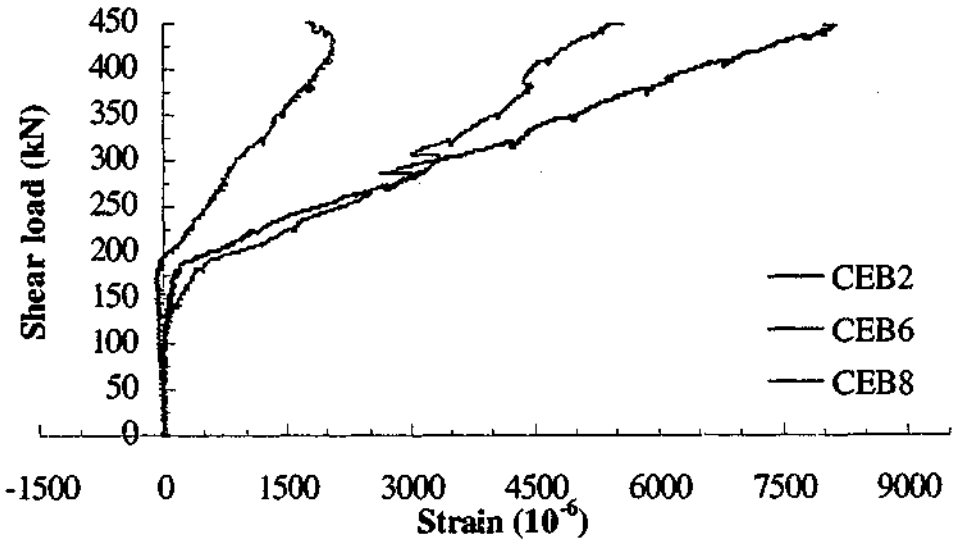

Figure 6.19 - Comparison of load strain responses of L-shaped CFRP reinforcement for beam '0.50D'

The location in the shear span where CFRP reinforcement gave the highest strain values were similar for all of the strengthened beams. The distances of these CFRP reinforcement from the support were 718 and 653 mm for beams '0.75D' and '0.50D' respectively. For beam '0.60D', two CFRP reinforcement locations gave equally high strain values. The distances of these reinforcement from the support were 528 and 823 mm respectively. Due to its relatively low stiffness, the CFRP reinforcement do not contribute to carrying any load until shear cracks had formed and propagated to a certain width. By this stage of loading, the crack orientations and propagation paths would have been fixed to a limited extent. The use of different CFRP reinforcement spacings did not affect significantly the region where the major shear cracks propagated.

The load level at which the CFRP reinforcement began to exhibit significant increase in strain values was similar for all the strengthened beams, which was approximately 150 kN. This load level was similar to the load level at which the internal steel shear reinforcement began to carry significantly more load. The placement of CFRP reinforcement at smaller spacings did not impede or delay the initial formation and propagation of shear cracks.

Outside the shear spans, all of the CFRP reinforcement closest to the point loads were observed to have undergone compression near the web-flange junction.

Post failure examination of the strengthened beams showed that these reinforcement did not exhibit any sign of debonding. Prior to failure, most of the CFRP reinforcement at the shear span were observed to have debonded. The failure modes for beams '0.75D' and '0.60D' were similar, which was CFRP anchorage failure at the soffit. Beam '0.50D' failed as a result of concrete surrounding the CFRP anchorage zone being torn away from the flange. In all cases, the beams failed in shear.

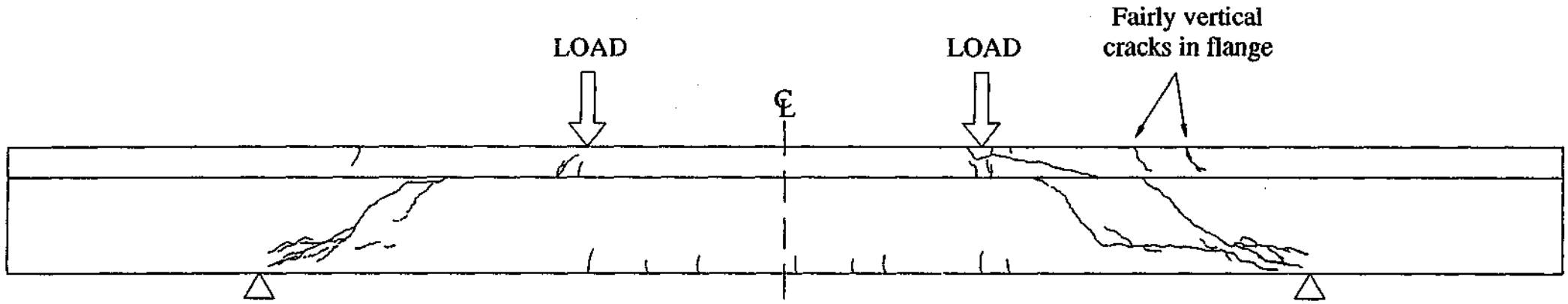

Figure 6.20 - Control beam post failure crack pattern

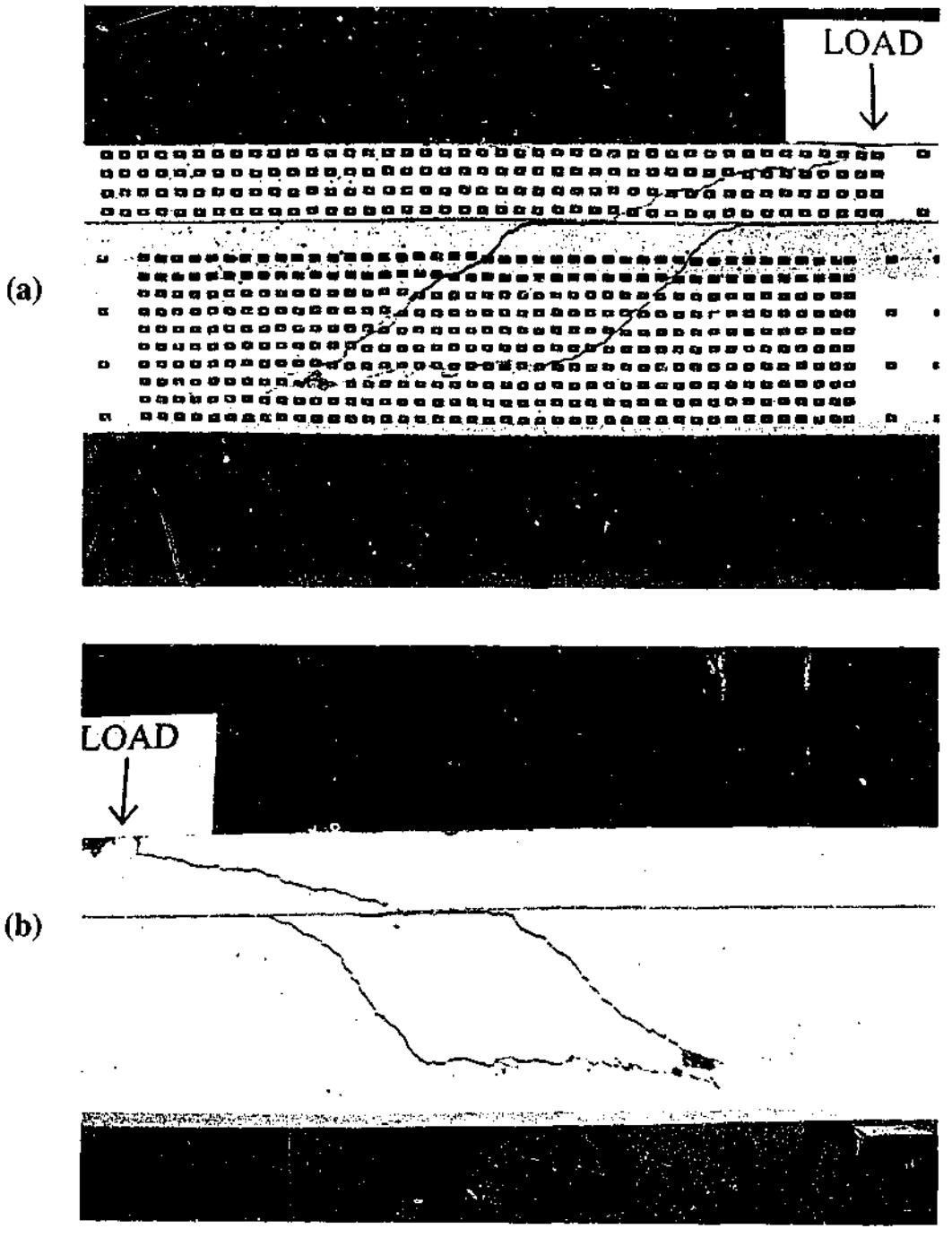

Figure 6.21 - Failure pattern for control beam at (a) side A and (b) side B

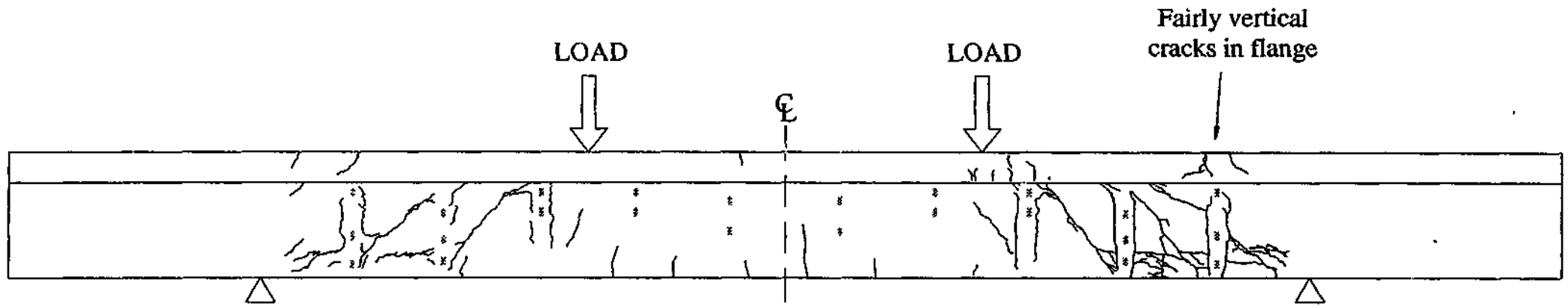

SIDE A

EAST ← → ***WEST***

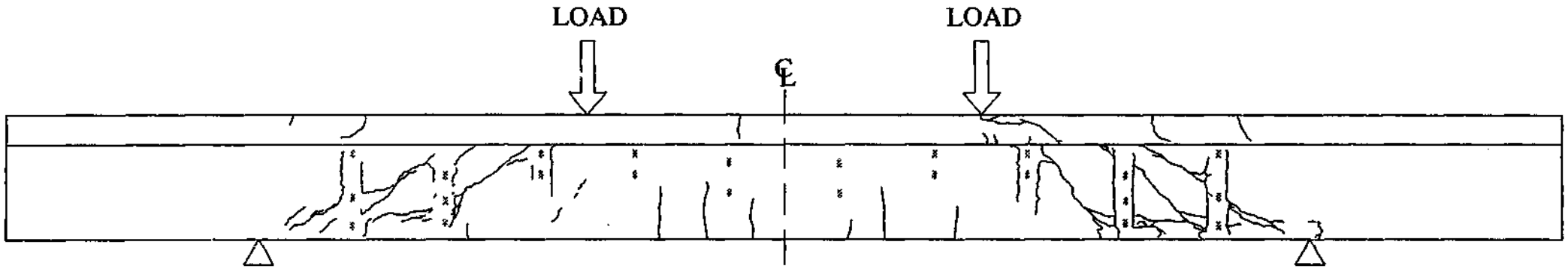

SIDE B

Figure 6.22 - Beam '0.75D' post failure crack pattern

(a)

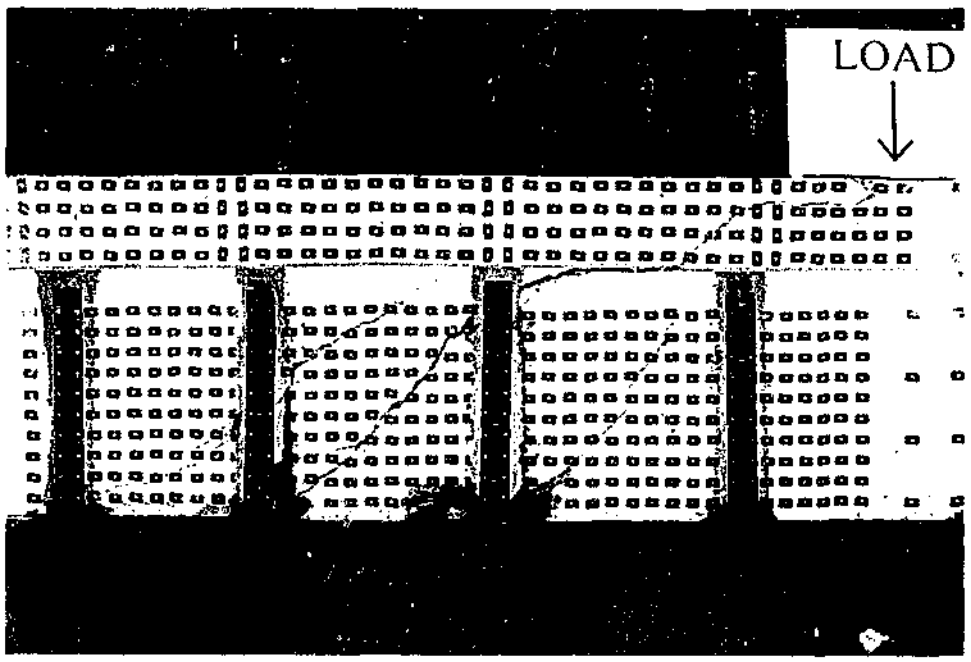

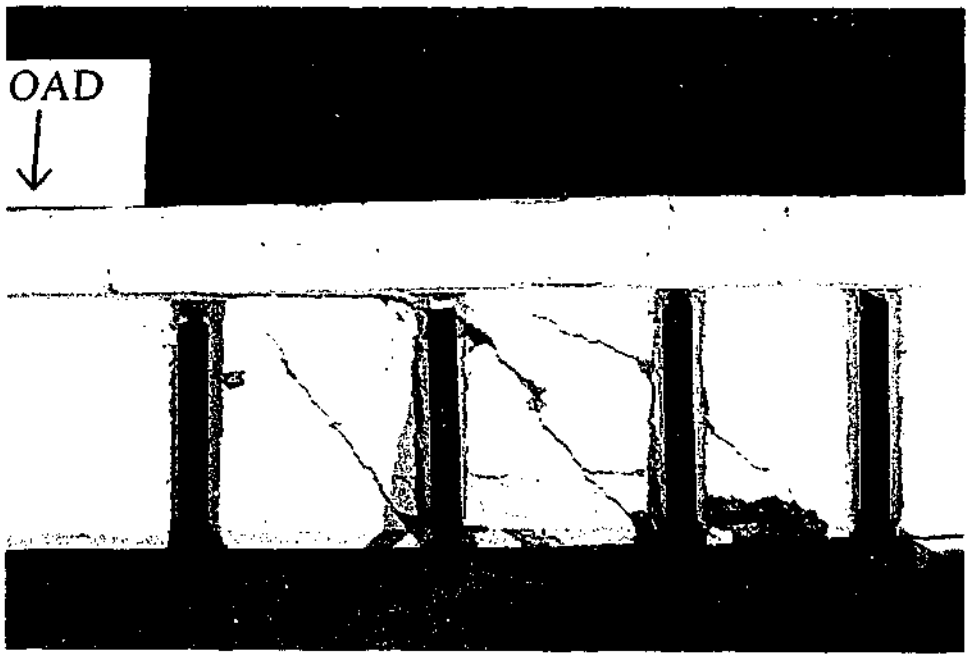

(b)

Figure 6.23 - Failure pattern for beam '0.75D' at (a) side A and (b) side B

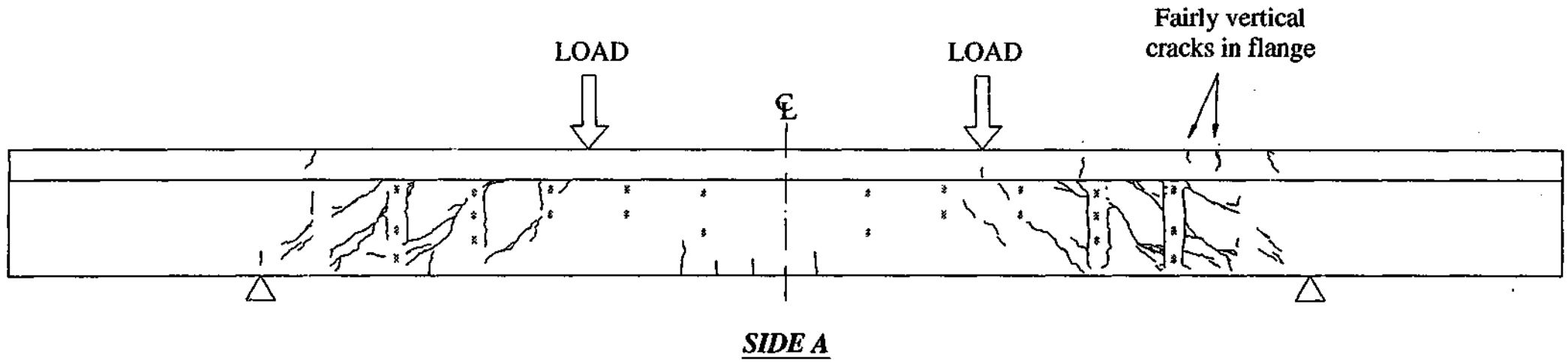

Figure 6.24 - Beam '0.60D' post failure crack pattern

(a)

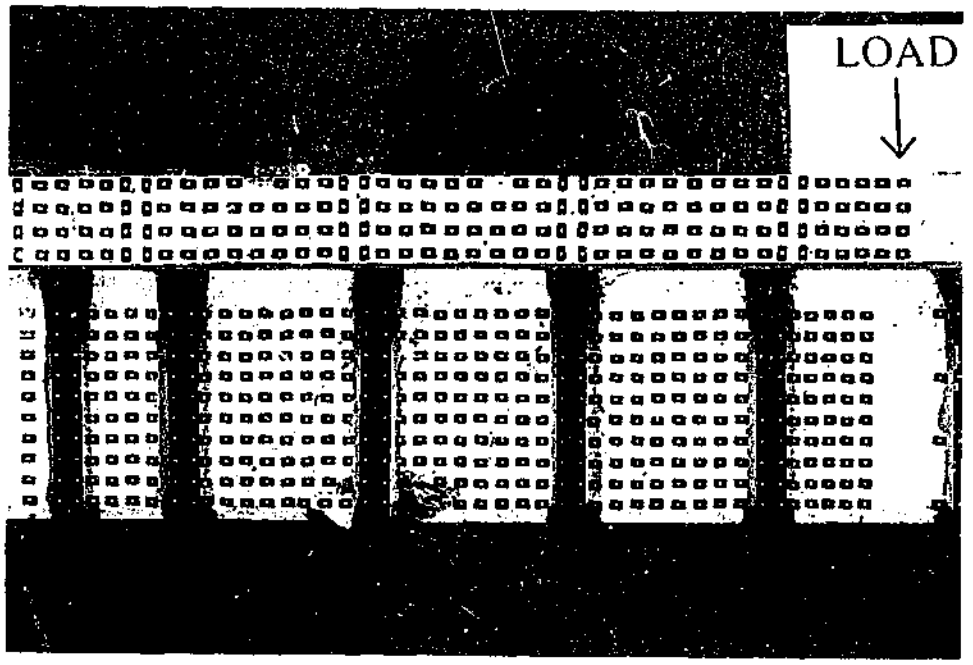

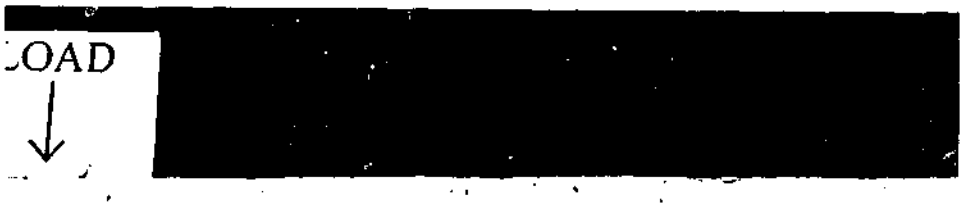

(b)

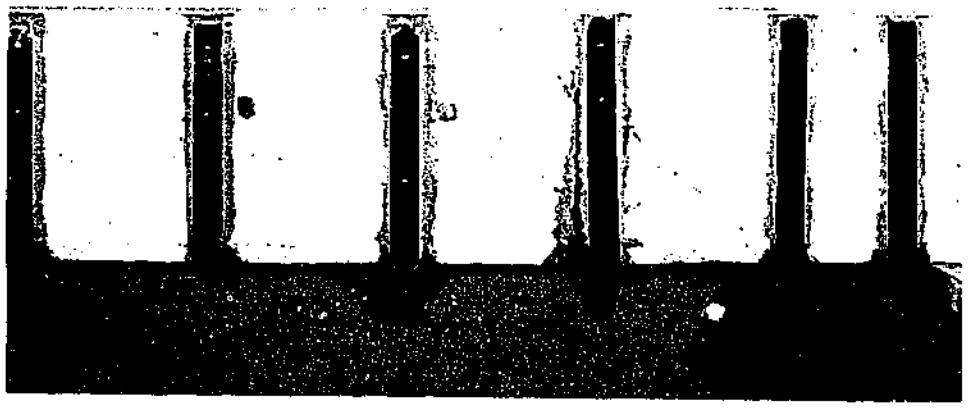

Figure 6.25 - Failure pattern for beam '0.60D' at (a) side A and (b) side B

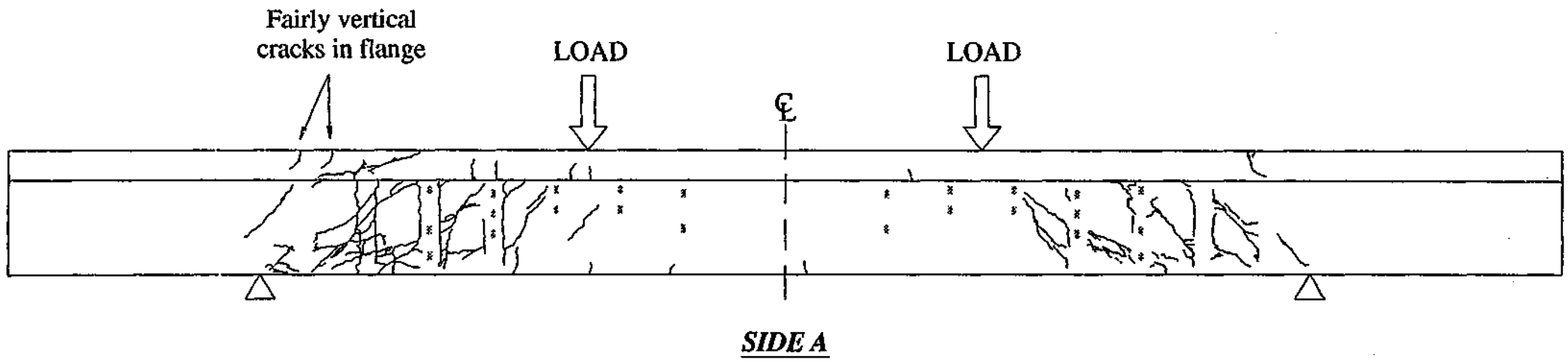

Figure 6.26 - Beam '0.50D' post failure crack pattern

(a)

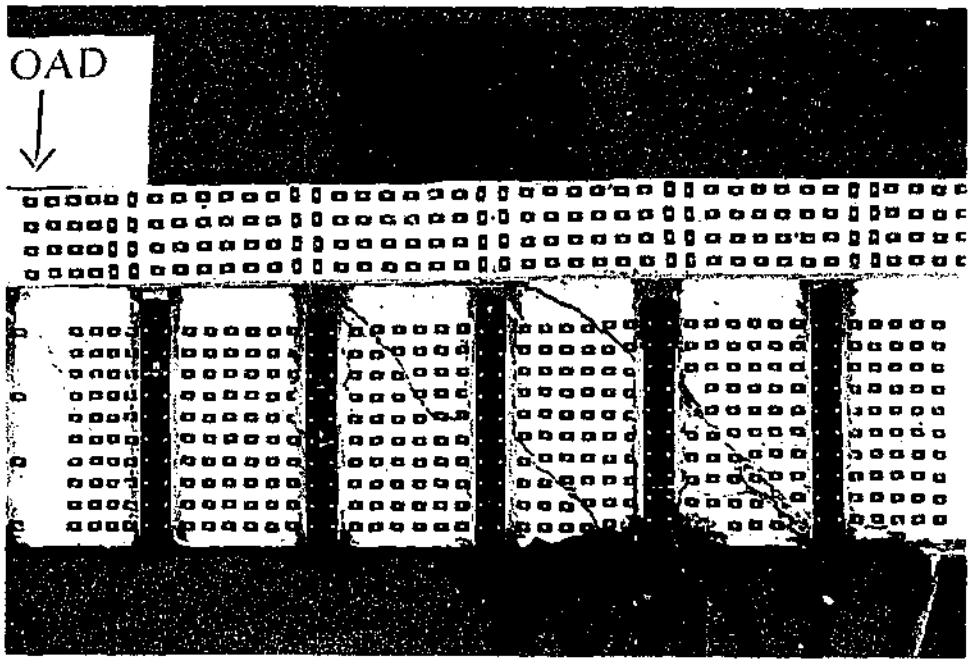

(b)

Figure 6.27 - Failure pattern for beam '0.50D' at (a) side A and (b) side B

6.2.6 Crack patterns

The crack patterns for the three strengthened beams are compared against the crack patterns of the control beam in Figure 6.31. The diagrams show the crack patterns at the failure span as observed on both sides of the beams. All of the beams except for beam '0.50D' failed in the west span. In the case of beam '0.50D', the crack patterns have been mirrored onto the west span to simplify comparisons with the control beam. The crack patterns for the control and strengthened beams are represented by solid and dotted lines respectively.

Prior to failure, two major shear cracks formed in the web at the west span of the control beam (Figure 6.21). The shear cracks propagated along the level of the top main flexural reinforcement towards the support. The average inclination angle of the shear cracks measured from the horizontal axis of the beam was 40°. Measurements were taken at mid depth on both sides of the web.

In beam '0.75D', three major shear cracks formed in the web of the shear span prior to failure (Figure 6.23). It was observed that the shear cracks did not propagate continuously along the level of the flexural reinforcement before failure. The average inclination angle of the two shear cracks closest to the point load was 51°. The average inclination angle of the shear crack closest to the support was 37°. The locations at which the major cracks formed were reasonably similar between the control beam and beam '0.75D'.

In beam '0.60D', two major shear cracks formed in the web between the second and fourth CFRP reinforcement from the support prior to failure (Figure 6.25). Minor shear cracks were observed to have formed close to the point load and supports. Along the level of the main flexural reinforcement, the cracks were less distinct and propagated less compared to the cracks observed in beam '0.75D'. The average inclination angle of the two major shear cracks was 47°. The locations at which the major shear cracks formed were reasonably similar between the control beam and beam '0.60D'.

In beam '0.50D', two major shear cracks were observed to have formed in the web between the first and fourth CFRP reinforcement from the support during loading (Figure 6.27). Minor shear cracks had formed between the fourth and fifth reinforcement and near the vicinity of the support. Near the support, the minor shear crack formed close to the major shear crack. Prior to and after failure, cracks along the level of the main flexural reinforcement were not distinctively noticeable. The average inclination angle of the major shear cracks was 45°. The major shear cracks in beam '0.50D' formed close to the locations of the shear cracks in the control beam.

In all of the beams, several fairly vertical cracks that were not part of the main diagonal crack can be observed to have formed in the flange as indicated in Figures 6.20, 6.22, 6.24 and 6.26. These cracks formed at very high load levels after the formation of diagonal cracks in the web. Figure 6.28 illustrates a possible deformation mechanism that causes the formation of such cracks where a section of the beam has been taken along the path of the shear crack. At the location where the shear crack intersects the main flexural reinforcement, the forces in the reinforcement are high. The high compressive forces in the flange effectively acts as rollers fixing horizontal movements of the beam. The force in the main reinforcement causes rotation of the concrete block about the roller support. In order to maintain compatibility in deformation, cracks form at the top of the beam at the location indicated in the figure. It should be pointed out that the cracks would only form if the concrete portions deform as rigid blocks. Photogrammetry measurement results in Section 7.3.2 show that the beams do deform as rigid blocks.

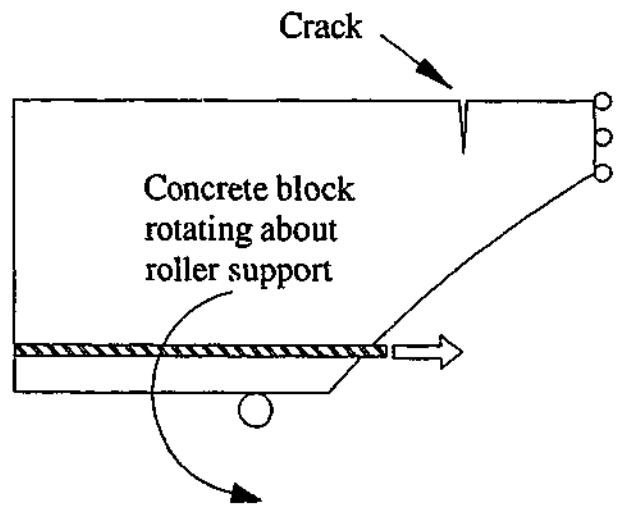

Figure 6.28 - Deformation mechanism of beam

In the control beam, a major diagonal crack had formed in the flange from the web-flange junction extending towards the load point (Figure 6.29). This diagonal crack had not been observed to form in any of the strengthened beams. On the top of the flange, longitudinal cracks were observed to have formed along the length of the control beam during loading. High compressive forces acting along the length of the flange resulted in cracking of concrete. Figure 6.30 shows the location of this longitudinal crack taken after failure had occurred. These cracks were observed to have formed in all of the strengthened beams. From the figure, it can also be observed that cracks perpendicular to the beam's length had formed at the location of the point load. This indicated crushing of concrete. These cracks did not form in any of the strengthened beams. Therefore, it is highly unlikely that crushing of concrete under the loading point had occurred in the control beam. It is simply due to the diagonal crack in the flange extending all the way up to the top of the flange.

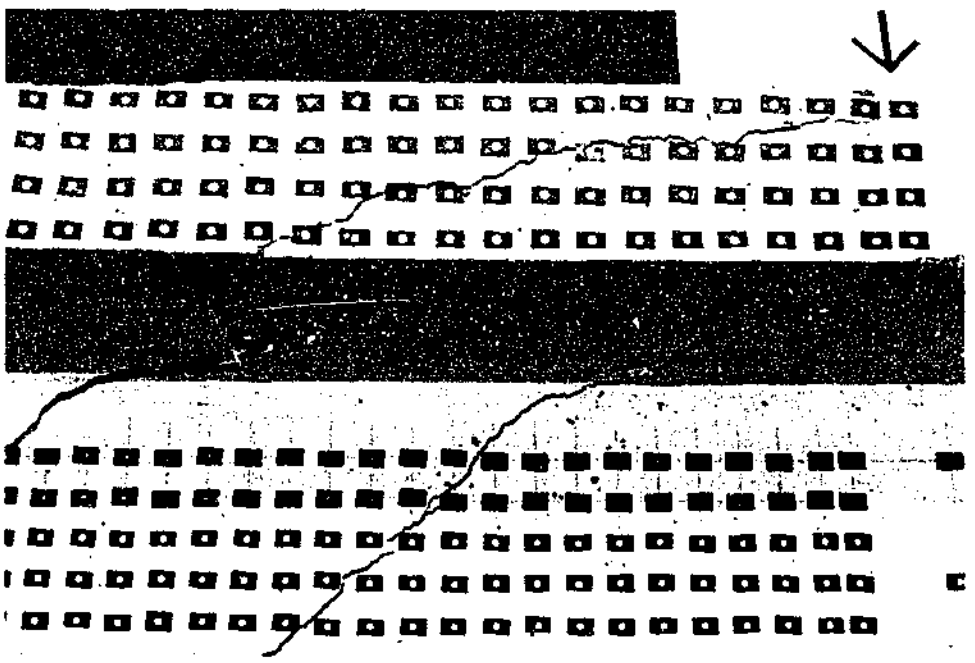

Figure 6.29 - Diagonal crack extending from web into flange of control beam

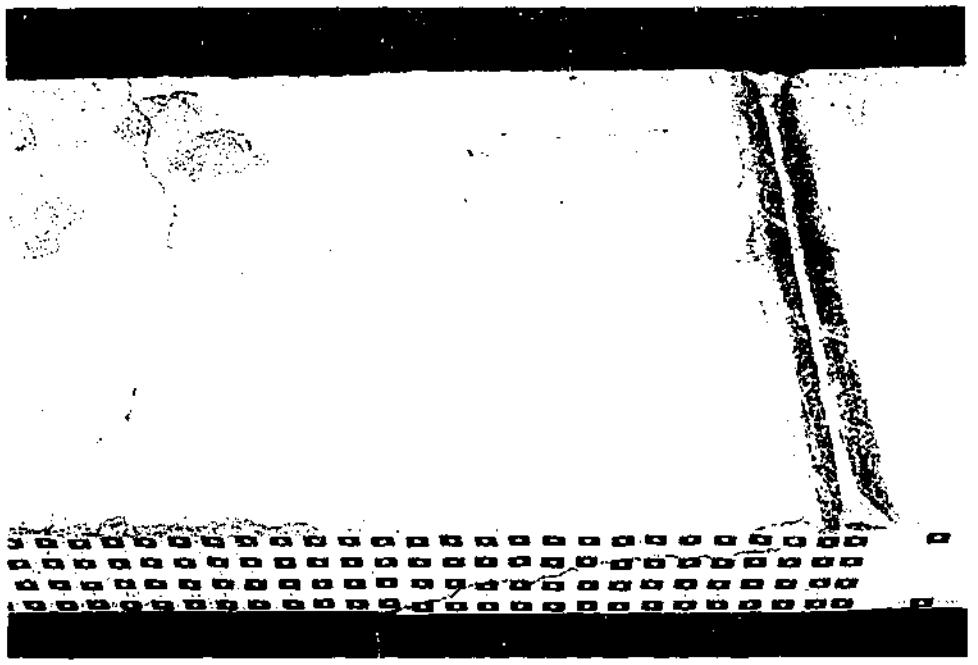

Figure 6.30 - Crack pattern on top of flange of control beam

Observations of the crack patterns indicated that the shear cracks in the strengthened beams formed at a slightly steeper angle compared to the shear cracks in the control beam. It is difficult to confirm this fact conclusively as experimental scatter exists even in beams of identical configurations. The shear crack inclination angle was similar between the strengthened beams. During testing, the crack widths were noticeably smaller in the strengthened beams compared to the crack widths in the control beam. In addition, cracks along the level of the main flexural reinforcement were less distinct or unnoticeable prior to and after failure. The locations of the major shear cracks that formed in the beams varied slightly between the strengthened beams and the control beam. Nevertheless, the locations of these shear cracks can be considered to be fairly similar for all the beams as different results can arise even in beams with identical configurations. In all the beams except for beam '0.75D', two major shear cracks formed in the shear span prior to failure. For beam '0.75D', the location of the third major shear crack coincided with the location of a minor shear crack observed in beam '0.60D' near the support. This crack was almost unnoticeable in beam '0.50D'. The strengthened beams with the CFRP reinforcement spaced closer together were more effective in restricting shear crack growth. Due to the additional shear capacity available, more minor shear cracks were observed to have formed in the web of strengthened beams compared to the control beam. It can be observed from Figure 6.31 that some cracks had formed in the web close to the location of the point load.

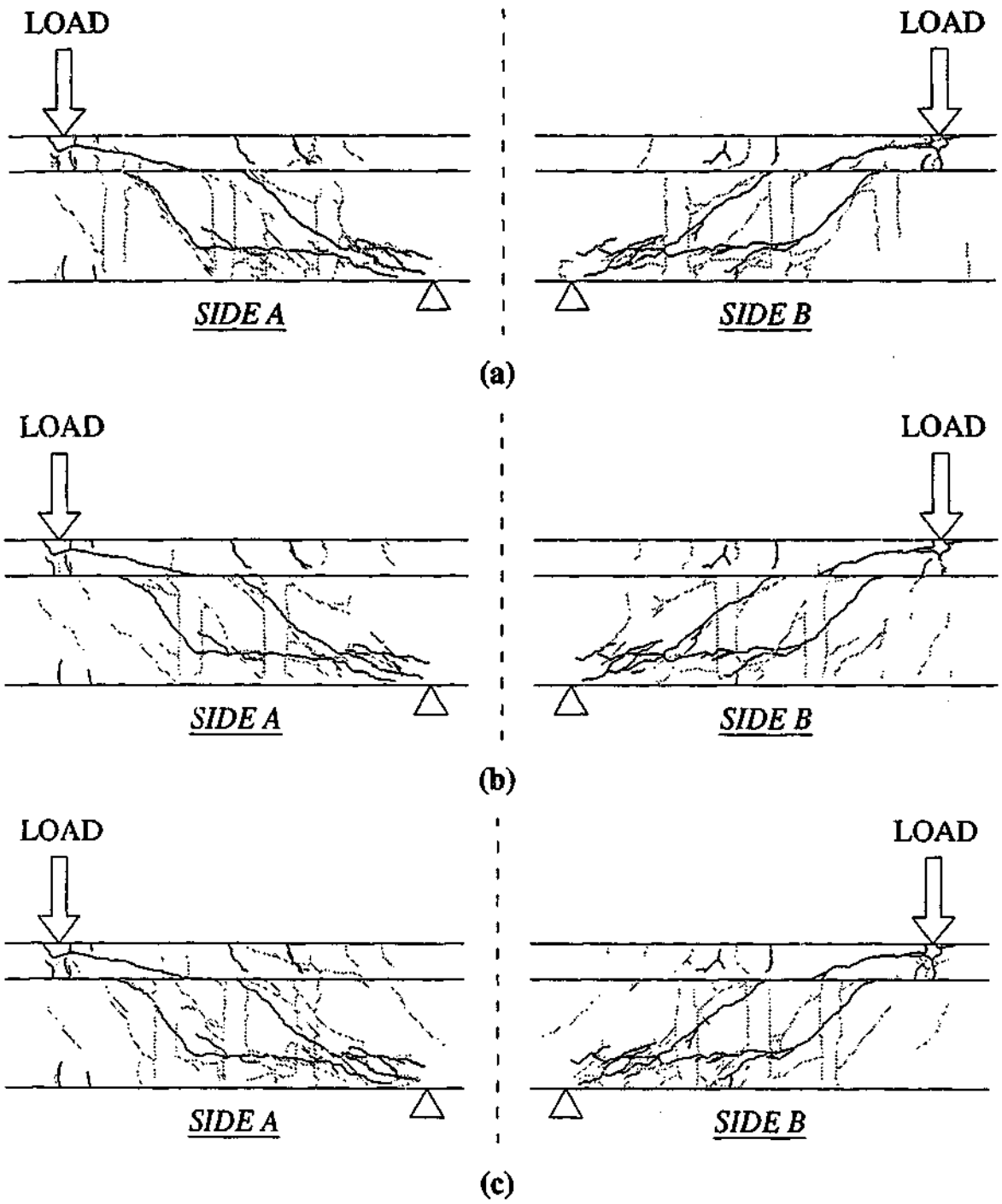

Figure 6.31 - Comparison of post failure crack patterns at failure span between control beam and beams (a) '0.75D' (b) '0.60D' and (c) '0.50D'

6.2.7 Comparison between CFRP and steel shear reinforcement

The tensile forces carried by the CFRP and steel shear reinforcement are compared in Figure 6.32. The y-axis in the plots corresponded to the support loads measured at the failure spans. One strain gauge from each CFRP reinforcement location was compared. The strain gauges selected were located near where shear

cracks had first crossed the CFRP reinforcement. In beam '0.60D', the internal shear reinforcement with gauges 1 and 2 were similarly located along the shear span with the CFRP reinforcement with gauges 1 to 3. In beam '0.50D', the internal shear reinforcement with gauges 3 and 4 were similarly located with the CFRP reinforcement with gauges 4 to 6. In beam '0.75D', none of the internal shear reinforcement were located at the same location as the CFRP reinforcement.

It can be observed clearly that the CFRP reinforcement contributed to carrying more loads at approximately the same load level as the internal shear reinforcement. At low load levels, both types of reinforcement exhibited similarly small strain values until the formation of shear cracks beyond which the response began to differ. At high load levels, the CFRP reinforcement carried significantly more load compared to the internal shear reinforcement.

(a)

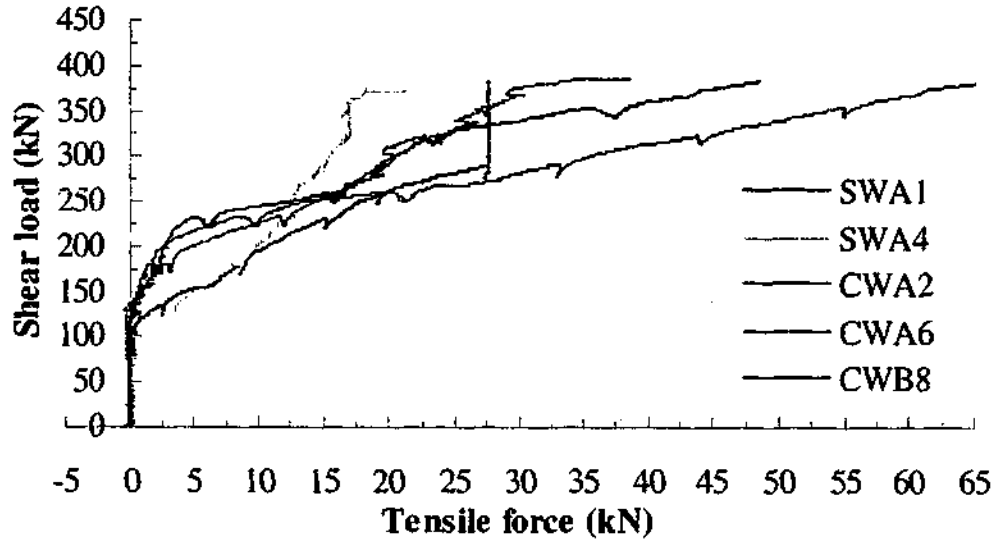

Figure 6.32 - Comparison of tensile forces between CFRP and steel shear reinforcement for beams (a) '0.75D' (b) '0.60D' and (c) '0.50D'

(b)

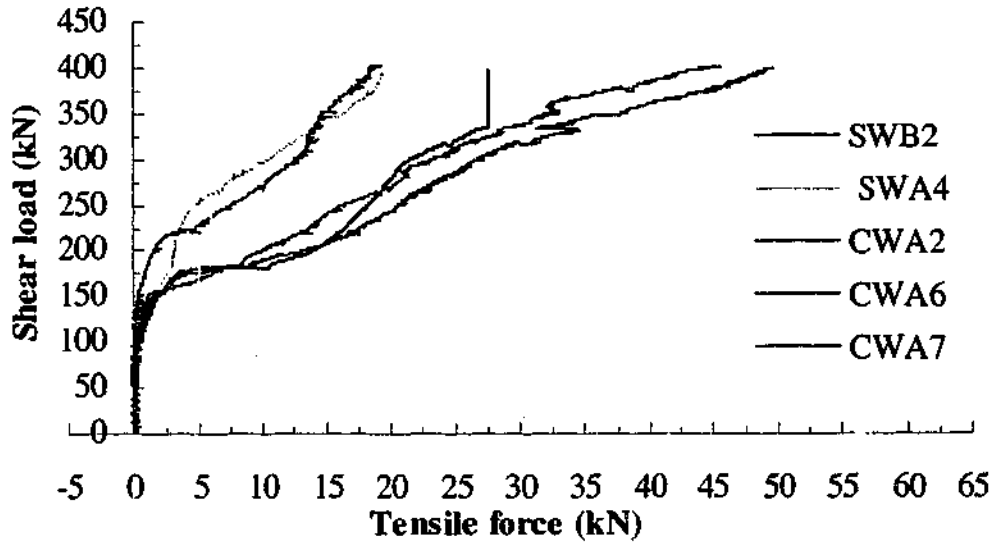

(c)

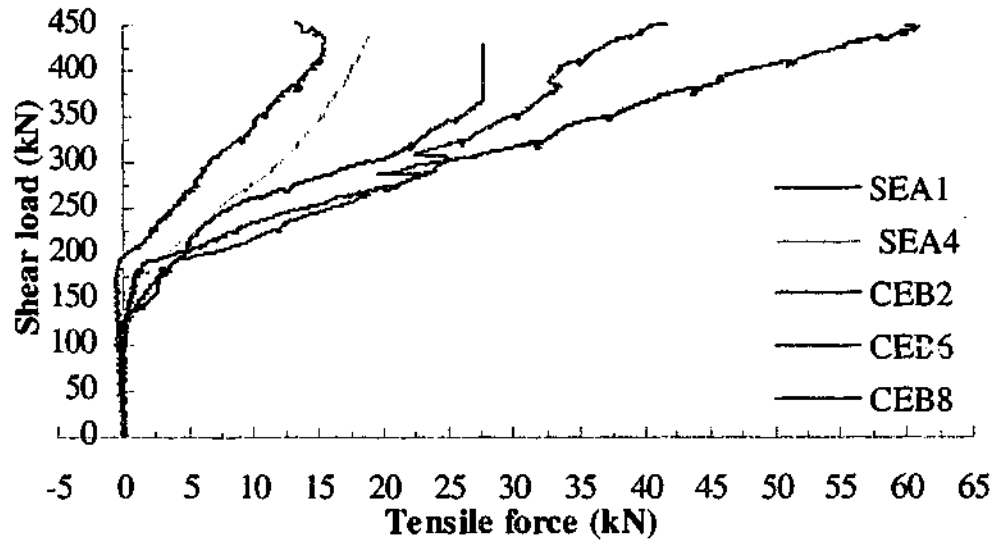

Figure 6.32 (continued) - Comparison of tensile forces between CFRP and steel shear reinforcement for beams (a) '0.75D' (b) '0.60D' and (c) '0.50D'

6.2.8 Slip behaviour between concrete and CFRP

Linear variable displacement transducers (LVDTs) were used to determine the slip between the CFRP plates and the concrete surface at selected locations. The locations of the LVDTs are illustrated in Figure 5.10. Figure 6.33 illustrates the complete load slip relationship between the CFRP plates and concrete for the shear strengthened beams. Slip measurements from the LVDT of both shear spans are shown. The load for each curve corresponds to the measured support load at the span where the LVDT is located. In Section 3.8.6, debonding of the bond specimens commenced when the slip range is from 0.016 to 0.05 mm. Due to the broad slip range, the corresponding ranges for all of the strengthened T-beams are not calculated. Since the concrete strengths of the bond specimens and T-beams are

comparable, it is assumed that the slip range for the T-beams and bond specimens is similar also. The discussion that follows refers primarily to the slip measurements taken at the beam span at which failure occurred.

For beam '0.75D', slip measurements were taken at the location of strain gauge 7. In Section 6.2.5, at the west span of the beam, it was reported that shear cracks propagated and intersected the CFRP plate near the vicinity of gauge 8. Thus, the CFRP plate debonded in the direction of gauge 8 to gauge 7. From Figure 6.33 (a) curve 'W1', it can be observed that the slip remained relatively small until the shear load level of 275 kN. Beyond this load level, the slip increased significantly with load. The load level corresponding to the slip value range of 0.016 to 0.05 mm indicated that debonding of the CFRP plate at the location of the LVDT occurred shortly within a few kilonewtons. According to Figure 6.8 (c), the load level corresponding to the critical strain level at the location of gauge 7 is approximately 270 kN, which is comparable to the load level using the LVDT. At the location of gauge 8, debonding of the CFRP plate occurred at a lower load level. Using the critical strain level value, this load level corresponds to approximately 200 kN as illustrated in Figure 6.8 (c). In Figure 6.2 (b), the second change in the overall beam stiffness at approximately 250 kN is therefore, partly due to the debonding of the CFRP plate. The slip measured at the east span showed similar trend to the west span.

For beam '0.60D', slip measurements were taken at the location of strain gauges 5 and 7. In Section 6.2.5, at the west span of the beam, it was reported that shear cracks propagated and intersected the CFRP plate near the vicinity of gauges 6 and 7. As expected, significant increase in the slip can be observed to occur first at location 'W2'. The slip at that location increases steadily in small magnitude with load until approximately 210 kN, beyond which the slip increases significantly with load. The CFRP plate became debonded at the location after a slight increase in load beyond this load level. At location 'W1', the slip value increased significantly with load at approximately 285 kN. Referring back to Figure 6.2 (c), this load level is close to the load level at which the second change in overall beam stiffness was observed. The observed stiffness change is the result of the debonding of the CFRP plate. According to Figure 6.12 (b) and (c), the load levels corresponding to the critical strain levels at the location of gauges 5 and 7 are approximately 250 and 230

kN, which is comparable to the load levels determined from the LVDTs. At the peak shear load, the slip value measured at location 'W1' was higher than the slip value measured at location 'W2'. Similar trends were observed at locations E1 and E2 at the east span of the beam.

For beam '0.50D', slip measurements were taken at the location of strain gauges 2 and 5. In Section 6.2.5, at the east span of the beam, it was reported that shear cracks propagated and intersected the CFRP plate near the vicinity of gauges 2 and 6. As expected, significant increase in the slip can be observed to occur first at location 'E1'. The slip remained relatively small until the shear load level of approximately 225 kN. Beyond this load level, the slip increases significantly with load. Slight increase beyond this load level resulted in the debonding of the CFRP plate at the location of the LVDT. At location 'E2', the slip increased significantly with load at approximately 285 kN. This load level coincides with the load level at which the second decrease in overall beam stiffness was observed in Figure 6.2 (d). The stiffness change is due to the debonding of the CFRP plate. According to Figure 6.16 (a) and (b), the load levels corresponding to the critical strain levels at the location of gauges 2 and 5 are approximately 203 and 260 kN, which is comparable to the load levels determined from the LVDTs. At the peak shear load, the slip values measured at location 'E1' and 'E2' were similar. The load slip relationships at similar location in the west span of the beam were different. This is due to the fact that at the west span, the shear cracks intersected the CFRP plates at slightly different locations.

The load range at which debonding occurs can be determined fairly well by using LVDTs. In all of the strengthened beams, the slip remained small until a particular load level beyond which it increased significantly. A slight increase in load beyond this load level resulted in the debonding of the CFRP plate.

(a)

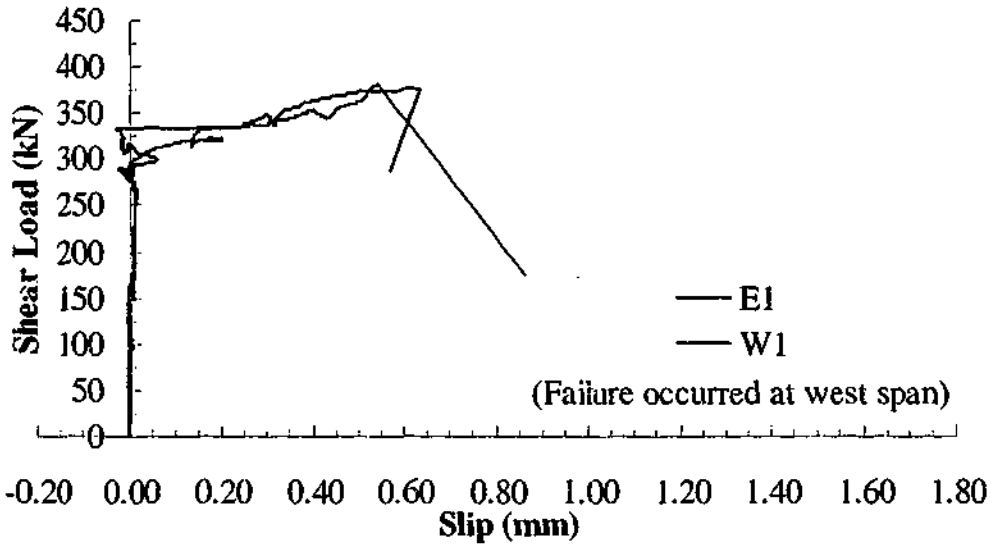

(b)

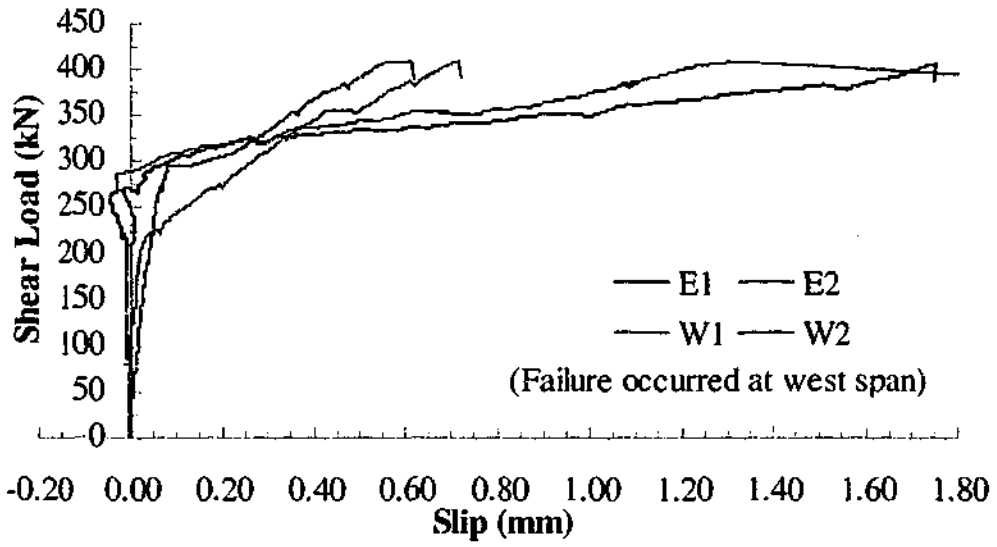

(c)

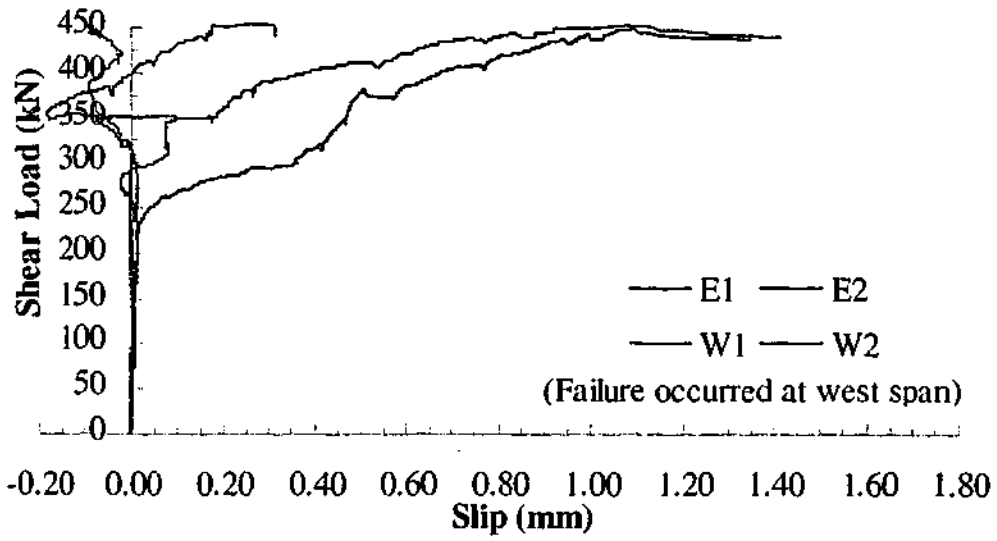

Figure 6.33 - Complete load slip behaviour for beams (a) '0.75D' (b) '0.60D' and (c) '0.50D'

6.3 Summary of findings

Four large-scale reinforced concrete T-beams, designed to the same specification, were fabricated and tested to failure. Three of the beams were strengthened with external L-shaped CFRP plates at the spacing of 0.75D, 0.60D and 0.50D where D is the overall depth of the beam. The control beam had no external reinforcement. The aim of the experiment was to investigate the effect on the failure mechanism and ultimate strength of varying the spacing of the external CFRP reinforcement. The overall depth and length of the beams were 490 mm and 6 m respectively. Each beam has a flange depth of 120 mm and a web width of 225 mm. The average compressive strength of the core samples taken from the beams at the time of testing was approximately 31.9 MPa. The yield strengths of the shear and main flexural reinforcement were 351 and 445 MPa respectively.

The shear capacity of the control beam was observed to be 247.1 kN. Increases in shear capacities of 54%, 61% and 81% compared to the control beam were achieved in the beams '0.75D', '0.60D' and '0.50D'. Failure was characterised by formation of large shear cracks and the separation of the CFRP laps at the soffit of the beam tearing away concrete at the bend zone. In all the beams except for beam '0.50D', failure occurred in the west span.

At the early stages of loading, it was observed from the shear load versus mid-span displacement responses that the stiffness of all the beams was almost similar to each other. At higher load level, the strengthened beams exhibited stiffer responses compared to the control beam. The presence of the external CFRP reinforcement had impeded shear crack propagation and growth. It was observed that for beams with closely spaced CFRP reinforcement, the shear crack widths and propagation were smaller and more limited at a given load.

Apart from the difference in the peak load reached, the main flexural reinforcement in the different T-beams exhibited almost identical load strain responses. The reinforcement strained linearly with load until structural failure. In all of the beams, the main reinforcement did not yield indicating that flexural tensile failure did not occur. The use of the external shear reinforcement did not increase the

flexural stiffness of the beams but had made possible the additional utilisation of the beams' flexural capacity.

From the load-strain response of the steel shear reinforcement, it was observed that the presence of the external CFRP reinforcement had an insignificant influence on the initial formation of shear cracks. For the strengthened beams, shear cracks formed at approximately the same load level as in the control beam. The shear load at which the stirrups began to carry significantly more loads was similar for all the beams. Beyond this load level, as the cracks started to widen sufficiently, the external CFRP reinforcement contributed to carrying part of the total shear load. This was characterised by the smaller stirrup strain readings at a given shear load in the strengthened beams compared to the strain readings in the control beam. The strain readings of the stirrups were generally smaller in beams with more closely spaced CFRP reinforcement. It was shown in all the beams that the stirrups closest to the supports at the failure spans yielded before the beams reached their respective peak shear loads. The stirrups closest to the point loads at the failure spans did not yield when failure occurred.

At the early stages of loading, similar to the internal shear reinforcement at the shear span, the CFRP reinforcement carried small load. In addition, both the CFRP reinforcement and internal shear reinforcement began to carry more shear load at similar shear load level. The CFRP reinforcement barely contributed to carrying the load until shear cracks had formed and propagated. The adhesive used had relatively low stiffness compared to concrete therefore the CFRP reinforcement would sustain load only when shear cracks had formed and propagated sufficiently. The CFRP reinforcement outside of the shear spans carried very low shear loads. It has been shown from the load-strain responses of the CFRP reinforcement that debonding initiated from the location of the shear cracks and propagated along the length of the CFRP reinforcement. Prior to failure, the strain readings indicated that significant portions of the CFRP reinforcement had debonded in all the strengthened beams.

Observations of the crack patterns indicated that the shear cracks in the strengthened beams formed at a slightly steeper angle compared to the shear cracks in the control beam. It is difficult to confirm this fact conclusively as experimental

scatter exists even in beams of identical configurations. The shear crack inclination angle was similar between the strengthened beams. During testing, the crack widths were noticeably smaller in the strengthened beams compared to the crack widths in the control beam. The locations of the major shear cracks that formed in the beams varied slightly between the strengthened beams and the control beam. Nevertheless, the locations of these shear cracks can be considered to be fairly similar for all the beams as different results can arise even in beams with identical configurations. In all the beams except for beam '0.75D', two major shear cracks formed in the shear span prior to failure. For beam '0.75D', the location of the third major shear crack coincided with the location of a minor shear crack observed in beam '0.60D' near the support. This crack was almost unnoticeable in beam '0.50D'. Due to the additional shear capacity available, more minor shear cracks were observed to have formed in the web of strengthened beams compared to the control beam.

The load range at which debonding of the CFRP reinforcement occurs can be determined fairly well by using LVDTs. In all of the strengthened beams, the slip remained small until a particular load level beyond which it increased significantly. A slight increase in load beyond this load level resulted in the debonding of the CFRP plate.

CHAPTER 7 - CLOSE-RANGE PHOTOGRAMMETRY

7.1 Introduction and scope

Photogrammetry is the process of obtaining precise measurements about physical objects by means of photography. There are several categories depending on the required applications. In the present study, close-range digital photogrammetry or vision metrology (VM) was used as part of the experimental program of the shear strengthened T-beams. An in-depth review of the methodology will not be carried out as it is beyond the scope of the present investigation. The method has been proven to be effective and has become a standard technique for precision industrial inspection. An overview of the principles of photogrammetry reported by Stirling (2001) is presented here.

Consider the case where an object is photographed as illustrated in Figure 7.1. A central perspective projection of the object is produced on the negative where the centre of the camera lens, O, is the perspective centre for the projection. It is generally considered that all rays of light from an object pass through a single point at the centre of the camera lens assembly. The point A on the object is imaged at a′ on the negative plane and at a on the positive plane with positive plate co-ordinates x_a, y_a. Similarly, an object point B is imaged at b′ on the negative plane and at b on the positive plane with positive plate co-ordinates x_b, y_b. The angle θ is recreated inside the camera by θ'. The ray which passes through the perspective centre, O, and intersects the film plane normal to it is the principal axis of the lens. This point of intersection is referred to as the principal point of the lens. It is the origin of the plate co-ordinate system. The distance between the perspective centre and the principal point is referred to as the principal distance or focal length of the lens. This is the z-co-ordinate of the camera co-ordinate system. For further details, readers are referred to the numerous publications available such as Kraus et al. (1993), Atkinson (1996), Armer (2001) and Mikhail et al. (2001).

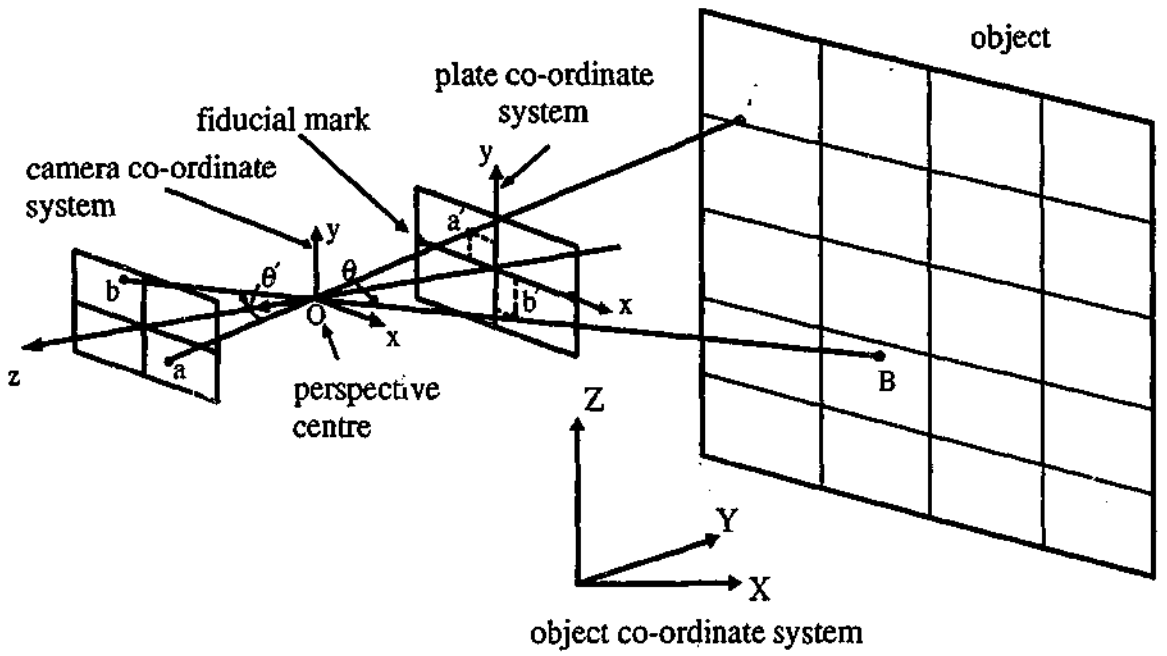

Figure 7.1 - Photogrammetric co-ordinate systems and the geometry of a central perspective projection (Armer (2001) - Figure 3.1)

The V-STARS system from Geodetic Services, Inc of Florida (GSI, 1996) was employed in the deformation monitoring of the T-beams. Monitoring points or targets were placed at selected locations on the beams' surface. The targets are dull coloured (black) rectangular labels with adhesive backing and a highly reflective circular dot in the centre. The centroid of the dot defines the position of the target. For each beam, using a specifically designed camera, three-dimensional digital photogrammetric measurements were made at twelve camera locations or epochs at selected load levels. The camera consists of a flash and digital data measurement device that records and stores information about the positions of the individual targets. The information is then processed in a separate computer workstation and results of the displacements of the individual targets are available within minutes of the imagery being recorded. The accuracy of the system is dependent mainly on the camera hardware, scale of the object and geometry of the survey. The camera hardware is related to factors such as resolution and lens specification. In the photogrammetry survey, co-ordinates of the targets are defined only in a relative sense. In processing the information, the results are scaled to correspond to the actual size of the object. The precision, hence accuracy of the results are scaled accordingly. Geometry of the survey relates to the number of epochs and their position. Typically, precision and accuracy of the data increases as the number of epochs used increases.

A detailed review of the mathematical formulation is not presented as it is beyond the scope of the present study. Readers are referred to the numerous publications available on digital close range photogrammetry in the literature. In the present investigation, the accuracy of the surveys surpasses 1:100,000. The length of the beams was six metres, which equates to an accuracy of ±0.06 mm. The accuracy of the system employed was adequate for the determination of the required displacements.

In the present study, photogrammetry was used to determine the displacement of a range of points on the beams' surface at selected load levels up to and after failure. Approximately 1500 targets were placed on each beam on the concrete surface as well as on the L-shaped CFRP plates. The aims of the photogrammetric measurements were to determine the shear crack width development with load and movements of the L-shaped CFRP plates relative to the concrete layer. Comparisons are carried out to determine the difference in the deformation mechanism across the four T-beams. Load-slip relationships of the L-shaped CFRP plates processed from the photogrammetric measurements are compared against experimental results of the T-beams.

7.2 Photogrammetry survey setup and procedure

The approximate locations of the photogrammetry monitoring points or targets on the control beam are illustrated in Figure 7.2. Further information on the target positions of the shear-strengthened beams is contained in Appendix C.1. Prior to application of the targets, the concrete surfaces were painted white to assist in locating cracks more easily. The targets were placed on one side of the beams at both the east and west spans. Each target was approximately 25 mm wide by 12.5 mm high. The diameter of the reflective dot in the centre was approximately 6.35 mm. A large number of the targets were placed at the shear spans to intercept shear crack formations. On the shear-strengthened beams, two rows of targets were placed along the length of each L-shaped CFRP plate. Figure 7.3 shows a photograph of the photogrammetry survey setup for beams '0.75D' and '0.50D'. Several targets were placed at the supports and actuators for cross checking against results obtained using stringpots.

During testing, loading of the specimens was paused intermittently to allow photogrammetry measurements to be taken. Table 7.1 summarises the approximate load levels at which measurements were taken. For beams '0.75D', '0.60D' and '0.50D', the load levels correspond to the average loads applied by both actuators. In the case of the control beam, the load levels shown correspond to the load applied by the east actuator. At high load levels, as it was not possible to predict accurately the failure load of the beams, measurements were taken at smaller load intervals. Each photogrammetry measurement took less than one minute to complete during which the actuators' displacements were held as stationary as possible. Since loading of the beams was by displacement control, slight decrease in the applied loads occurred during each photogrammetry measurement as internal forces redistributed within the beam. This appeared as 'dips' in the load-displacement curves illustrated in Figure 6.1. These 'dips' were more noticeable at high load levels. Some difficulties were encountered in maintaining the actuators at a fixed position for the photogrammetry measurements. As outlined previously in Section 5.7, loading through displacement control was achieved by controlling the output pressure of the hydraulic distributor system to the actuators. There was a delay in the system responding to the adjustments made by the computer program. At each load level, the displacement applied by the actuators drifted slightly during the photogrammetry measurements. During each photogrammetry survey, the displacements were slightly different from epoch to epoch. Nevertheless, as can be observed in the sections to follow, the photogrammetry results obtained were not affected significantly. The drifts in the applied displacements were very small and insignificant. In addition, the pausing of the load for such a short period of time did not affect the failure load nor the behaviour of the beams significantly.

The location of each target was defined in terms of the cartesian co-ordinates system (x, y, z). The orientations of the x-, y- and z-axes are illustrated in the figures. In all of the beams, the origin (0,0,0) was set at the location of the left most target closest to the bottom of the beam in the west span.

Table 7.1 - Approximate load levels of actuators at which photogrammetry measurements were taken

Control beam*	Beam '0.75D'	Beam '0.60D'	Beam '0.50D'
0 kN	0 kN	0 kN	0 kN
60 kN	40 kN	40 kN	40 kN
90 kN	90 kN	80 kN	80 kN
120 kN	135 kN	135 kN	140 kN
140 kN	170 kN	180 kN	180 kN
180 kN	230 kN	220 kN	225 kN
210 kN	255 kN	265 kN	270 kN
265 kN	280 kN	315 kN	320 kN
310 kN	315 kN	345 kN	345 kN
Post Failure	350 kN	380 kN	380 kN
-	Post Failure	Post Failure	405 kN
-	-	-	435 kN
-	-	-	Post Failure

* Based on load level of east actuator

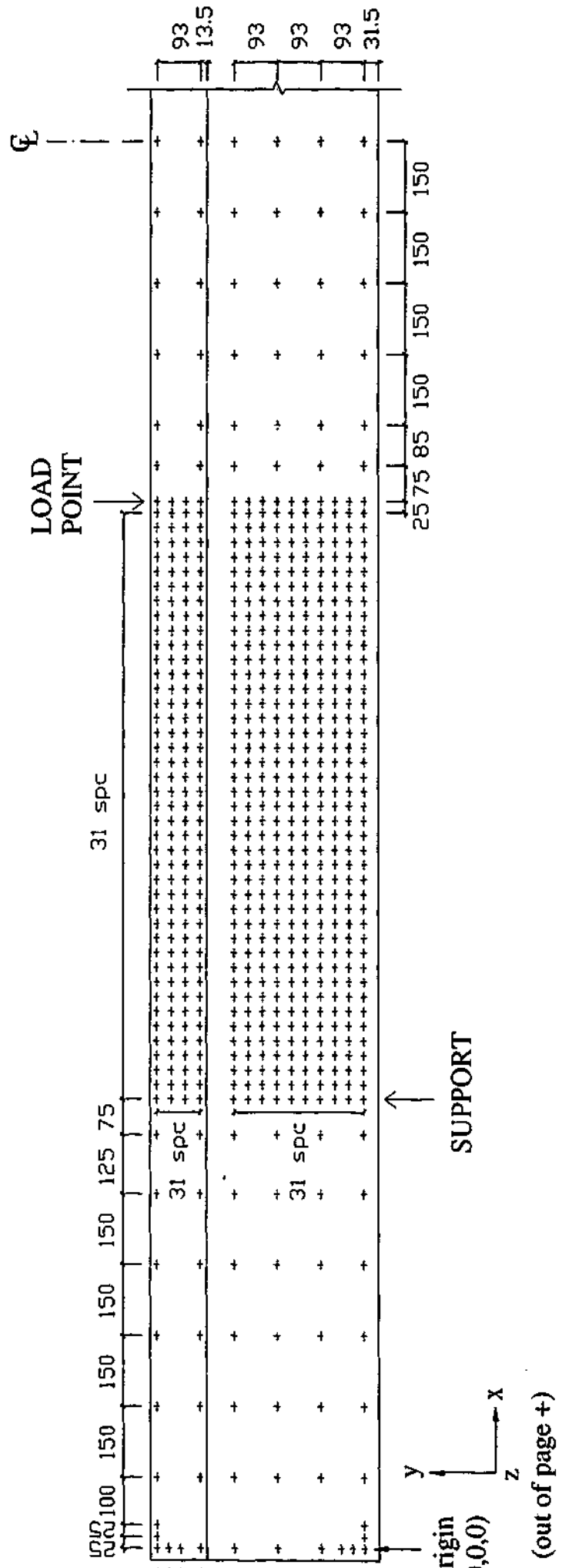

Figure 7.2 - Locations of targets on control beam

(a)

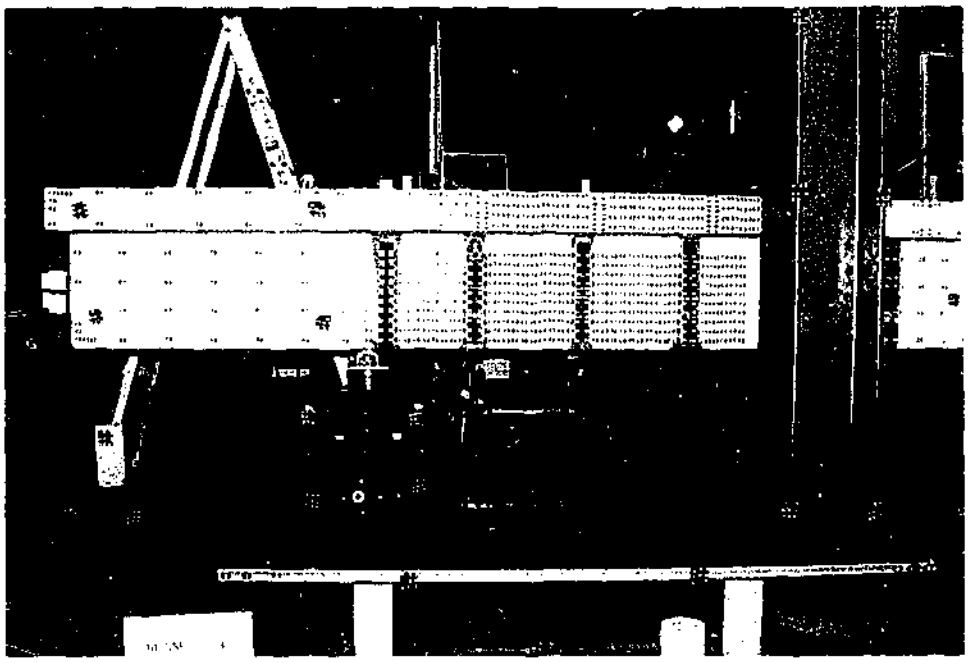

(b)

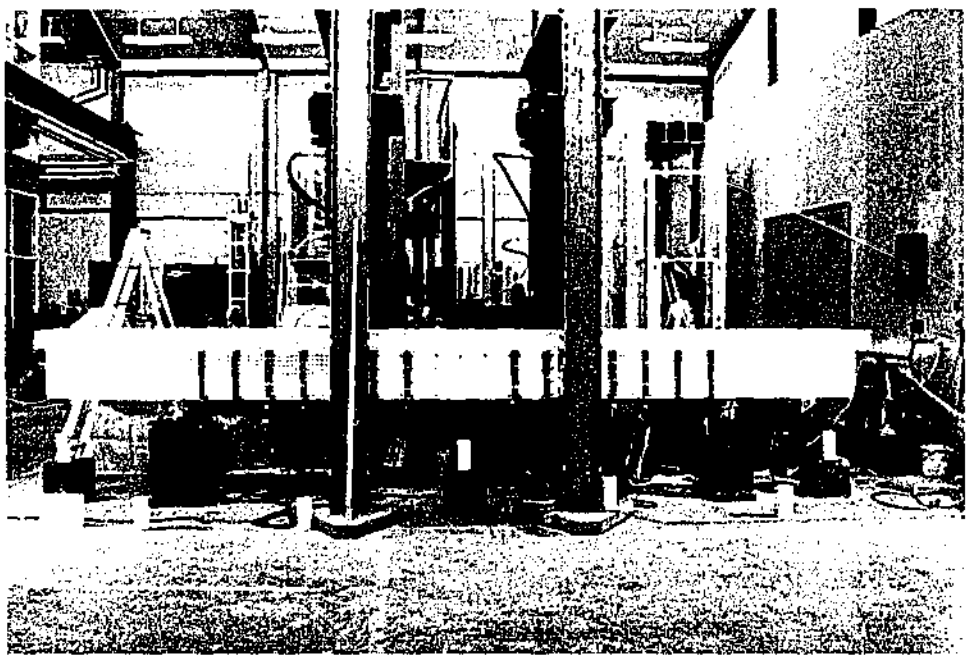

Figure 7.3 - Photogrammetry targets location of beams (a) '0.75D' and (b) '0.50D'

7.3 Presentation and interpretation of photogrammetry results

7.3.1 Load deflection behaviour

Figure 7.4 and Figure 7.5 compare the load-deflection behaviour, at selected locations of the control beam, obtained using photogrammetry measurements and stringpots. The figures show the applied load versus beam deflections at the load points and support load versus mid-span deflections of the control beam. The displacements of single photogrammetry targets closest to the soffit of the beams at the midspan and load points were compared with displacement results obtained from the stringpots under the beams. For the photogrammetry survey, only the vertical co-ordinates of the targets, the y-values, were used in determining the displacements at different load levels. The displacements of the targets were obtained by subtracting the corresponding values at each load level from the reference values taken at 0 kN. The photogrammetry results obtained at post failure are not included in the figures. The discrete points in the graphs designated as 'x' represent the load level at which photogrammetry measurements were taken. Straight broken lines are plotted between two consecutive points to give the full load-deflection curves.

For the control beam, it can be observed that the photogrammetry measurements were in close agreement with the stringpot results. Slight differences exist due to the photogrammetry targets located at a higher level than the points where the stringpots were attached. For all the strengthened beams, the photogrammetry measurements were also in close agreement with the stringpot results. Further information on the load deflection responses of these beams is contained in Appendix C.2.

(a)

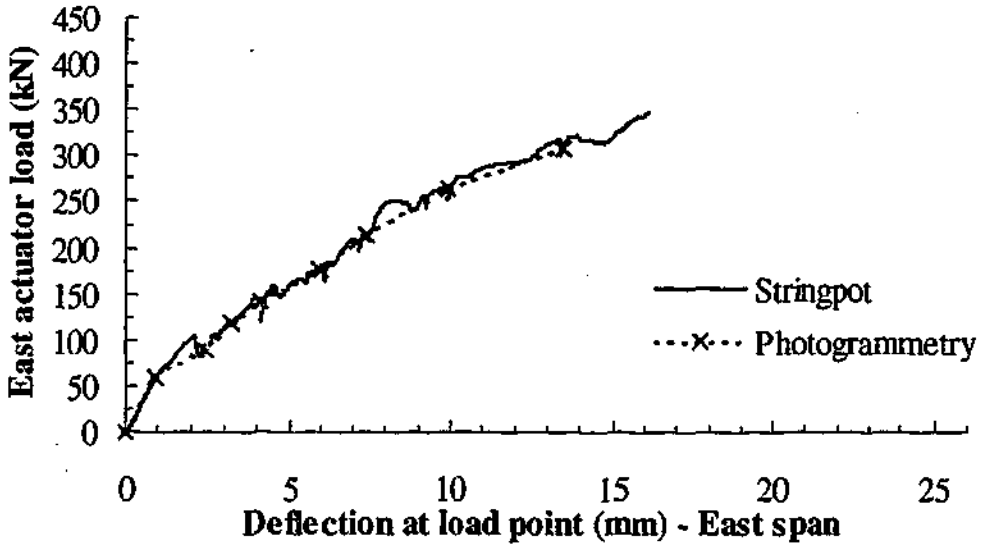

(b)

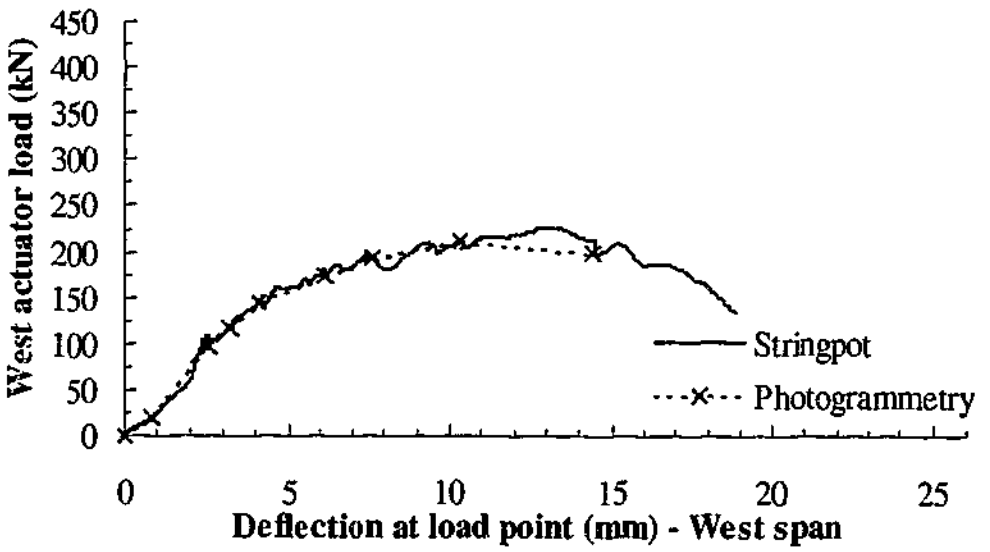

Figure 7.4 - Actuator load versus deflection behaviour for control beam from stringpot and photogrammetry measurements

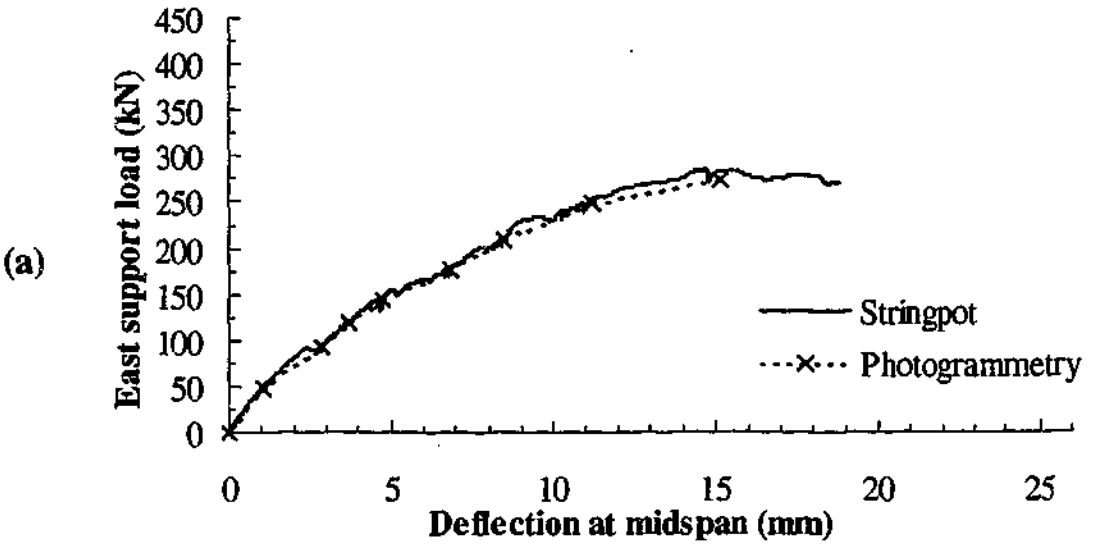

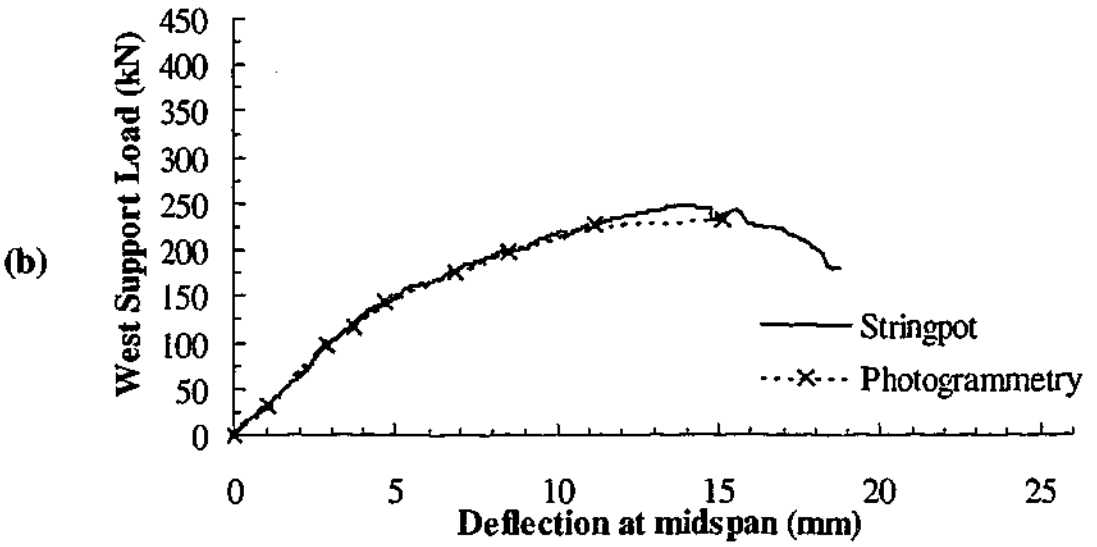

Figure 7.5 - Support load versus deflection behaviour of control beam from stringpot and photogrammetry measurements

7.3.2 Beam deformation

The displacements of the targets, hence beam deformations at the failure span are illustrated in Figure 7.7 to Figure 7.10. Each line shows the displacement of the targets from zero loading to the load level of the photogrammetry survey taken prior to failure. The lengths of the lines simply indicate the relative magnitude of the displacements and are not to scale. Illustrations in (a) show the displacements of the targets with respect to an external stationary point, which in this case was the ground. Illustrations in (b) show the displacements of the targets on the beams with respect to the targets on the concrete overhang at the support, which are held stationary. In processing the photogrammetry results, all targets on the concrete overhang were held fixed to act as a rigid block. Unlike the shear span, the concrete overhang at the

support was a non-critical section. Cracks were not observed to have formed at this section. Therefore, the concrete overhang were assumed to rotate and displace as a rigid block. It can be observed from the illustrations in (a) that the assumption is reasonable. Targets on the overhang appear to rotate and displace uniformly about the support. The path of the shear crack that had formed on the beams can be seen more clearly. Red coloured lines represent the displacements of targets located on the external L-shaped CFRP reinforcement.

Referring to the control beam in Figure 7.7 (a), the concrete overhang displaced almost like a rigid block about the support. At the midspan, the targets displace mainly in the vertical direction. At the shear span, targets on one side of the shear cracks closest to the mid-span displaced diagonally. In illustration (b), these targets displaced fairly vertically with respect to the targets on the concrete overhang. Significant portions of the targets on the web and flange in the shear span on the upper side of the shear crack can be observed to have remained stationary with the concrete overhang. The paths of the two shear cracks in the web are clearly identified by the sudden change in length of the lines. In the flange, however, the crack paths are not as distinct. There was a subtle change in the displacement of the targets at approximately 520 mm horizontal distance from the support. The targets on the flange on the concrete overhang up to this point remained almost stationary. Beyond this point, the targets can be observed to rotate almost uniformly about a point. This indicated that this flange portion displaced almost as a rigid block. To facilitate such movements, vertical cracks must form and this was confirmed with observations of vertical cracks in the beam. In the web, it can be observed clearly that the shear deformation mechanism was simply the separation of two rigid blocks of concrete at the location of the shear crack closest to the support. Further along into the shear span, the same mechanism occurred at the location of the second shear crack. The displacements of the blocks were almost vertical with respect to each other, which intuitively suggested the absence of aggregate interlock. However, by resolving the displacement into a normal and shear component along the plane of the crack, it can be observed from Figure 7.6 that there is a shear component along the crack plane. The magnitude of the shear displacement is small compared to the normal displacement and therefore the effect of aggregate interlock can be considered to be

minor. If the resultant displacement is perpendicular to the crack plane, the effect of aggregate interlock is negligible.

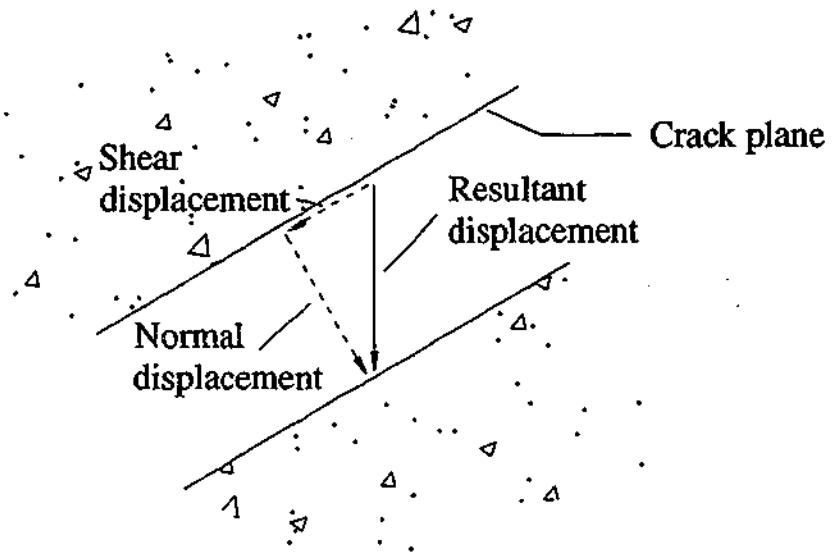

Figure 7.6 - Displacement along crack plane (diagrammatic)

Figure 7.8 to Figure 7.10 show the displacement of the targets from zero loading to 350, 380 and 435 kN for beams '0.75D', '0.60D' and '0.50D' respectively. Although the load levels at which the photogrammetry survey was taken were higher compared to the load level in the control beam, the location of the shear cracks on the figure for the strengthened beams were not as apparent as the control beam. The scales of the displacements were kept equal in all of the beams. The figures confirm conclusively that the external L-shaped CFRP reinforcement have reduced the shear crack width and limited its propagation. The general deformation mechanisms of the strengthened beams do not differ significantly from the control beam. Similar to the control beam, it can be observed from illustrations (b) that the concrete overhang and a portion of the web and flange in the shear span remained fairly stationary. Near the lower side of the shear crack closest to the support, targets on both the concrete and CFRP plates at the shear span displaced almost vertically with respect to the concrete overhang. Although additional shear cracks have formed in the strengthened beams, the deformation mechanisms were quite similar to the one described previously for the control beam apart from the crack widths and magnitude of the deformation. The rigid blocks displaced almost vertically with respect to each other at the location of the shear crack, which implies that the CFRP plates were loaded mainly along the

longitudinal direction. Therefore, it can be assumed that the CFRP plates act simply as external tension ties, which are anchored at the flange and bottom of the beam.

The presence of the external CFRP shear reinforcement did not alter the basic shear deformation mechanism of the T-beams investigated herein. The external reinforcement limited the shear crack width and therefore the overall vertical deflection of the beam. The effect of aggregate interlock decreases with increasing crack width. Conversely, it increases with decreasing crack width. The effect of aggregate interlock was therefore more significant in the strengthened beams compared to the control beam. Neglecting the contributions of the external CFRP reinforcement, this implied that the shear capacities were higher in the strengthened beams compared to the control beam. The external CFRP reinforcement had increased the shear capacity of the T-beams simply by limiting the shear crack widths.

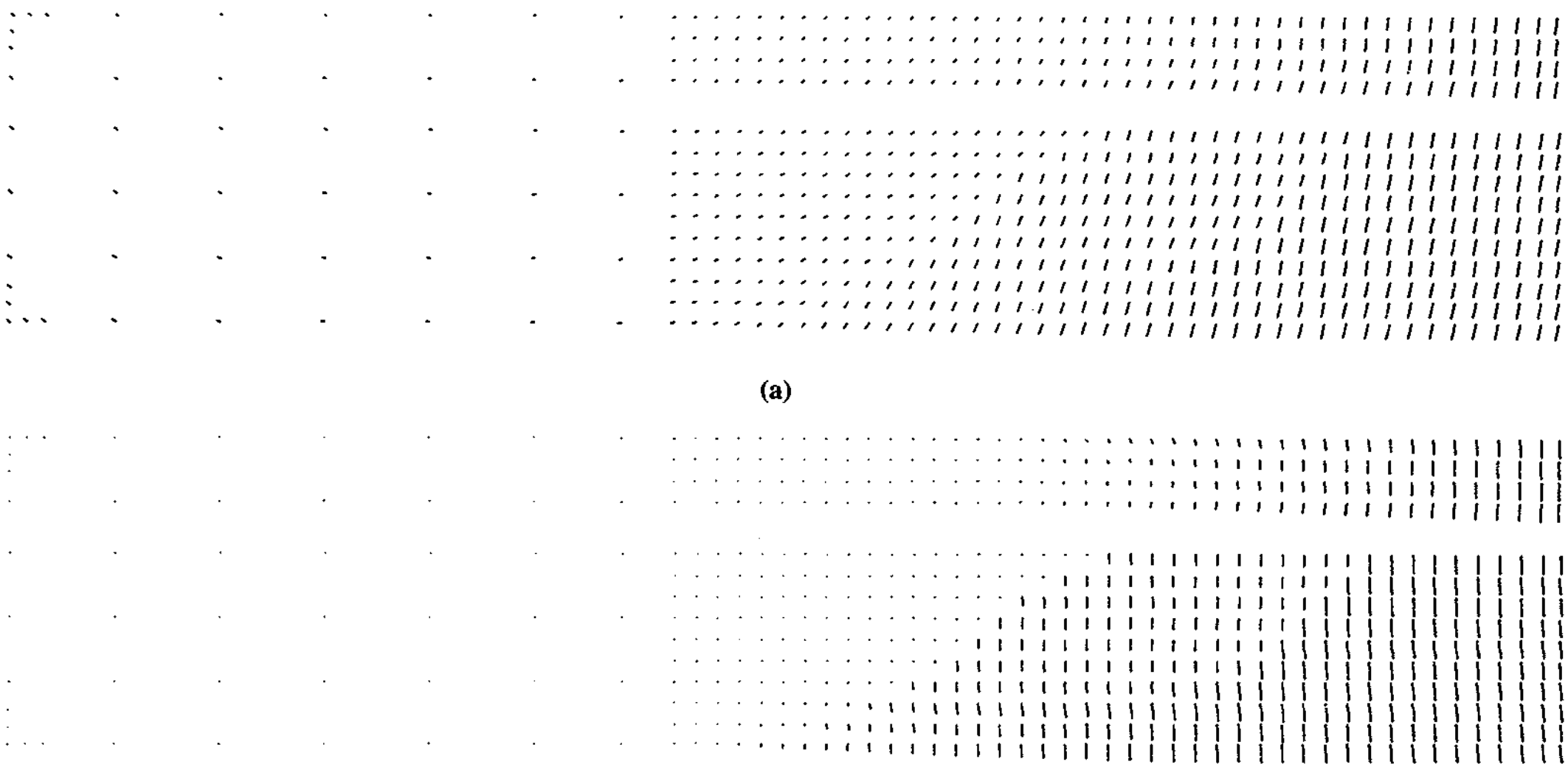

(a)

(b)

Figure 7.7 - Control beam deformation with respect to (a) external stationary point and (b) concrete overhang

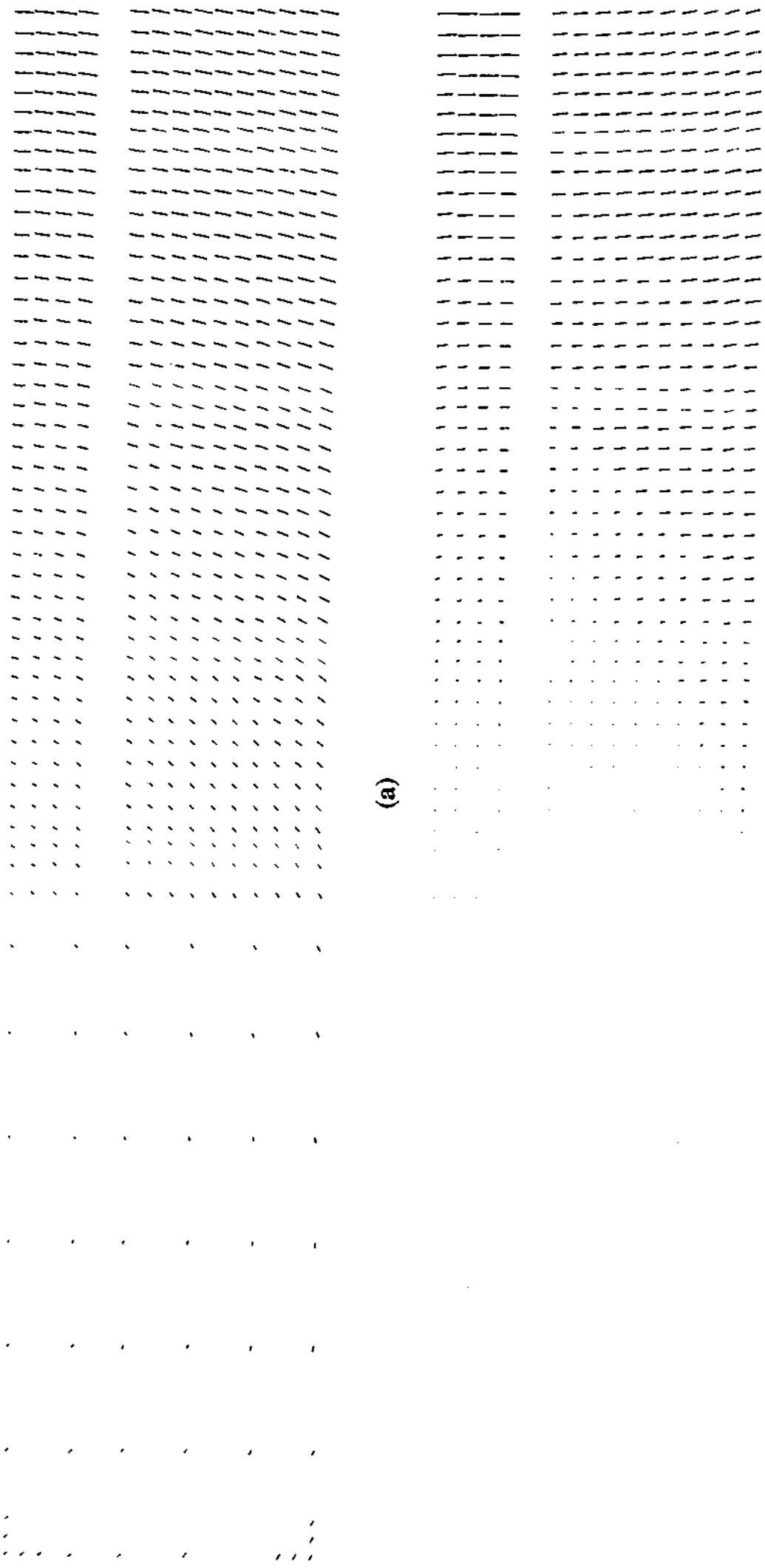

Figure 7.8 - Beam '0.75D' deformation with respect to (a) external stationary point and (b) concrete overhang

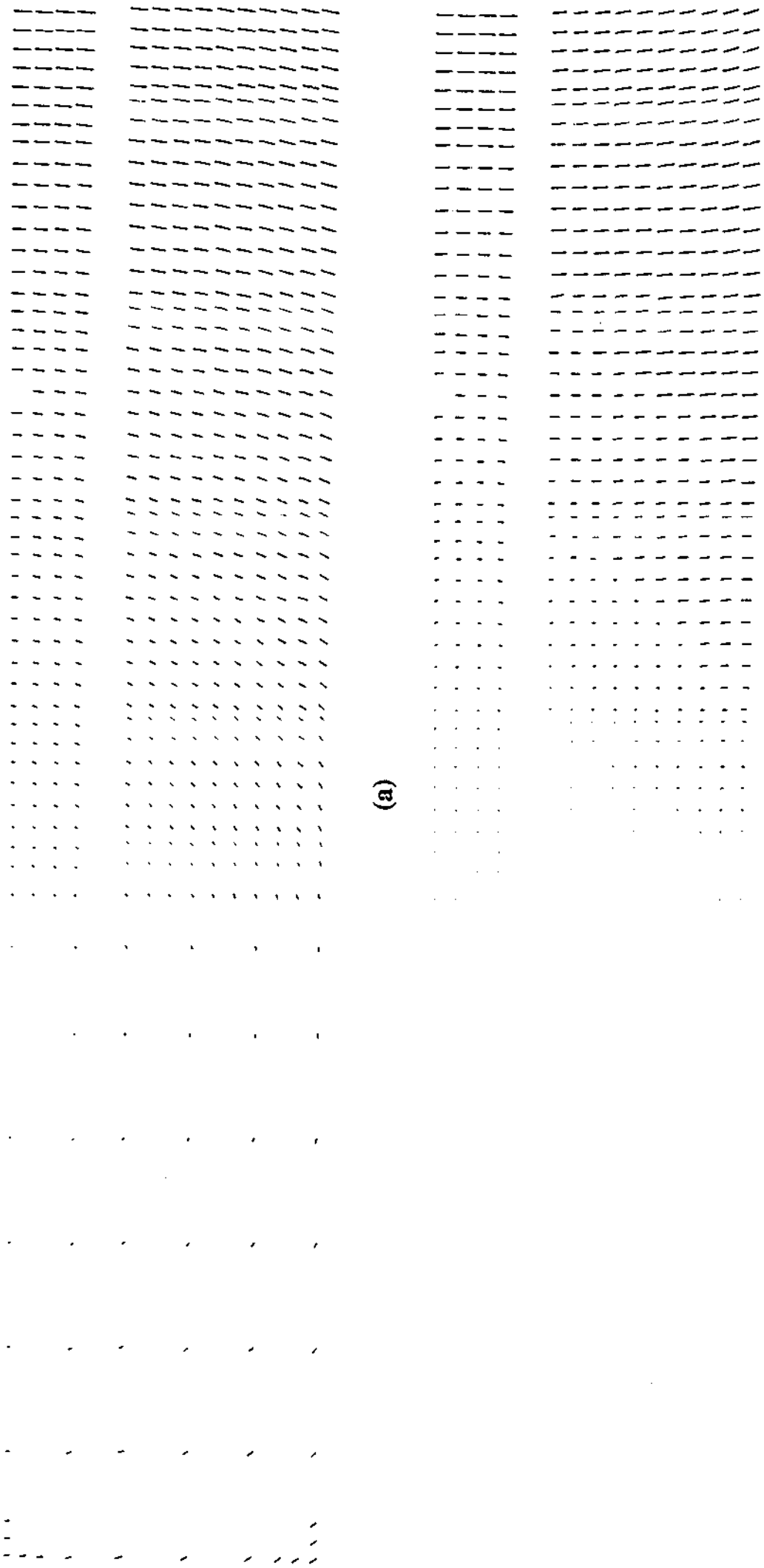

Figure 7.9 - Beam '0.60D' deformation with respect to (a) external stationary point and (b) concrete overhang

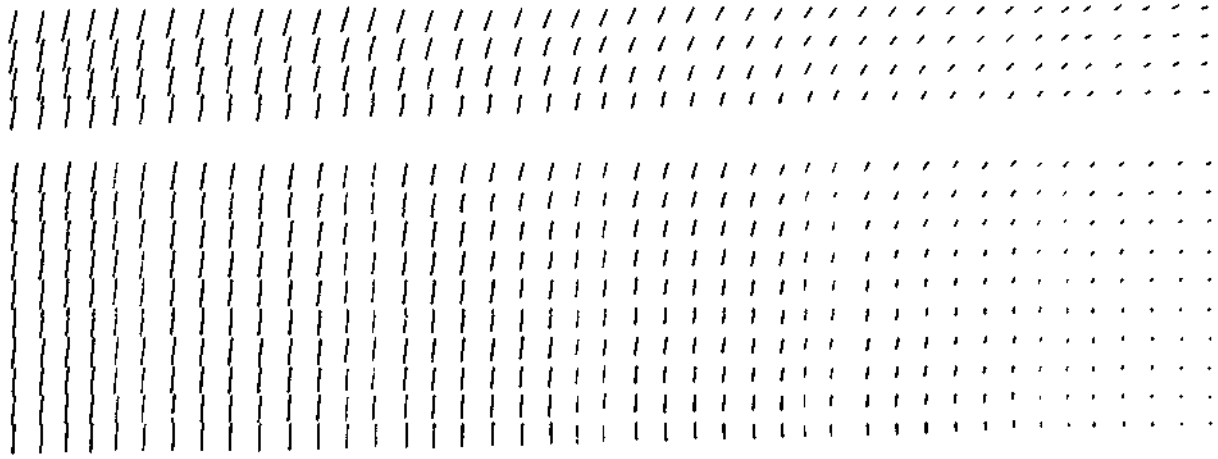

(a)

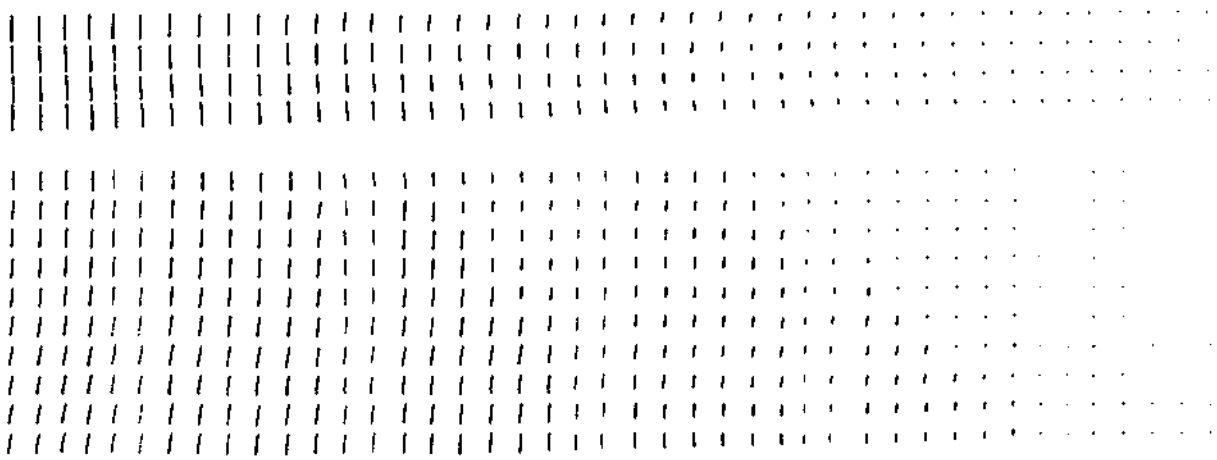

(b)

Figure 7.10 - Beam '0.50D' deformation with respect to (a) external stationary point and (b) concrete overhang

7.3.3 Shear crack width development

The shear crack width along the web depth at different load levels is reported in this section. As discussed previously in Section 6.2.6, before failure, two major shear cracks were observed to have formed in the web of the failure span of all the beams except for beam '0.75D'. In the latter, three major shear cracks had formed. These crack patterns have been reproduced alongside the L-shaped CFRP plates and photogrammetry targets, drawn as faded '+' signs, in Figure 7.11. Each major shear crack is assigned a number '1' or '2' and in the case of beam '0.75D', the third shear crack assigned number '3'. At a given load level, the crack width at a particular beam depth is approximated using the displacement records of two targets. In the drawings, red lines joining the centres of two targets indicate the target sets used to obtain the crack width profile along the beam depth. Target pairs are chosen as close as possible to the shear cracks and such that the angle formed at the intersection of the straight line joining the centres of the target pairs and shear crack is as close as possible to 90°. It can be observed from Figure 7.11 that several targets were intersected by the shear cracks. The displacements of these targets are examined individually to determine which side of the shear crack they had shifted with. In the present investigation, the majority of these targets displaced relative to both sides of the shear crack. These targets were omitted and the next nearest target was used instead. In the graphs, some curves appear as discontinuous lines as targets on the L-shaped CFRP plates were not considered. The crack width at a given depth was approximated using Equation 7.1, where x and y refers to the horizontal and vertical co-ordinates of the targets. The subscripts 'L' and 'R' refer to the location of the targets, that is, left and right of the shear crack. The shear load level at a given time is denoted by 'i' where '0' corresponds to the initial photogrammetry survey taken at the time of zero loading. The out-of-plane displacements were not taken into account in the equation. Displacements in this direction were minor and have an insignificant effect on the crack width. At a given target pair location, the depth of the shear crack is taken as the point of intersection between the line joining the centres of the target pair and the shear crack, measured from the soffit of the beam which is assumed to be at zero depth.

$$\text{Width}_i \approx \sqrt{\left((x_{L,i} - x_{L,0}) - (x_{R,i} - x_{R,0})\right)^2 + \left((y_{L,i} - y_{L,0}) - (y_{R,i} - y_{R,0})\right)^2} \qquad (7.1)$$

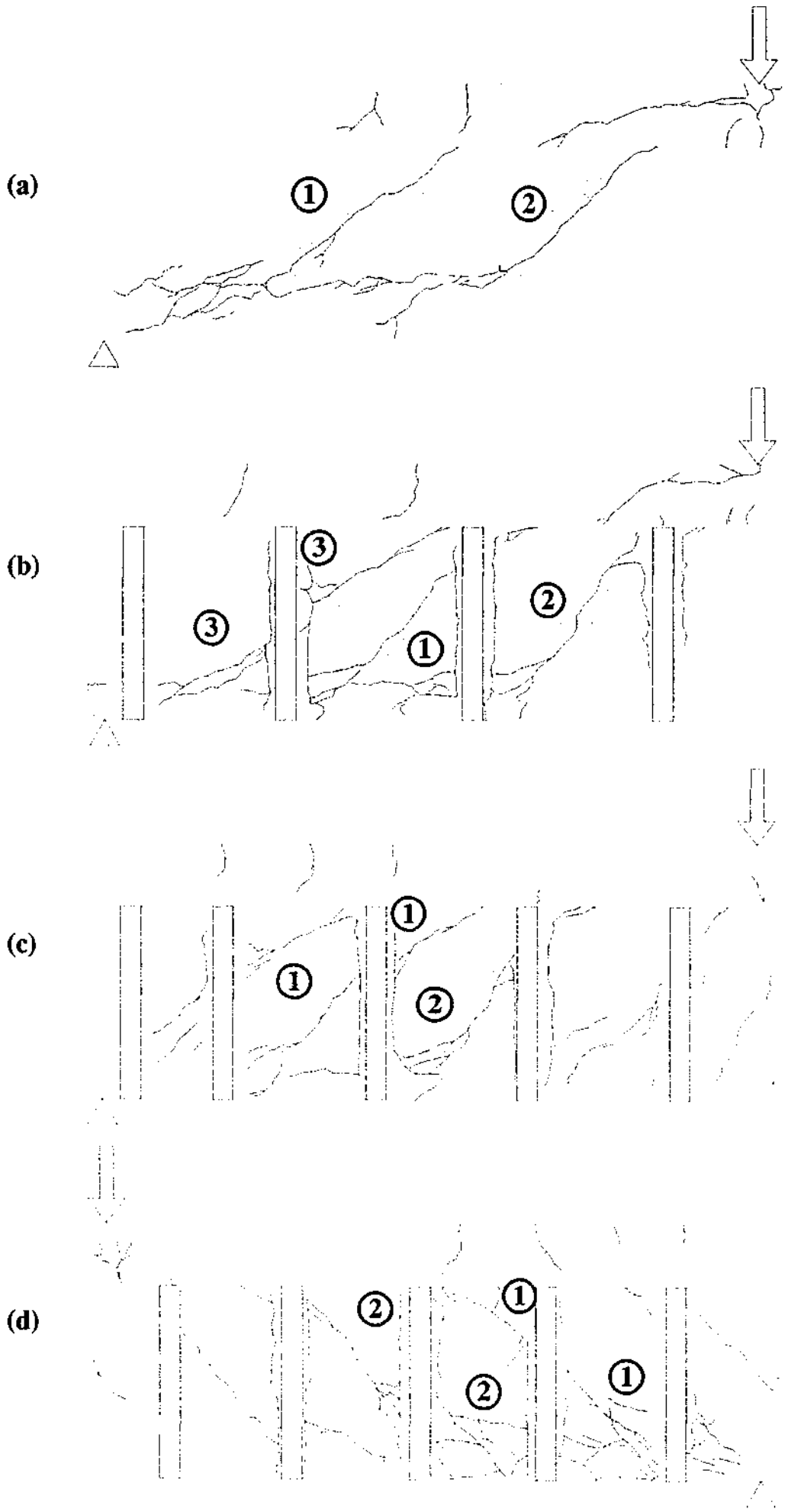

Figure 7.11 - Location of targets used in approximating the shear crack width in (a) control beam (b) beam '0.75D' (c) beam '0.60D' and (d) beam '0.50D'

Figure 7.12 to Figure 7.15 illustrates the shear crack width profile along the web depth of the T-beams at various stages of loading. The crack width was approximated based on data sets where targets on the concrete overhang in the failure span are held stationary. The load levels shown in the plots correspond to the average support load levels at the failure span at the time each survey was executed. In all of the beams, the plots show that the shear cracks either had not formed or remained relatively small at low shear load levels. At higher load levels, the crack widths can be observed to increase with load. The increase in crack width between two consecutive load levels is significantly more in the control beam than in the strengthened beams. At the final survey, the maximum average crack width developed in the control beam, beams '0.75D', '0.60D' and '0.50D' was 4.4, 2.1, 1.7 and 2.5 mm respectively. Despite being subjected to a higher load level, the crack widths were smaller in the strengthened beams compared to the control beam. The implication is that the effect of aggregate interlock is enhanced in the strengthened beams. Therefore, the contribution from the concrete to the capacity of the beams is increased. The contribution to the shear capacity of the strengthened T-beams does not come entirely from the external shear reinforcement but also from the concrete through the effect of aggregate interlock.

(a)

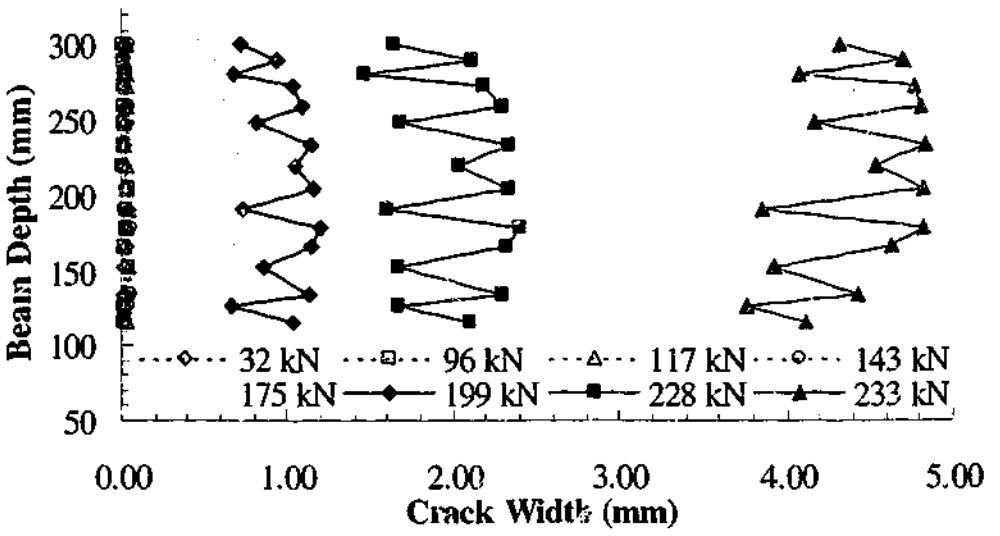

(b)

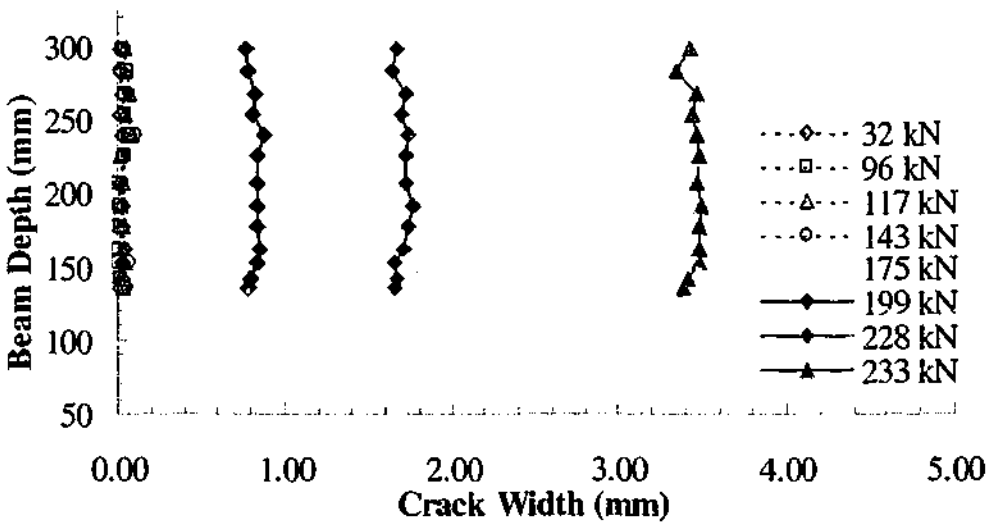

Figure 7.12 - Crack width development of shear cracks (a) '1' and (b) '2' along control beam web depth

(a)

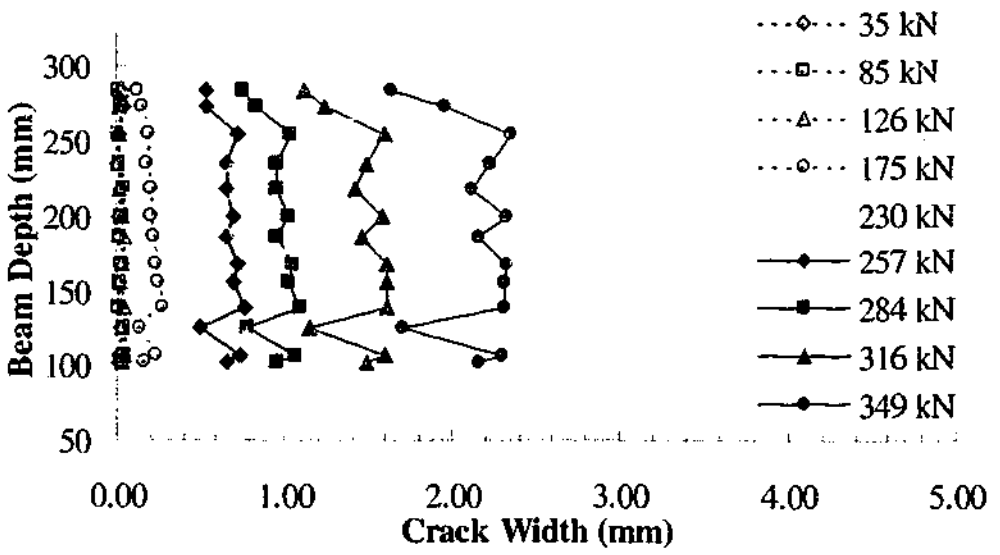

Figure 7.13 - Crack width development of shear cracks (a) '1' (b) '2' and (c) '3' along beam '0.75D' web depth

(b)

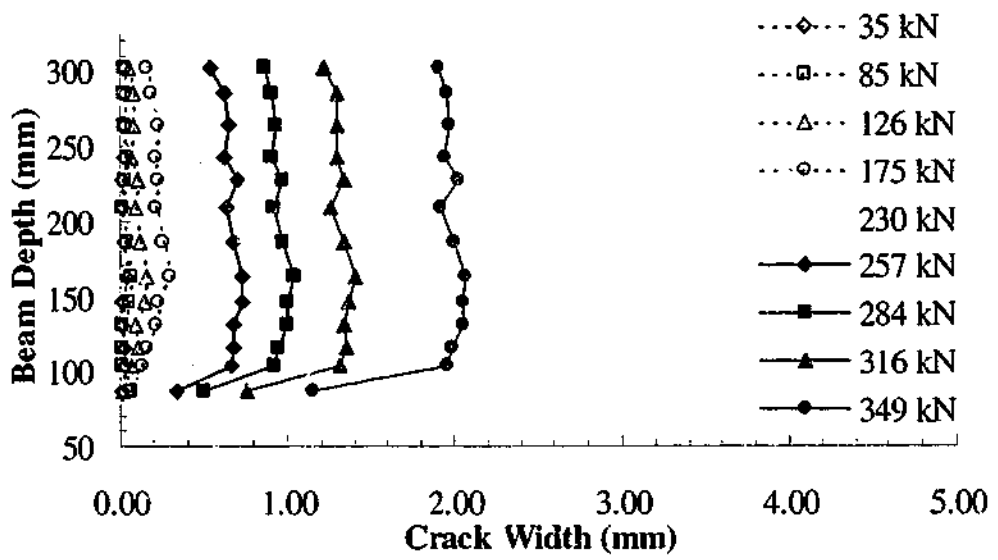

(c)

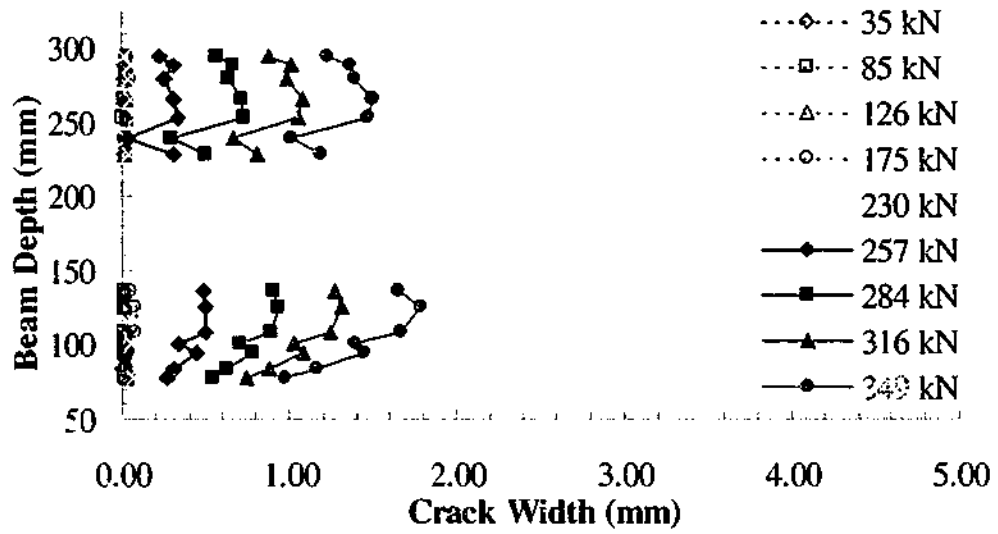

Figure 7.13 (continued) - Crack width development of shear cracks (a) '1' (b) '2' and (c) '3' along beam '0.75D' web depth

(a)

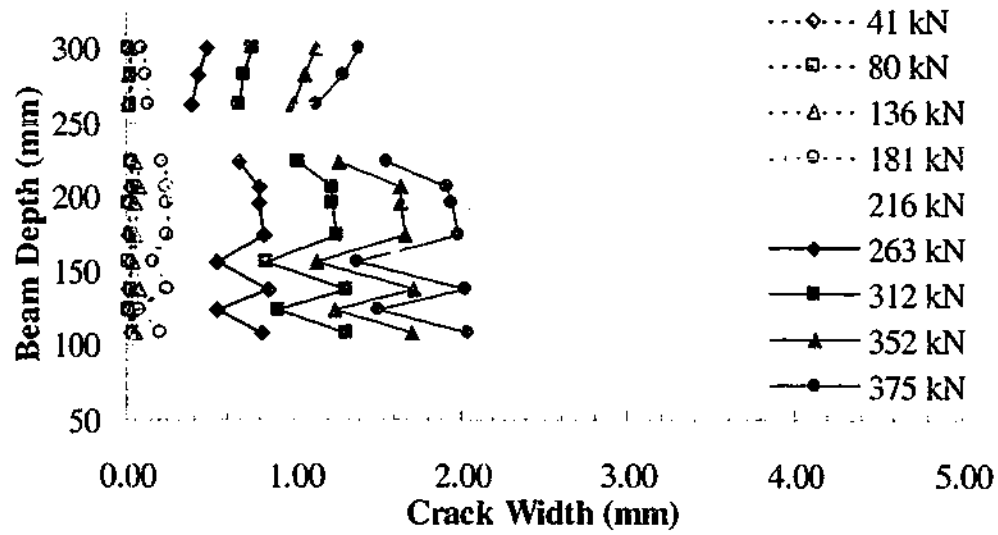

Figure 7.14 - Crack width development of shear cracks (a) '1' and (b) '2' along beam '0.60D' web depth

(b)

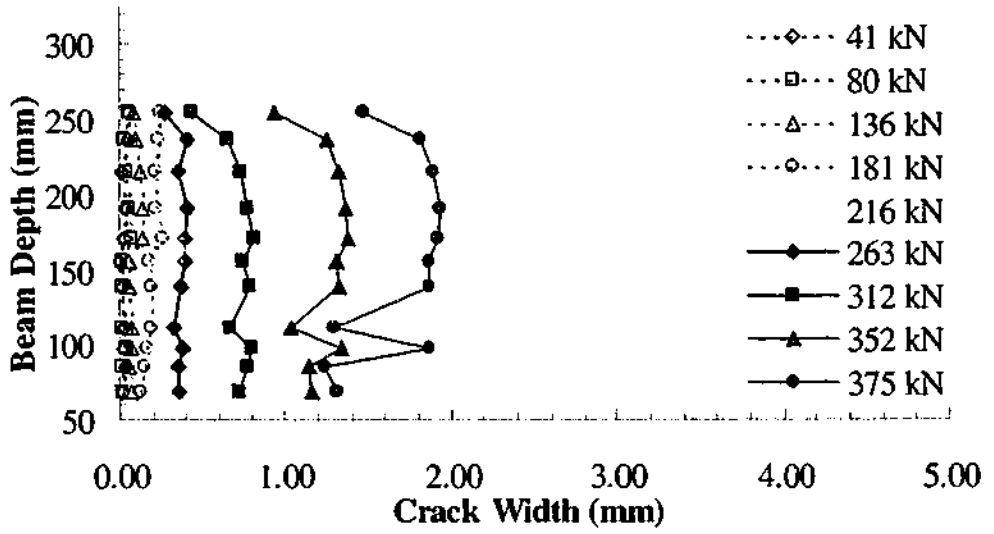

Figure 7.14 (continued) - Crack width development of shear cracks (a) '1' and (b) '2' along beam '0.60D' web depth

(a)

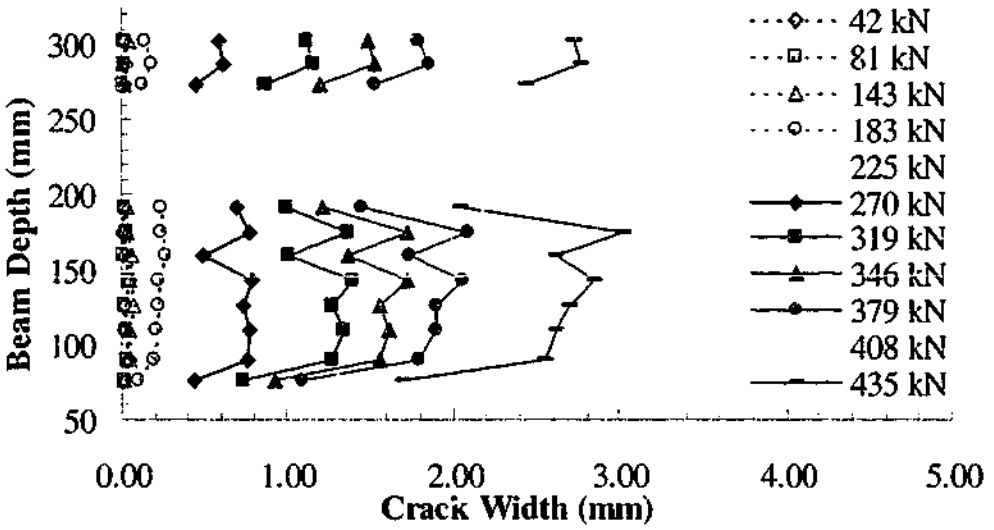

(b)

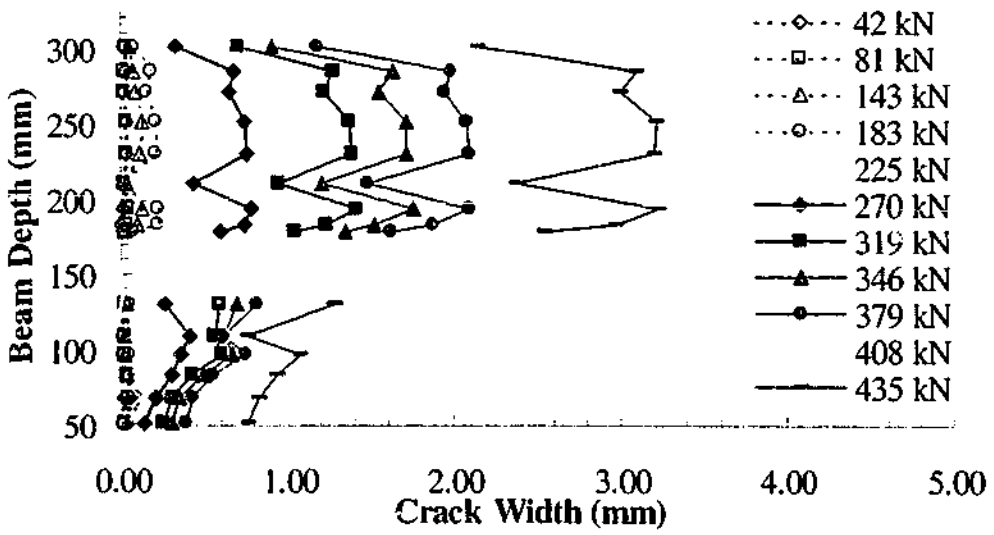

Figure 7.15 - Crack width development of shear cracks (a) '1' and (b) '2' along beam '0.50D' web depth

Figure 7.16 and Figure 7.17 compare the crack width development of shear cracks '1' and '2' at similar load levels across all the beams. The locations of the major shear cracks '1' and '2' formed at roughly similar locations in all of the beams. Referring to Figure 7.11 (b), shear crack '3' in beam '0.75D' appear to be a more appropriate choice compared to shear crack '1' for the comparison in Figure 7.16. However, the crack width of shear crack '3' at any given load level was smaller compared to the crack width of shear crack '1' and therefore omitted from the figure. The shear load levels of each beam are shown in the figure.

(a)

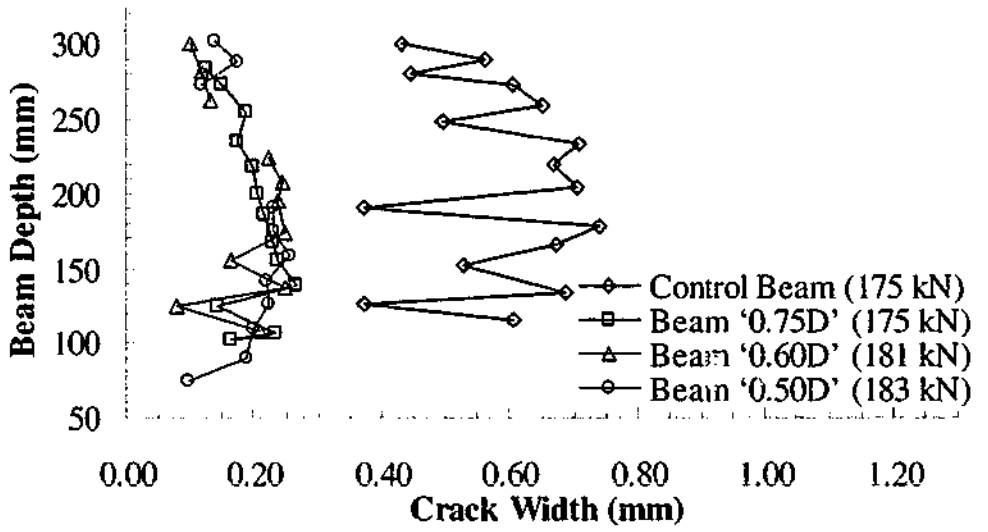

(b)

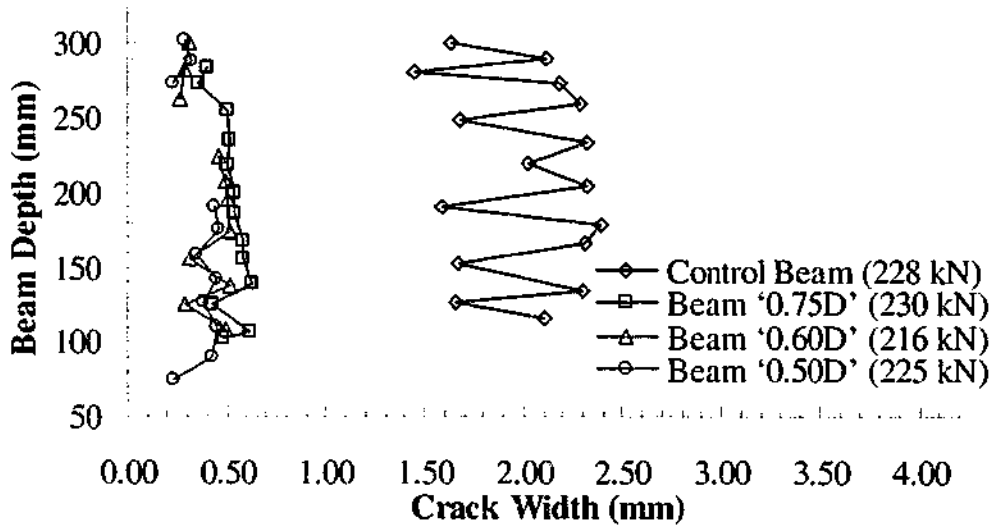

Figure 7.16 - Comparison of shear crack '1' width at approximate shear load levels of (a) 180 (b) 225 (c) 316 (d) 349 and (e) 377 kN

(c)

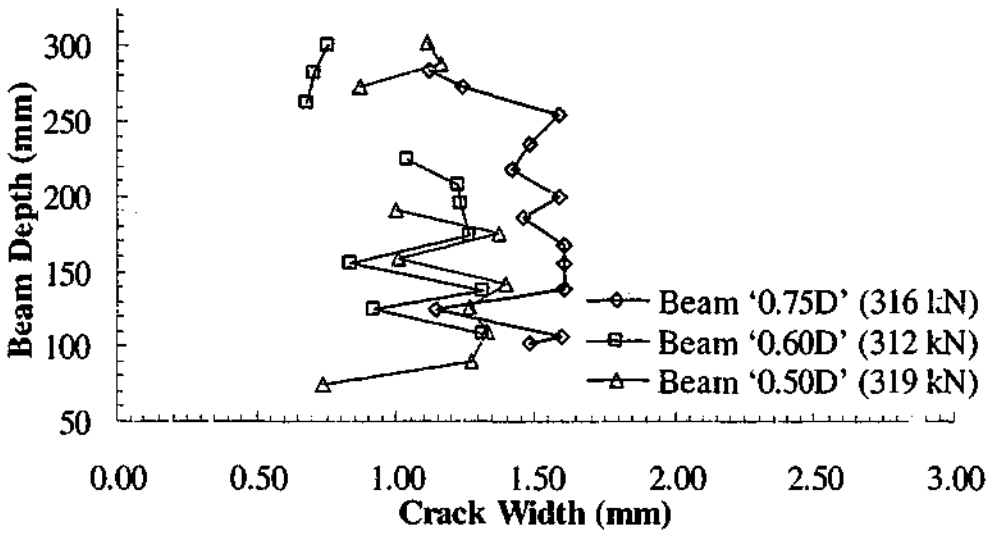

(d)

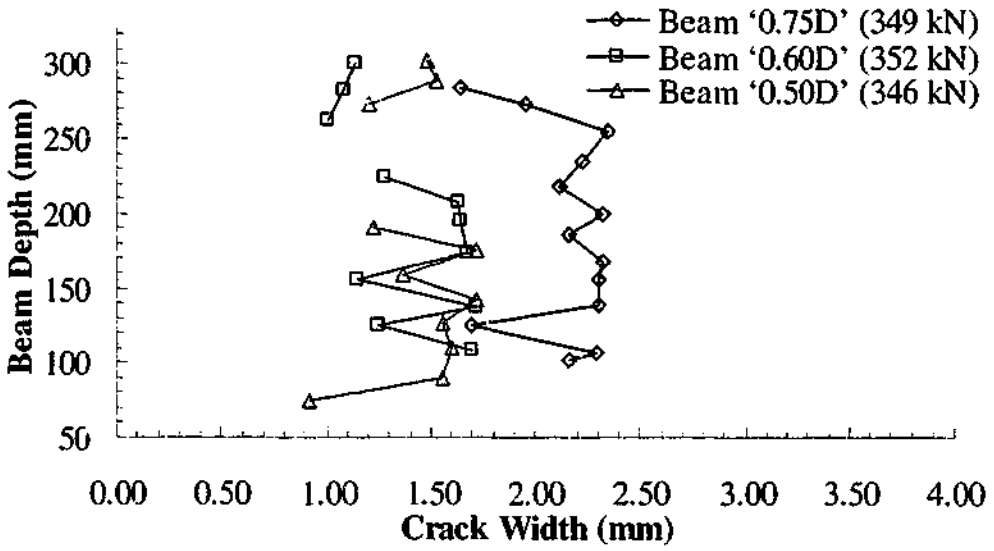

(e)

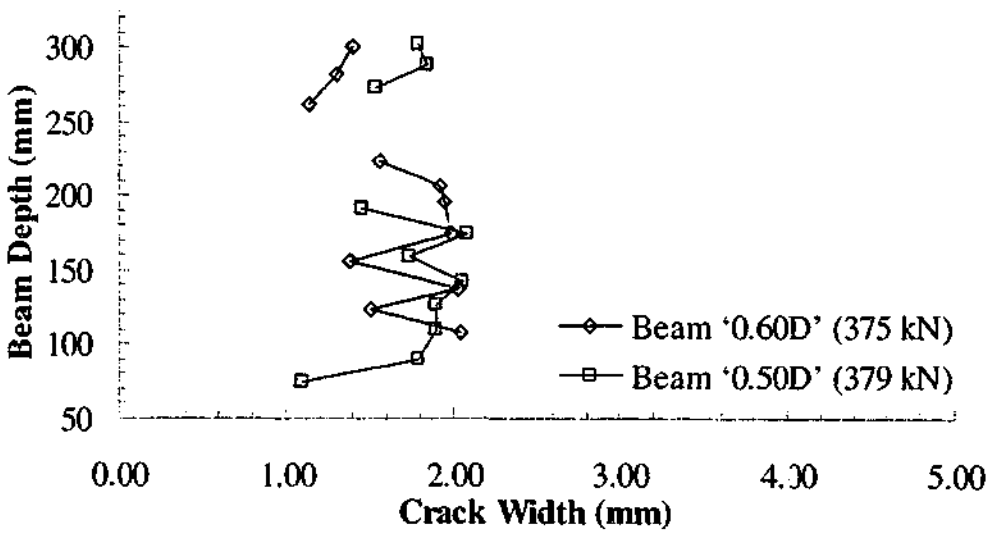

Figure 7.16 (continued) - Comparison of shear crack '1' width at approximate shear load levels of (a) 180 (b) 225 (c) 316 (d) 349 and (e) 377 kN

(a)

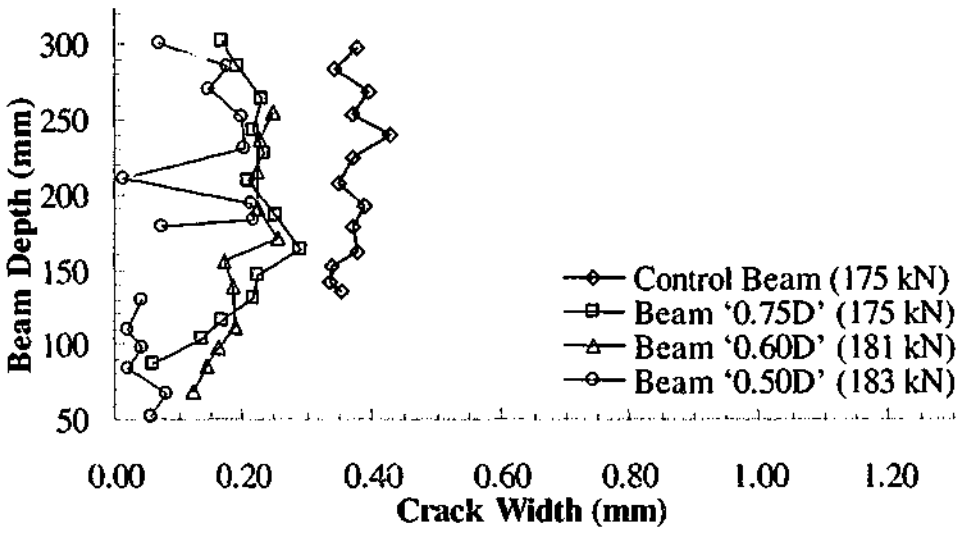

(b)

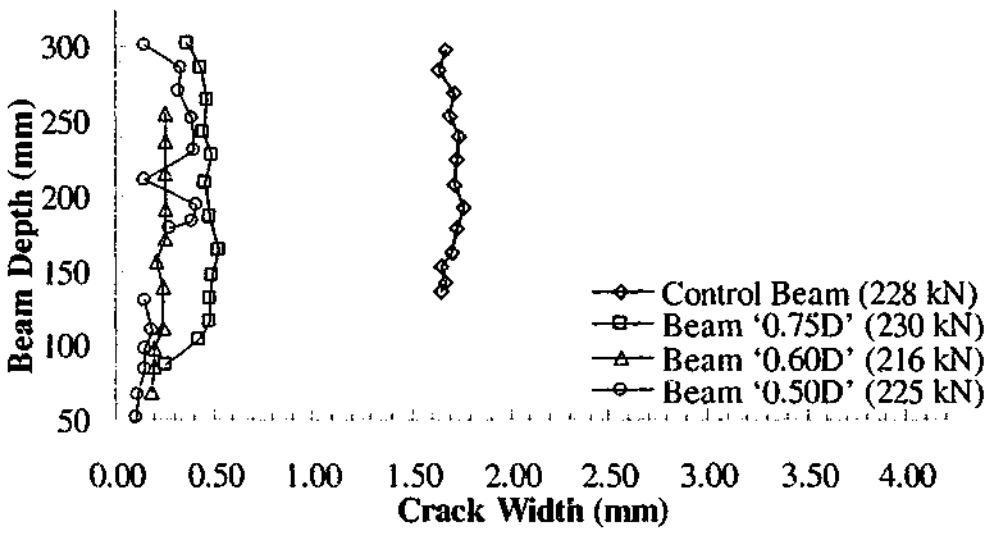

(c)

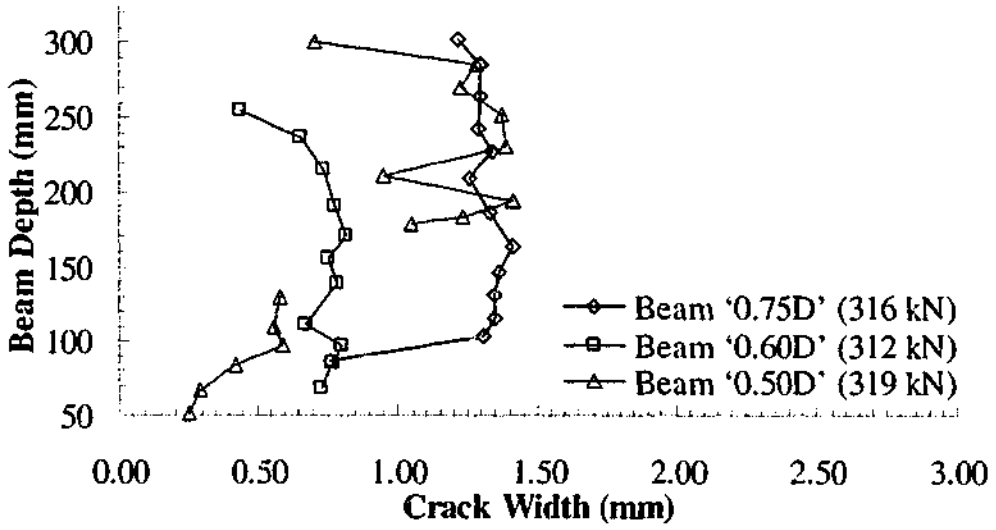

Figure 7.17 - Comparison of shear crack '2' width at approximate shear load levels of (a) 180 (b) 225 (c) 316 (d) 349 and (e) 377 kN

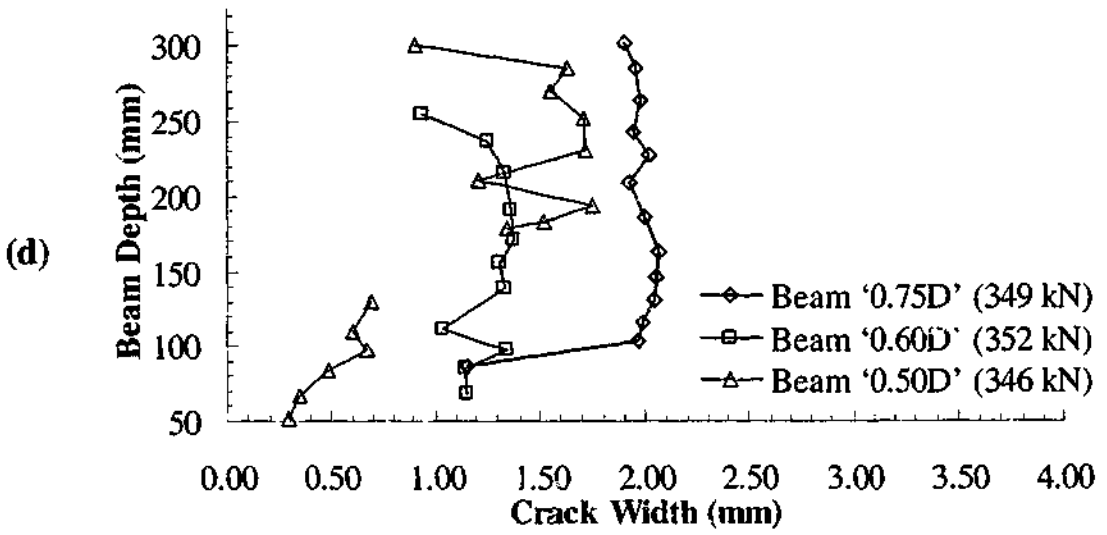

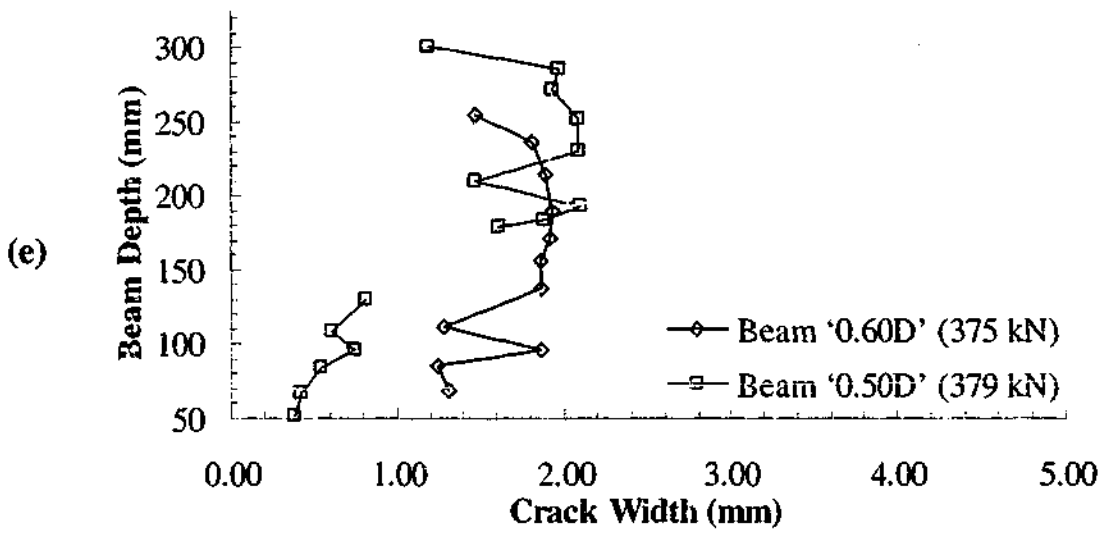

Figure 7.17 (continued) - Comparison of shear crack '2' width at approximate shear load levels of (a) 180 (b) 225 (c) 316 (d) 349 and (e) 377 kN

For a given load, it can be observed the crack width is smaller in the strengthened beams compared to the control beam. The crack widths have been reduced by at least half in the strengthened beams. It is difficult to determine distinct difference in the crack widths of beams '0.60D' and '0.50D' at any given load. Nevertheless, the crack widths are generally smaller than the crack widths in beam '0.75D'.

Figure 7.18 and Figure 7.19 compare the average width development of shear cracks '1' and '2' in each of the beams. At each load level, the average crack width was calculated using all the data points that have been illustrated previously in Figure 7.16 and Figure 7.17. In all of the beams, it can be observed that beyond the

service load levels, the width of shear crack '1' is generally larger than the width of shear crack '2'. In beam '0.75D', the average crack width of shear crack '3' is smaller compared to shear cracks '1' and '2' at any given load level. In beam '0.60D', the average crack width of shear crack '2' was slightly larger than the average crack width in shear crack '1' at the time of the final survey.

(a)

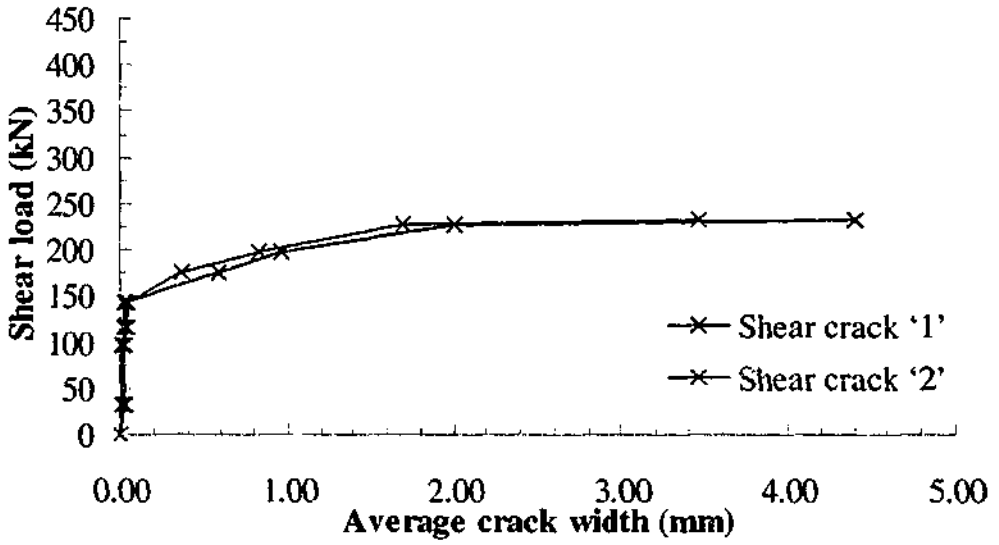

(b)

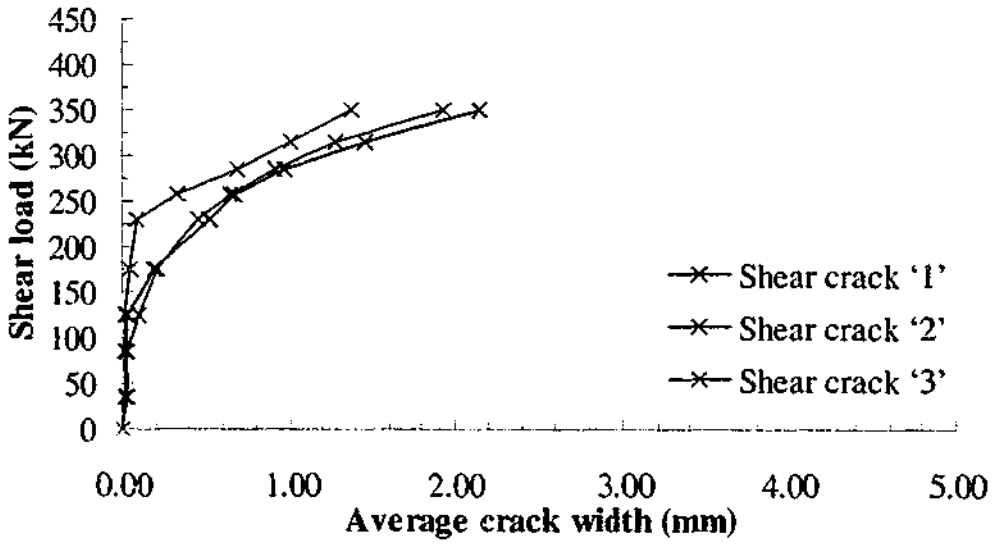

Figure 7.18 - Comparison of shear cracks '1' and '2' in (a) control beam and (b) beam '0.75D'

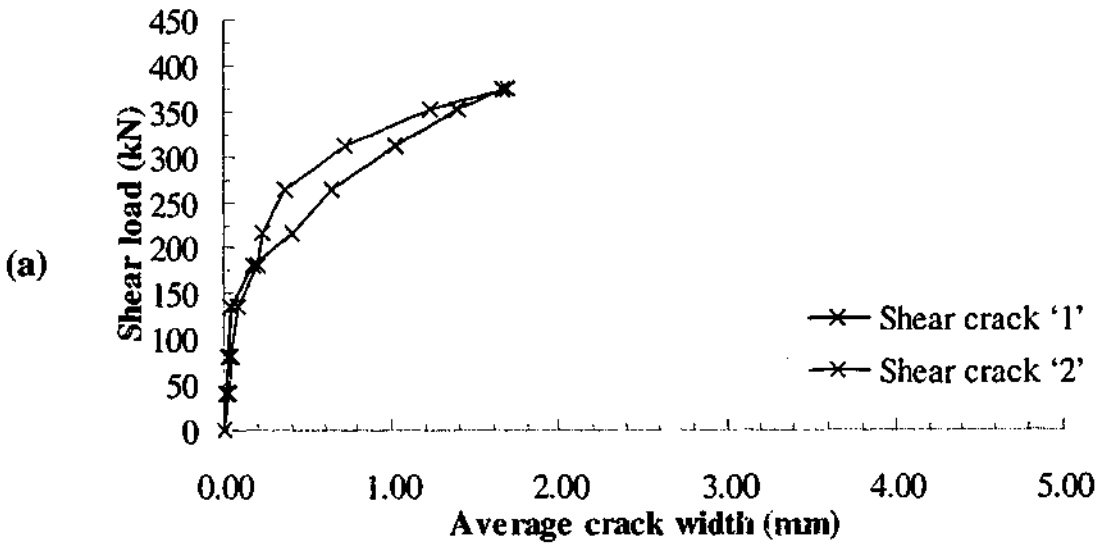

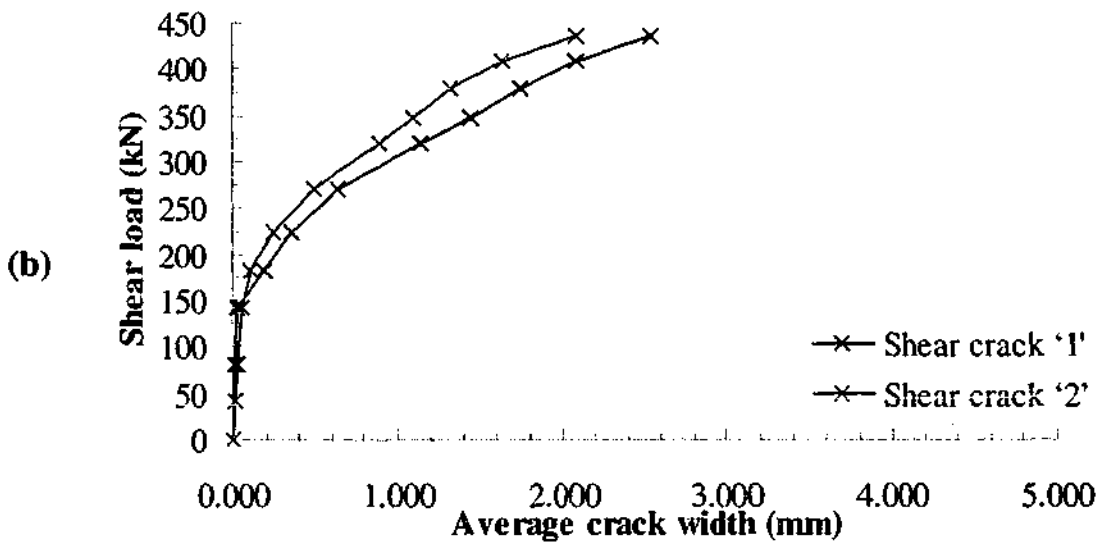

Figure 7.19 - Comparison of shear cracks '1' and '2' in (a) beam '0.60D' and (b) beam '0.50D'

Figure 7.20 compares the average crack width development of shear cracks '1' and '2' across the four T-beams. Beyond the service load level, it can be observed clearly that at any given load level, the average crack widths of both shear cracks '1' and '2' were larger in the control beam compared to all of the strengthened beams. At high load levels, the average crack widths were smaller in beam '0.75D' compared to beams '0.60D' and '0.50D'. The average crack width developments in beams '0.60D' and '0.50D' were fairly similar for most of the loading. The smaller crack widths imply that the effect of aggregate interlock is enhanced in the strengthened beams compared to the control beam. In addition, it follows that concrete contribution to the shear capacity in beams '0.60D' and '0.50D' is slightly higher compared to beam '0.75D'.

(a)

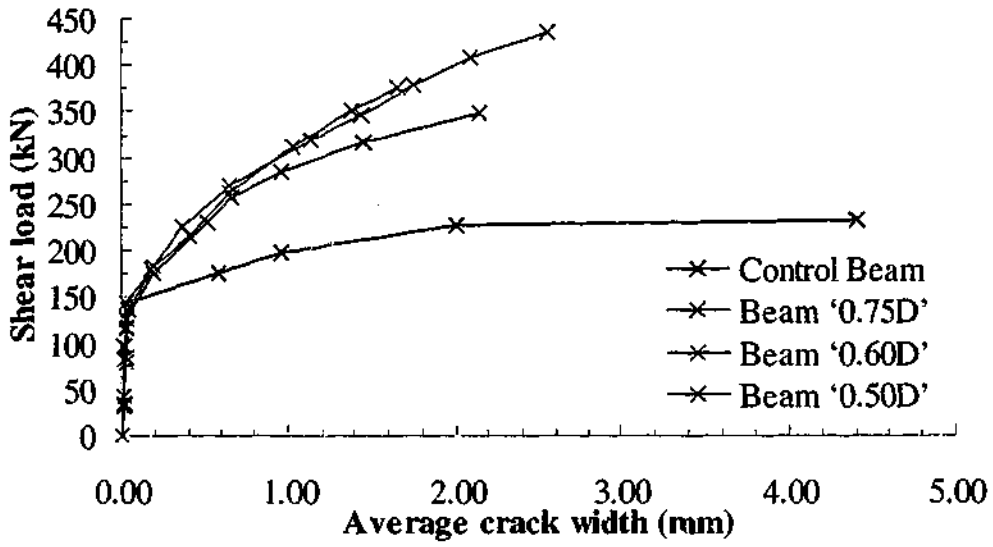

(b)

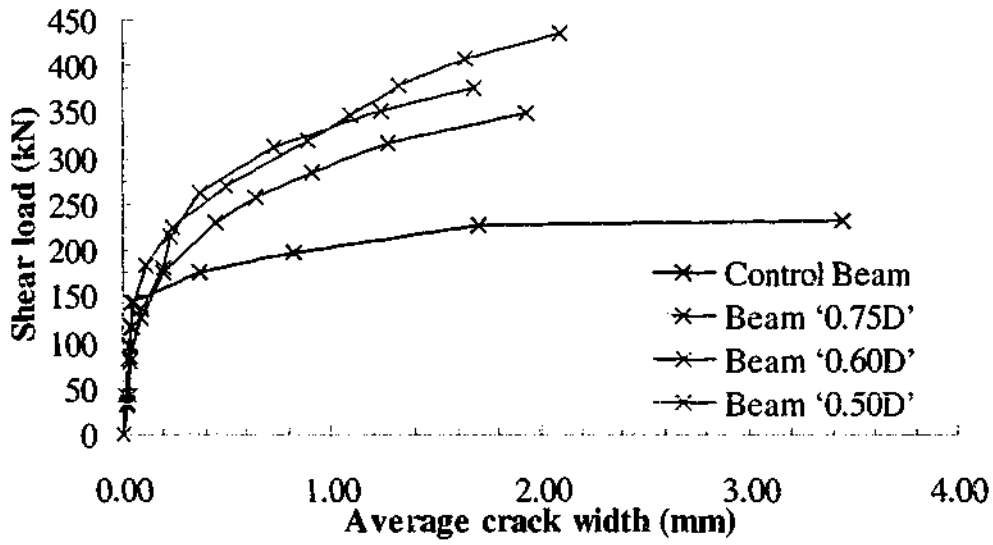

Figure 7.20 - Comparison of average width development of shear cracks (a) '1' and (b) '2'

Using advanced photogrammetry measurements, it has been shown quantitatively that the presence of the external L-shaped CFRP reinforcement has restricted the shear crack width development and propagation. This implies that the effect of aggregate interlock becomes more significant, hence, increasing the contribution of the concrete to the shear capacity of the beam. During loading, the crack widths in the strengthened beams are significantly smaller compared to the control beam. There is no clear difference in crack widths between beam '0.60D' and beam '0.50D' but they are generally smaller compared to beam '0.75D'.

7.3.4 Slip behaviour between CFRP reinforcement and concrete

From the photogrammetry measurements, it is possible to acquire the slip or relative displacement between the L-shaped CFRP reinforcement and concrete at various points of the web depth. In this section, slip is defined as the relative movement between the CFRP and concrete layer. Displacement records of the two columns of targets on the concrete surface next to the individual L-shaped CFRP reinforcement and on the CFRP themselves were used to determine the slip behaviour. The slip was approximated using Equation 7.2, where the subscripts 'cfrp' and 'conc' refer to targets on the L-shaped CFRP reinforcement and concrete surface respectively. The shear load level at a given time is denoted by 'i' where '0' corresponds to the initial photogrammetry survey taken at the time of zero loading. Since the load was carried primarily by the L-shaped CFRP reinforcement along its length, only the vertical component (y-direction) of the targets' displacement records was considered in the equation. At each CFRP location, two slip behaviour profiles can be obtained, one from each side of the CFRP. The displacement data of targets on one side of the CFRP are used in conjunction with the displacement data of targets on the concrete of the same side to produce the slip profile. Ideally, slip should be measured between the CFRP and the concrete layer immediately below it. Nevertheless, the concrete layer next to the CFRP reinforcement are representative of the behaviour of the concrete layer directly under the CFRP. In the figure, the label CFRP '1' refers to the external shear reinforcement first from the support with increasing numbers being the ones that follows. The results presented in the figures herein are based on data sets where targets on the concrete overhang in the failure span are held stationary.

$$Slip_i \approx (y_{cfrp,i} - y_{cfrp,0}) - (y_{conc,i} - y_{conc,0}) \tag{7.2}$$

Figure 7.21 to Figure 7.24 shows the slip behaviour along the control beam depth of the L-shaped CFRP plates in the failure shear span at selected load levels. In the figures, the beam depth refers to the height of the individual targets on the CFRP plate from the soffit of the beam, which is taken as zero. Similar to the figures in the previous section, the average support load levels at the failure span at the time of the surveys are outlined in the figures.

At low load levels, the slip between the CFRP reinforcement and concrete in all of the strengthened T-beams is insignificant or very small. The slip remained relatively small until at higher shear load levels, that is, when shear cracks have begun to form. At a given shear load level, the magnitude of slip is larger near locations where the shear cracks intercepted the CFRP reinforcement compared to locations further away from the shear crack. The slip between the CFRP and concrete decreases steadily the further away the targets are from the shear cracks. The shape of the slip profile along the web depth from the shear crack is almost exponential in all of the strengthened beams.

In Section 3.3.6, it has been observed from testing of the bond specimens that the slip range at which debonding of the CFRP plate from the concrete occurs in the range of 0.016 to 0.05 mm. Since the concrete strength of the bond specimens and T-beams are fairly similar, it is assumed that the slip range at which debonding occurs is similar also. It was stated earlier that the accuracy of the photogrammetry measurements used in the present study was ±0.06 mm. Although the slip range is smaller than the accuracy of the photogrammetry system, at higher load levels where slip is larger, the accuracy is more than adequate to determine whether or not debonding has occurred. Referring to the post-failure crack pattern shown in Figure 7.11, it is clear from the figures of the slip profiles that debonding initiates from the location where the shear crack crossed the CFRP reinforcement. For a given CFRP at a particular depth, the slip values on the left and right sides of the CFRP differ from each other. This was due to the shear crack crossing the CFRP reinforcement at an angle that resulted in an uneven debonded zone along the width of the CFRP reinforcement.

In CFRP '1' of beam '0.75D', the slip is relatively small compared to other CFRP reinforcement, indicating that there was little or no debonding of CFRP from the concrete. As for CFRP '2' of beam '0.75D', Figure 7.22 indicates that the entire portion of the CFRP above shear crack '3' shown in Figure 7.11 has debonded at the time of the final survey. At the time of the final survey, significant portions of CFRP '2', '3' and '4' have debonded from the concrete layer. At the bottom of the beam, the magnitude of slip on the right side of the CFRP is relatively large. The bend zone acts as an anchor for the CFRP reinforcement and is a region of high stress

concentration. A similar behaviour is observed for CFRP '3' as well. The post failure crack pattern illustrated in Figure 7.11 (b) shows that shear cracks '1' and '2' extended to the bottom of CFRP '2' and '3'. It was possible that the CFRP may have debonded because of the shear crack. However, it was more likely due to a combination of localised deformation of concrete and debonding. The concrete portion directly under the CFRP at the bend zone was subjected to localised compression whereas the concrete portion close to the CFRP was not confined at all. At the bottom of both CFRP '2' and '3', the slip values at the right side at the time of the final survey are significantly higher compared to the slip values at the left side. The large slip values can be used as an indication of the imminent failure of the CFRP anchorage at the bend zone. At the time of the final survey, the slip at the bend zone of CFRP '2' was the highest.

The general trends in the slip behaviour in beams '0.60D' and '0.50D' are similar to the slip behaviour of beam '0.75D'. The behaviour was consistent with the observed post failure crack patterns illustrated in Figure 7.11. Further information on the slip behaviour along the depth of the L-shaped plates for beams '0.60D' and '0.50D' is contained in Appendix C.3.

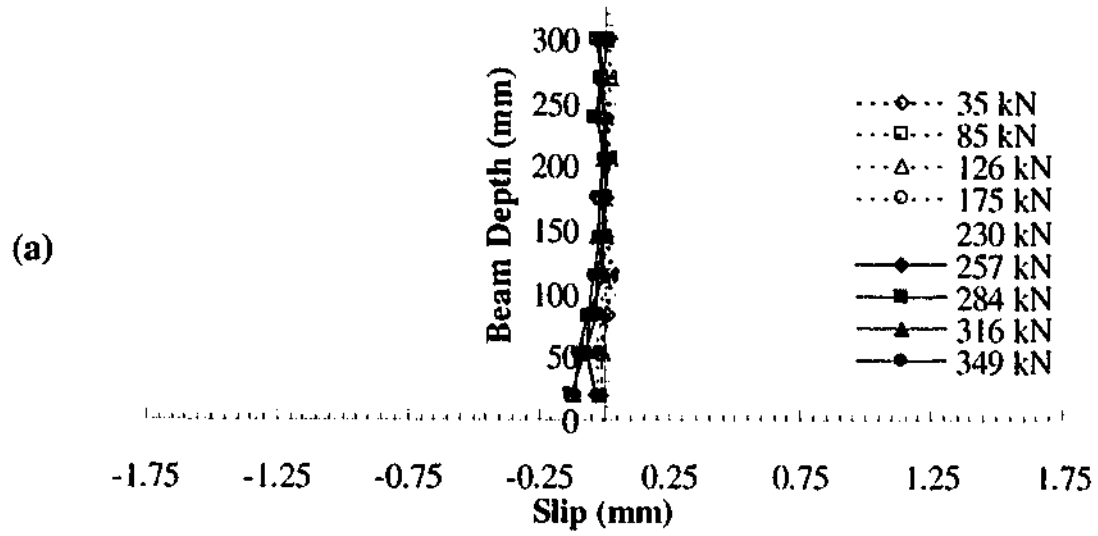

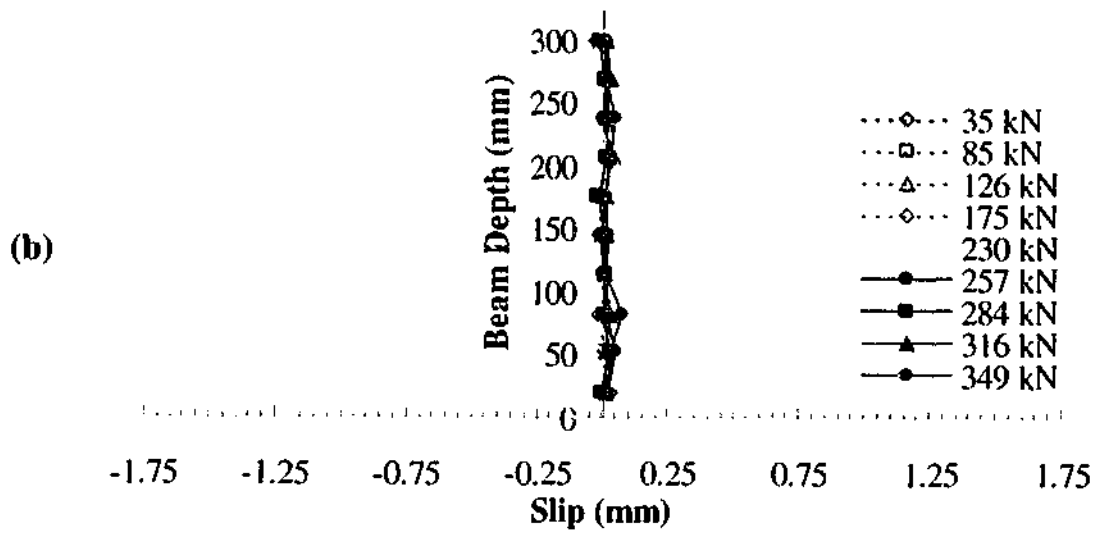

Figure 7.21 - Slip behaviour of CFRP '1' in beam '0.75D' at (a) left side and (b) right side

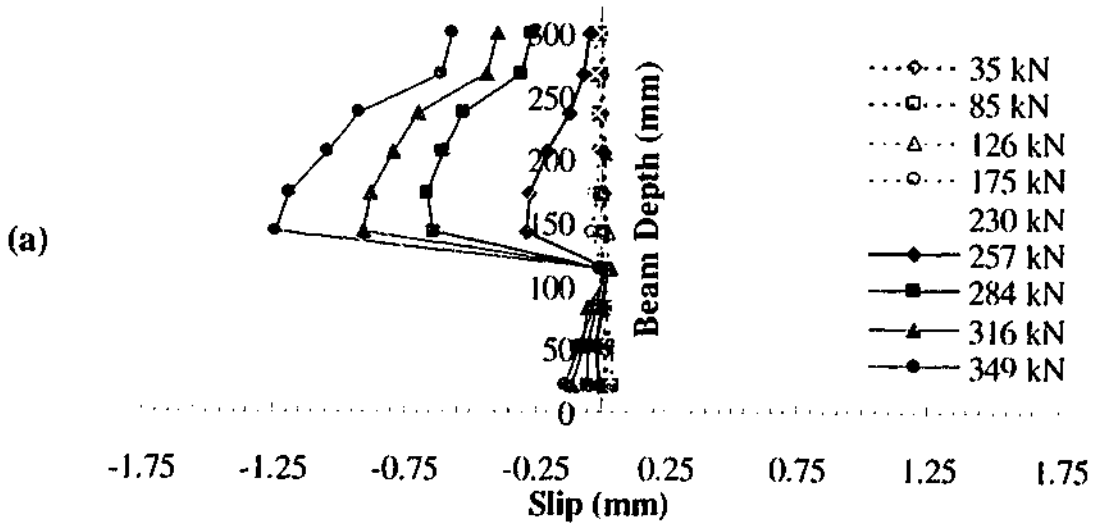

Figure 7.22 - Slip behaviour of CFRP '2' in beam '0.75D' at (a) left side and (b) right side

(b)

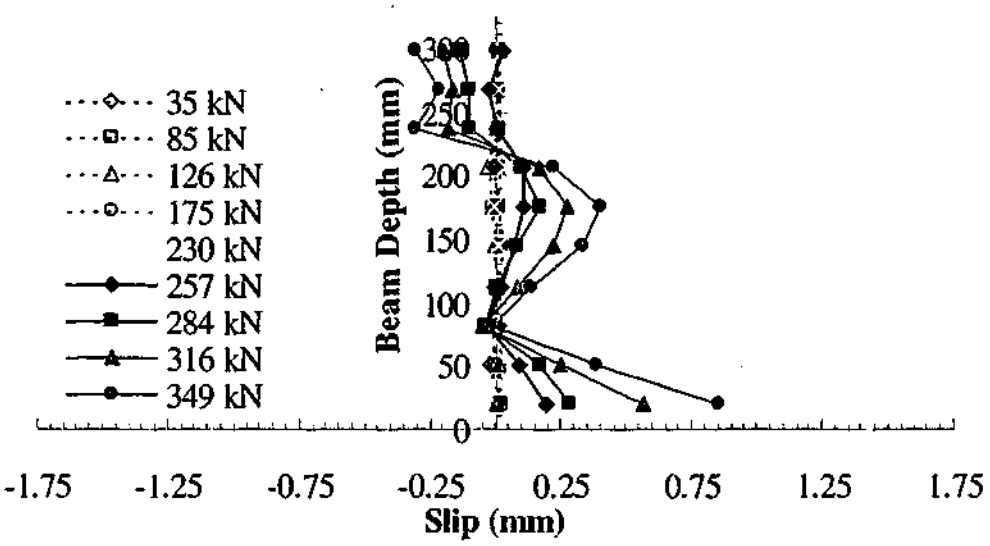

Figure 7.22 (continued) - Slip behaviour of CFRP '2' in beam '0.75D' at (a) left side and (b) right side

(a)

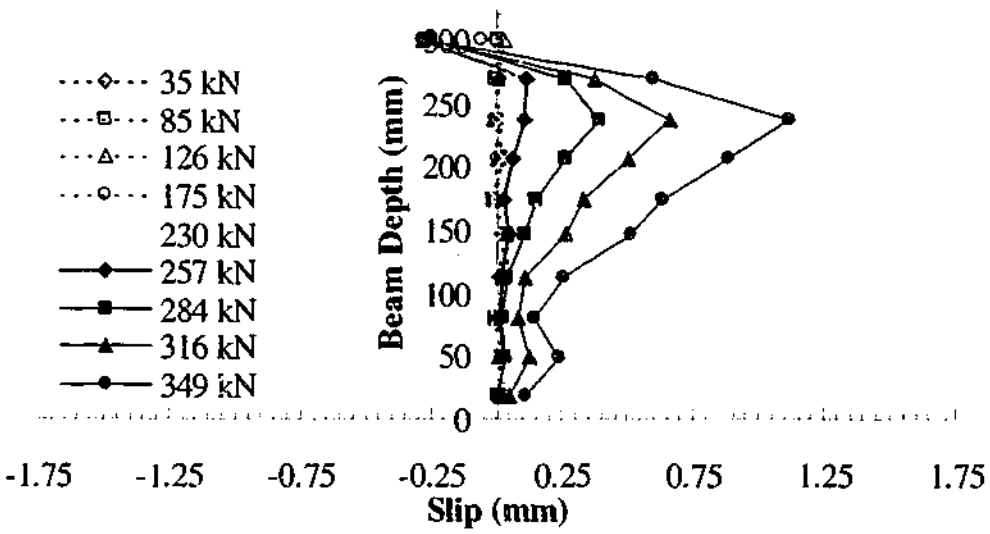

(b)

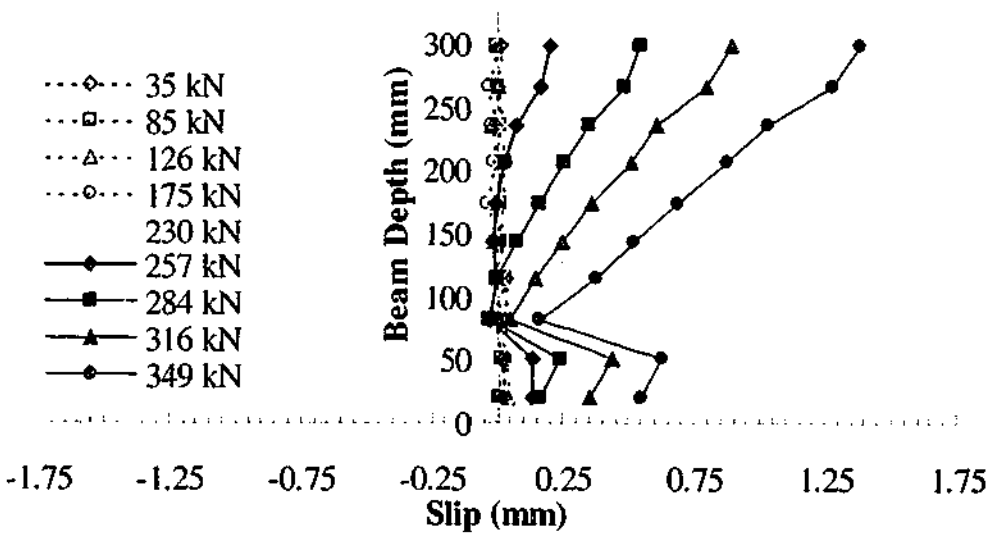

Figure 7.23 - Slip behaviour of CFRP '3' in beam '0.75D' at (a) left side and (b) right side

(a)

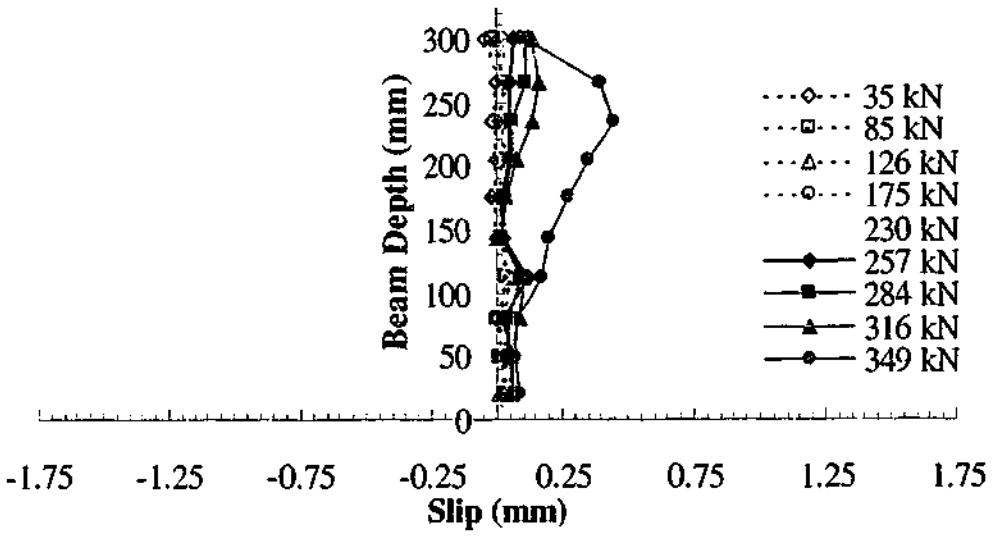

(b)

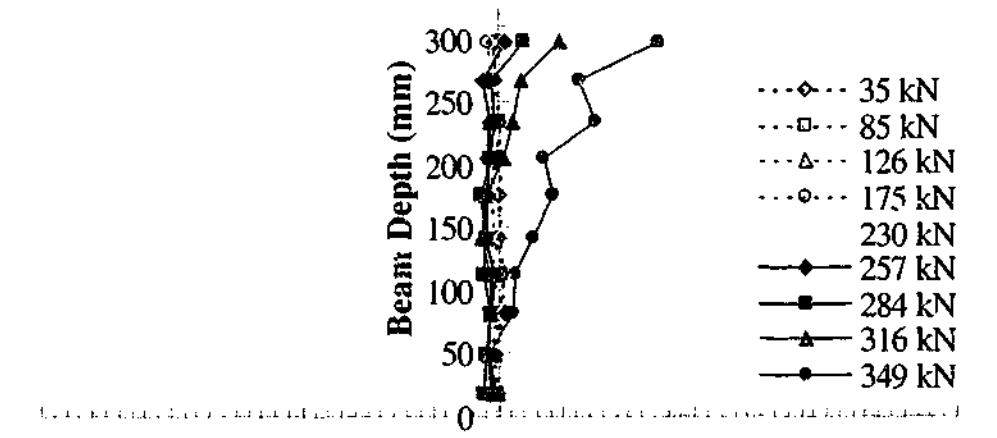

Figure 7.24 - Slip behaviour of CFRP '4' in beam '0.75D' at (a) left side and (b) right side

The slip behaviour obtained using photogrammetry measurements and LVDTs as presented in Section 6.2.8 are compared in Figure 7.25 to Figure 7.27. Since the LVDTs and targets were placed on opposing sides of the beams, targets located at heights similar or closest to the LVDTs are adopted for the comparison. The height of the targets and LVDTs are illustrated in the figures. In the T-beams, the LVDTs were mounted onto the concrete surface hence slip was measured with reference to the concrete. The steel fixtures on the CFRP were adhered to two locations along the width. In the case of the photogrammetry measurements, the displacement data of three targets per location were used to calculate slip for comparison with slip obtained from the LVDTs, one on the concrete and two on the CFRP. The slip adopted in the figures corresponded to the average of the slip

between the targets on both sides of the CFRP with respect to the target on the concrete. The slip was approximated using Equation 7.2, however, with reference to the concrete instead. Despite the LVDTs and photogrammetry targets being located at different sides of the beams, the figures show that the slip behaviour obtained from both measurement systems are comparable. The general trends in the slip behaviour are similar although the photogrammetry measurements are less accurate compared to the LVDTs' measurements. Both measurement systems showed small slip values at low load levels followed by a large increase after shear cracks had formed. This implies that the CFRP reinforcement on both sides of the beams debonded quite uniformly.

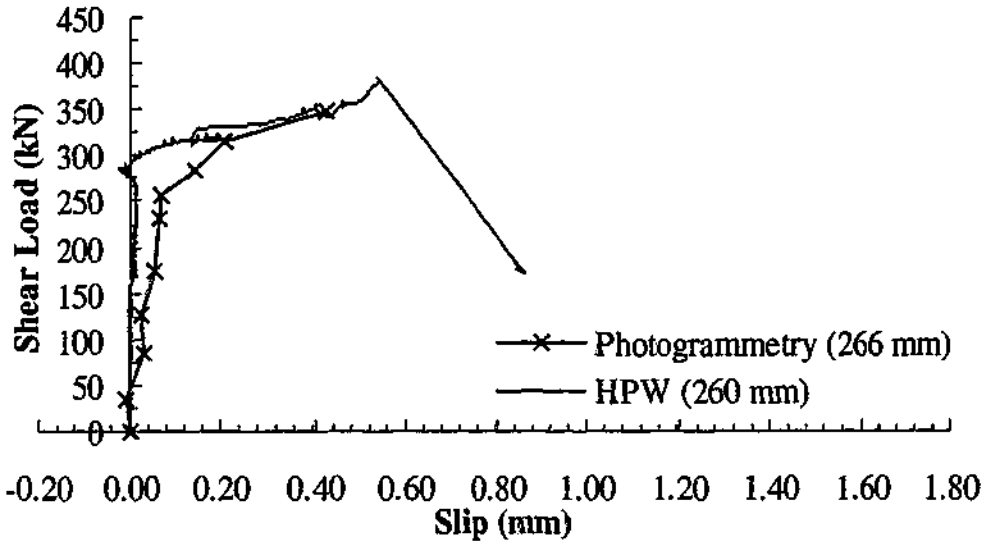

Figure 7.25 - Comparison of slip measured with LVDT and photogrammetry for beam '0.75D'

(a)

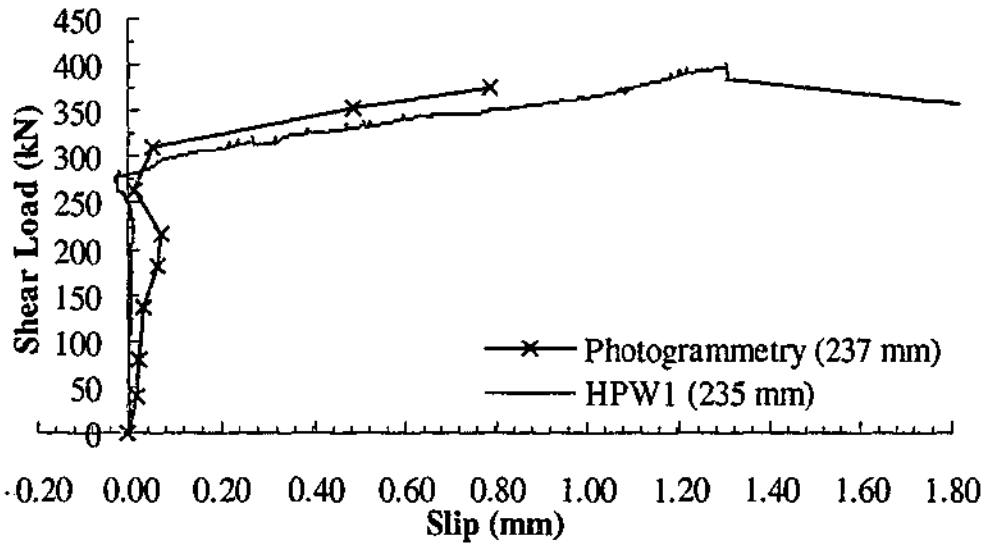

(b)

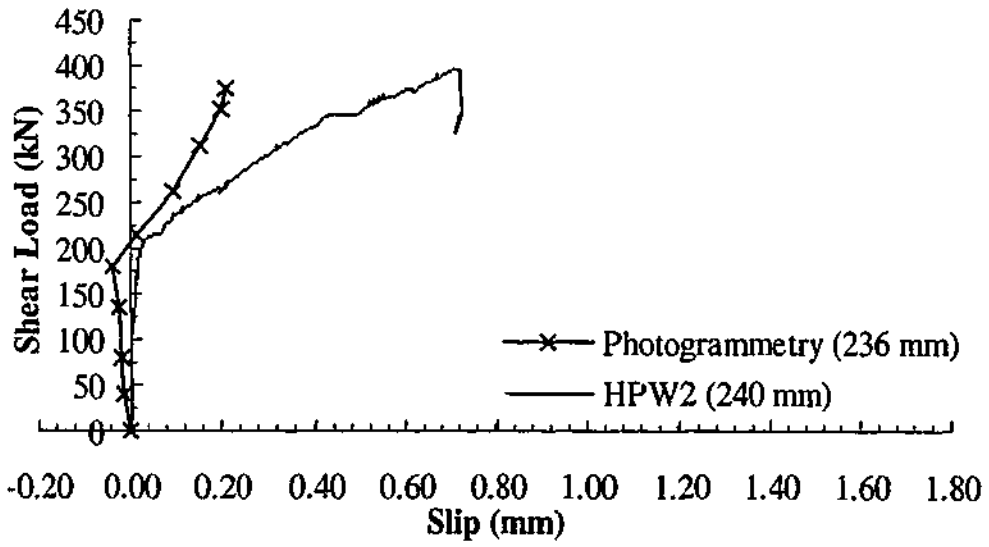

Figure 7.26 - Comparison of slip measured with LVDT and photogrammetry for beam '0.60D' at (a) HPW1 and (b) HPW2

(a)

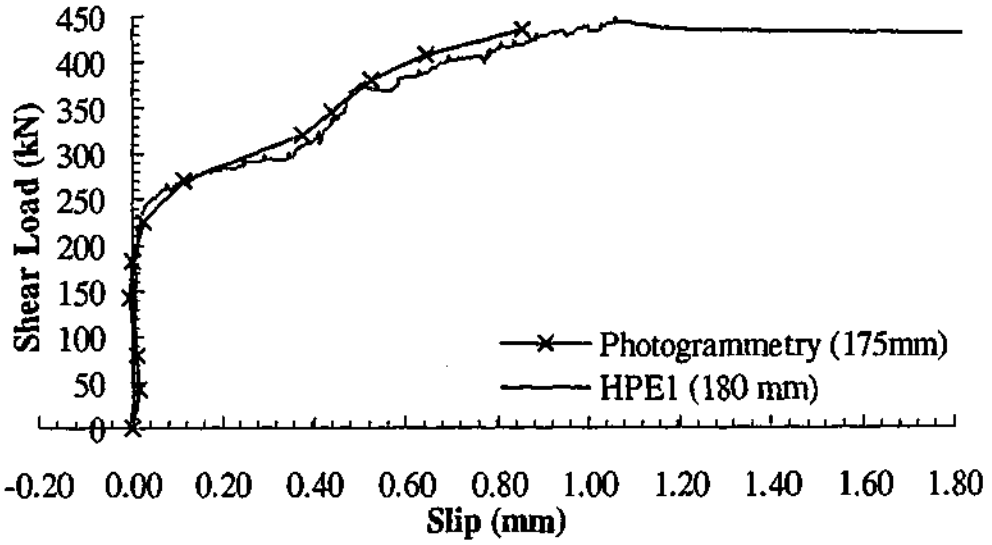

(b)

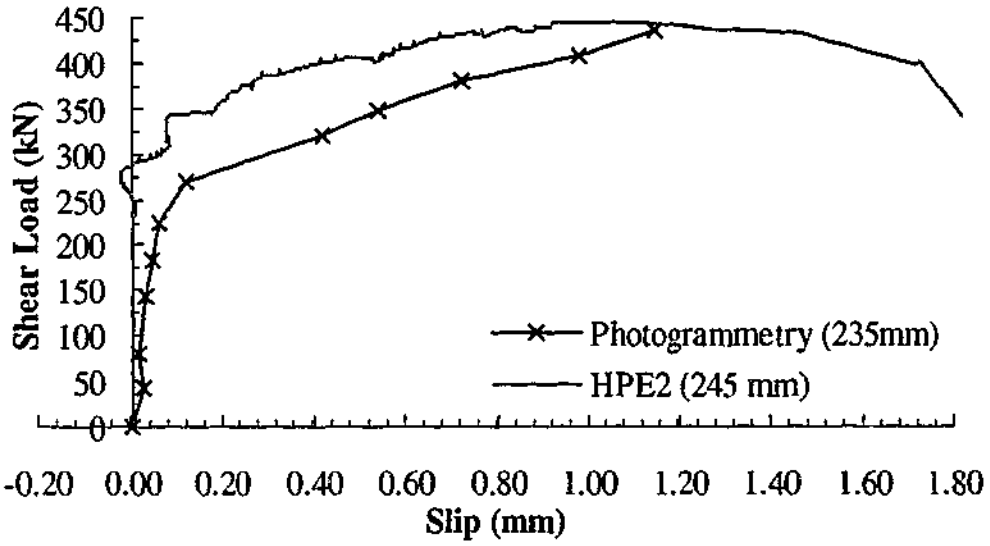

Figure 7.27 - Comparison of slip measured with LVDT and photogrammetry for beam '0.50D' at (a) HPE1 and (b) HPE2

Using advanced photogrammetry measurements, it has been shown that the majority of the CFRP reinforcement at the failure shear span exhibited high slip values at the time of the final survey. By using the slip range obtained from the bond specimens as an indicator of debonding, the high slip values observed in the T-beams indicated that the CFRP reinforcement had debonded. At low shear load levels, there was negligible slip between the CFRP reinforcement and concrete until when shear cracks had begun to form. The magnitude of slip is larger near locations where the shear cracks had crossed the CFRP reinforcement compared to locations further away from the shear crack. At high shear load levels, slip was significant near the bend zone of several CFRP in all of the beams. The slip behaviour obtained from both the photogrammetry targets and LVDTs are comparable despite being located at different

sides of the beams. This implies that debonding occurred quite uniformly at both sides of the beam at the same CFRP location.

7.4 Strain in CFRP reinforcement

The strain development in the CFRP reinforcement at the failure shear span of the beams are reported. The strain on one side of the CFRP reinforcement at a given time was calculated by dividing the difference in the vertical displacements of only the top and bottom most targets by the initial difference in height between the two targets. The strain in the CFRP is then the average of the values of both sides of the CFRP. In calculating strain, the low accuracy of the photogrammetry system necessitates the use of targets separated by the greatest distance. There are ten rows of targets on the CFRP spaced at approximately 31 mm. The accuracy of the photogrammetry measurement is 0.06 mm, which equates to a strain accuracy of approximately ±1935 με. The force corresponding to this strain accuracy is approximately ±14.5 kN (Force = E x ε x Area). However, by taking the strain over a longer length, say 279 mm, the strain accuracy increases to ±215 με, which equates to a force in the CFRP of approximately ±1.6 kN. This assumes that the strain in the CFRP reinforcement is uniform over 279 mm, which is not realistic. Nevertheless, the results obtained still provide a good indication of the strain level in the CFRP.

Figure 7.28 illustrates the average strain development in the individual CFRP reinforcement at the failure shear span of the strengthened beams. Similar to the observations of strain gauges on the CFRP reinforcement, the average strain obtained from the photogrammetry measurements remained fairly small at the initial stages of loading. Upon the formation of shear cracks, the average strain can be observed to increase significantly with the shear load level.

In beam '0.75D', a significant increase in the tensile strain occurred first in CFRP '2' and '3'. This implied that a significant proportion of the shear load was transferred through the CFRP in this section of the shear span. The low average strain in CFRP '1' throughout loading indicated that only small amount of shear force was transferred through this CFRP. Therefore, this section of the shear span is a non-critical region. At the time of the final survey, CFRP '2' and '3' exhibited very high

average strain values. This is consistent with the observation of anchorage failure at the bend zone of the two CFRP. CFRP '3' exhibited the highest average strain at the time of the final survey. This is similar to the results obtained from the strain gauges whereby the average strain values of the gauges on CFRP '3' were the highest at the peak load. It is possible that failure had occurred first at the anchorage of CFRP '3'. The average force in CFRP '3' at the time of the final survey was approximately 44.7 kN.

In beam '0.60D', the first significant increase in tensile strain occurred in CFRP '3' followed by CFRP '4' and then CFRP '2'. The strain in CFRP '1' remained relatively small for most of the loading until approximately 310 kN, beyond which the strain increased slightly. CFRP '3' exhibited the highest average strain at the time of the final survey, which is consistent with the observation of anchorage failure at the bend zone of the CFRP reinforcement. The average force in the CFRP was approximately 41.9 kN. It is also consistent with the observation that the strain gauges on CFRP '3' exhibited the highest average strain at the peak load.

In beam '0.50D', the increase in tensile strain occurred first in CFRP '2' followed by CFRP '3' and then CFRP '4'. The strain in CFRP '1' remained relatively small for most of the loading until approximately 275 kN, beyond which the strain increased slightly. CFRP '3' exhibited the highest average strain at the time of the final survey with an average force of approximately 55.9 kN. The average strain as measured by the strain gauges on CFRP '3' was also the highest at the peak load.

The general trends in the CFRP load-strain behaviour from the photogrammetry measurements and strain gauges are consistent with each other. The average strain in the CFRP reinforcement remained fairly small at the initial stages of loading, which increased significantly with load upon the formation of shear cracks. The locations of the CFRP reinforcement subjected to the most load obtained from photogrammetry measurements are consistent with observations from strain gauges in all of the beams.

(a)

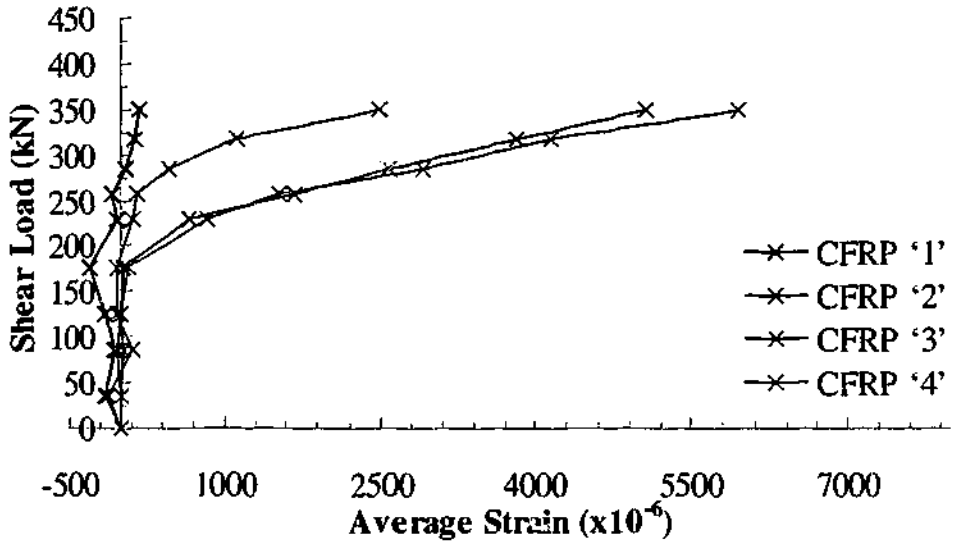

(b)

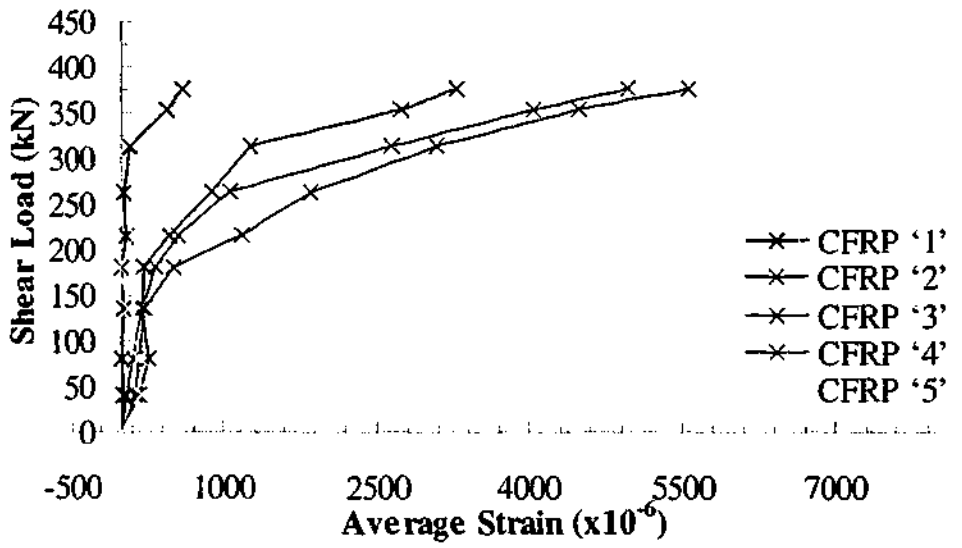

(c)

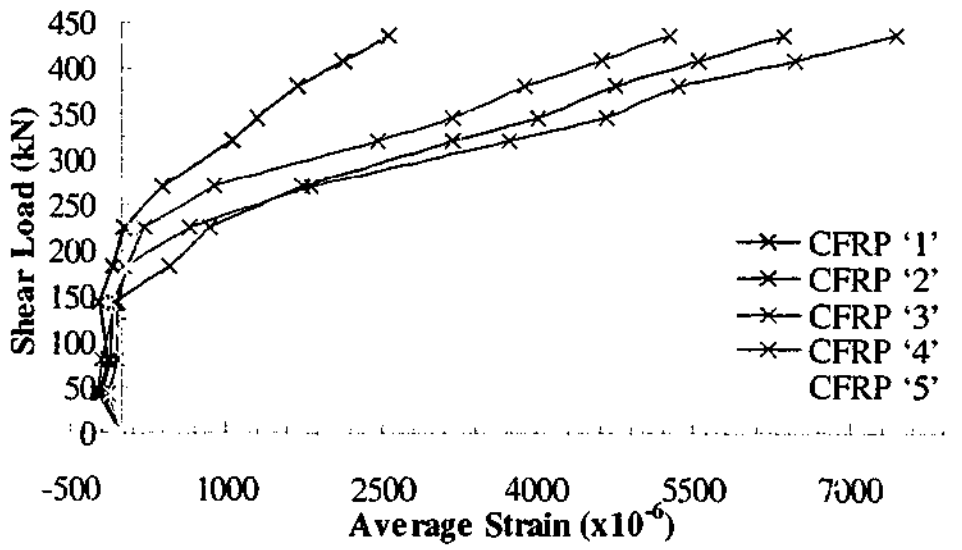

Figure 7.28 - Average strain development in CFRP of beams (a) '0.75D' (b) '0.60D' and (c) '0.50D'

7.5 Summary of findings

An advanced photogrammetry measurement technique was used to determine the shear deformation mechanisms of the T-beams, crack width development, slip behaviour between the CFRP reinforcement and the concrete and average strain of the CFRP reinforcement. It has been shown that the presence of the external CFRP shear reinforcement did not alter the basic shear deformation mechanism of the T-beams investigated herein. The deformation mechanisms in the strengthened beams were still similar to the control beam except that the width of the shear cracks was smaller. Therefore, existing equations used in the prediction of the shear capacity of reinforced concrete beams can be extended to include the contributions from the CFRP reinforcement. In the web, the shear deformation mechanisms were simply the separation of two rigid blocks of concrete at the locations of the shear cracks. The rigid blocks displaced almost vertically with respect to each other. In all of the beams, the concrete overhang displaced as a rigid block.

The widths of the two major shear cracks in the web of the T-beams were compared and it has been shown quantitatively that the crack widths were significantly smaller in the strengthened beams compared to the control beam. There was no clear difference in the crack widths of the beams with CFRP reinforcement spacing of 0.60D and 0.50D. However, they were smaller than the crack widths in beam '0.75D'. The smaller shear crack widths in the strengthened beams imply that the effect of aggregate interlock is more significant, therefore, the concrete contribution to the shear capacity of the beams increases.

The load-slip relationships between the CFRP reinforcement and concrete at the failure span were reported for each beam. In all of the beams, it was shown that the slip was insignificant at low load levels. It remained so until when shear cracks had begun to form. The slip was observed to be higher near locations where the shear cracks had intercepted the CFRP reinforcement compared to locations further away. The shape of the slip profile along the web depth from the shear crack is almost exponential. At the time of the final survey, the slip profiles indicated that significant portions of critically loaded CFRP reinforcement had debonded in all of the beams.

At high shear load levels, slip was observed to be significant near the bend zone of several CFRP in all of the beams. Comparisons of the slip measured using photogrammetry and LVDTs were carried out and it was found that both measurement systems gave similar results. This indicated that debonding had occurred quite uniformly at both sides of the beam at the same CFRP location.

The average strain development in the individual CFRP reinforcement at the failure shear span was also reported. Similar to the observations of strain gauges on the CFRP reinforcement, the average strain obtained from the photogrammetry measurements remained fairly small at the initial stages of loading. Upon the formation of shear cracks, the average strain can be observed to increase significantly with the shear load level. The locations of the CFRP reinforcement subjected to the most load obtained from photogrammetry measurements are consistent with observations from strain gauges.

In the present study, the photogrammetry measurement technique has provided much valuable information regarding behaviour of the different components of the beams with minimal preparation. To get similar amount of information using conventional measurement devices may prove to be too cumbersome and time consuming.

CHAPTER 8 - NON-LINEAR FINITE ELEMENT MODELLING OF T-BEAMS

8.1 Introduction and scope

In this section, the short-term behaviour of the four T-beams outlined in Chapters 5 and 6 were numerically modelled using the finite element method (FEM). Numerical analyses based on the non-linear approach were carried out with the aims of confirming the applicability of FEM in modelling FRP web bonded beams and of supplementing experimental results. In the literature, studies on numerical analyses of reinforced concrete beams using the finite element method are numerous. Different modelling methodologies were reported that uses various types of material models, element types and solution strategies. Studies on finite element modelling of reinforced concrete beams externally bonded with FRP plates or sheets, however, are limited particularly in the area of shear strengthening. In studies where flexural strengthening were reported, slip between the FRP and concrete layer was modelled using interface elements simulating the behaviour of the adhesive layer. In the case of shear strengthening, however, there does not appear to be any study reported in the literature regarding the finite element modelling of beams with slip behaviour between the FRP and concrete elements. All the studies assumed perfect bond between the FRP and concrete layer (Kaliakin et al. (1996), Arduini et al. (1997), Malek and Saadatmanesh (1998a), Tedesco et al. (1999), Adhikary et al. (2000) and Potisuk et al. (2001)). The implication of such assumption is that beam failure due to FRP debonding cannot occur. This may lead to incorrect prediction of behaviour of beams in cases where FRP debonding dominates. In the present investigation, both cases of perfect bond and slip between the concrete and FRP elements are modelled.

In the absence of lateral or out-of plane forces in the T-beams, two-dimensional analysis (plane stress) was adopted in the study. In the experiment, failure of the shear strengthened T-beams was characterised by opening of the CFRP overlap at the soffit with concrete pieces torn away at the CFRP bend zone. The localised failure was three dimensional in nature with the bend zone representing a region of high stress concentration. A 2D analysis will not simulate the localised

stress concentration at the bend zone or debonding of the CFRP but it is the intention of the present study to take a simplistic approach in modelling. The numerical analyses may predict a higher shear capacity for the strengthened beam, which may otherwise, fail sooner due to the localised stress concentration at the bend zone. However, from the experiment, the strains in the CFRP plates prior to failure were known. The experimental value can be used as an upper limit of the CFRP contribution in which to terminate the numerical analyses. As the 2D analysis may be overly simplistic, a three-dimensional (3D) analysis was also used in the study. It will later be established from both the 2D and 3D analyses that there were no indications of stress concentration in the concrete layer in the bend zone.

For the 2D analysis, the finite element models were created using four-node quadrilateral isoparametric plane stress elements. Initially, the models were created using higher order eight-node plane stress elements but difficulties were encountered in achieving results similar or even remotely close to the experiments. The analyses terminated prematurely due to non-convergence of solution despite adopting very relaxed convergence criteria or varying the load steps. Since the beam failure mode is that of shear, increasing the concrete shear retention factor significantly did not improve the solution either. The eight-node plane stress element models were numerically unstable. Nevertheless, selected results are presented for comparison against the four-node plane stress element models. For the 3D analysis, the finite element models were created using eight-node isoparametric solid brick elements. Preliminary analyses of models created using higher order twenty-node solid brick elements were also carried out but did not yield appreciable differences in the numerical results. In order to reduce the computational effort, subsequent analyses employed the eight-node elements. Selected results of the twenty-node elements are also presented for comparison against the eight-node element models.

The aims of the finite element modelling are to develop a general methodology for the modelling of the experimental T-beams both in a 2D and 3D environment, confirm the applicability of the FEM in modelling web bonded beams and supplement the experimental results. In its current form, the finite element method cannot simulate the type of failure observed in the experimental beams. It is the intention of the current study to establish whether or not the numerical models can

simulate the experimental trends adequately. The same non-linear finite element code described in Chapter 4 was used. The first phase of the numerical study involved the development of an accurate finite element model or base model of the control beam. Due to geometric constraints such as the CFRP plate location, it was necessary to generate three different base models, one for each of the shear-strengthened beams. The quality of the base models was assessed by comparing the numerical results with actual experimental measurements of the control beam. The second phase of the numerical study involved the simulation of the three base models with the presence of the external CFRP reinforcement.

8.2 Finite element idealisation

8.2.1 Two-dimensional finite element mesh (2D FE mesh)

The 2D finite element meshes generated for the various beams are illustrated in Figure 8.1. Since the cross-sectional geometry of the beams, loading and boundary conditions were symmetrical about the centreline, only half a beam was modelled. The concrete and CFRP plate were modelled using four-node quadrilateral isoparametric plane stress element (Q8MEM) shown in Figure 8.2. The element has eight degrees of freedom (dof) with two displacements, u_x and u_y, at each node. A 2 x 2 Gaussian integration scheme was adopted. The element size was maintained at or close to 52 mm x 52 mm for the concrete elements and 41.71 mm x 52 mm for the CFRP plate elements. Ten elements formed the entire depth of the beam with three elements used to represent the flange depth. The aspect ratios (length over height) were kept as close as possible to 1 with a maximum of approximately 2.

In models where slip between the concrete and CFRP plate was taken into account, the slip was modelled using the structural interface element (L8IF) shown in Figure 8.3. The element is similar to the structural interface element adopted in the finite element analysis of the bond specimens (CL12I) but based on linear interpolation and the 3-point Newton-Cotes integration scheme. The CFRP layer was superimposed on top of the concrete layer separated by the interface elements in between. Since the L-shaped CFRP plate was well anchored in the flange and soffit of the beam, it was assumed that perfect bond existed between the CFRP and concrete layer at these locations in the models. This means that the CFRP and concrete

elements share the same nodes in the flange and at the bottom of the beam as illustrated in Figure 8.4. In the web, there were two sets of nodes separating the concrete and CFRP layer. The interface elements were placed at both sides of the CFRP plate, allowing separate movements at each side. In models where perfect bond between the concrete and CFRP layer was assumed, the concrete and CFRP layer share the same nodes throughout. In the figure, the CFRP layer has been drawn at an offset from the concrete layer for the purpose of showing the position of the interface elements. In the model, no gaps existed between the concrete and CFRP element layer.

All the steel reinforcement in the T-beams, except for the transverse reinforcement in the flange, was modelled as embedded bars in the concrete elements hence assuming full strain compatibility or perfect bond between the two components. For the main flexural reinforcement, this assumption was considered to be reasonable since deformed bars were used. In the case of the shear reinforcement and longitudinal reinforcement in the flange, such assumption was made for the purpose of simplifying creation of the finite element mesh. Figure 8.5 shows the position of the steel reinforcement, drawn as broken lines, in the finite element mesh. The main flexural reinforcement is simplified in the model by ignoring the bent-up portion in the concrete overhang. The longitudinal reinforcement in the flange was also modelled.

In the experimental beams, a spreader beam was placed under each actuator to distribute the load over a small area. In the finite element model, a 25-mm thick steel plate, modelled using Q8MEM elements, was added at the load location to provide a more even load distribution and avoid stress concentration problems. The steel plate elements were assumed to have linear elastic properties.

The concrete elements directly under the load point and above the support were subjected to high compressive forces and preliminary analyses have revealed that these concrete elements underwent crushing, which caused the analyses to terminate prematurely. In the experimental beam, localised crushing in the region around the load points and supports were not observed to have occurred. To overcome the problem of localised crushing in the finite element models, selected

concrete elements around the load point and support were assumed to have linear elastic properties. The locations of the elements are shown in Figure 8.1.

The model was supported vertically at the base and horizontally at the beam's centreline with roller supports. Load was applied by means of a prescribed vertical displacement to a single node in the steel plate element. In all the models, concrete cracking was based on the smeared model approach. The same mesh was used for models created using higher order eight-node quadrilateral isoparametric plane stress elements (CQ16M). Models with bonded CFRP using the eight-node quadrilateral elements were not created since the results of the base models were inaccurate.

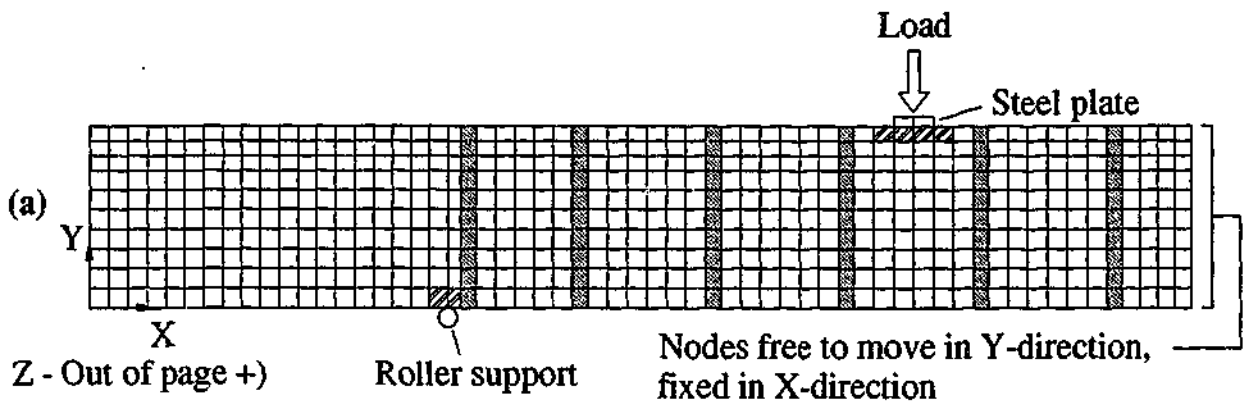

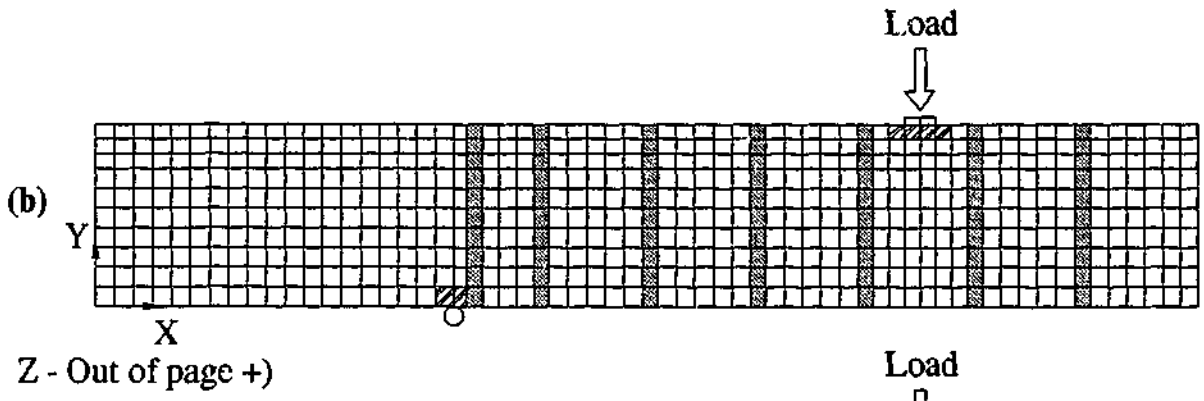

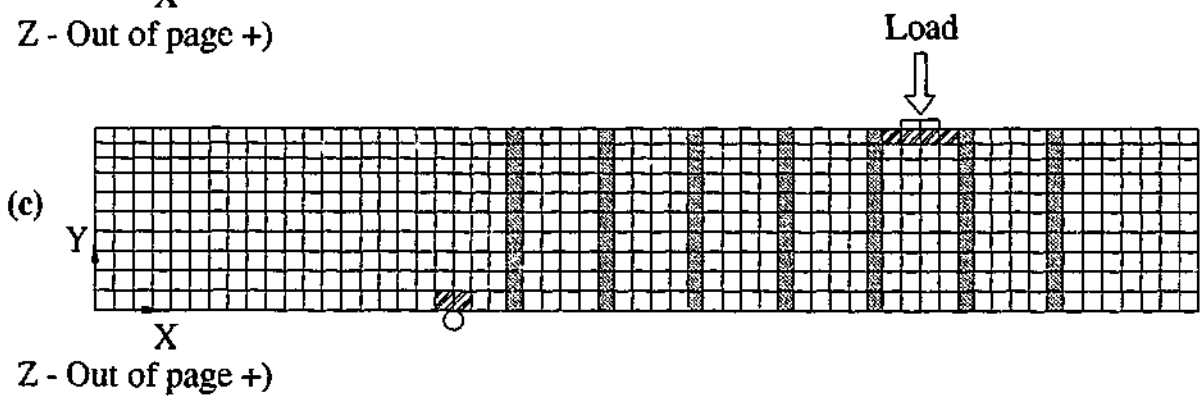

▨ - Concrete elements with elastic properties only (prevent localised crushing)
▩ - CFRP element location

Figure 8.1 - 2D FE mesh of beams (a) '0.75D' (b) '0.60D' and (c)'0.50D'

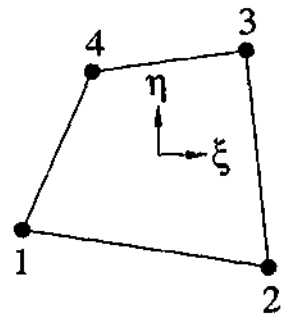

Figure 8.2 - Four-node quadrilateral isoparametric plane stress element (Q8MEM)

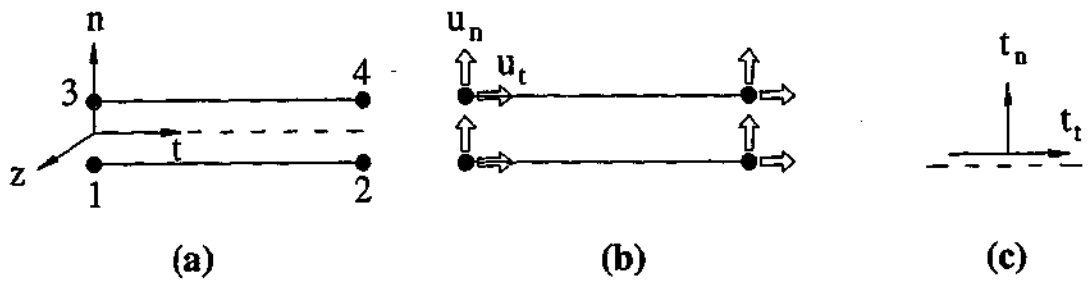

Figure 8.3 - 2+2 nodes structural interface elements (L8IF) (a) topology (b) displacements (c) tractions

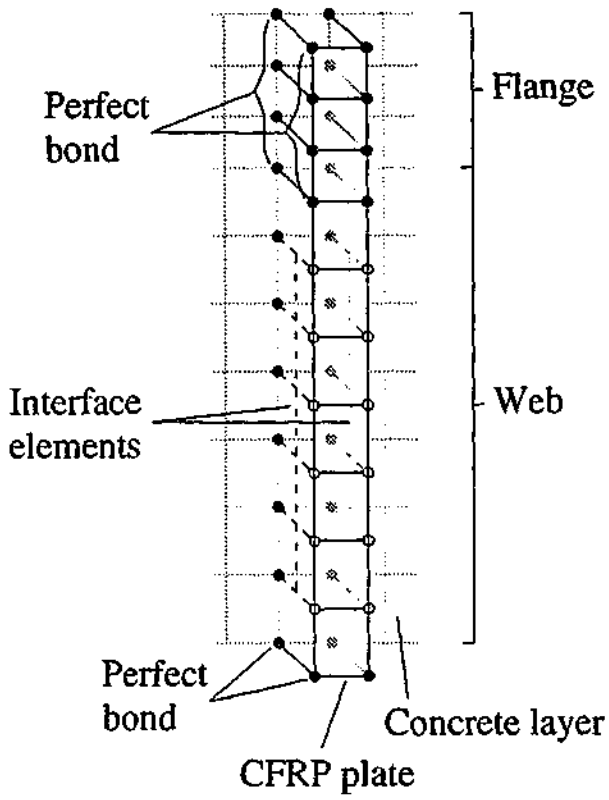

Figure 8.4 - Location of interface element in 2D FE mesh

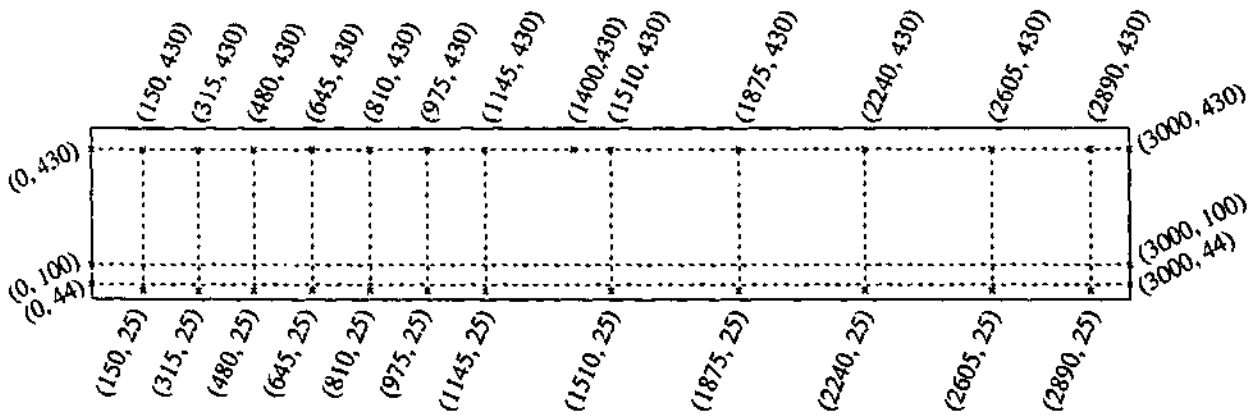

Figure 8.5 - Position of steel reinforcement in 2D FE mesh

8.2.2 Three-dimensional finite element mesh (3D FE mesh)

The 3D finite element meshes generated for the various beams are illustrated in Figure 8.6. As the beams were symmetrical about its length and width, only a quarter of the beam was modelled with the appropriate boundary conditions imposed. This reduced significantly the computational time and resource required in the numerical analyses. The concrete was modelled using the eight-node isoparametric solid brick element (HX24L) illustrated in Figure 8.7. The element has twenty four degrees of freedom with three displacements, u_x, u_y and u_z, at each node. A 2 x 2 x 2 Gaussian integration scheme was adopted. Compared to 2D analyses, the computational time and resource required for 3D analyses are significantly more. For that reason, the 3D mesh is coarser than the 2D mesh illustrated previously. The concrete element size in the web was maintained at or close to 50 mm x 55 mm x 60 mm. In the flange, the concrete element size was maintained at or close to 40 mm x 55 mm x 60mm. Ten brick elements formed the entire depth of the beam with three elements forming the flange depth.

The CFRP plate was modelled using the four-node quadrilateral isoparametric plane stress element Q8MEM (Figure 8.2). Plane stress elements were used due to the fact that forces carried by the CFRP plate were mainly in the in-plane direction. Out-of-plane forces were considered to be negligible. In addition, the CFRP plate has low bending stiffness. The CFRP element size was maintained at approximately 41.71 x 52.

The structural interface elements (L8IF) were modelled in a similar manner described for the 2D meshes. Figure 8.9 illustrates the location at which slip was modelled and perfect bond between the CFRP and concrete elements were assumed. The CFRP plate lap at the soffit was modelled as well and assumed to be perfectly bonded to the concrete elements. In the flange, the CFRP plate element was inserted between two concrete elements. Similar to the 2D models, no gaps existed between the concrete and CFRP element layer.

In the 2D meshes, the flexural reinforcement steel bars were modelled as single embedded bar reinforcement with the equivalent area. In the 3D meshes, the steel bars were modelled individually. Figure 8.10 illustrates the location of the steel

reinforcement in the 3D mesh. The flexural reinforcement started and terminated at the end faces of the models. The transverse reinforcement in the flange was also modelled. The first transverse reinforcement was positioned at 200 mm from the beam end and subsequent reinforcement at spacing of 200 mm until the mid-span.

In the 3D meshes, the steel plate under the load point was modelled as in the case of the 2D meshes. A line load was applied across the entire width of the flange, which resembled the experimental loading more closely. In the experiments, the spreader beam under each actuator was very stiff as it had been reinforced with additional stiffeners and steel plates. In the models, it was assumed that the line load displaced uniformly in the models. Load was applied by means of a prescribed vertical displacement to the entire row of nodes. Similar to the 2D models, the concrete elements near the load point and support were assumed to have linear elastic properties to prevent localised crushing.

The model was supported vertically at the base with roller support. At the mid-span, the nodes were free to displace vertically and laterally but were restrained longitudinally. At the mid-width, the nodes were free to displace vertically and longitudinally but were restrained laterally. In all the models, concrete cracking was based on the smeared model approach. The same mesh was used for models created using the higher order twenty-node isoparametric solid brick element (CHX60) illustrated in Figure 8.8. Models with bonded CFRP using the twenty-node solid brick elements were not created since the base models gave inaccurate results.

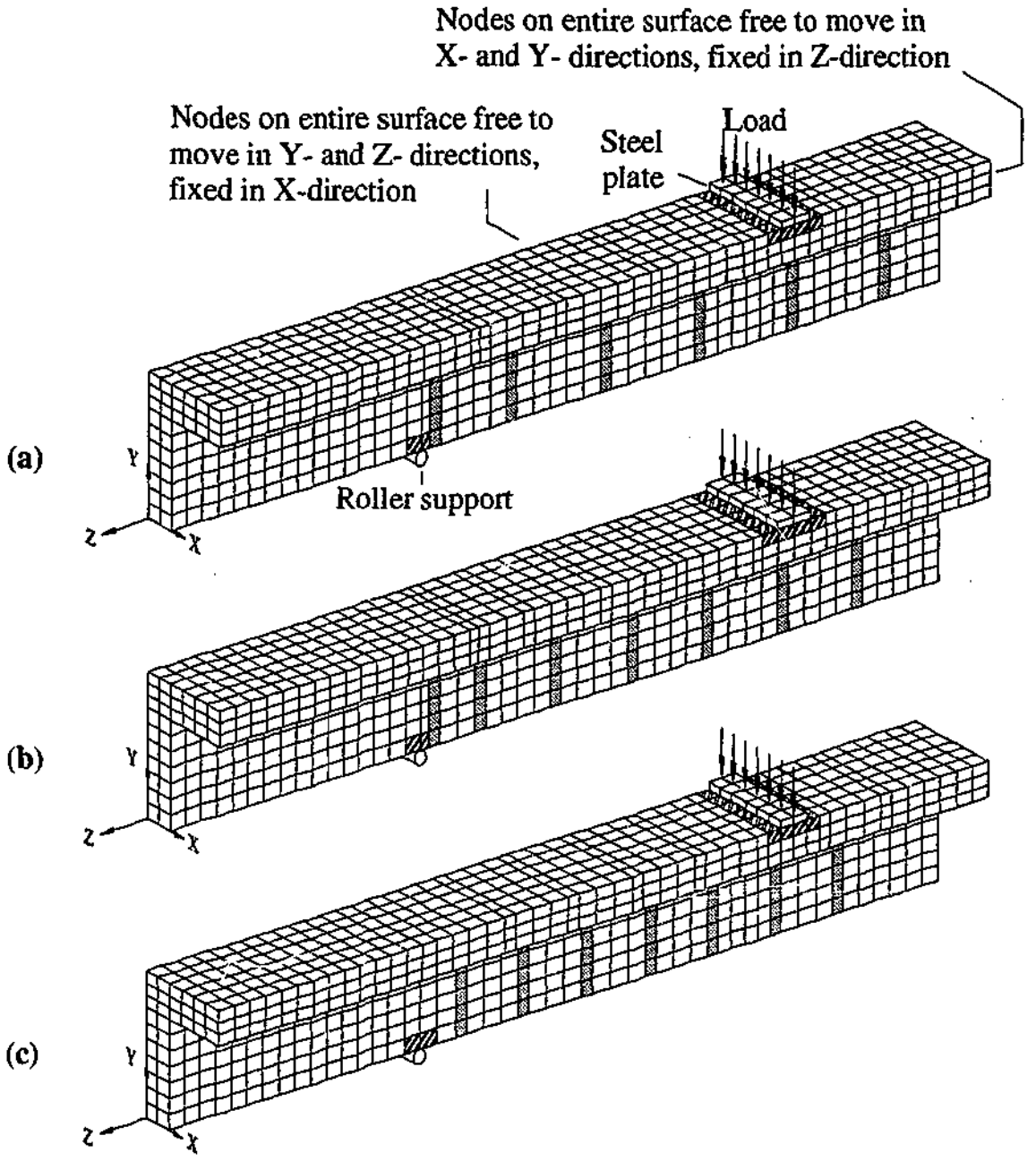

- Concrete elements with elastic properties only (prevent localised crushing)

- CFRP element location

Figure 8.6 - 3D finite element mesh of beams (a) '0.75D' (b) '0.60D' and (c)'0.50D'

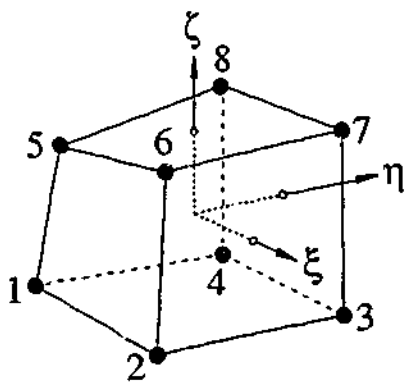

Figure 8.7 - Eight-node isoparametric solid brick element (HX24L)

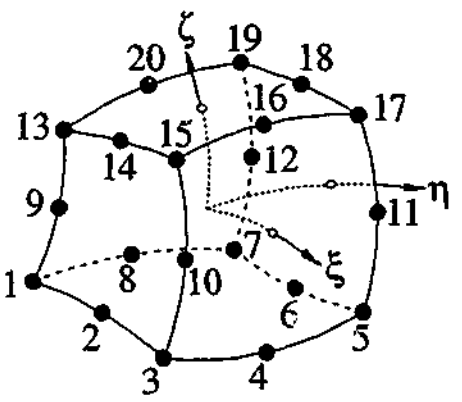

Figure 8.8 - Twenty-node isoparametric solid brick element (CHX60)

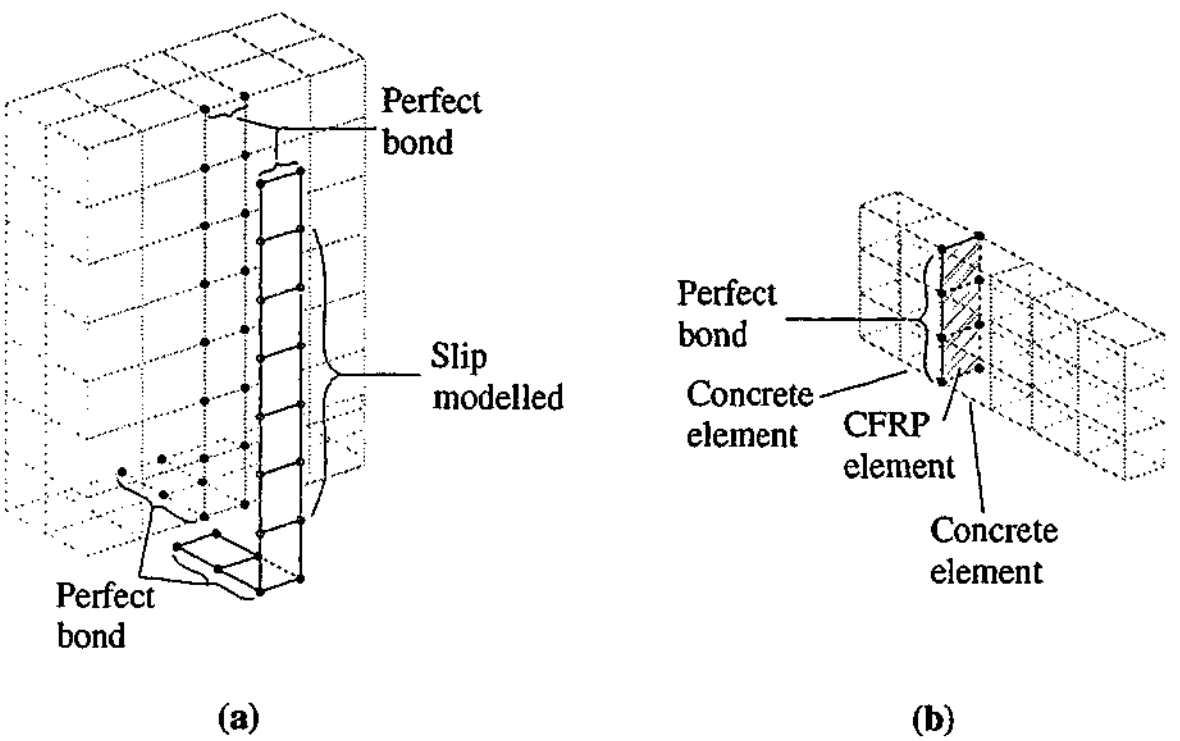

Figure 8.9 - Modelling of CFRP element in 3D mesh in (a) web and (b) flange

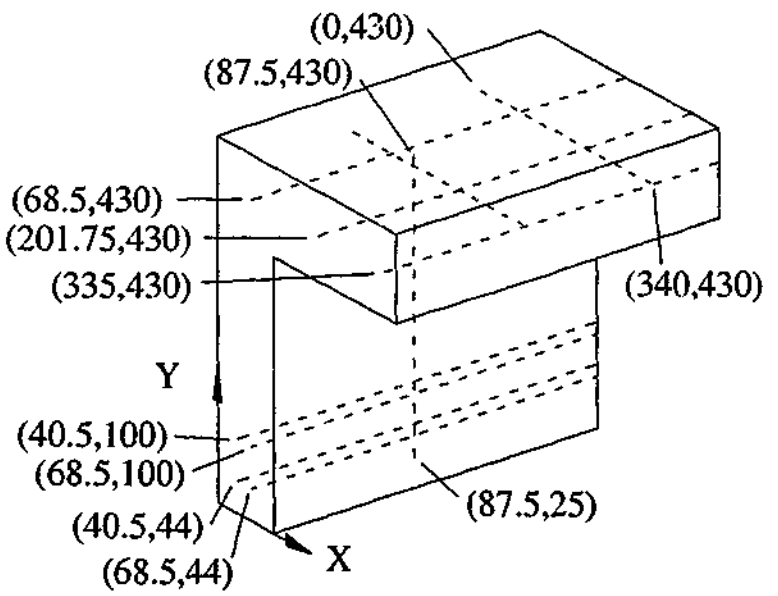

Figure 8.10 - Position of steel reinforcement in 3D finite element mesh

8.3 Material models

8.3.1 Concrete

The behaviour of the concrete was modelled using the same model that had been used in the numerical analyses of the bond specimens, which was the total strain-based constitutive model. A brief description of the model has been reported in Section 4.3.1. In the analyses, the input for the T-beam models was similar to the input for the bond specimen models. The Young's modulus was determined in accordance to SAI (2001) given by Equation 4.1. The density of concrete, ρ, was assumed as 2400 kg/m^3 and the Poisson's ratio, ν, was taken as equal to 0.2. The tensile strength of the concrete was determined using Equation 4.2. The average compressive strength of the core samples of the experimental T-beams was approximately 31.9 MPa. This value was adopted for all the models. The behaviour of the concrete in compression was described by the function of Thorenfeldt et al. (1987), illustrated in Figure 4.4 (a). In tension, the behaviour was based on a bilinear stress-strain relationship illustrated in Figure 4.4 (b). The fracture energy, G_f^I, was estimated using Equation 4.3 and Table 4.1, based on the maximum aggregate size of 14 mm. The values used in all the finite element models are summarised in Table 8.1.

Table 8.1 - Concrete properties adopted in finite element models

Properties	Values
Young's Modulus (MPa)	28555
Poisson's ratio	0.2
Compressive strength (MPa)	31.9
Tensile strength (MPa)	2.26
Fracture energy (Nmm/mm^2)	0.0648

In the bond specimen model, the shear stiffness of cracked concrete was assumed to be constant at 5% (β = 0.05) of the full shear stiffness of uncracked concrete. This value was adopted in the bond specimen models for numerical stability. The shear retention factor, β, is used to account for the effect of aggregate interlock in the concrete. The loading and deformation mechanism of the bond specimens was such that the effect of aggregate interlock was minor. In the case of the T-beams, the shear retention factor is an important parameter because shear

mechanism dominates the beam behaviour and failure mode. The shear stiffness of cracked concrete depends on numerous factors including but not limited to the amount of steel reinforcement present, concrete strength, aggregate size, crack width and stresses normal to the crack. The complex interaction between these factors makes it difficult if not impossible to determine the shear stiffness of the cracked concrete. In the finite element models, a trial and error approach was adopted. Several shear retention factor values were investigated in the base models (without CFRP plates) to determine the effects on the results. By comparing with the experimental results, an appropriate value was selected and subsequently used in the shear strengthened beam models. In the 2D models, the β values of 0.025, 0.05, 0.10 and 0.20 were investigated. It was found that the β value of 0.05 in all the base models gave comparable results to the control beam in the experiment. This value was used in the shear strengthened beam models.

According to the photogrammetry results in Chapter 7, the presence of the external CFRP shear reinforcement had limited the shear crack width in the strengthened beams. It can then be argued that the effect of aggregate interlock was significantly more in the strengthened beams compared to the control beam. This means that the use of a higher β value in the strengthened beam model is justified. However, the exact increase in the β value is unknown. Nevertheless, the initial value of $\beta = 0.05$ was adopted in all the strengthened beam models and the numerical results compared with the experimental results. This allows the determination of the increase in the beam's shear capacity due to the contribution of the CFRP plate only and difference in the predicted peak load in the different beams. It is intended to establish whether or not the numerical model can model the trend of increasing shear load capacity with decreasing CFRP reinforcement without increasing the β value. Higher β values of 0.06 and 0.07 were investigated to determine the difference in the predicted peak load, if any, between the different strengthened beams.

For the concrete elements directly under the load and above the support, linear elastic properties were assumed.

8.3.2 Steel reinforcement

The main flexural and shear steel reinforcement in the finite element models were assumed to be an isotropic linear elastic material up until the yield point. Yielding of the reinforcement was based on the Von Mises yield criterion with strain hardening. The values of Young's Modulus and yield stresses adopted in the models were based on the tensile tests performed and are summarised in Table 8.2. For the flexural reinforcement in the beam flange and the steel plate under the load point, a linear-elastic material was assumed.

Table 8.2 - Steel properties adopted in finite element models

Bar type	Young's modulus (MPa)	Yield stress (MPa)
Main flexural reinforcement	188502	445
Shear reinforcement	204411	351
Flexural reinforcement in flange	200000*	400
Steel plate	200000*	-

* Properties not tested. Value was assumed

8.3.3 CFRP plate

The CFRP plate was modelled as an orthotropic linear elastic material with properties described in the experimental aspect of the study. The assumption of linear elastic behaviour is reasonable since it was observed in the experimental beams that failure was governed by concrete fracturing. Table 8.3 summarises the CFRP plate properties used in the finite element models. Several of the CFRP properties were assumed as tests were not carried out and the manufacturer provided no information. The Young's Modulus in the lateral direction was assumed to be five percent of the Young's Modulus in the longitudinal direction with the shear modulus assumed at three percent. Since loading is mainly along the longitudinal direction of the CFRP plate, the contribution in stiffness in the lateral direction is insignificant given the unidirectional property of the plate and small width compared to its length. The effect on the overall behaviour of the beam is insignificant as it is localised to the region of concrete where the strips were bonded. Therefore, the use of exact values for the properties in the lateral direction is not as crucial as in the longitudinal direction.

Parametric studies into the effects on the beam behaviour of varying the properties of the CFRP plate were not carried out. It has been established from the finite element analyses of the bond specimens that variations in the longitudinal stiffness of the CFRP plate between 125000 and 155000 MPa do not have a significant effect on the general bond behaviour of the models. The shear transfer mechanism between the concrete and CFRP plate is fairly similar in the case of the bond specimens and T-beams. In both cases, loading is mainly in the longitudinal direction of the CFRP plate and debonding occurs in the concrete layer. In the 2D and 3D models, the thickness of the CFRP plates was set at 2.62 mm (2 x 1.31) and 1.31 mm respectively.

Table 8.3 - CFRP plate properties adopted in finite element models

Properties	Values
Young's Modulus (MPa) - longitudinal	137345
*Young's Modulus (MPa) - lateral	6867
*Poisson's ratio, ν_{xy}	0.3
*Shear modulus, G_{xy} (MPa)	4120

* Properties not tested. Value was assumed

8.3.4 Bond behaviour between concrete and CFRP plate

The bond behaviour between the concrete and CFRP plate was modelled using the structural interface element shown in Figure 8.3. In the 2D models, the bond behaviour was modelled instead of the adhesive layer because it was not possible to simulate debonding of the CFRP plate. Debonding occurs as a result of localised shearing of the concrete layer directly under the CFRP plate and in a plane stress model, there is only a single plane of concrete elements. The interface element is assigned properties to simulate the general bond behaviour between the CFRP plate and concrete layer including the debonding of the CFRP. In the 3D models, a different approach was adopted. Unlike the 2D models, the out-of-plane behaviour was simulated in the 3D models. Debonding of the CFRP due to cracking in the concrete can be modelled. Therefore, the adhesive layer properties adopted for the bond specimen models in Section 4.5.1.1 can be used. Introducing debonding characteristics into the interface element can weaken the structure as the debonding

effect is taken into account twice. However, there are only two layers of concrete elements under the CFRP plate elements and so the mesh size used may be too coarse to model the localised shearing of the concrete layer directly under the CFRP plate elements. As a result, debonding of the CFRP element layer may not be simulated properly. Figure 8.11 shows an example of shearing of the concrete layer under the CFRP plate in a coarse mesh and fine mesh. It is clear that to ensure shearing of the concrete layer is as close as possible to the CFRP plate, a fine mesh is required. To be able to model correctly and accurately the debonding of the CFRP due to shearing of the concrete layer would require a mesh density similar or close to those created for the bond specimens. This is undesirable because the computational time and resource required would increase significantly particularly for a 3D model. As a compromise, the shear stiffness modulus of the interface elements can be reduced to account for the coarseness of the mesh.

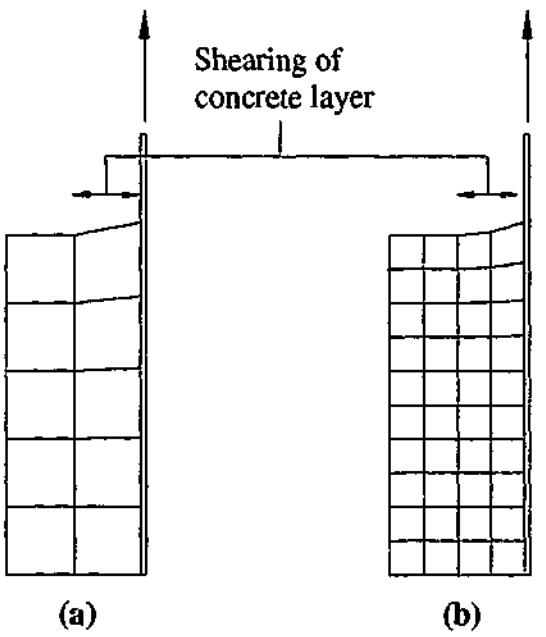

Figure 8.11 - Shearing of concrete layer in (a) coarse mesh and (b) fine mesh

For the 2D models, the bond behaviour between the concrete and CFRP plate was simulated using a simple bond-slip model based on the numerical results of the bond specimen models. Figure 4.10 from Section 4.5.1.4, which illustrates the load slip behaviour of the finite element bond models with various bonded length, has been reproduced herein as Figure 8.12. The concrete strength adopted in the models was 30 MPa, which is comparable to the concrete strength adopted in the T-beam models. The load shown in the figure corresponds to the total load applied to the model and

the slip is measured at the locations shown in Figure 4.7. By dividing the load with the effective bonded area of the joint, the average shear stress development illustrated in Figure 8.13 is obtained. The effective bond length of the bond specimens as determined from the finite element analyses was reported earlier to be approximately 145 mm. The effective bond area is then the product of the CFRP width and the lesser of the bonded length or 145 mm.

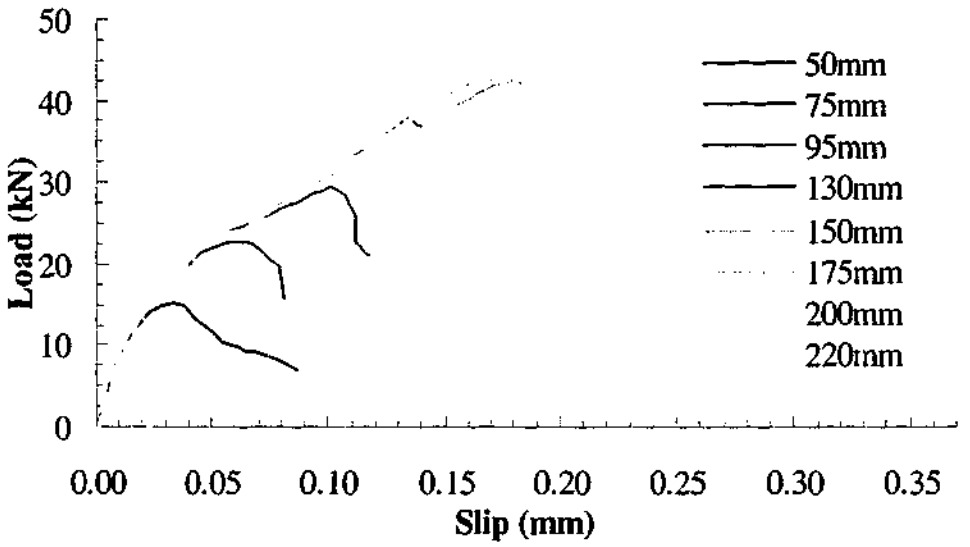

Figure 8.12 - Load slip behaviour of finite element bond specimens

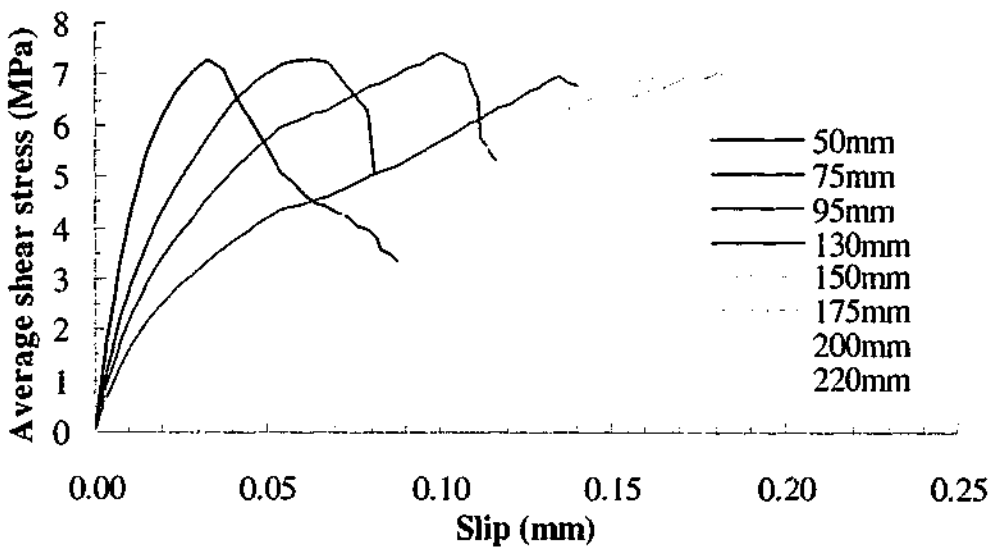

Figure 8.13 - Average shear stress development of finite element bond specimens

The responses shown in Figure 8.13 account for deformations in the concrete, adhesive, CFRP and most importantly debonding due to cracking in the concrete layer. Therefore, a simple bond-slip model for the interface elements can be

obtained from the figure. The issue now arises as to which bond lengths should be adopted in the 2D T-beam models. In the T-beam models, the element size in the web is approximately 52 mm x 52 mm. Therefore, the average shear stress versus slip response of the 50 mm was adopted as the basis of the bond slip model. Six bond slip models (D_{22}) were investigated for the interface elements of the 2D T-beam models, four of which are shown below in Figure 8.14. The other two bond models are the assumptions of perfect bond and no bond between the CFRP and concrete elements. In the case of the 'No bond' model, the CFRP reinforcement is still anchored at the flange and soffit of the beam. There are simply no interface elements between the concrete and CFRP at the beam web (see Figure 8.4 and Figure 8.9). The peak stress of the bond slip models is set at 7.3 MPa. 'BS4' is similar to 'BS1' except that force is continuously transferred to the CFRP layer once the peak shear stress is reached. The normal stiffness modulus of the interface elements (D_{11}) is assumed to be constant at 487 N/mm^2/mm, which corresponds to the slope of the bond slip model 'BS1'. In the 2D models, the 'thickness' or transfer width of the interface element was set at 41.71 mm.

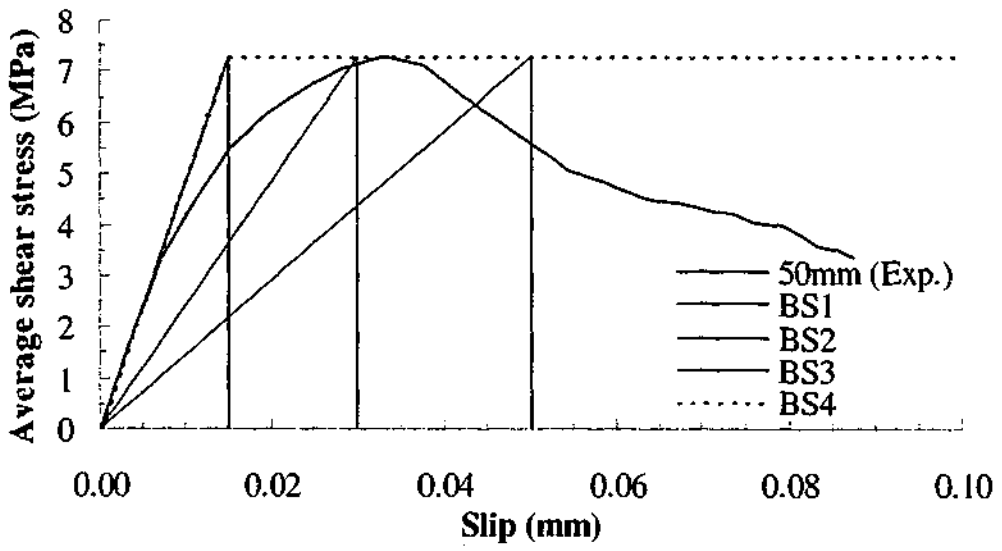

Figure 8.14 - Bond-slip models for interface elements of 2D T-beam models

For the 3D models, three bond slip models were investigated for the interface elements as outlined in Table 8.4. Bond slip model 'LS1' has material properties similar to the interface elements of the bond specimen models in Section 4.5.1.1. Bond slip 'LS2' was set as the slope of the 2D bond slip model 'BS1'. The 'thickness' or transfer width of the interface element was set at 20.855 mm.

Table 8.4 - Bond slip models for interface elements of 3D T-beam models

Bond slip model	D_{11} (N/mm^3)	D_{22} (N/mm^3)
Perfect bond (PB)	-	-
LS1	4266	1557
LS2	4266	487

8.4 Solution procedure

Several numerical methods can be used to solve for non-linear problems. In the present study, the combined incremental-iterative procedure has been used. In the 2D models, load was 'applied' in increments of 0.2 mm initially and then at smaller increments, which was selected subjectively on a case by case basis. In the 3D models, the initial increments were set to 0.3 mm to reduce the computational time required. The increments adopted in the analyses gave comparable results to the experimental control beam. Preliminary analyses using smaller initial load steps to the above generally gave comparable results to the experimental control beam but computational time required was significant longer and more susceptible to premature solution divergence. At each load step of the analysis, the modified Newton-Raphson iterative scheme was used to bring the internal forces to an acceptable level of equilibrium, which was set subjectively. The convergence criterion adopted was based on the energy norm criterion expressed as Equation 4.7. The criterion adopted for the T-beam analyses were less strict compared to the bond specimen analyses. The tolerance for convergence was set to 0.0005 as a compromise between computational time and accuracy of the solutions. The maximum number of iterations for each load step was set to 300.

Similar to the bond specimens, cracking of concrete in the T-beams was modelled by the smeared cracking method. As a result, the discrete shear cracks observed in the experimental T-beams cannot be replicated exactly in the finite element models. The use of the smeared cracking approach also means that the fracture type failure of concrete at the bend zone and separation of the flange from the web as observed in the experimental beam '0.50D' cannot be simulated exactly. The numerical failure point and hence peak load can be difficult to determine. Unlike the bond specimen models, the load-displacement curves of the T-beam models showed a

gradual decrease in stiffness with little or no plateauing followed by either a sudden drop in the load or solution divergence. The numerical models did not exhibit any softening behaviour. The criterion for 'failure' of the T-beam was initially assumed as the point at which the sudden drop in the load occurred or solution diverged. The step sizes leading up to this point were then reduced accordingly and the model reanalysed again. This process was repeated until the step sizes leading up to the failure point were reduced generally to 0.05 mm or 0.025 mm. 'Failure' of the beam model can then be assumed to have occurred. Due to the complex mechanism involved in shear deformation, the experimental peak load may not be predicted exactly by the finite element models. In the current investigation, the numerical solution was considered to be good when the predicted peak load was within 10 to 20% of the experimental peak load. Similar to the bond specimen models, irregularities in the load-displacement curves of the models such as sudden drop in load before peak load has been reached, flattening of the curve and sudden change in the stiffness are examined as well and logically assessed.

8.5 Results of non-linear finite element analyses

8.5.1 Verification of the finite element base models

8.5.1.1 Introduction

To verify that the finite element base models are simulating the behaviour of the experimental control beam properly, four items from the experimental and numerical results are compared. They are the load displacement behaviour, crack patterns at failure, and the load strain development in the steel shear and flexural reinforcement. Three different base models, one for each of the shear-strengthened beams, were generated for both 2D and 3D analyses as illustrated in Figure 8.1 and Figure 8.6. The reader is reminded that the base models have no external CFRP reinforcement. Due to the difference in CFRP reinforcement location, three different meshes were generated, one for each of the shear-strengthened beams. The concrete and steel properties used in the analyses are summarised in Table 8.1 and Table 8.2. The shear retention factor β used in the models was 0.05.

8.5.1.2 Load displacement behaviour

The load displacement behaviour of the experiment and finite element models are compared in Figure 8.15. For both the 2D and 3D models, the displacement of the beam was obtained from a single node. The node was located at the bottom of the beam at the line or intersection of the planes of symmetry. The load shown in the plots corresponds to the applied load, which is the same as the support load. The load displacement curves were plotted either up to the step at which significant decrease in the load carried by the beam was first observed or up to the step prior to solution divergence. The experimental curve shown in the plots correspond to the shear load versus mid-span deflection behaviour of the control beam at the failure (west) span.

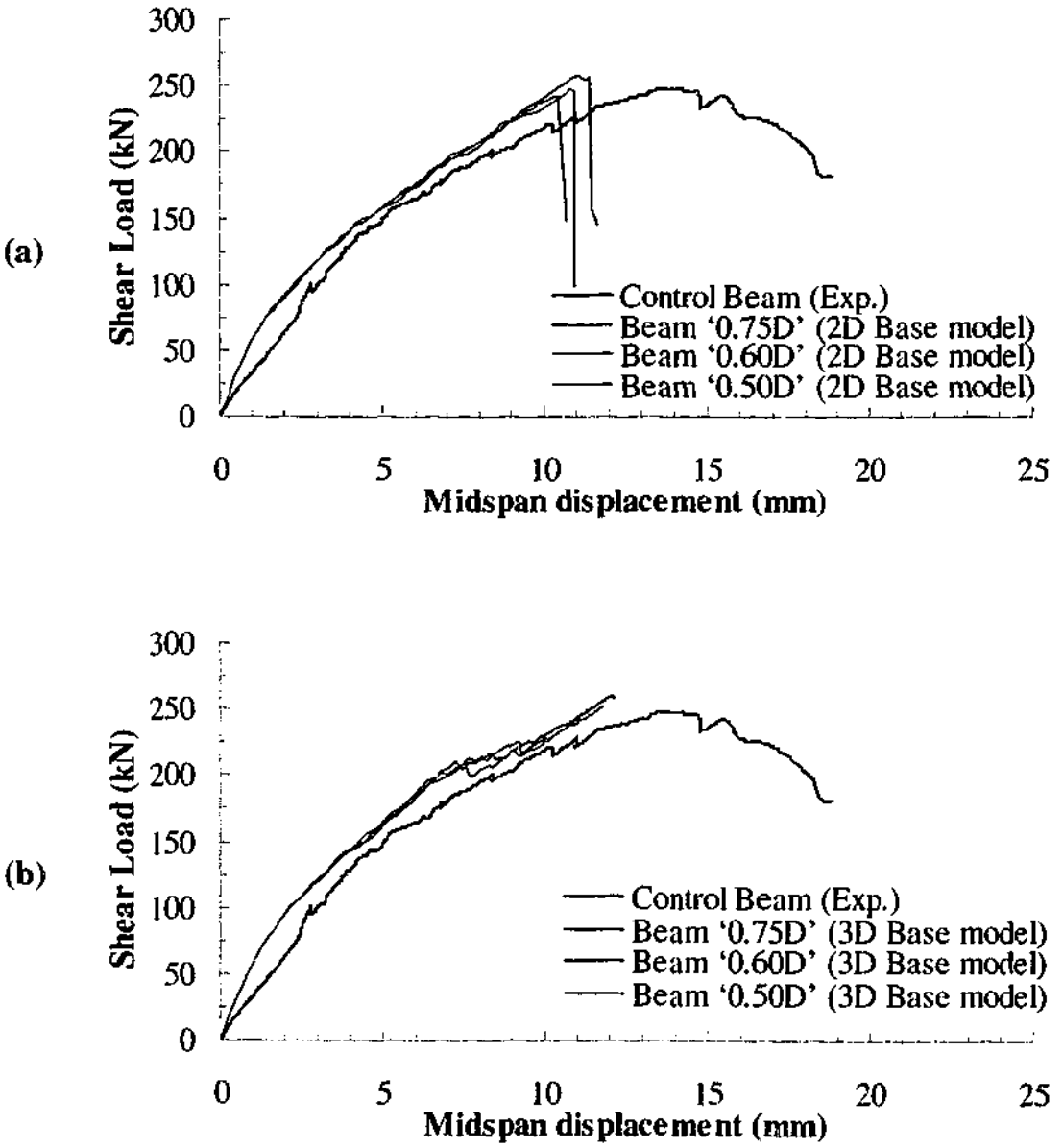

Figure 8.15 - Load displacement behaviour of control beam and numerical analyses of (a) 2D base models (4-node) and (b) 3D base models (8-node)

In both the 2D and 3D analyses, it can be observed that the load slip behaviour of the experiment and numerical models were comparable. At the early stages of loading, the numerical models exhibited slightly higher stiffness compared to the experimental beam. This is partially attributed to the equilibrium iteration process to balance the internal forces with the external applied forces to within a prescribed tolerance. In general, a stricter tolerance (convergence criteria) will yield a less stiff response but will require significantly more computational effort. Another possible reason for the discrepancy in the stiffness is that slack exists in the in the experimental environment. This can result in a less stiff response in the load displacement behaviour of the beam. Between the shear load level of 100 to 200 kN, the numerical and experimental stiffness of the load displacement curves were similar. Beyond this load level until the peak load, the numerical models exhibited a stiffer response compared to the experiment beam. This is attributed to the smeared crack approach adopted for concrete cracking in the numerical analyses. In the models, the discrete continuous shear cracks observed in the experimental beams were modelled as discontinuous cracks distributed over a band of elements. In the experiment, the opening of the shear crack is concentrated to a single continuous crack location whereas in the finite element models, the opening of the shear crack is distributed over several discontinuous locations. As a result, the deformation of the beam at a given load is smaller in the finite element models compared to the experimental beam hence the stiffer response in the load deflection behaviour. The higher stiffness at first loading and at higher load levels resulted in the displacement at the peak load to be smaller in the finite element models compared to the experimental beam. Nevertheless, based on the material models and properties outlined earlier, the predicted peak shear loads were reasonably close to the experiment.

As mentioned in Section 8.4, it can be observed that the numerical models do not exhibit any softening behaviour. In the 2D models, failure was characterised by a sudden and significant decrease in load. In the 3D models, failure was characterised by a solution divergence. The shear cracks had formed and propagated to such an extent that further increase in load or deformation cannot be sustained. In addition, it has been established in Section 8.5.1.4 that the stirrups had yielded. The combination of shear cracks and steel yielding caused the sudden load decrease observed in the 2D

solution divergence. Both the 2D and 3D models gave comparable responses from the start of the loading to approximately 200 kN. Beyond this load level, the 3D models exhibited a less stiff response compared to the 2D models.

The load displacement behaviour of the 2D and 3D higher order element base models of beam '0.75D' are illustrated in Figure 8.16. In the 2D model, the peak load achieved was approximately 145 kN, which was significantly smaller than the experiment peak load of 247.1 kN. As mentioned in Section 8.1, the analyses terminated prematurely due to non-convergence of solution despite adopting very relaxed convergence criteria or varying the load steps. Increasing the concrete shear retention factor significantly did not improve the solution either. The 3D 20-node model gave comparable load displacement response to the experimental control beam but required significantly more computational effort than the 3D 8-node model. Apart from difference in the peak load achieved, the load displacement responses of the 2D and 3D models were similar. Preliminary analyses of the base models of beams '0.60D' and '0.50D' gave similar results. Due to numerical instability of the 2D models and increased computational effort required in the 3D models, further investigation into models using the higher order element models were not pursued.

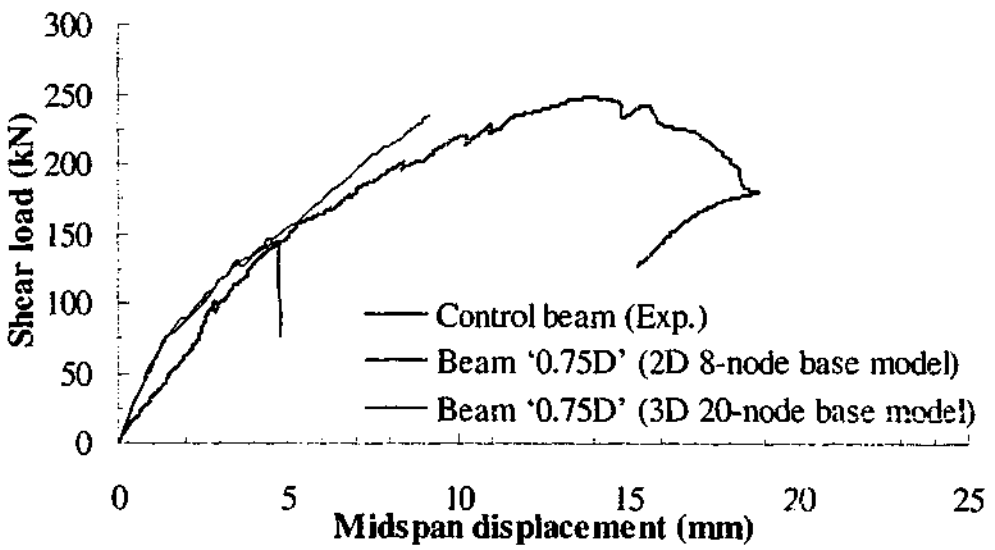

Figure 8.16 - Load displacement behaviour of control beam and numerical analyses of 2D (8-node) and 3D (20-node) base models of beam '0.75D'

8.5.1.3 Behaviour of main flexural reinforcement

The behaviour of the main flexural reinforcement of the experiment and finite element models is compared in Figure 8.17. The experimental result corresponds to readings of strain gauge MWB of the control beam (see Figures 5.4 and 5.7). For the 2D models, the strain results were obtained from a single gaussian point of the bottom main flexural reinforcement directly under the load point. In the case of the 3D models, the strain results were obtained from the bottom and outermost flexural reinforcement. The load-strain curves were plotted up to the step at which peak load was reached. The load shown in the plots corresponds to the applied load, which is the same as the support load.

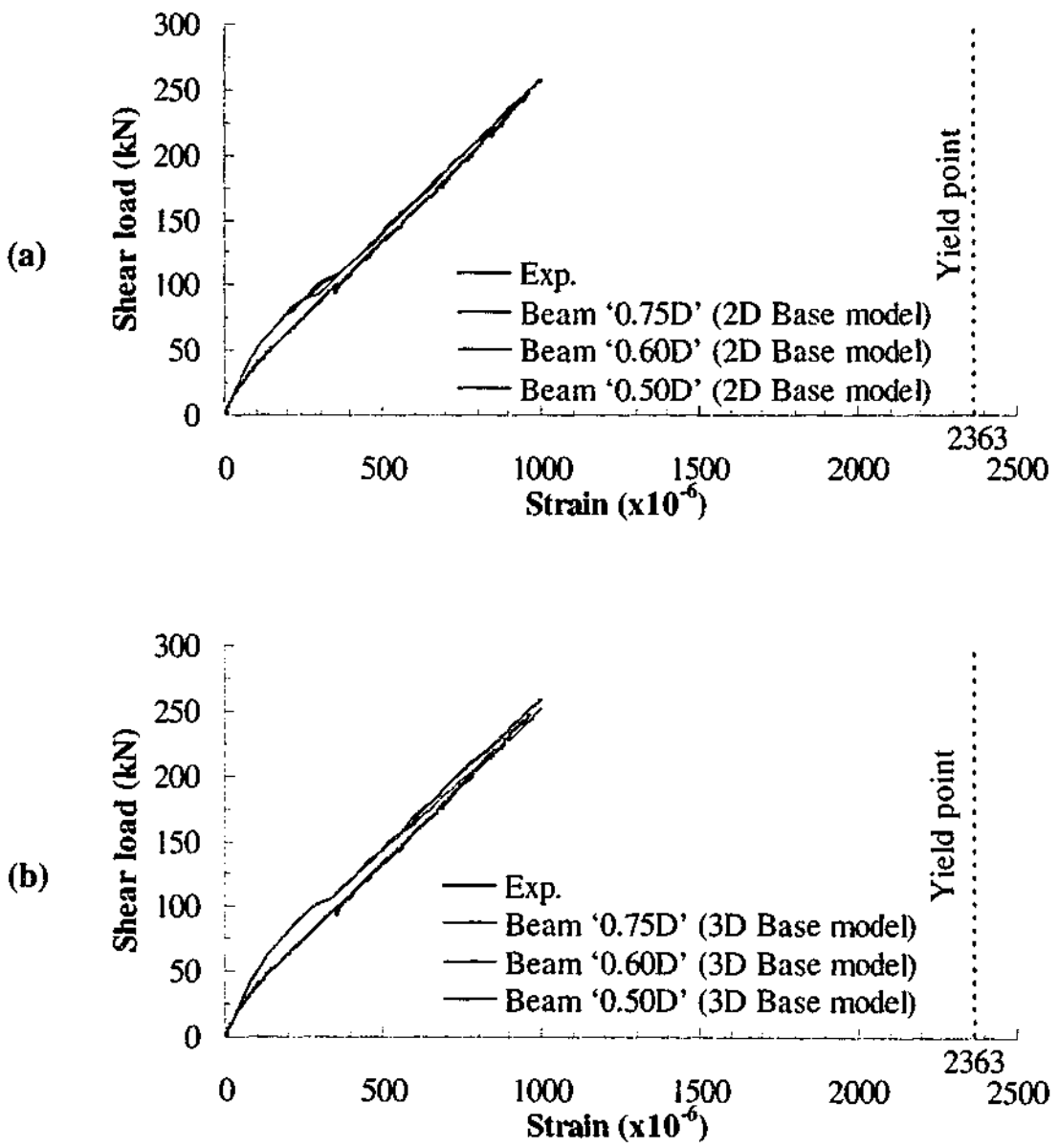

Figure 8.17 - Behaviour of the main flexural reinforcement of the control beam and (a) 2D base models (4-node) and (b) 3D base models (8-node)

Apart from the higher initial stiffness, it can be observed from the plots that the 2D and 3D models gave similar load strain response to the experimental control beam. Similar to the experiment, the reinforcement strained fairly linearly with load until the peak load. The main reinforcement did not yield indicating that flexural failure did not occur. Although perfect bond between the concrete and reinforcement was assumed, the numerical results gave comparable results to the experiment.

8.5.1.4 Behaviour of shear reinforcement

Figure 8.18 to Figure 8.23 compare the shear reinforcement behaviour of the 2D and 3D FE models with the experimental control beam. The locations of the stirrups being compared are illustrated in Figure 5.3. Figures (a) and (b) show the load strain responses of the stirrup in the shear span closest to the support and load point respectively. For the finite element models, the strain results were obtained from single gaussian point (S1 to S4) located closest to the actual position of the strain gauge in the experimental control beam. The load-strain curves were plotted up to the step at which peak load was reached.

(a)

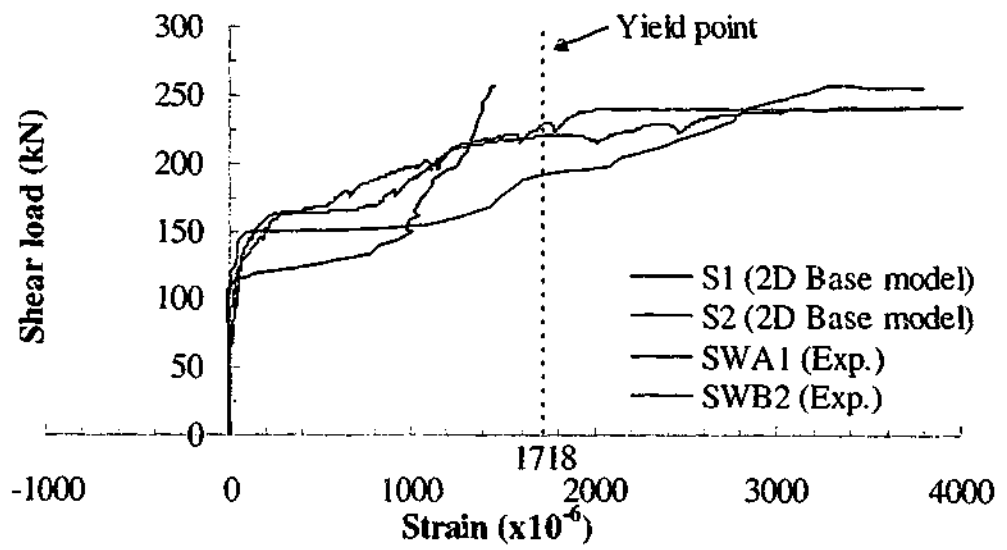

Figure 8.18 - Behaviour of shear reinforcement of the control beam and beam '0.75D' 2D base models (4-node) at stirrup locations (a) S1, S2 and (b) S3, S4

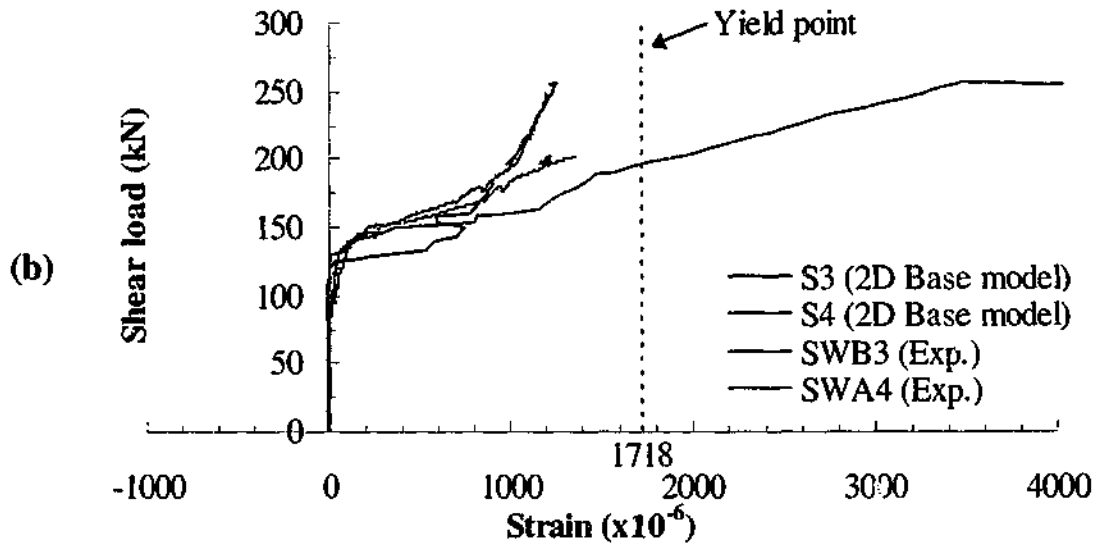

Figure 8.18 (continued) - Behaviour of shear reinforcement of the control beam and beam '0.75D' 2D base models at stirrup locations (a) S1, S2 and (b) S3, S4

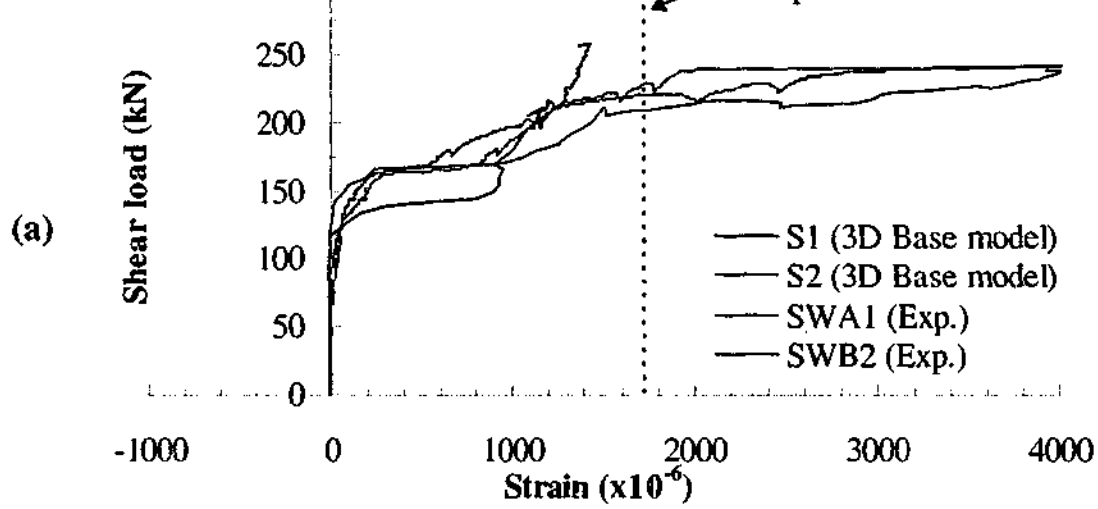

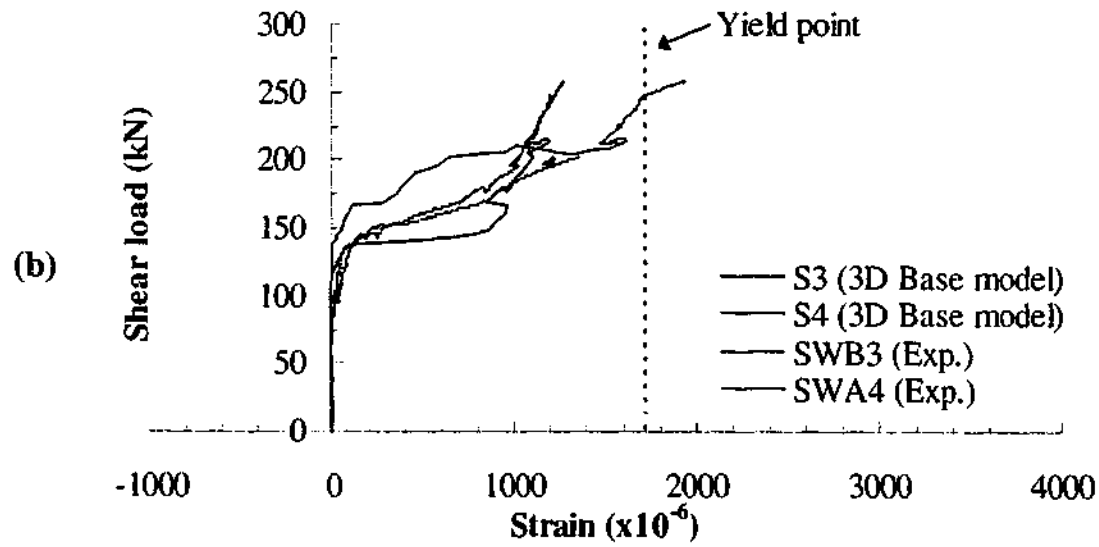

Figure 8.19 - Behaviour of shear reinforcement of the control beam and beam '0.75D' 3D base models (8-node) at stirrup locations (a) S1, S2 and (b) S3, S4

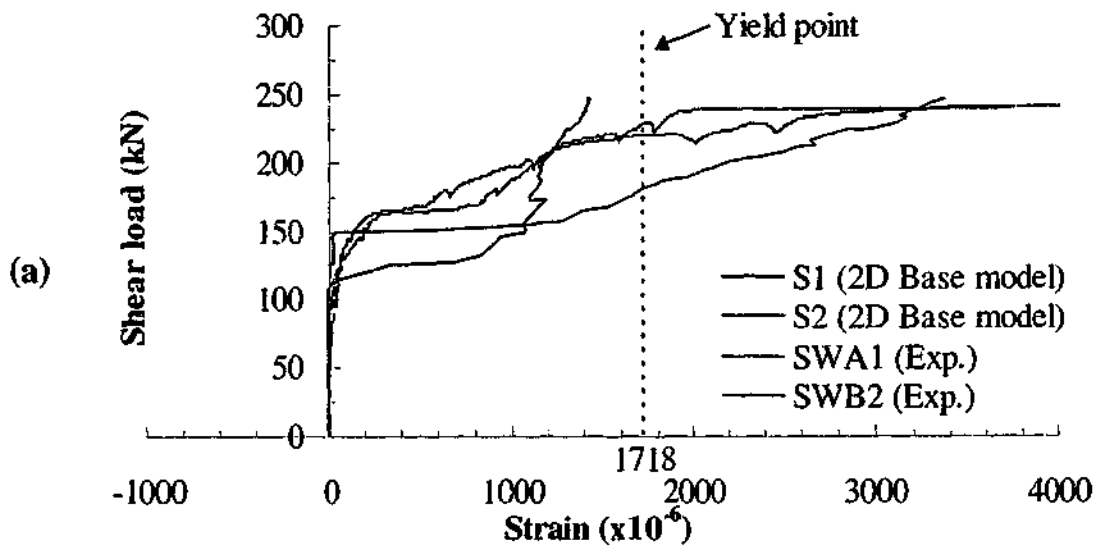

Figure 8.20 - Behaviour of shear reinforcement of the control beam and beam '0.60D' 2D base models (4-node) at stirrup locations (a) S1, S2 and (b) S3, S4

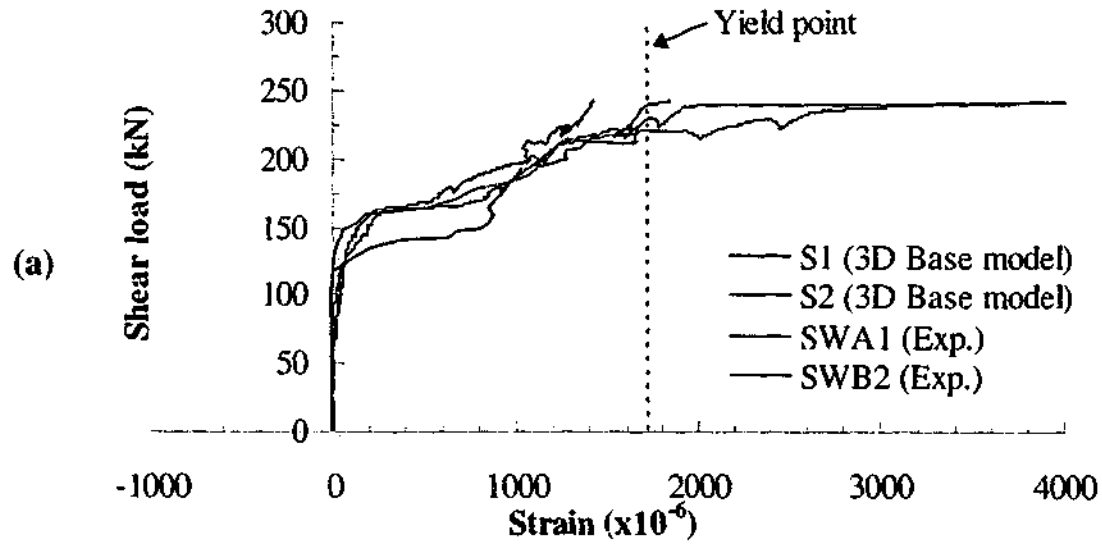

Figure 8.21 - Behaviour of shear reinforcement of the control beam and beam '0.60D' 3D base models (8-node) at stirrup locations (a) S1, S2 and (b) S3, S4

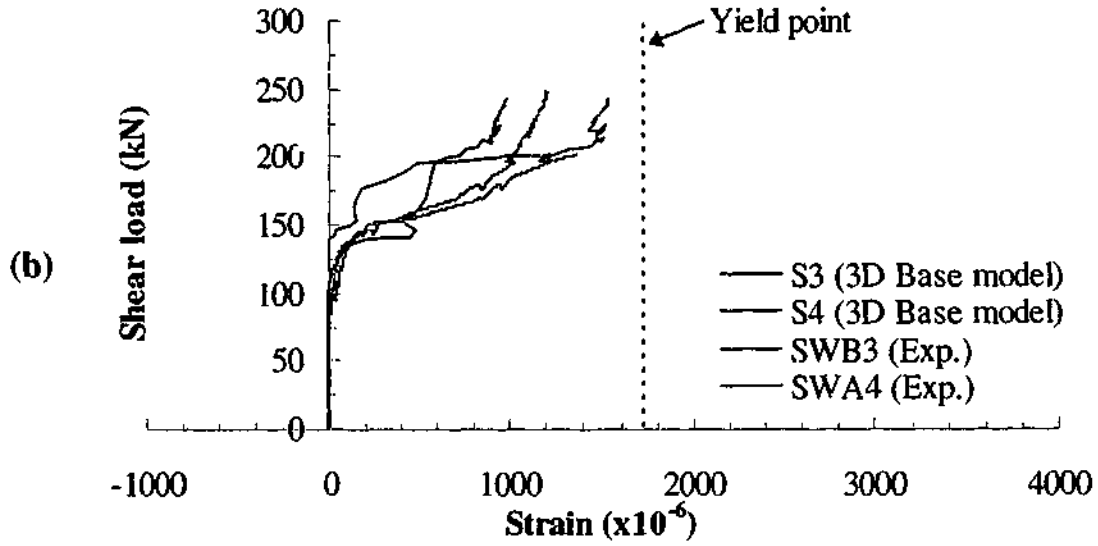

Figure 8.21 (continued) - Behaviour of shear reinforcement of the control beam and beam '0.60D' 3D base models at stirrup locations (a) S1, S2 and (b) S3, S4

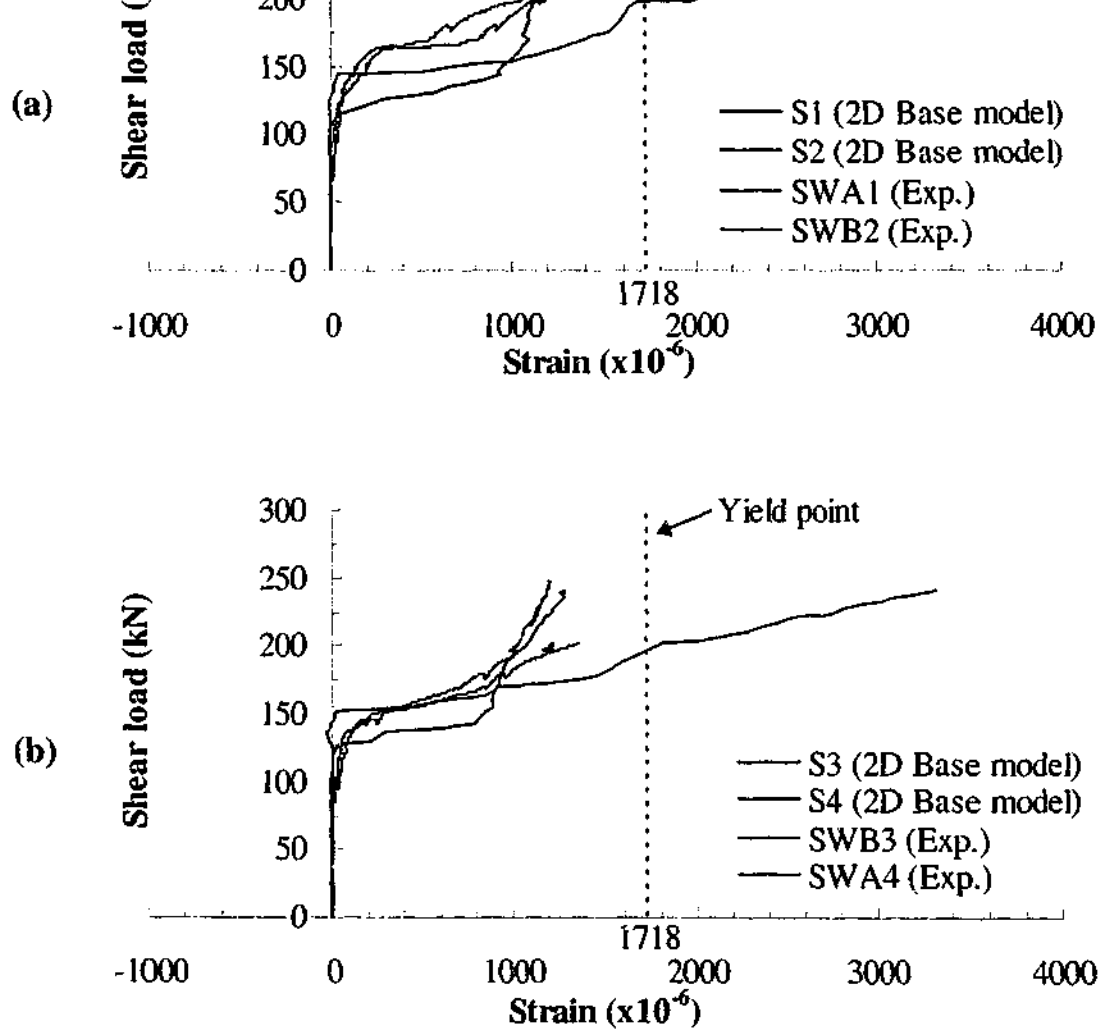

Figure 8.22 - Behaviour of shear reinforcement of the control beam and beam '0.50D' 2D base models (4-node) at stirrup locations (a) S1, S2 and (b) S3, S4

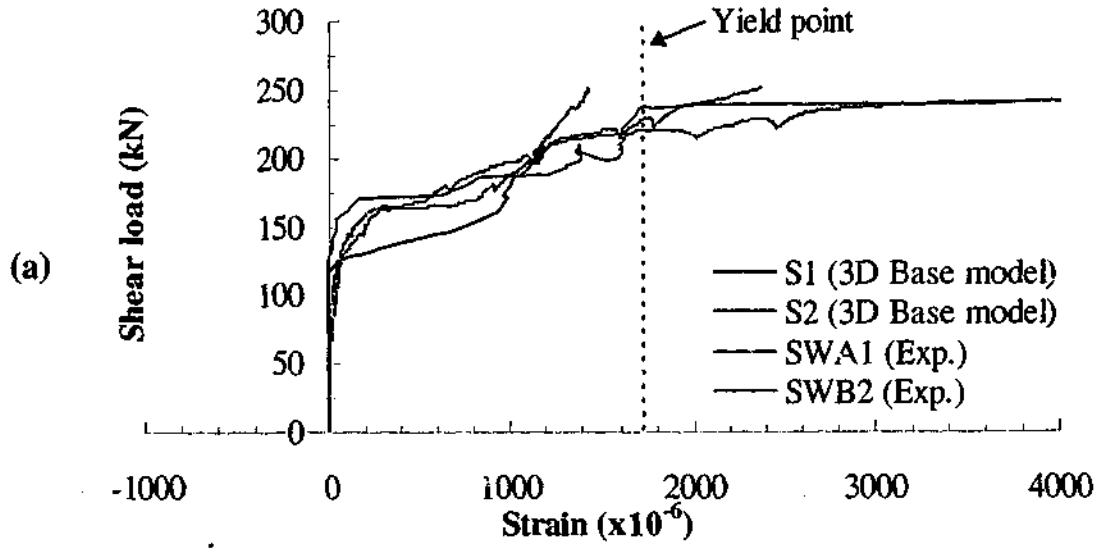

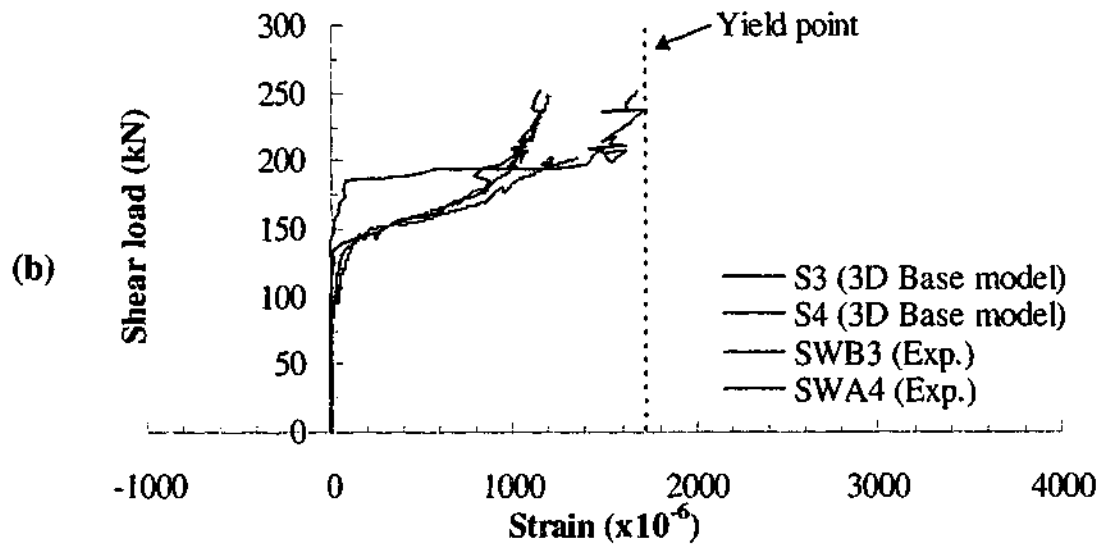

Figure 8.23 - Behaviour of shear reinforcement of the control beam and beam '0.50D' 3D base models (8-node) at stirrup locations (a) S1, S2 and (b) S3, S4

It can be observed from the plots that the experimental load strain responses of the stirrups are simulated adequately by the 2D and 3D models. The general trend predicted by the FE models is similar to the experimental results. The load level at which the strain began to increase significantly is comparable to the experimental beam. In the experiment, the second stirrup from the support in the shear span yielded before the peak shear loads were reached at approximately 230 kN. The stirrup closest to the load point in the shear span did not yield when failure occurred. It should be noted that the reading from the strain gauge SWA4 became erratic sometime before failure of the beam. Therefore only a partial load strain response has been shown. The load strain response of SWA4 indicated that the stirrup would have yielded if it continued its current trend but other strain gauges on the same stirrups

strongly indicated otherwise (see Figure B.2). In the finite element models, the curves S1 indicate that the stirrup did not yield but curves S2 indicate otherwise. This is attributed to the assumption of perfect bond between the stirrup and concrete elements. In the experiment, slip between the stirrups and surrounding concrete allows for a more uniform loading along the entire stirrup length. In the finite element models, the strains are high at the location of concrete elements that have cracked or are subjected to high forces. Since perfect bond between the stirrups and concrete elements are assumed, this means that the strains in the stirrups will be high as well and are localised to those particular concrete element locations. In order to determine whether the stirrup has yielded or not in the finite element models, the average strain along the entire length was calculated at the peak load. This approach gives a good indication of the yield status of the stirrups in the FE models. Table 8.5 summarises the average strain of the two stirrups in the FE base models at the peak load. In both the 2D and 3D models, the values indicated that the stirrup nearest to the support yielded whereas the stirrup nearest to the load point did not yield. This is consistent with the experimental results. The strain results indicate that the FE base models failed in shear due to yielding of the stirrup.

Table 8.5 - Average strain of stirrup in FE base models at the peak load

F.E. model	Stirrup nearest support (με)	Stirrup nearest load point (με)
Beam '0.75D' (2D Base model)	2448	1539
Beam '0.60D' (2D Base model)	2588	1430
Beam '0.50D' (2D Base model)	2347	1389
Beam '0.75D' (3D Base model)	2970	1570
Beam '0.60D' (3D Base model)	2724	1301
Beam '0.50D' (3D Base model)	2760	1624

Note - Yield strain = 1718 με

8.5.1.5 Crack pattern

The crack patterns of different base models at the peak load step are illustrated in Figure 8.24 and Figure 8.25. The crack patterns were obtained by plotting vectors of tensile strains normal to the crack direction of fully open crack at the integration points. Only crack strains that have exceeded the softening branch of

the tension model illustrated in Figure 4.4 (b) were plotted. The length of the line is relative to the crack strains of the element. The longer the line, the higher the crack strains. The lines are also assigned three different colours depending on the crack strains to allow easy identification. High crack strains are shown as red lines, medium crack strains as green lines and small crack strains as blue lines. It should be noted that the crack strains are relative to the individual model only. They are not the same between different models even though the line length is the same. The figures merely give an indication of the crack strain distribution along the beam. In both the 2D and 3D models, the cracks are not in the direction of the principal stresses. The post failure crack pattern from the experiment control beam has been superimposed on top of the numerical crack pattern for comparison and is represented by continuous black lines.

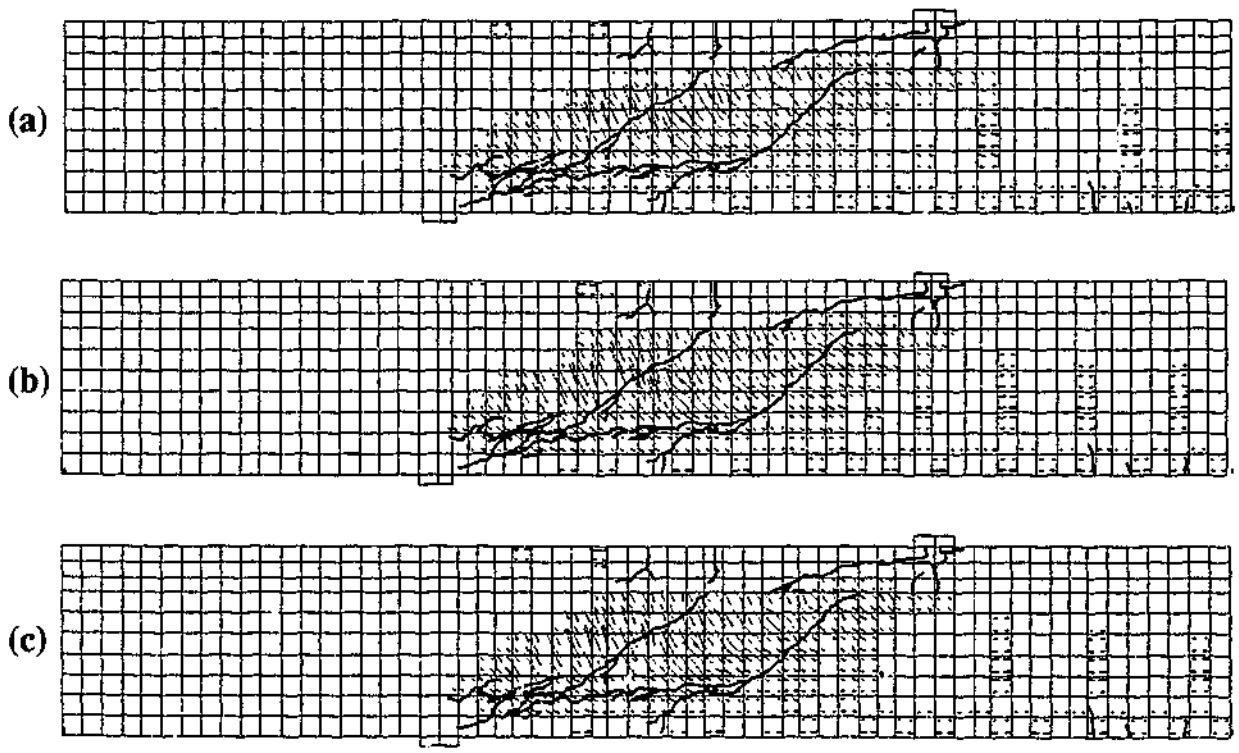

Figure 8.24 - Experimental crack patterns and corresponding predicted crack tensile strains of 2D base models (4-node) of beams (a) '0.75D' (b) '0.60D' and (c) '0.50D'

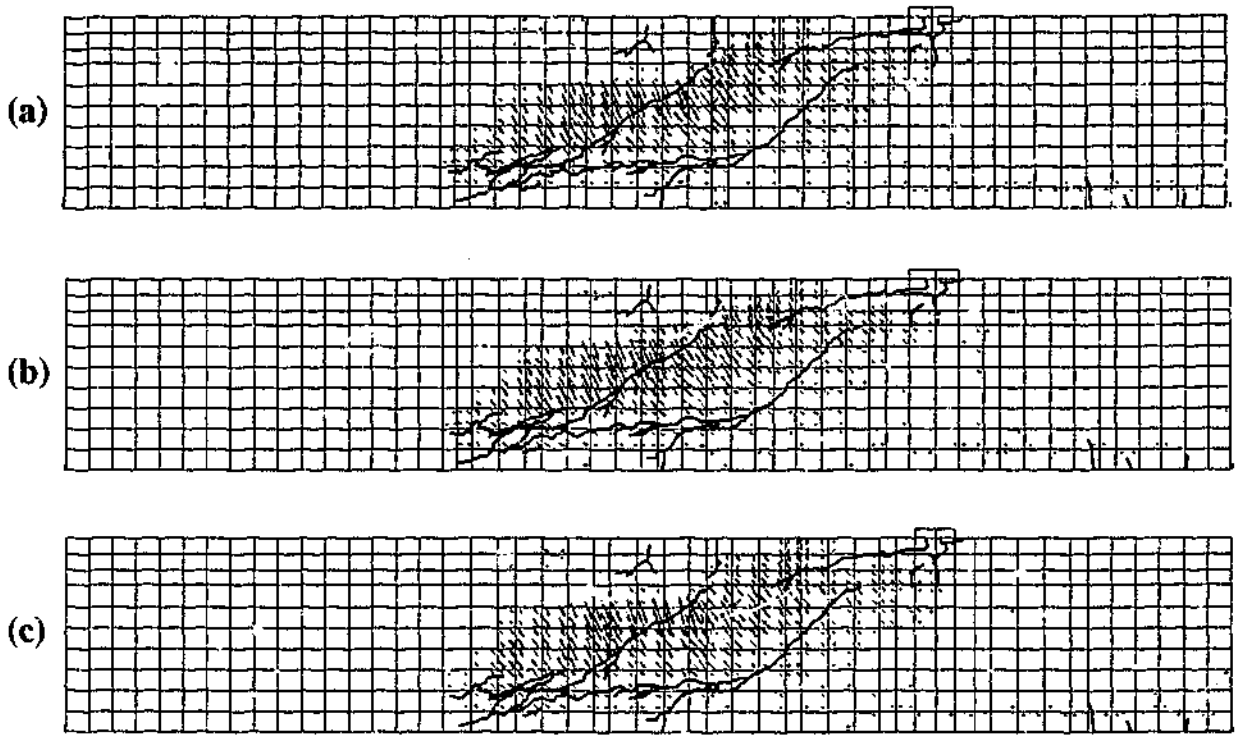

Figure 8.25 - Experimental crack patterns and corresponding predicted crack tensile strains of 3D base models (8-node) of beams (a) '0.75D' (b) '0.60D' and (c) '0.50D'

Based on the solution procedure described earlier, the base models gave comparable crack patterns to the experiments. As expected, the shear cracks in the numerical models were distributed over several elements forming a path from the support towards the load point. The locations of the cracks cover the path of the two distinct shear cracks observed in the experiment. The 2D base models have simulated flexural cracks near the mid-span. In the 3D base models, the flexural cracks were less noticeable. In the experiment, it was observed that the shear crack from the web had extended into the flange towards the load point. This has also been simulated to a limited extent by the numerical models.

In the models, high crack strains (red lines) concentrate around the location of the experimental shear crack closest to the support. The crack strains were lower along the path of the experimental shear crack closest to the load point. This is consistent with the results obtained from the photogrammetry measurement. Referring back to Figures 7.21 (a), the average crack width of shear crack '1' (shear crack closest to support) is noticeable larger than the average crack width of shear crack '2' at the time of the final survey. In the 3D models, a band of cracks has

concentrated around the location of the experimental shear crack closest to the support.

The crack patterns of the 2D and 3D base models of beam '0.75D' created using the 8-node plane stress elements and 20-node solid brick elements are illustrated in Figure 8.26. The crack patterns shown were obtained at the peak load step. In the 2D model, it can be observed that a band of cracks has concentrated along the path of the experimental shear crack closest to the load point. Cracks did not form near the location of the experimental shear crack closest to the support. As a result, the predicted load capacity of the beam was significantly lower compared to the experiment. The band of cracks represent a source of numerical instability and it is possible that the 2D 8-node plane stress elements model was more susceptible to the numerical instability compared to the 2D 4-node plane stress elements model. This may have prevented the formation of the second band of crack nearer to the support. The crack patterns of the 3D base model were comparable to the experimental crack patterns. Bands of cracks had formed around the location of the two experimental shear cracks. Computational time required, however, was significantly more compared to the 8-noded solid brick element model. Preliminary analyses of the base models of beams '0.60D' and '0.50D' created using the higher order elements gave similar trends.

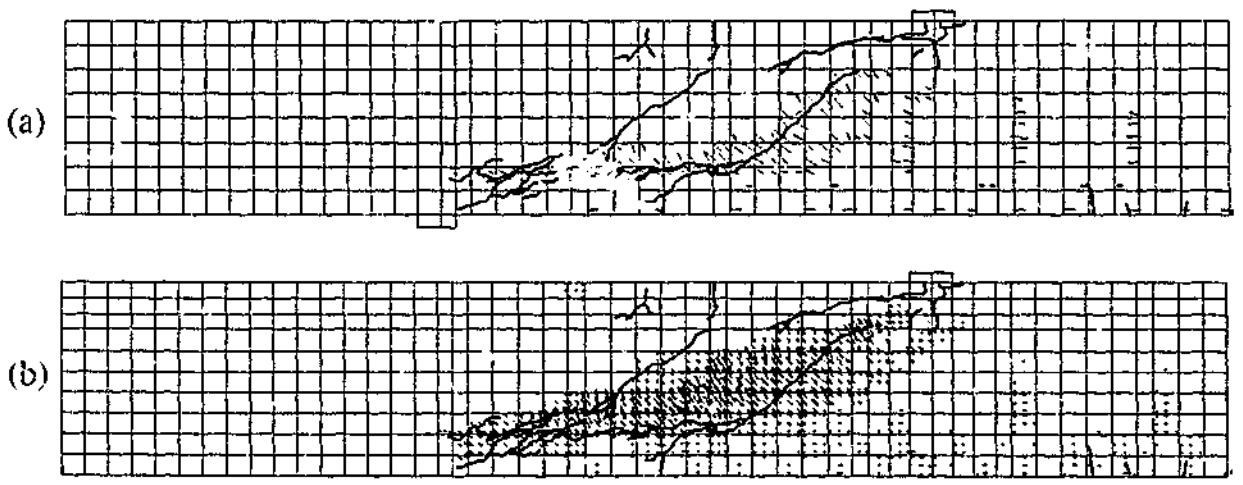

Figure 8.26 - Experimental crack patterns and corresponding predicted crack tensile strains of base models of beam '0.75D' in (a) 2D (8noded) and (b) 3D (20noded)

8.5.1.6 Validity of model

The 2D 4-node plane stress elements model and 3D 8-node solid brick elements model, with the material models and properties adopted, produced comparable results to the experiment. The numerical peak loads were comparable to the experimental peak loads. The crack patterns, load-deflection response and load strain response of the stirrup and flexural reinforcement were similar to the experimental results, with the trends simulated adequately. Therefore, it can be considered that the results of the finite element models are valid. In the section to follow, an investigation is carried out to determine the effect of varying the shear retention factor β using the models with material properties outlined earlier as the basis for comparison.

The results of the 2D and 3D base models of beam '0.75D' created using 8-node plane stress elements and 20-node solid brick elements models were also presented. The predicted shear load capacity of the 2D model was not comparable to the experimental peak load. In the 3D models, comparable results to the experiments were achieved but significantly more computational effort was required. Further investigation into models using the higher order element models was not pursued.

8.5.2 Effect of varying shear retention factor β in base models

8.5.2.1 Introduction

In the current study, the shear retention factor β is an important parameter because shear mechanism dominates the beam behaviour and failure mode. Therefore, the effects of varying the concrete strength on the peak load, load-slip behaviour and strain distribution profiles were investigated. Numerical models with β values of 0.025, 0.10 and 0.20 were adopted for all the base models. All other material properties have remained the same as the base model. The determination of 'failure' of the models is based on the criterion used for the base models described earlier.

8.5.2.2 Load displacement behaviour

Figure 8.27 to Figure 8.29 illustrates the load displacement behaviour of the base models with varying shear retention factors. In general, the load capacity

increases as the shear retention factor β increases. Both the 2D and 3D models exhibited similar trends. At the early stages of loading, the stiffness is identical across the models with different β. Beyond the service load level when shear cracks have formed, models with a higher β value exhibit a stiffer response compared to models with a lower β value. Since the cracked concrete is capable of carrying more shear load, the propagation and growth of shear cracks are impeded. Subsequently, smaller and fewer cracks resulted in smaller beam deformation.

In all the models, the β value of 0.05 gave the closest peak load value compared to the experiment result. The load displacement response is fairly similar in models with β values of 0.025 and 0.05, except for the predicted peak load. However, the difference in the predicted peak load varies between 20 to 50 kN, which can be considered to be insignificant in view of the fact that experimental scatter of such magnitude is not uncommon even in shear critical beams of identical configurations. Therefore, small variation to the β value within such a low range will not affect the load displacement response or the predicted peak load significantly. However, doubling the β value to 0.10 yielded a significant increase in the load capacity of the beam to approximately 400 kN. In the case of β of 0.20, the load capacity of the beam increases to approximately 500 kN. An increase in the β value does not increase the concrete strength but merely allow more shear load to be carried by the cracked concrete. This will result in an increase in the load carried by the neighbouring uncracked concrete elements also. A higher value of β would then mean a larger force carried by the cracked concrete and the load transferred to a larger band of surrounding concrete elements. This potentially increases the area over which more cracks can form thereby increasing the beams shear load carrying capacity. It will be shown later that that more cracks were observed to have formed in the web in models with higher β value. An increase in the β value has allowed the cracks to distribute over a wider area. More force is required to form these cracks and as a result, the shear capacity of the beam increases.

(a)

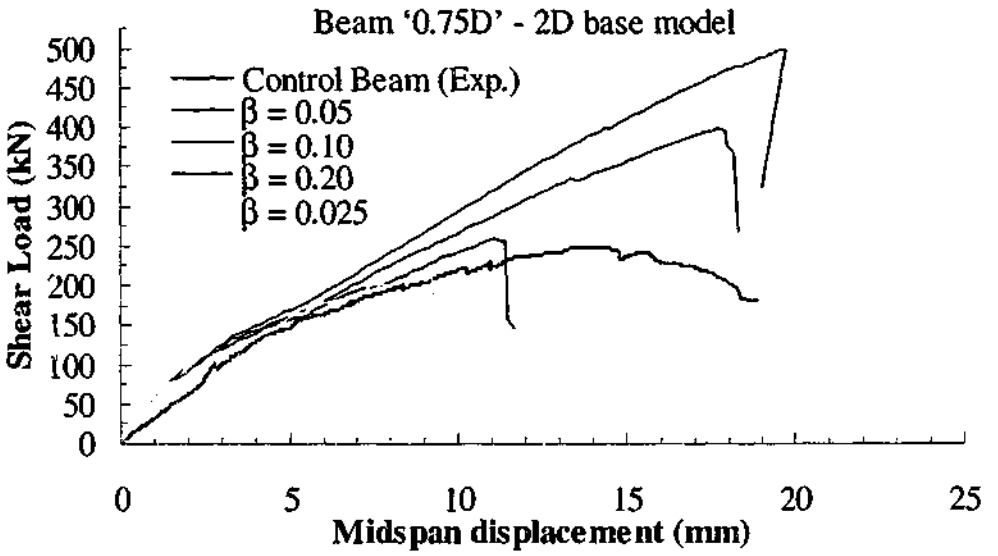

(b)

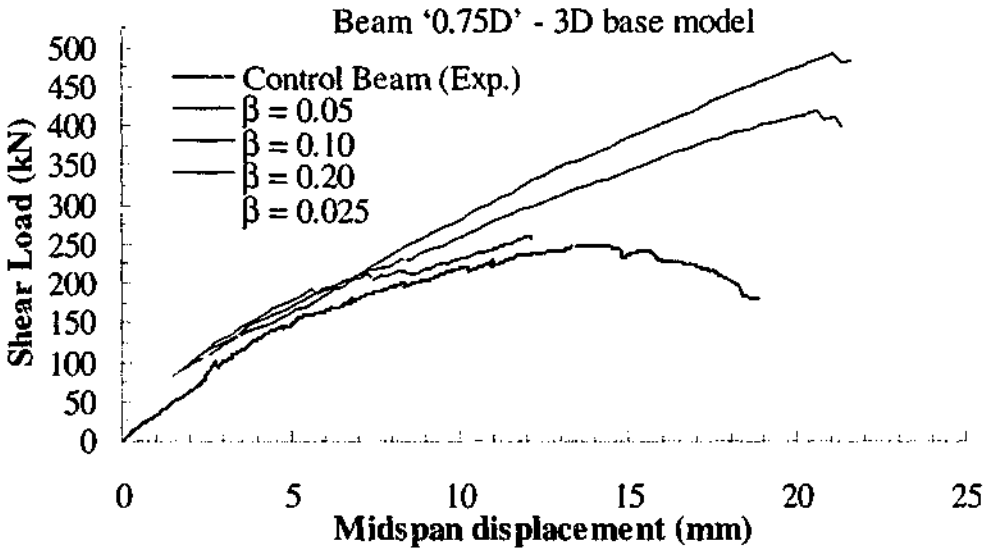

Figure 8.27 - Effect of varying β on load displacement behaviour of beam '0.75D' in (a) 2D base models and (b) 3D base models

(a)

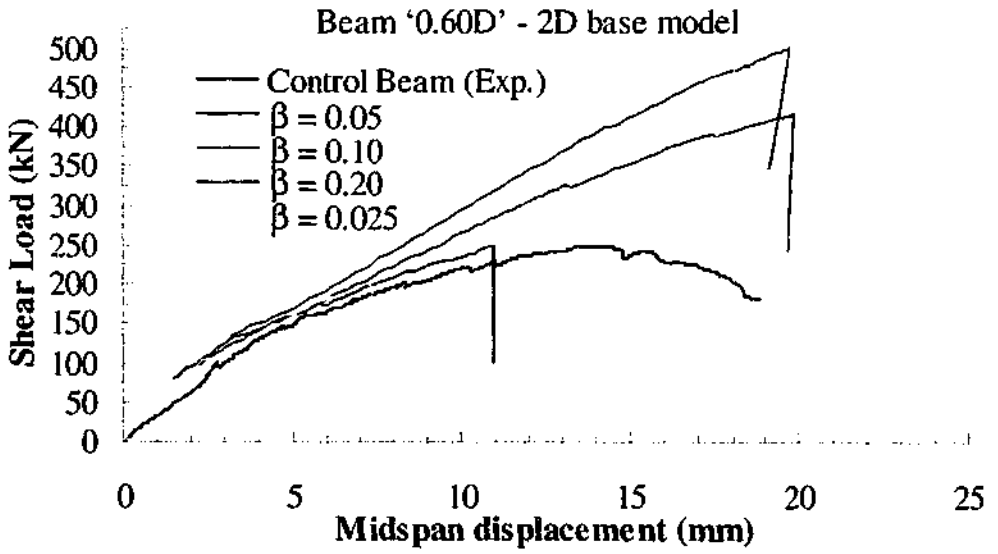

Figure 8.28 - Effect of varying β on load displacement behaviour of beam '0.60D' in (a) 2D base models and (b) 3D base models

(b)

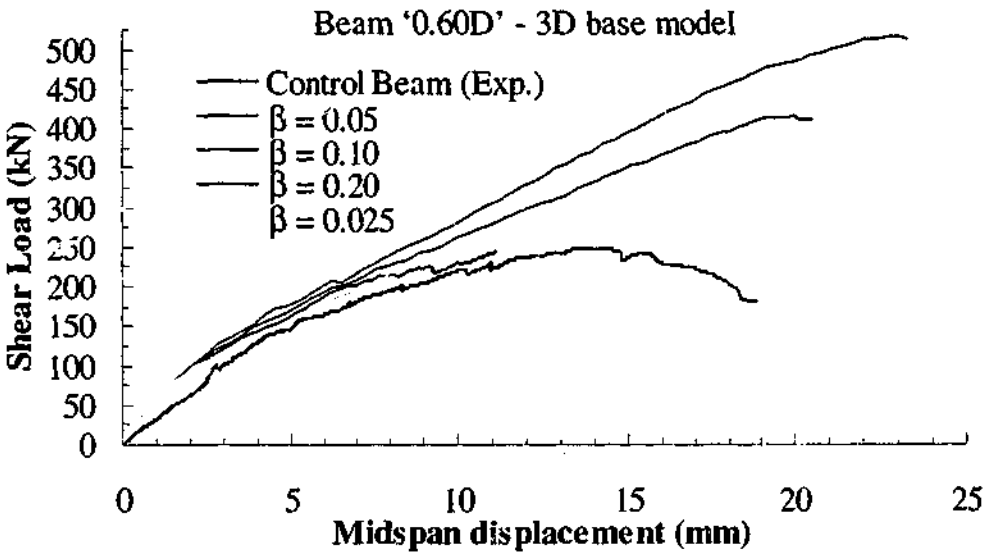

Figure 8.28 (continued) - Effect of varying β on load displacement behaviour of beam '0.60D' in (a) 2D base models and (b) 3D base models

(a)

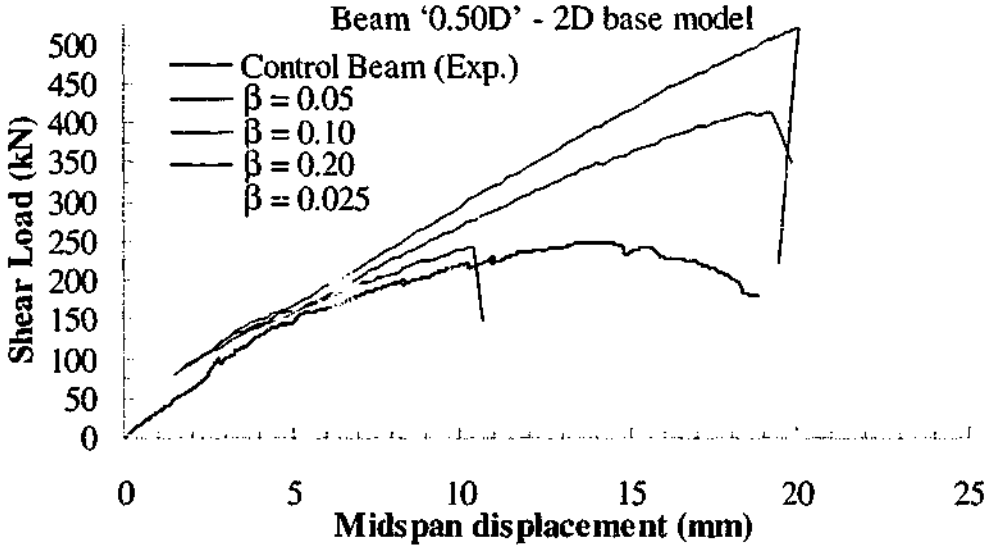

(b)

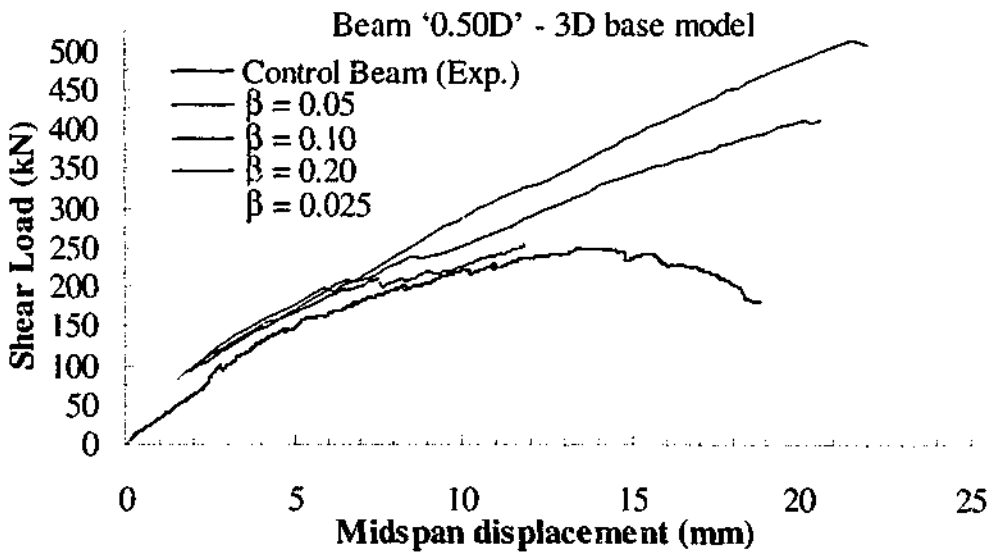

Figure 8.29 - Effect of varying β on load displacement behaviour of beam '0.50D' in (a) 2D base models and (b) 3D base models

8.5.2.3 Behaviour of main flexural reinforcement

The main flexural reinforcement responses of the base models of beam '0.75D' with varying β are compared in Figure 8.30. The strain results were obtained from the same location previously described in Section 8.5.1.3. Apart from the difference due to the peak load reached, it can be observed that the load strain responses were similar across all the models. In both the 2D and 3D models, the main reinforcement strained linearly with load until structural failure. There is no noticeable difference in the flexural stiffness of the beams. In general, the higher the β value, the higher the strain reached in the main reinforcement. In all of the models, the main reinforcement did not yield indicating that flexural tensile failure did not occur. Similar trends and behaviour to what have been described herein were also observed in the base models of beams '0.60D' and '0.50D'. Further information on the load strain responses of these models is contained in Appendix D.1.

(a)

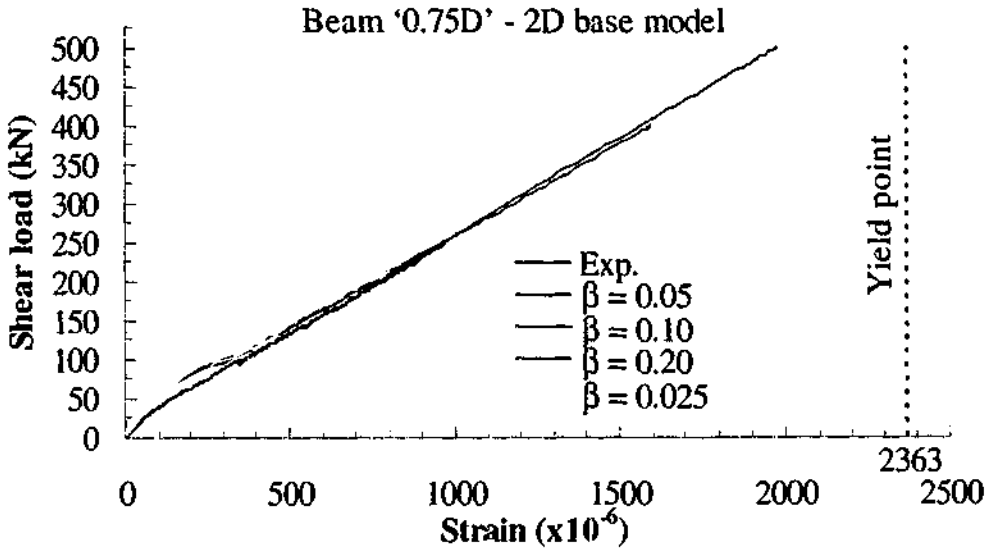

(b)

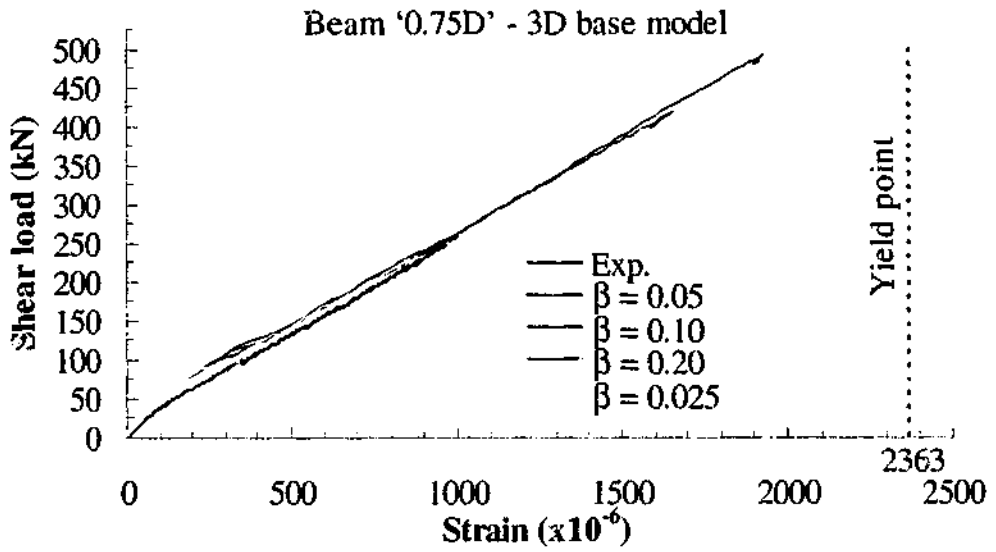

Figure 8.30 - Effect of varying β on main reinforcement load strain responses of beam '0.75D' in (a) 2D base models and (b) 3D base models

8.5.2.4 Behaviour of shear reinforcement

The shear reinforcement responses at location S2 and S4 of the base models of beam '0.75D' with varying β are compared in Figure 8.31 and Figure 8.32. The strain results were obtained from the same location previously described in Section 8.5.1.4. In both the 2D and 3D models, it can be observed that the load strain responses are similar in the various models at the early stages of loading. The strains in the stirrups at the locations S2 and S4 were insignificant indicating that little or no load were being carried. The load level at which the strains in the stirrups began to increase significantly was similar in all the models, which was approximately at 150 kN. At this stage, the load strain responses of the models still remained fairly similar to each other. At high load levels, there is a general trend that the larger the shear

retention factor, the smaller the strain hence force carried by the stirrups at a given load. This indicates that the shear load carried by the cracked concrete increases with increasing β.

With the exception of the peak load, the load strain response is fairly similar in models with β values of 0.025 and 0.05. This implied that the contribution of concrete in carrying the shear load is insignificant within such a low range. Similar trends and behaviour to what have been described herein were also observed in the base models of beams '0.60D' and '0.50D'. Further information on the load strain responses of these models is contained in Appendix D.2.

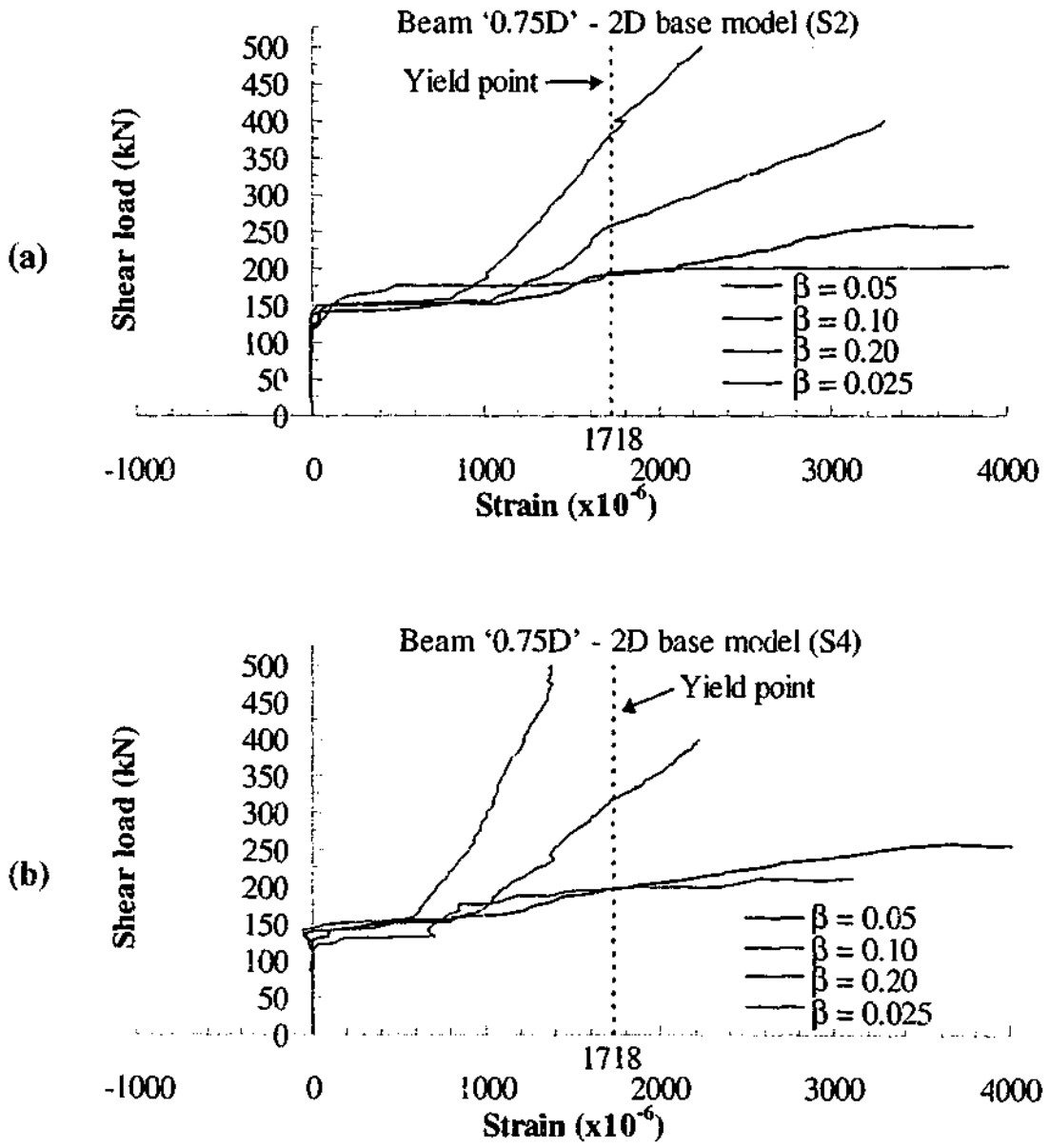

Figure 8.31 - Effect of varying β on shear reinforcement load strain responses of 2D base models of beam '0.75D' at stirrup locations (a) S2 and (b) S4

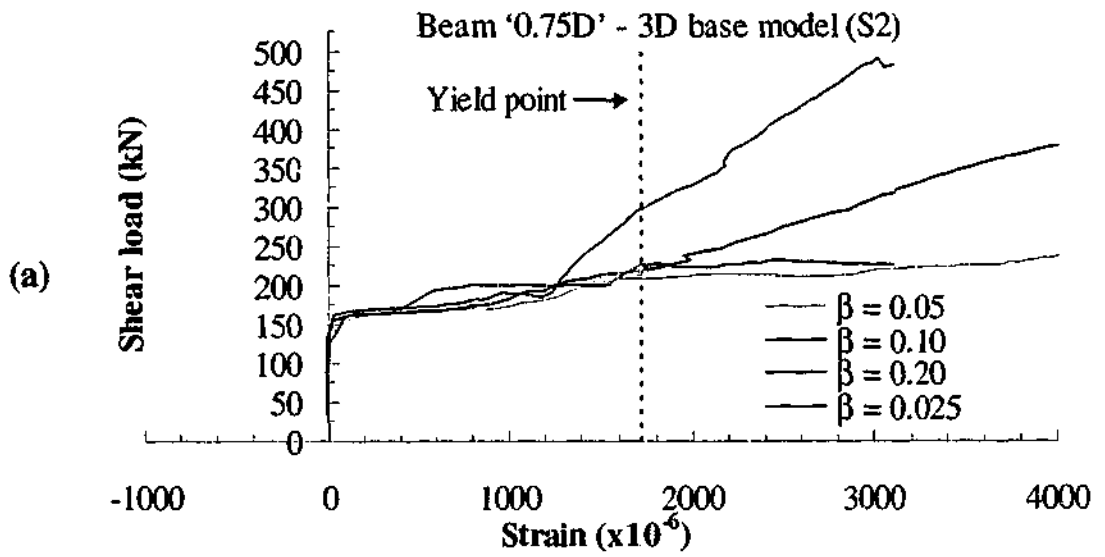

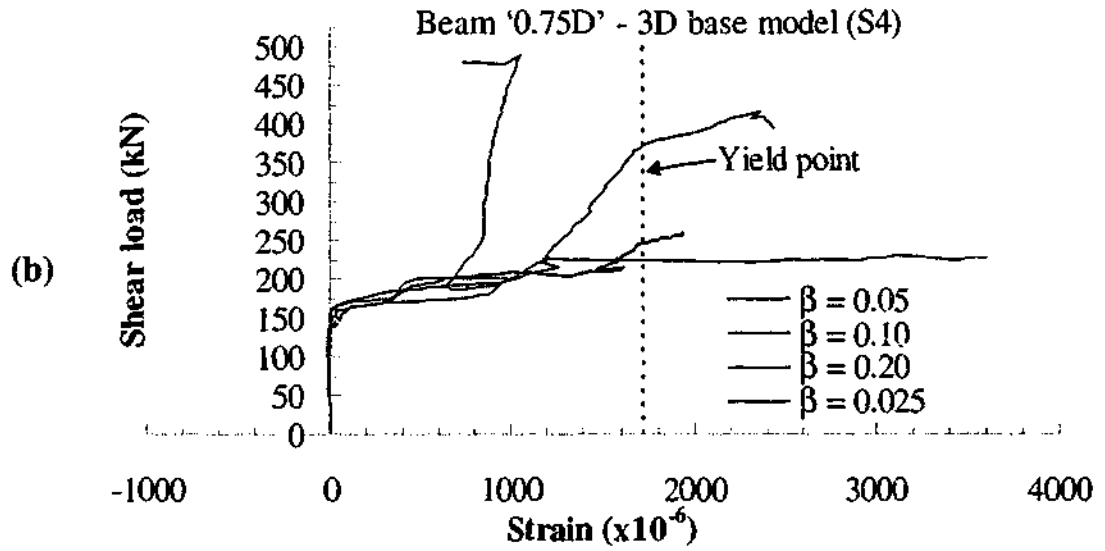

Figure 8.32 - Effect of varying β on shear reinforcement load strain responses of 3D base models of beam '0.75D' at stirrup locations (a) S2 and (b) S4

8.5.2.5 Crack pattern

Figure 8.33 and Figure 8.34 illustrate the crack patterns of the beam '0.75D' base models with varying β value. The crack patterns shown were obtained at the peak load step and correspond to crack strains exceeding the softening branch of the tension model illustrated in Figure 4.4 (b).

In the 2D models, it can be observed that cracks had covered significant portions of the web in the shear span at each of the models' respective peak loads. The number of cracks and therefore the area covered increases with the β value. As a result, the shear capacity of the beam increases. The cracks cover the path of the two distinct shear cracks observed in the experiment. The locations where high crack

strains occur, indicated as red lines, vary slightly from model to model. In the model with β of 0.025, it can be observed that these high crack strains formed a diagonal path in the general direction of the support to the load point. The location of this diagonal band of high crack strains had formed close to the experimental shear crack nearest to the load point. As the β value increases, the angle between this diagonal band and longitudinal axis of the beam becomes smaller. The critical section of the beam changes with the shear retention factor. Similar trends were observed in the 3D models as well.

Flexural cracks near the mid-span were not as apparent in the 3D models compared to the 2D models. Nevertheless, the load strain behaviour of the 2D and 3D models are similar as indicated in Figure 8.30.

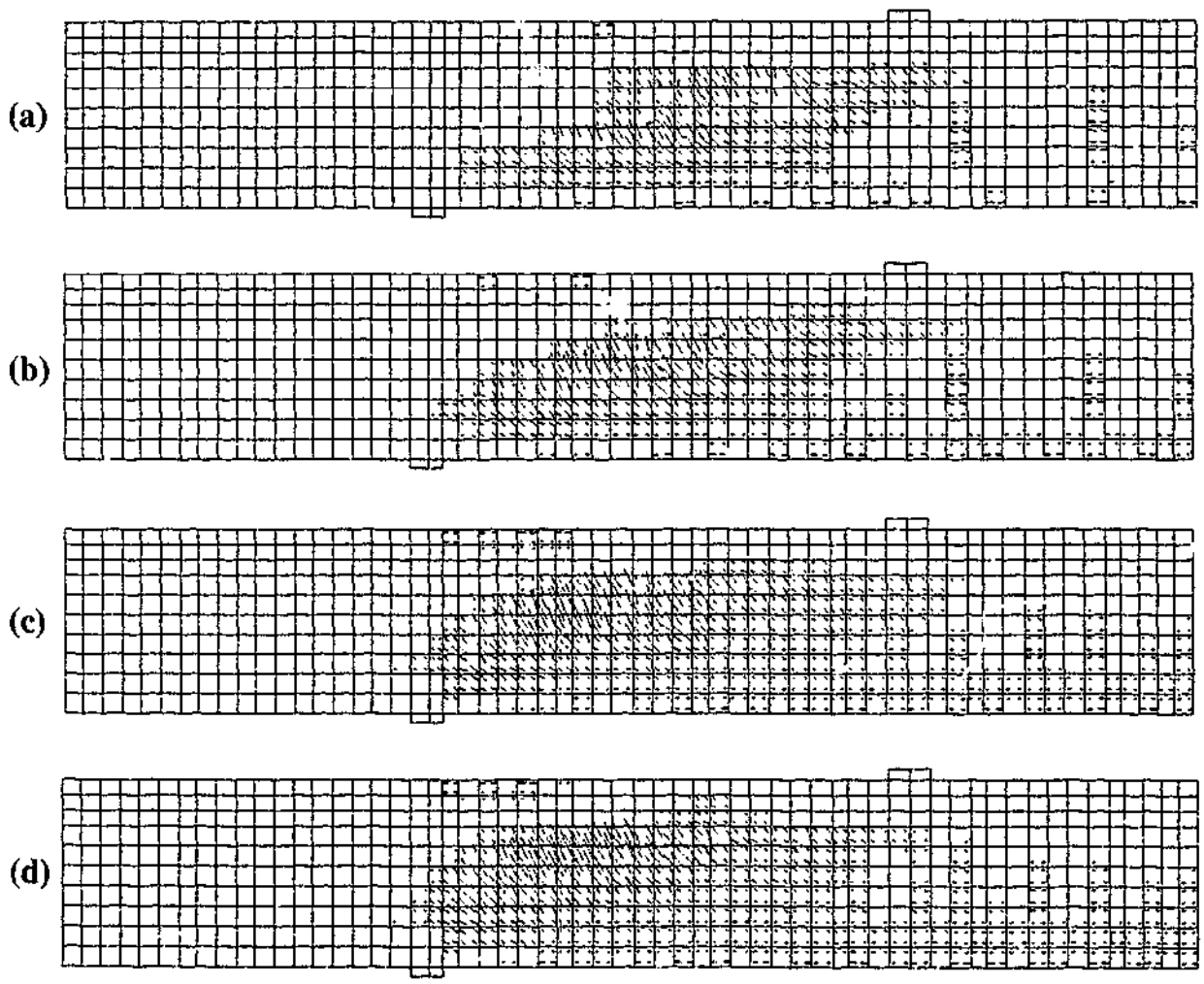

Figure 8.33- Predicted crack tensile strain patterns of 2D base models (4-node) of beam '0.75D' with β of (a) 0.025 (b) 0.05 (c) 0.10 and (d) 0.20

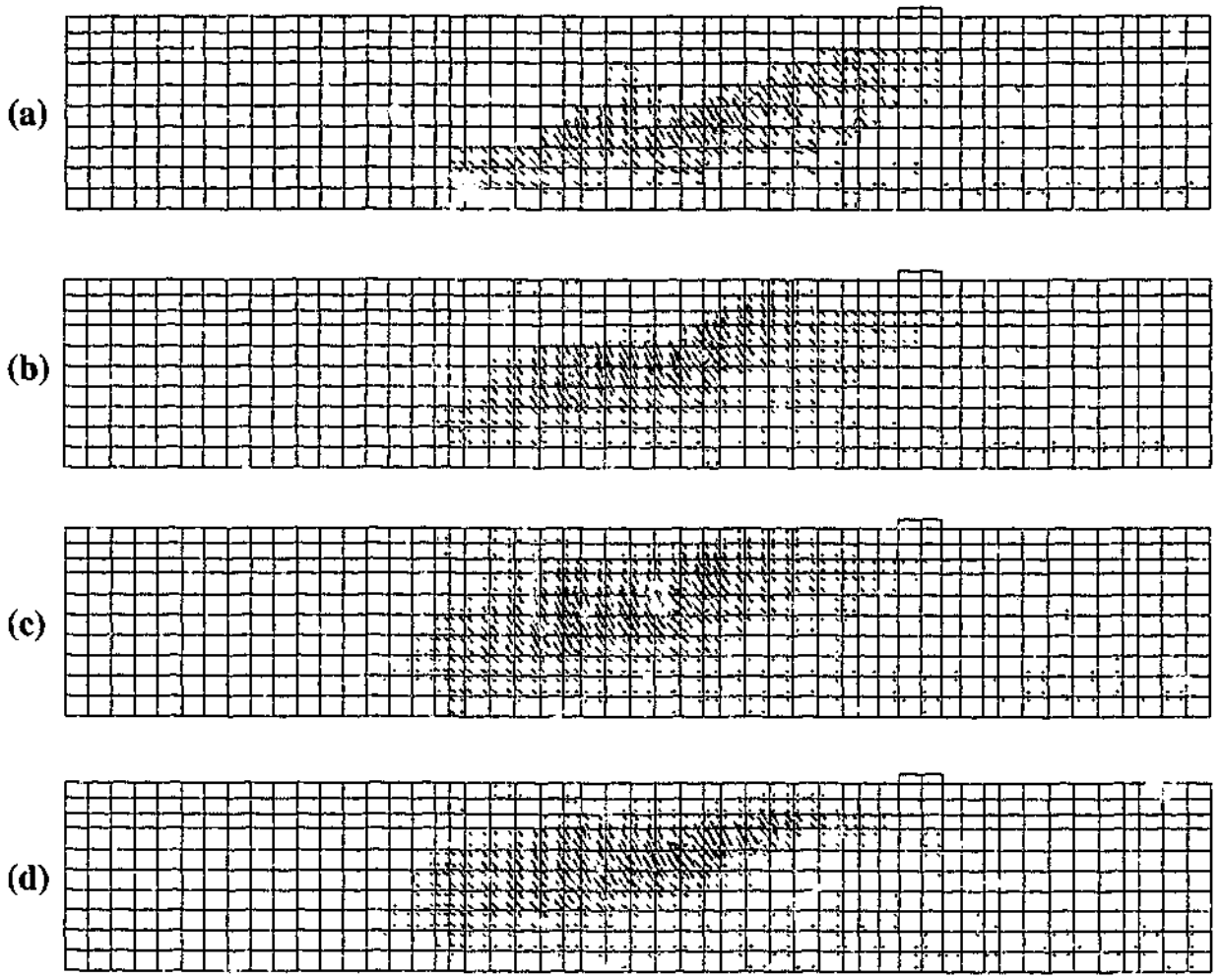

Figure 8.34 - Predicted crack tensile strain patterns of 3D base models (8-node) of beam '0.75D' with β of (a) 0.025 (b) 0.05 (c) 0.10 and (d) 0.20

8.5.2.6 Summary

The effects of varying the shear retention factor β on the behaviour of the base models were investigated in this section. It was found that the load capacity increases with the shear retention factor. The model with the β value of 0.05 gave the closest peak load value compared to the experiment result. The load displacement response is fairly similar in models with β values of 0.025 and 0.05, except for the predicted peak load. The difference in the predicted peak load of these two models can be considered to be insignificant. Small variation to the β value within such a low range will not affect the load displacement response or the predicted peak load significantly. As for the behaviour of the main flexural reinforcement, apart from the difference due to the peak load reached, the load strain responses were similar across all the models with different shear retention factor. The main reinforcement strained linearly with load until structural failure with no noticeable difference in the flexural stiffness of the beams. The higher the β value, the higher the strain reached in the

main reinforcement. In all of the models, the main reinforcement did not yield indicating that flexural tensile failure did not occur. The load strain responses of the shear reinforcement were also similar in the various models at the early stages of loading. The strains in the stirrups were insignificant indicating that little or no load was being carried. The load level at which the strains in the stirrups began to increase significantly was also similar in all the models, which was approximately at 150 kN. At high load levels, there is a general trend that the larger the shear retention factor, the smaller the strain hence force carried by the stirrups at a given load. This indicates that the shear load carried by the cracked concrete increases with increasing β. With the exception of the peak load, the load strain response of the stirrup is fairly similar in models with β values of 0.025 and 0.05. This implied that the contribution of concrete in carrying the shear load is insignificant within such a low range.

At the peak load step, it was shown that cracks had covered significant portions of the web in the shear span of the various models. The number of cracks and therefore the area covered increases with the β value. An increase in the β value has allowed the cracks to distribute over a wider area. More force is required to form these cracks and as a result, the shear capacity of the beam increases. The locations of where high crack strains occur were observed to form a diagonal path in the general direction of the support to the load point. As the β value increases, the angle between this diagonal band of high crack strains and longitudinal axis of the beam becomes smaller. The critical section of the beam changes with the shear retention factor. From the findings of this section, the shear retention factor of 0.05 was adopted for the beam models.

8.5.3 Effect of varying interface behaviour between CFRP and concrete layer in 2D strengthened beam models with β = 0.05

8.5.3.1 Introduction

In this section, the behaviour of the 2D beam models strengthened with CFRP plates are investigated, assuming various bond slip models (see Figure 8.14) between the CFRP and concrete layer. The shear retention factor β of all the models was kept at 0.05. The effects on the load displacement, steel reinforcement and CFRP plate responses and crack patterns were investigated.

8.5.3.2 Load displacement behaviour

Figure 8.35 compares the load displacement behaviour of the experimental strengthened beams with their respective 2D numerical counterparts with different bond slip models. An explanation of the various bond slip models is given in Section 8.3.4 and illustrated in Figure 8.14. The numerical results of the base models (without CFRP reinforcement) from Section 8.5.1.2 have been included as well.

At low load levels, it can be observed that all the numerical models exhibited stiffer responses compared to the experiments. The reason for this behaviour has been explained in Section 8.5.1.2. The responses of the strengthened beam models are identical to their respective base models. The responses predicted by the numerical models were comparable to the experiments until about approximately half of the ultimate load levels of the experimental beams. At higher load levels, the numerical models exhibited a stiffer response for each of the experimental beams. For each beam type, the predicted load level varies depending on the bond slip model adopted. For the 'Perfect bond' model of beam '0.75D', the predicted load capacity is significantly higher compared to the experiment. In the case of the 'No bond' model, the predicted load capacity is lower than the experiment. This means that by introducing any bond slip models, the predicted load capacity will lie anywhere between the shear capacities predicted by the 'Perfect bond' and 'No bond' models. The numerical results illustrated in Figure 8.35 confirm this fact. Similar trends and results were also observed for the numerical models of beams '0.60D' and '0.50D'. However, it should be noted that the failure mode of the numerical models is different to the experimental failure modes. Nevertheless, the numerical models have simulated the experimental trend that the shear capacity is higher in beams with the external CFRP reinforcement compared to beams without the external CFRP reinforcement.

In all the beams, the predicted shear capacities vary only slightly between the models 'BS1', 'BS2' and 'BS3'. It is difficult to establish any trend between the different bond-slip models in each beam type. However, the predicted shear capacities of models 'BS4' are consistently higher than the models 'BS1', 'BS2' and 'BS3'. In all the beams, the responses of the models 'BS4' are similar to the 'Perfect bond' models except that the peak loads attained are only slightly lower. Referring

back to Figure 8.14, load is continuously transferred from the concrete in the web to the CFRP reinforcement for the models 'BS4'. Unlike models 'BS1', 'BS2' and 'BS3', there is no debonding in models 'BS4'.

(a)

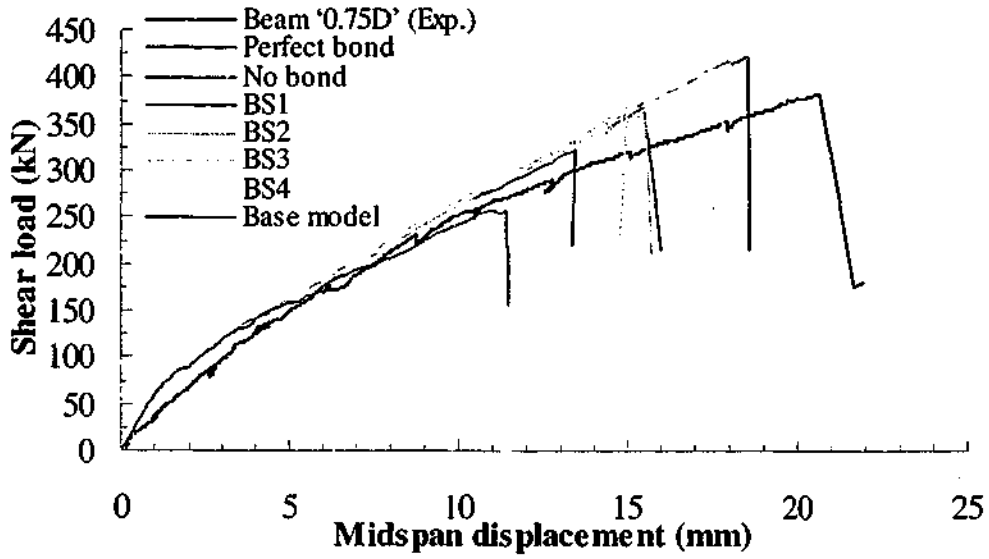

(b)

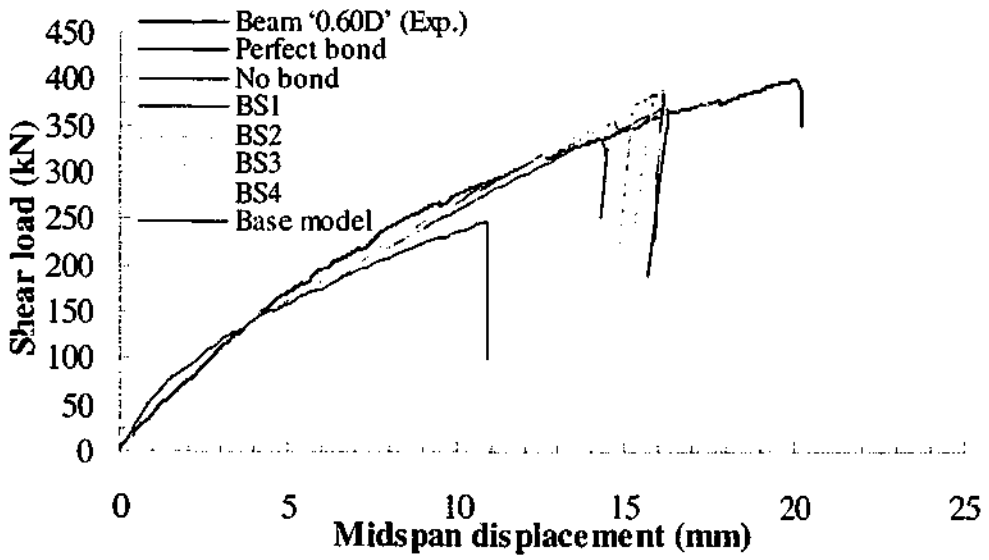

(c)

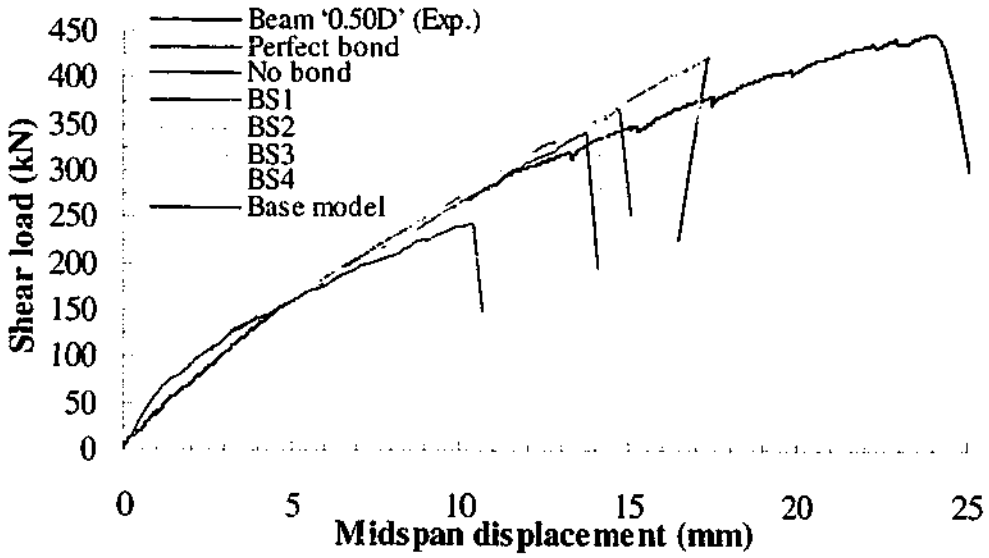

Figure 8.35 - Comparison of experimental and 2D numerical load displacement behaviour of beams (a) '0.75D' (b) '0.60D' and (c) '0.50D'

Figure 8.36 and Figure 8.37 compare the load displacement responses of the different T-beam models with identical bond slip models. It can be observed that the responses, in general, are similar for all the different beams. Although the beams have different CFRP spacing, the predicted peak loads are fairly close to each other. There is no noticeable trend in the predicted peak load with varying CFRP spacing in the beams. At high shear load levels, models of beam '0.50D' exhibited stiffer responses compared to models of beams '0.75D' and '0.60D'. The failure mode of all the models is the same, which has been established in Section 8.5.3.6 to be most likely shear compression failure. This implies that variation in the CFRP spacing has an insignificant effect on the shear capacity of the T-beams in the 2D numerical models adopted herein. In the experiments, it has been established in Chapter 7 that shear crack widths were significantly smaller in the strengthened beams compared to the control beam. In addition, the shear crack widths of beams '0.60D' and '0.50D' were smaller than the crack widths in beam '0.75D'. This implies that the effect of aggregate interlock is more significant, therefore, the concrete contribution to the shear capacity of the beams increases with a smaller CFRP spacing. In terms of finite element modelling, this translates to an increase in the shear retention factor β. It was initially suspected that the β value of 0.05 may have been too small and have resulted in similarity in the predicted shear capacities achieved in the different T-beams. Investigation into the effects of varying the β value carried out in Section 8.5.4 has established that this is not the case. For a given bond slip model, the predicted shear capacities of the different T-beams were similar regardless of the CFRP spacing. Therefore, it is justifiable to increase the shear retention factors in beams with smaller CFRP spacing. The finite element models did not account fully for the effects of CFRP spacing in the different T-beams.

(a)

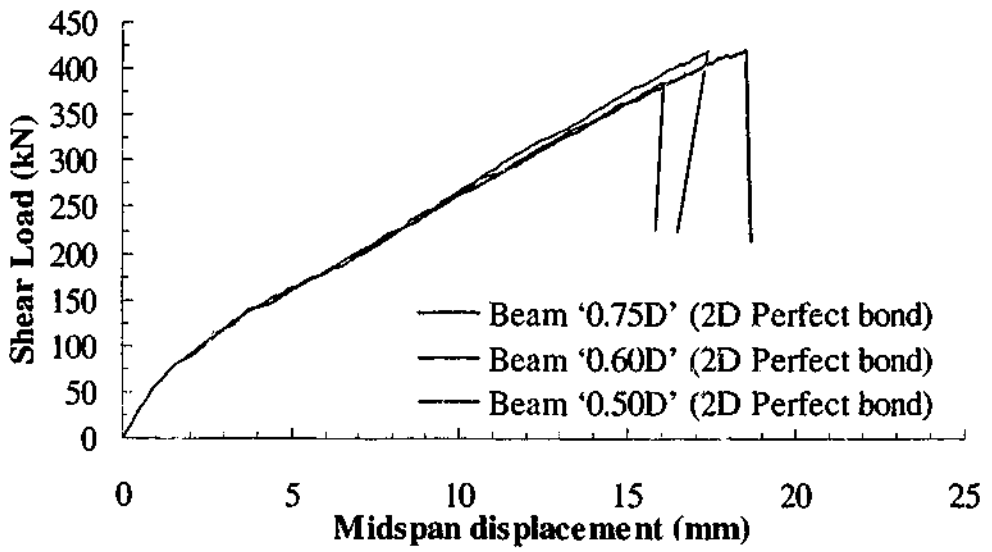

(b)

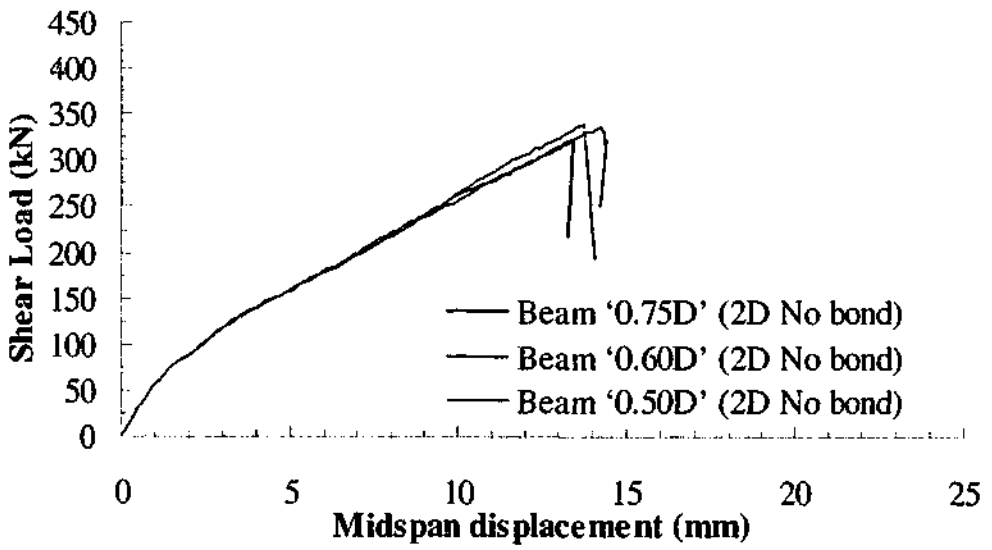

(c)

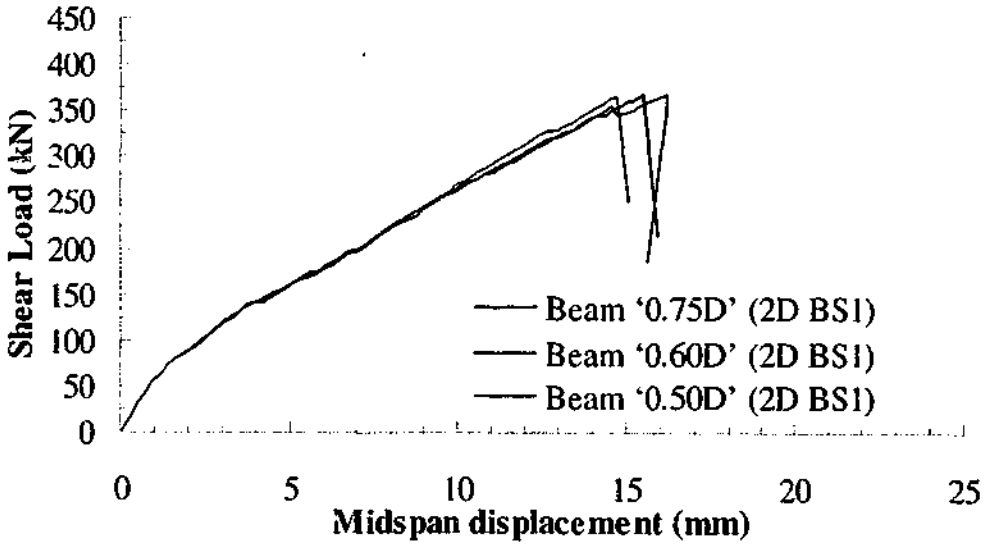

Figure 8.36 - Comparison of numerical load displacement behaviour of 2D models with (a) Perfect Bond (b) No bond and (c) BS1

(a)

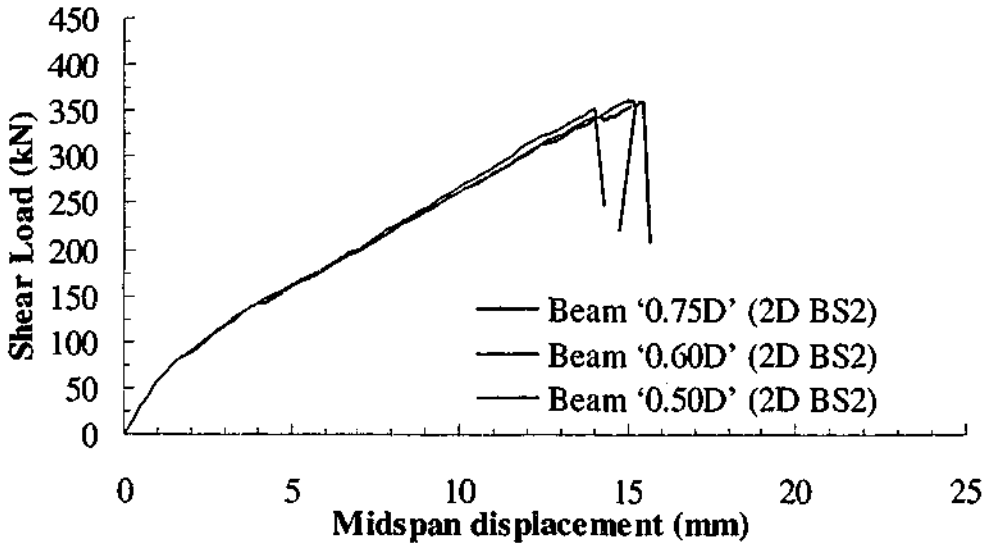

(b)

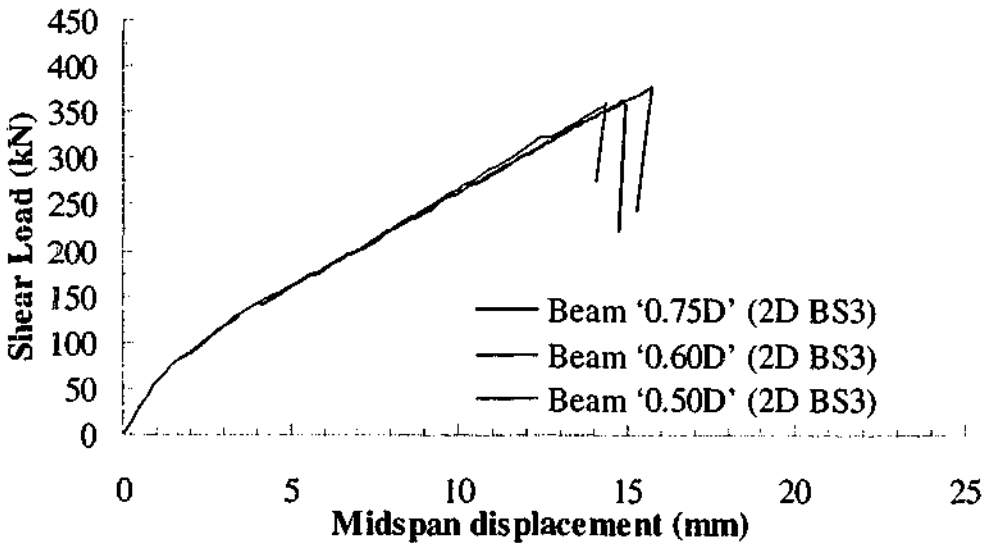

(c)

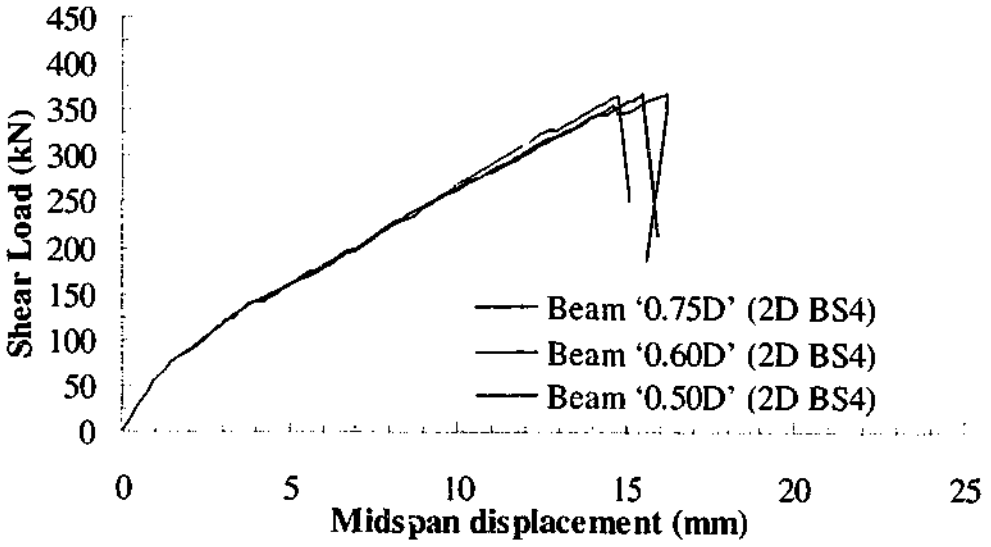

Figure 8.37 - Comparison of numerical load displacement behaviour of 2D models with (a) BS2 (b) BS3 and (c) BS4

8.5.3.3 Behaviour of the main flexural reinforcement

Figure 8.38 compares the main reinforcement responses of the experimental strengthened beams with their respective numerical counterparts. Apart from the difference due to the peak load reached, it can be observed that the load strain responses were similar across all the models. The main reinforcement strained linearly with load until structural failure. The main reinforcement did not yield indicating that flexural failure did not occur. The numerical responses were similar to the experiments.

(a)

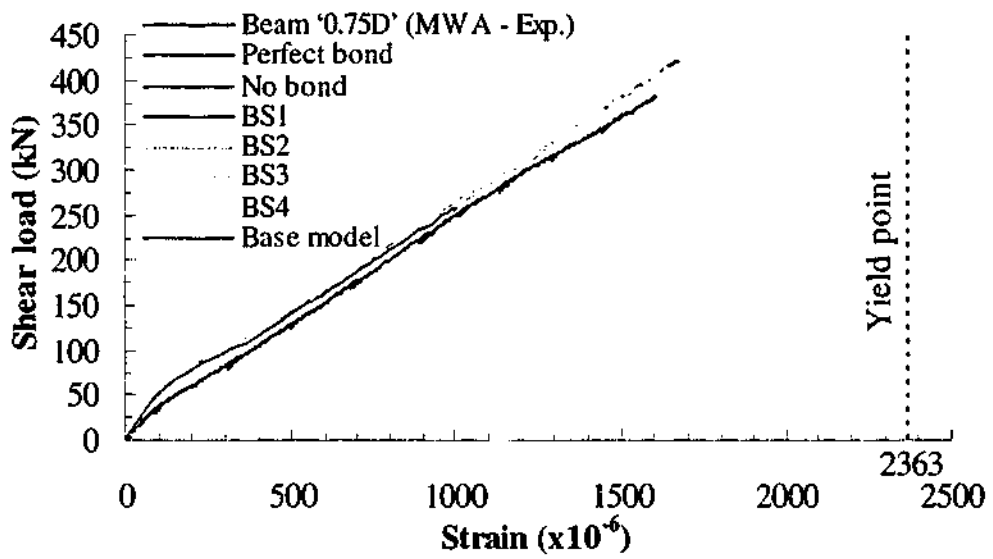

(b)

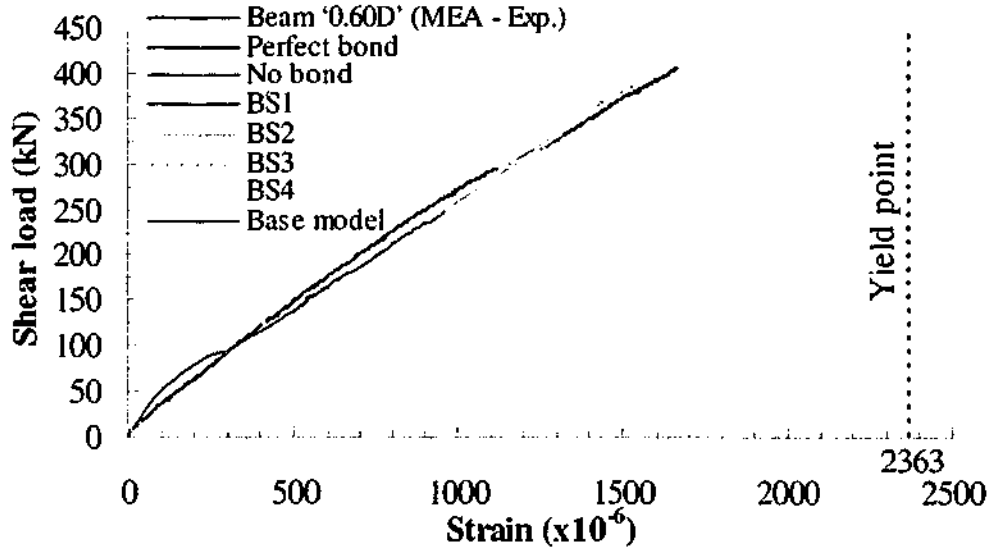

Figure 8.38 - Comparison of experimental and 2D numerical main reinforcement behaviour of beams (a) '0.75D' (b) '0.60D' and (c) '0.50D'

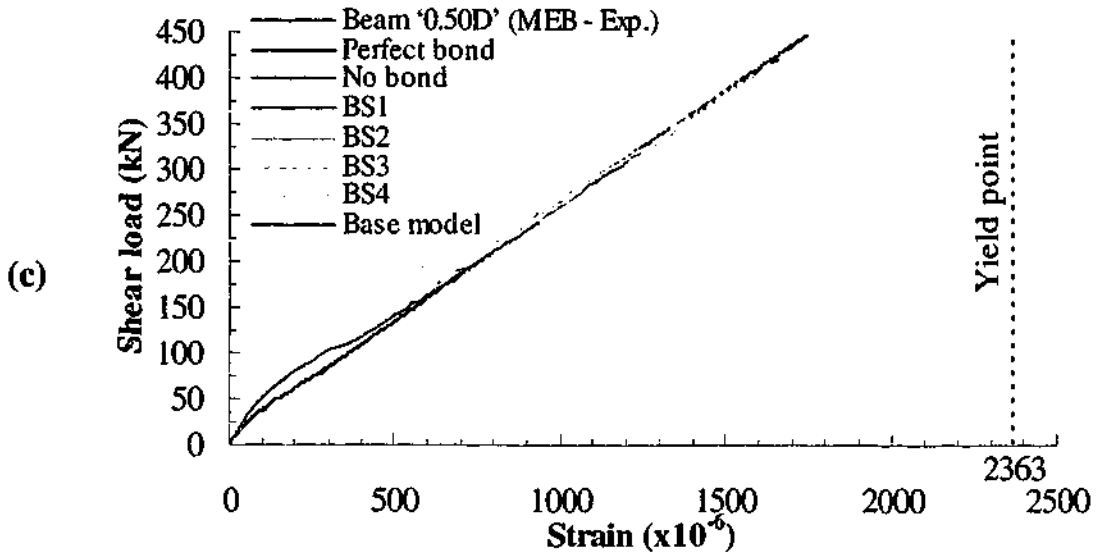

Figure 8.38 (continued) - Comparison of experimental and 2D numerical main reinforcement behaviour of beams (a) '0.75D' (b) '0.60D' and (c) '0.50D'

8.5.3.4 Behaviour of shear reinforcement

Figure 8.39 to Figure 8.41 compare the shear reinforcement load strain responses of the experimental and numerical results at selected locations. The numerical results of the base models (without CFRP reinforcement) from Section 8.5.1.4 have also been included. At low load levels, it can be observed that the shear reinforcement exhibited very small strains in all the numerical models as well as the experimental T-beams. In the numerical models, the load level at which the strain in the reinforcement began to increase significantly was comparable to the experiments. At higher load levels, the response predicted by the numerical models deviated significantly from the experimental results but the general trend remained similar. This is partly due to the assumption of perfect bond between the concrete and stirrups. At a given load level, the strain hence load carried by the stirrups in the numerical models is significantly higher compared to the experiments even for the 'Perfect bond' models. This implies that the contribution of the CFRP reinforcement to carrying the load is significantly less in the numerical models compared to the experiments. Beyond the service load levels, it can be observed that the strain in the stirrups is lower in the strengthened beam models compared to the base models at a given load level. This indicates that part of the shear load has been carried by the CFRP reinforcement but the contribution is minor. In each beam type, the load strain responses vary only slightly between the different bond slip models. The general trend remained similar. The 'Perfect bond' and 'No bond' models represent two

extreme cases of the bond slip behaviour and it can be observed that the load strain curves for the models 'BS1', 'BS2', 'BS3' and 'BS4' lie within these two models.

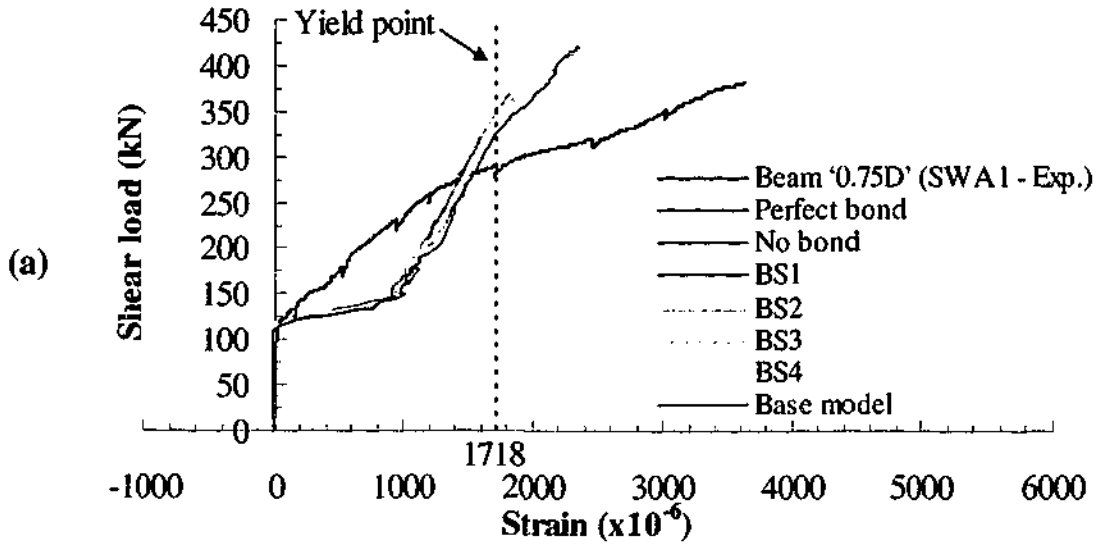

Figure 8.39 - Comparison of shear reinforcement behaviour of beam '0.75D' 2D models at stirrup locations (a) S1 and (b) S4

(a)

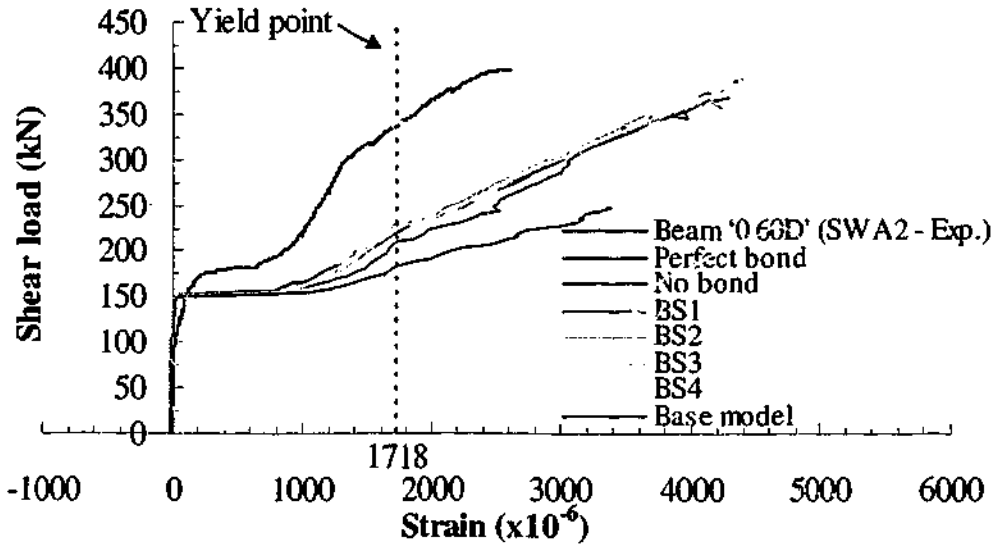

(b)

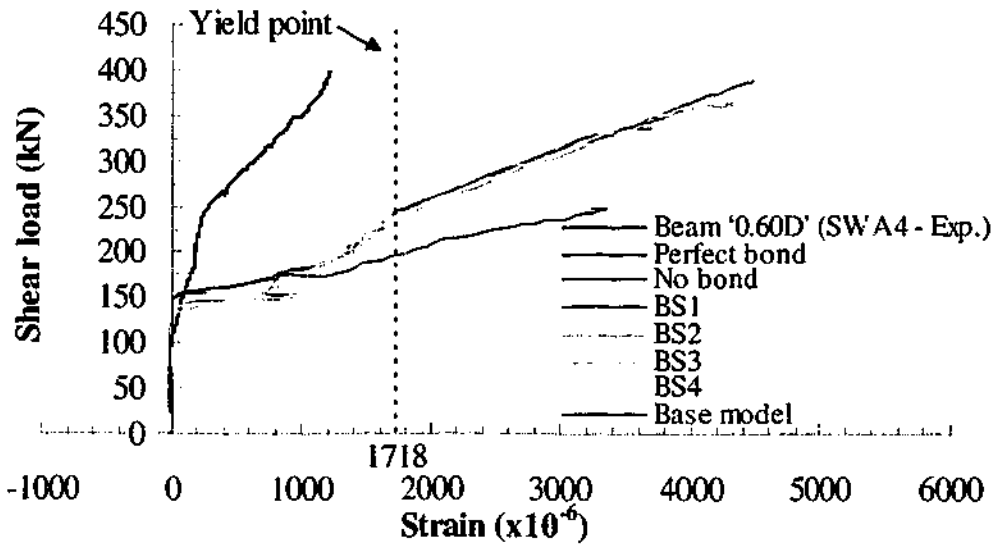

Figure 8.40 - Comparison of shear reinforcement behaviour of beam '0.60D' 2D models at stirrup locations (a) S2 and (b) S4

(a)

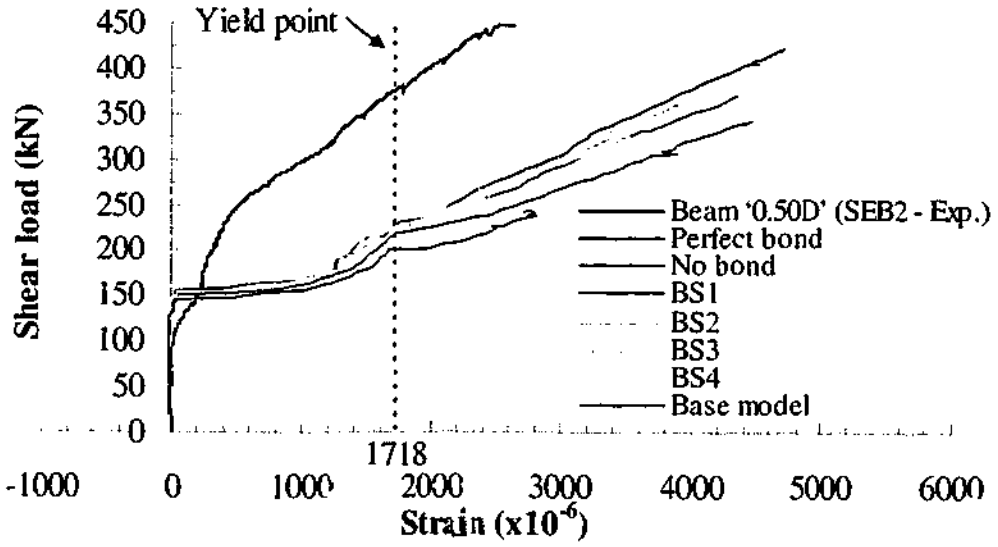

Figure 8.41 - Comparison of shear reinforcement behaviour of beam '0.50D' 2D models at stirrup locations (a) S2 and (b) S4

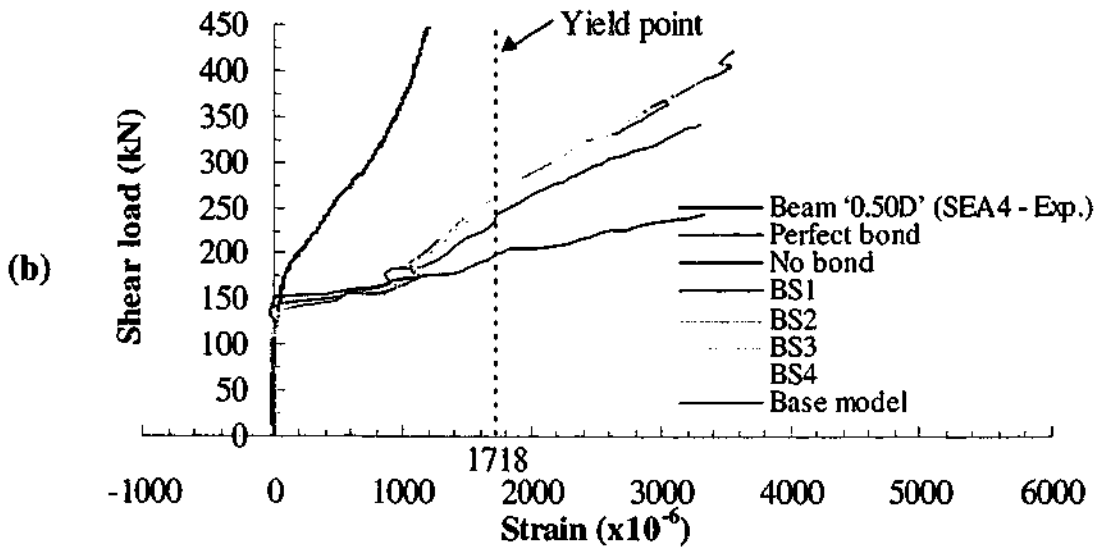

Figure 8.41 (continued) - Comparison of shear reinforcement behaviour of beam '0.50D' 2D models at stirrup locations (a) S2 and (b) S4

Figure 8.42 compares the load strain responses at location 'S4' of the 'Perfect bond' and 'No bond' models. It can be observed that the responses are fairly similar in the different T-beams. Nevertheless, there is a general trend that the smaller the CFRP spacing, the smaller the strain hence load carried by the shear reinforcement. The differences in the numerical responses are not as distinct compared to differences in the experimental responses illustrated in Figures 6.6 and 6.7. The results presented herein indicated that the CFRP reinforcement does not contribute significantly to carrying the shear load compared to the experiments. The stirrups still carry significant portions of the shear load. Variations in the bond slip models adopted yielded only slight but insignificant difference in the response. In the numerical models, the load carried by the stirrups is only slightly less in the strengthened beam models compared to the base models. Although, the comparisons between the experimental beams and numerical models have been made at selected locations, the results presented still give a good indication of the overall behaviour of the shear reinforcement in the numerical models.

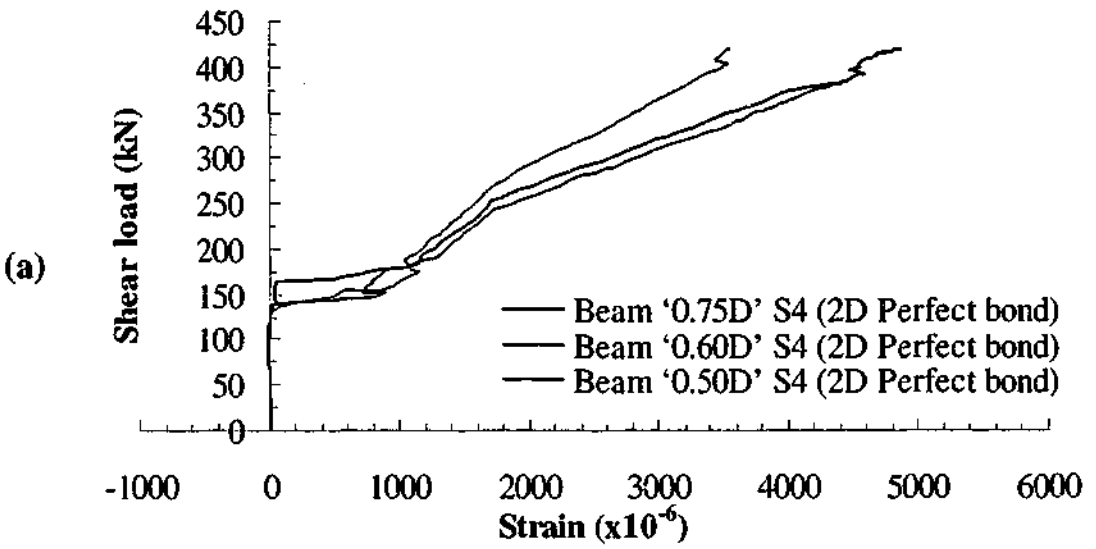

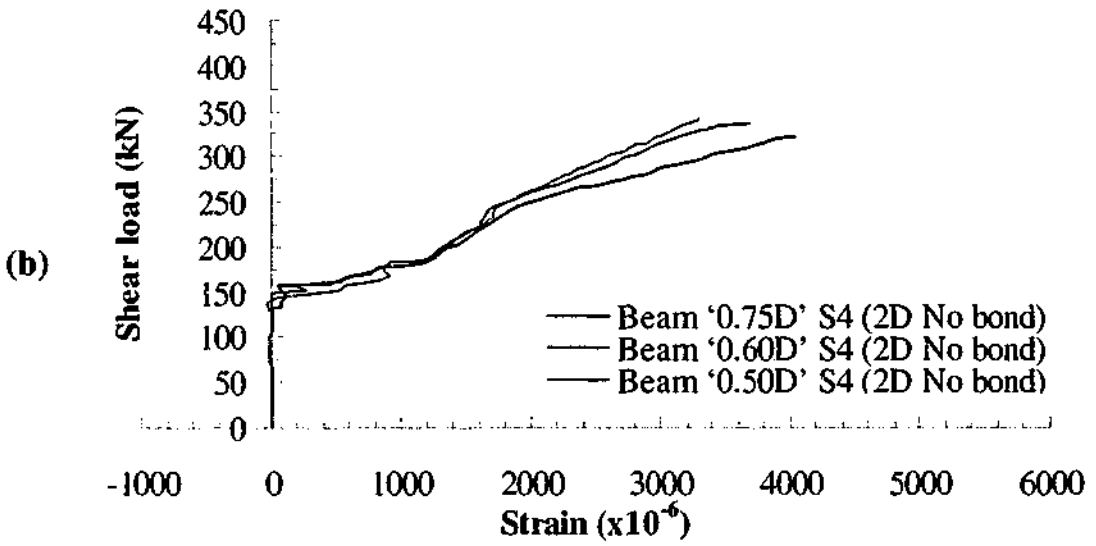

Figure 8.42 - Comparison of shear reinforcement behaviour at location S4 of 2D models with (a) 'Perfect bond' and (b) 'No bond'

8.5.3.5 Strain contours of L-shaped CFRP reinforcement

The strain contours of the L-shaped CFRP plates from the various bond slip models of the different T-beams are illustrated in Figure 8.43 to Figure 8.45. All the CFRP reinforcement on each beam is presented including the CFRP plates outside of the shear span. The strain contours shown were taken at the peak load step of each model.

Similar to experimental observations, the CFRP plates outside of the shear span carry very low shear loads in all the numerical models. In beam '0.75D', the strain contours indicated that the second and third CFRP reinforcement were the most critically loaded plates regardless of the bond slip models adopted. This was

consistent with the strain gauge results from the experiments. For beam '0.60D', the most critically loaded plates were the third and fourth CFRP reinforcement from the support. This was also consistent with the strain gauge results from the experiments. The models also indicated that the second CFRP reinforcement from the support was subjected to fairly high shear loads. In the experiments, strain gauges were not bonded to the CFRP reinforcement at this location and so it is difficult to establish the level of strain in the CFRP plate. For beam '0.50D', the most critically loaded plates were the second and third CFRP reinforcement from the support. The second CFRP reinforcement from the support were not instrumented with strain gauges in the experiments and so it is difficult to establish the level of strain in the CFRP plate. Nevertheless, the numerical models have provided valuable insight into the level of strain in the CFRP plates at these locations. The locations of the CFRP reinforcement subjected to significant shear loads were consistent between the numerical models and experimental results.

The maximum level of strain achieved in the CFRP plates in the numerical models, however, were significantly less compared to the level of strain achieved in the CFRP plates in the experiments. Generally, the numerically predicted strains in the CFRP are lower than the measured ones at any given load. For example, referring to the 'Perfect Bond' model of beam '0.75D', it can be observed that the maximum strain level achieved in the model is approximately 7000 με, which occurred at the third CFRP reinforcement from the support. The numerical shear load level at which this occurred is approximately 420 kN. This is significantly less compared to the strain level of 8884 με (refer to Table 6.4) achieved in the experimental beam '0.75D'. The experimental shear load level is approximately 370 kN. At other CFRP locations, the trend is similar. Introducing bond slip behaviour through interface elements only reduces the load carried by the CFRP reinforcement further. As a result, the strain level in the CFRP reinforcement is even smaller. Similar trends were observed in the numerical models of beams '0.60D' and '0.50D'. Regardless of the bond models used, the force transferred to the CFRP reinforcement is significantly less compared to the experiments at any given load level. This has resulted in the internal shear reinforcement still carrying significant shear loads in the numerical models. Increasing the stiffness of the CFRP reinforcement in the numerical models

may improve the solution but the stiffness value used no longer represents the actual property of the CFRP.

In all the models except the 'No bond' case, the level of strain in the bottom most elements of the CFRP reinforcement is significantly lower compared to the maximum strain achieved at their respective CFRP location. This indicates that the concrete elements at these locations were not subjected to localised stress concentration. Observations of the stress contours of the concrete elements at these locations revealed that this is the case.

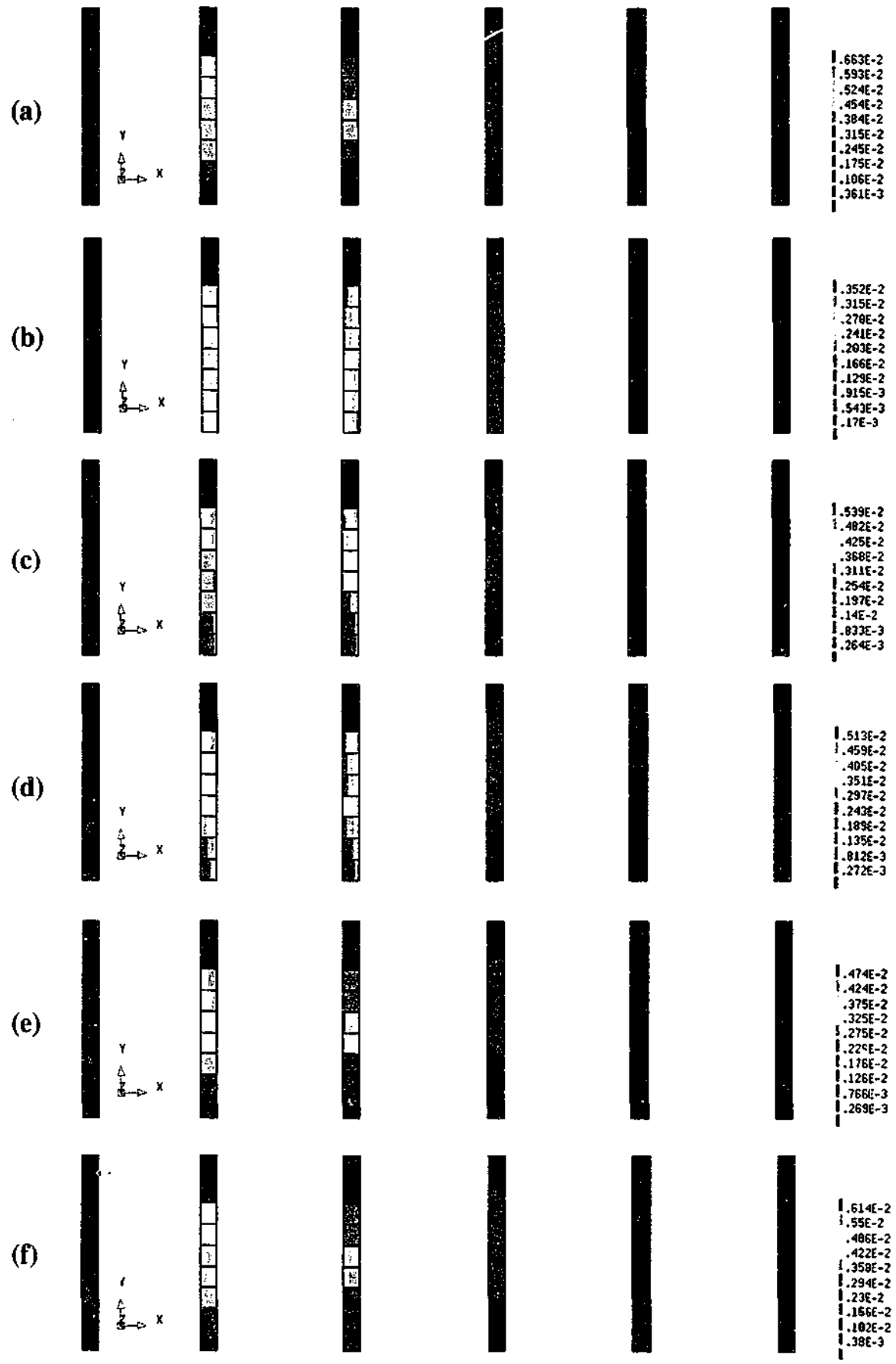

Figure 8.43 - Strain in CFRP of beam '0.75D' 2D models with (a) Perfect Bond (b) No bond (c) BS1 (d) BS2 (e) BS3 and (f) BS4

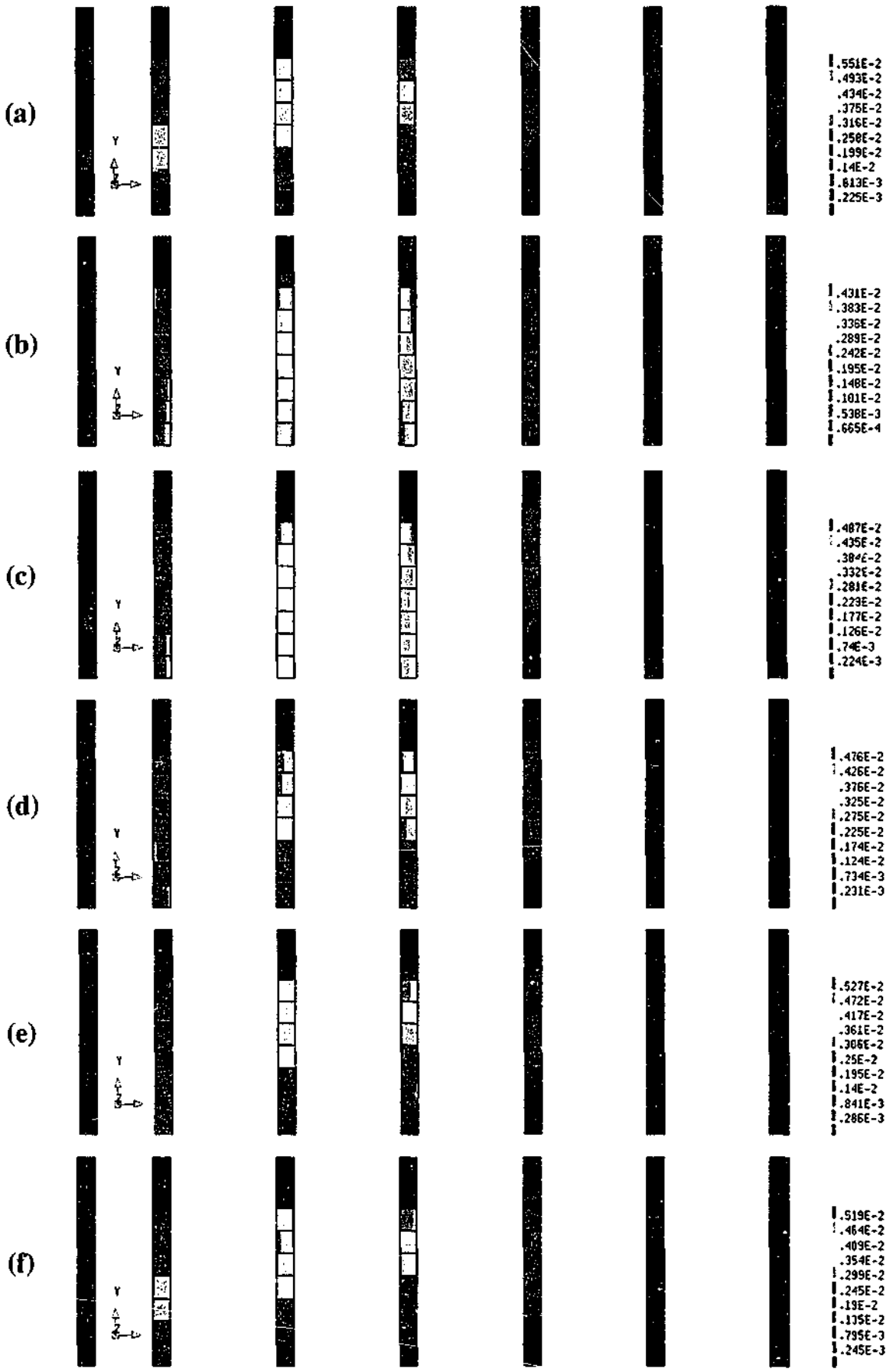

Figure 8.44 - Strain in CFRP of beam '0.60D' 2D models with (a) Perfect Bond (b) No bond (c) BS1 (d) BS2 (e) BS3 and (f) BS4

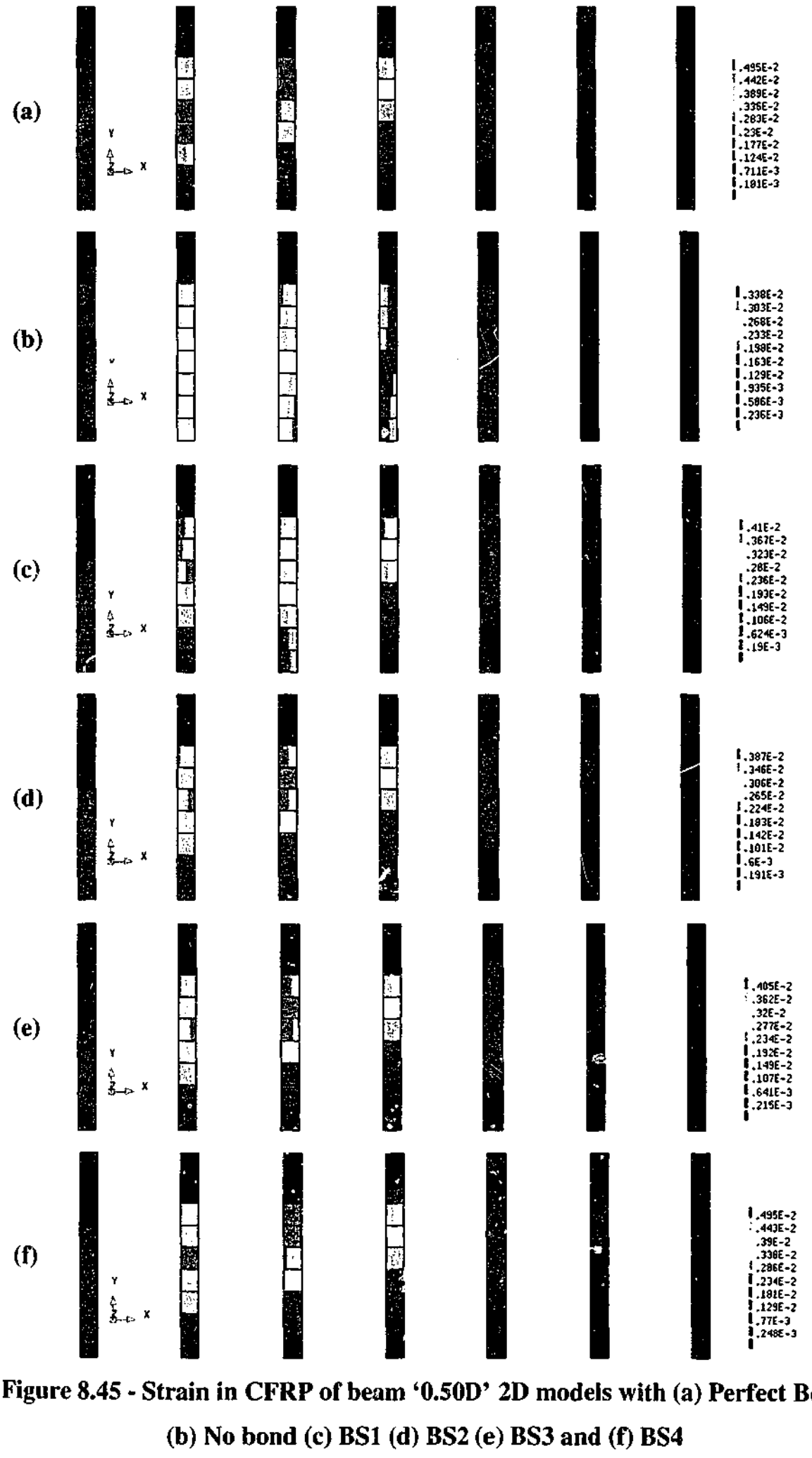

Figure 8.45 - Strain in CFRP of beam '0.50D' 2D models with (a) Perfect Bond (b) No bond (c) BS1 (d) BS2 (e) BS3 and (f) BS4

8.5.3.6 Crack pattern

The crack patterns of the 'Perfect bond' and 'No bond' models of the different T-beams are illustrated in Figure 8.46 to Figure 8.48. The crack patterns were obtained at the peak load step of each respective model. The post failure crack patterns of the experimental strengthened beams have been superimposed on top of the numerical crack patterns for comparison and are represented by continuous black lines.

For each of the different T-beam models, it can be observed that the crack patterns of the 'Perfect bond' and 'No bond' models are similar to each other. The location of the band of high crack strains is similar between the two models. In view of the fact that the 'Perfect bond' and 'No bond' models represent two extreme cases of bond slip behaviour and that the crack patterns are similar between these two models, it is certain that the crack patterns of the other bond slip models will be similar as well. It can be observed that the crack patterns across the different T-beam models are also similar. Cracks have formed extensively in the web along the shear span.

At the peak load step, a band of high crack strains has formed a fairly diagonal path in the general direction from the support towards the load point. Towards the direction of the load point, it can be observed that this band of high crack strains formed along several elements directly under the flange. Nearer to the load point, cracks formed in several elements at the bottom of the flange. The results reported in Sections 8.5.3.3 and 8.5.3.4 have indicated that the main flexural reinforcement did not yield whereas the shear reinforcement yielded when the peak load was reached. Principal stresses approaching the concrete compressive strength were observed in concrete elements at the top layer of the flange near the load point. The combination of these factors and the crack patterns shown in the figures indicated that the numerical models most likely failed in shear compression. In experiments, shear compression failure was characterised by the formation of diagonal tension crack, which had formed in the web, propagating along the web-flange junction into the flange towards the load point. The reduction of the area of the compression zone in the flange and high shear forces caused the concrete to crush near the load point. Unlike flexural compression failure, the main flexural reinforcement has not yielded.

The increase in the shear crack width in the web due to yielding of the shear reinforcement allows the propagation of the shear crack into the flange.

In the models, the band of high crack strains (red lines) formed closer to the location of the experimental shear crack '1' (refer to Figure 7.14). The crack strains were lower along the path of the experimental shear crack '2'. This is consistent with the results obtained from the photogrammetry measurement. Referring back to Figure 7.21 and Figure 7.22, the average crack width of shear crack '1' is generally larger than the average crack width of shear crack '2'.

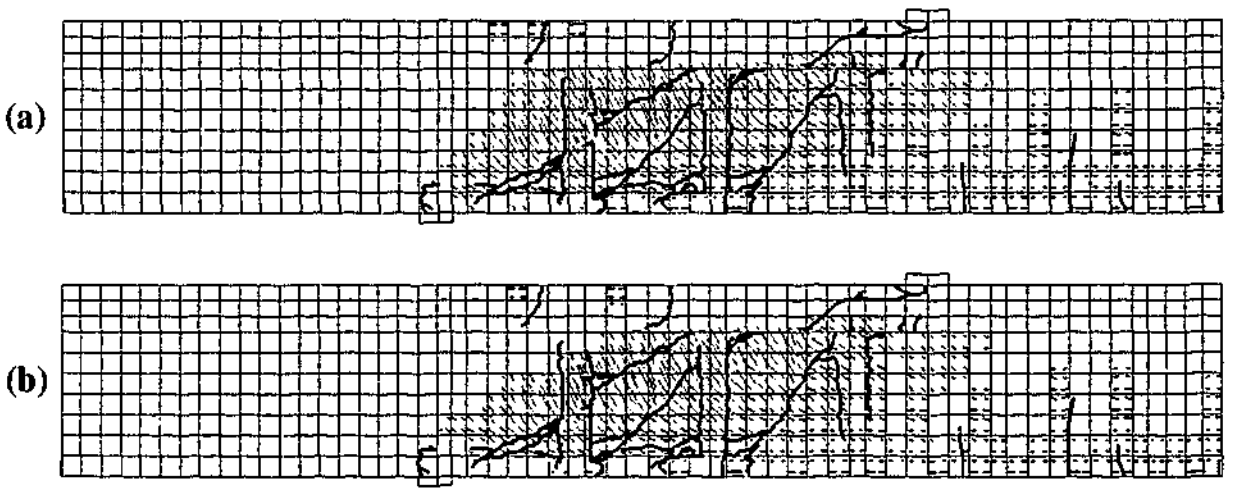

Figure 8.46 - Experimental crack patterns and corresponding predicted crack tensile strains of beam '0.75D' 2D models with (a) Perfect bond and (b) No bond

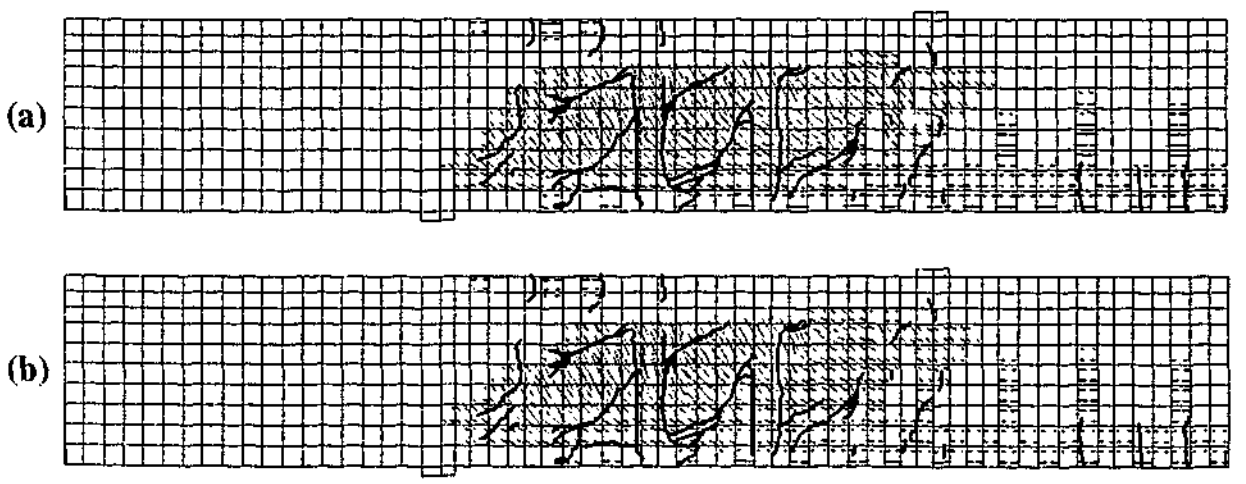

Figure 8.47 - Experimental crack patterns and corresponding predicted crack tensile strains of beam '0.60D' 2D models with (a) Perfect bond and (b) No bond

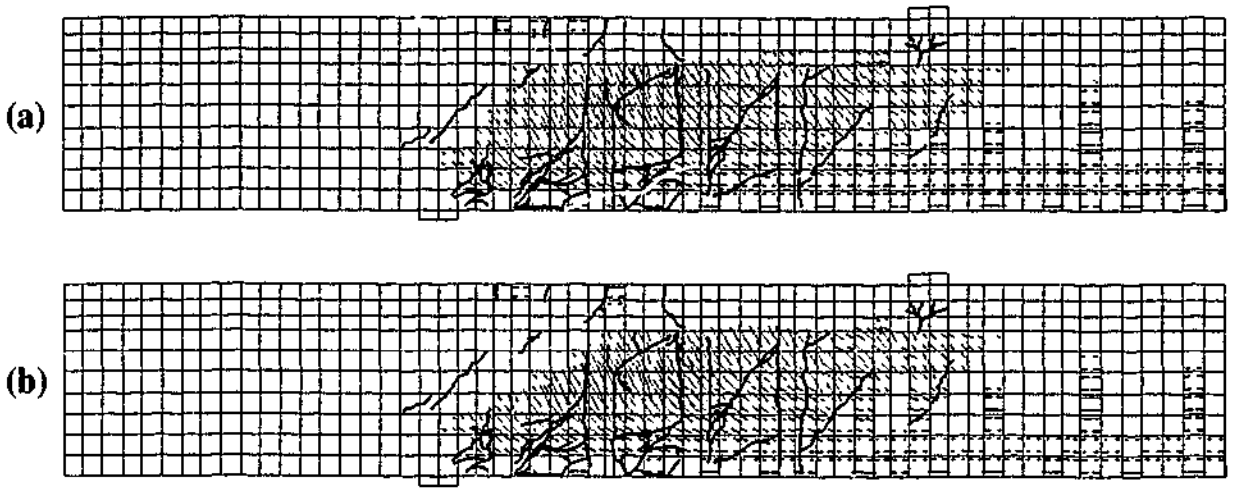

Figure 8.48 - Experimental crack patterns and corresponding predicted crack tensile strains of beam '0.50D' 2D models with (a) Perfect bond and (b) No bond

8.5.3.7 Summary

The effects of varying the interface behaviour between the CFRP and concrete layer in the 2D strengthened beam models with shear retention factor β of 0.05 were investigated in this section. For each beam type, the load displacement responses vary slightly depending on the bond slip models used. It was found that variation in the CFRP spacing has an insignificant effect on the shear capacity of the T-beams in the 2D numerical models adopted herein. For a given bond slip model, the predicted shear capacities were similar across all the different T-beam models.

As for the behaviour of the main flexural reinforcement, apart from the difference due to the peak load reached, the load strain responses were similar across all the models. The main reinforcement strained linearly with load until structural failure with no noticeable difference in the flexural stiffness of the beams. In all of the models, the main reinforcement did not yield indicating that flexural tensile failure did not occur.

The load strain responses of the shear reinforcement were similar in the various models at the early stages of loading. The strains in the stirrups were insignificant indicating that little or no load was being carried. The load level at which the strains in the stirrups began to increase significantly was also similar in all the models, which was approximately at 150 kN. At high load levels, the responses differ between the experiments and numerical models. The responses indicated that

the CFRP reinforcement does not contribute significantly to carrying the shear load compared to the experiments. For each T-beam model, variations in the bond slip models adopted yielded only slight but insignificant difference in the response of the shear reinforcement. The load carried by the stirrups is only slightly less in the strengthened beam models compared to their respective base models. The levels of strain achieved in the CFRP plates in the numerical models were significantly less compared to the levels of strain achieved in the CFRP plates in the experiments.

The crack patterns at the peak load level were similar across all the T-beam models regardless of the bond slip models adopted. This indicated that the beam failed in a similar fashion, which was established to be most likely shear compression failure. Although the finite element models did not account fully for the effects of CFRP spacing in the different T-beams, they have been proven to be capable of simulating most of the trends observed in the experimental beams adequately.

8.5.4 Effect of varying shear retention factor β in 2D strengthened beam models 'BS1'

8.5.4.1 Introduction

The effect of varying the shear retention factor β on the behaviour of the 2D strengthened beam model with bond slip property 'BS1' are reported in this section. The shear retention factors of 0.06 and 0.07 were investigated. The effects on the load displacement, steel reinforcement and CFRP plate responses and crack patterns were investigated.

8.5.4.2 Load displacement behaviour

The load-displacement responses of the different T-beam models with varying β values are compared in Figure 8.49 and Figure 8.50. As expected, the predicted shear capacities of the individual beam increases with β. The responses were similar for most of the loading regime. At higher shear load levels, the models with higher β values exhibited stiffer responses. In Figure 8.50, it can be observed that for a given β value, the peak load levels achieved between the different T-beam models were similar. At high load levels, the stiffness varies slightly between the beams but there is no noticeable trend between the CFRP spacing and beam stiffness.

(a)

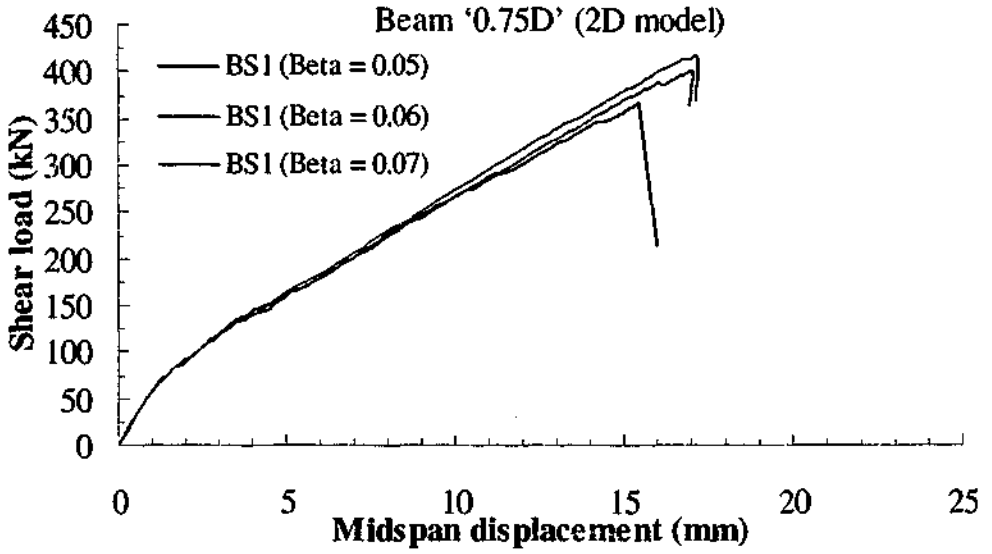

(b)

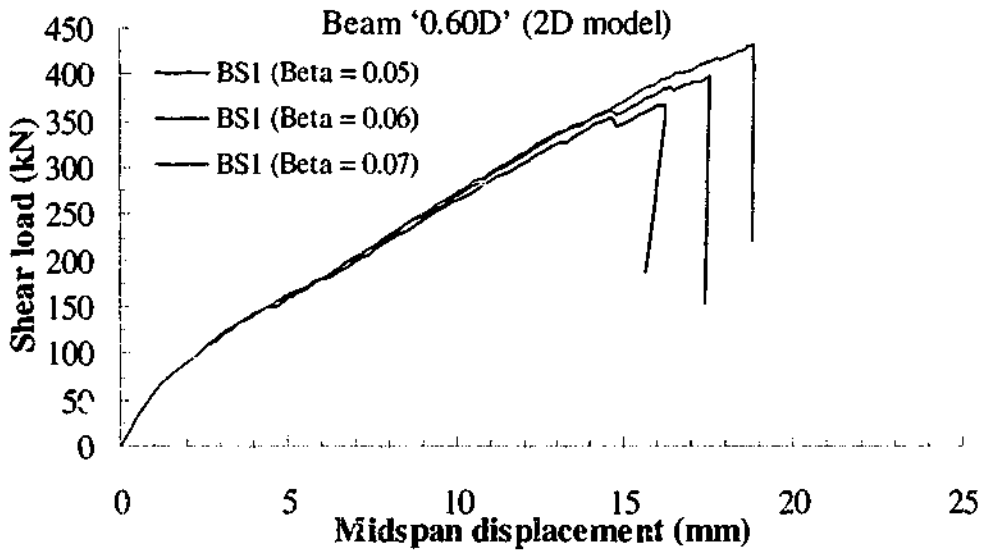

(c)

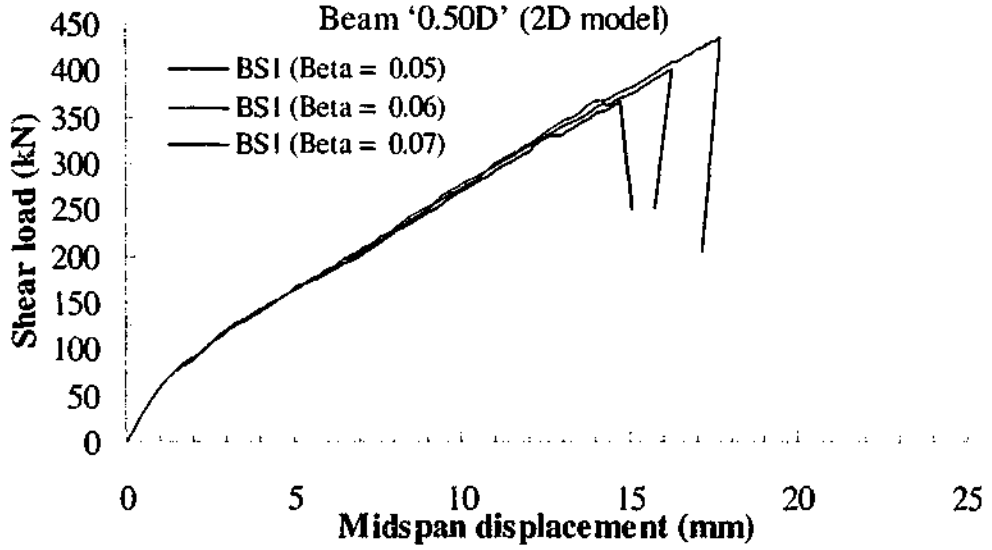

Figure 8.49 - Comparison of load displacement responses of 2D models 'BS1' with varying β values in beams (a) '0.75D' (b) '0.60D' and (c) '0.50D'

(a)

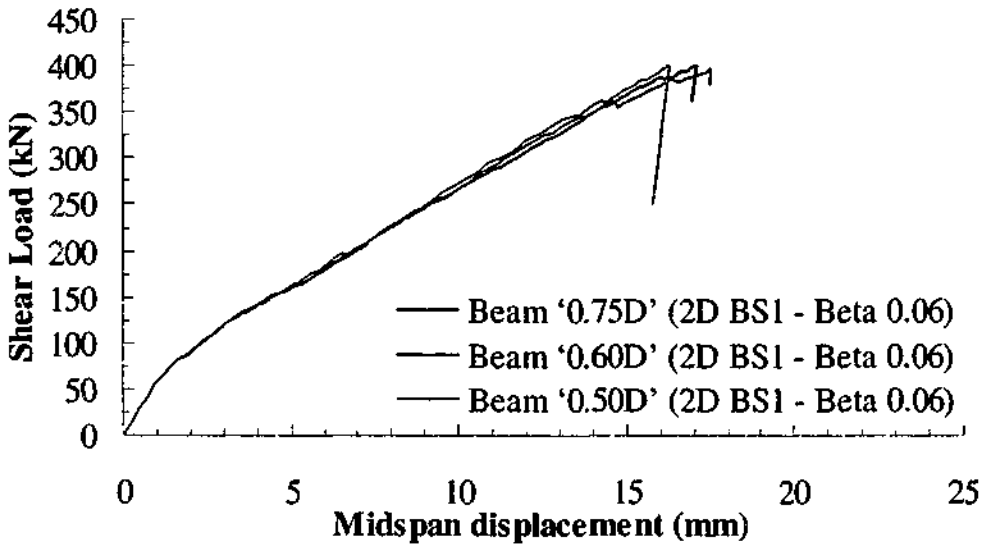

(b)

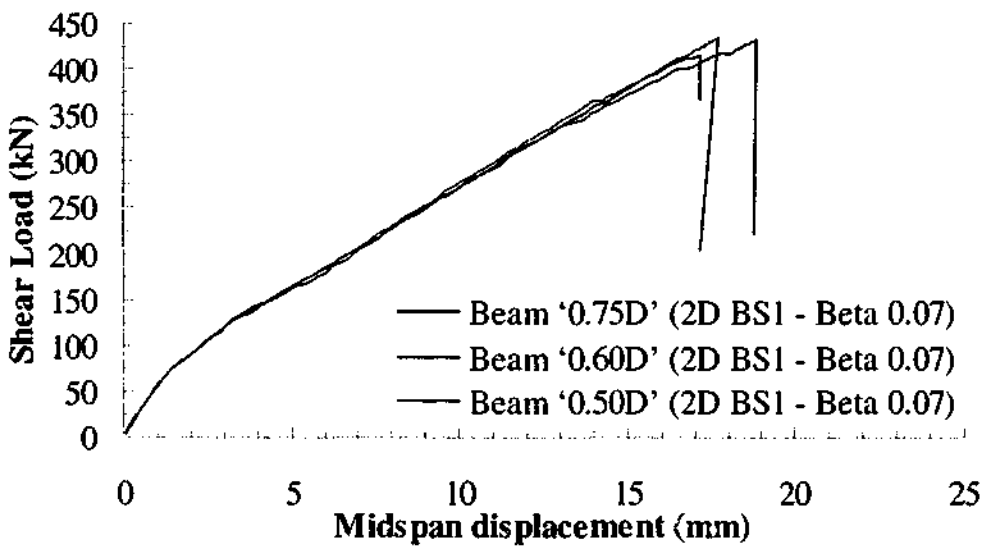

Figure 8.50 - Comparison of load displacement responses of 2D models 'BS1' in different T-beams with β values of (a) 0.06 and (b) 0.07

8.5.4.3 Behaviour of the main flexural reinforcement

Figure 8.51 compares the main reinforcement behaviour of the different T-beam models with varying β value. Apart from the difference due to the peak load reached, it can be observed that the load strain responses were similar in all the models. The main reinforcement strained linearly with load until structural failure. The main reinforcement did not yield indicating that flexural failure did not occur.

(a)

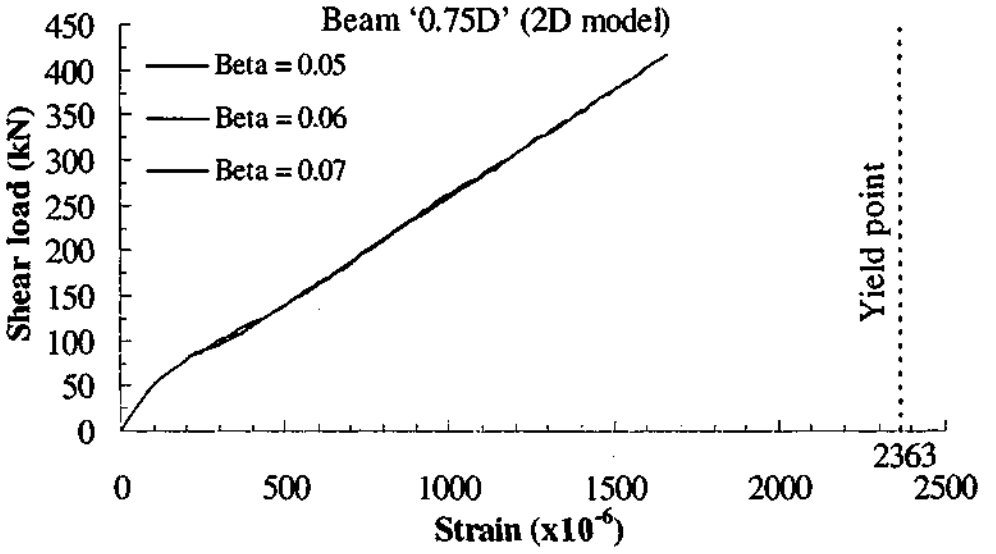

(b)

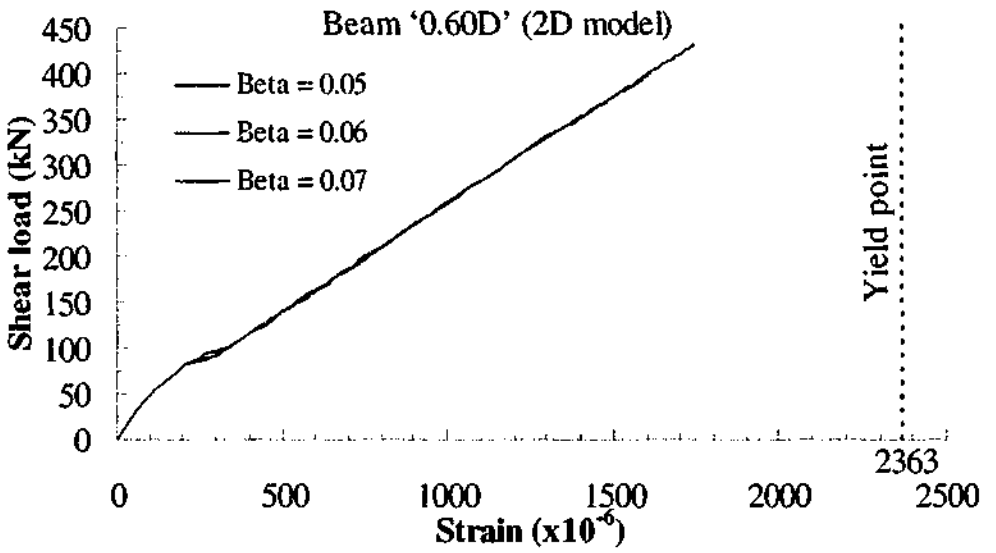

(c)

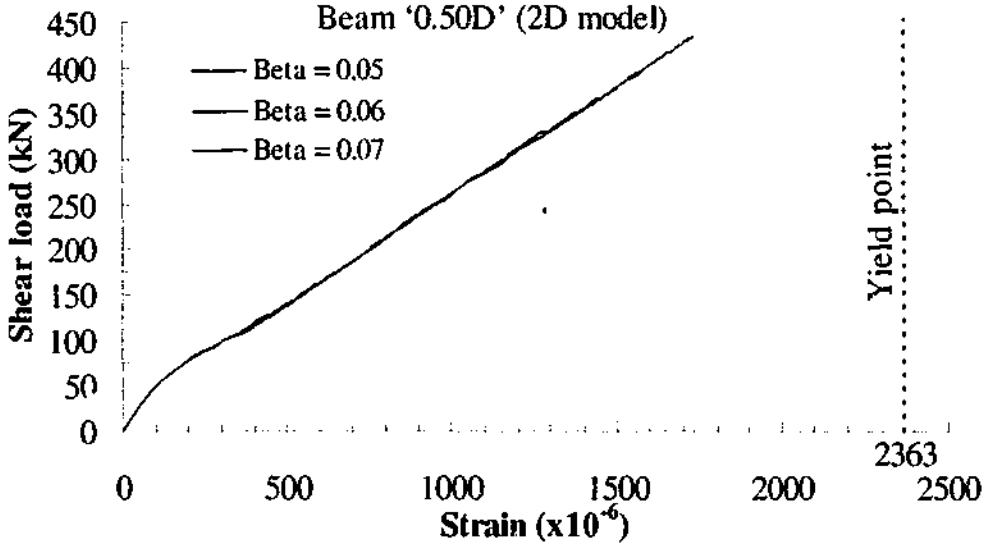

Figure 8.51 - Comparison of main flexural reinforcement responses of 2D models 'BS1' with varying β values in beams (a) '0.75D' (b) '0.60D' and (c) '0.50D'

8.5.4.4 Behaviour of shear reinforcement

The load strain responses of the shear reinforcement at the location 'S4' are compared in Figure 8.52. At low load levels, it can be observed that the shear reinforcement exhibited very small strains in all the numerical models. At higher load level, there is a general trend whereby the strain hence load carried by the shear reinforcement becomes smaller as the β value increases. The results are consistent with those presented previously in Section 8.5.2.4.

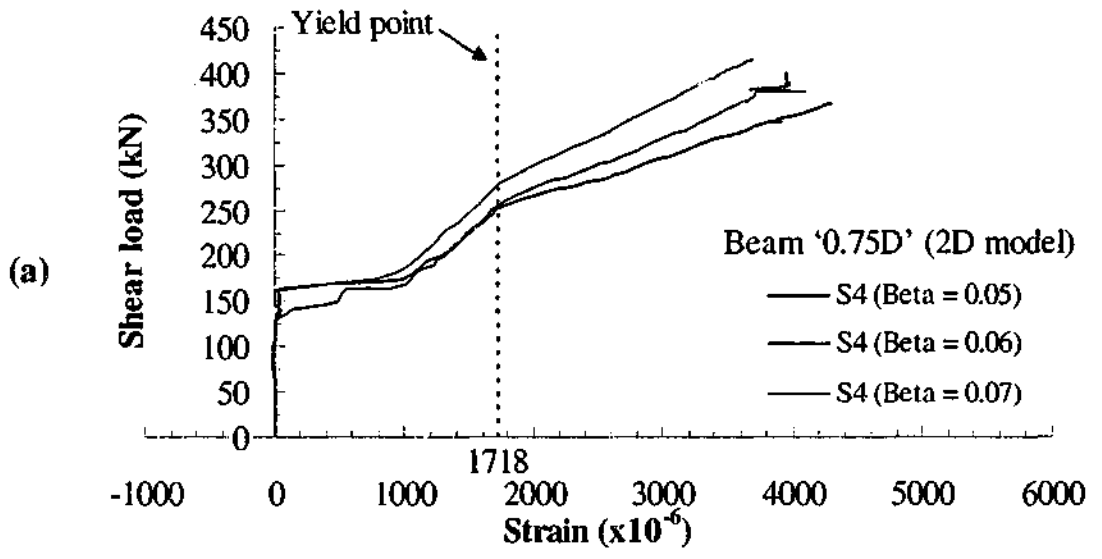

Figure 8.52 - Comparison of shear reinforcement responses at location S4 with varying β values in 2D beams (a) '0.75D' (b) '0.60D' and (c) '0.50D'

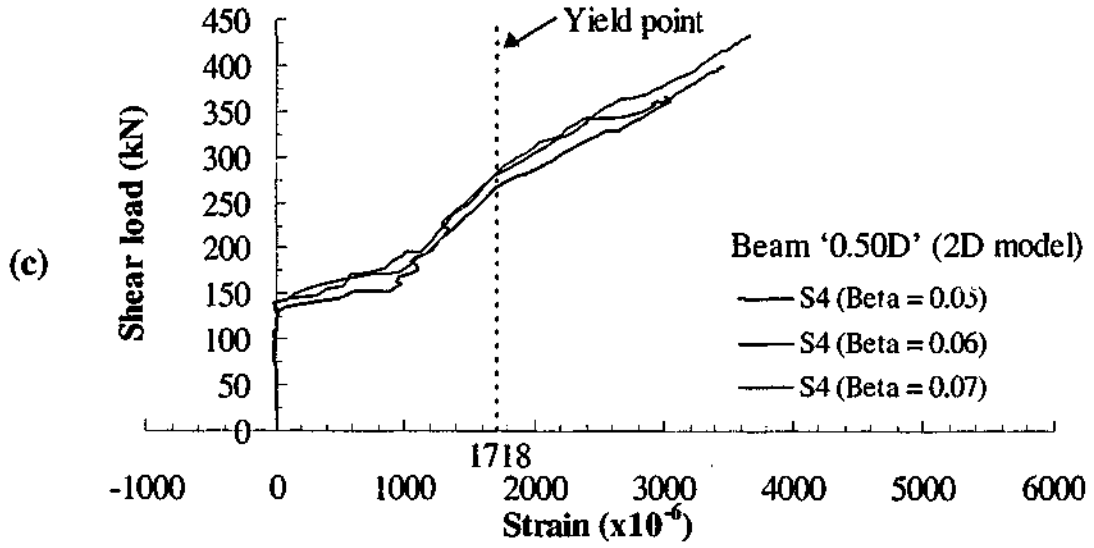

Figure 8.52 (continued) - Comparison of shear reinforcement responses at location S4 with varying β values in 2D beams (a) '0.75D' (b) '0.60D' and (c) '0.50D'

Figure 8.53 compares the load strain responses of the different T-beam models with the same β value. It can be observed that the responses are fairly similar in the different T-beams. There is a general trend that the smaller the CFRP spacing, the smaller the strain hence load carried by the shear reinforcement. Similar to the results in Section 8.5.3.4, the differences in the numerical responses are not as distinct compared to differences in the experimental responses illustrated in Figures 6.6 and 6.7. This indicated that the CFRP reinforcement does not contribute significantly to carrying the shear load compared to the experiments even when higher β values were adopted. The stirrups still carry significant portions of the shear load. This has resulted in the predicted shear capacities to be similar despite the fact that the CFRP spacings in the models were different.

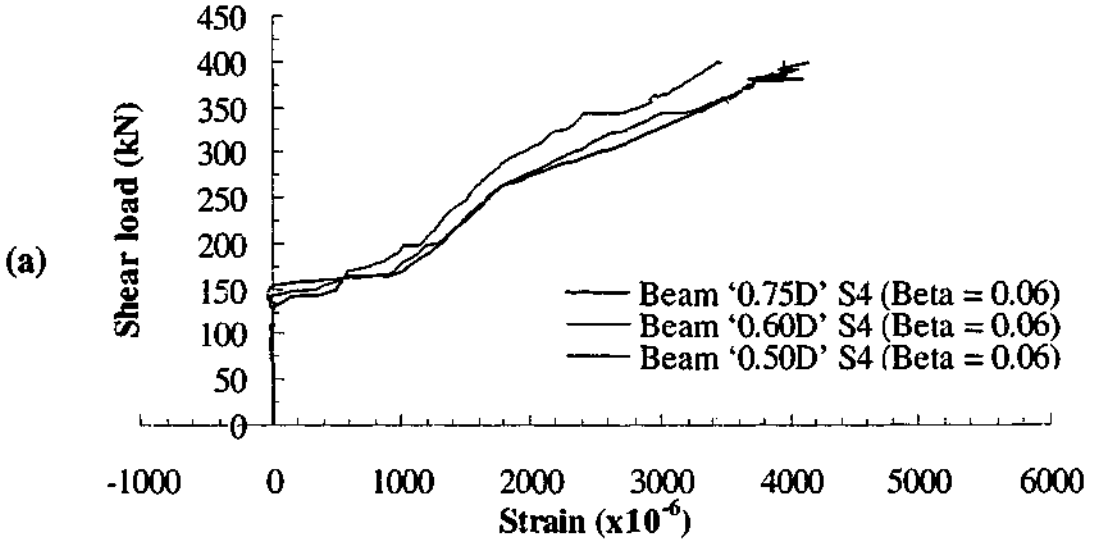

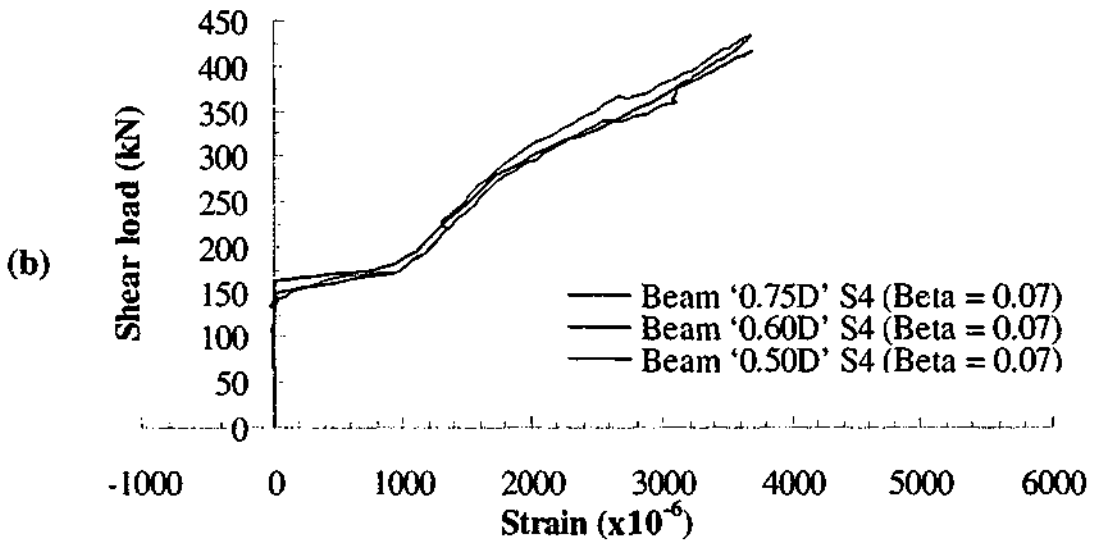

Figure 8.53 - Comparison of shear reinforcement responses of 2D models 'BS1' at location S4 with β values of (a) 0.06 and (b) 0.07

8.5.4.5 Strain contours of L-shaped CFRP reinforcement

The strain contours of the L-shaped CFRP plates at the peak load step of the models 'BS1' with varying β values are illustrated in Figure 8.54 to Figure 8.56. It can be observed from the figures that the most critically loaded CFRP reinforcement in the different T-beams remained the same as reported previously in Section 8.5.3.5.

In all beams except beam '0.75D', the level of strain achieved in the CFRP plates increases with increases in the β value. This is mostly due to the increase in the shear capacity of the T-beams following the increase in β. The maximum level of strain achieved in the CFRP, however, was still significantly less compared to the level of strain achieved in the CFRP plates in the experiments.

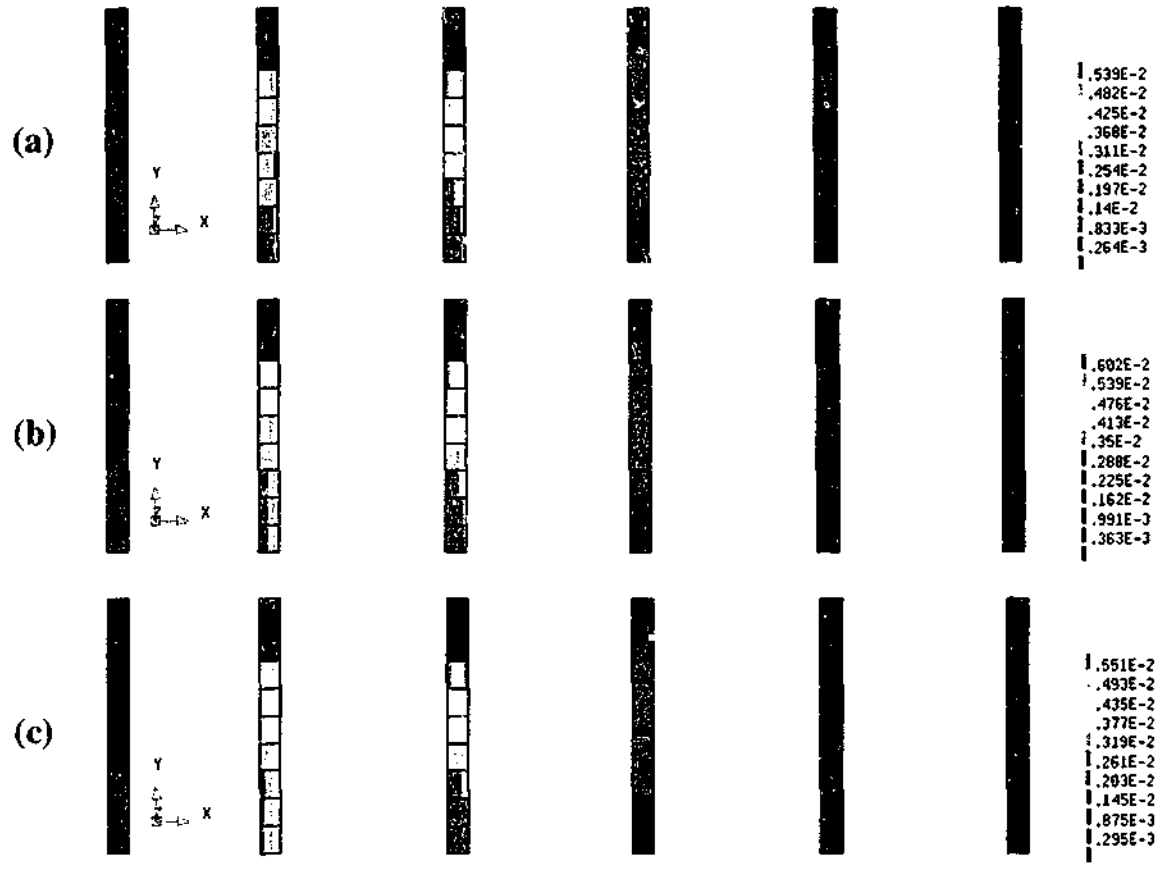

Figure 8.54 - Strain in CFRP of beam '0.75D' 2D 'BS1' models with β of (a) 0.05 (b) 0.06 and (c) 0.07

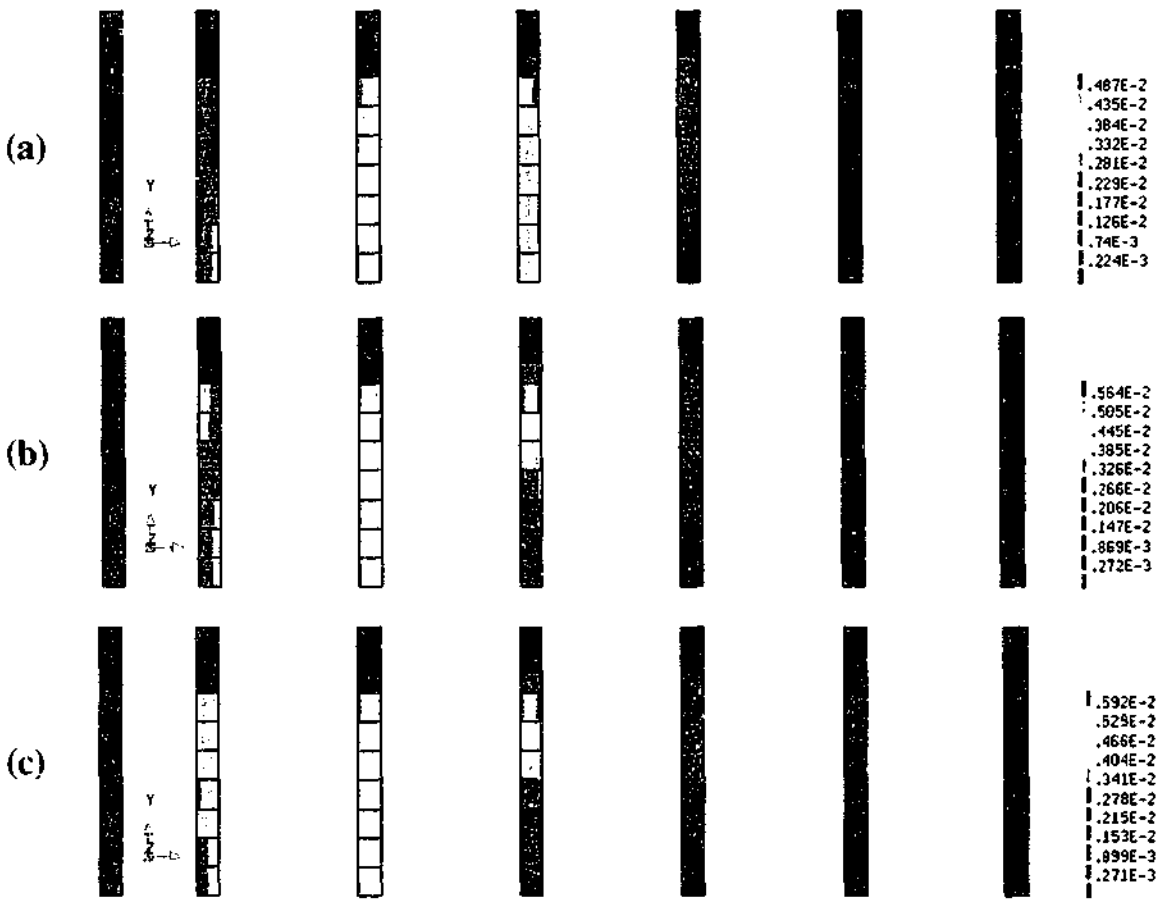

Figure 8.55 - Strain in CFRP of beam '0.60D' 2D 'BS1' models with β of (a) 0.05 (b) 0.06 and (c) 0.07

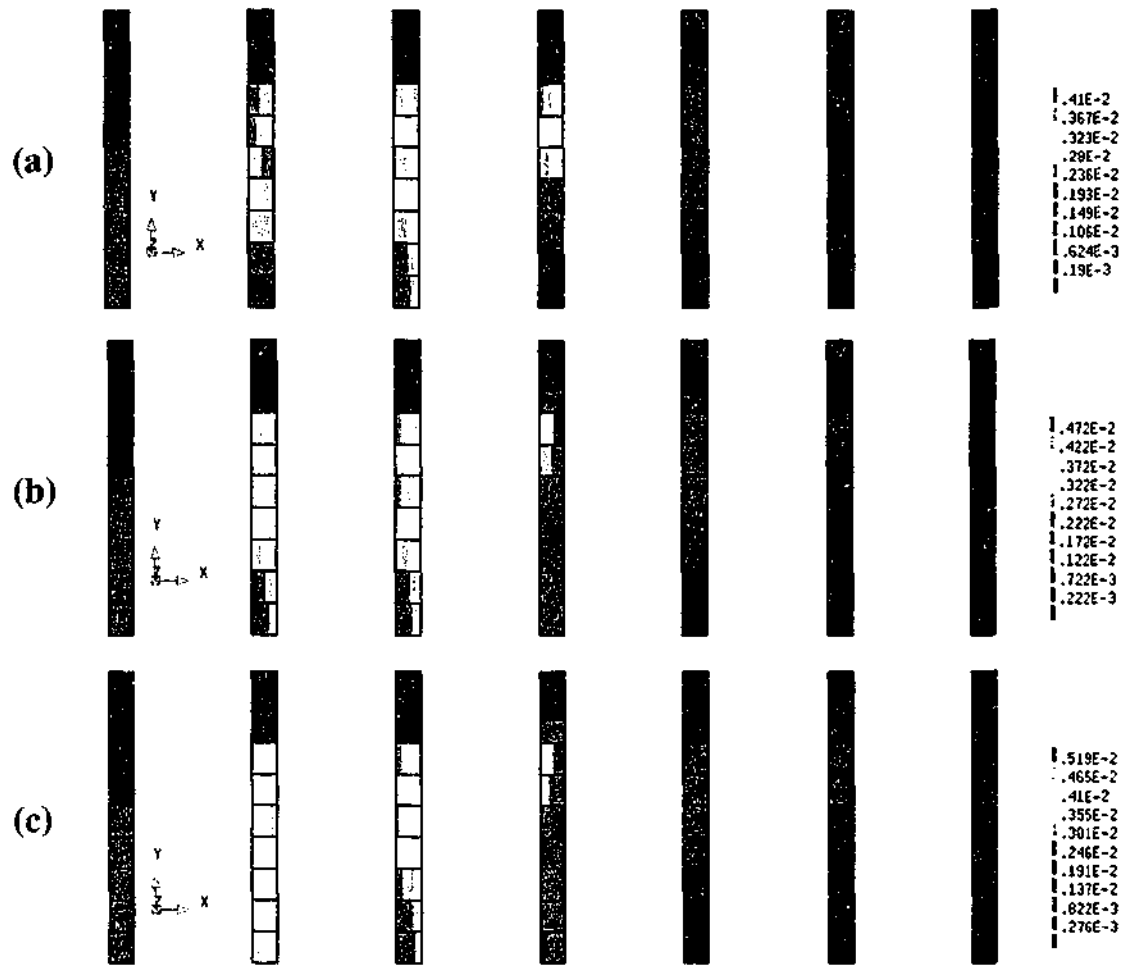

Figure 8.56 - Strain in CFRP of beam '0.50D' 2D 'BS1' models with β of (a) 0.05 (b) 0.06 and (c) 0.07

8.5.4.6 Crack pattern

The crack patterns of the models 'BS1' of the different T-beams with varying β values are compared in Figure 8.57 to Figure 8.59. The crack patterns were obtained at the peak load step of each respective model. It can be observed from the figures that the crack patterns are similar across the entire T-beam models. The locations of the band of high crack strains are similar in all the models. The results presented herein and in Sections 8.5.4.3 and 8.5.4.4 indicate that the beams most likely failed in shear compression.

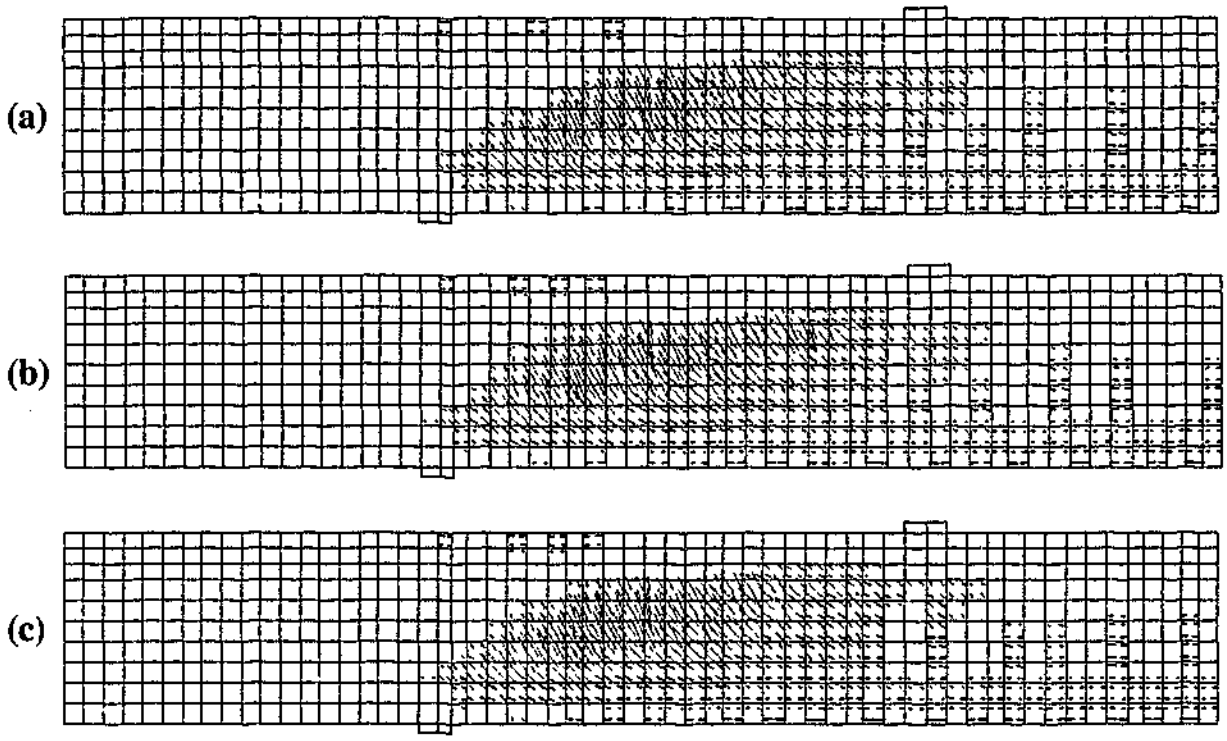

Figure 8.57 - Predicted crack tensile strain patterns of beam '0.75D' 2D 'BS1' models with β of (a) 0.05 (b) 0.06 and (c) 0.07

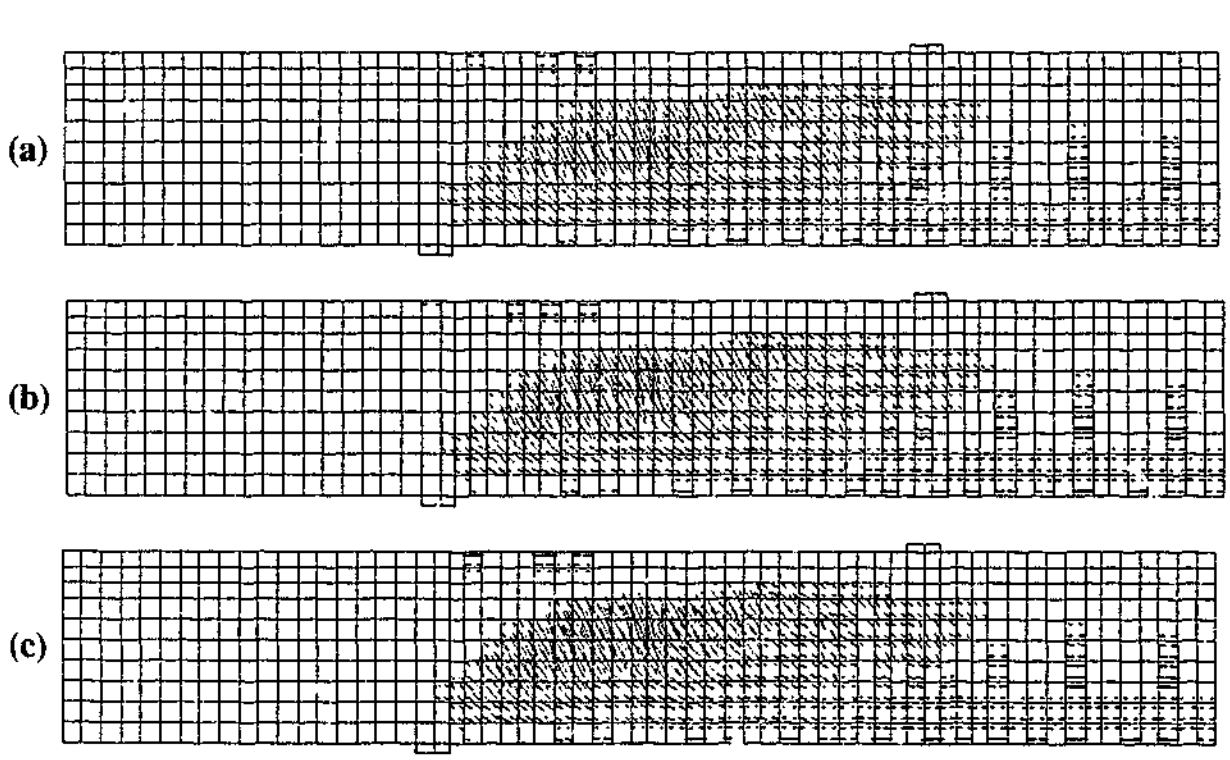

Figure 8.58 - Predicted crack tensile strain patterns of beam '0.60D' 2D 'BS1' models with β of (a) 0.05 (b) 0.06 and (c) 0.07

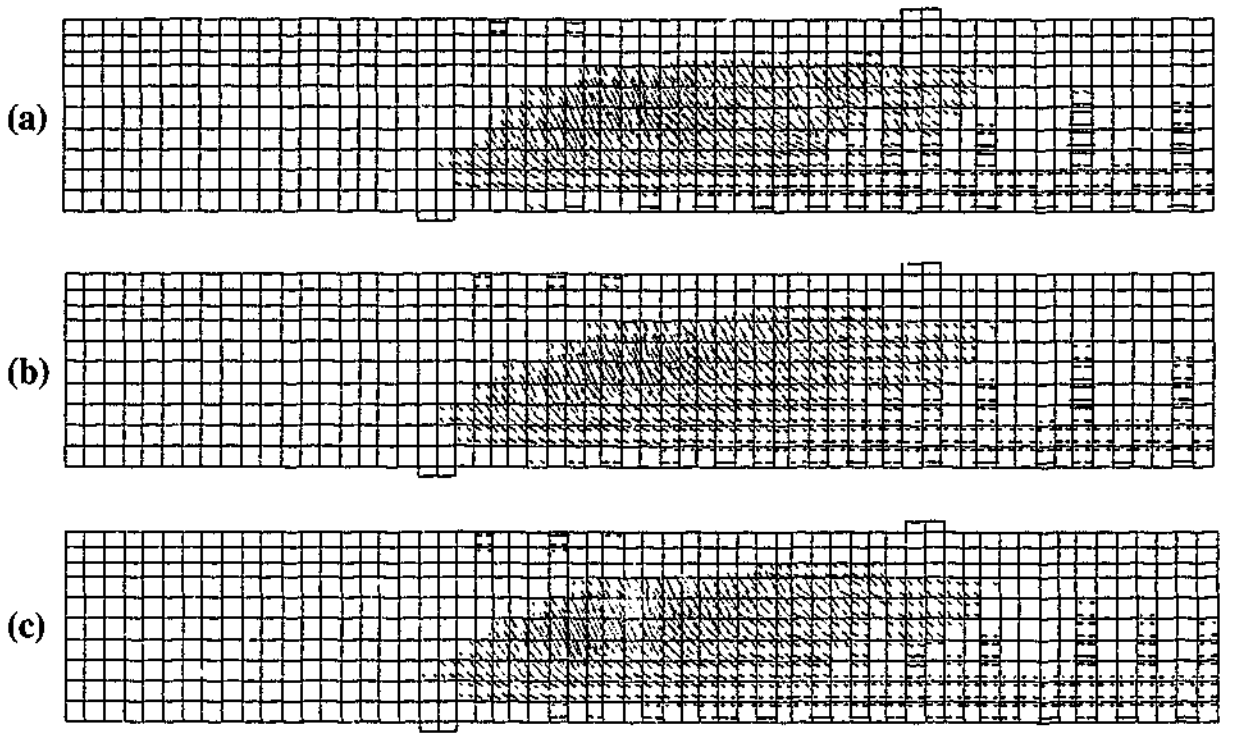

Figure 8.59 - Predicted crack tensile strain patterns of beam '0.50D' 2D 'BS1' models with β of (a) 0.05 (b) 0.06 and (c) 0.07

8.5.4.7 Summary

The effects of varying the shear retention factor β in the 2D T-beam models with bond slip property 'BS1' were investigated in this section. As expected, the load capacity of the T-beams increases with the shear retention factor. Similar to the results presented in Section 8 5.3.2, variation in the CFRP spacing has an insignificant effect on the shear capacity of the T-beams in the 2D numerical models adopted herein. The predicted shear capacities were similar across all the different T-beam models for a given β.

For the main flexural reinforcement, apart from the difference due to the peak load reached, the load strain responses were similar across all the models. The main reinforcement strained linearly with load until structural failure with no noticeable difference in the flexural stiffness of the beams. In all of the models, the main reinforcement did not yield indicating that flexural tensile failure did not occur.

The load strain responses of the shear reinforcement were similar in the various models at the early stages of loading. The strains in the stirrups were insignificant indicating that little or no load was being carried. The load level at

which the strains in the stirrups began to increase significantly was also similar in all the models. At higher load level, there is a general trend whereby the strain hence load carried by the shear reinforcement becomes smaller as the β value increases. In addition, there is a general trend that the smaller the CFRP spacing, the smaller the strain hence load carried by the shear reinforcement. However, the differences in the numerical responses are not as distinct compared to differences in the experimental responses illustrated in Figures 6.6 and 6.7. The crack patterns at the peak load level were similar across all the T-beam indicating that the beams failed in a similar fashion, which was established to be most likely shear compression failure.

The main finding of this section is that the contribution of the CFRP reinforcement in carrying the shear load of the T-beams is significantly less in the numerical models compared to the experiments. This is evident from the strain contour plot of the CFRP reinforcement obtained at the peak load and the load strain responses of the shear reinforcement. The level of strain in the CFRP reinforcement is significantly smaller compared to its experimental counterpart at a given load level. The load carried by the stirrups was significantly higher in the experiments than in the numerical models. This may be partly attributed to the smeared crack approach used in modelling cracking of concrete. In the experiments, discrete cracks that formed in the beams concentrate within a small region in the web. In the numerical models, the cracks are distributed over a band of elements therefore reducing the load that can be transferred to the CFRP reinforcement. To a lesser extent, the assumption of perfect bond between the stirrups and concrete elements has allowed more loads being transferred to the stirrups.

8.5.5 Effect of varying interface behaviour between CFRP and concrete layer in 3D strengthened beam models with β = 0.05

8.5.5.1 Introduction

In this section, the behaviour of the 3D strengthened beam models assuming various bond slip models (refer to Table 8.4) between the CFRP and concrete layer are investigated. The shear retention factor β of all the models was kept at 0.05. The effects on the load displacement, steel reinforcement and CFRP plate responses and crack patterns were investigated.

8.5.5.2 Load displacement behaviour

Figure 8.60 compares the load displacement behaviour of the experimental strengthened beams with their respective 3D numerical counterparts with different bond slip models. The numerical results of the base models (without CFRP reinforcement) from Section 8.5.1.2 have also been included. Similar to the 2D strengthened beam models, it can be observed that the responses of the strengthened beam models are identical to their respective base models at low shear load levels. The responses predicted by the numerical models were comparable to the experiments for most of the loading. At higher load levels, the numerical models exhibited stiffer responses compared to the experiments.

For each beam type, the predicted load capacities of the various bond slip models were fairly similar to each other. The figures indicate a trend whereby the predicted load capacities decrease with a reduction in the shear stiffness of the interface elements. However, it is difficult to establish conclusively that this is the case because the predicted load capacities were within 5% of each other. Introducing debonding characteristics into the interface elements as in the case of the 2D models will no doubt reduce the load capacities of the beams. The differences in the predicted load capacities may also be more apparent. However, this weakens the structure unnecessarily as the debonding effect is taken into account twice. The solution may be improved by increasing the number of elements in the lateral direction but will require significant computational effort and resources. Nevertheless, the results show that changes in the bond slip models do affect the overall beam behaviour. The 3D numerical models have also simulated the experimental trend that the shear capacity is higher in beams with the external CFRP reinforcement compared to beams without the external CFRP reinforcement.

For beam '0.75D', the predicted load capacities of the models are significantly higher compared to the experiment. For beams '0.60D' and '0.50D', the predicted load capacities were closer to the experiments. However, it should be noted that the failure mode of the numerical models is different to the experimental failure modes. In fact, the failure mode is similar to the 2D models and that is shear compression failure. The additional lateral dimension simulated in the 3D models did not result in a significant difference in overall behaviour from the 2D models.

(a)

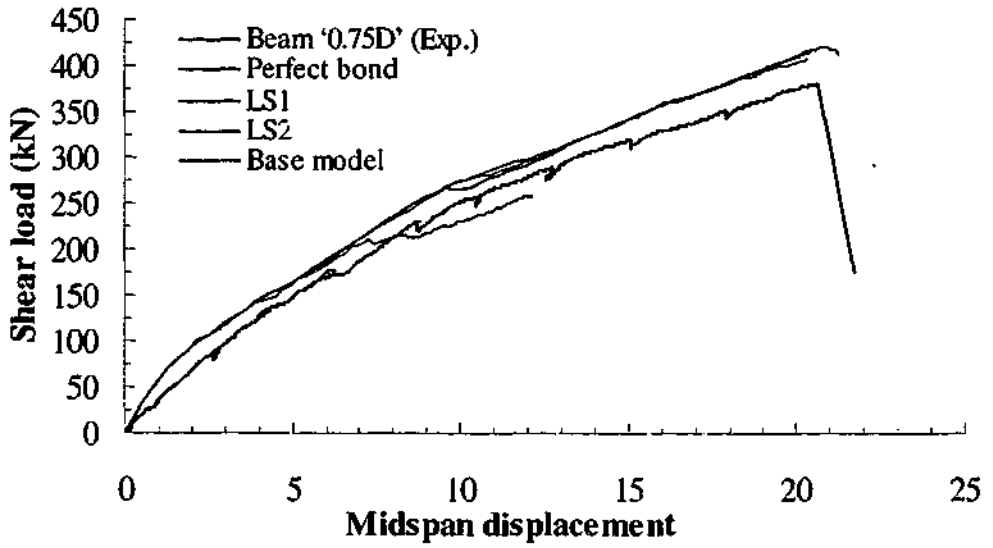

(b)

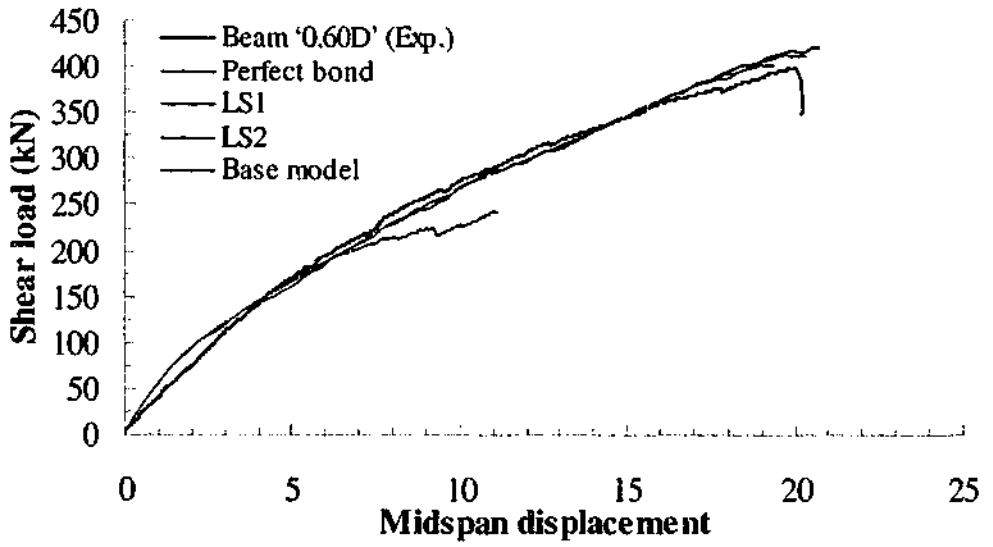

(c)

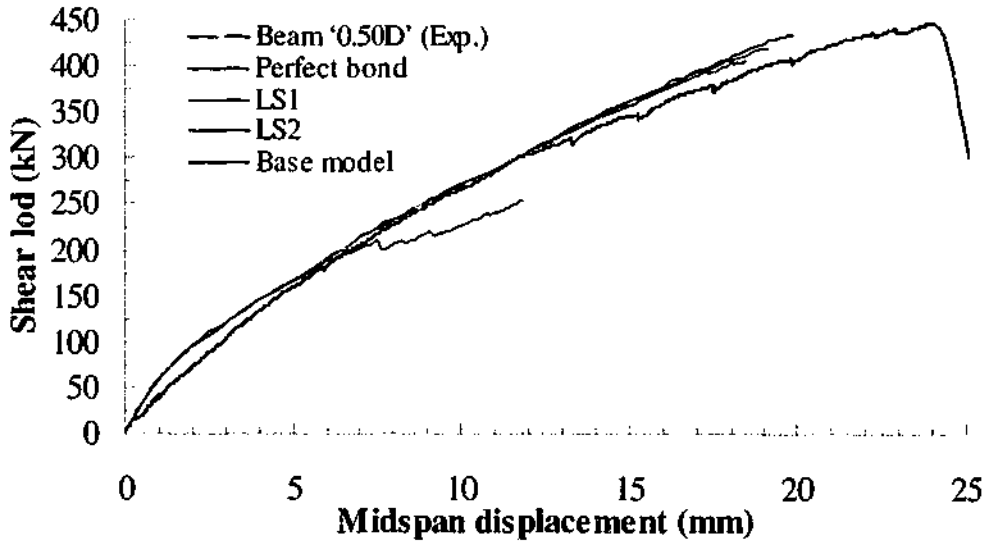

Figure 8.60 - Comparison of experimental and 3D numerical load displacement behaviour of beams (a) '0.75D' (b) '0.60D' and (c) '0.50D'

Figure 8.61 compares the load displacement responses of the different T-beam models with identical bond slip models. It can be observed that the responses, in general, are similar for all the different beams. Similar to the 2D models, the predicted peak loads are fairly close to each other despite the fact that the beams have different CFRP spacing,. There is no noticeable trend in the predicted peak load with varying CFRP spacing in the beams. However, there is a general trend whereby the response is stiffer in the beam with smaller CFRP spacing at high shear load levels. The failure mode of all the models is the same, which has been established in Section 8.5.5.6 to be most likely shear compression failure. Similar to the 2D models, this implies that variation in the CFRP spacing has an insignificant effect on the shear capacity of the T-beams in the 3D numerical models as well. Increasing the shear retention factor β of the concrete elements (refer to Section 8.5.6) yielded similar outcome. For a given bond slip model, the predicted shear capacities of the different T-beams were similar regardless of the CFRP spacing. The finite element models did not account fully for the effects of CFRP spacing in the different T-beams.

(a)

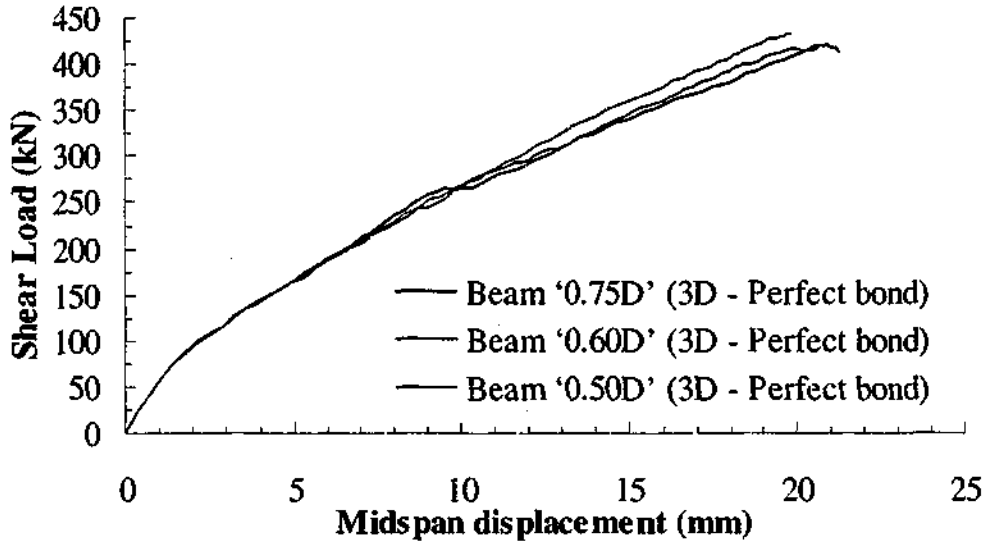

(b)

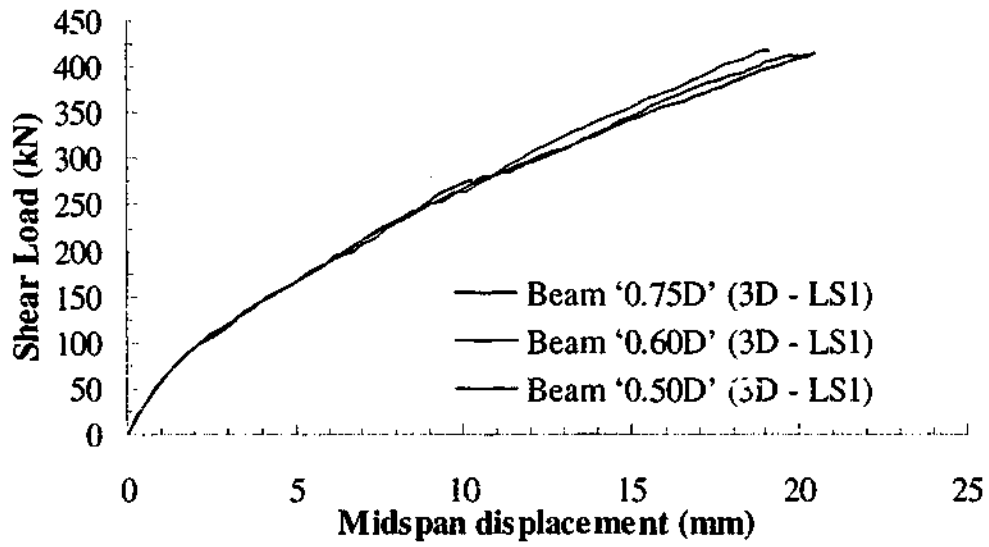

(c)

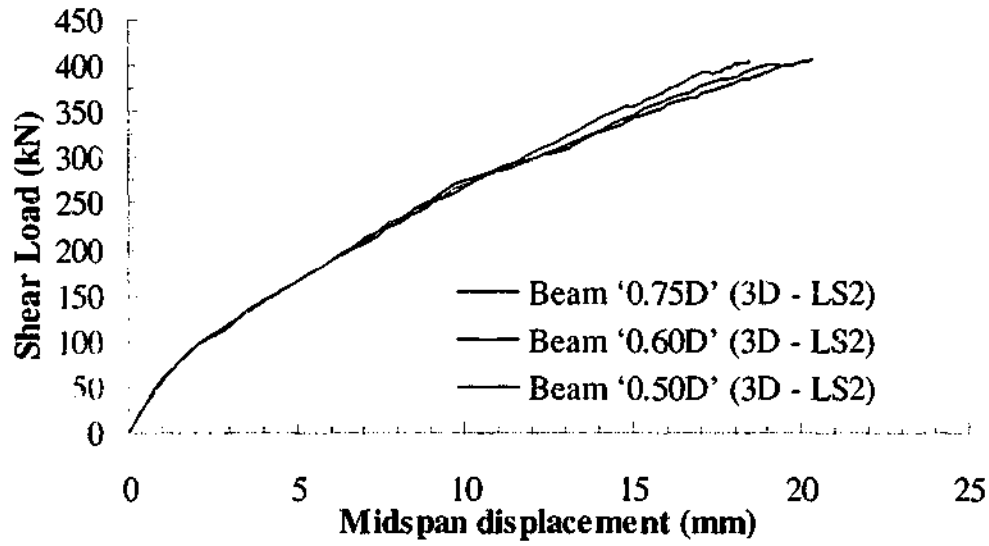

Figure 8.61 - Comparison of numerical load displacement behaviour of 3D models with (a) Perfect Bond (b) LS1 and (c) LS2

8.5.5.3 Behaviour of main reinforcement

Figure 8.62 compares the main reinforcement behaviour of the experimental strengthened beams with their respective numerical counterparts. Apart from the difference due to the peak load reached, it can be observed that the load strain responses were similar across all the models. The main reinforcement strained linearly with load until structural failure. The main reinforcement did not yield indicating that flexural failure did not occur. The numerical responses were similar to the experiments.

(a)

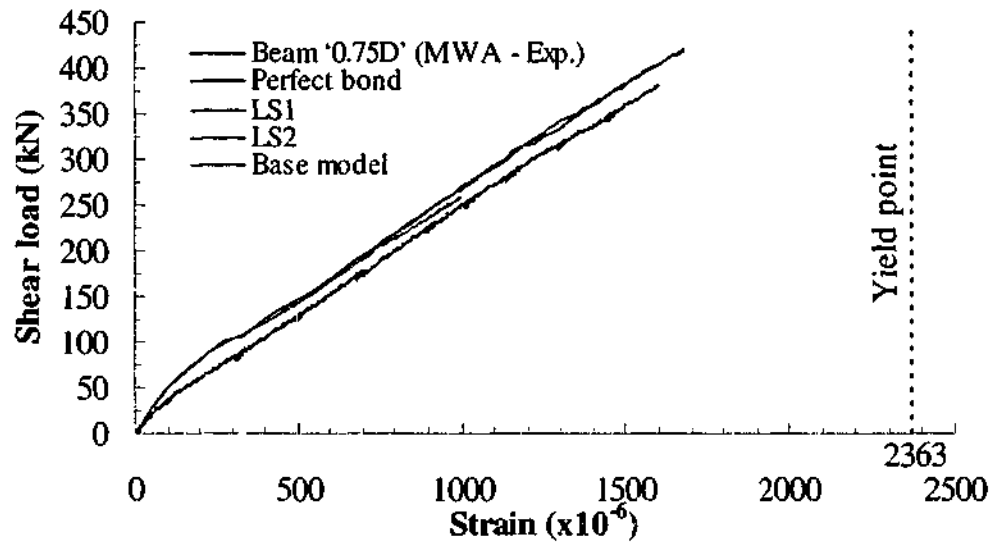

(b)

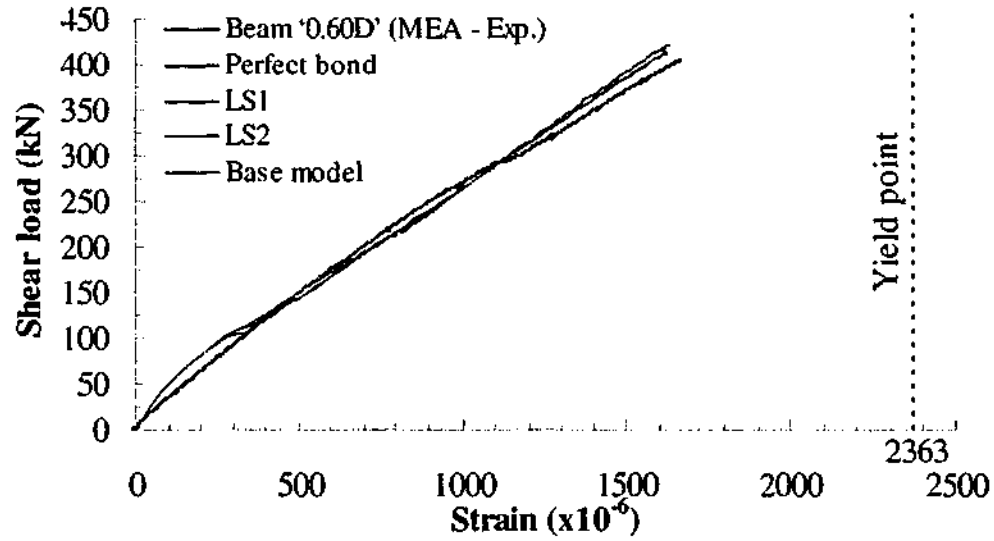

Figure 8.62 - Comparison of experimental and 3D numerical main reinforcement behaviour of beams (a) '0.75D' (b) '0.60D' and (c) '0.50D'

(c)

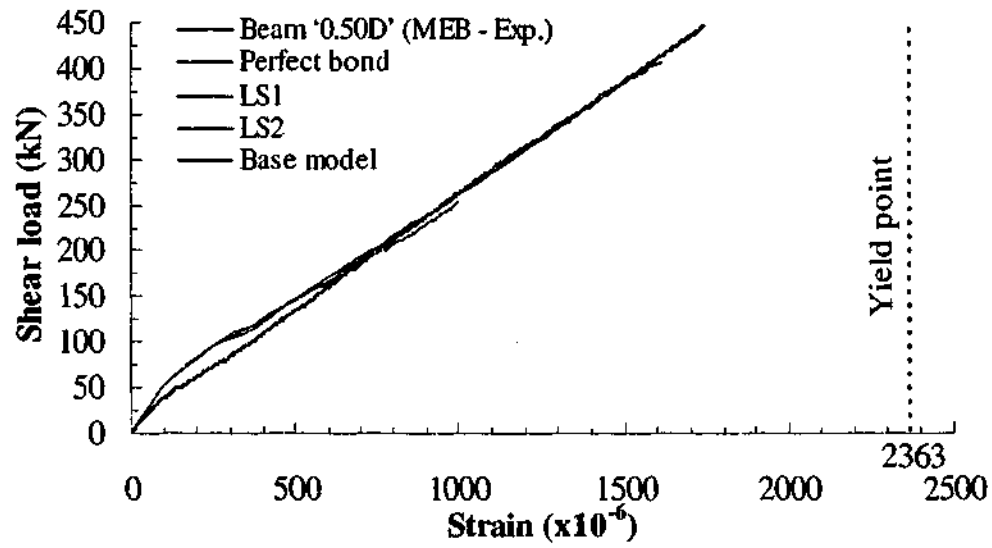

Figure 8.62 (continued) - Comparison of experimental and 3D numerical main reinforcement behaviour of beams (a) '0.75D' (b) '0.60D' and (c) '0.50D'

8.5.5.4 Behaviour of shear reinforcement

Figure 8.63 to Figure 8.65 compare the shear reinforcement load strain responses of the experimental and numerical results at selected locations. Similar to the 2D models, the shear reinforcement exhibited very small strains in all the numerical models at low shear load levels. In the numerical models, the load level at which the strain in the reinforcement began to increase significantly was comparable to the experiments. At higher load levels, the response predicted by the numerical models deviated significantly from the experimental results but the general trend remained similar. Similar to the 2D models, this is partly due to the assumption of perfect bond between the concrete and stirrups. Beyond the service load levels, it can be observed that the strain in the stirrups is generally lower in the strengthened beam models compared to the base models at a given load level. This indicates that part of the shear load has been carried by the CFRP reinforcement but the contribution is minor. For each beam type, the load strain responses vary only slightly between the different bond slip models. The figures do not indicate any trend between the strain in the stirrups and bond slip models.

(a)

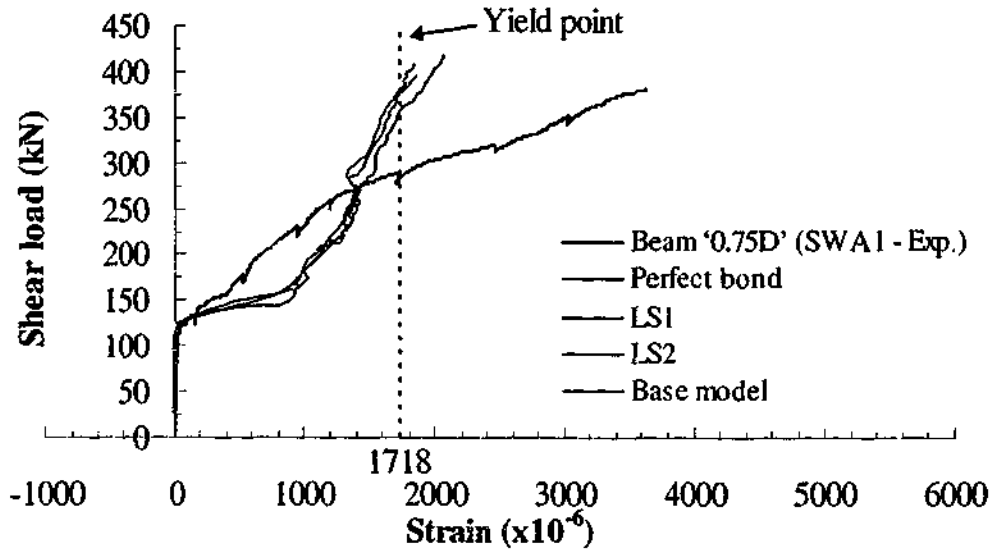

(b)

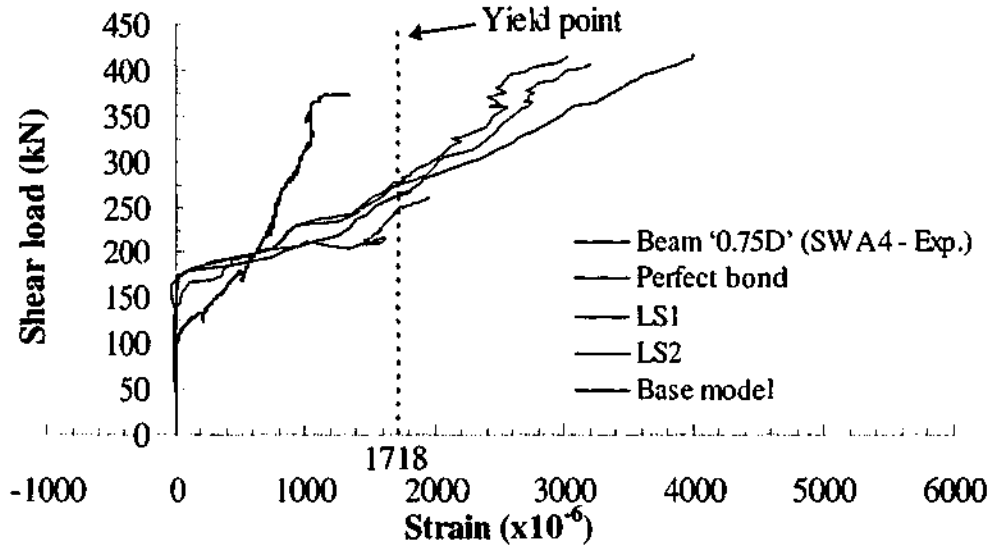

Figure 8.63 - Comparison of shear reinforcement behaviour of beam '0.75D' 3D models at stirrup locations (a) S1 and (b) S4

(a)

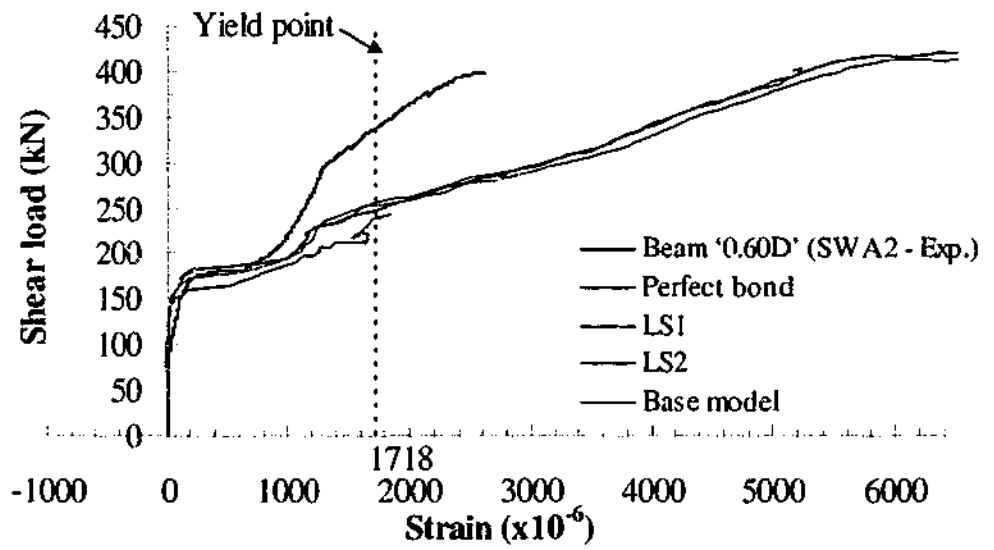

Figure 8.64 - Comparison of shear reinforcement behaviour of beam '0.60D' 3D models at stirrup locations (a) S2 and (b) S4

(b)

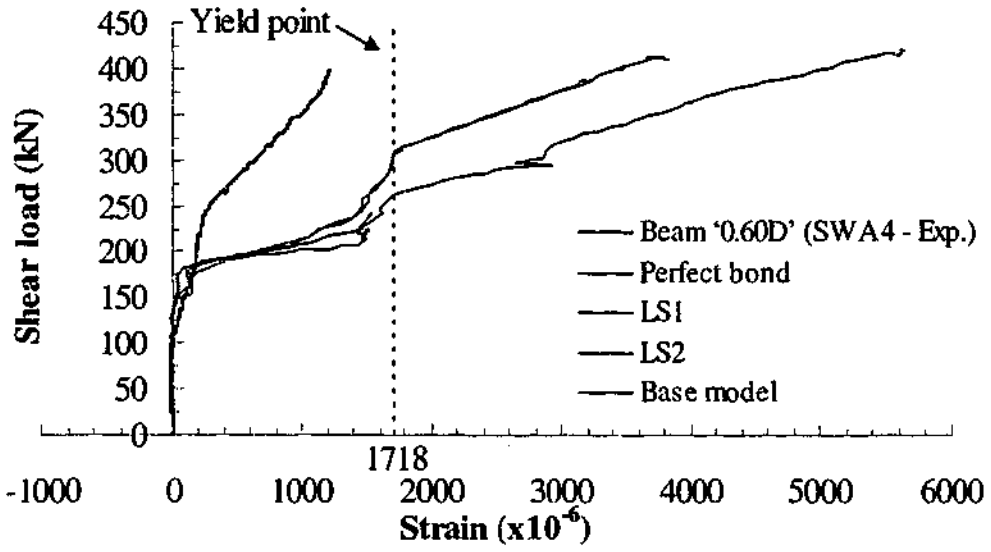

Figure 8.64 (continued) - Comparison of shear reinforcement behaviour of beam '0.60D' 3D models at stirrup locations (a) S2 and (b) S4

(a)

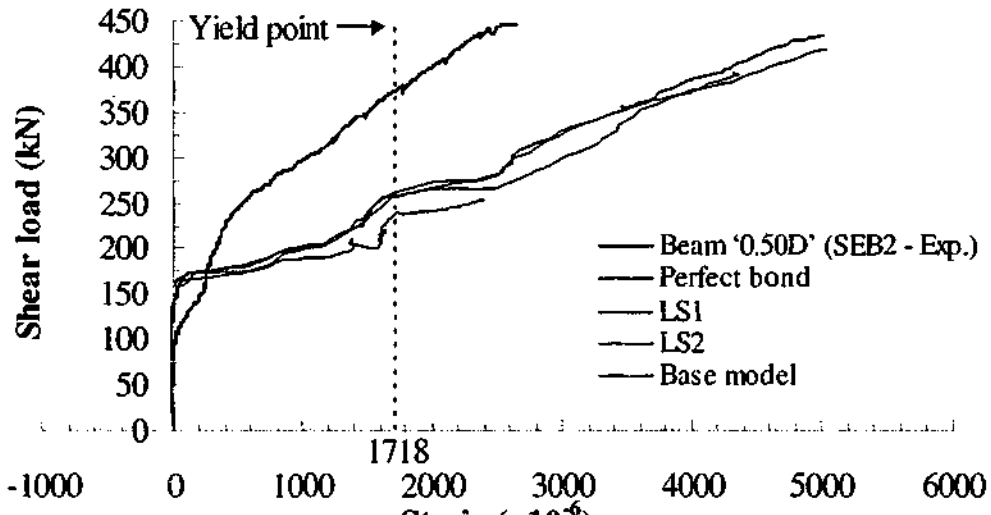

(b)

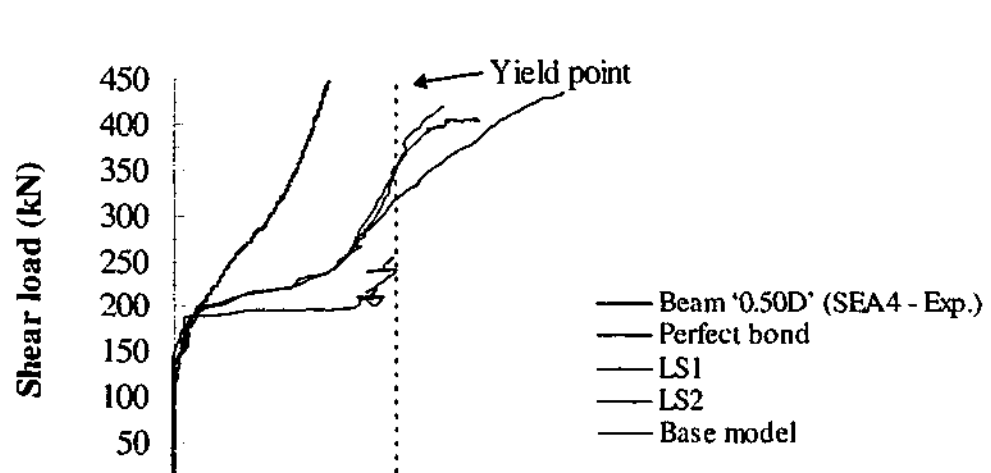

Figure 8.65 - Comparison of shear reinforcement behaviour of beam '0.50D' 3D models at stirrup locations (a) S2 and (b) S4

Figure 8.66 compares the load strain responses at location 'S4' of the 'Perfect bond' and 'LS2' models. It can be observed that the responses are fairly similar in the different T-beams. In the 2D models in Section 8.5.3.4, there is a general trend that the smaller the CFRP spacing, the smaller the strain hence load carried by the shear reinforcement. This trend is not observed in the 3D models in Figure 8.66. Although, the comparisons between the experimental beams and numerical models have been made at selected locations, the results presented still gives a good indication of the overall behaviour of the shear reinforcement in the numerical models.

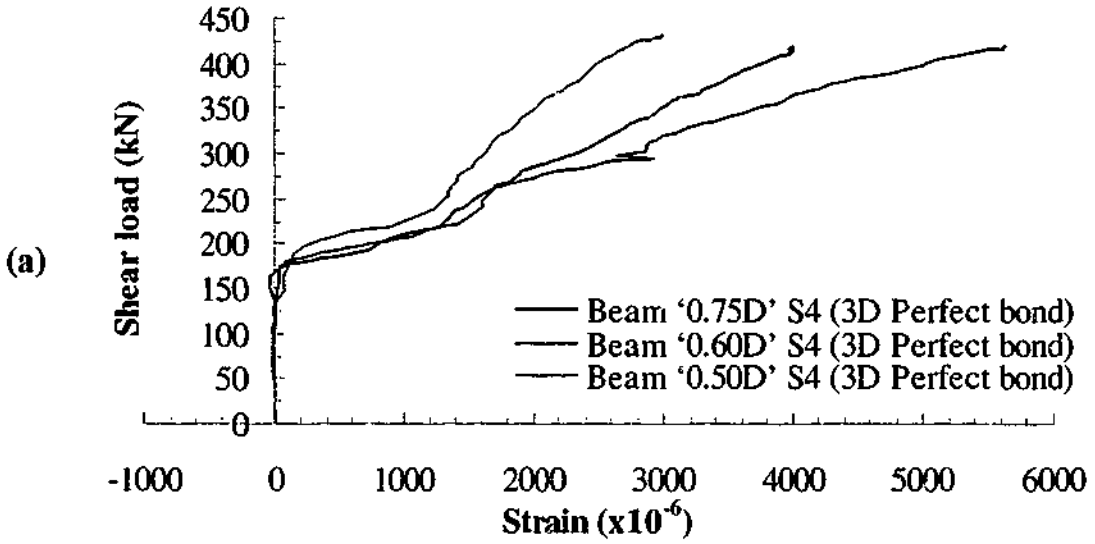

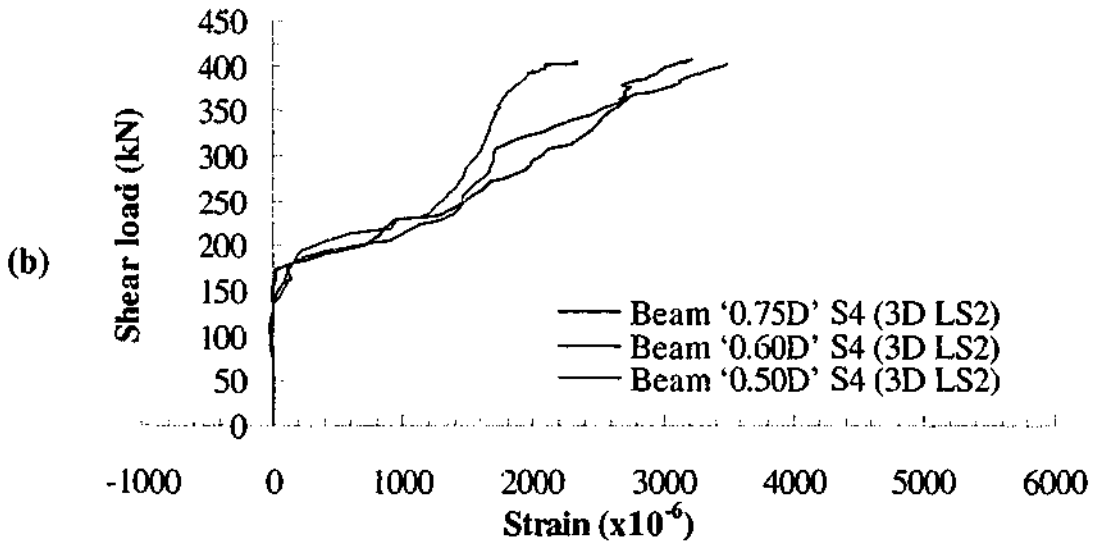

Figure 8.66 - Comparison of shear reinforcement behaviour at location S4 of 3D models with (a) 'Perfect bond' and (b) 'LS2'

8.5.5.5 Strain contours of L-shaped CFRP reinforcement

The strain contours of the L-shaped CFRP plates from the various models are illustrated in Figure 8.67 to Figure 8.69. The strain contours shown were taken at the peak load step of each model. The CFRP plates outside of the shear span carry very low shear loads in all the numerical models. The locations of the most critically loaded CFRP plates in the different T-beams were identical to the 2D models. Similar to the 2D models, the maximum level of strain achieved in the CFRP plates in the numerical models were also significantly less compared to the level of strain achieved in the CFRP plates in the experiments. Regardless of the bond models used, the force transferred to the CFRP reinforcement is significantly less compared to the experiments at any given load level. This has resulted in the internal shear reinforcement still carrying significant shear load in the numerical models. In using a bond slip model with infinite stiffness (Perfect bond) to one with low stiffness (LS2), it can be observed from the figures that there is a trend for high strains to localise to a particular location and to fewer CFRP elements.

In all the models, the level of strain in the bottom most elements of the CFRP reinforcement is significantly lower compared to the maximum strain achieved at their respective CFRP location. This indicates that the concrete elements at these locations were not subjected to localised stress concentration. Observations of the stress contours of the concrete elements at these locations revealed that this is the case.

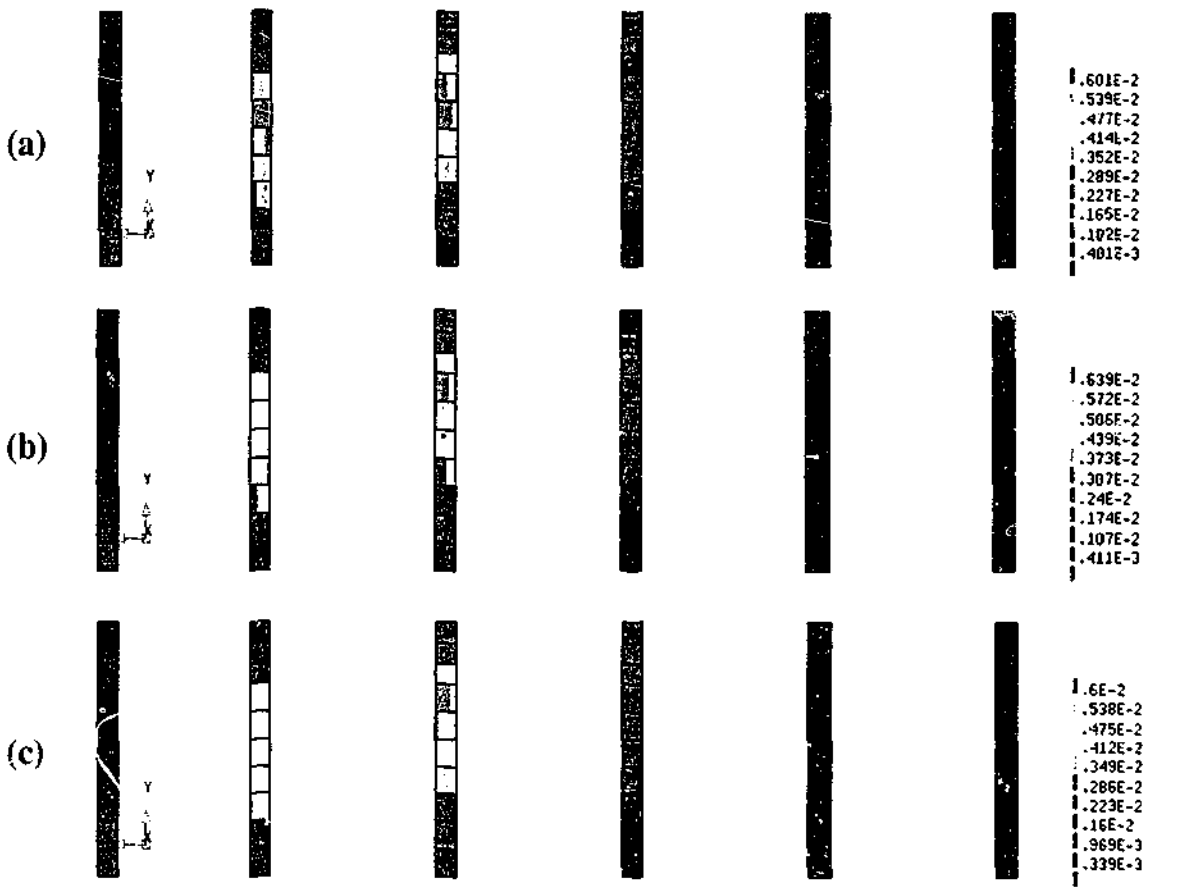

Figure 8.67 - Strain in CFRP of beam '0.75D' 3D models with (a) Perfect Bond (b) LS1 and (c) LS2

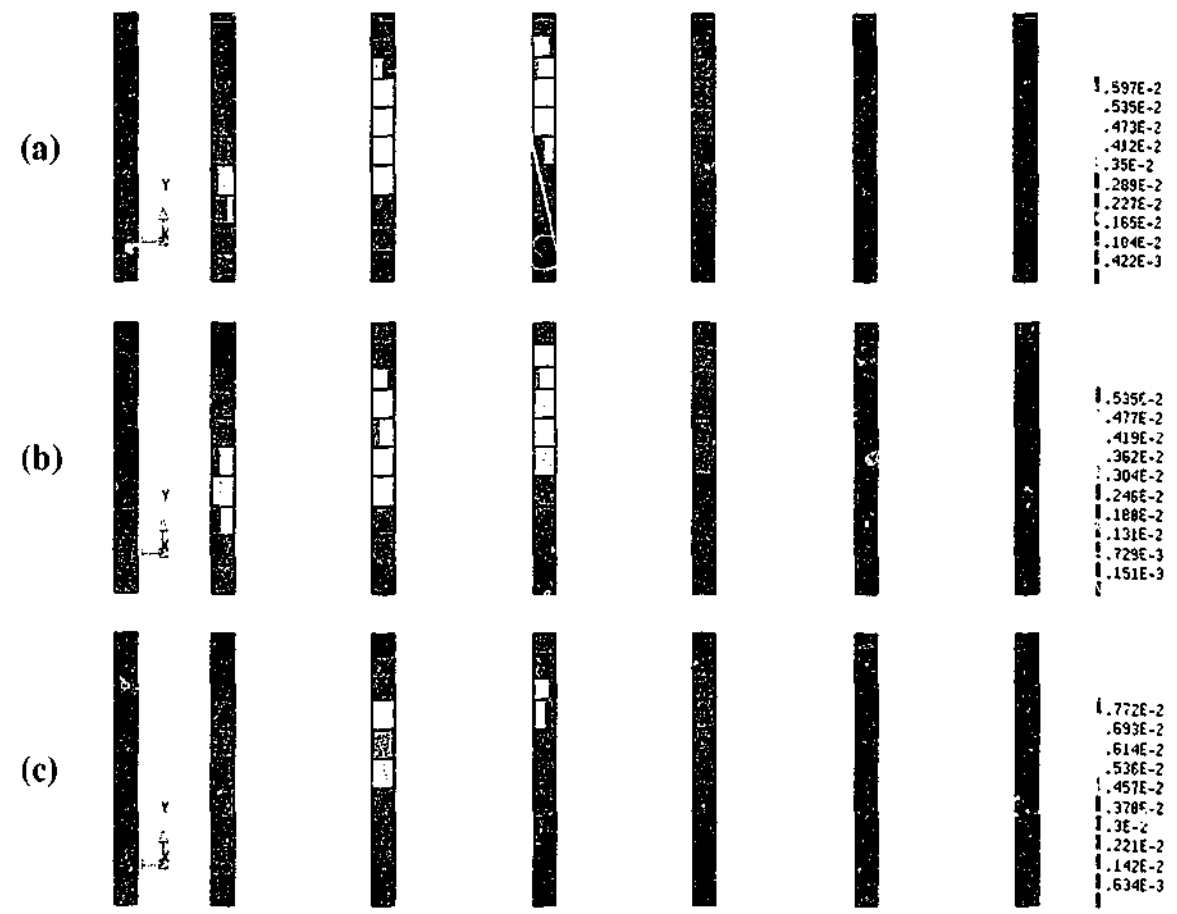

Figure 8.68 - Strain in CFRP of beam '0.60D' 3D models with (a) Perfect Bond (b) LS1 and (c) LS2

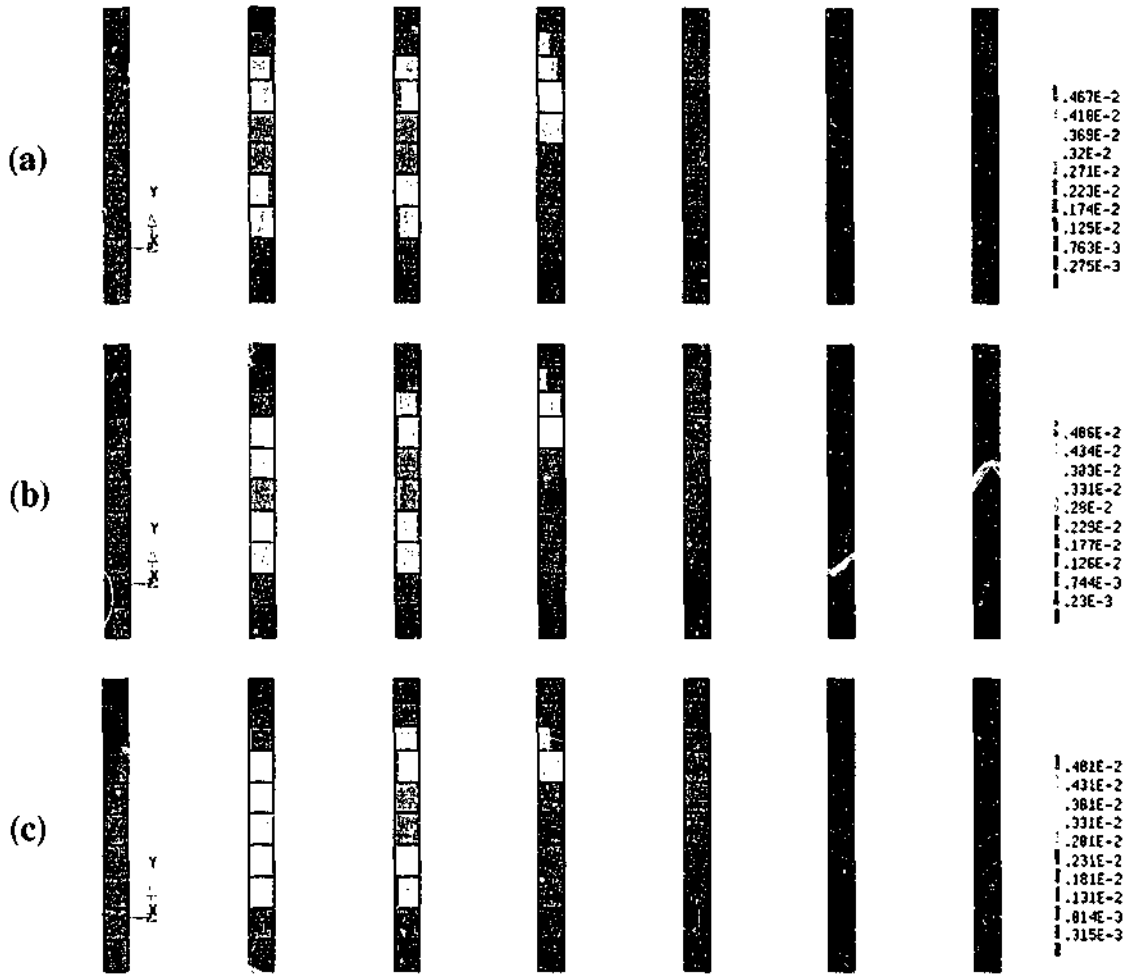

Figure 8.69 - Strain in CFRP of beam '0.50D' 3D models with (a) Perfect Bond (b) LS1 and (c) LS2

8.5.5.6 Crack pattern

The crack patterns of the 'Perfect bond' and 'LS2' models of the different T-beams are illustrated in Figure 8.70 to Figure 8.72. For each beam type, it can be observed that the crack patterns are similar to each other. The location of the band of high crack strains is similar between the two models. There is little difference in the crack patterns between the different T-beam models. Cracks have formed extensively in the web along the shear span. The characteristics of the crack patterns are similar to those described for the 2D models in Section 8.5.3.6. The results reported in Sections 8.5.5.3 and 8.5.5.4 have indicated that the main flexural reinforcement did not yield whereas the shear reinforcement yielded when the peak load was reached. Principal stresses approaching the concrete compressive strength were observed in concrete elements at the top layer of the flange near the load point. The combination of these factors and the crack patterns shown in the figures indicated that the 3D numerical models most likely failed in shear compression.

In the models of beams '0.75D' and '0.60D', the band of high crack strains (red lines) formed closer to the location of the experimental shear crack '1' (refer to Figure 7.14) than the location of the experimental shear crack '2'. This is consistent with the results obtained from the photogrammetry measurement. Referring back to Figure 7.21 and Figure 7.22, the average crack width of shear crack '1' is generally larger than the average crack width of shear crack '2'. In the models of beam '0.50D', the band of high crack strains formed almost halfway between the experimental shear cracks '1' and '2'.

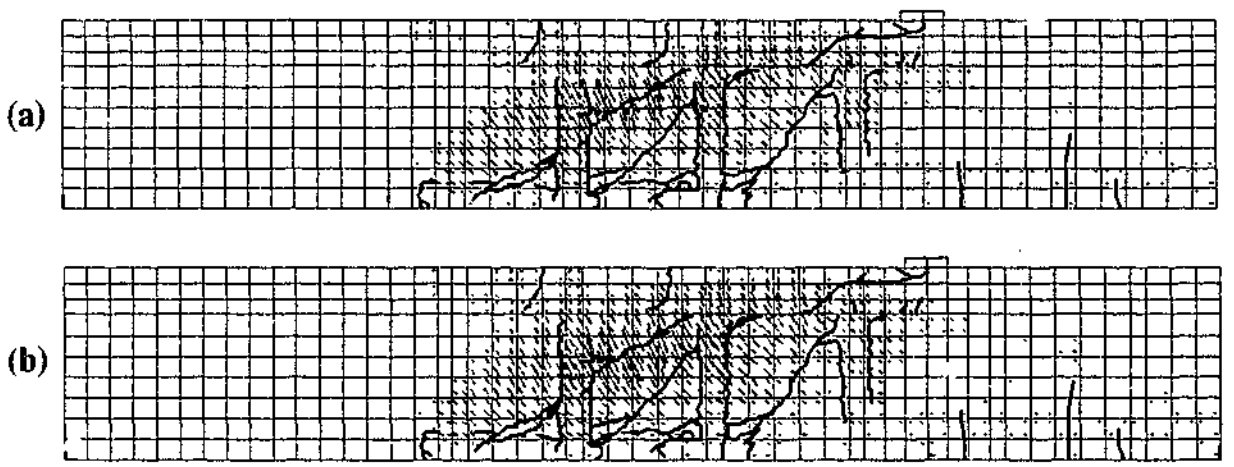

Figure 8.70 - Experimental crack patterns and corresponding predicted crack tensile strains of beam '0.75D' 3D models with (a) Perfect bond and (b) LS2

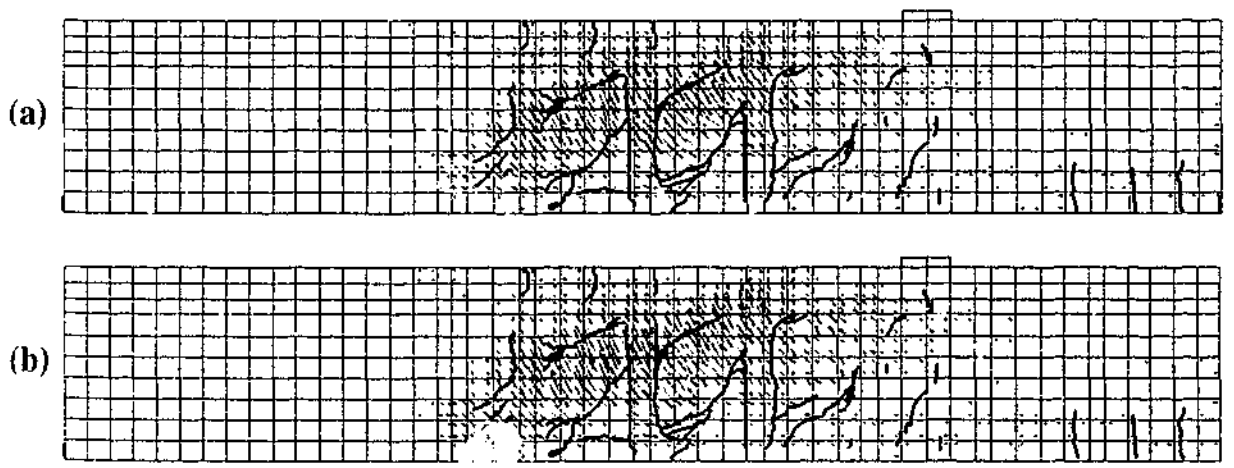

Figure 8.71 - Experimental crack patterns and corresponding predicted crack tensile strains of beam '0.60D' 3D models with (a) Perfect bond and (b) LS2

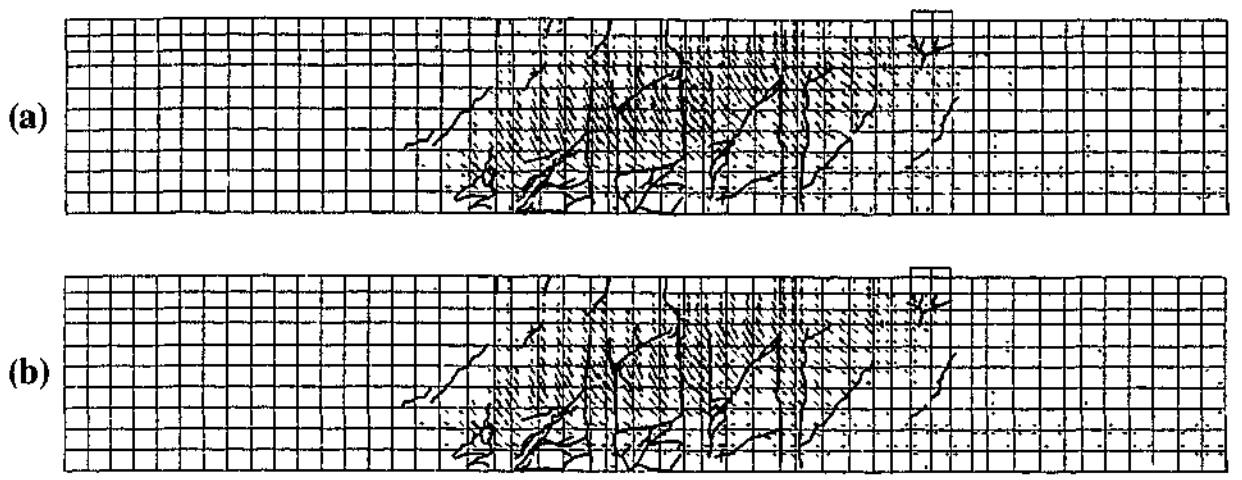

Figure 8.72 - Experimental crack patterns and corresponding predicted crack tensile strains of beam '0.50D' 3D models with (a) Perfect bond and (b) LS2

8.5.5.7 Summary

The effects of varying the interface behaviour between the CFRP and concrete layer in the 3D strengthened beam models with shear retention factor β of 0.05 were investigated in this section. For each beam type, the load displacement responses were similar between the various bond slip models. The results indicated a trend whereby the predicted load capacities decrease with a reduction in the shear stiffness of the interface elements. Variation in the CFRP spacing has an insignificant effect on the shear capacity of the T-beams in the 3D numerical models adopted herein. For a given bond slip model, the predicted shear capacities were similar across all the different T-beam models.

As for the behaviour of the main flexural reinforcement, apart from the difference due to the peak load reached, the load strain responses were similar across all the models. The main reinforcement strained linearly with load until structural failure with no noticeable difference in the flexural stiffness of the beams. In all of the models, the main reinforcement did not yield indicating that flexural tensile failure did not occur.

The load strain responses of the shear reinforcement in the 3D models were generally similar to the 2D models of Section 8.5.3.4. At low shear load levels, the strains in the stirrups were insignificant indicating that little or no load was being carried. The load level at which the strains in the stirrups began to increase

significantly was also similar in all the models. At high load levels, the responses differ between the experiments and numerical models. For each beam type, the load strain responses vary only slightly between the different bond slip models. The figures do not indicate any trend between the strain in the stirrups and bond slip models.

Similar to the 2D models, the levels of strain achieved in the CFRP plates in the numerical models were significantly less compared to the levels of strain achieved in the CFRP plates in the experiments. In using a bond slip model with infinite stiffness (Perfect bond) to one with low stiffness (LS2), it can be observed from the figures that there is a trend for high strain to localise to a particular location and to fewer CFRP elements.

The crack patterns at the peak load level were similar across all the T-beam models regardless of the bond slip models adopted. All the beam models failed in a similar fashion, which was established to be most likely shear compression failure. Although the finite element models did not account fully for the effects of CFRP spacing in the different T-beams, they have been proven to be capable of simulating most of the trends observed in the experimental beams adequately. In general, the results obtained from the 3D models were similar to the 2D models.

8.5.6 Effect of varying shear retention factor β in 3D strengthened beam models 'LS1'

8.5.6.1 Introduction

The effect of varying the shear retention factor β on the behaviour of the 3D strengthened beam model with bond slip property 'LS1' are reported in this section. The shear retention factors of 0.06 and 0.07 were investigated. The effects on the load displacement, steel reinforcement and CFRP plate responses and crack patterns were investigated.

8.5.6.2 Load displacement behaviour

The load-displacement responses of the different T-beam models with varying β values are compared in Figure 8.73 and Figure 8.74. As expected, the

predicted shear capacities of the individual beam increases with β. The responses were similar for most of the loading regime. At higher shear load levels, the models with higher β values exhibited stiffer responses. In Figure 8.74, it can be observed that for a given β value, the peak load levels achieved between the different T-beam models were similar as in the case of the 2D models in Section 8.5.4.2. At higher shear load levels, there is a general trend where the load-displacement responses were stiffer in beam models with smaller CFRP spacing. In the 2D models, there is no noticeable trend between the CFRP spacing and beam stiffness.

(a)

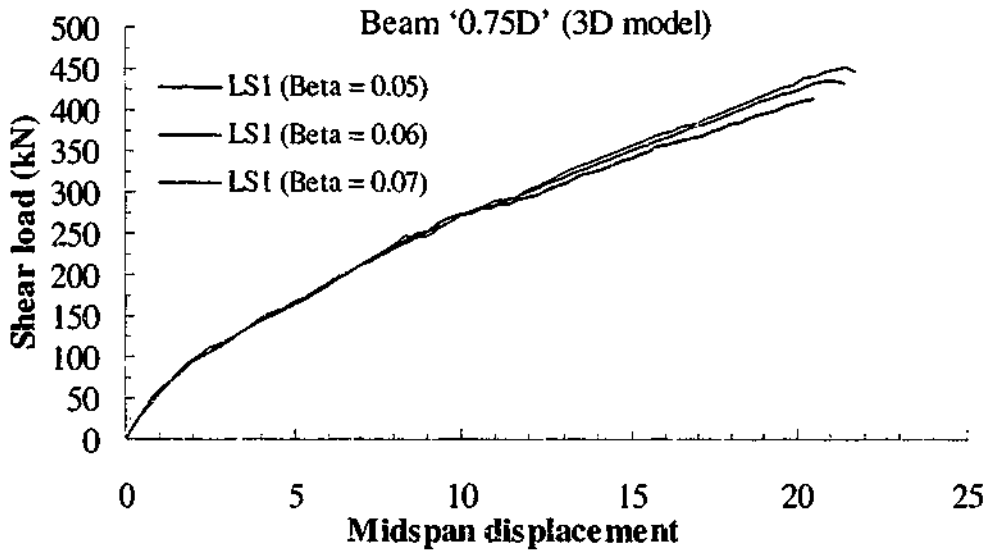

(b)

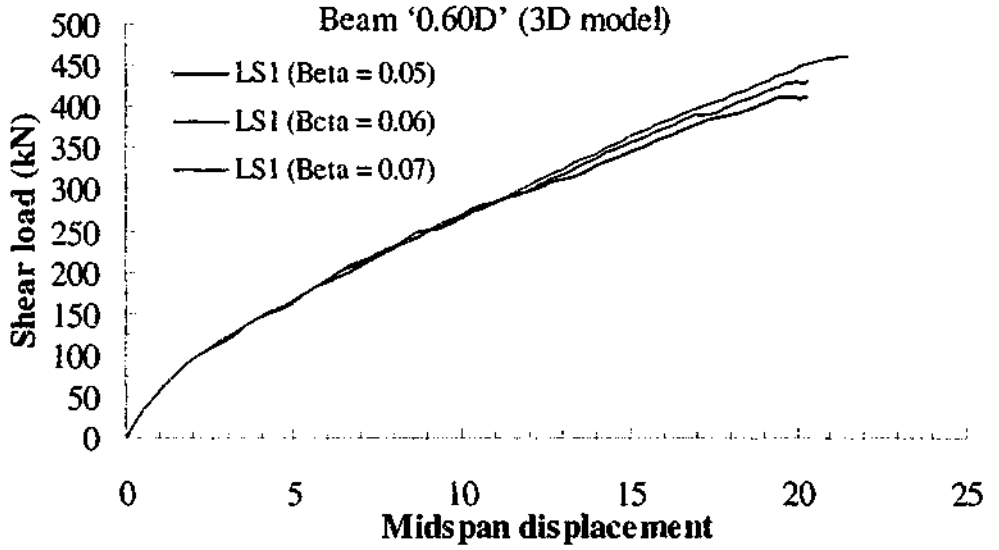

Figure 8.73 - Comparison of load displacement responses of 3D models 'LS1' with varying β values in beams (a) '0.75D' (b) '0.60D' and (c) '0.50D'

(c)

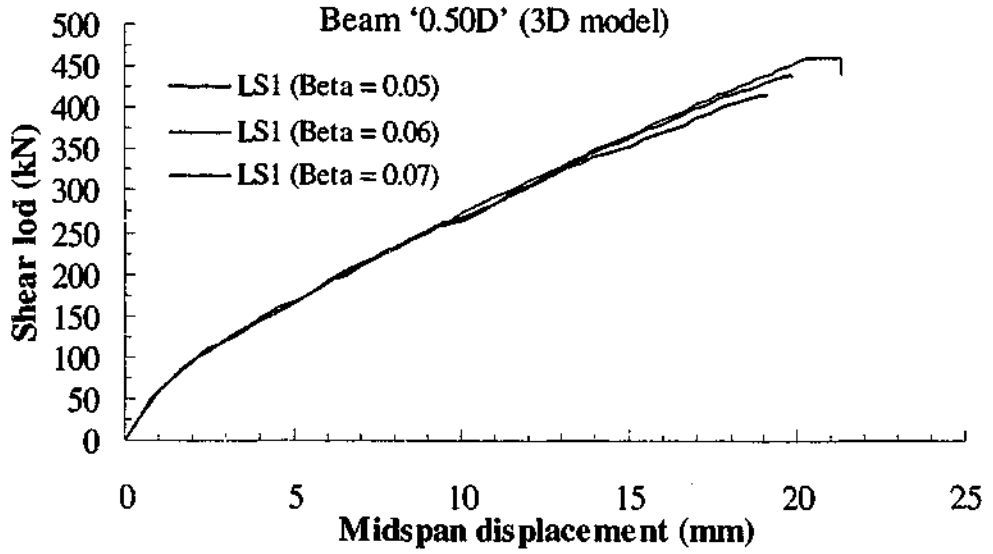

Figure 8.73 (continued) - Comparison of load displacement responses of 3D models 'LS1' with varying β in beams (a) '0.75D' (b) '0.60D' and (c) '0.50D'

(a)

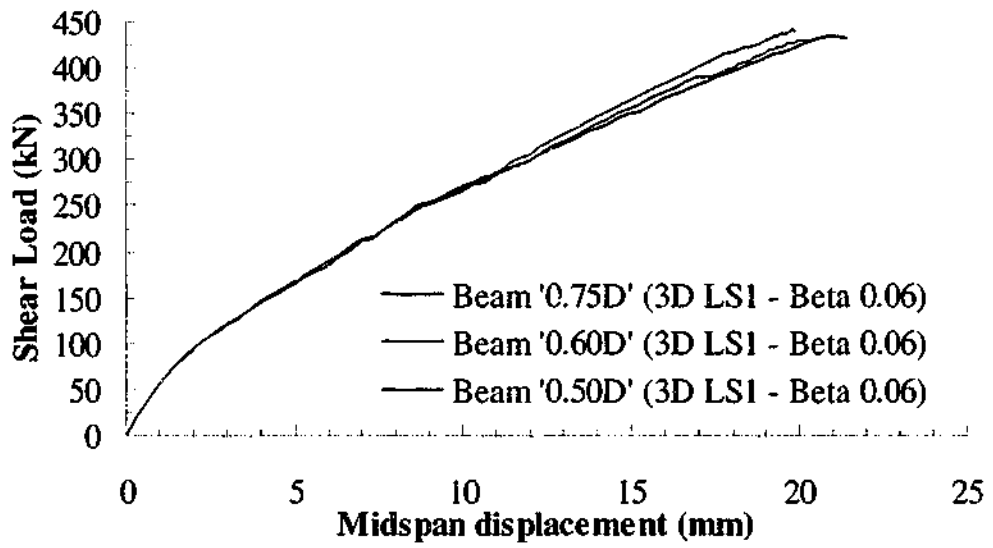

(b)

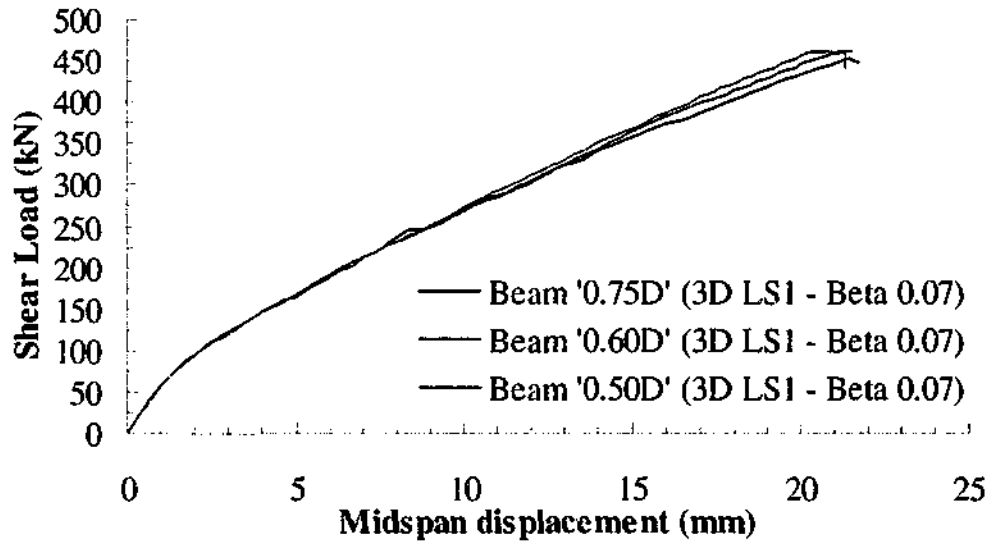

Figure 8.74 - Comparison of load displacement responses of 3D models 'LS1' in different T-beams with β values of (a) 0.06 and (b) 0.07

8.5.6.3 Behaviour of main reinforcement

Figure 8.75 compares the main reinforcement behaviour of the different T-beam models with varying β value. Apart from the difference due to the peak load reached, it can be observed that the load strain responses were similar in all the models. The main reinforcement strained linearly with load until structural failure. The main reinforcement did not yield indicating that flexural failure did not occur. The trends were similar to those reported for the 2D models in Section 8.5.4.3.

(a)

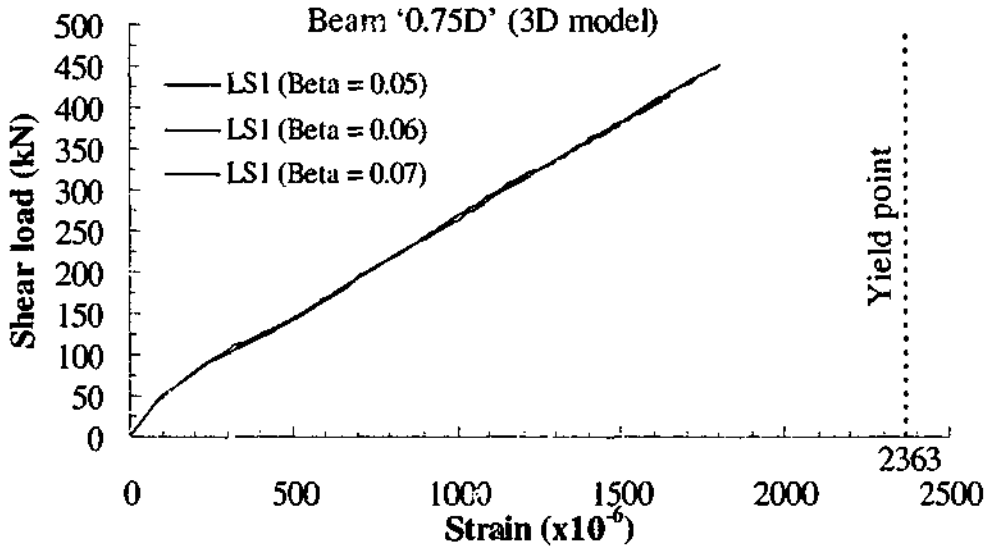

(b)

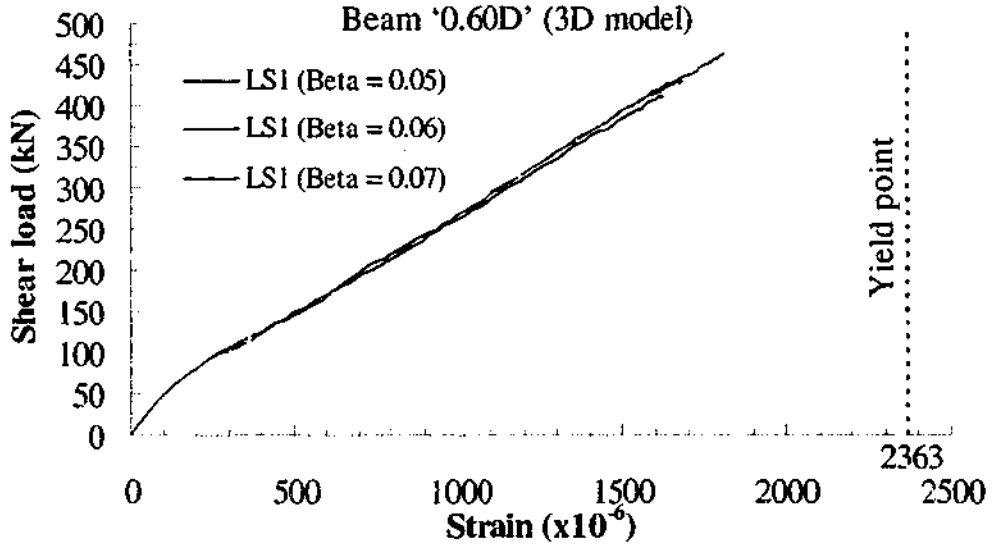

Figure 8.75 - Comparison of main flexural reinforcement responses of 3D models 'LS1' with varying β values in beams (a) '0.75D' (b) '0.60D' and (c) '0.50D'

(c)

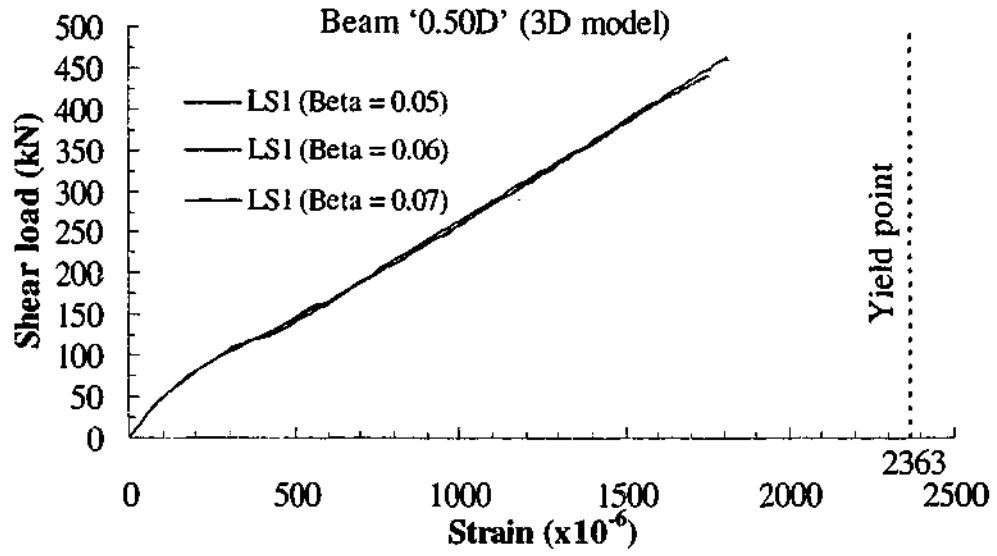

Figure 8.75 (continued) - Comparison of main flexural reinforcement responses of 3D models 'LS1' with varying β in beams (a) '0.75D' (b) '0.60D' and (c) '0.50D'

8.5.6.4 Behaviour of shear reinforcement

The load strain responses of the shear reinforcement at the location 'S4' are compared in Figure 8.76. At low load levels, it can be observed that the shear reinforcement exhibited very small strains in all the numerical models. Unlike the 2D models in Section 8.5.4.4, there is no noticeable trend between the strain and shear retention factor in the 3D models. In the 2D models, there is a general trend whereby the strain in the stirrups becomes smaller as the β value increases. Nevertheless, the general trend in the shear reinforcement responses of the 3D models is similar.

Figure 8.77 compares the load strain responses of the different T-beam models with the same β value. It can be observed that the responses are fairly similar in the different T-beams. For a given shear retention factor, there is no noticeable trend between the strain in the stirrups and CFRP spacing. In the 2D models, there is a general trend that the smaller the CFRP spacing, the smaller the strain hence load carried by the shear reinforcement.

(a)

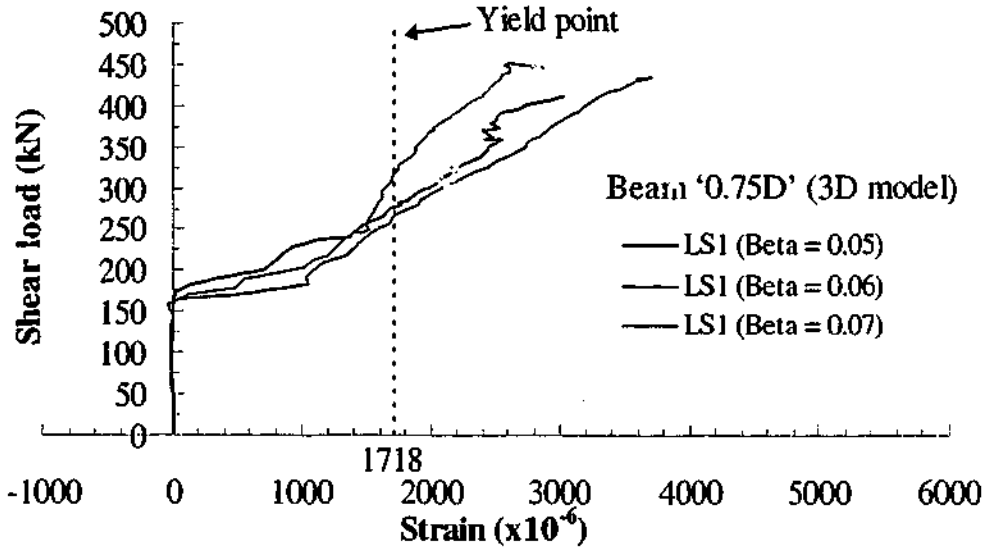

(b)

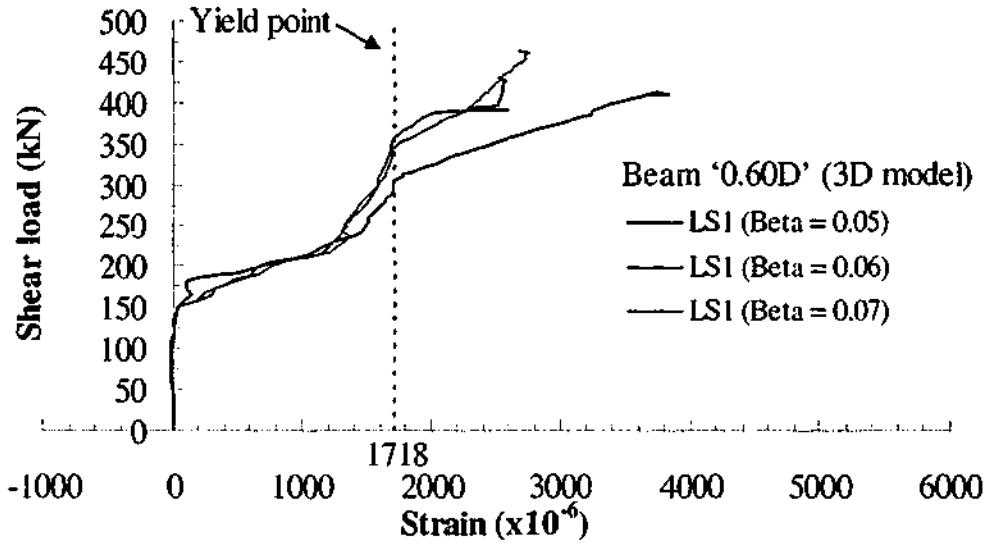

(c)

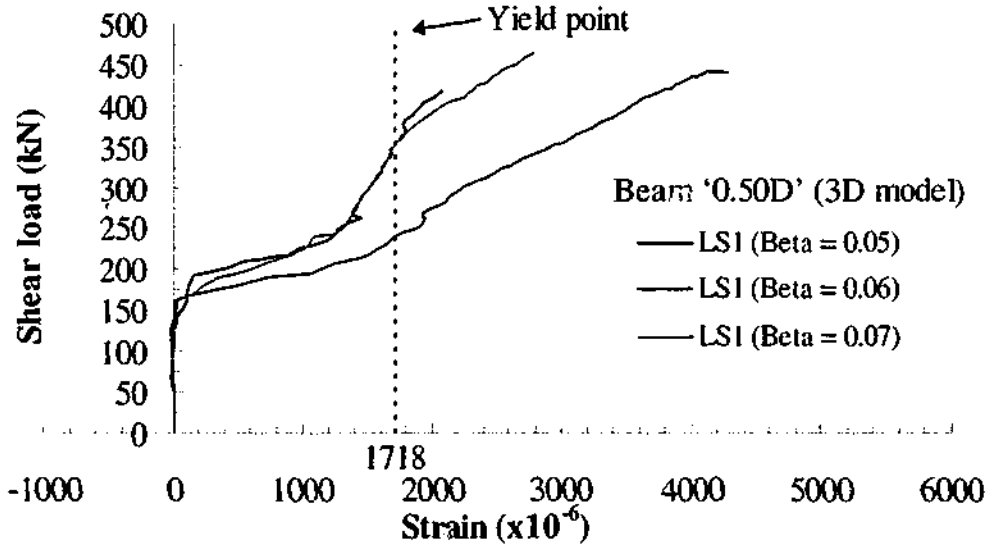

Figure 8.76 - Comparison of shear reinforcement responses at location S4 with varying β values in 3D beams (a) '0.75D' (b) '0.60D' and (c) '0.50D'

(a)

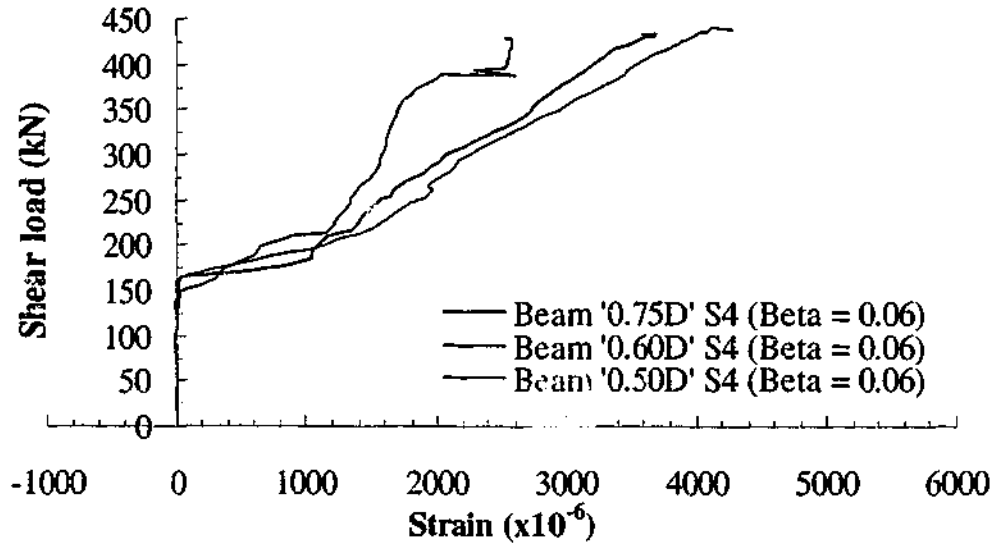

(b)

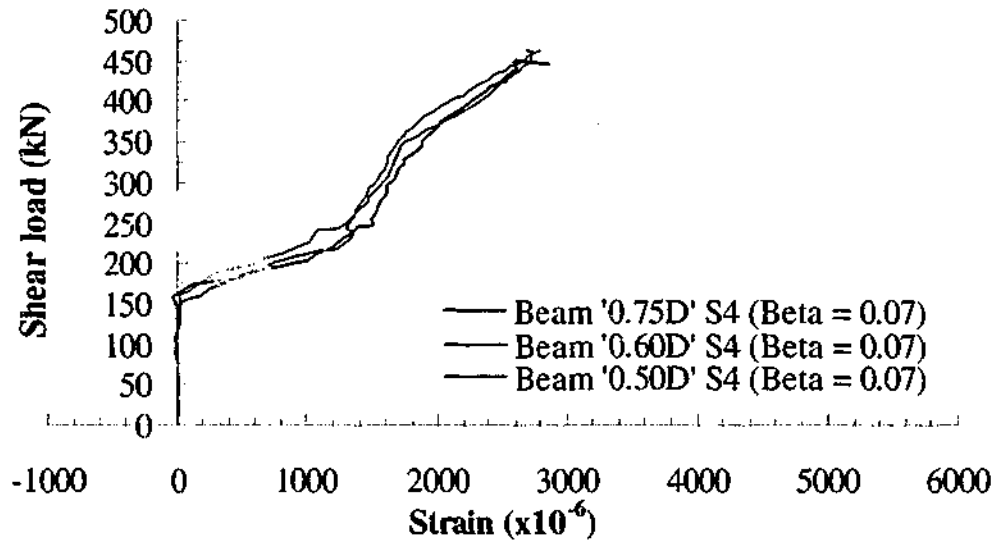

Figure 8.77 - Comparison of shear reinforcement responses of 3D models 'LS1' at location S4 with β values of (a) 0.06 and (b) 0.07

8.5.6.5 Strain contours of L-shaped CFRP reinforcement

The strain contours of the L-shaped CFRP plates at the peak load step of the models 'LS1' with varying β values are illustrated in Figure 8.78 to Figure 8.80. It can be observed from the figures that the most critically loaded CFRP reinforcement in the different T-beams remained the same as reported previously in Section 8.5.5.5.

Similar to the 2D models in Section 8.5.4.5, the levels of strain achieved in the CFRP plates increase with increases in the β value. This is mostly due to the increase in the shear capacity of the T-beams following the increase in β. However, the maximum level of strain achieved in the CFRP was still significantly less compared to the level of strain achieved in the CFRP plates in the experiments. This

has resulted in the steel shear reinforcement still carrying significant portions of the shear load.

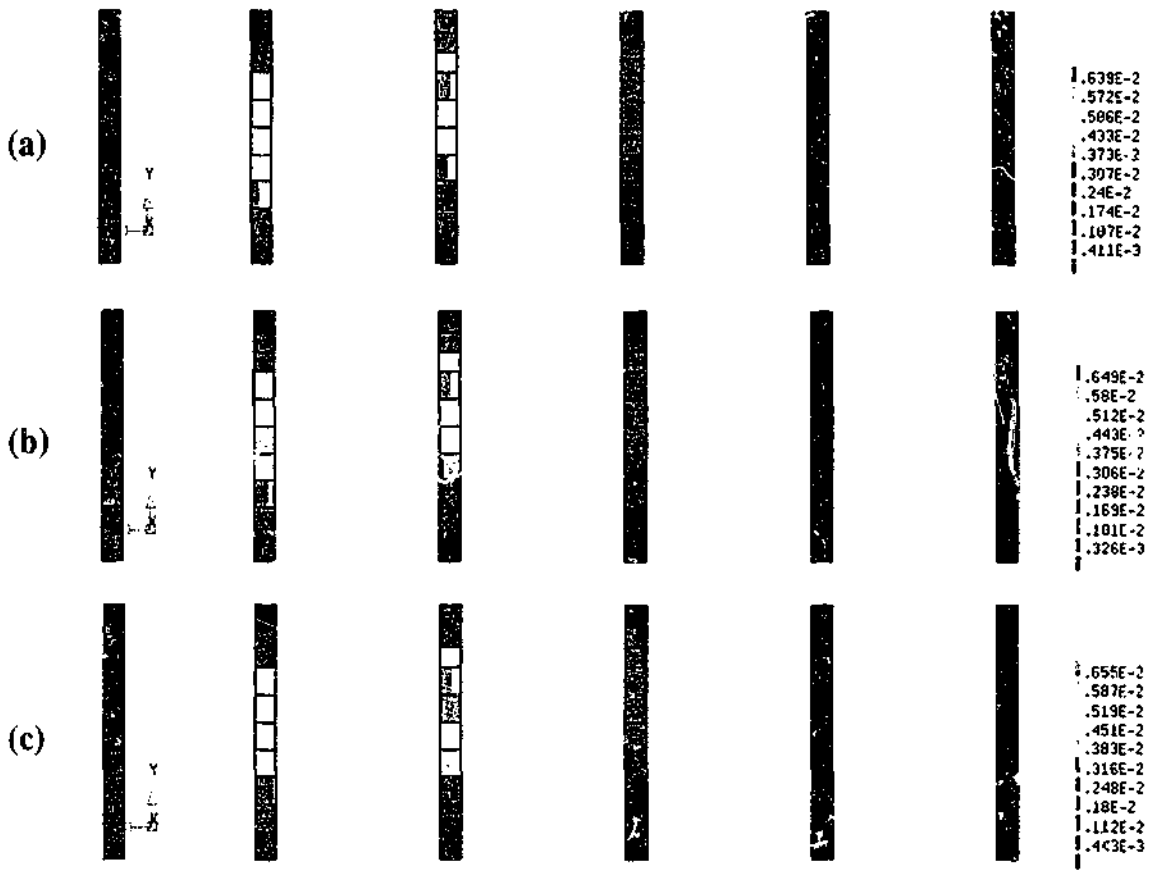

Figure 8.78 - Strain in CFRP of beam '0.75D' 3D 'LS1' models with β of (a) 0.05 (b) 0.06 and (c) 0.07

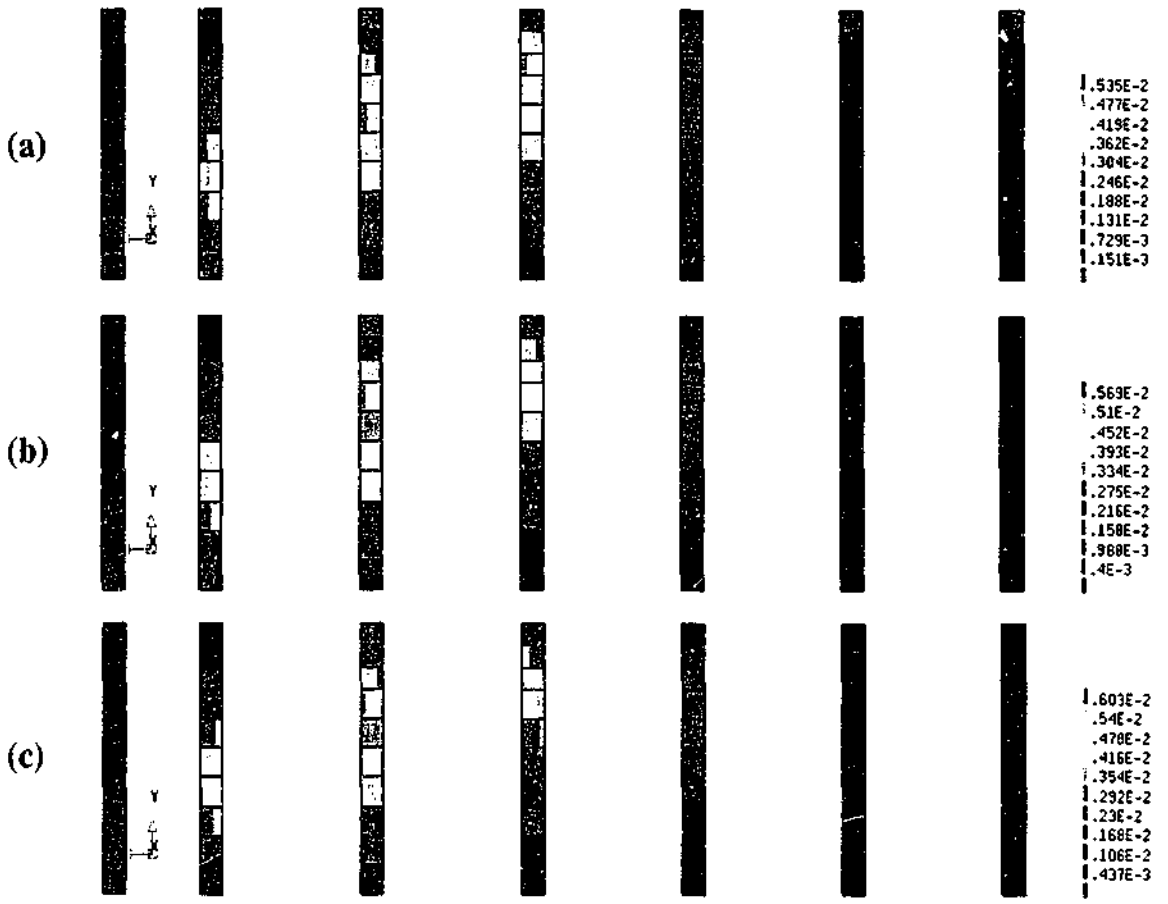

Figure 8.79 - Strain in CFRP of beam '0.60D' 3D 'LS1' models with β of (a) 0.05 (b) 0.06 and (c) 0.07

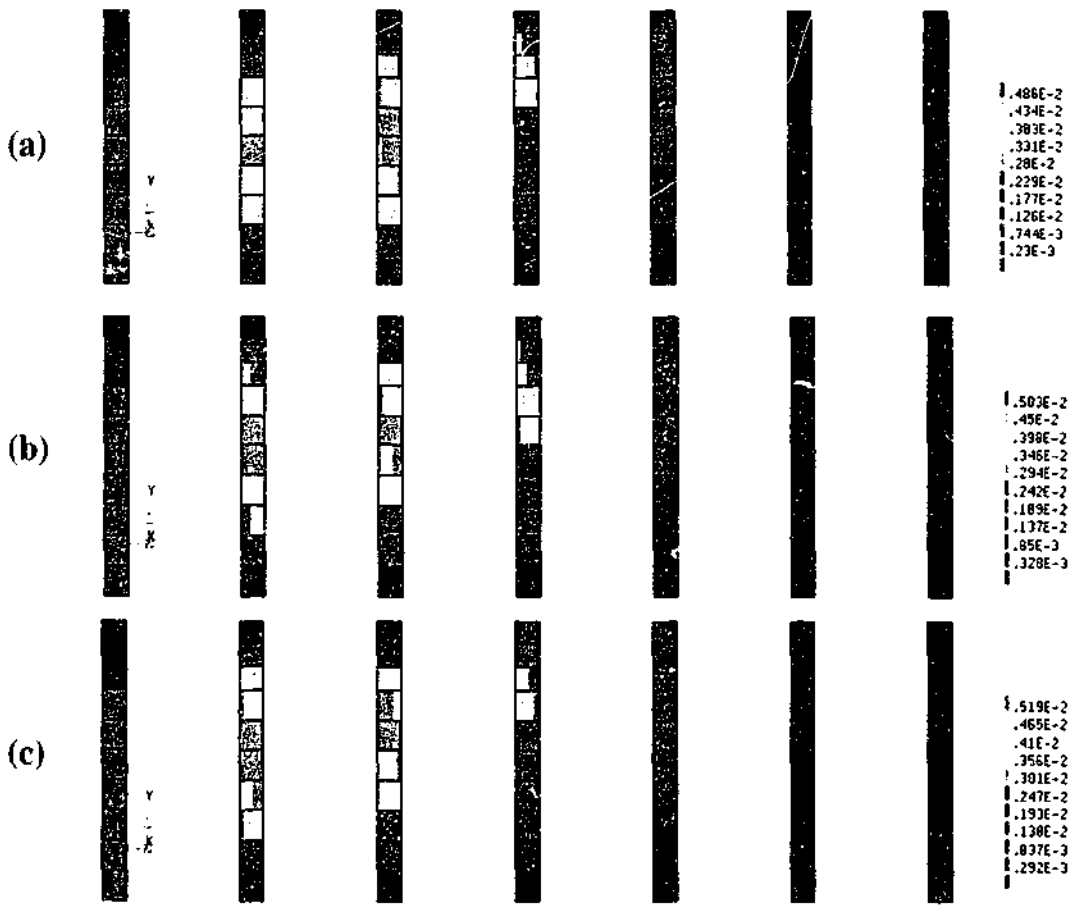

Figure 8.80 - Strain in CFRP of beam '0.50D' 3D 'LS1' models with β of (a) 0.05 (b) 0.06 and (c) 0.07

8.5.6.6 Crack pattern

The crack patterns of the models 'LS1' of the different beam types with varying β values are compared in Figure 8.81 to Figure 8.83. In general, the crack patterns are similar across the entire T-beam models. The locations of the band of high crack strains are similar in all the models. Considering the results reported in Sections 8.5.6.3 and 8.5.6.4 and crack patterns presented herein, the beams most likely failed in shear compression.

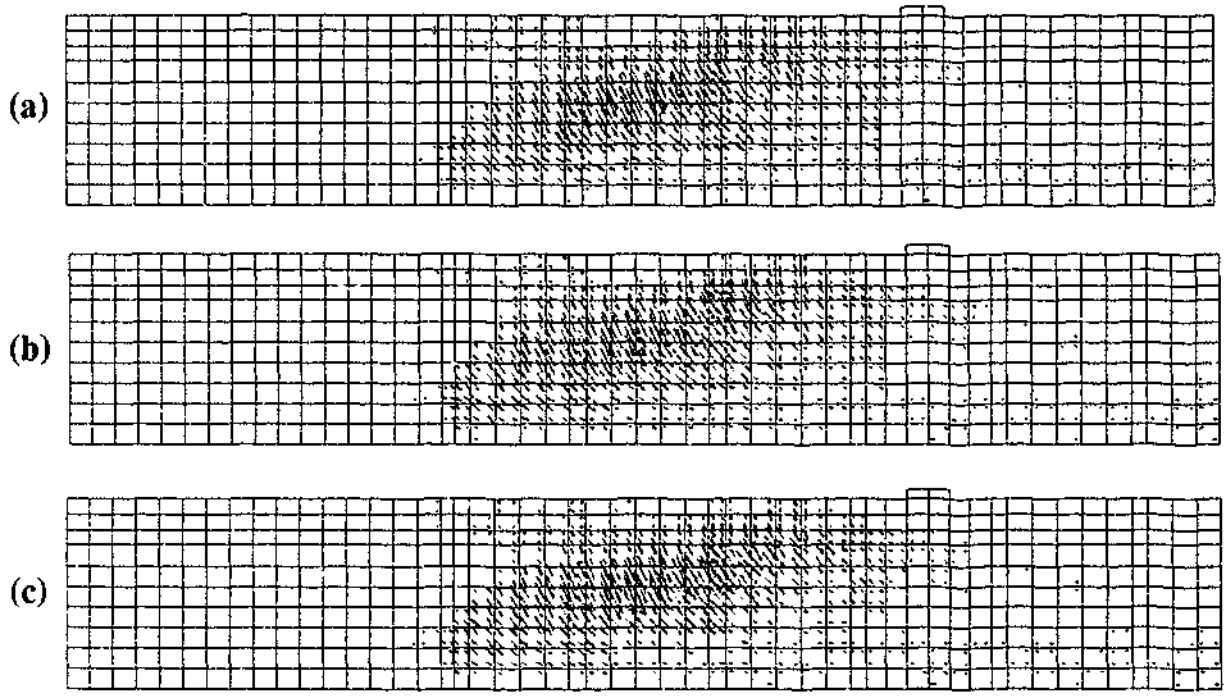

Figure 8.81 - Predicted crack tensile strain patterns of beam '0.75D' 3D 'LS1' models with β of (a) 0.05 (b) 0.06 and (c) 0.07

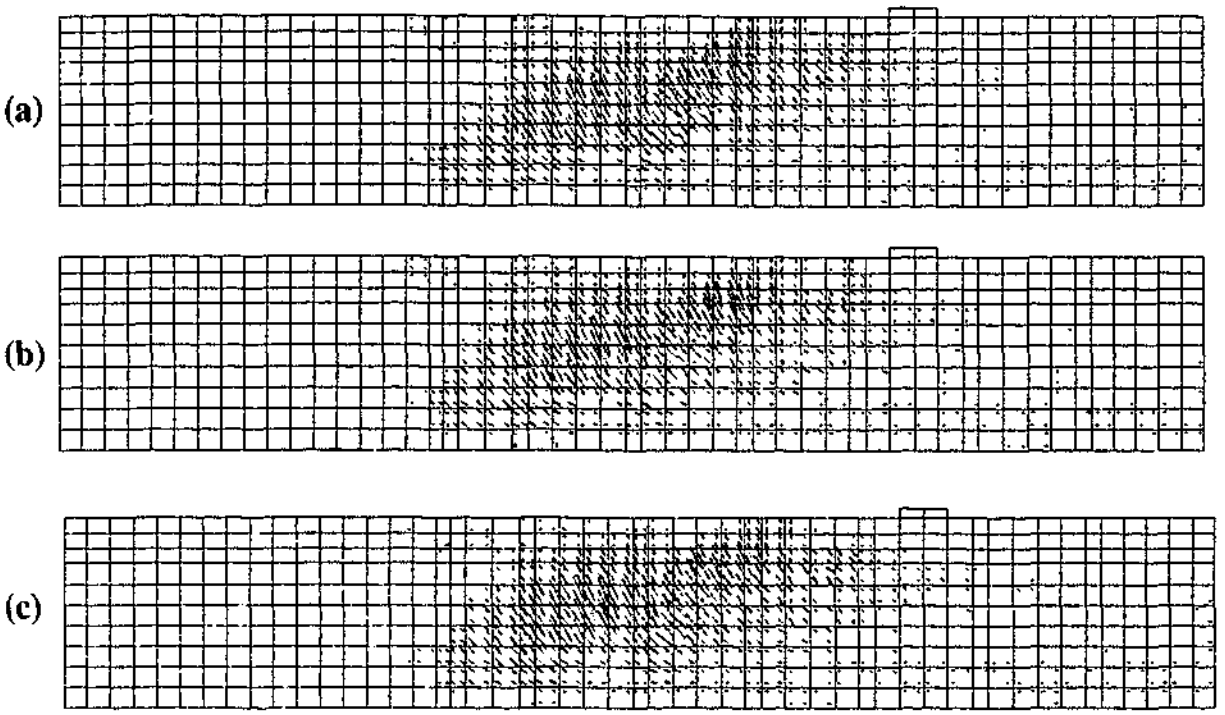

Figure 8.82 - Predicted crack tensile strain patterns of beam '0.60D' 3D 'LS1' models with β of (a) 0.05 (b) 0.06 and (c) 0.07

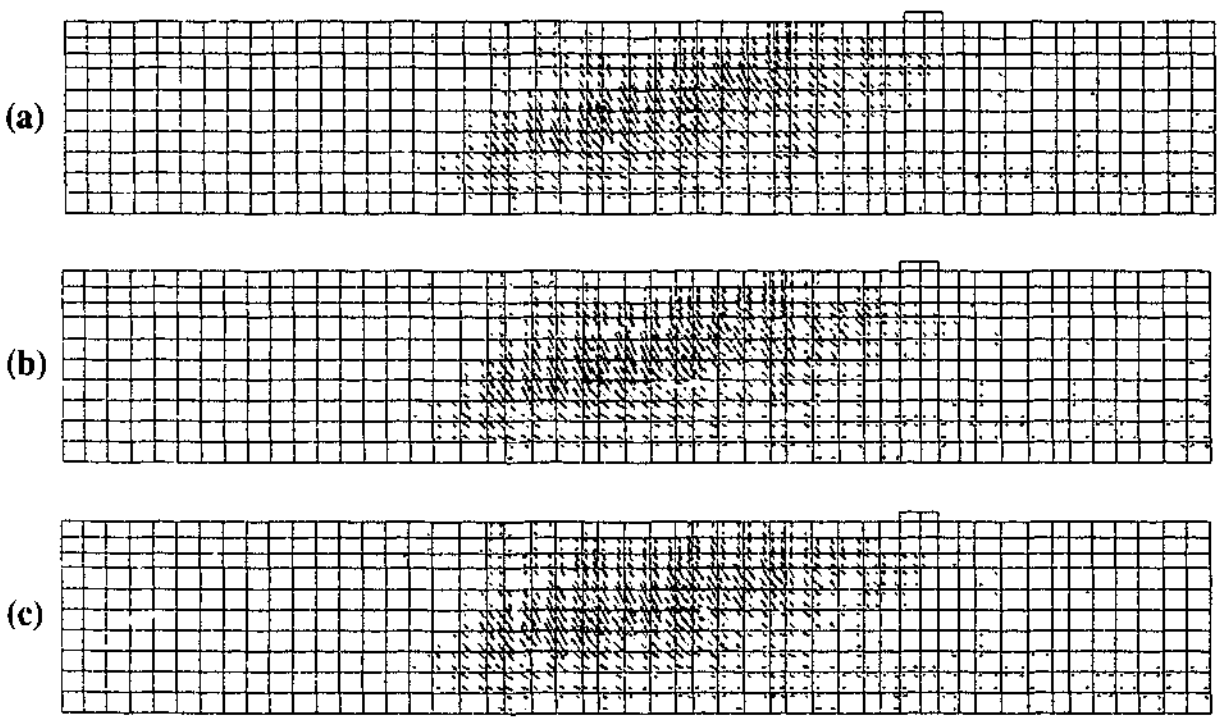

Figure 8.83 - Predicted crack tensile strain patterns of beam '0.50D' 3D 'LS1' models with β of (a) 0.05 (b) 0.06 and (c) 0.07

8.5.6.7 Summary

The effects of varying the shear retention factor β in the 3D T-beam models with bond slip property 'LS1' were investigated in this section. As expected, the load capacity of the T-beams increases with the shear retention factor. Similar to the

results presented in Section 8.5.5.2, variation in the CFRP spacing has an insignificant effect on the shear capacity of the T-beams in the 3D numerical models adopted herein. The predicted shear capacities were similar across all the different T-beam models for a given β.

For the main flexural reinforcement, apart from the difference due to the peak load reached, the load strain responses were similar across all the models. The main reinforcement strained linearly with load until structural failure with no noticeable difference in the flexural stiffness of the beams. In all of the models, the main reinforcement did not yield indicating that flexural tensile failure did not occur.

The load strain responses of the shear reinforcement were similar in the various models at the early stages of loading. The strains in the stirrups were insignificant indicating that little or no load was being carried. The load level at which the strains in the stirrups began to increase significantly was also similar in all the models. Unlike the 2D models in Section 8.5.4.4, there is no noticeable trend between the strain and shear retention factor in the 3D models. In the 2D models, there is a general trend whereby the strain in the stirrups becomes smaller as the β value increases. In addition, for a given shear retention factor, there is no noticeable trend between the strain in the stirrups and CFRP spacing.

The crack patterns at the peak load level were similar across all the T-beams indicating that the beams failed in a similar fashion, which was established to be most likely shear compression failure.

The main finding of this section is that the contribution of the CFRP reinforcement in carrying the shear load of the T-beams is significantly less in the numerical models compared to the experiments. This is evident from the strain contour plot of the CFRP reinforcement obtained at the peak load and the load strain responses of the shear reinforcement. The level of strain in the CFRP reinforcement is significantly smaller compared to its experimental counterpart at a given load level. The load carried by the stirrups was significantly higher in the experiments than in the numerical models.

8.6 Summary of findings

In this section, a general methodology for the modelling of reinforced concrete T-beams web-bonded with FRP both in a 2D and 3D environment has been presented. The finite element models used to analyse the experimental control beam proved to be capable of modelling the general trends and behaviour reasonably accurately. In the numerical base models where there are no external CFRP reinforcement, the peak loads, load-deflection response, load strain response of the stirrup and flexural reinforcement and crack patterns were comparable to the experimental results, with the trends simulated accurately. The shear retention factor β in these base models was 0.05.

An investigation into the effects of varying the shear retention factor β in the numerical base models was also carried out. It was found that the load capacity increases with the shear retention factor. The main flexural reinforcement responses were similar across all the models with different shear retention factor. The main reinforcement strained linearly with load until structural failure with no noticeable difference in the flexural stiffness of the beams. The higher the β value, the higher the strain reached in the main reinforcement. The main reinforcement did not yield indicating that flexural tensile failure did not occur. For the shear reinforcement, there is a general trend that the larger the shear retention factor, the smaller the strain hence force carried by the stirrups at a given load. This indicates that the shear load carried by the cracked concrete increases with increasing β. From the crack patterns obtained, it was found that the number of cracks and therefore the area covered increases with the β value. An increase in the β value has allowed the cracks to distribute over a wider area. More force is required to form these cracks and as a result, the shear capacity of the beam increases.

In the case of the shear-strengthened beams, the 2D and 3D finite element models used proved to be capable of modelling the general trends and behaviour reasonably well but with several limitations. The fracture type failure of the concrete at the bend zone and separation of the flange from the web cannot be simulated exactly. In the numerical strengthened beam models, the failure mode was shear compression. In addition, the finite element models did not account fully for the

effects of CFRP spacing in the different T-beams. The predicted load capacities were similar despite the fact that the CFRP spacings in the models were different. This was partly due to the maximum level of strain achieved in the CFRP plates in the numerical models being significantly less compared to the level of strain achieved in the CFRP plates in the experiments. The numerical results show that the stirrups still carried significant portions of the shear loads. This may be partly attributed to the smeared crack approach used in modelling cracking of concrete. In the experiments, discrete cracks that formed in the beams concentrate within a small region in the web. In the numerical models, the cracks are distributed over a band of elements therefore reducing the load that can be transferred to the CFRP reinforcement. To a lesser extent, the assumption of perfect bond between the stirrups and concrete elements has allowed more loads being transferred to the stirrups. This has resulted in the numerical models to fail in the same manner. Nevertheless, the numerical models have simulated the experimental trend that the shear capacity is higher in beams with the external CFRP reinforcement compared to beams without the external CFRP reinforcement. The locations of the most critically loaded CFRP reinforcement were consistent between the numerical models and experimental beams. The numerical models have also provided valuable insight into the level of strain in CFRP plates where strain gauges were not bonded in the experimental beams. The crack patterns produced from the numerical models were comparable to the experimental beams. The locations of where high crack strains were observed to have formed were consistent with the location of the experimentally observed discrete shear cracks. In addition, the locations of where the high crack strains occur were consistent with the crack width results obtained from the photogrammetry measurement.

An investigation was carried out on the effects of varying the bond slip behaviour between the CFRP and concrete elements. In the current investigation, the FRP system used was such that FRP end anchorage was provided. In the strengthened beam models, the predicted load level, steel reinforcement and CFRP plate responses vary depending on the bond slip model adopted. The variation in the responses although small in the current study, will become an important factor in cases where there is no FRP end anchorage and debonding of the FRP dominates. The present investigation highlights the importance of using a proper bond slip model

in situations where FRP debonding dominates. The assumption of perfect bond between the CFRP and concrete elements is unjustifiable in these cases.

The effects of varying the shear retention factor β in selected strengthened beam models were also investigated. The load capacity of the T-beams increases with the shear retention factor. However, variation in the CFRP spacing has an insignificant effect on the shear capacity of the T-beams. The predicted shear capacities were similar across all the different T-beam models for a given β. The finite element models did not account fully for the effects of CFRP spacing in the different T-beams even when higher β values were adopted. According to the photogrammetry results in Chapter 7, the presence of the external CFRP shear reinforcement had limited the shear crack width in the strengthened beams. It can then be argued that the effect of aggregate interlock was significant more in the strengthened beams compared to the control beam. This means that the use of a higher β value is justified in strengthened beams with smaller CFRP spacing.

In summary, the finite element method proved to be capable of modelling the general trends and behaviour of the experimental T-beams reasonably well. It may be used as an aid to designing FRP web bonded beams.

CHAPTER 9 - SHEAR STRENGTH OF T-BEAM USING EXISTING PREDICTION MODELS

9.1 Introduction

In Section 2.4, a review of existing models to predict the shear strength of reinforced concrete beams shear strengthened with externally bonded FRP was carried out. It was found that earlier models were too simplistic in that key parameters such as concrete strength, FRP failure mode and strengthening configurations were not considered all together. The more recent models proposed by Triantafillou and Antonopoulos (2000), Neale (2001) and Chen and Teng (2003a, c) are more sophisticated addressing all the key parameters at once. In this section, the applicability of these three models in the case of shear strengthening with prefabricated L-shaped CFRP were determined by comparing the predicted and experimental results.

The general expression used to calculate the shear strength of a strengthened reinforced concrete beam is given by Equation 2.1. The contributions from the concrete and steel stirrups, V_c and V_s were calculated according to the guidelines of four existing design codes. The design standards used are the Australian code SAI (2001), American code ACI Committee 318 (1999), Canadian code CSA (1994) and European code ENV 1992-1-1 (1991). For a more appropriate comparison against experimental results, the material and partial safety factors in all the prediction models are taken to be equal to one. The FRP, steel reinforcement and concrete properties are known from testing. The concrete characteristic strength f'_c is taken to be equal to the mean compressive strength f_{cm}. Table 9.1 summarises the dimension and property values used in the prediction models

Table 9.1 - Dimension and property values used in prediction models

Beam dimensions and properties	FRP dimensions and properties
Overall depth ⇒ D = 490 mm	FRP ⇒ E_{frp} = 137345 MPa
Flange width ⇒ b_f = 720 mm	FRP thickness ⇒ t_{frp} = 1.31 mm
Flange thickness ⇒ t_f = 120 mm	FRP width ⇒ w_{frp} = 41.71 mm
Web thickness ⇒ b_w = 225 mm	FRP spacings ⇒ s_{frp} = 365 mm (Beam '0.75D') ⇒ s_{frp} = 295 mm (Beam '0.60D') ⇒ s_{frp} = 245 mm (Beam '0.50D')
Effective depth ⇒ d = 418 mm	
Depth to centroid of outermost layer of tensile reinforcement ⇒ d_o = 446 mm	
Cross sectional area of tensile reinforcement ⇒ A_{st} = 4926 mm^2	
Steel stirrup spacing ⇒ s = 365 mm	Fracture strain ⇒ ε_{frpu} = 0.015 (assumed) Fracture stress ⇒ f_{frpu} = 2060 MPa (approximated)
Cross sectional area of shear reinforcement ⇒ A_{sv} = 157.1 mm^2	
Mean compressive strength of concrete f_{cm} = 31.9 MPa	
Yield strength of stirrups $f_{sy.f}$ = 351.1MPa	

9.2 Results and discussion of shear strength prediction models

The concrete and stirrup contribution to the shear strength using the various design standards outlined is summarised in Table 9.2. The shear strength predicted using the European code coincided with the experiment value. Apart from the European code, the shear strength that was predicted by all the other codes were conservative with the Canadian code being the most conservative. It can be observed that concrete and stirrup contribution to the shear strength as predicted by the Australia code were consistently higher compared to the American and Canadian codes. It should be noted that the discrepancy in the predicted values between the various design codes is due to different methodology and parameters adopted. Further information on the assumptions and workings of calculations is presented in Appendix E.2.

Table 9.2 - Existing shear strength of T-beams according to various design standards

Design standards	Shear strength			$V_{predicted} / V_{exp}$*
	V_c	V_s	$V_c + V_s$	
Australian code SAI (2001)	147.9	67.4	215.3	0.87
American code ACI Committee 318 (1999)	117.6	63.2	180.8	0.73
Canadian code CSA (1994)	106.2	63.2	169.4	0.69
European code ENV 1992-1-1 (1991)	190.2	56.9	247.1	1.00

* - V_{exp} = 247.1 kN (Control beam)

The contribution of the external FRP reinforcement to the shear strength of the T-beams using the various design standards outlined is summarised in Table 9.3. For the experimental results, the contribution of the FRP reinforcement to the shear strength was obtained by simply deducting the shear capacity of the control beam from the shear capacity of the different strengthened beams. Although the concrete strength varies between the different T-beams, the difference is insignificant. The shear strengths predicted by all the models were conservative with the model proposed by Chen and Teng (2003a, c) the most conservative and Neale (2001) the least conservative.

Table 9.3 - FRP contribution to shear strength according to various design models

Prediction model	Shear strength (kN)		$V_{predicted} / V_{frp-exp}$*
	V_{frp}	$V_{frp-exp}$*	
Triantafillou and Antonopoulos (2000)	77.4	133.9	0.58 (S_{frp} = 0.75D)
	95.7	151.2	0.63 (S_{frp} = 0.60D)
	115.2	199.1	0.58 (S_{frp} = 0.50D)
Neale (2001)	80.6	133.9	0.60 (S_{frp} = 0.75D)
	99.7	151.2	0.66 (S_{frp} = 0.60D)
	120.1	199.1	0.60 (S_{frp} = 0.50D)
Chen and Teng (2003a, c)	39.8	133.9	0.30 (S_{frp} = 0.75D)
	48.4	151.2	0.32 (S_{frp} = 0.60D)
	57.1	199.1	0.29 (S_{frp} = 0.50D)

* - Obtained by simply deducting shear capacity of the control beam from shear capacity of the strengthened beams

In Section 2.4, the single most important parameter of the prediction models is the effective FRP strain in the models by Triantafillou and Antonopoulos (2000) and Neale (2001) or the average FRP shear stress in the model by Chen and Teng (2003a, c). The values predicted by these models and those obtained from the strain gauges of the experimental beams are compared in Table 9.4. In the model by Chen and Teng (2003a, c), the average FRP shear stress is converted into its equivalent effective FRP strain by dividing the value by the tensile modulus of the CFRP, which was reported to be 137345 MPa. The predicted average FRP shear stress is contained in Appendix E.3.3. For the experimental beams, the effective FRP strain was assumed to be the average of the maximum strain recorded at the two most critically loaded CFRP reinforcement of the failure span. Referring to Tables 6.4 to 6.6, this corresponds to the CFRP reinforcement bonded with the strain gauges 1, 2, 3 and 4, 5, 6. The effective FRP strain was calculated by taking the average of the four strain values of the CFRP reinforcement at both sides A and B of the beams. Given the limited number of strain gauges bonded on the CFRP reinforcement, it is difficult to determine exactly the effective FRP strain in the experimental beams. The values shown in the table serve only as an indication.

Table 9.4 - Comparison of numerical and experiemental effective FRP strain

Prediction model	Effective FRP strain	
	Numerical	Experimental
Triantafillou and Antonopoulos (2000)	5000	7685 (S_{frp} = 0.75D)
	5000	6778 (S_{frp} = 0.60D)
	5000	6788 (S_{frp} = 0.50D)
Neale (2001)	4000	7685 (S_{frp} = 0.75D)
	4000	6778 (S_{frp} = 0.60D)
	4000	6788 (S_{frp} = 0.50D)
Chen and Teng (2003a, c)	2577*	7685 (S_{frp} = 0.75D)
	2526*	6778 (S_{frp} = 0.60D)
	2476*	6788 (S_{frp} = 0.50D)

* - Converted into equivalent effective FRP strain from average FRP shear stress

The large discrepancy observed between the predicted and experimental values in Table 9.3 is partly due to the predicted effective FRP strain being significantly smaller than the experimental values as summarised in Table 9.4. In the prediction models by Triantafillou and Antonopoulos (2000) and Neale (2001), the effective FRP strain was limited to a maximum value of 5000 and 4000 με

respectively. This was to ensure that the integrity of the concrete is maintained and the effect of aggregate interlock mechanism is not lost. Disregarding these limits and using the experimental instead of the calculated effective FRP strain values, Table 9.5 summarises the contribution of the FRP to the shear strength according to the various design models. For the model by Chen and Teng (2003a, c), the effective FRP strain is converted into its equivalent average FRP shear stress by multiplying the value by the tensile modulus of the CFRP. It can be observed that the predicted values are closer to the experimental values. The model by Neale (2001) over predicted the contribution of the FRP. Excluding the prediction model by Chen and Teng (2003a, c), the upper limit imposed on the effective FRP strain resulted in the significant underestimation of the FRP contribution. In addition, the predicted values presented in Table 9.3 exclude any material or code safety factors. Inclusion of these factors will further underestimate the predicted values. For the CFRP strengthening system used in the present study, the limit imposed on the effective FRP strain could be raised. However, the longitudinal shear strength of the beams should also be checked to ensure that the web does not separate from the flange as observed in the experimental beam '0.50D'. Checks for the potential failure by separation of the CFRP laps at the soffit of the beam are not accounted for by any of the three models used herein. Given the low effective FRP strains or average FRP shear stress predicted by the models, this check may be unnecessary. Further study is required to study this phenomenon.

Table 9.5 - FRP contribution to shear strength according to various design models based on experimental effective FRP strain values

Prediction model	Shear strength (kN)		$V_{predicted} / V_{frp-exp}$*
	V_{frp}	$V_{frp-exp}$*	
Triantafillou and Antonopoulos (2000)	118.9	133.9	0.89 (S_{frp} = 0.75D)
	129.7	151.2	0.86 (S_{frp} = 0.60D)
	156.4	199.1	0.79 (S_{frp} = 0.50D)
Neale (2001)	154.8	133.9	1.16 (S_{frp} = 0.75D)
	169.0	151.2	1.12 (S_{frp} = 0.60D)
	203.8	199.1	1.02 (S_{frp} = 0.50D)
Chen and Teng (2003a, c)	118.8	133.9	0.89 (S_{frp} = 0.75D)
	129.7	151.2	0.86 (S_{frp} = 0.60D)
	156.4	199.1	0.79 (S_{frp} = 0.50D)

* - Obtained by simply deducting shear capacity of the control beam from shear capacity of the strengthened beams

In Chapter 7, it has been shown quantitatively that the crack widths were significantly smaller in the strengthened beams compared to the control beam. This implies that the effect of aggregate interlock is enhanced in the strengthened beams compared to the control beam. Therefore, the contribution of the concrete to the existing shear capacity of the beam increases. It also follows that concrete contribution to the shear capacity in beams '0.60D' and '0.50D' is slightly higher compared to beam '0.75D' since the shear crack widths were smaller. This effect has not been accounted for in any of the three prediction models presented herein.

In summary, the three models gave very conservative predictions of the FRP contribution to the shear strength. These prediction models can be used in the design of beams shear strengthened with the prefabricated L-shaped CFRP strengthening system used in the present study.

CONCLUSIONS

Concluding remarks

Most previous studies of strengthening of reinforced concrete beams using advanced FRP materials have investigated flexure with only limited research done in shear. The research undertaken herein investigated the short-term behaviour of T-beams shear strengthened with prefabricated L-shaped CFRP plates. The CFRP plates were bonded to the soffit and web of the beams extending into the flange.

As part of the experimental programme, four large-scale reinforced concrete beams were fabricated and tested to failure. All beams were designed to exhibit shear failure. The effect on the beam behaviour of varying the spacing of the external reinforcement was investigated. The spacings considered were 0.75D, 0.60D and 0.50D where D is the overall depth of the beam. The control beam had no external reinforcement. To gain a better understanding of the bond behaviour between the CFRP and concrete and the mechanisms that occur in the T-beams under loading, thirteen CFRP-concrete bond specimens were fabricated and tested. Advanced photogrammetry measurement techniques were used to study the behaviour of the T-beams with and without shear strengthening. Shear crack width development with load and movements of the L-shaped CFRP plates relative to the concrete layer were compared between the T-beams. Numerical modelling of the T-beams and bond specimens using the non-linear finite element method was carried out to supplement the experimental results. The applicability of three existing beam shear strength prediction models were also investigated and compared against experimental results.

An increase in the ultimate shear capacity with reference to the control beam of 54%, 61% and 81% was achieved in beams '0.75D', '0.60D, and '0.50D'. The control beam failed due to the formation of two large shear cracks. Failure in the strengthened beams was characterised by formation of large shear cracks and the separation of the CFRP laps at the soffit of the beam tearing away concrete at the bend zone. It was found from the T-beam tests that the presence of the external shear reinforcement did not affect significantly the initial stiffness of the strengthened

beams compared to the control beam at first loading. The placement of CFRP reinforcement at smaller spacings did not impede or delay the initial formation and propagation of shear cracks. The shear cracks formed at similar load levels in all the beams. In the stirrups, the strains were generally smaller in beams with more closely spaced CFRP reinforcement. Shear cracks were observed to be smaller in the strengthened beams compared to the shear cracks in the control beam.

Results from the photogrammetry measurement show that the deformation mechanisms in the strengthened beams were similar to the control beam except that the width of the shear cracks was smaller. Therefore, existing equations used in the prediction of the shear capacity of reinforced concrete beams can be extended to include the contributions from the CFRP reinforcement. The web shear crack widths were established quantitatively to be significantly smaller in the strengthened beams compared to the control beam. There was no clear difference in the crack widths of the beams with CFRP reinforcement spacing of 0.60D and 0.50D. However, they were smaller than the crack widths in beam '0.75D'. The smaller shear crack widths in the strengthened beams imply that the effect of aggregate interlock is more significant, therefore, the concrete contribution to the shear capacity of the beams increases. Slip between the CFRP plate and concrete was insignificant until when shear cracks have begun to form. At high load levels, the slip profiles indicated that significant portions of critically loaded CFRP reinforcement had debonded in the beams.

Experimental testing of the CFRP-concrete joint tensile specimens has established the effective bond length to be approximately 120 mm, which was based on a simple bilinear curve fit of the peak load versus bond length graph. In all of the specimens, the strain profile in the CFRP plate along the joint shows an exponential curve at the early stages of loading. At the ultimate load, the strain distribution shows combination of a linear and exponential curve. The numerical results of the finite element models were in good agreement with the experimental results. The peak loads, load slip behaviour, strain distribution profile in the CFRP plate and crack patterns were predicted reasonably accurately by the numerical models. Parametric studies were carried out to determine the effects of varying concrete strength, adhesive stiffness and CFRP stiffness. For the values investigated herein, it was

found that the concrete strength had a significant effect on the peak load carried by the models. The effect on the slip behaviour and strain distribution profile of the CFRP plate was minor. Variations in the adhesive and CFRP plate stiffness did not have a significant effect on the peak load, slip behaviour and strain distribution profile of the CFRP plate.

A general methodology for the modelling of the reinforced concrete T-beams web-bonded with FRP both in a 2D and 3D environment has been presented. The finite element models used to analyse the experimental control beam proved to be capable of modelling the general trends and behaviour reasonably accurately. In the case of the shear-strengthened beams, the 2D and 3D finite element models used proved to be capable of modelling the general trends and behaviour reasonably well but with several limitations. The fracture type failure of the concrete at the bend zone and separation of the flange from the web cannot be simulated exactly. In the numerical strengthened beam models, the failure mode was shear compression. In addition, the finite element models did not account fully for the effects of CFRP spacing in the different T-beams. The predicted load capacities were similar despite the fact that the CFRP spacings in the models were different. Nevertheless, the numerical models have simulated the experimental trend that the shear capacity is higher in beams with the external CFRP reinforcement compared to beams without the external CFRP reinforcement. The locations of the most critically loaded CFRP reinforcement were consistent between the numerical models and experimental beams. The numerical models have also provided valuable insight into the level of strain in CFRP plates where strain gauges were not bonded in the experimental beams. The crack patterns produced from the numerical models were comparable to the experimental beams. The investigation carried out on the effects of varying the shear retention factor β in the numerical base models has shown that the load capacity increases with the shear retention factor. In the shear reinforcement, there is a general trend that the larger the shear retention factor, the smaller the strain hence force carried by the stirrups at a given load. This indicates that the shear load carried by the cracked concrete increases with increasing β. An investigation was also carried out on the effects of varying the bond slip behaviour between the CFRP and concrete elements. In the current investigation, the FRP system used was such that FRP end

anchorage was provided. In the strengthened beam models, the predicted load level, steel reinforcement and CFRP plate responses varies depending on the bond slip model adopted. The variation in the responses although small in the current study, will become an important factor in cases where there is no FRP end anchorage and debonding of the FRP dominates. The present investigation highlights the importance of using a proper bond slip model in situations where FRP debonding dominates. The assumption of perfect bond between the CFRP and concrete elements is unjustifiable in these cases. The effects of varying the shear retention factor β in selected strengthened beam models were also investigated. The load capacity of the T-beams increases with the shear retention factor. However, variation in the CFRP spacing has an insignificant effect on the shear capacity of the T-beams. The predicted shear capacities were similar across all the different T-beam models for a given β. The finite element models did not account fully for the effects of CFRP spacing in the different T-beams even when higher β values were adopted. According to the photogrammetry results in Chapter 7, the presence of the external CFRP shear reinforcement had limited the shear crack width in the strengthened beams. It can then be argued that the effect of aggregate interlock was significant more in the strengthened beams compared to the control beam. This means that the use of a higher β value is justified in strengthened beams with smaller CFRP spacing. The finite element method may be used as an aid to designing FRP web bonded beams.

The three existing beam shear strength models investigated gave very conservative predictions of the FRP contribution to the shear strength. These prediction models can be used in the design of beams shear strengthened with the prefabricated L-shaped CFRP strengthening system used in the present study.

Recommendations for further study

Further research will be required in several areas of the present study. In the area of CFRP-concrete bond behaviour, additional experimental work will be required to verify the numerical results of the finite element models presented in Chapter 4. Experimental investigation into the effects of varying concrete strength, adhesive stiffness and CFRP stiffness should be carried out. Further experimental and analytical work will also be required to develop a relationship for modelling of the

bond behaviour that can accommodate the combined effects of varying concrete strength, composite geometries and properties and specimen configurations. The model proposed by Chen and Teng (2001) accounts for all these effects but additional experimental works are required to increase confidence in and verify the robustness of the model.

In the case of the T-beams, further experimental investigations may include varying the steel shear reinforcement spacing, concrete strength, cross-sectional dimensions or the shear-span over effective depth ratio, a_v/d. The experimental investigations may also be extended to study the effects of cyclic or repeated loading and effects of loading over the negative moment regions such as supports. The experimental database on T-beams shear strengthened using the L-shaped cured laminate plates is still very limited. Studies should also be conducted to investigate the CFRP lap separation mechanism observed at the soffit of the experimental T-beams herein. A model accounting for this failure mechanism should be developed and incorporated into the existing prediction models. In Chapter 7, it has been shown quantitatively that the crack widths were significantly smaller in the strengthened beams compared to the control beam. The smaller shear crack widths in the strengthened beams imply that the effect of aggregate interlock is more significant, therefore, the concrete contribution to the shear capacity of the beams increases. Further investigation may be carried out to determine the contribution of aggregate interlock on the total shear capacity. This may be achieved by combining the photogrammetry measurements of crack widths and sliding presented in this thesis with existing models for aggregate interlock shear.

For the finite element analyses, further investigation can be carried out to improve the material models. In the present study, the smeared crack approach was adopted in the T-beam analyses. Future investigation may consider using the discrete crack approach based on fracture mechanics.

REFERENCES

ACI Committee 318 (1999), Building Code Requirements for Structural Concrete (318M-99) and Commentary (318RM-99), American Concrete Institute, Michigan, USA.

ACI Committee 440 (1999), Guidelines for the selection, design, and installation of fiber reinforced polymer (FRP) systems for external strengthening of concrete structures, American Concrete Institute, Michigan, USA.

Adhikary, B. B., Mutsuyoshi, H. and Sano, M. (2000), "Shear strengthening of reinforced concrete beams using steel plates bonded on beam web: experiments and analysis", *Construction and Building Materials*, Vol. 14, No. 5, pp. 237-244.

Aldinger, T. I. and Fultz, B. S. (1989), "Keys to successfully preparing concrete for coating", *Journal of Protective Coatings & Linings*, Vol. 6, No. 5, pp. 34-40.

Al-Mahaidi, R. and Taplin, G. (1998), Analysis of the load testing results of the Old Kiewa Valley Highway Bridge over Yackadandah Creek, *Report to VicRoads*, Department of Civil Engineering, Monash University, Melbourne, Australia

Al-Mahaidi, R., Taplin, G. and Giufre, A. (2000), "Load distribution and shear strength evaluation of old concrete T-beam bridges", *Journal of the Transportation Research Board, Transporation Research Record*, Vol. 1, No. 1696, pp. 52-62.

Al-Sulaimani, G. J., Sharif, A., Basunbul, I. A., Baluch, M. H. and Ghaleb, B. N. (1994), "Shear repair for reinforced concrete by fiberglass plate bonding", *ACI Structural Journal*, Vol. 91, No. 4, pp. 458-464.

Arduini, M., Di Tommaso, A. and Manfroni, O. (1996), Failure mechanisms of concrete beams reinforced with FRP flexible sheets. Advanced composite materials in bridges and structures : 2nd International Conference, Montréal, Québec, Canada

August 11-14, 1996, Montreal, Quebec, Société canadienne de génie civil, pp. 253-260.

Arduini, M., Nanni, A., Di Tommaso, A. and Focacci, F. (1997), Shear response of continuous RC beams strengthened with carbon FRP sheets. Non-Metallic (FRP) Reinforcement for Concrete Structures: Proceedings of the Third International Symposium (FRPRCS-3), Sapporo, Japan, Japan Concrete Institute, pp. 459-466.

Aridome, Y., Kanakubo, T., Furuta, T. and Matsui, M. (1998), "Ductility of T-shape RC beams strengthened by CFRP sheet", *Transactions of the Japan Concrete Institute*, Vol. 20, pp. 117-124.

Armer, G. S. T., Ed. (2001). Monitoring and assessment of structures. London, England, Spon Press.

ASTM (1995), Standard test method for tensile properties of polymer matrix composite materials, American Society for Testing and Materials D3039/D3039M, West Conshohocken, PA, USA

Atkinson, K. B. (1996). Close range photogrammetry and machine vision. Caithness, Scotland, Whittles Pub.

Bizindavyi, L. and Neale, K. W. (1999), "Transfer lengths and bond strength for composites bonded to concrete", *Journal of Composites for Construction*, Vol. 3, No. 4, pp. 153-160.

Bleibler, A., Meier, H. and Steiner, W. (1998), External strengthening of reinforced concrete structures using bonded CFRP plates - Latest developments and world-wide experiences. Australasian Structural Engineering Conference, Auckland, New Zealand, pp. 141-149.

Brosens, K. and Van Gemert, D. (1997), Anchoring stresses between concrete and carbon fibre reinforced laminates. Non-Metallic (FRP) Reinforcement for Concrete

Structures: Proceedings of the Third International Symposium (FRPRCS-3), Sapporo, Japan, Japan Concrete Institute, pp. 271-278.

CEB-FIP (1993), Model Code 1990: design code, Comité Euro-International du Béton - Fédération Internationale de la Précontrainte, Thomas Telford, 1993, London, England, 437 pp.

Chaallal, O., Nollet, M. J. and Perraton, D. (1998a), "Shear strengthening of RC beams by externally bonded side CFRP strips", *Journal of Composites for Construction*, Vol. 2, No. 2, pp. 111-114.

Chaallal, O., Nollet, M.-J. and Perraton, D. (1998b), "Strengthening of reinforced concrete beams with externally bonded fiber-reinforced-plastic plates: design guidelines for shear and flexure", *Canadian Journal of Civil Engineering*, Vol. 25, No. 4, pp. 692-704.

Chajes, M. J., Finch, W. W., Jr., Januszka, T. F. and Thomson, T. A., Jr. (1996), "Bond and force transfer of composite material plates bonded to concrete", *ACI Structural Journal*, Vol. 93, No. 2, pp. 208-217.

Chajes, M. J., Januszka, T. F., Mertz, D. R., Thomson, T. A., Jr. and Finch, W. W., Jr. (1995), "Shear strengthening of reinforced concrete beams using externally applied composite fabrics", *ACI Structural Journal*, Vol. 92, No. 3, pp. 295-303.

Chajes, M. J., Thomson, T. A. J., Januszka, T. F. and Finch, W. W. J. (1994), "Flexural strengthening of concrete beams using externally bonded composite materials". *Construction & Building Materials*, Vol. 8, No. 3, pp. 191-201.

Chen, J. F. and Teng, J. G. (2001), "Anchorage strength models for FRP and steel plates bonded to concrete", *Journal of Structural Engineering ASCE*, Vol. 127, No. 7, pp. 784-791.

Chen, J. F. and Teng, J. G. (2003a), "Shear capacity of FRP-strengthened RC beams: FRP debonding", *Construction and Building Materials*, Vol. 17, No. 1, pp. 27-41.

Chen, J. F. and Teng, J. G. (2003b), "Shear capacity of FRP-strengthened RC beams: FRP rupture", *Journal of Structural Engineering ASCE* (Accepted for publication).

CSA (1994), Design of concrete structures CSA-A23.3-94, Canadian Standards Association, Rexdale, Ontario.

Czaderski, C. (2002), Shear strengthening with prefabricated CFRP L-shaped plates. IABSE Symposium Melbourne: Towards a Better Built Environment - Innovation, Sustainability, Information Technology, Melbourne, Australia.

de Witte, F. C. and Jansen, J., Eds. (2000). Diana - Finite Element Analysis 'User's Manual Introduction and Utilities Release 7.2'. Delft, The Netherlands, TNO Building and Construction Research.

de Witte, F. C. and Kikstra, W. P., Eds. (2000). Diana - Finite Element Analysis 'User's Manual Nonlinear Analysis Release 7.2'. Delft, The Netherlands, TNO Building and Construction Research.

Deniaud, C. and Cheng, J. J. R. (2001), "Shear behavior of reinforced concrete T-beams with externally bonded fiber-reinforced polymer sheets", *ACI Structural Journal*, Vol. 98, No. 3, pp. 386-394.

Dolan, B. E., Hamilton, H. R. I. and Dolan, C. W. (1998), "Strengthening with bonded FRP laminate", *Concrete International*, Vol. 20, No. 6, pp. 51-55.

Dolan, C. W., Rider, W., Chajes, M. J. and DeAscanis, M. (1992), Prestressed concrete beams using non-metallic tendons and external shear reinforcement. Fiber-reinforced plastic reinforcement for concrete structures - international symposium, ACI SP-138, Detroit, American Concrete Institute, pp. 475-495.

EMPA (1998a), Testing of CFRP shear strips on reinforced concrete T-beams T1 and T2, Swiss Federal Laboratories for Materials Testing and Research, Dubendorf, Switzerland, 39 pp.

EMPA (1998b), Testing of CFRP shear strips on flexural beam T3, Swiss Federal Laboratories for Materials Testing and Research, Dubendorf, Switzerland, 17 pp.

ENV 1992-1-1 (1991), Eurocode 2: Design of Concrete Structures Part 1: General Rules and Rules for Buildings, European Committee for Standardization (draft for development).

GSI, 1996. Geodetic Services, Inc. V-Stars [on-line], [http://www.geodetic.com].

Horiguchi, T. and Saeki, N. (1997), Effect of test methods and quality of concrete on bond strength of CFRP sheet. Non-Metallic (FRP) Reinforcement for Concrete Structures: Proceedings of the Third International Symposium (FRPRCS-3), Sapporo, Japan, Japan Concrete Institute, pp. 265-270.

Hutchinson, R., Abdelrahman, A., Rizkalla, S. and Smith, G. (1997), Shear strengthening using FRP sheets for a highway bridge in Manitoba, Canada. Non-Metallic (FRP) Reinforcement for Concrete Structures: Proceedings of the Third International Symposium (FRPRCS-3), Sapporo, Japan, Japan Concrete Institute, pp. 531-538.

Izumo, K., Asamizu, T., Saeki, N. and Shimura, K. (1997), "Shear strengthening of PRC members by fiber sheets", *Transactions of the Japan Concrete Institute*, Vol. 19, pp. 105-112.

Izumo, K., Asamizu, T., Saeki, N. and Shimura, K. (1998), "Bond behaviour of aramid and carbon fiber sheeting", *Transactions of the Japan Concrete Institute*, Vol. 20, pp. 269-278.

JSCE (1996), Standard specification for design and construction of concrete structures - Part 1 (Design), Japan Society of Civil Engineers, Tokyo, Japan

Kaliakin, V. N., Chajes, M. J. and Januszka, T. F. (1996), "Analysis of concrete beams reinforced with externally bonded woven composite fabrics", *Composites Part B:Engineering*, Vol. 27, No. 3-4, pp. 235-244.

Kamiharako, A., Maruyama, K., Takada, K. and Shimomura, T. (1997), Evaluation of shear contribution of FRP sheets attached to concrete beams. Non-Metallic (FRP) Reinforcement for Concrete Structures: Proceedings of the Third International Symposium (FRPRCS-3), Sapporo, Japan, Japan Concrete Institute, pp. 467-474.

Khalifa, A., Alkhrdaji, T., Nanni, A. and Lansburg, S. (1999), "Anchorage of surface mounted FRP reinforcement", *Concrete International*, Vol. 21, No. 10, pp. 49-54.

Khalifa, A., Gold, W. J., Nanni, A. and Aziz Abdel, M. I. (1998), "Contribution of externally bonded FRP to shear capacity of RC flexural members", *Journal of Composites for Construction*, Vol. 2, No. 4, pp. 195-202.

Khalifa, A. and Nanni, A. (2000), "Improving shear capacity of existing RC T-section beams using CFRP composites", *Cement & Concrete Composites*, Vol. 22, No. 3, pp. 165-174.

Kraus, K., Waldhäusl, P. and Stewardson, P. (1993). Photogrammetry. Bonn, Germany, Dümmler's Verlag.

Lee, Y. J., Boothby, T. E., Bakis, C. E. and Nanni, A. (1999), "Slip modulus of frp sheets bonded to concrete", *Journal of Composites for Construction*, Vol. 3, No. 4, pp. 161-167.

Macdonald, M. D. and Calder, A. J. J. (1982), "Bonded steel plating for strengthening concrete structures", *International Journal of Adhesion and Adhesives*, No. 4, pp. 119-127.

Maeda, T., Asano, Y., Sato, Y., Ueda, T. and Kakuta, Y. (1997), A study on bond mechanism of carbon fiber sheet. Non-Metallic (FRP) Reinforcement for Concrete Structures: Proceedings of the Third International Symposium (FRPRCS-3), Sapporo, Japan, Japan Concrete Institute, pp. 279-286.

Malek, A. M. and Saadatmanesh, H. (1998a), "Analytical study of reinforced concrete beams strengthened with web-bonded fiber reinforced plastic pla..s or fabrics", *ACI Structural Journal*, Vol. 95, No. 3, pp. 343-352.

Malek, A. M. and Saadatmanesh, H. (1998b), "Ultimate shear capacity of reinforced concrete beams strengthened with web-bonded fiber-reinforced plastic plates", *ACI Structural Journal*, Vol. 95, No. 4, pp. 391-399.

Meier, U. (1997), Repair using advanced composites. International Conference : Composite Construction - Conventional and Innovative, IABSE, Innsbruck, Austria, pp. 113-123.

Mikhail, E. M., McGlone, J. C. and Bethel, J. S. (2001). Introduction to modern photogrammetry. New York ; Chichester, Wiley.

Miyauchi, K., Inoue, S., Nishibayashi, S. and Tanaka, Y. (1997), "Shear behavior of reinforced concrete beam strengthened with CFRP sheet", *Transactions of the Japan Concrete Institute*, Vol. 19, pp. 97-104.

Nakaba, K., Kanakubo, T., Furuta, T. and Yoshizawa, H. (2001), "Bond behavior between fiber-reinforced polymer laminates and concrete", *ACI Structural Journal*, Vol. 98, No. 3, pp. 359-367.

Neale, K. (2001). Strengthening reinforced concrete structures with externally-bonded fibre reinforced polymers - design manual no. 4. ISIS, Winnipeg, Manitoba, Canada.

Norris, T., Saadatmanesh, H. and Ehsani, M. R. (1997), "Shear and flexural strengthening of R/C beams with carbon fiber sheets", *Journal of Structural Engineering ASCE*, Vol. 123, No. 7, pp. 903-911.

Potisuk, T., Kachlakev, D. I., Miller, T. H. and Yim, S. C. S. (2001), Effects of shear strengthening with GFRP on reinforced concrete beams. 46th International SAMPE Symposium and Exhibition, pp. 1759-1771.

SAA (1991), Methods for tensile testing of metals, Australian Standard AS1391-1991, Standards Australia Association, Sydney, Australia.

SAA (1999), Methods of testing concrete - Method 9: Determination of the compressive strength of concrete specimens, Australian Standard AS1012.9-1999, Standards Australia Association, Sydney, Australia.

Saadatmanesh, H. and Ehsani, M. R. (1989), "Application of fiber-composites in civil engineering", *Proceedings of the Sessions Related to Structural Materials at Structures Congress '89. Publ by ASCE, New York, NY, USA*, Vol. 89, pp. 526-535.

SAI (2001), Concrete structures, Australian Standard AS3600-2001, Standards Australia International, Sydney, Australia.

Sakai, Y., Ushijima, S., Hayashi, S. and Sano, T. (1997), Mechanical characteristics of carbon fiber sheet with methyl methacrylate resin. Non-Metallic (FRP) Reinforcement for Concrete Structures: Proceedings of the Third International Symposium (FRPRCS-3), Sapporo, Japan, Japan Concrete Institute, pp. 243-250.

Sato, Y., Tanaka, T., Ueda, T. and Ono, S. (1996), "Shear behavior of RC beams reinforced with carbon fiber sheet", *Transactions of the Japan Concrete Institute*, Vol. 18, No. , pp. 137-142.

Sato, Y., Ueda, T., Kakuta, Y. and Ono, S. (1997), Ultimate shear capacity of reinforced concrete beams with carbon fiber sheet. Non-Metallic (FRP) Reinforcement for Concrete Structures: Proceedings of the Third International Symposium (FRPRCS-3), Sapporo, Japan, Japan Concrete Institute, pp. 499-506.

Selby, R. G. and Vecchio, F. J. (1993), Three-dimensional constitutive relations for reinforced concrete, Department of Civil Engineering, University of Toronto, Ontario, Canada

Shahawy, M. and Beitelman, T. E. (1999), "Static and fatigue performance of RC beams strengthened with CFRP laminates", *Journal of Structural Engineering ASCE*, Vol. 125, No. 6, pp. 613-621.

Sharif, A., Al-Sulaimani, G. J., Basunbul, I. A., Baluch, M. H. and Husain, M. (1995), "Strengthening of shear-damaged RC beams by external bonding of steel plates", *Magazine of Concrete Research*, Vol. 47, No. 173, pp. 329-334.

Spadea, G., Bencardino, F. and Swamy, R. N. (1998), "Structural behavior of composite RC beams with externally bonded CFRP", *Journal of Composites for Construction*, Vol. 2, No. 3, pp. 132-137.

Stirling, D. (2001). Photogrammetry - theory and technology. Monitoring and assessment of structures. G. S. T. Armer. London, England, Spon Press: 167.

Taerwe, L., Khalil, H. and Matthys, S. (1997), Behaviour of RC beams strengthened in shear by external CFRP sheets. Non-Metallic (FRP) Reinforcement for Concrete Structures: Proceedings of the Third International Symposium (FRPRCS-3), Sapporo, Japan, Japan Concrete Institute, pp. 483-490.

Täljsten, B. (1994), "Plate bonding. Strengthening of existing concrete structures with epoxy bonded plates of steel or fibre reinforced plastics", Doctoral Thesis, Lulea University of Technology, Sweden.

Täljsten, B. (1997), "Defining anchor lengths of steel and CFRP plates bonded to concrete", *International Journal of Adhesion & Adhesives*, Vol. 17, No. 4, pp. 319-327.

Taplin, G. and Al-Mahaidi, R. (1999), An experimental and theoretical investigation of the shear strength of model reinforced concrete T-beams, *Report to VicRoads*, Department of Civil Engineering, Monash University, Melbourne, Australia.

Taplin, G. and Al-Mahaidi, R. (2000), An experimental investigation of shear critical T-beams. Canadian Society for Civil Engineering Annual Conference and 3rd Structural Specialty Conference, London, Ontario, Canada.

Tedesco, J. W., Stallings, J. M. and El-Mihilmy, M. (1999), "Finite element method analysis of a concrete bridge repaired with fiber reinforced plastic laminates", *Computers and Structures*, Vol. 72, No. 1-3, pp. 379-407.

Teng, J. G., Chen, J. F., Smith, S. T. and Lam, L. (2002). FRP strengthened rc structures. Chichester, England, John Wiley & Sons, Ltd.

Thorenfeldt, E., Tomaszewicz, A. and Jensen, J. J. (1987), Mechanical properties of high-strength concrete and application in design. Utilization of high strength concrete: proceedings: symposium in Stavanger, Norway, June 15-18, 1987, Stavanger, Norway, Tapir Publishers, Trondheim.

Toutanji, H. and Ortiz, G. (2001), "The effect of surface preparation on the bond interface between FRP sheets and concrete members", *Composite Structures*, Vol. 53, No. 4, pp. 457-462.

Triantafillou, T. C. (1998), "Shear strengthening of reinforced concrete beams using epoxy-bonded FRP composites", *ACI Structural Journal*, Vol. 95, No. 2, pp. 107-115.

Triantafillou, T. C. and Antonopoulos, C. P. (2000), "Design of concrete flexural members strengthened in shear with FRP", *Journal of Composites for Construction*, Vol. 4, No. 4, pp. 198-205.

Triantafillou, T. C. and Plevris, N. (1992), "Strengthening of RC beams with epoxy-bonded fibre-composite materials", *Materials & Structures*, Vol. 25, pp. 201-211.

Uji, K. (1992), "Improving shear capacity of existing reinforced concrete members by applying carbon fiber sheets", *Transactions of the Japan Concrete Institute*, Vol. 14, pp. 253-266.

Umezu, K., Fujita, M., Nakai, H. and Tamaki, K. (1997), Shear behavior of RC beams with aramid fiber sheet. Non-Metallic (FRP) Reinforcement for Concrete Structures: Proceedings of the Third International Symposium (FRPRCS-3), Sapporo, Japan, Japan Concrete Institute, pp. 491-498.

Van Gemert, D. (1980), "Force transfer in epoxy bonded steel/concrete joints", *International Journal of Adhesion and Adhesives*, No. 1, pp. 67-72.

Vecchio, F. J. and Collins, M. P. (1986), "The Modified Compression-Field Theory for Reinforced Concrete Elements Subjected to Shear", *ACI Journal*, Vol. 83, No. 2, pp. 219-231.

Ziraba, Y. N., Baluch, M. H., Basunbul, I. A., Sharif, A. M., Azad, A. K. and Al-Sulaimani, G. J. (1994), "Guidelines toward the design of reinforced concrete beams with external plates", *ACI Structural Journal*, Vol. 91, No. 6, pp. 639-646.

APPENDIX A

A.1 T-beam geometries and material properties consideration

The T-beam geometries and material properties considered in the design of the T-beams are summarised in Table A.1 to Table A.3. As the objective of the tests was to study the failure mode of the L-shaped CFRP plate strengthening system, the test beams were designed to have significantly higher flexural capacity than the shear capacity. The dimensions of the T-beams were based on the Kiewa Valley Highway Bridge, designed in 1916, which was a typical bridge constructed in periods when provisions were less severe than current design requirements. The bridge has an average span of 7.213 metres with a 150 mm thick concrete slab integrated with four beams. The overall depth of the beams including the slab is 610 mm with a web width of 280 mm.

Six beam scales ranging from 50% to 100% with different flexural reinforcement configurations were considered. To minimise the range of beam configurations, the shear reinforcement spacing in all the beams was set to the maximum allowable by SAI (2001), which was 0.75D where D is the overall depth of the member. The area of shear reinforcement was set to the minimum area allowable by SAI (2001), expressed as $A_{sv.min}$ (= $0.35b_vs/f_{sy.f}$). The calculated stirrup diameter was set to match the nearest available sizes. The bar type considered was limited to plain round bars with yield stresses ($f_{sy.f}$) of 250 MPa (Table A.1) and 350 MPa (Table A.2). For the flexural reinforcement, the bar sizes considered were varied from 16 to 32 mm with the smaller sizes used for smaller scale beams and larger sizes for larger scale beams. In Table A.1 and Table A.2, the bar type investigated was limited to deformed bars with yield stress (f_{sy}) of 500 MPa. The concrete strengths considered were 25 and 30 MPa, which were the typical strength of old bridges.

For each beam, the margin between shear failure and flexural failure was calculated. The margin was expressed as the ratio between the load corresponding to the ultimate moment capacity and the shear failure load. The flexural strength was

calculated using bending theory whereas the shear strength was calculated using a computer program that utilised the modified compression field theory (MCFT) developed by Vecchio and Collins (1986). Details of the program are outlined in the study by Al-Mahaidi and Taplin (1998) and Al-Mahaidi et al. (2000). The contribution of the L-shaped CFRP plates was calculated independently. It was assumed that shear cracks would intersect two CFRP plates on each side. Based on the study carried out by EMPA (1998a), it was assumed that each strip would contribute up to 55% of its ultimate load capacity before failing by concrete debonding. The ultimate tensile capacity of each CFRP plate was assumed to be 126 kN. The shear strength of the beam was calculated to be the total of the load contributed by the CFRP plates and the load obtained using the MCFT.

From the results of Table A.1 and Table A.2, the 80% beam scale was deemed feasible and was considered for further investigation. A more refined set of calculations was carried out on the beam configuration with 8 main bars of 28 mm diameter, the results of which are summarised in Table A.3. To account for variations in the material properties, the concrete strength of 25, 30 and 35 MPa and flexural reinforcement yield stresses of 450 and 500 MPa were considered. The steel shear reinforcement available was assumed to have a yield stress of 350 MPa. The beam configurations investigated have ratio of flexural capacity to shear capacity larger than one. The beam with the concrete strength of 30 MPa and flexural reinforcement yield stress of 450 MPa was adopted for the experimental program.

Table A.1 - Geometries and material properties considered for scale beams with stirrup yield stress of 250 MPa

Scale	Beam details	d (mm)	Main bar dia. (mm)	No. of main bars	A_{st} (mm^2)	Stirrup dia. req. (mm)	Actual stirrup dia. (mm)	No. of legs	f'_c (MPa)	M_u (kNM) AS3600	$V_{measured}$ (kN) AS3600	$V_s + V_c$ (kN) MCFT	V_{cfrp} (kN) Approx.	V_{shear} (kN)	$V_{measured}/V_{shear}$
E = 200,000 MPa, Yield stresses = 500 MPa (main bars) & 250 MPa (stirrups), $a_v/d = 3.0$, $V_{cfrp} = 4 \times (55\% \times 126\ kN) = 277.2\ kN$															
100%	$b_f = 900$ mm $b_w = 280$ mm $t_f = 150$ mm D = 610 mm S = 458 mm $A_{sv.min} = 179\ mm^2$	538	28	8	4926	10.7	10	2	25	1166.5	722.7	296.5	277.2	573.7	1.26
		538	28	10	6158	10.7	10	2	25	1406.0	871.1	313.6	277.2	590.8	1.47
		532	32	8	6434	10.7	10	2	25	1433.9	898.4	313.4	277.2	590.6	1.52
		538	28	8	4926	10.7	10	2	30	1192.9	739.1	312.9	277.2	590.1	1.25
		538	28	10	6158	10.7	10	2	30	1449.9	898.3	330.9	277.2	608.1	1.48
		532	32	8	6434	10.7	10	2	30	1486.0	931.1	331.3	277.2	608.5	1.53
90%	$b_f = 810$ mm $b_w = 250$ mm $t_f = 135$ mm D = 550 mm S = 413 mm $A_{sv.min} = 144\ mm^2$	486	24	8	3619	9.6	10	2	25	784.3	537.9	246.1	277.2	523.3	1.03
		480	28	8	4926	9.6	10	2	25	1004.8	697.8	262.4	277.2	539.6	1.29
		474	32	6	4825	9.6	10	2	25	974.0	685.0	258.5	277.2	535.7	1.28
		486	24	8	3619	9.6	10	2	30	800.2	548.8	260.0	277.2	537.2	1.02
		480	28	8	4926	9.6	10	2	30	1035.4	719.0	276.6	277.2	553.8	1.30
		474	32	6	4825	9.6	10	2	30	1002.7	705.1	272.0	277.2	549.2	1.28
80%	$b_f = 720$ mm $b_w = 225$ mm $t_f = 120$ mm D = 490 mm S = 368 mm $A_{sv.min} = 116\ mm^2$	438	20	8	2513	6.1	6	4	25	498.8	379.6	191.2	277.2	468.4	0.81
		432	24	6	2714	6.1	6	4	25	526.1	405.9	193.0	277.2	470.2	0.86
		432	24	8	3619	6.1	6	4	25	674.7	520.6	206.7	277.2	483.9	1.08
		420	32	6	4825	6.1	6	4	25	762.3	605.0	215.9	277.2	493.1	1.23
		438	20	8	2513	6.1	6	4	30	507.4	386.2	201.1	277.2	478.3	0.81
		432	2	6	2714	6.1	6	4	30	536.1	413.7	203.4	277.2	480.6	0.86
		432	24	8	3619	6.1	6	4	30	692.6	514.4	217.7	277.2	494.9	1.08
		420	32	6	4825	6.1	6	4	30	852.2	676.3	228.0	277.2	505.2	1.34

Table A.1 (continued) - Geometries and material properties considered for scale beams with stirrup yield stress of 250 MPa

75%	b_f = 675 mm b_w = 210 mm t_f = 115 mm D = 460 mm S = 345 mm $A_{sv.min}$ = 101 mm^2	409	20	8	2513	5.7	6	4	25	458.9	374.0	179.9	277.2	457.1	0.82
		403	24	8	3619	5.7	6	4	25	613.1	507.1	192.6	277.2	469.8	1.08
		403	24	6	2714	5.7	6	4	25	482.7	399.3	180.1	277.2	457.3	0.87
		397	28	6	3695	5.7	6	4	25	611.4	513.3	192.2	277.2	469.4	1.09
		391	32	6	4825	5.7	6	4	25	635.3	541.6	201.7	277.2	478.9	1.13
		409	20	8	2513	5.7	6	4	30	468.1	381.5	188.4	277.2	465.6	0.82
		403	24	8	3619	5.7	6	4	30	634.1	524.5	203.4	277.2	480.6	1.09
		403	24	6	2714	5.7	6	4	30	493.4	408.1	190.3	277.2	467.5	0.87
		397	28	6	3695	5.7	6	4	30	634.2	532.5	202.6	277.2	479.8	1.11
		391	32	6	4825	5.7	6	4	30	746.0	636.0	212.8	277.2	490.0	1.30
60%	b_f = 540 mm b_w = 170 mm t_f = 90 mm D = 365 mm S = 274 mm $A_{sv.min}$ = 65 mm^2	326	16	8	1608	3.7	3.2	6	25	233.8	239.2	110.9	277.2	388.1	0.62
		320	20	6	1885	3.7	3.2	6	25	262.7	273.8	113.6	277.2	390.8	0.70
		314	24	6	2714	3.7	3.2	6	25	320.1	340.0	122.2	277.2	399.4	0.85
		308	28	6	3695	3.7	3.2	6	25	320.1	346.7	128.4	277.2	405.6	0.85
		302	32	4	3217	3.7	3.2	6	25	307.2	339.3	122.9	277.2	400.1	0.85
		326	16	8	1608	3.7	3.2	6	30	238.5	244.1	117.3	277.2	394.5	0.62
		320	20	6	1885	3.7	3.2	6	30	269.2	280.5	120.5	277.2	397.7	0.71
		314	24	6	2714	3.7	3.2	6	30	357.9	380.2	129.8	277.2	407.0	0.93
		308	28	6	3695	3.7	3.2	6	30	376.5	407.8	???	277.2	277.2	1.47
		302	32	4	3217	3.7	3.2	6	30	361.0	398.7	130.7	277.2	407.9	0.98
50%	b_f = 450 mm b_w = 140 mm t_f = 75 mm D = 305 mm S = 229 mm $A_{sv.min}$ = 45 mm^2	274	12	8	905	3.1	3.2	6	25	113.2	137.8	79.8	277.2	357.0	0.39
		268	16	6	1206	3.1	3.2	6	25	142.5	177.4	84.4	277.2	361.6	0.49
		262	20	6	1885	3.1	3.2	6	25	185.3	235.9	91.6	277.2	368.8	0.64
		256	24	6	2714	3.1	3.2	6	25	185.1	241.2	96.7	277.2	373.9	0.65
		274	12	8	905	3.1	3.2	6	30	114.9	139.9	83.8	277.2	361.0	0.39
		268	16	6	1206	3.1	3.2	6	30	145.7	181.3	88.9	277.2	366.1	0.50
		262	20	6	1885	3.1	3.2	6	30	207.4	264.1	97.0	277.2	374.2	0.71
		256	24	6	2714	3.1	3.2	6	30	217.9	283.9	???	277.2	277.2	1.02

Table A.2 - Geometries and material properties considered for scale beams with stirrup yield stress of 350 MPa

Scale	Beam details	d (mm)	Main bar dia. (mm)	No. of main bars	A_{st} (mm^2)	Stirrup dia. req. (mm)	Actual stirrup dia. (mm)	No. of legs	f'_c (MPa)	M_u (kNM) AS3600	V_{moment} (kN) AS3600	V_s+V_c (kN) MCFT	V_{cfrp} (kN) Approx.	V_{shear} (kN)	V_{moment}/V_{shear}
E = 200,000 MPa, Yield stresses = 500 MPa (main bars) & 250 MPa (stirrups), a_v/d = 3.0, V_{cfrp} = 4 x (55% x 126 kN) = 277.2 kN															
100%	b_f = 900 mm b_w = 280 mm t_f = 150 mm D = 610 mm S = 458 mm $A_{sv.min}$ = 128 mm^2	538	28	8	4926	9.0	10	2	25	1166.5	722.7	313.9	277.2	591.1	1.22
		538	28	10	6158	9.0	10	2	25	1406.0	871.1	326.8	277.2	604.0	1.44
		532	32	8	6434	9.0	10	2	25	1433.9	898.4	330.7	277.2	607.9	1.48
		538	28	8	4926	9.0	10	2	30	1192.9	739.1	331.6	277.2	608.8	1.21
		538	28	10	6158	9.0	10	2	30	1449.9	898.3	345.9	277.2	623.1	1.44
		532	32	8	6434	9.0	10	2	30	1486.0	931.1	348.5	277.2	625.7	1.49
90%	b_f = 810 mm b_w = 250 mm t_f = 135 mm D = 550 mm S = 413 mm $A_{sv.min}$ = 103 mm^2	486	24	8	3619	8.1	10	2	25	784.3	537.9	265.1	277.2	542.3	0.99
		480	28	8	4926	8.1	10	2	25	1004.8	697.8	280.3	277.2	557.5	1.25
		474	32	6	4825	8.1	10	2	25	974.0	685.0	278.2	277.2	555.4	1.23
		486	24	8	3619	8.1	10	2	30	800.2	548.8	277.9	277.2	555.1	0.99
		480	28	8	4926	8.1	10	2	30	1035.4	719.0	295.3	277.2	572.5	1.26
		474	32	6	4825	8.1	10	2	30	1002.7	705.1	291.8	277.2	569.0	1.24
80%	b_f = 720 mm b_w = 225 mm t_f = 120 mm D = 490 mm S = 368 mm $A_{sv.min}$ = 83 mm^2	438	20	8	2513	7.3	6	2	25	498.8	379.6	181.6	277.2	458.8	0.83
		432	24	6	2714	7.3	6	2	25	526.1	405.9	182.9	277.2	460.1	0.88
		432	24	8	3619	7.3	6	2	25	674.7	520.6	196.1	277.2	473.3	1.10
		418	28	8	4926	7.3	10	2	25	758.6	599.6	240.0	277.2	517.2	1.16
		420	32	6	4825	7.3	6	2	25	762.3	605.0	204.6	277.2	481.8	1.26
		438	20	8	2513	7.3	6	2	30	507.4	386.2	191.6	277.2	468.8	0.82
		432	24	6	2714	7.3	6	2	30	536.1	413.7	193.0	277.2	470.2	0.88
		432	24	8	3619	7.3	6	2	30	692.6	534.4	208.2	277.2	485.4	1.10
		418	28	8	4926	7.3	10	2	30	860.3	680.1	253.3	277.2	530.5	1.28
		420	32	6	4825	7.3	6	2	30	852.2	676.3	218.3	277.2	495.5	1.36

Table A.2 (continued) - Geometries and material properties considered for scale beams with stirrup yield stress of 350 MPa

75%	b_f = 675 mm b_w = 210 mm t_f = 115 mm D = 460 mm S = 345 mm $A_{sv,min}$ = 72 mm^2	409	20	8	2513	6.8	6	2	25	458.9	374.0	169.2	277.2	446.4	0.84
		403	24	8	3619	6.8	6	2	25	613.1	507.1	183.0	277.2	460.2	1.10
		403	24	6	2714	6.8	6	2	25	482.7	399.3	171.3	277.2	448.5	0.89
		397	28	6	3695	6.8	6	2	25	611.4	513.3	182.0	277.2	459.2	1.12
		391	32	6	4825	6.8	6	2	25	635.3	541.6	190.1	277.2	467.3	1.16
		409	20	8	2513	6.8	6	2	30	468.1	381.5	178.9	277.2	456.1	0.84
		403	24	8	3619	6.8	6	2	30	634.1	524.5	192.9	277.2	470.1	1.12
		403	24	6	2714	6.8	6	2	30	493.4	408.1	180.0	277.2	457.2	0.89
		397	28	6	3695	6.8	6	2	30	634.2	532.5	192.7	277.2	469.9	1.13
		391	32	6	4825	6.8	6	2	30	746.0	636.0	203.0	277.2	480.2	1.32
60%	b_f = 540 mm b_w = 170 mm t_f = 90 mm D = 365 mm S = 274 mm $A_{sv,min}$ = 47 mm^2	323	16	8	1608	5.4	6	2	25	231.6	239.0	120.4	277.2	397.6	0.60
		317	20	6	1885	5.4	6	2	25	260.1	273.5	123.2	277.2	400.4	0.68
		311	24	6	2714	5.4	6	2	25	315.9	338.6	131.8	277.2	409.0	0.83
		305	28	6	3695	5.4	6	2	25	315.8	345.2	138.0	277.2	415.2	0.83
		299	32	4	3217	5.4	6	2	25	303.1	337.9	132.4	277.2	409.6	0.82
		323	16	8	1608	5.4	6	2	30	236.3	243.8	126.1	277.2	403.3	0.60
		317	20	6	1885	5.4	6	2	30	266.5	280.2	129.3	277.2	406.5	0.69
		311	24	6	2714	5.4	6	2	30	354.1	379.5	139.2	277.2	416.4	0.91
		305	28	6	3695	5.4	6	2	30	371.5	406.0	???	277.2	277.2	1.46
		299	32	4	3217	5.4	6	2	30	356.1	397.0	140.4	277.2	417.6	0.95
50%	b_f = 450 mm b_w = 140 mm t_f = 75 mm D = 305 mm S = 229 mm $A_{sv,min}$ = 32 mm^2	274	12	8	905	3.2	3.2	4	25	113.2	137.8	265.1	277.2	542.3	0.25
		268	16	6	1206	3.2	3.2	4	25	142.5	177.4	128.8	277.2	406.0	0.44
		262	20	6	1885	3.2	3.2	4	25	185.3	235.9	141.1	277.2	418.3	0.56
		256	24	6	2714	3.2	3.2	4	25	185.1	241.2	150.3	277.2	427.5	0.56
		274	12	8	905	3.2	3.2	4	30	114.9	139.9	???	277.2	277.2	0.50
		268	16	6	1206	3.2	3.2	4	30	145.7	181.3	136.0	277.2	413.2	0.44
		262	20	6	1885	3.2	3.2	4	30	207.4	264.1	149.4	277.2	426.6	0.62
		256	24	6	2714	3.2	3.2	4	30	217.9	283.9	159.2	277.2	436.4	0.65

Table A.3 - Geometries and material properties considered for 80% scale beams with stirrup yield stress of 350 MPa

Scale	Beam details:	d (mm)	Main bar dia. (mm)	No. of main bars	Stirrup dia. req. (mm)	Actual stirrup dia. (mm)	No. of legs	f'_c (MPa)	Main bar f_{sy} (MPa)	M_u (kNM) AS3600	$V_{maximum}$ (kN) AS3600	$V_s + V_c$ (kN) MCFT	V_{cfrp} (kN) Approx.	V_{shear} (kN)	$V_{maximum}$ /V_{shear}
E = 200,000 MPa, Yield stresses = 350 MPa (stirrups), $a_v/d = 3.0$, $V_{cfrp} = 4 \times (55\% \times 126\ kN) = 277.2\ kN$															
80%	$b_f = 720$ mm $b_w = 225$ mm $t_f = 120$ mm D = 490 mm S = 368 mm $A_{st} = 4926\ mm^2$ $A_{sv.min} = 83\ mm^2$	418	28	8	7.3	10	2	30	500	860.3	680.1	253.3	277.2	530.5	1.28
		418	28	8	7.3	10	2	30	450	792.8	626.7	253.3	277.2	530.5	1.18
		418	28	8	7.3	10	2	35	500	887.9	701.9	263.2	277.2	540.4	1.30
		418	28	8	7.3	10	2	35	450	811.9	641.8	263.2	277.2	540.4	1.19
		418	28	8	7.3	10	2	25	500	758.6	599.6	240.0	277.2	517.2	1.16
		418	28	8	7.3	10	2	25	450	755.6	597.3	240.0	277.2	517.2	1.15

A.2 Shear crack patterns (Taplin and Al-Mahaidi (1999, 2000))

The shear crack patterns of T-beams in the study by Taplin and Al-Mahaidi (1999) and Taplin and Al-Mahaidi (2000) are reproduced in Figure A.1 below. The numbers correspond to the beams used in the study. Crack patterns from both sides of the beam on one shear span were sketched.

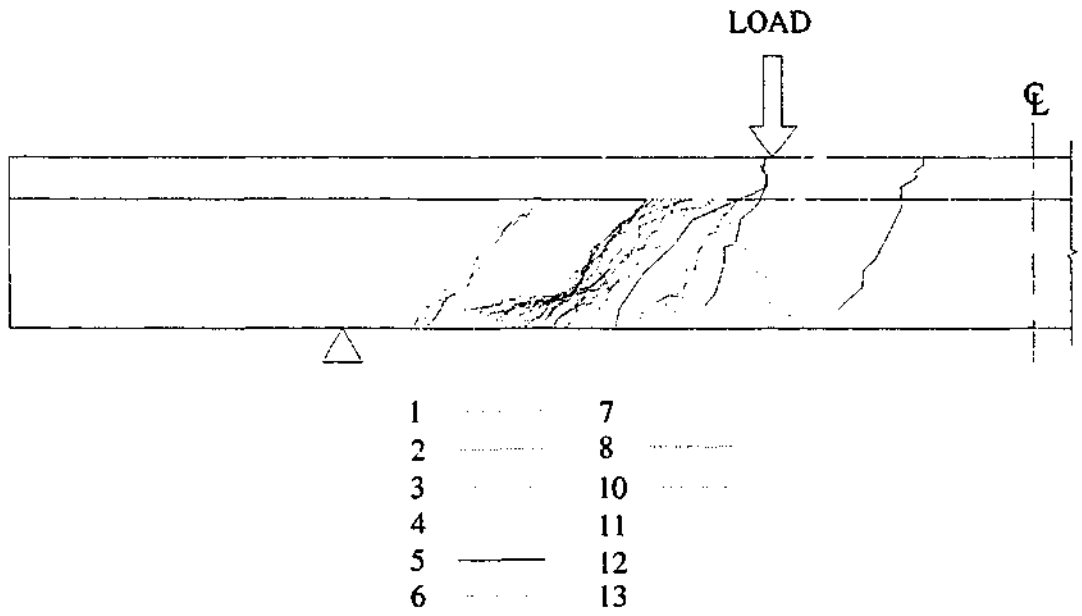

Figure A.1 - Shear crack patterns of T-beams (Taplin and Al-Mahaidi (1999))

A.3 Concrete mix design and properties of T-beams

The concrete mix design used for the fabrication of the T-beams is outlined in Table A.4. The concrete strength development with time is illustrated in Figure A.2.

Table A.4 - Concrete mix design for T-beams

A.C.H. Goliath Type GP Portland Cement (kg/m^3)	242
Maximum Aggregate Size (mm)	14
Pioneer Kilmore 14/10 mm coarse aggregates (kg/m^3)	980
Pioneer Kilmore Crusher Fines (kg/m^3)	200
Pioneer Bacchus Marsh Sand (SSD*) (kg/m^3)	840
Nominal Slump (mm)	80
Water Cement Ratio	0.66
Water Reducing Admixture (ml)	As required
Air Entraining Admixture (ml)	As required

* Saturated and Surface Dry

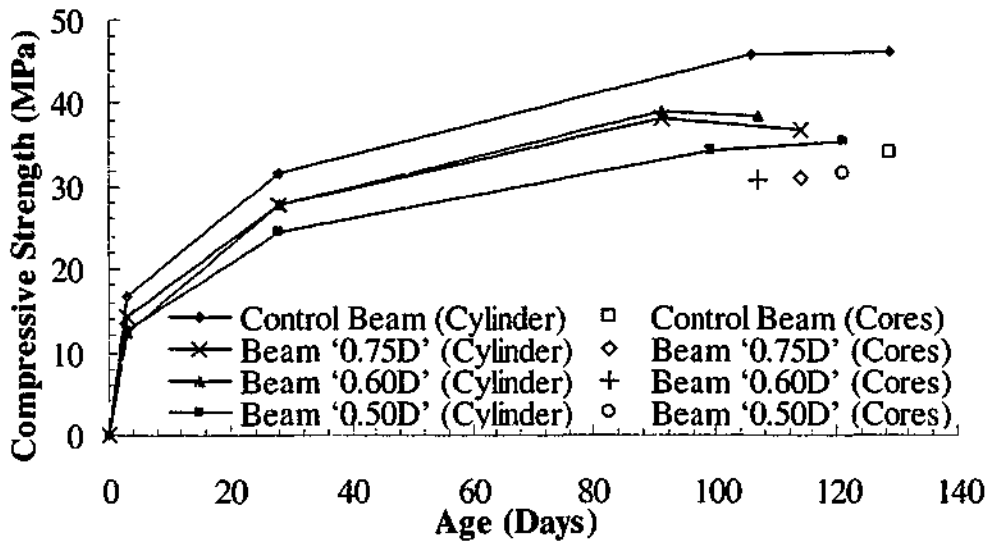

Figure A.2 - Concrete strength development with time

A.4 Steel reinforcement

The typical stress strain responses of the steel reinforcement used in the T-beams are illustrated in Figure A.3 and Figure A.4. The bar type R10 did not have a distinct yield point and exhibited strain hardening until rupture. The bar type Y28 possessed a distinct yield point with a long plateau followed by strain hardening until rupture.

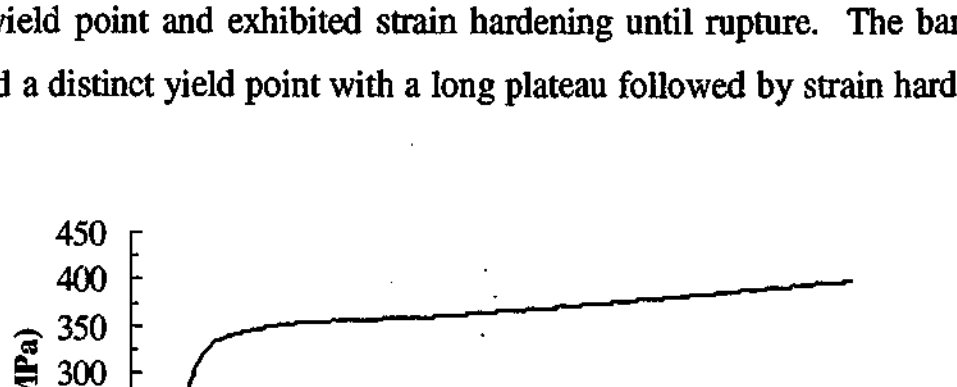

Figure A.3 - Typical stress-strain profile for reinforcement type R10

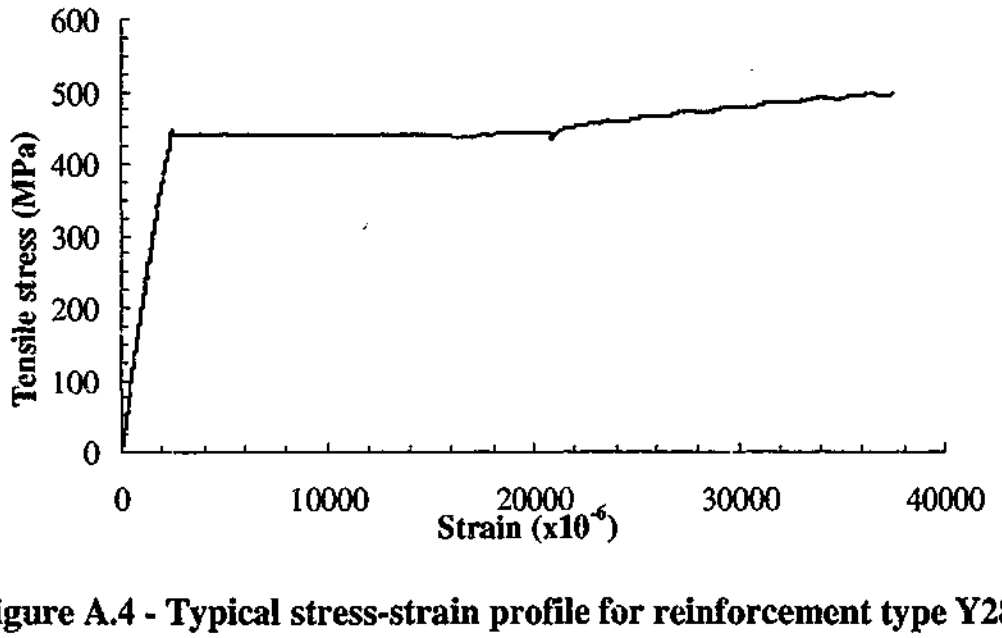

Figure A.4 - Typical stress-strain profile for reinforcement type Y28

A.5 Sika CarboShear L Plates strengthening system

Tension test coupons were cut to the required length from the L-shaped CFRP plates. Each coupon had an overall length of 320 mm and average width of 41.71 mm. To prevent gripping damage, woven fibreglass fabrics were used as tab materials. The fibreglass used was a 0/90° bi-directional woven fabric with a fibre distribution ratio of 45% to 55%. The fibreglass weighed approximately 180 grams per square metre. The tabs were formed in 'steps' using 2 layers of fibreglass (Figure A.5) bonded to the specimen using a rubber modified two parts epoxy 'Redux 420A'.

The tension tests were carried out using a 250 kN MTS Instron testing machine with adjustable hydraulic grips. Strain readings were measured using an extensometer with a gauge length of 25 mm. The load was applied at a constant displacement rate of 1 mm/min with strain, stroke displacement and load readings recorded every 0.5 seconds. The grip pressure was set to 8 MPa. Prior to each test, the width and thickness of each coupon were measured across three points. The tests were carried out in accordance to ASTM (1995).

The results of the tension tests including the ultimate tensile stress reached are tabulated in Table A.5. All the specimens failed in a similar manner, which was longitudinal splitting along the fibres across the entire width (Figure A.6). The specimens failed in a brittle and explosive manner. The ultimate tensile stresses recorded varied significantly to the value reported by EMPA (1998a). The researchers reported a significantly higher tensile strength of 2190 MPa. Premature failure due to high stress concentration near the grips may have contributed to this discrepancy. Nevertheless, the tensile elastic modulus obtained is consistent with the value of 139,900 MPa reported by EMPA (1998a). The tensile capacity is not an important variable as it has been shown in the present study that tensile failure of the CFRP L-shaped plates did not occur. A typical stress-strain curve for the CFRP is illustrated in Figure A.7. The CFRP exhibits linear elastic behaviour until failure.

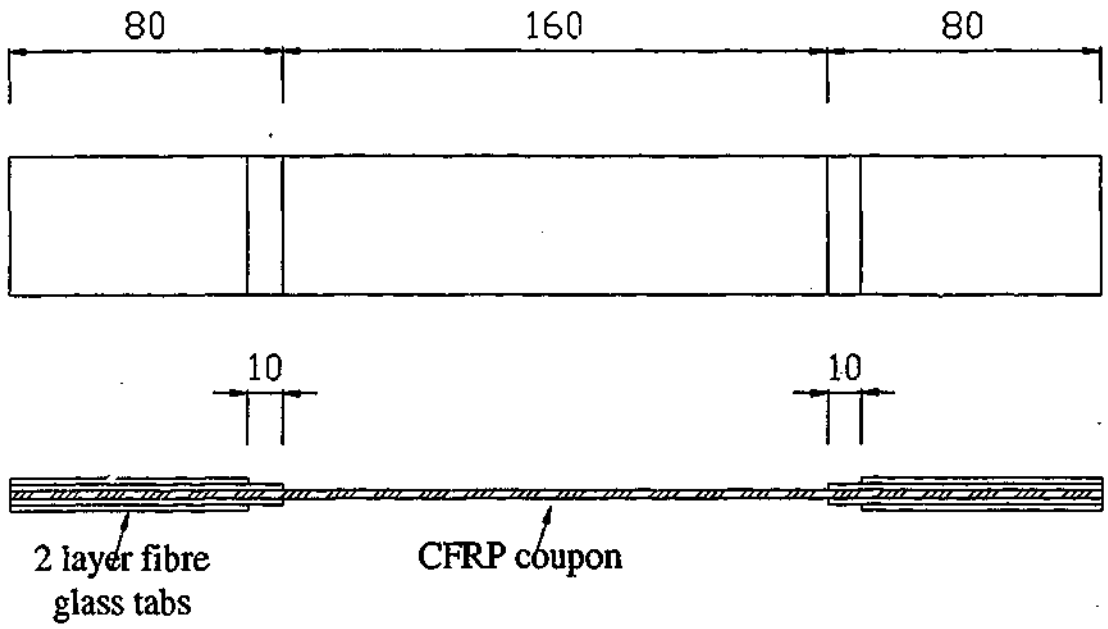

Figure A.5 - CFRP tension test coupon

Table A.5 - Test results of CFRP tensile coupons

Specimen No.	Average thickness (mm)	Average width (mm)	Tensile elastic modulus (MPa)	Ultimate tensile stress (MPa)
1	1.33	41.75	135667	1744.0
2	1.25	41.82	138714	1940.3
3	1.31	41.65	136714	1835.4
4	1.34	41.63	138286	1742.3
Average	1.31	41.71	137345	-

Figure A.6 - Failure of CFRP tensile coupons

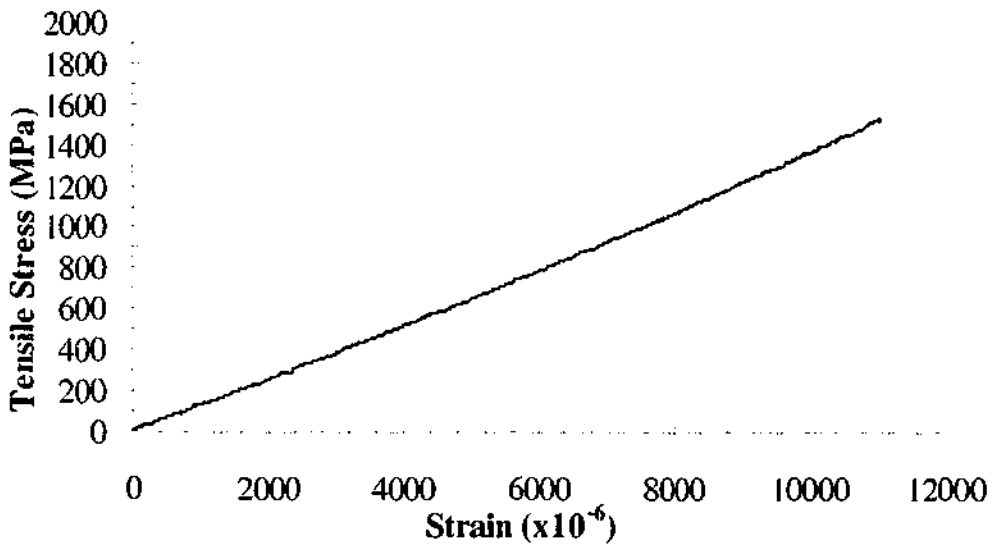

Figure A.7 - Typical stress-strain curve for L-shaped CFRP plate

APPENDIX B

B.1 Load strain behaviour of main flexural reinforcement

The load strain behaviour of the main flexural reinforcement in the control and strengthened T-beams are illustrated in Figure B.1. Two strain gauges were bonded on the main flexural reinforcement of each beam, one for each shear span directly under the loading points. The strain gauges were bonded to the bottom and outermost bars at opposing sides. Figure B.1 (c) shows only result from one strain gauge as the second strain gauge was damaged during concrete pouring. The load illustrated in the figures corresponds to the measured support loads at the span where the strain gauges were bonded.

In all of the beams, the results indicated that the main flexural reinforcement did not reach yield at failure. The responses at the east and west spans were similar except in beam '0.60D'.

(a)

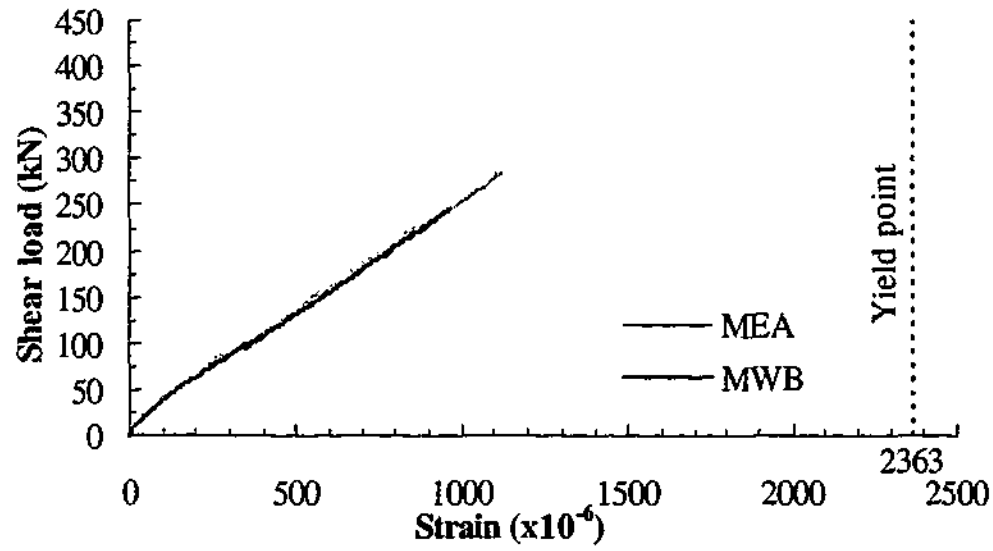

Figure B.1 - Load versus strain behaviour of main flexural reinforcement for (a) control beam (b) beam '0.75D' (c) beam '0.60D' and (d) beam '0.50D'

(b)

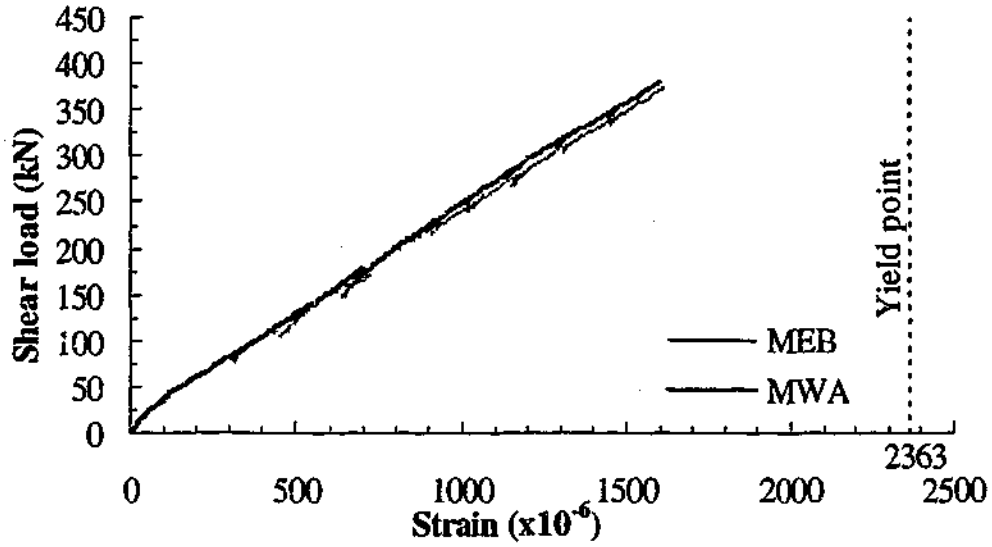

(c)

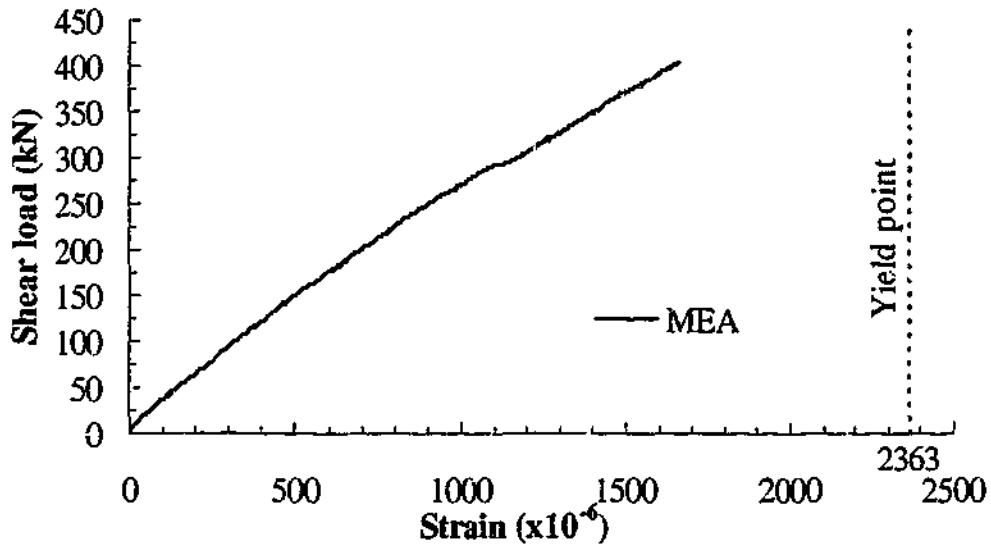

(d)

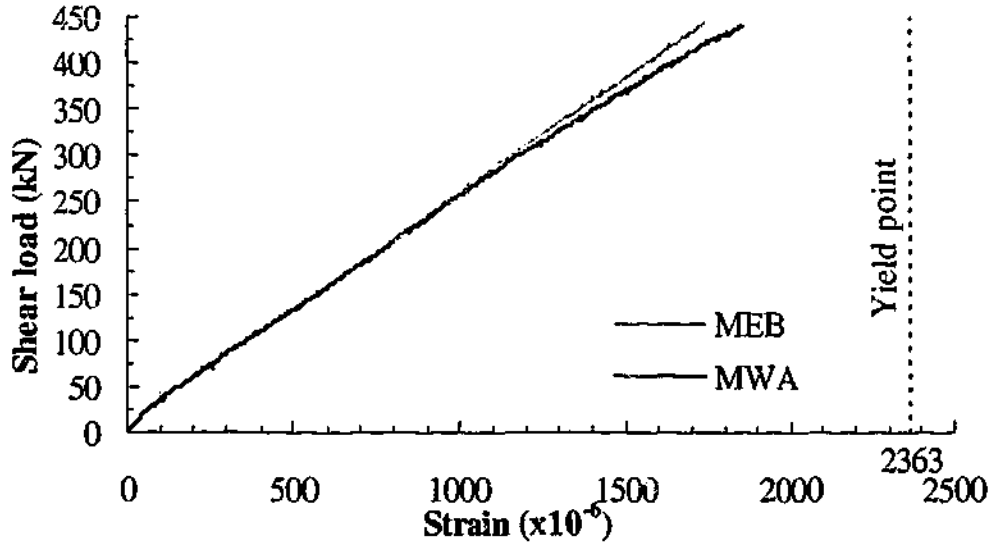

Figure B.1 (continued) - Load versus strain behaviour of main flexural reinforcement for (a) control beam (b) beam '0.75D' (c) beam '0.60D' and (d) beam '0.50D'

B.2 Load strain behaviour of shear reinforcement

The load strain behaviour of the steel shear reinforcement or stirrups in the T-beams are illustrated in Figure B.2 to Figure B.5. In each beam, strain gauges were bonded to both legs of two stirrups located in the shear spans. The load shown in the diagram corresponds to the measured support loads at the span where the stirrups were located. The result of gauge SWA2 in beam '0.75D' has been omitted as it was damaged during pouring of the concrete.

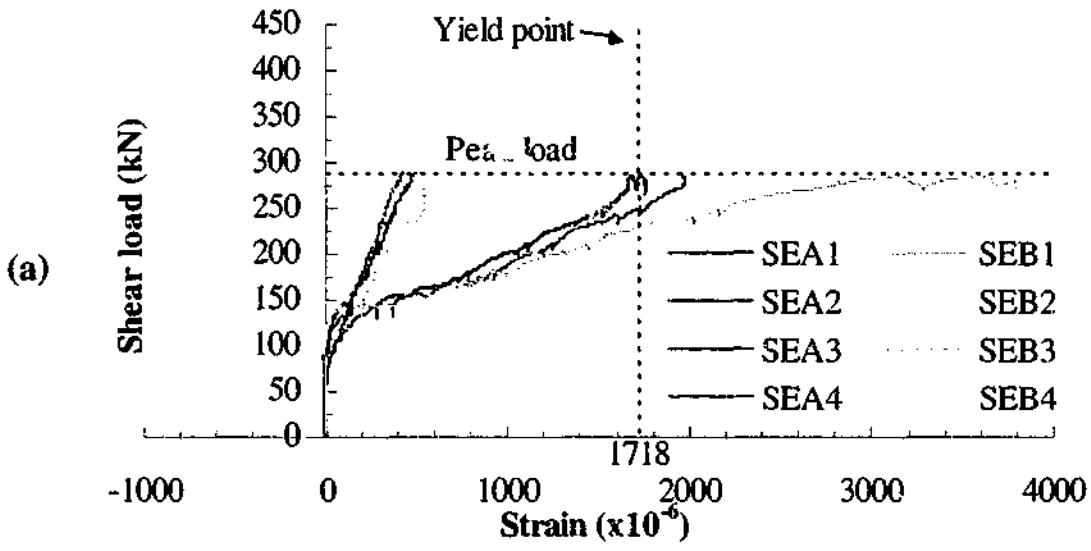

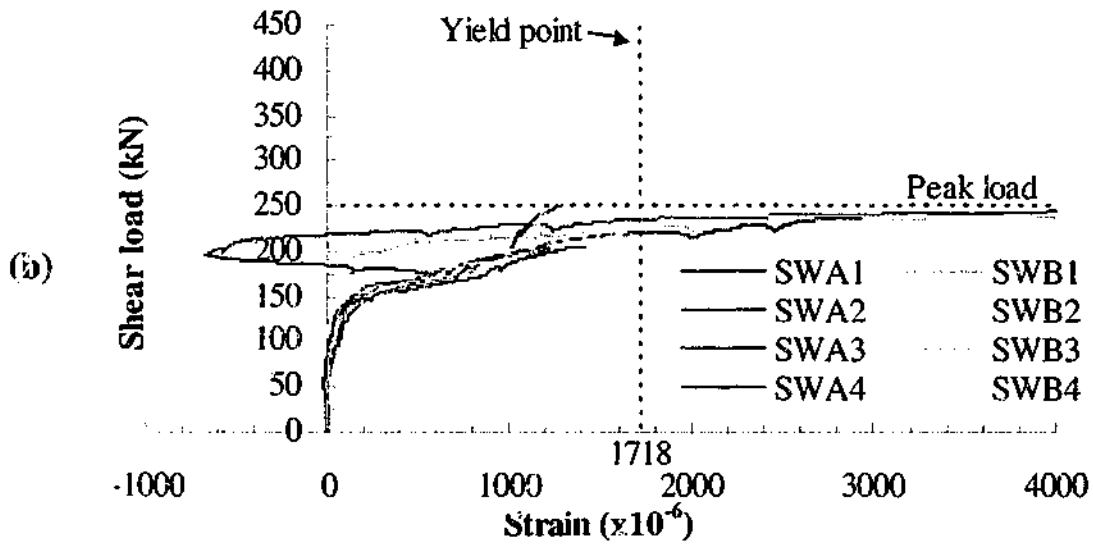

Figure B.2 - Load versus strain behaviour of stirrups in control beam at (a) east span and (b) west span

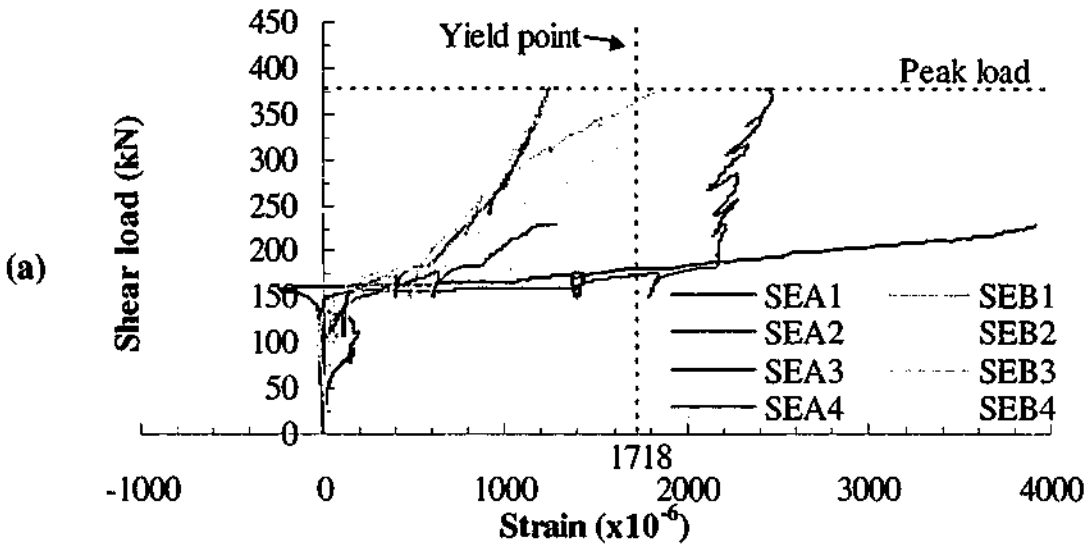

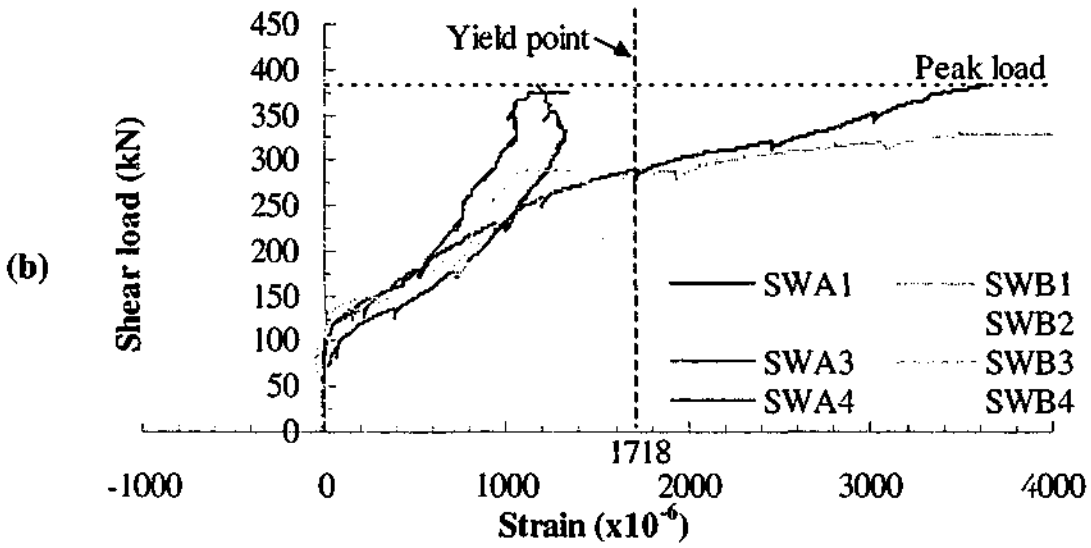

Figure B.3 - Load versus strain behaviour of stirrups in beam '0.75D' at (a) east span and (b) west span

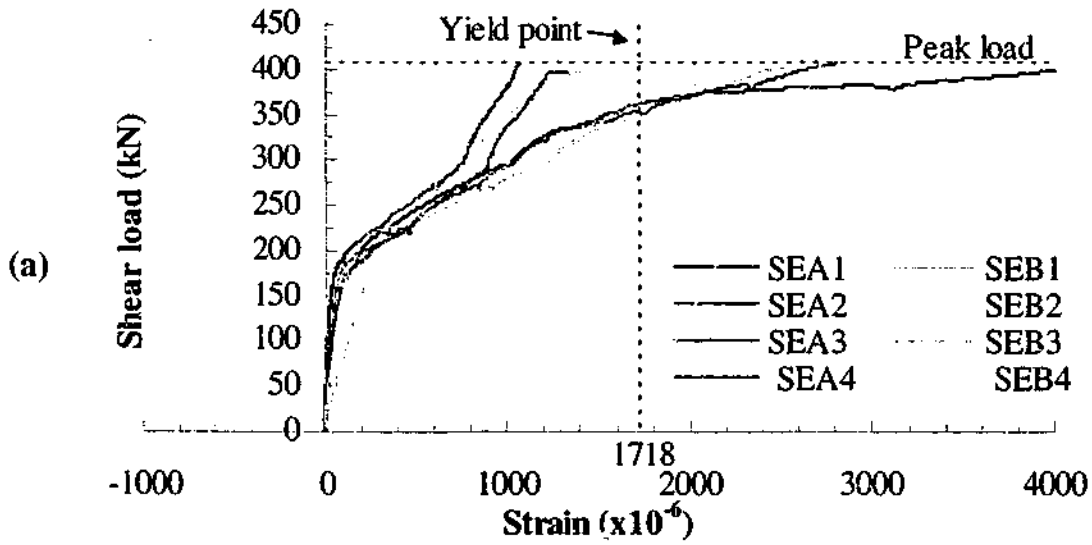

Figure B.4 - Load versus strain behaviour of stirrups in beam '0.60D' at (a) east span and (b) west span

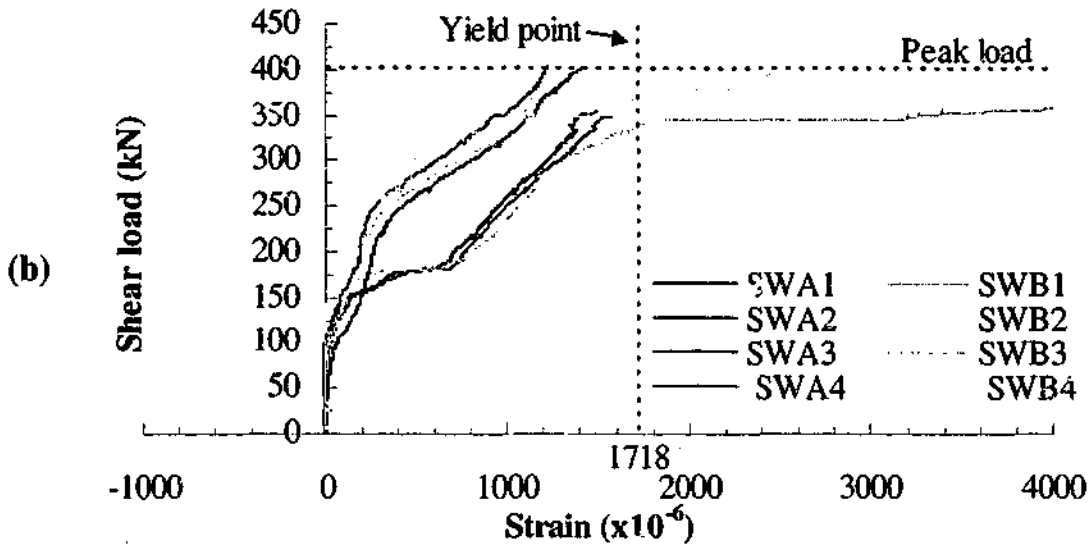

Figure B.4 (continued) - Load versus strain behaviour of stirrups in beam '0.60D' at (a) east span and (b) west span

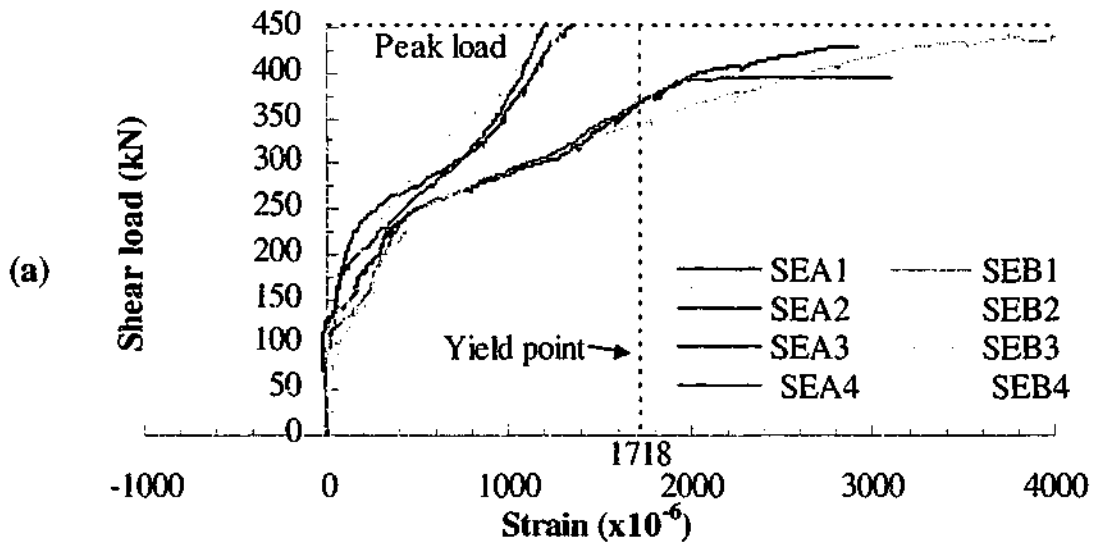

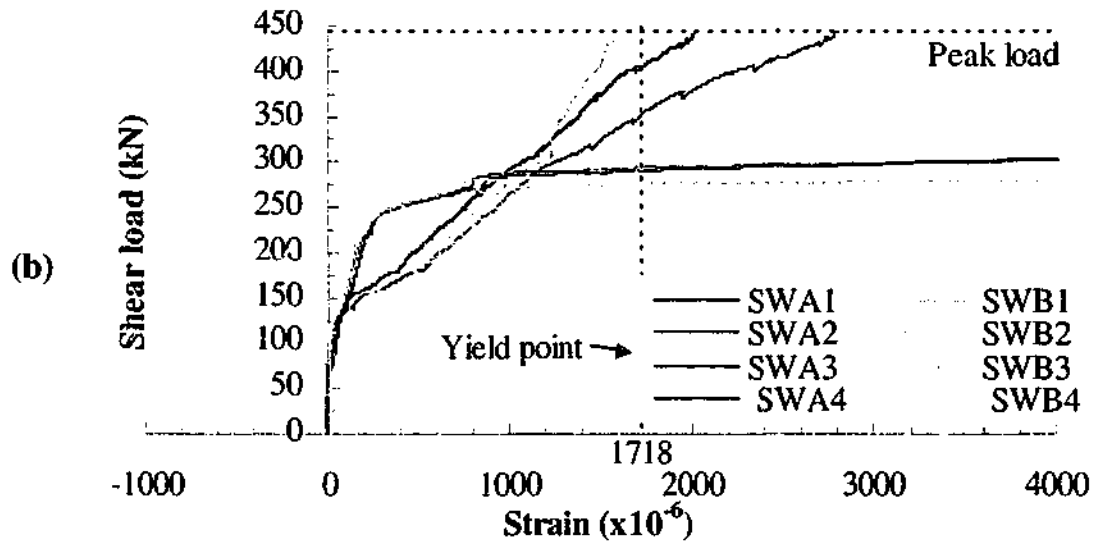

Figure B.5 - Load versus strain behaviour of stirrups in beam '0.50D' at (a) east span and (b) west span

B.3 Load strain behaviour of L-shaped CFRP plates

The load strain behaviour of the L-shaped CFRP plates on the shear strengthened beams are illustrated in Figure B.6 to Figure B.8. On each beam, forty-eight strain gauges were bonded on the L-shaped CFRP plates, twelve each side per shear span. The positions of the strain gauges are detailed in Figure 5.5. The load shown in the diagram corresponds to the measured support loads at the span where the strain gauges were located.

(a)

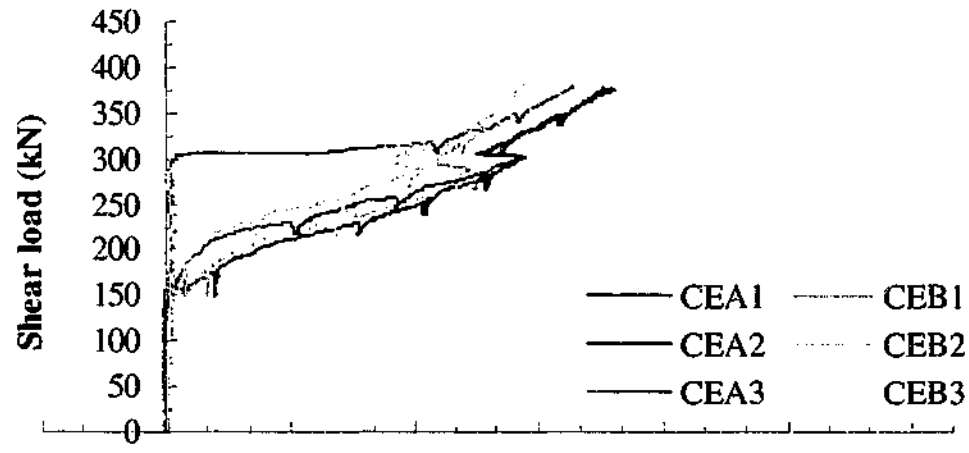

(b)

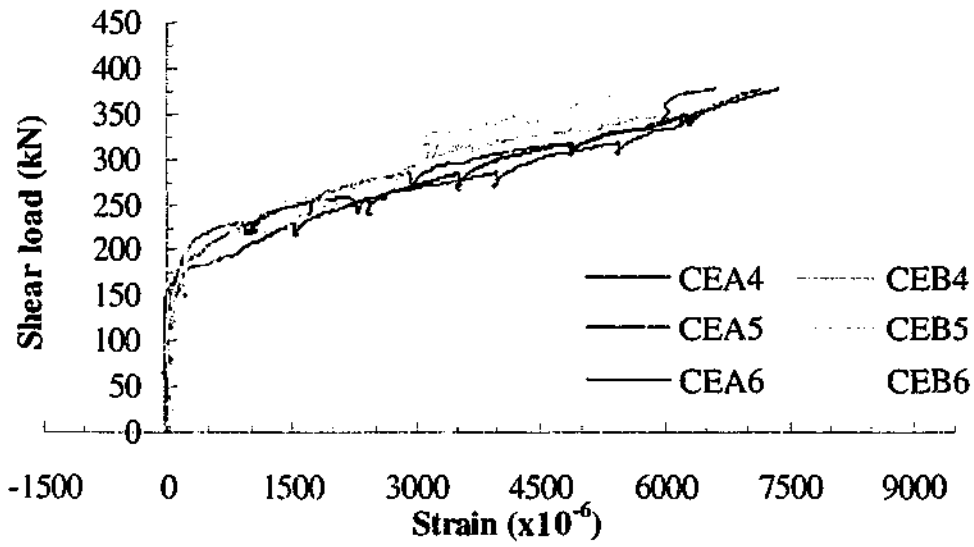

Figure B.6 - Load versus strain behaviour of L-shaped CFRP reinforcement on the east span of beam '0.75D'

(c)

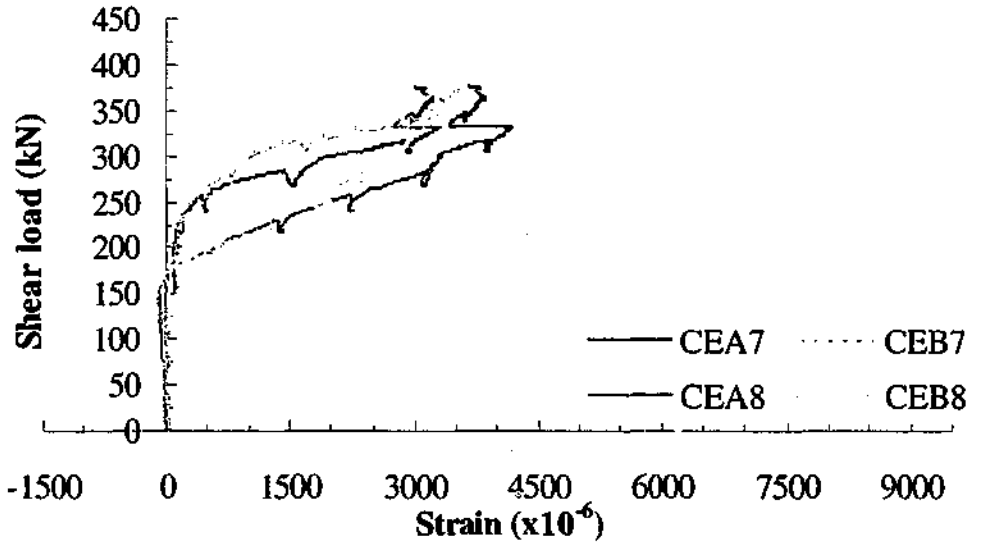

(d)

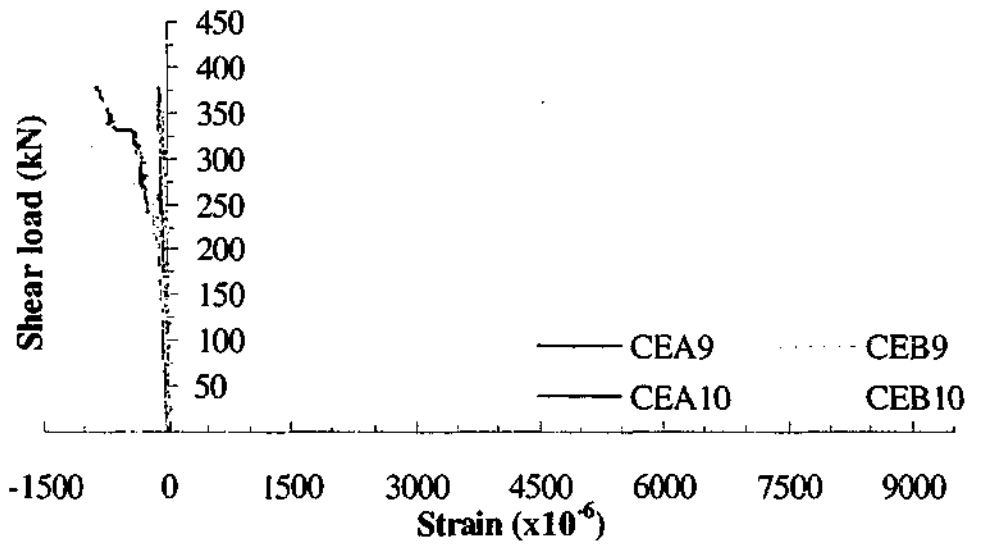

(e)

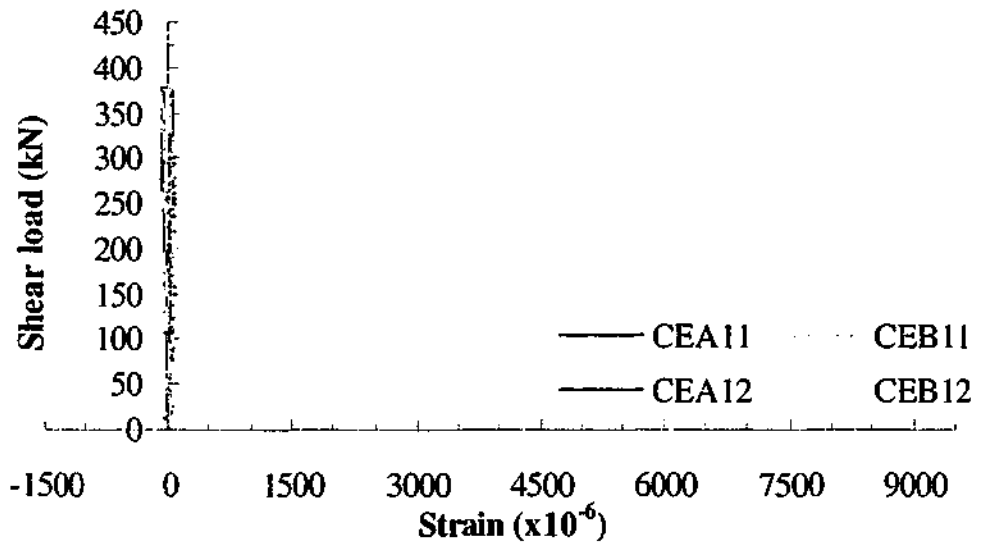

Figure B.6 (continued) - Load versus strain behaviour of L-shaped CFRP reinforcement on the east span of beam '0.75D'

(a)

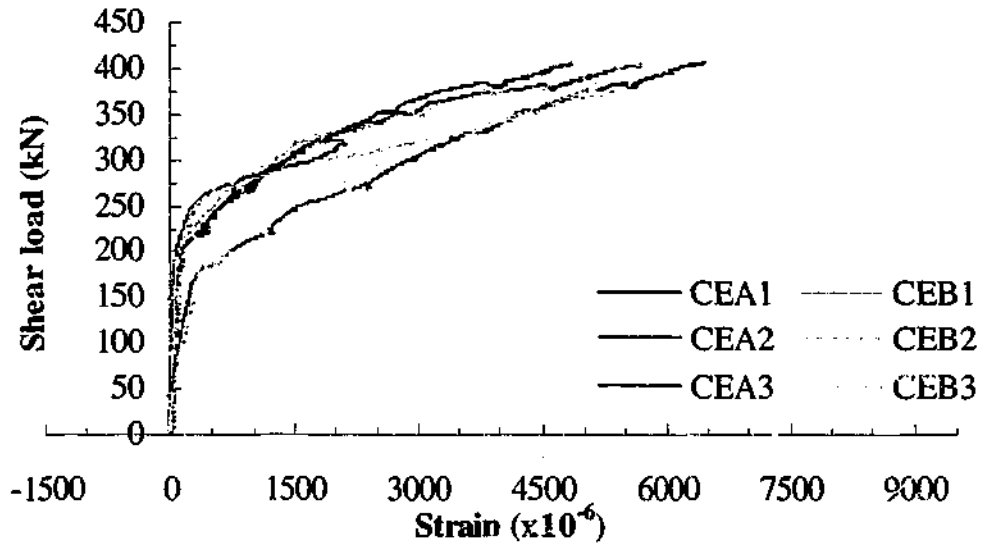

(b)

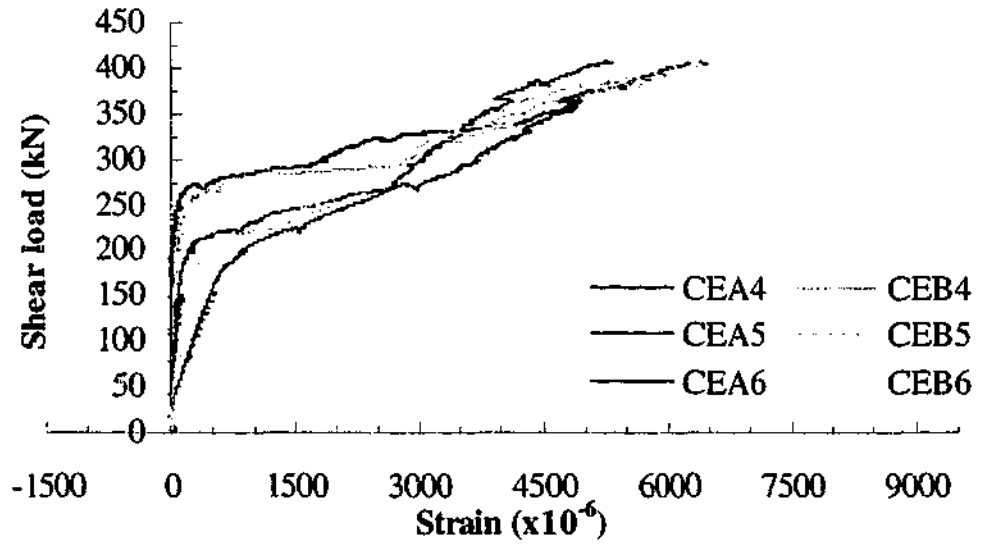

(c)

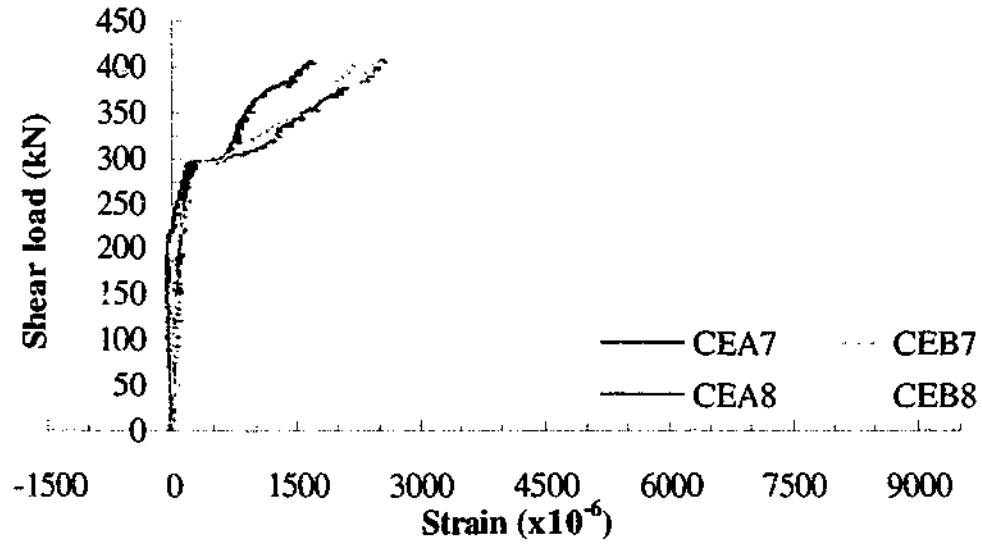

Figure B.7 - Load versus strain behaviour of L-shaped CFRP reinforcement on the east span of beam '0.60D'

(d)

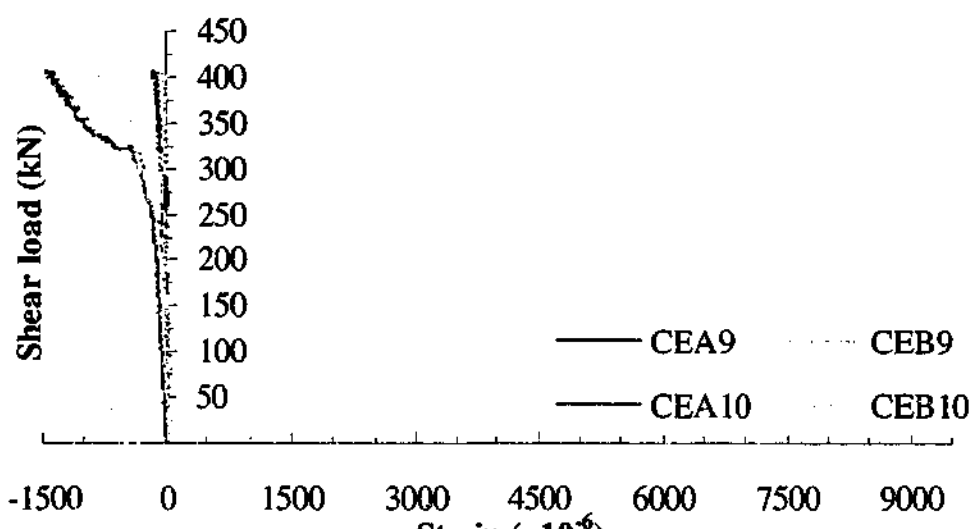

(e)

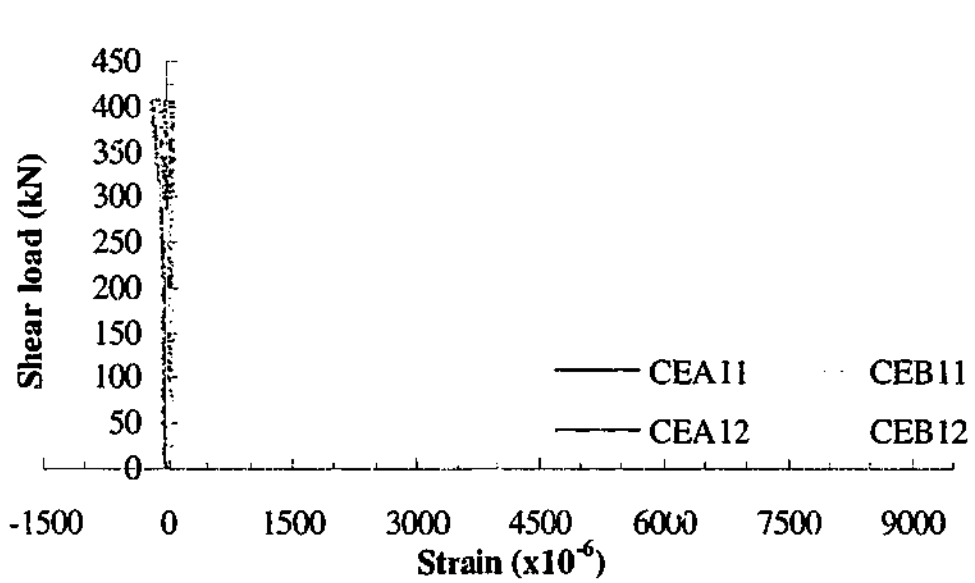

Figure B.7 (continued) - Load versus strain behaviour of L-shaped CFRP reinforcement on the east span of beam '0.60D'

(a)

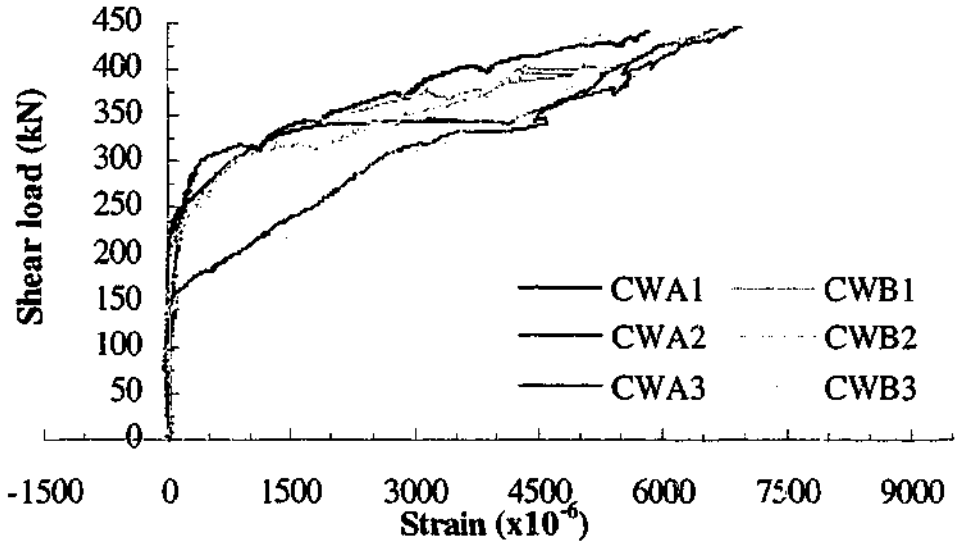

(b)

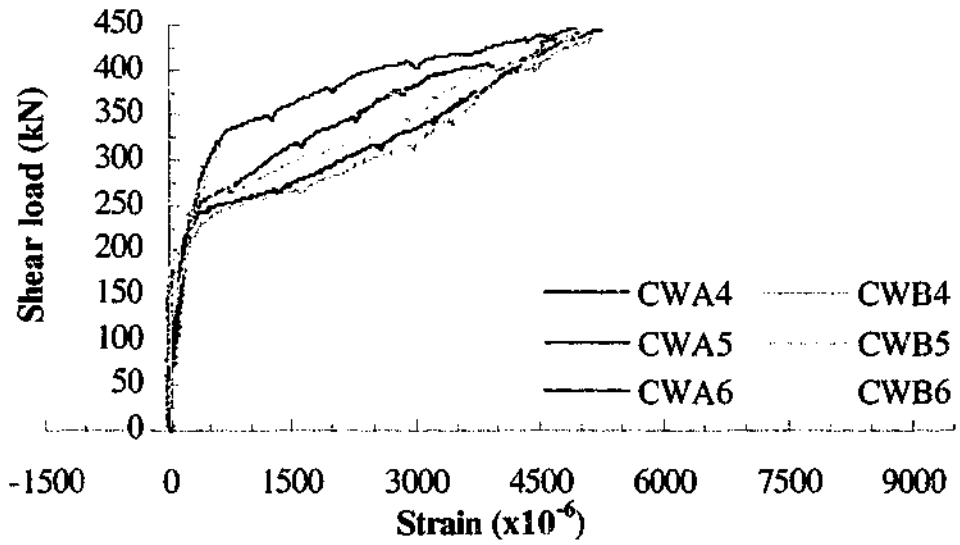

(c)

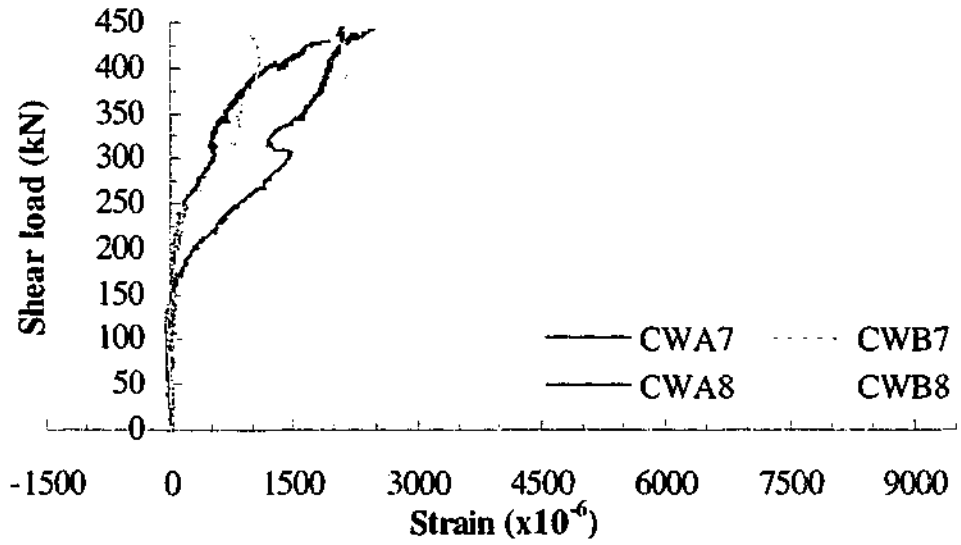

Figure B.8 - Load versus strain behaviour of L-shaped CFRP reinforcement on the west span of beam '0.50D'

(d)

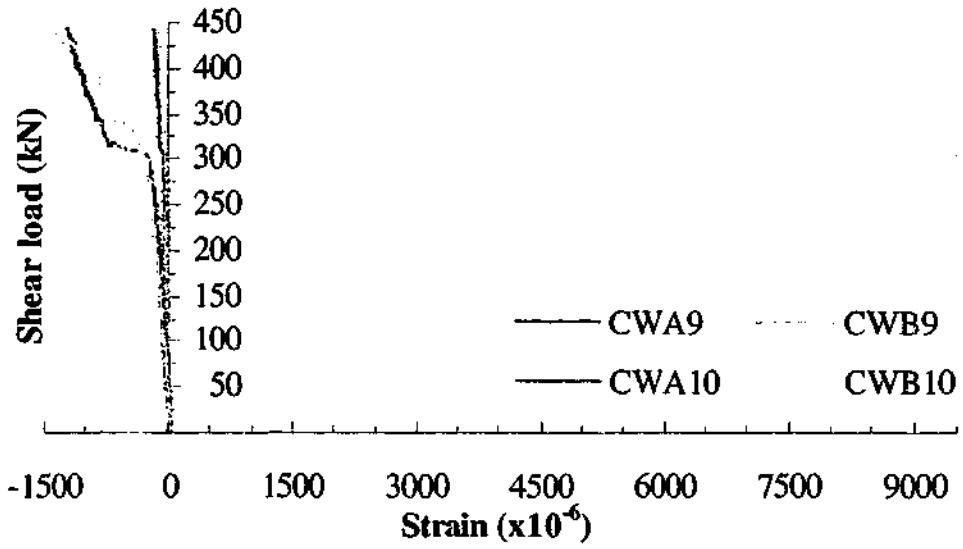

(e)

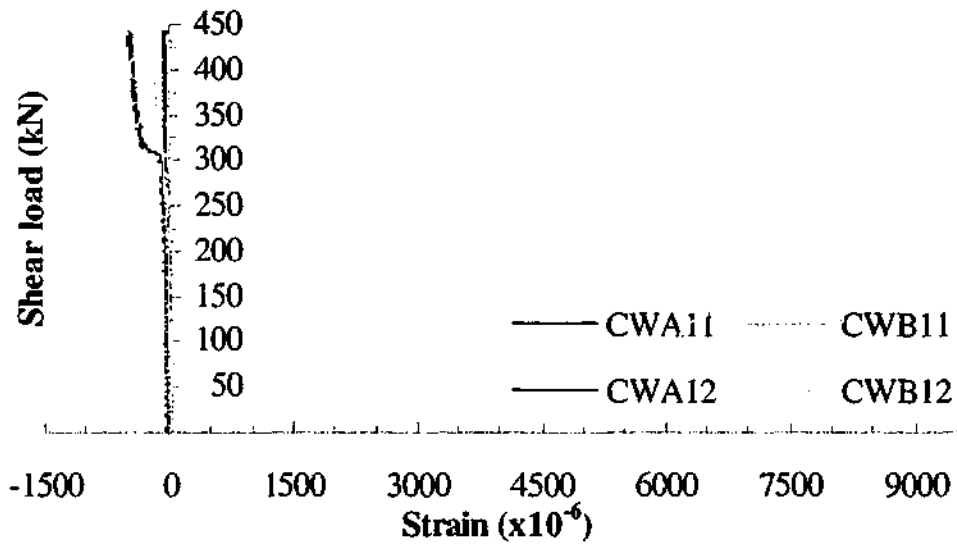

Figure B.8 (continued) - Load versus strain behaviour of L-shaped CFRP reinforcement on the west span of beam '0.50D'

APPENDIX C

C.1 Locations of photogrammetry monitoring points

The approximate locations of the photogrammetry monitoring points or targets on the T-beams beam are illustrated in Figure C.1 to Figure C.4. The targets were placed on one side of the beams at both the east and west spans. Each target was approximately 25 mm wide by 12.5 mm high. The diameter of the reflective dot in the centre was approximately 6.35 mm. A large number of the targets were placed at the shear spans to intercept shear crack formations. On the shear-strengthened beams, two rows of targets were placed along the length of each L-shaped CFRP plate. Several targets were placed at the supports and actuators for cross checking against results obtained using stringpots.

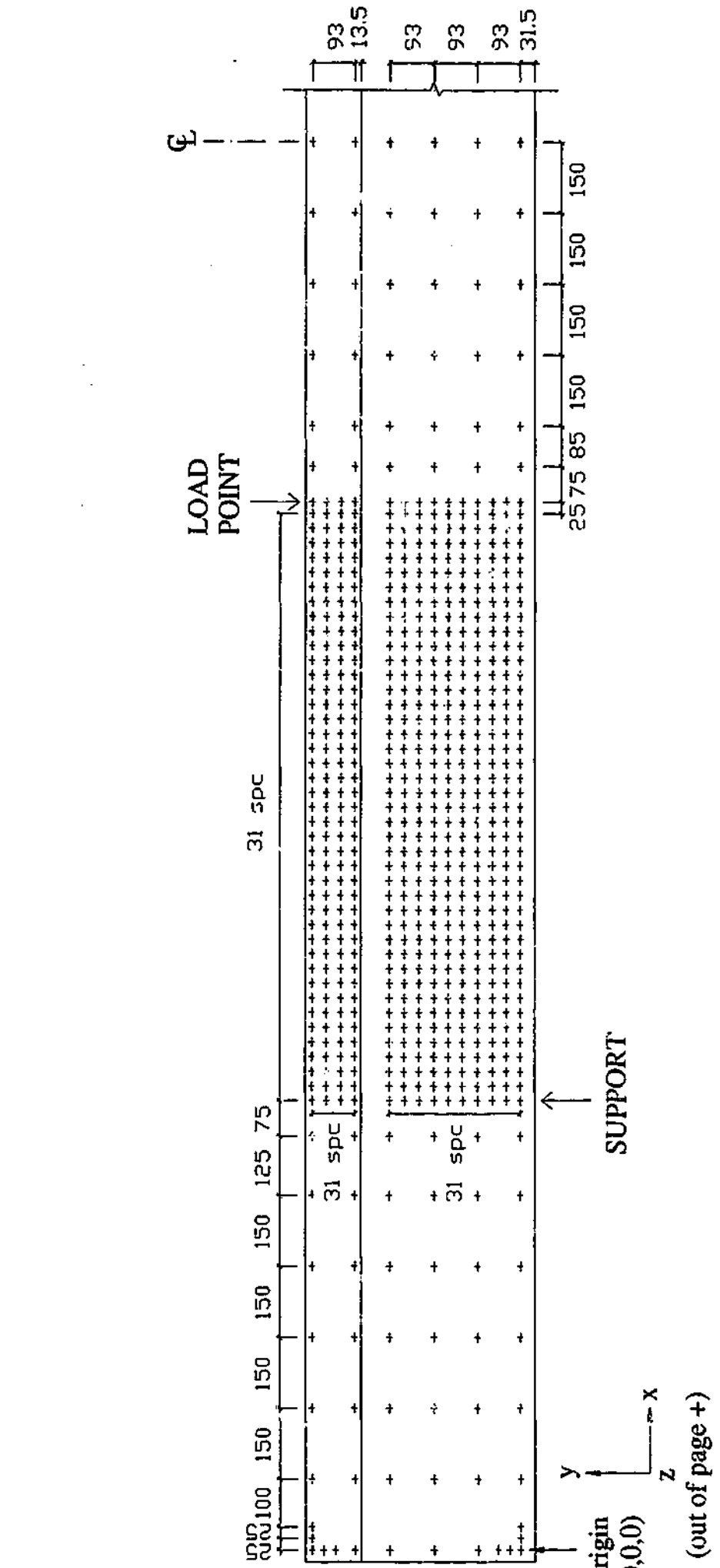

Figure C.1 - Locations of targets on control beam

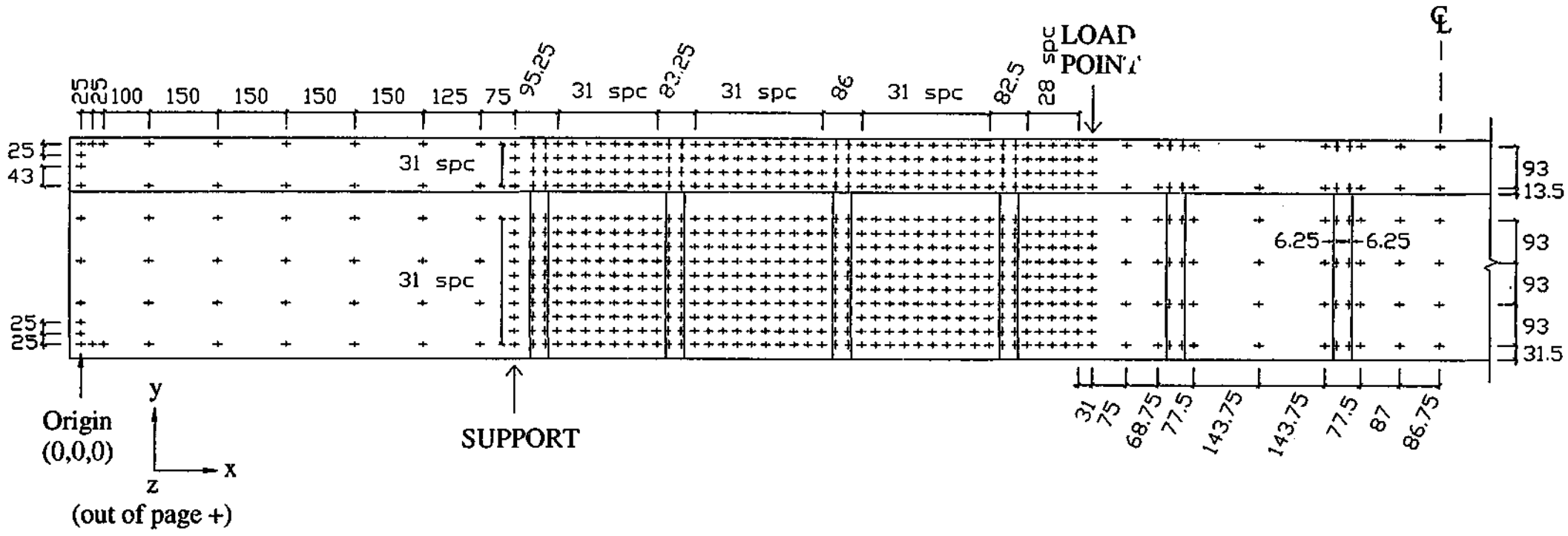

Figure C.2 - Locations of targets on beam '0.75D'

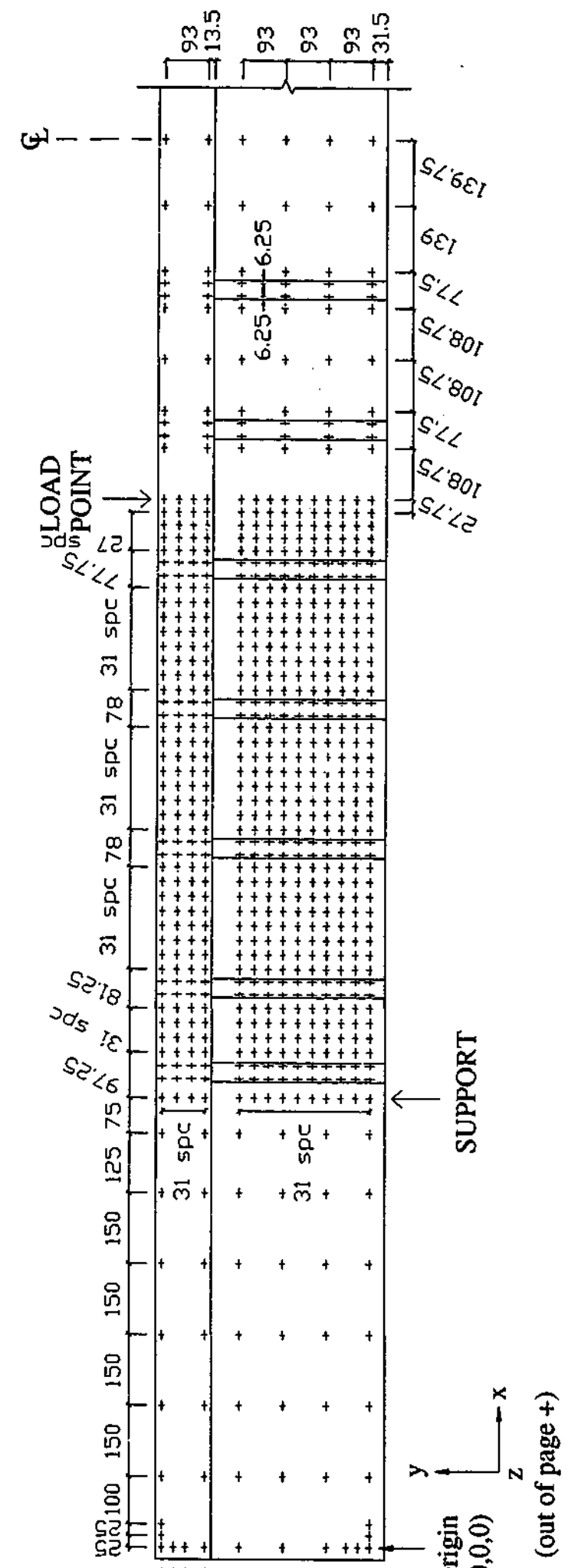

Figure C.3 - Location of targets on beam '0.60D'

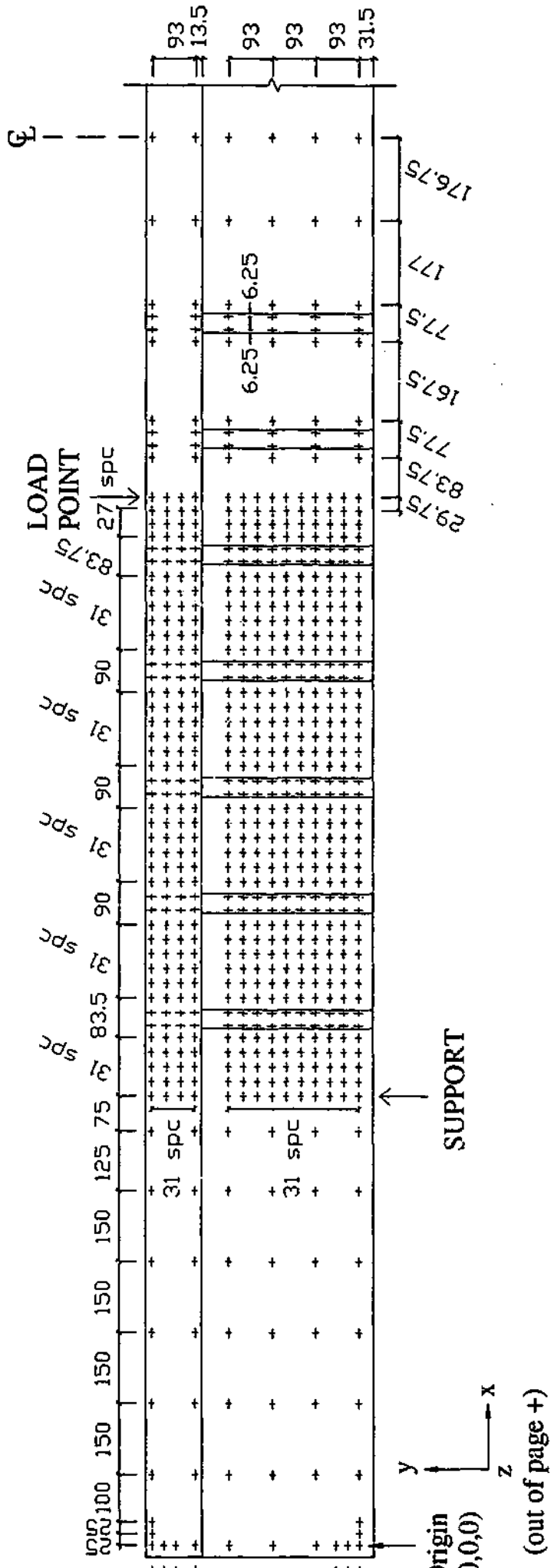

Figure C.4 - Locations of targets on beam '0.50D'

C.2 Load deflection behaviour from photogrammetry measurements

Figure C.5 to Figure C.12 compare the load-deflection behaviour, at selected locations of all the beams, obtained using photogrammetry measurements and stringpots. The figures show the applied load versus beam deflections at the load points and support load versus mid-span deflections. The locations of the targets used in the comparison are reported in Section 7.3.1.

(a)

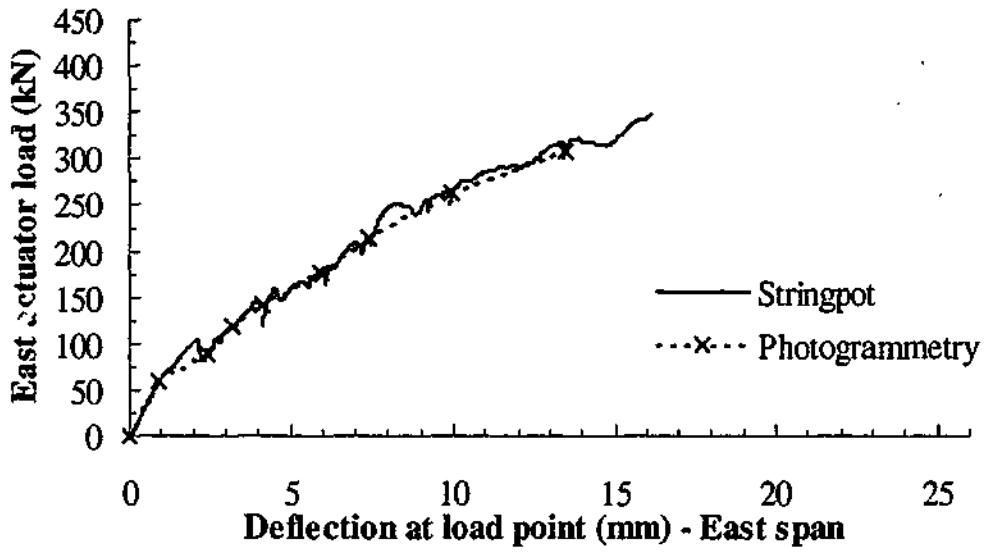

(b)

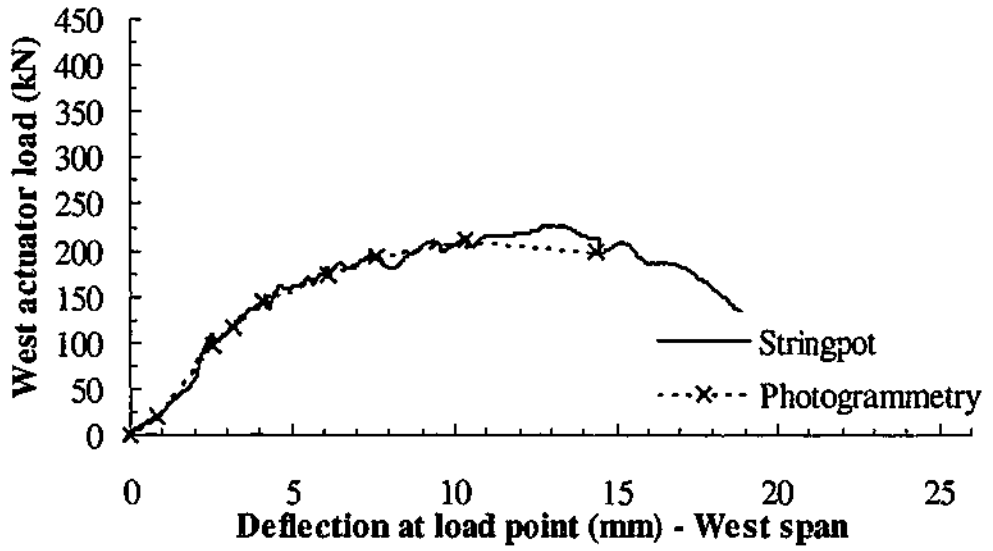

Figure C.5 - Actuator load versus deflection behaviour for control beam from stringpot and photogrammetry measurements

(a)

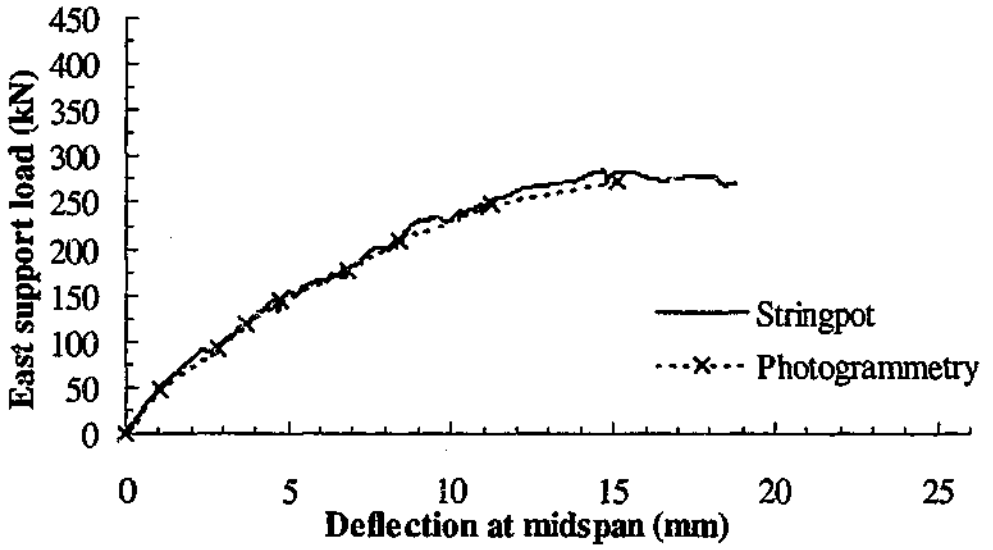

(b)

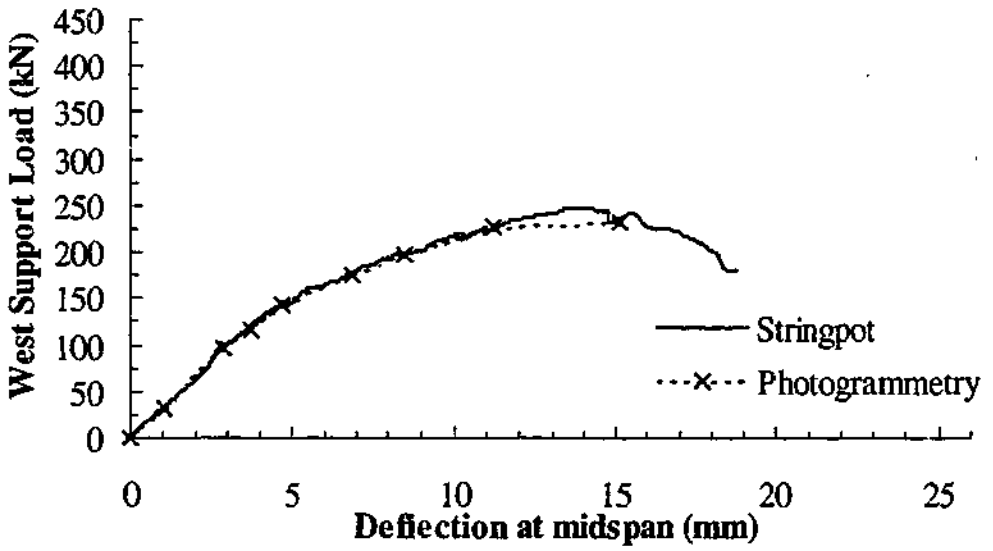

Figure C.6 - Support load versus deflection behaviour of control beam from stringpot and photogrammetry measurements

(a)

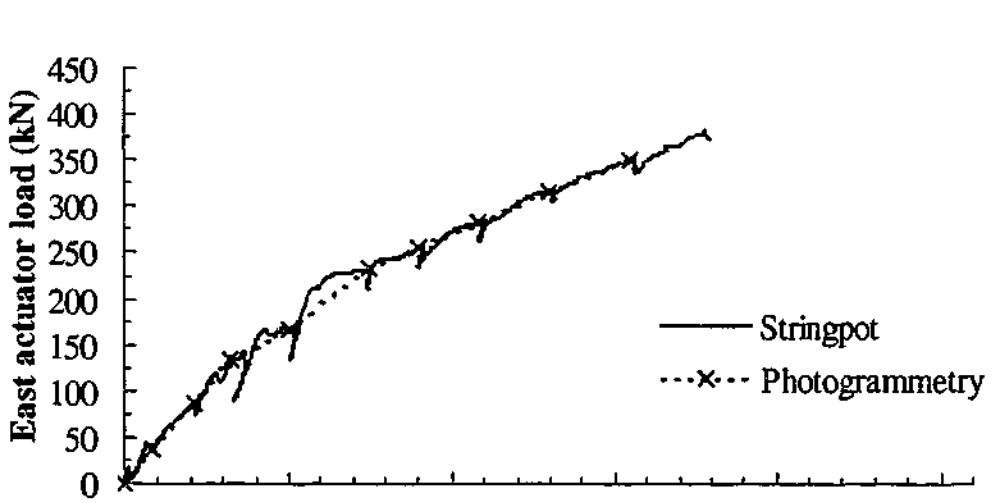

Figure C.7 - Actuator load versus deflection behaviour for beam '0.75D' from stringpot and photogrammetry measurements

(b)

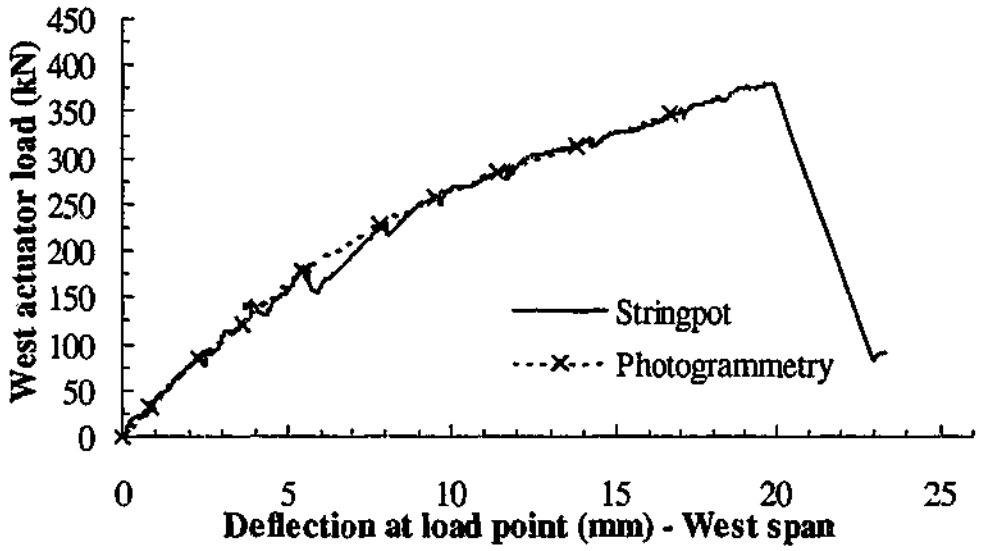

Figure C.7 (continued) - Actuator load versus deflection behaviour for beam '0.75D' from stringpot and photogrammetry measurements

(a)

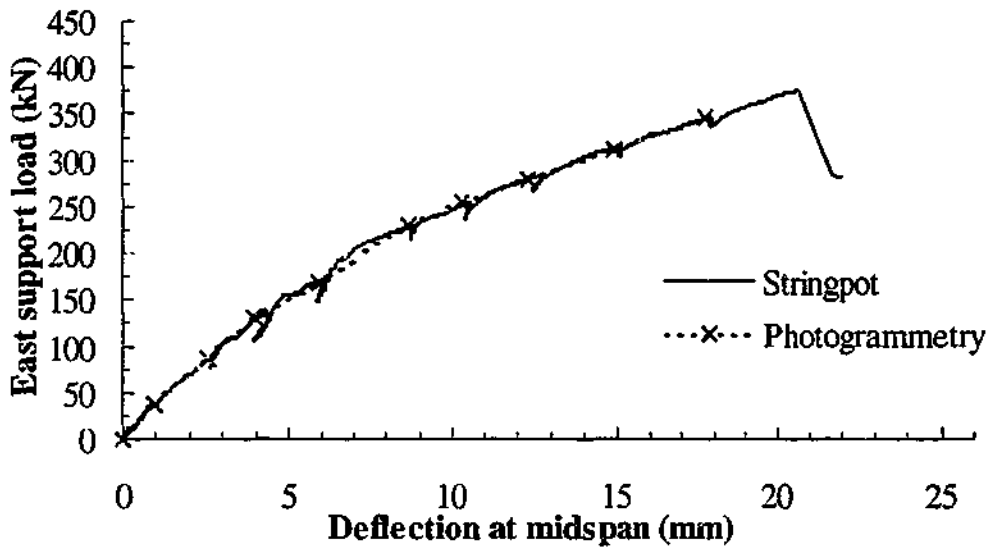

(b)

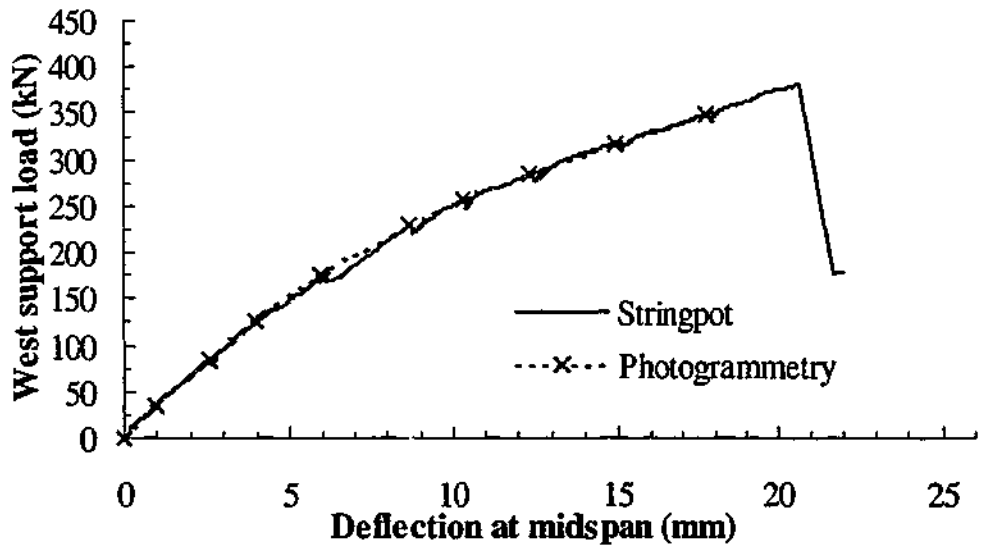

Figure C.8 - Support load versus deflection behaviour of beam '0.75D' from stringpot and photogrammetry measurements

(a)

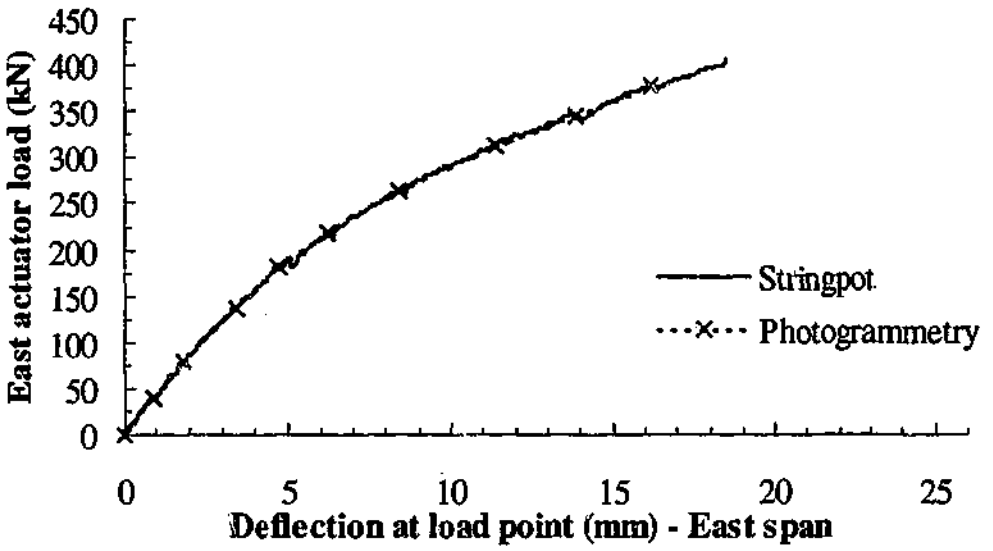

(b)

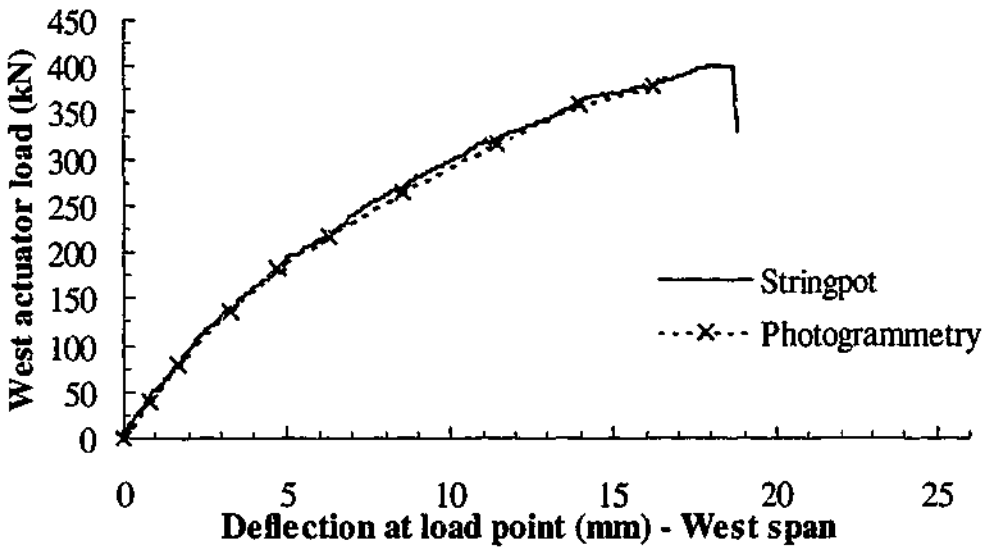

Figure C.9 - Actuator load versus deflection behaviour for beam '0.60D' from stringpot and photogrammetry measurements

(a)

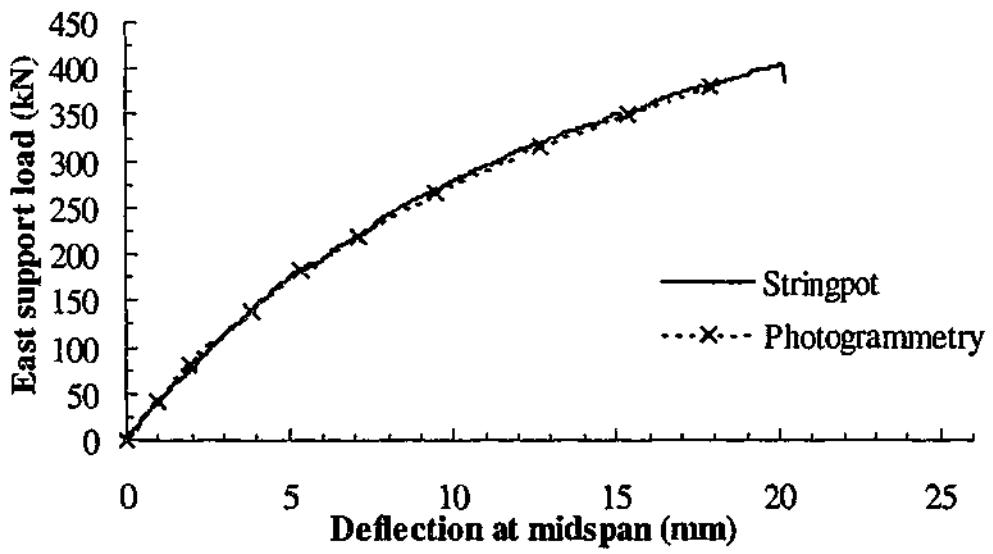

Figure C.10 - Support load versus deflection behaviour of beam '0.60D' from stringpot and photogrammetry measurements

(b)

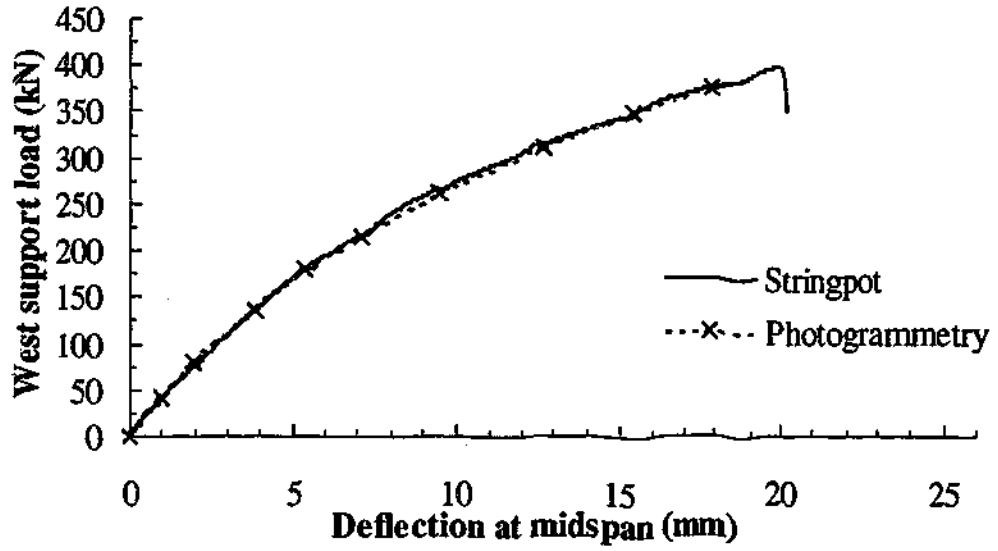

Figure C.10 (continued) - Support load versus deflection behaviour of beam '0.60D' from stringpot and photogrammetry measurements

(a)

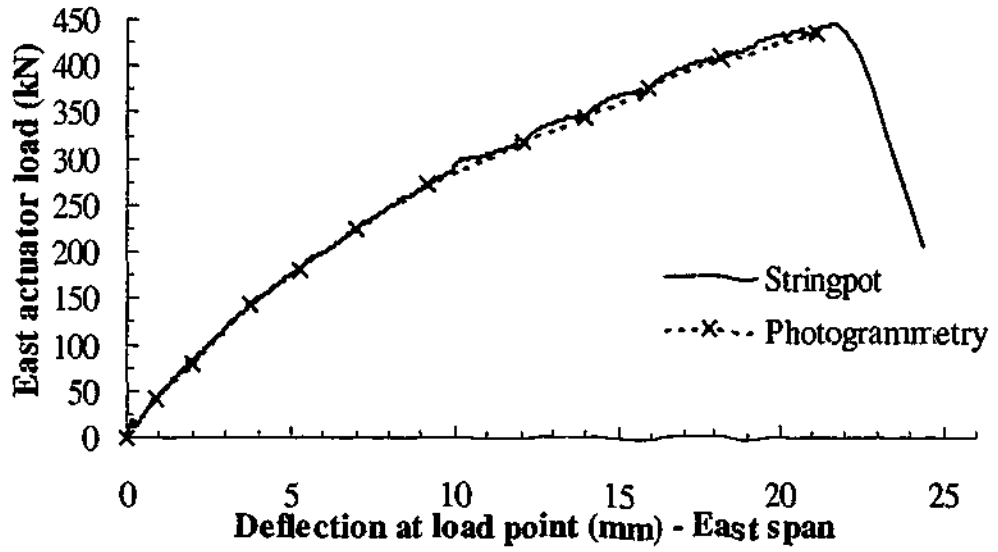

(b)

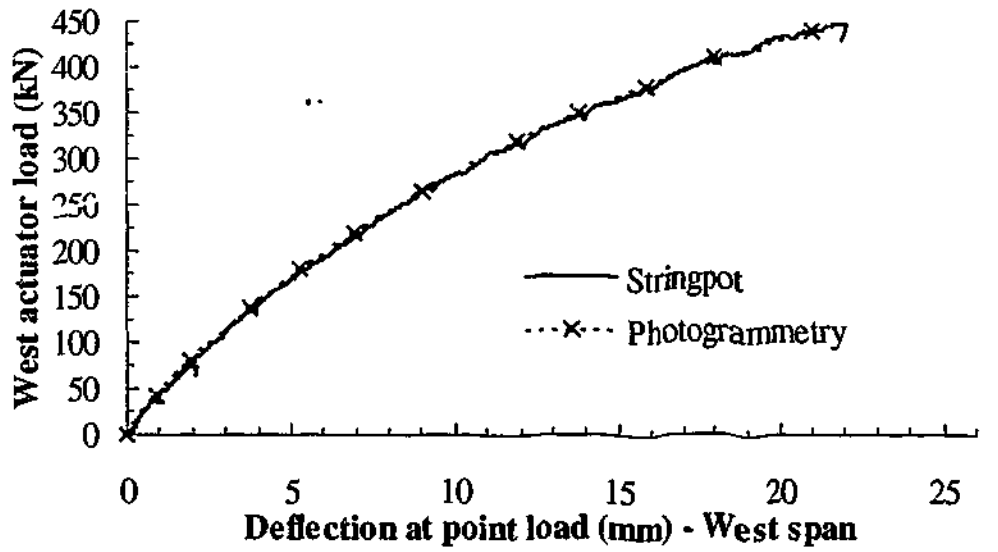

Figure C.11 - Actuator load versus deflection behaviour for beam '0.50D' from stringpot and photogrammetry measurements

(a)

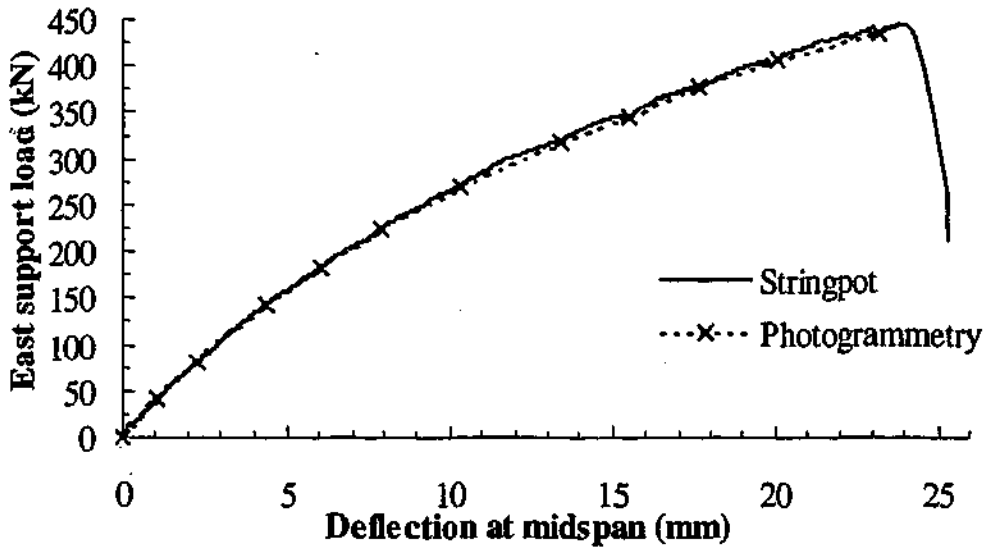

(b)

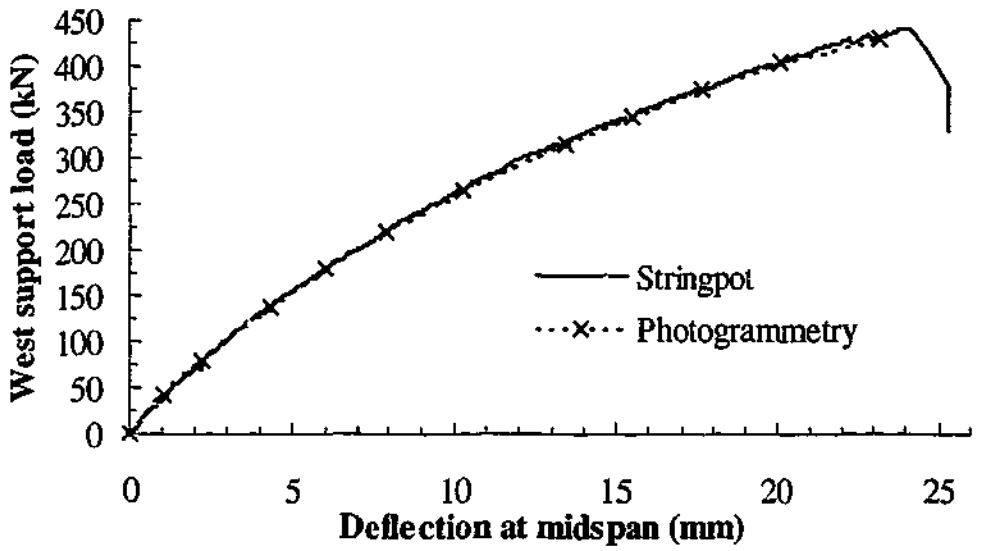

Figure C.12 - Support load versus deflection behaviour of beam '0.50D' from stringpot and photogrammetry measurements

C.3 Slip behaviour between CFRP reinforcement and concrete

Figure C.13 to Figure C.26 shows the slip behaviour along the beam depth of the L-shaped CFRP plates in the failure shear span at selected load levels. In the figures, the beam depth refers to the height of the individual targets on the CFRP plate from the soffit of the beam, which is taken as zero. The load levels shown in the plots correspond to the average support load levels at the failure span at the time each survey was executed.

(a)

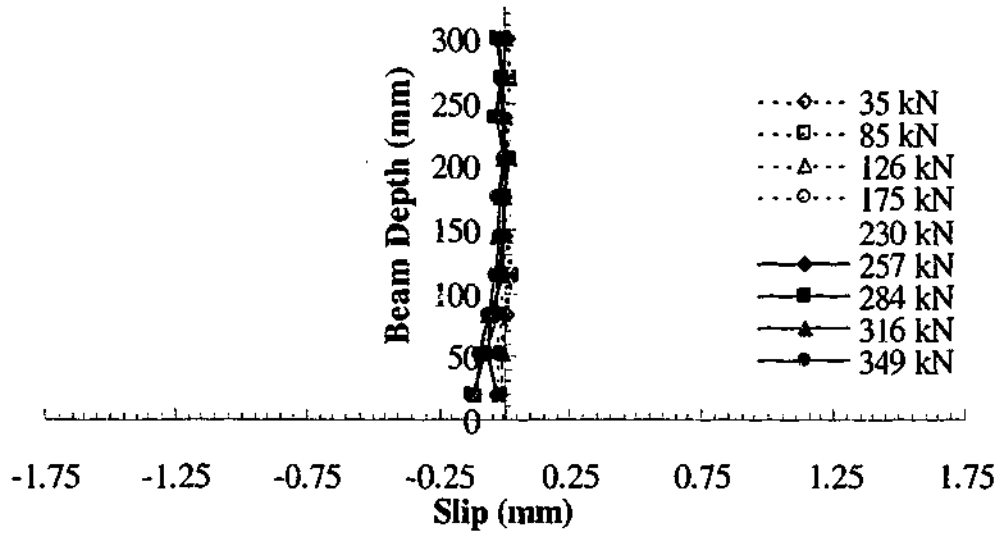

(b)

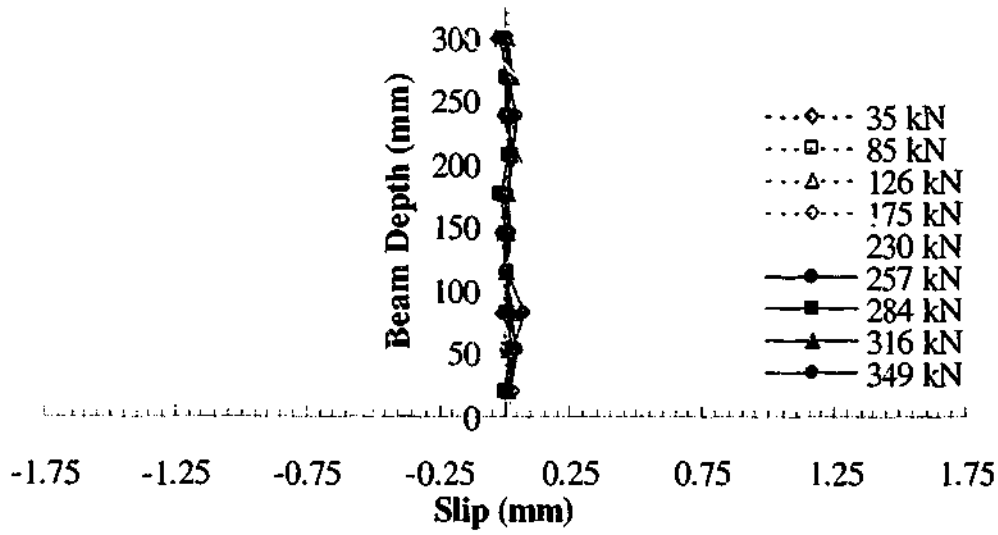

Figure C.13 - Slip behaviour of CFRP '1' in beam '0.75D' at (a) left side and (b) right side

(a)

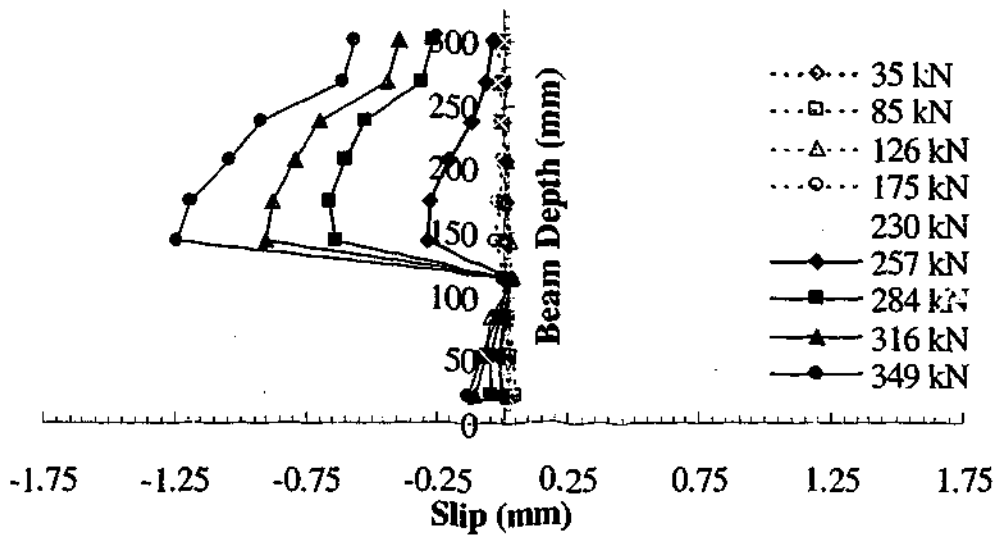

(b)

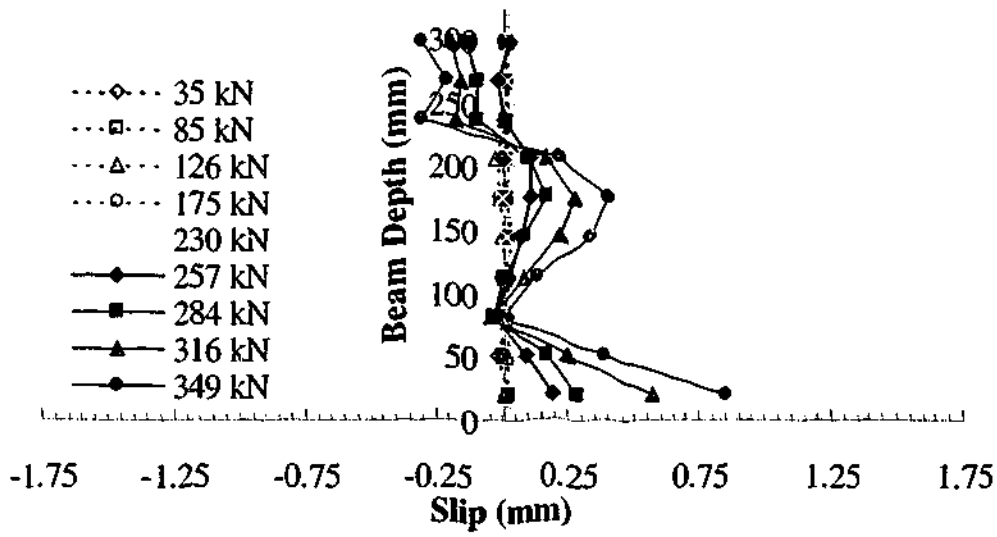

Figure C.14 - Slip behaviour of CFRP '2' in beam '0.75D' at (a) left side and (b) right side

(a)

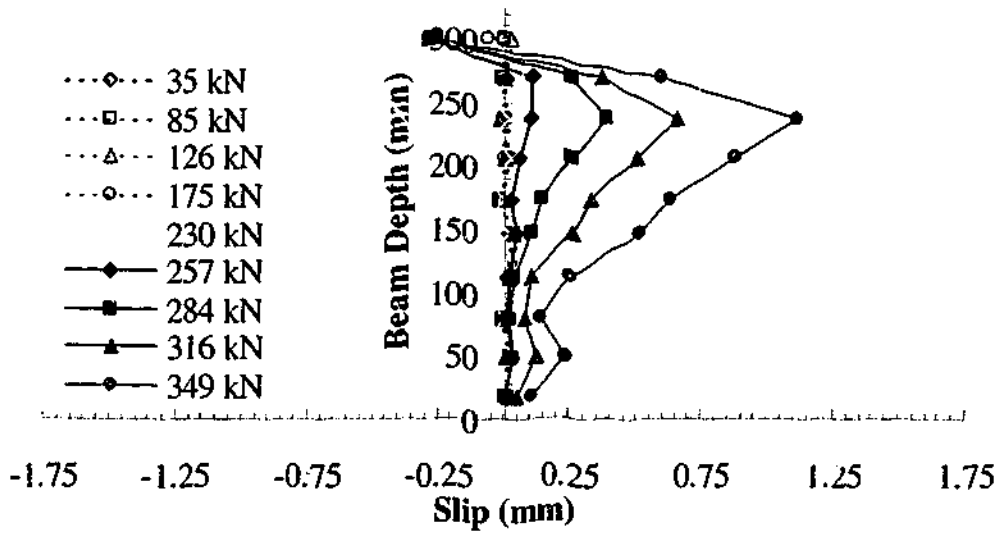

Figure C.15 - Slip behaviour of CFRP '3' in beam '0.75D' at (a) left side and (b) right side

(b)

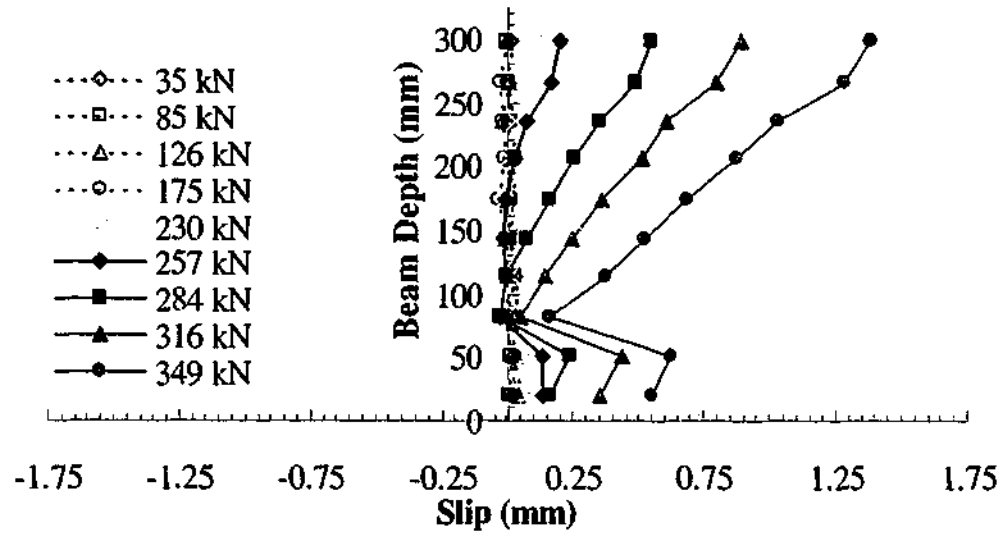

Figure C.15 (continued) - Slip behaviour of CFRP '3' in beam '0.75D' at (a) left side and (b) right side

(a)

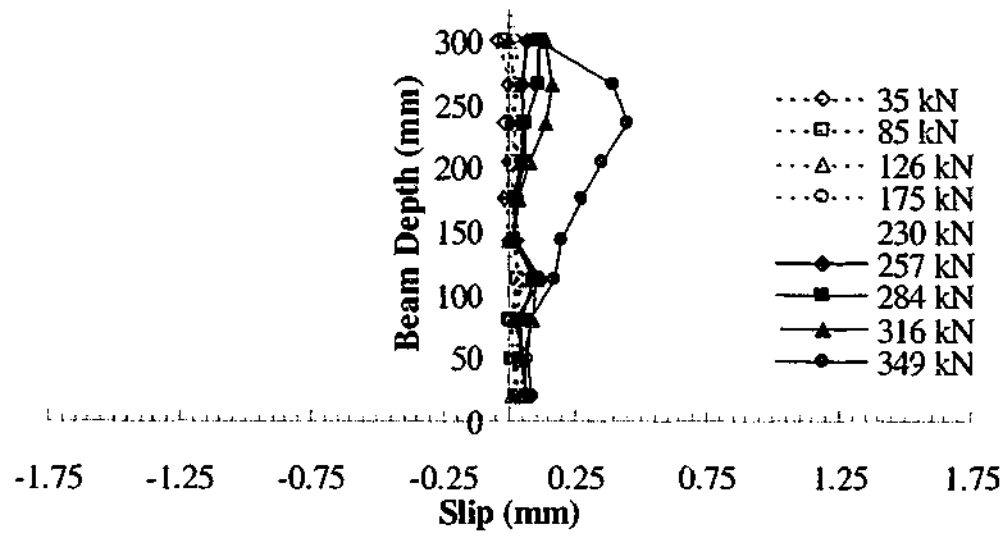

(b)

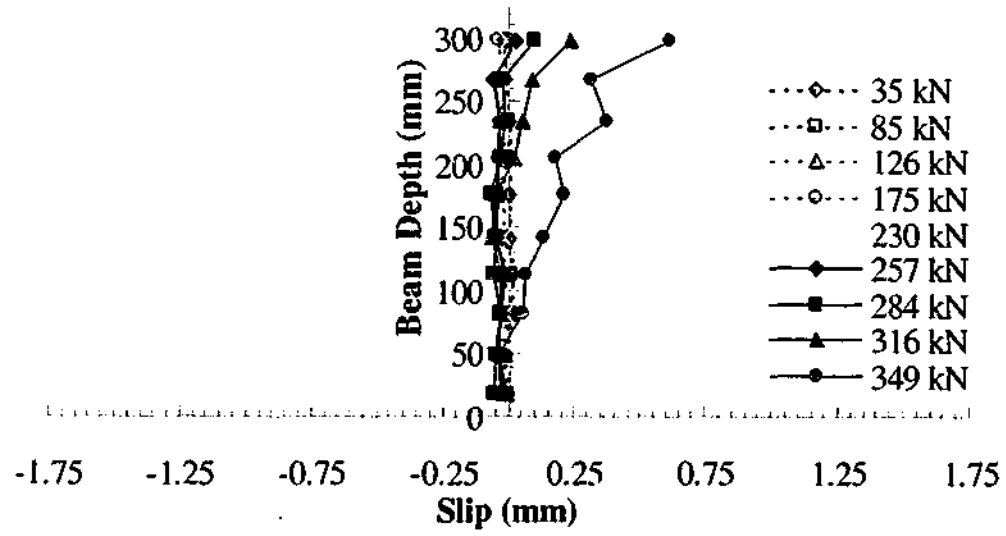

Figure C.16 - Slip behaviour of CFRP '4' in beam '0.75D' at (a) left side and (b) right side

(a)

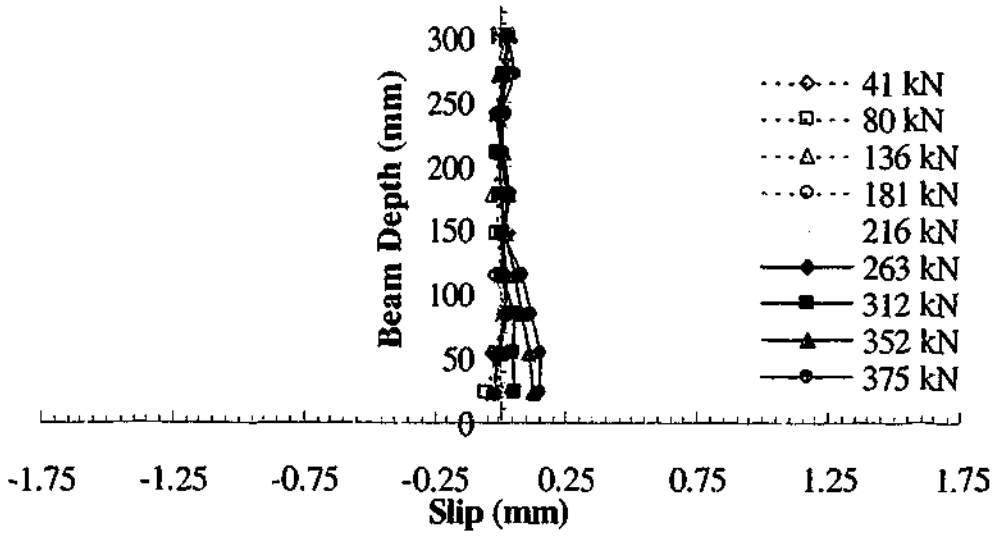

(b)

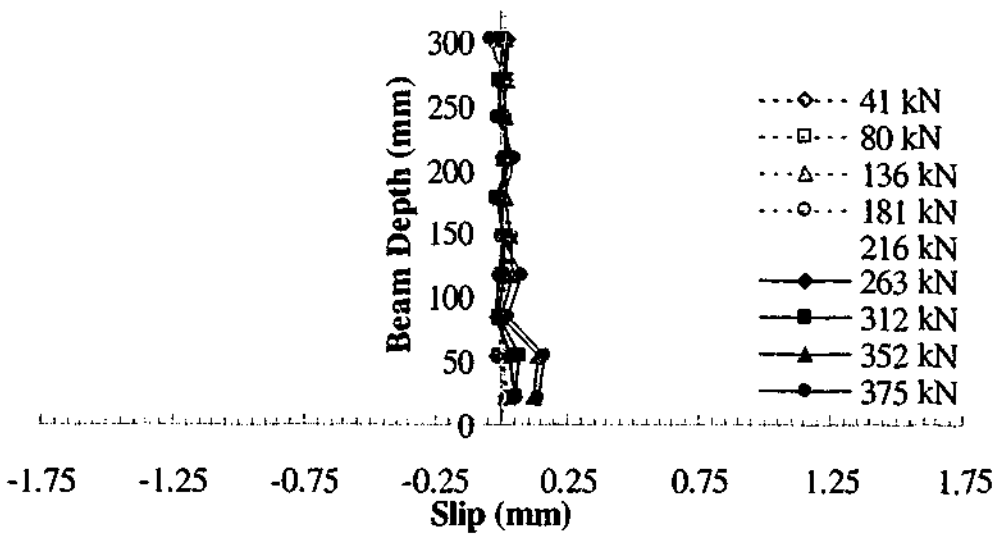

Figure C.17 - Slip behaviour of CFRP '1' in beam '0.60D' at (a) left side and (b) right side

(a)

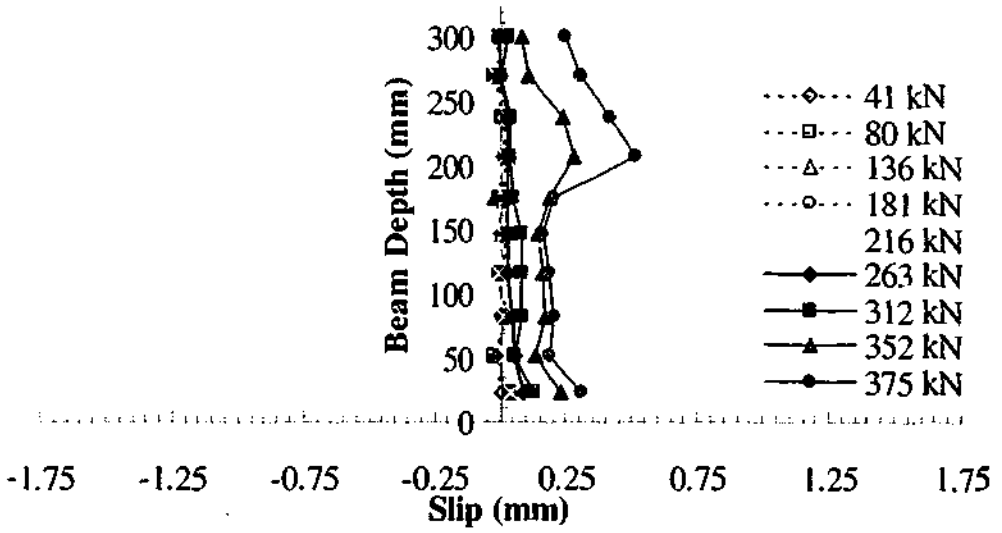

Figure C.18 - Slip behaviour of CFRP '2' in beam '0.60D' at (a) left side and (b) right side

(b)

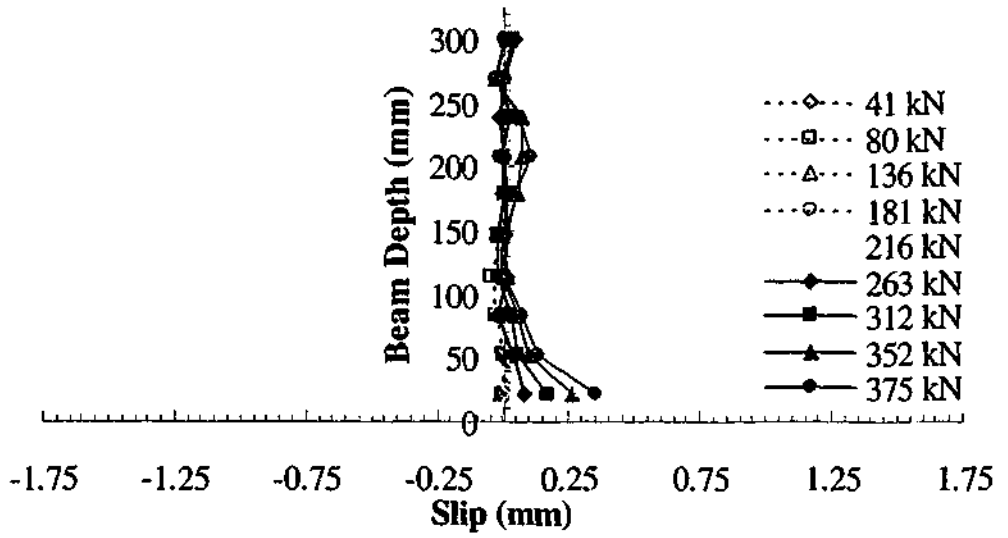

Figure C.18 (continued) - Slip behaviour of CFRP '2' in beam '0.60D' at (a) left side and (b) right side

(a)

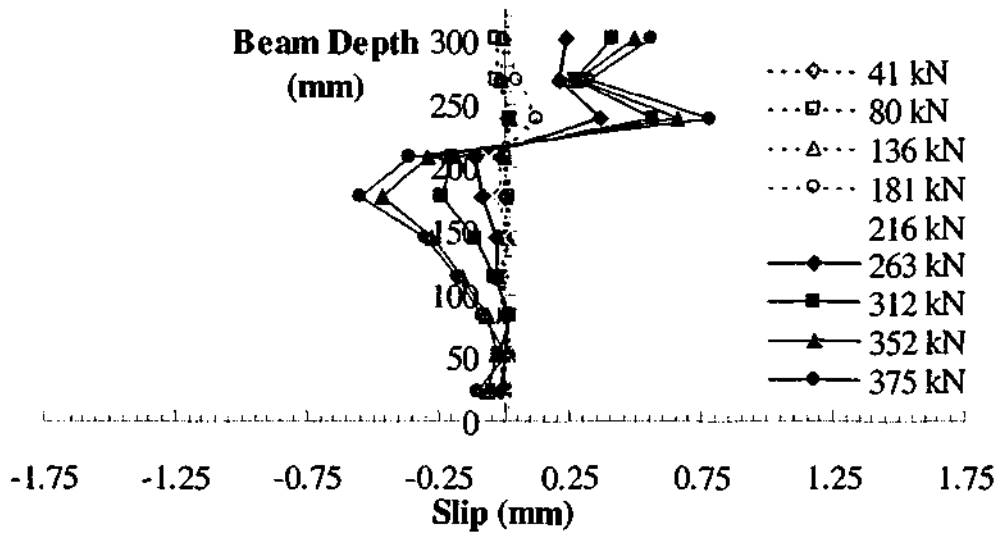

(b)

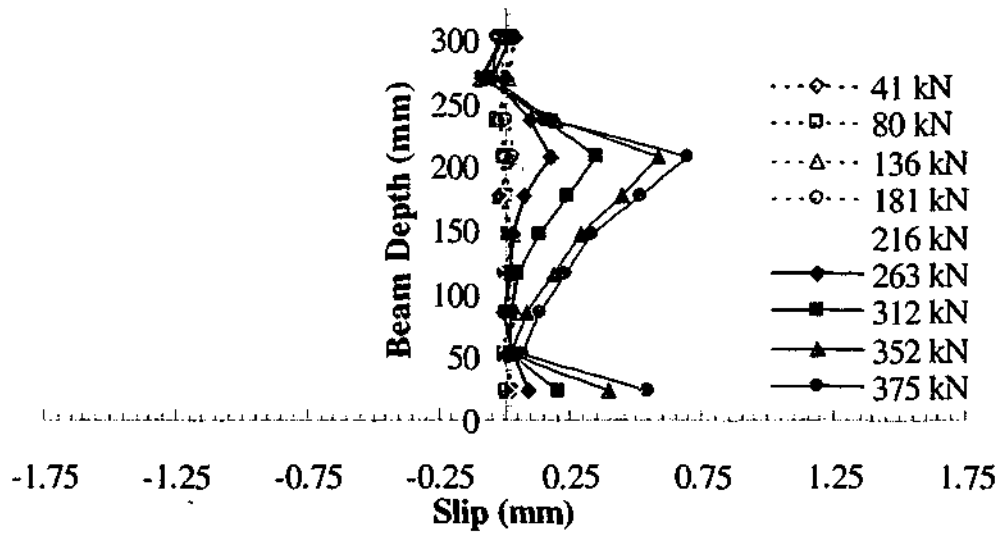

gure C.19 - Slip behaviour of CFRP '3' in beam '0.60D' at (a) left side and (b) right side

(a)

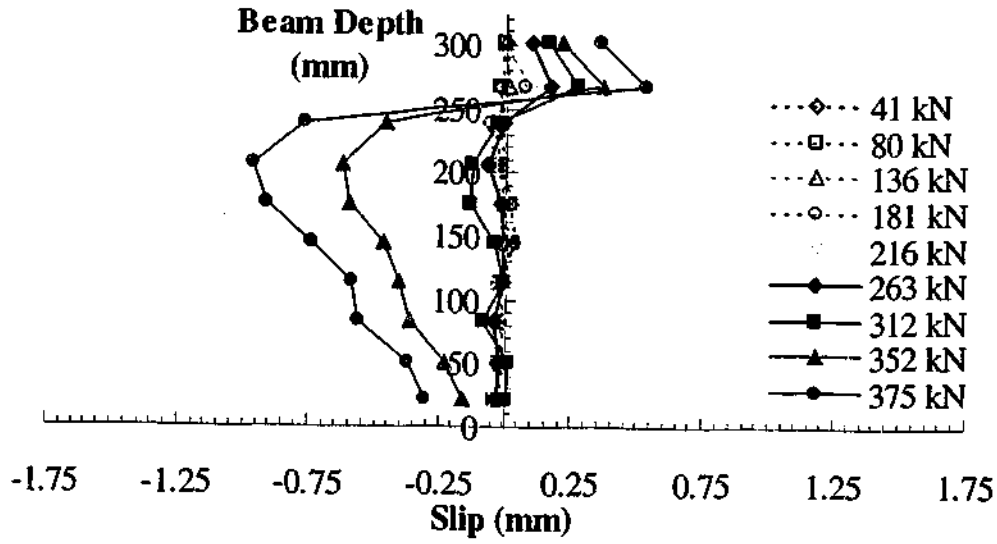

(b)

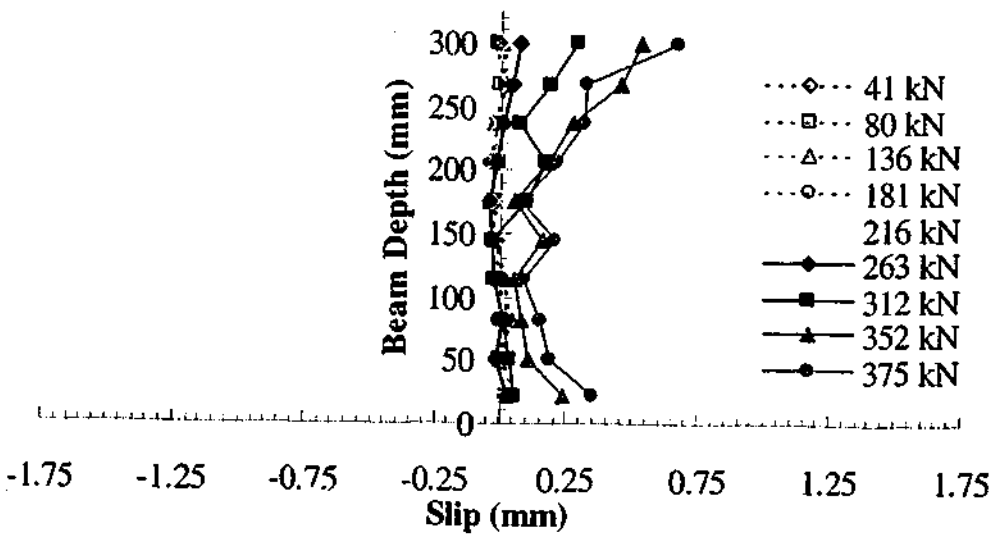

Figure C.20 - Slip behaviour of CFRP '4' in beam '0.60D' at (a) left side and (b) right side

(a)

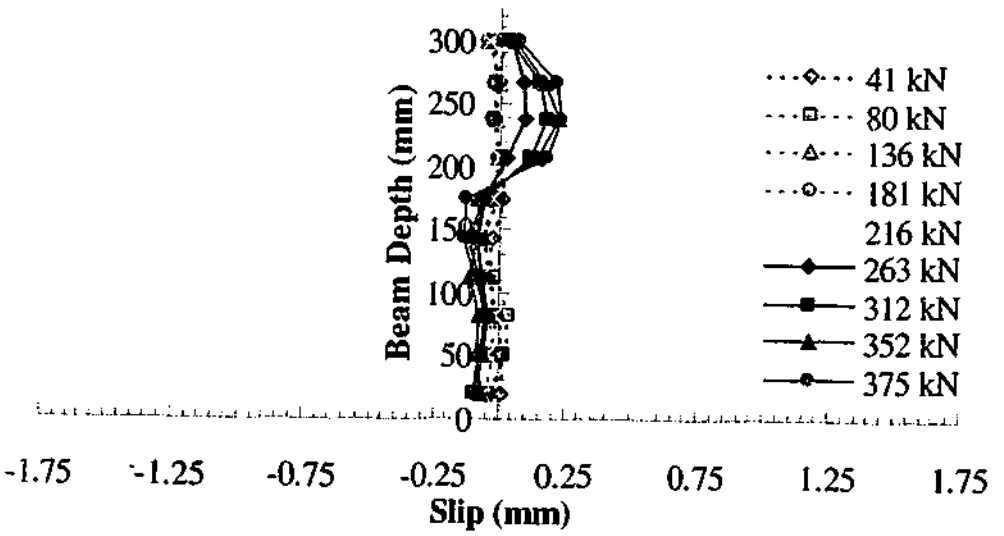

gure C.21 - Slip behaviour of CFRP '5' in beam '0.60D' at (a) left side and (b) right side

(b)

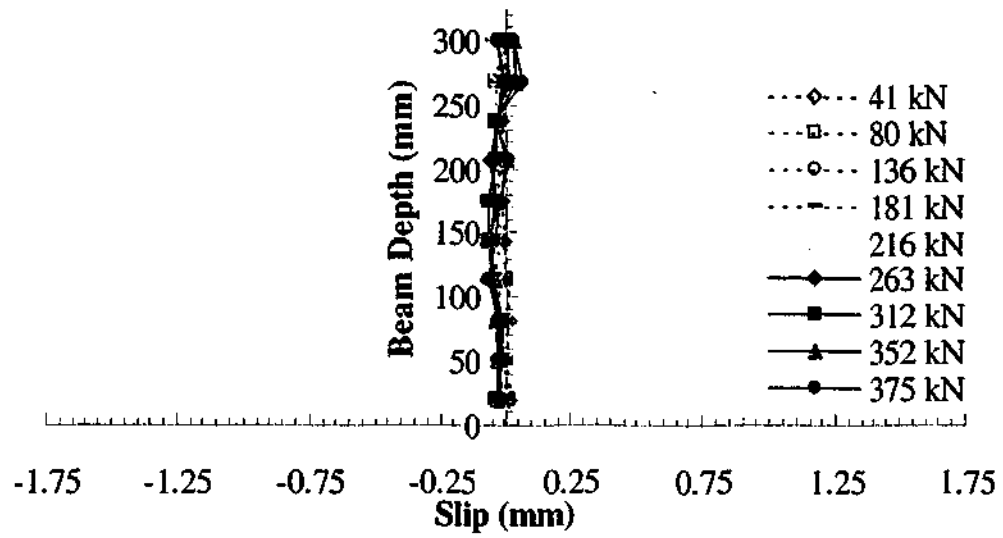

Figure C.21 (continued) - Slip behaviour of CFRP '5' in beam '0.60D' at (a) left side and (b) right side

(a)

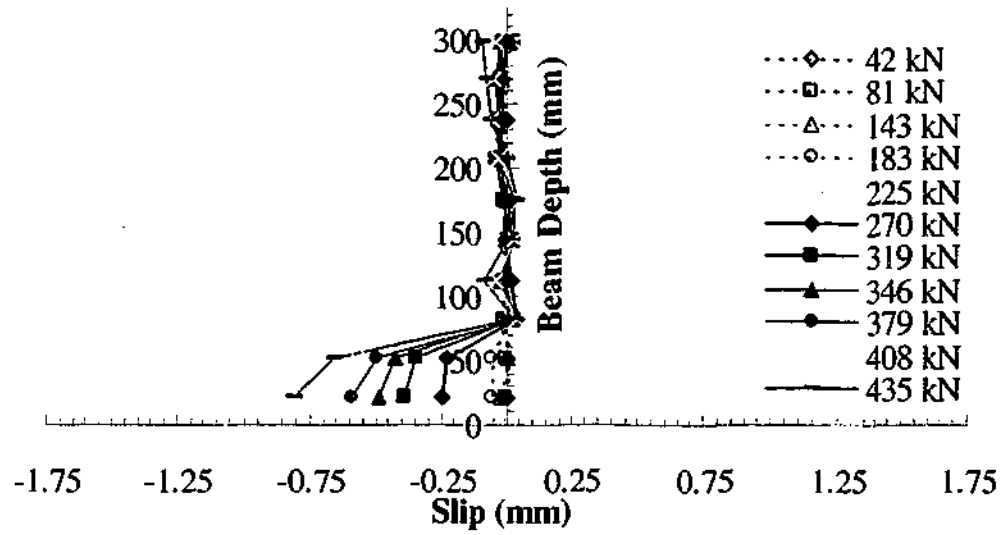

(b)

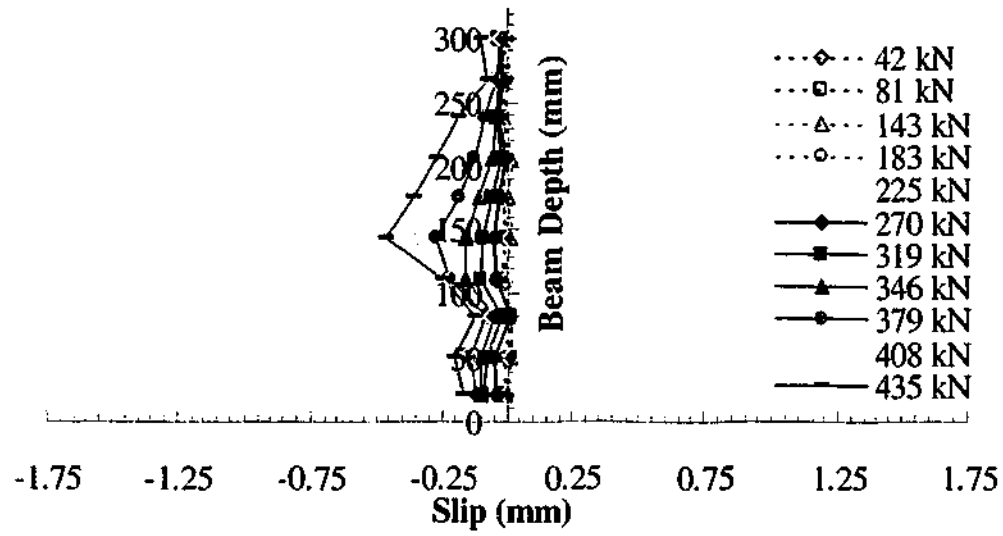

igure C.22 - Slip behaviour of CFRP '1' in beam '0.50D' at (a) left side and (b) right side

(a)

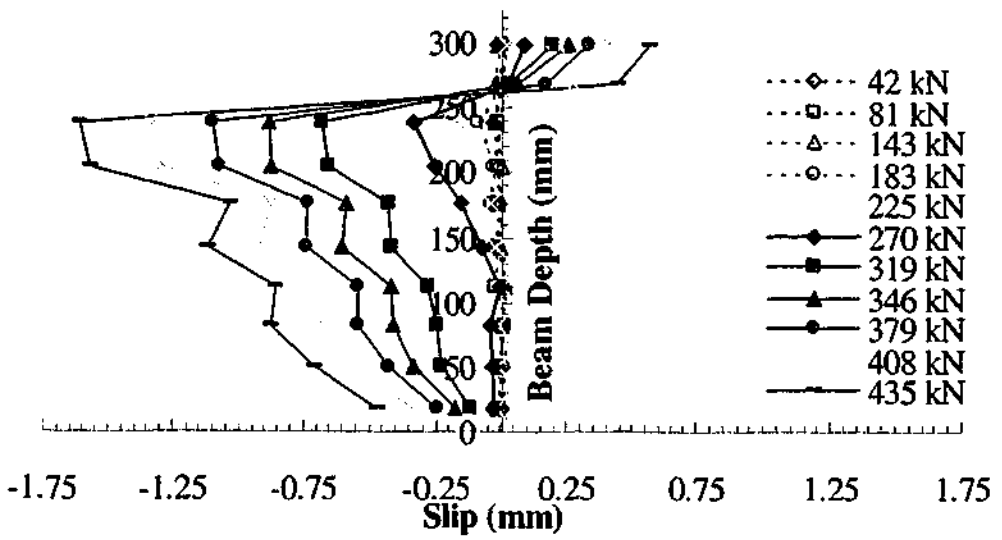

(b)

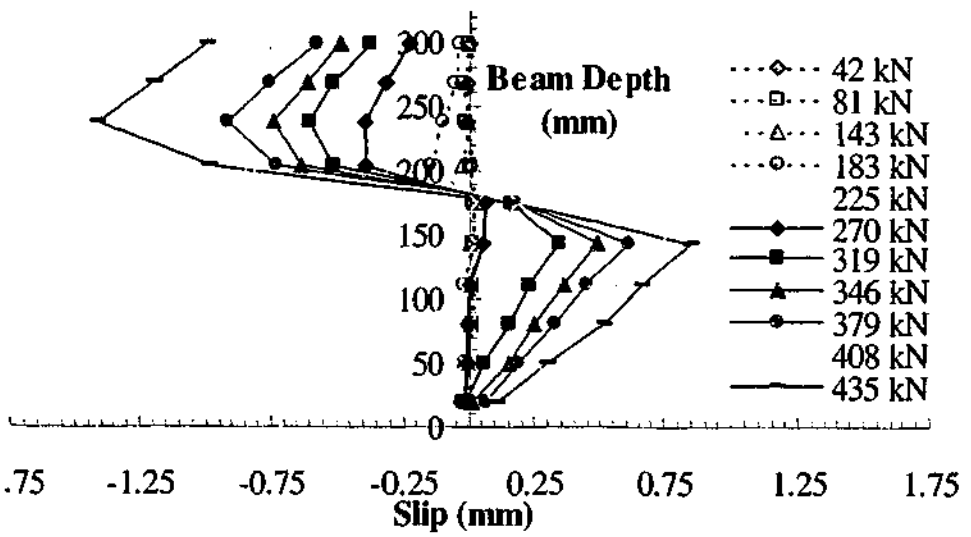

Figure C.23 - Slip behaviour of CFRP '2' in beam '0.50D' at (a) left side and (b) right side

(a)

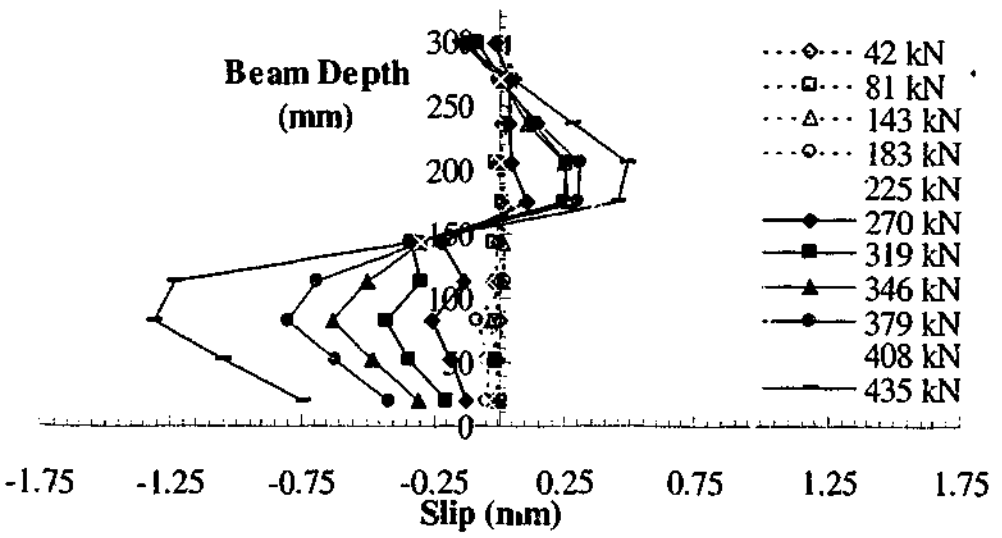

Figure C.24- Slip behaviour of CFRP '3' in beam '0.50D' at (a) left side and (b) right side

(b)

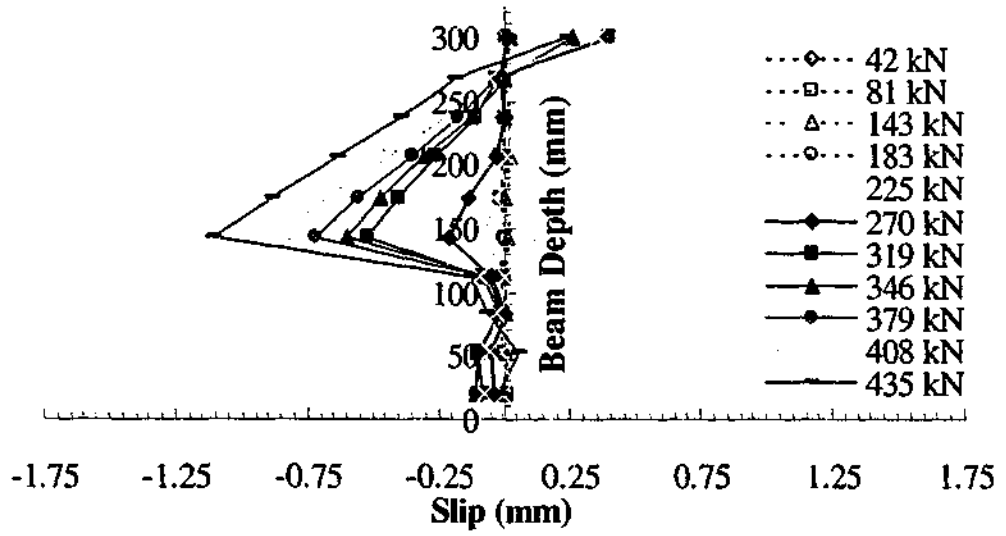

Figure C.24 (continued) - Slip behaviour of CFRP '3' in beam '0.50D' at (a) left side and (b) right side

(a)

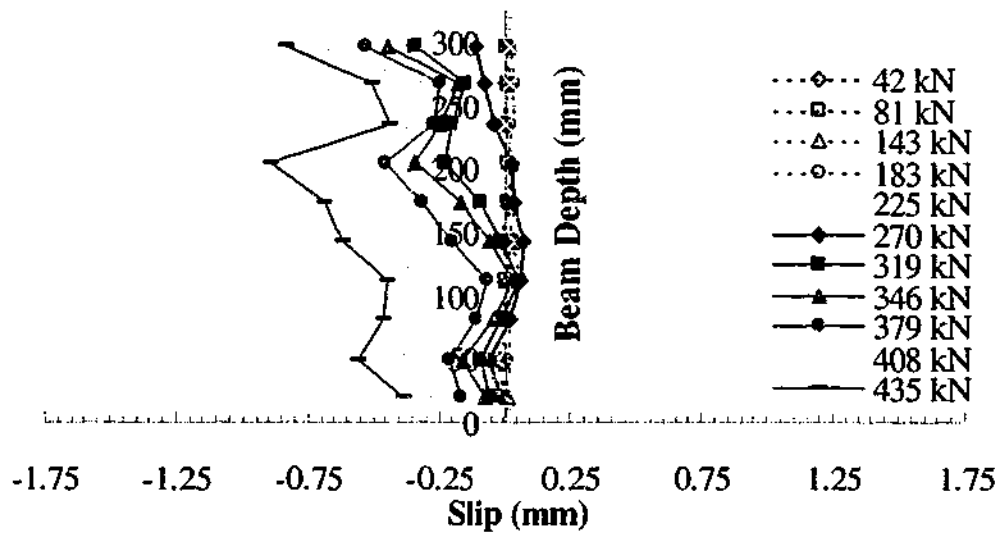

(b)

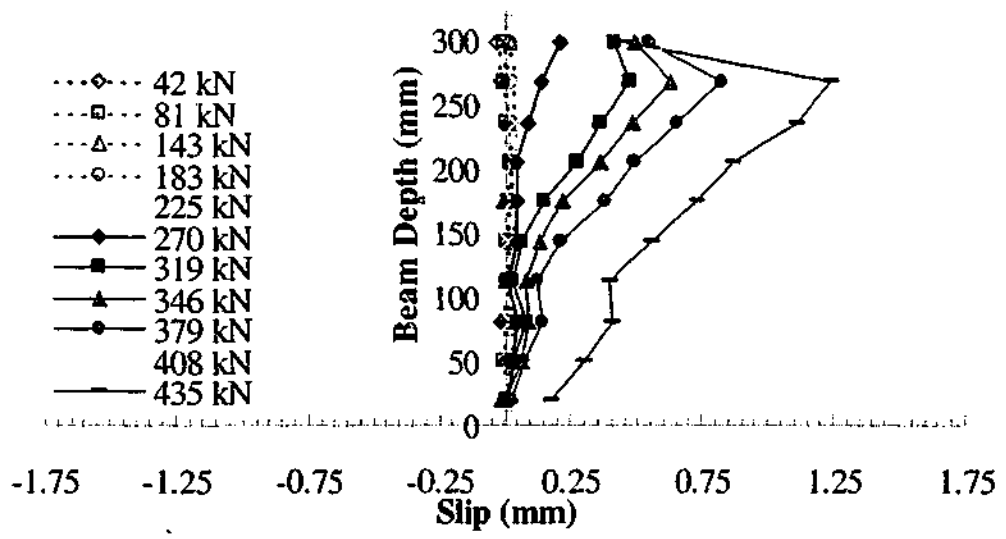

Figure C.25 - Slip behaviour of CFRP '4' in beam '0.50D' at (a) left side and (b) right side

(a)

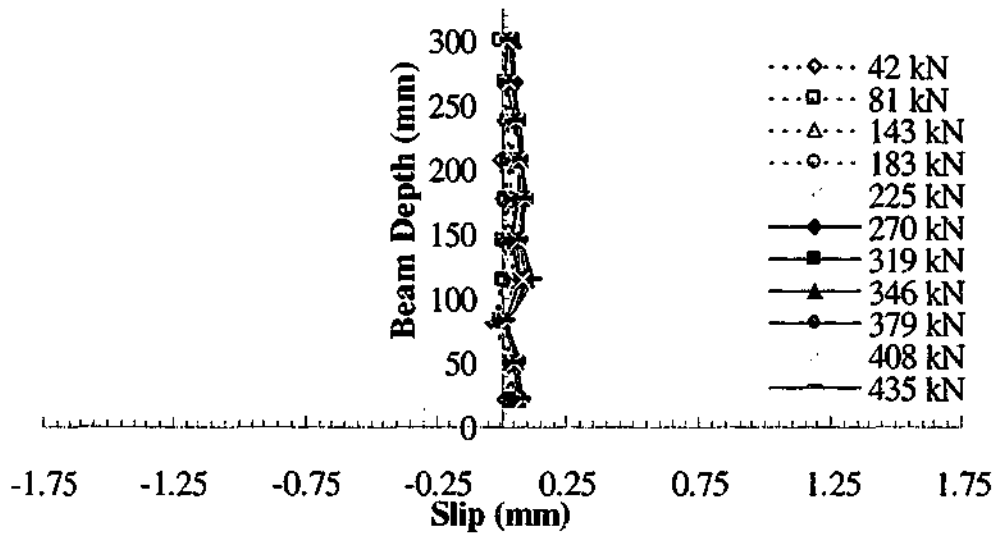

(b)

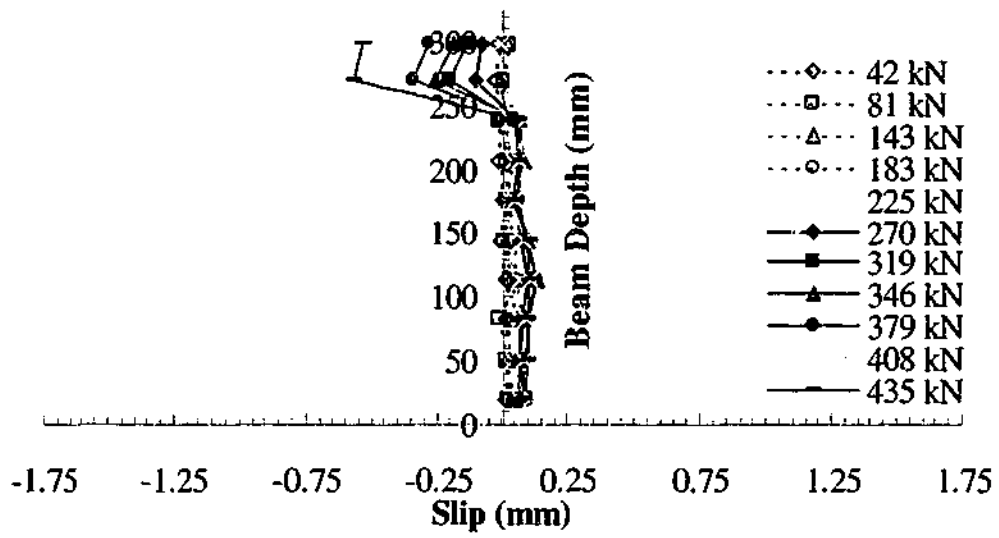

Figure C.26 - Slip behaviour of CFRP '5' in beam '0.50D' at (a) left side and (b) right side

APPENDIX D

D.1 Effect of varying β on main flexural reinforcement behaviour of finite element base models

Figure D.1 to Figure D.3 illustrate the main flexural reinforcement responses of the strengthened beam finite element base models with varying shear retention factor β. The experimental result in the figures corresponds to readings of strain gauge MWB of the control beam (see Figures 5.4 and 5.7).

(a)

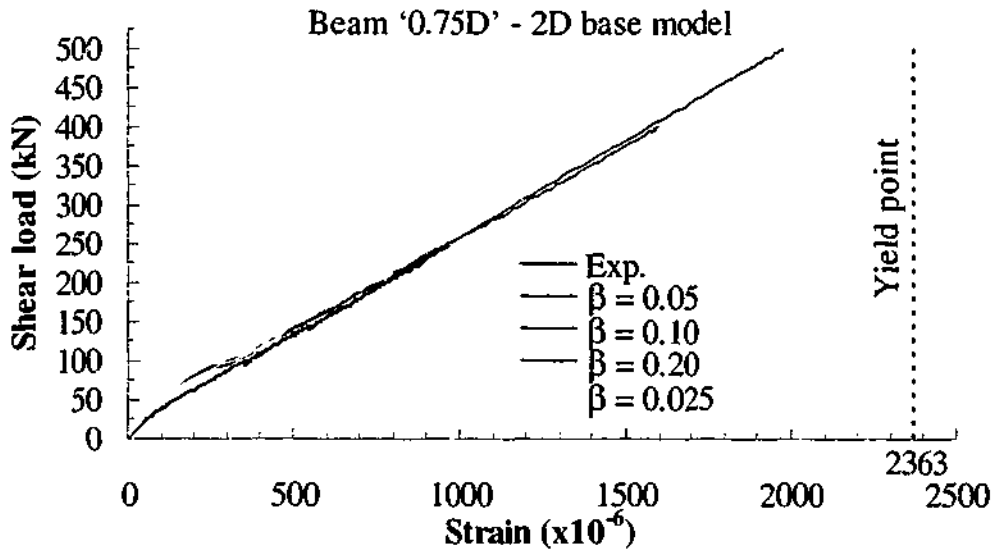

(b)

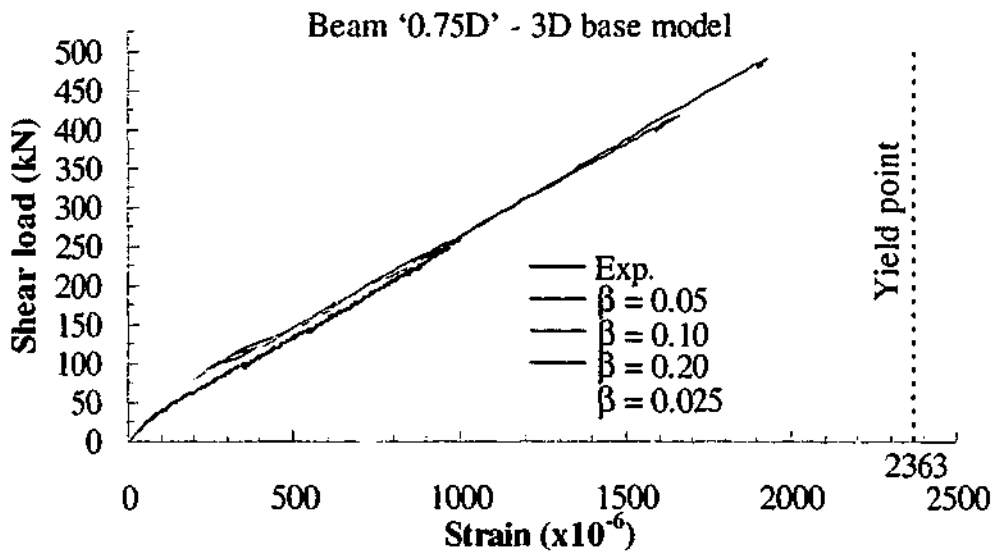

Figure D.1 - Effect of varying β on main reinforcement load strain responses of beam '0.75D' in (a) 2D base models and (b) 3D base models

(a)

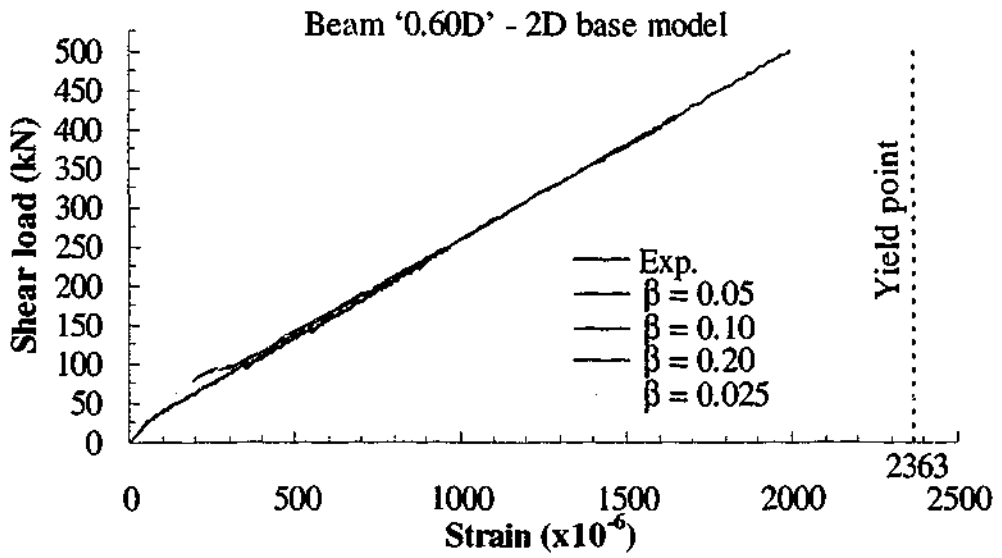

(b)

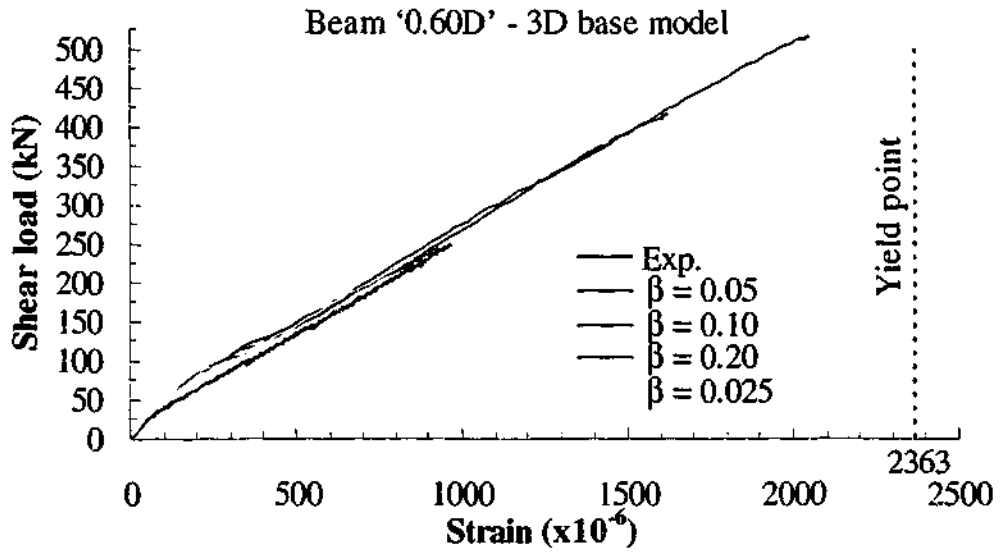

Figure D.2 - Effect of varying β on main reinforcement load strain responses of beam '0.60D' in (a) 2D base models and (b) 3D base models

(a)

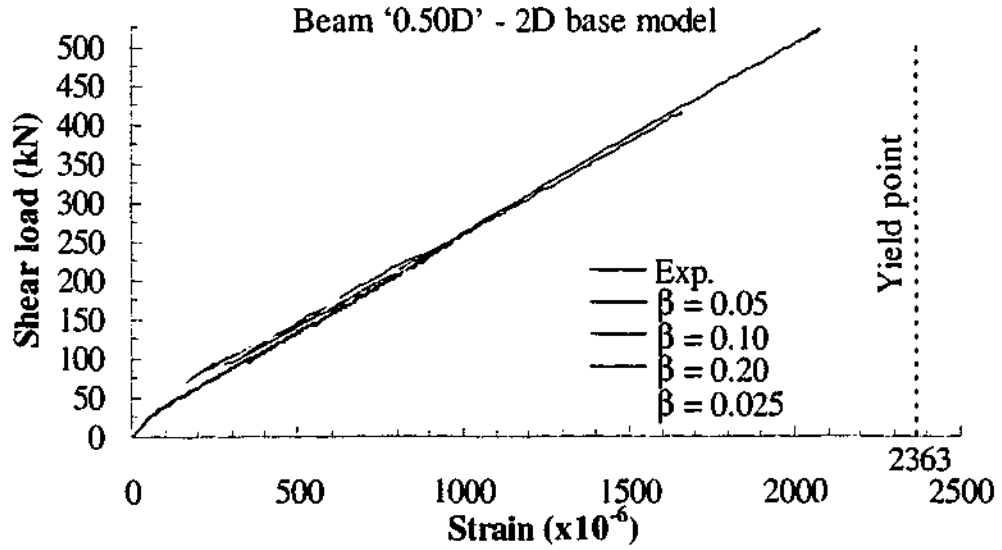

Figure D.3 - Effect of varying β on main reinforcement load strain responses of beam '0.50D' in (a) 2D base models and (b) 3D base models

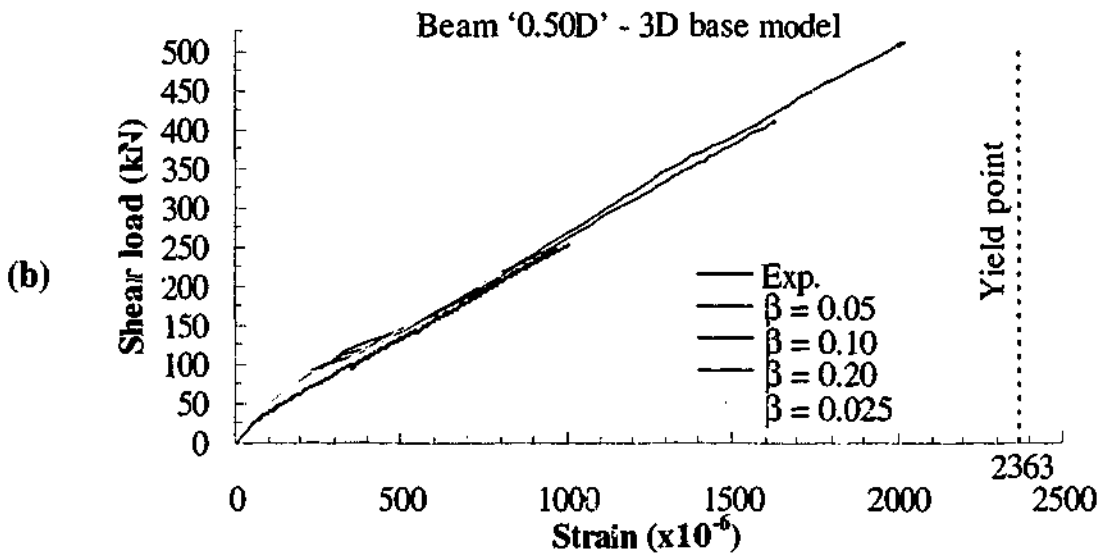

Figure D.3 (continued) - Effect of varying β on main reinforcement load strain responses of beam '0.50D' in (a) 2D base models and (b) 3D base models

D.2 Effect of varying β on the shear reinforcement behaviour of finite element base models

Figure D.4 to Figure D.9 illustrate the shear reinforcement responses of the strengthened beam finite element base models with varying shear retention factor β.

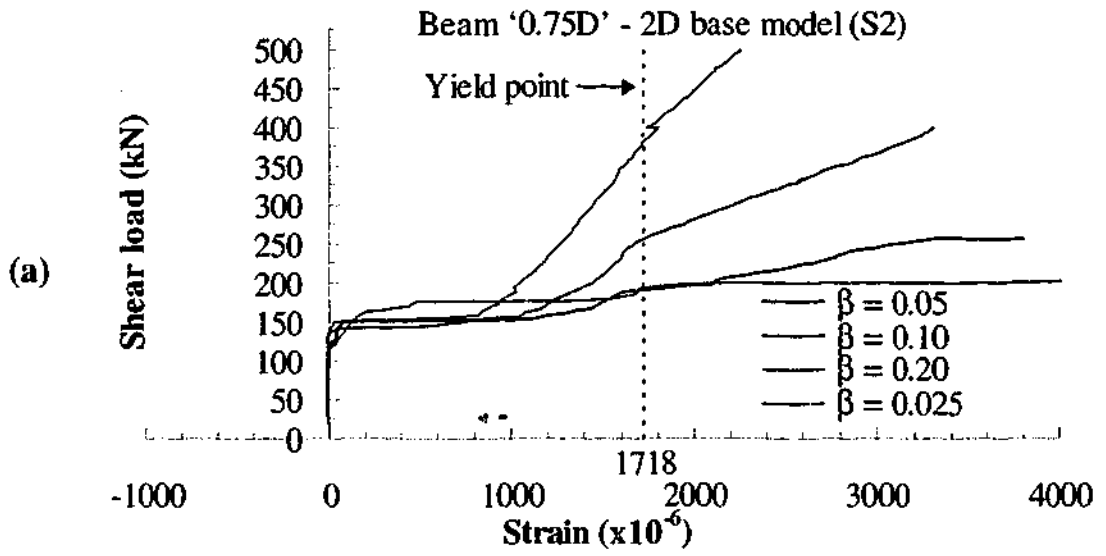

Figure D.4 - Effect of varying β on shear reinforcement load strain responses of 2D base models of beam '0.75D' at stirrup locations (a) S2 and (b) S4

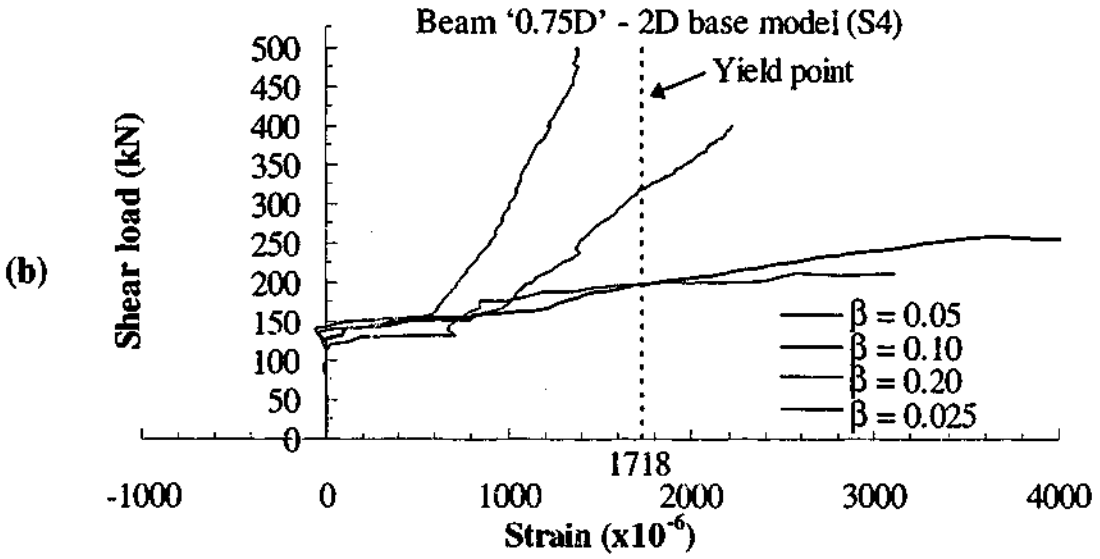

Figure D.4 (continued) - Effect of varying β on shear reinforcement load strain responses of 2D base models of beam '0.75D' at stirrup locations (a) S2 & (b) S4

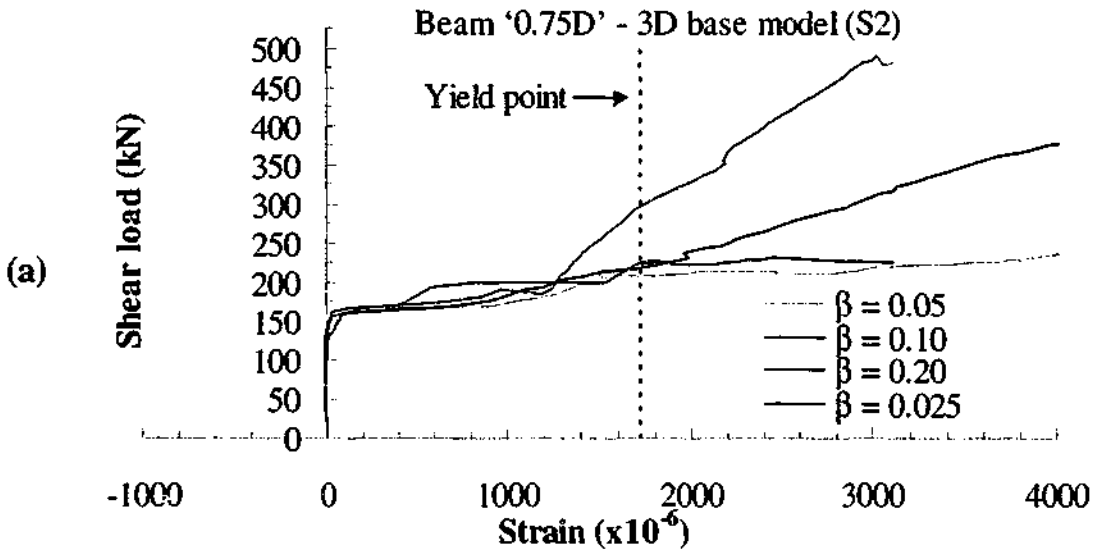

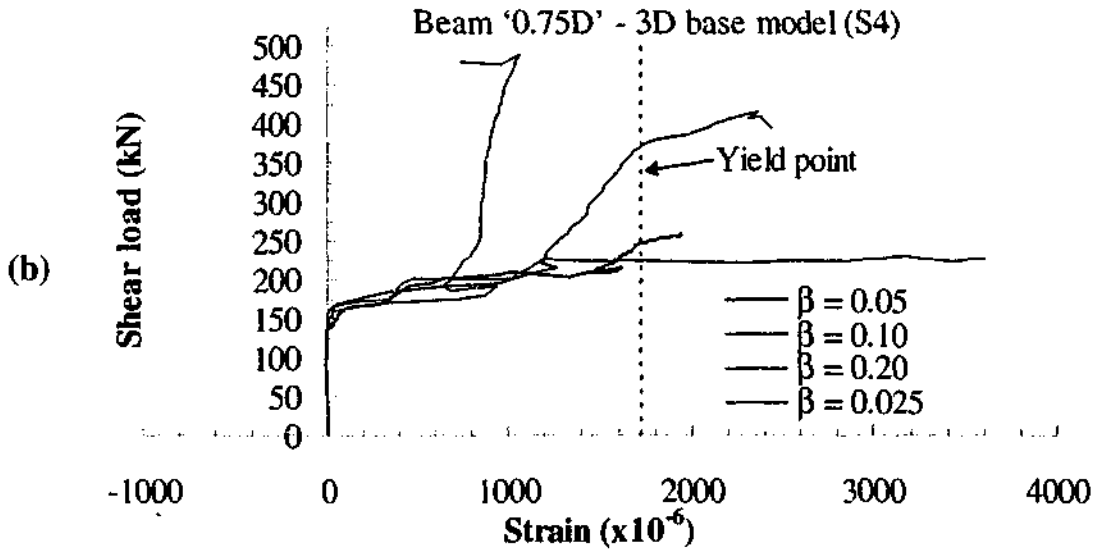

igure D.5 - Effect of varying β on shear reinforcement load strain responses of 3D base models of beam '0.75D' at stirrup locations (a) S2 and (b) S4

(a)

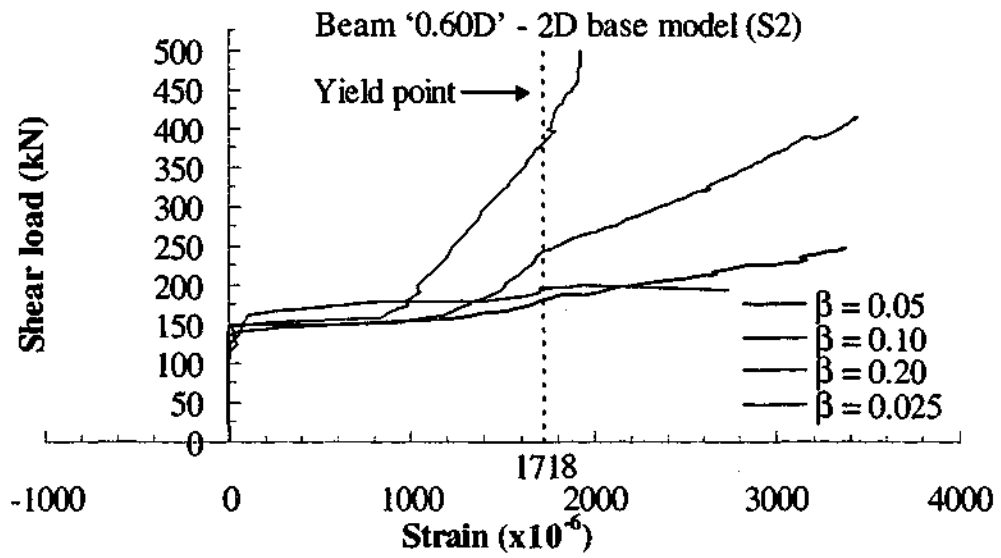

(b)

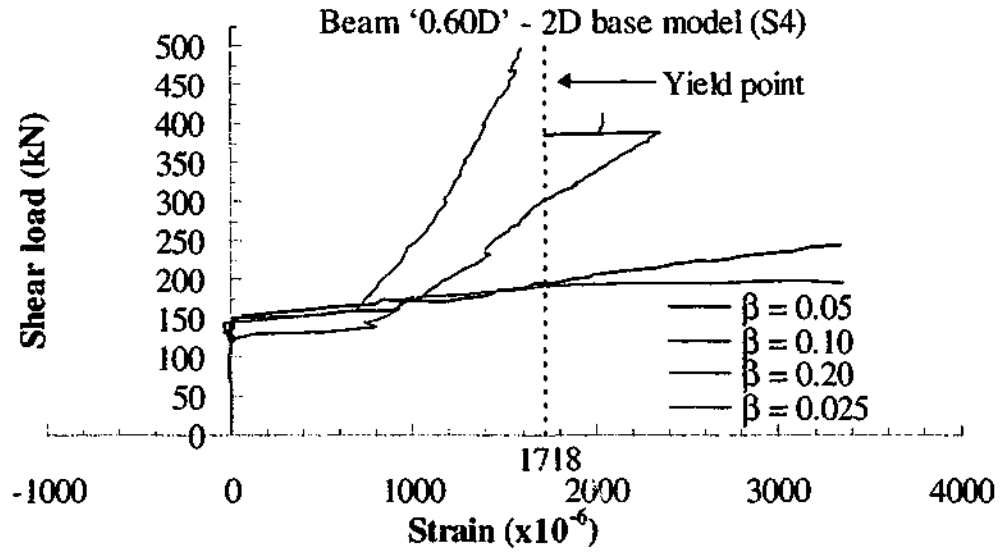

Figure D.6 - Effect of varying β on shear reinforcement load strain responses of 2D base models of beam '0.60D' at stirrup locations (a) S2 and (b) S4

(a)

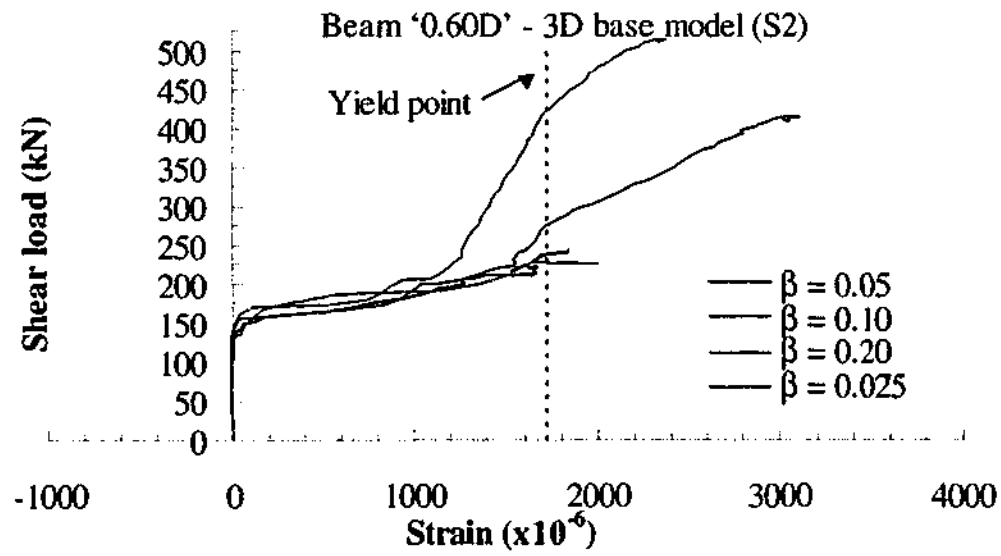

Figure D.7 - Effect of varying β on shear reinforcement load strain responses of 3D base models of beam '0.60D' at stirrup locations (a) S2 and (b) S4

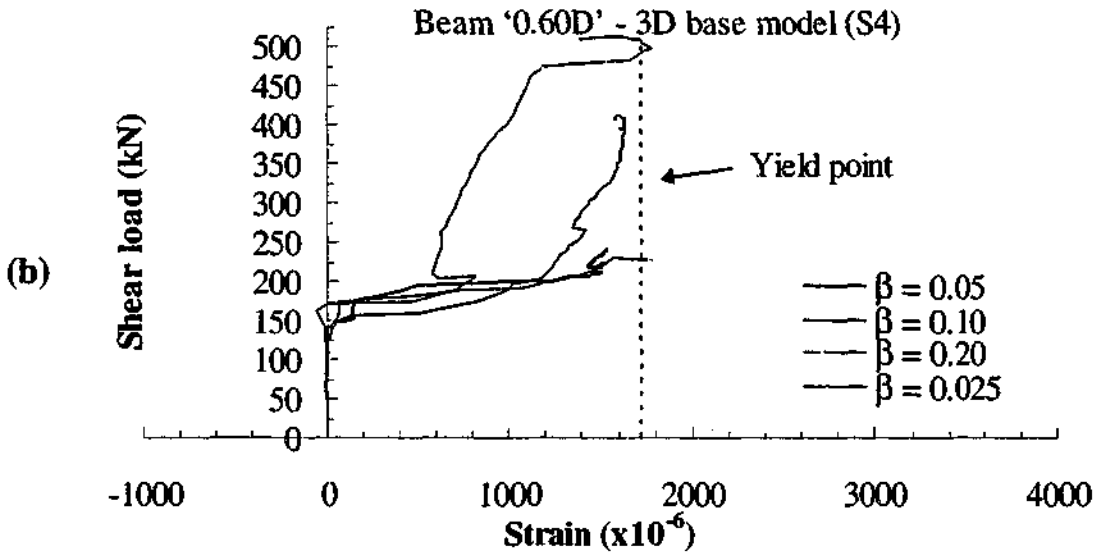

(b)

Figure D.7 (continued) - Effect of varying β on shear reinforcement load strain responses of 3D base models of beam '0.60D' at stirrup locations (a) S2 & (b) S4

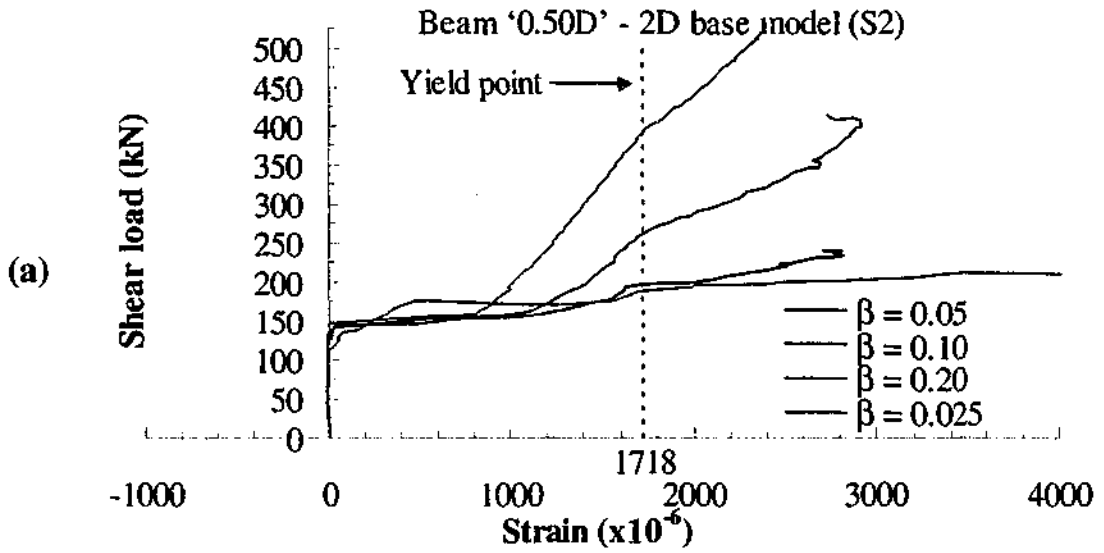

(a)

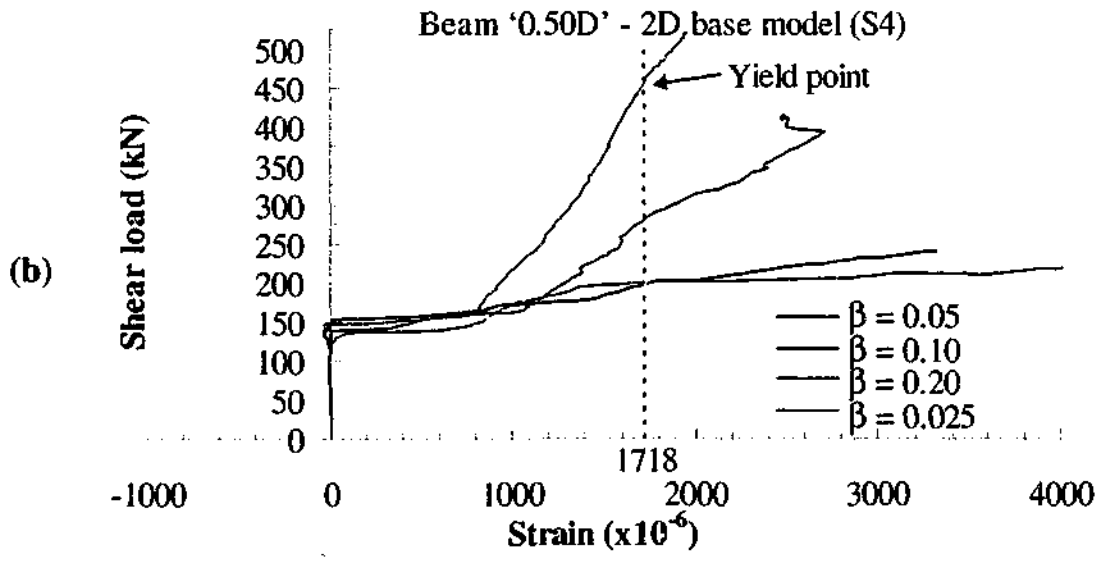

(b)

Figure D.8 - Effect of varying β on shear reinforcement load strain responses of 2D base models of beam '0.50D' at stirrup locations (a) S2 and (b) S4

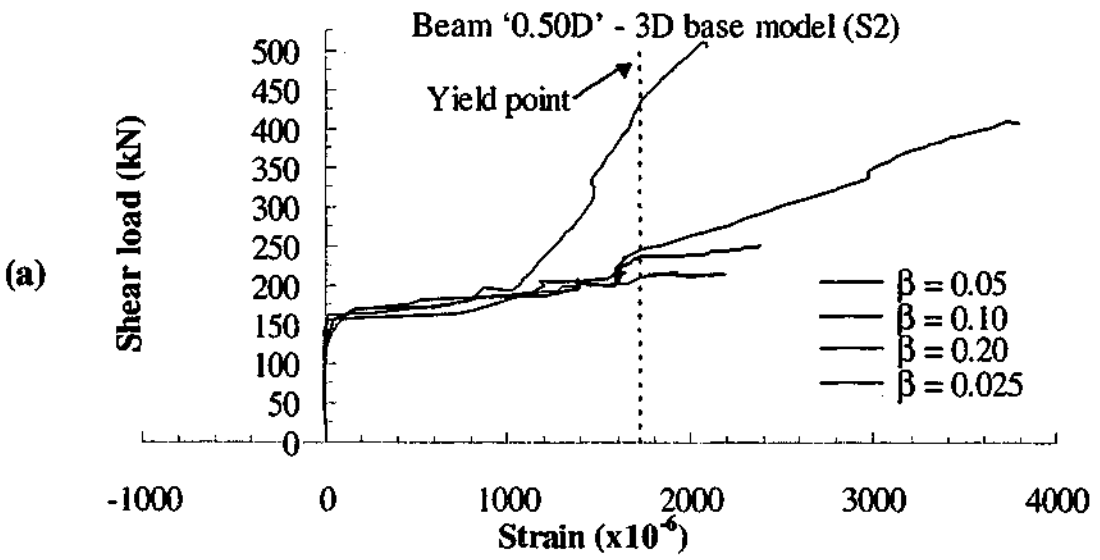

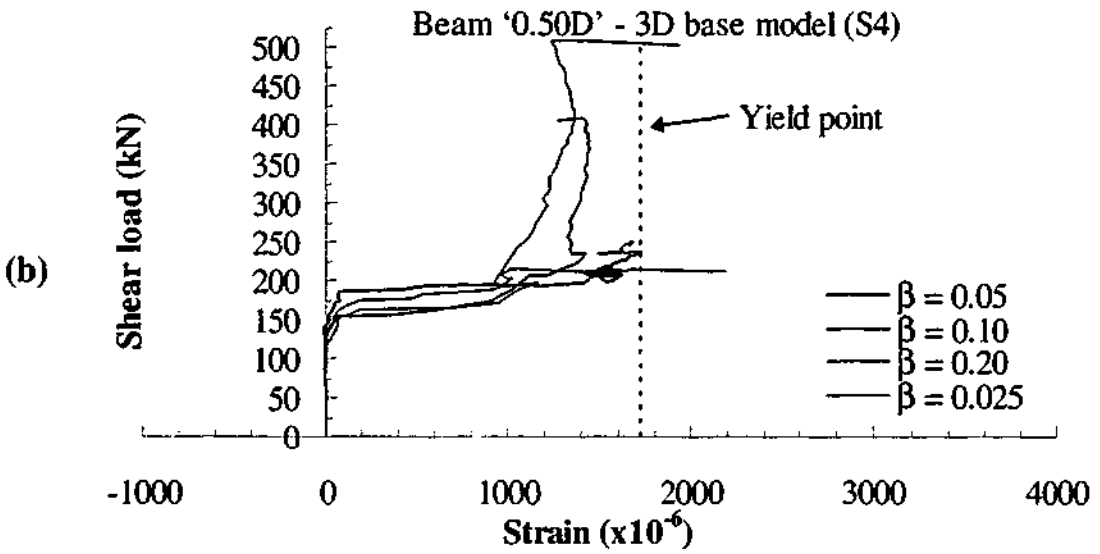

Figure D.9 - Effect of varying β on shear reinforcement load strain responses of 3D base models of beam '0.50D' at stirrup locations (a) S2 and (b) S4

D.3 Effect of varying β on the crack pattern of finite element base models

Figure D.10 to Figure D.15 illustrate the crack patterns of the finite element strengthened beam base models with varying shear retention factor β. The crack patterns shown were obtained at the peak load step of each respective model.

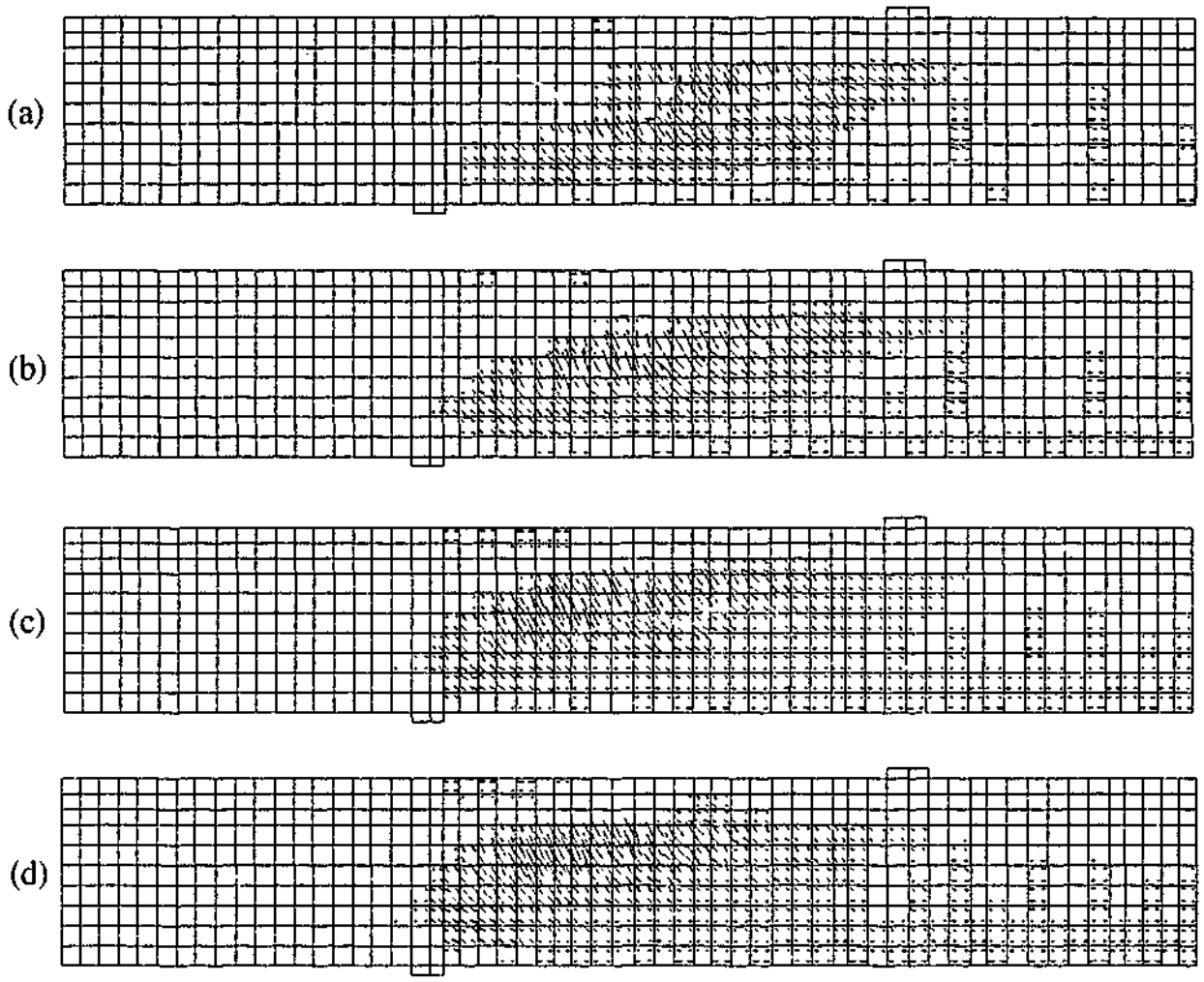

Figure D.10 - Predicted crack tensile strain patterns of 2D base models (4-node) of beam '0.75D' with β of (a) 0.025 (b) 0.05 (c) 0.10 and (d) 0.20

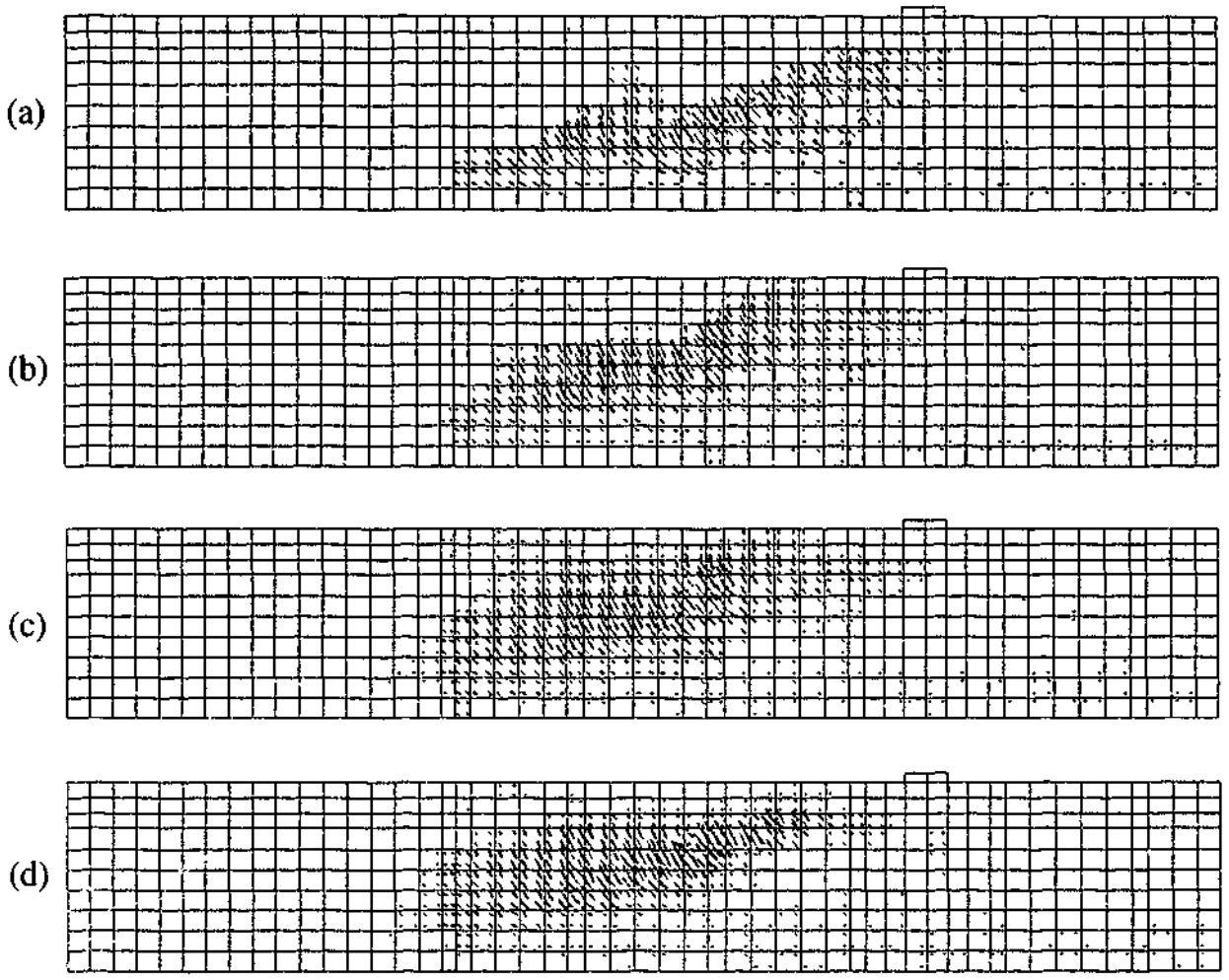

Figure D.11 - Predicted crack tensile strain patterns of 3D base models (8-node) of beam '0.75D' with β of (a) 0.025 (b) 0.05 (c) 0.10 and (d) 0.20

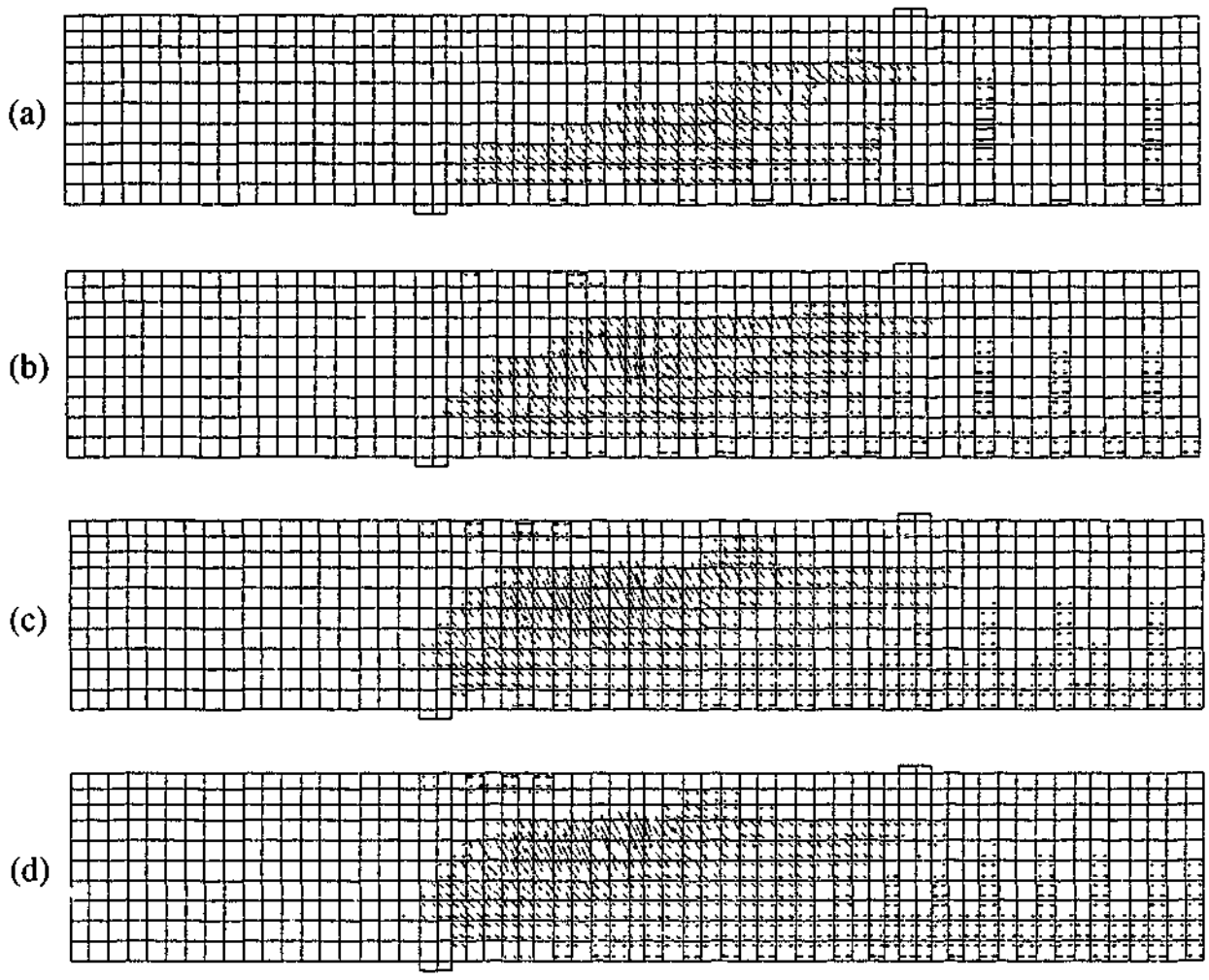

Figure D.12 - Predicted crack tensile strain patterns of 2D base models (4-node) of beam '0.60D' with β of (a) 0.025 (b) 0.05 (c) 0.10 and (d) 0.20

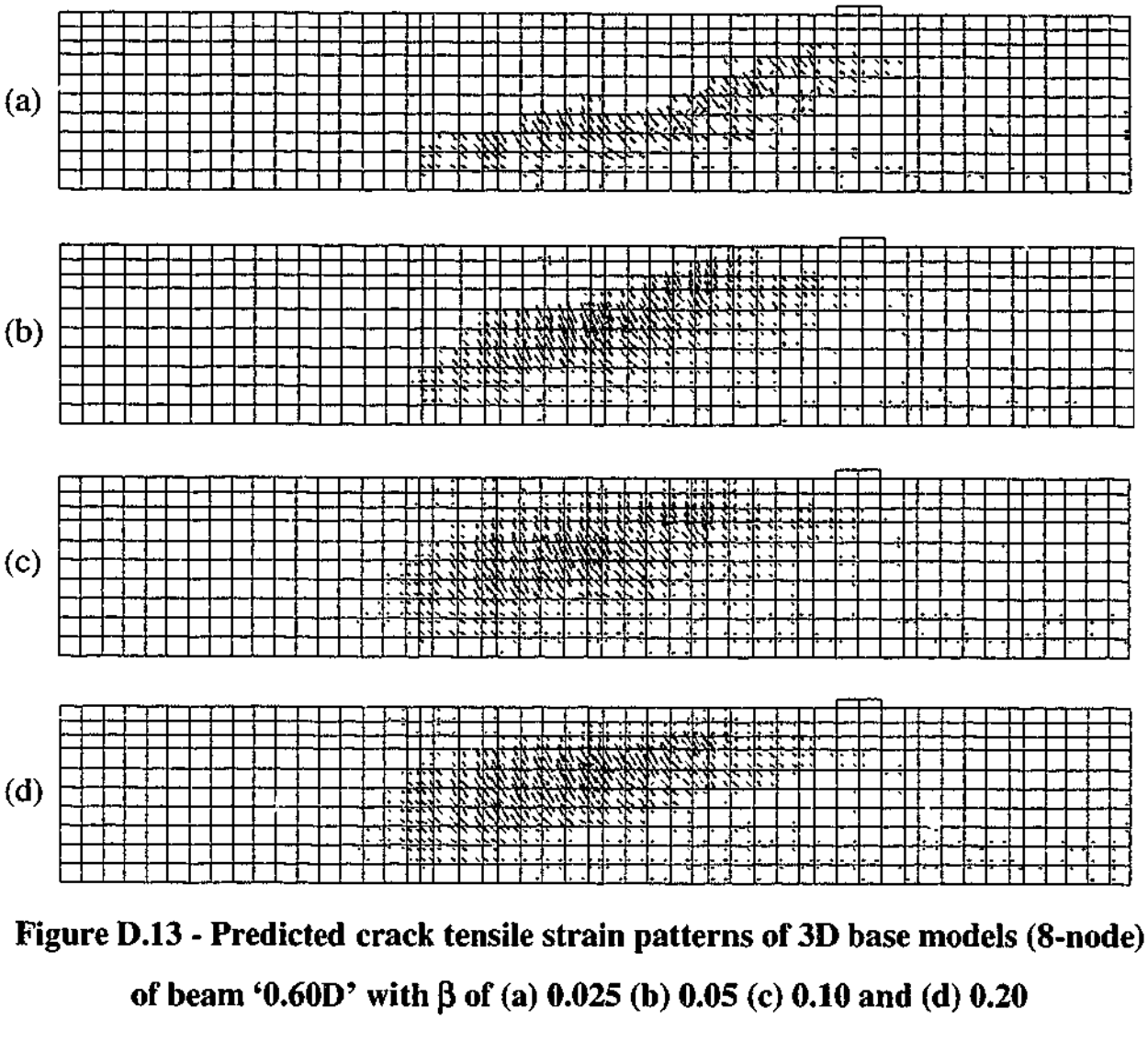

Figure D.13 - Predicted crack tensile strain patterns of 3D base models (8-node) of beam '0.60D' with β of (a) 0.025 (b) 0.05 (c) 0.10 and (d) 0.20

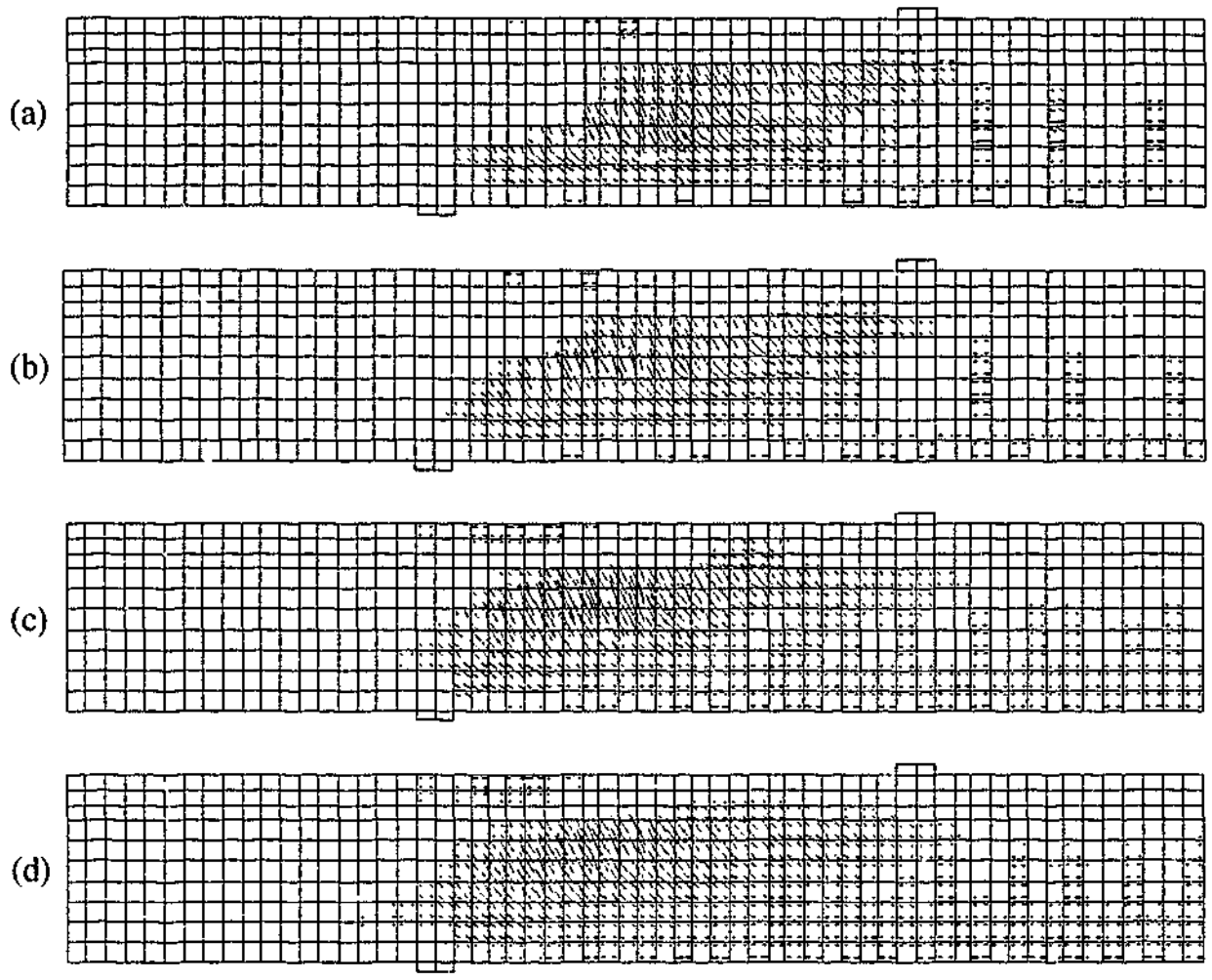

Figure D.14 - Predicted crack tensile strain of 2D base models (4-node) of beam '0.50D' with β of (a) 0.025 (b) 0.05 (c) 0.10 and (d) 0.20

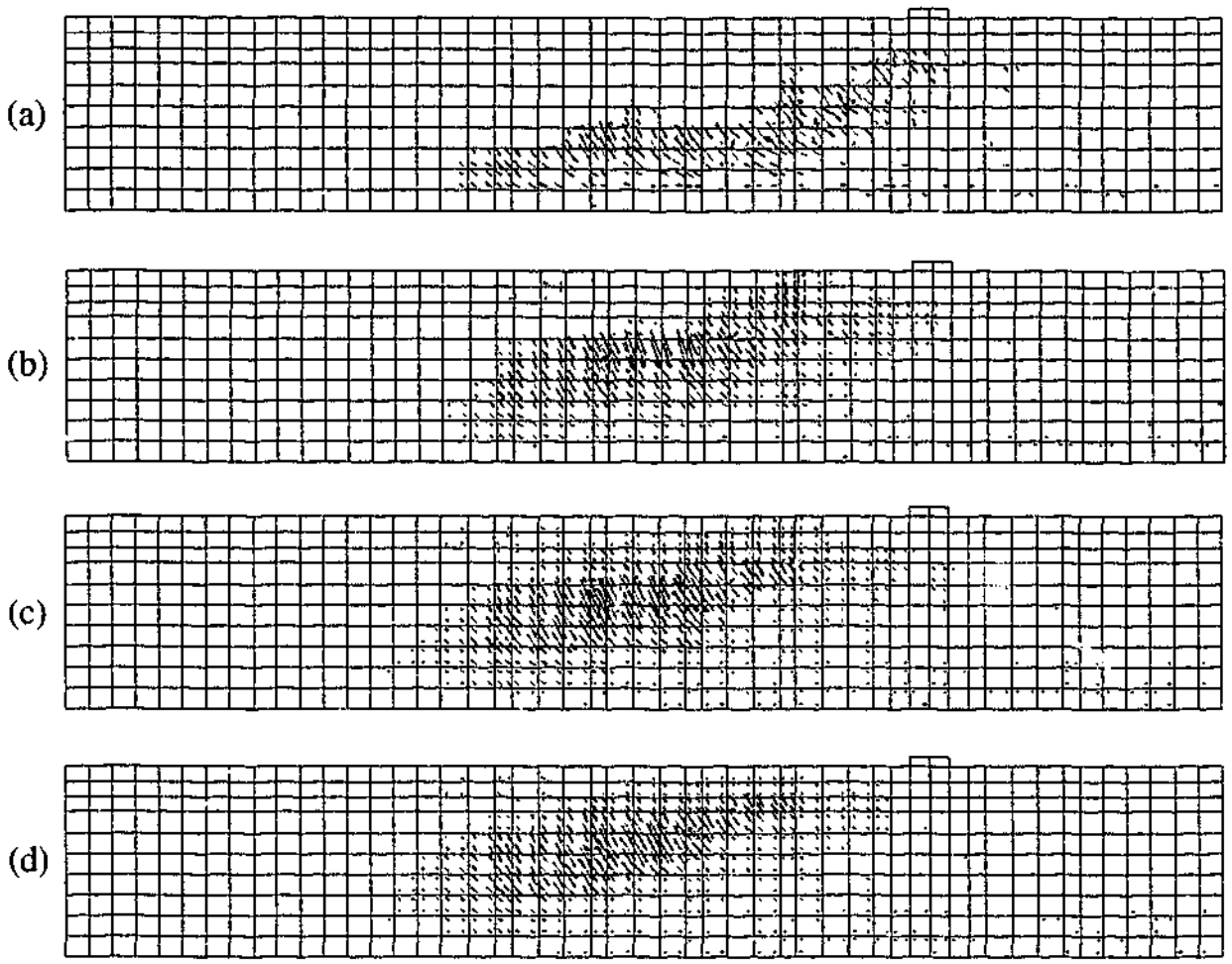

Figure D.15 - Predicted crack tensile strain patterns of 3D base model (8-node) of beam '0.50D' with β of (a) 0.025 (b) 0.05 (c) 0.10 and (c) 0.20

APPENDIX E

E.1 Calculations of T-beams shear strength using existing prediction models

In this section, the workings and calculations of the FRP prediction models reported by Triantafillou and Antonopoulos (2000), Neale (2001) and Chen and Teng (2003a, c) based on the dimensions and configurations of the T-beams in the current study are shown and reported. Only equations in the publications that are applicable to the current study are reproduced here. Table E.1 summarises the common values used in all the prediction models. The contribution of the concrete and internal steel shear reinforcement to the shear capacity of the beam was determined using four different design standards. The design standards used are based on the Australian code SAI (2001), American code ACI Committee 318(1999), Canadian code CSA (1994) and European code ENV 1992-1-1 (1991). For a more appropriate comparison against experimental results, the material and partial safety factors in all the prediction models are taken to be equal to one. The FRP, steel reinforcement and concrete properties are known from testing. The concrete characteristic strength f'_c is taken to be equal to the mean compressive strength f_{cm}.

Table E.1 - Dimension and property values used in prediction models

<table>
<tr><th>Beam dimensions and properties</th><th>FRP dimensions and properties</th></tr>
<tr><td>Overall depth ⇒ D = 490 mm</td><td>FRP ⇒ E_{frp} = 137345 MPa</td></tr>
<tr><td>Flange width ⇒ b_f = 720 mm</td><td>FRP thickness ⇒ t_{frp} = 1.31 mm</td></tr>
<tr><td>Flange thickness ⇒ t_f = 120 mm</td><td>FRP width ⇒ w_{frp} = 41.71 mm</td></tr>
<tr><td>Web thickness ⇒ b_w = 225 mm</td><td rowspan="4">FRP spacings
⇒ s_{frp} = 365 mm (Beam '0.75D')
⇒ s_{frp} = 295 mm (Beam '0.60D')
⇒ s_{frp} = 245 mm (Beam '0.50D')</td></tr>
<tr><td>Effective depth ⇒ d = 418 mm</td></tr>
<tr><td>Depth to centroid of outermost layer of tensile reinforcement ⇒ d_o = 446 mm</td></tr>
<tr><td>Cross sectional area of tensile reinforcement ⇒ A_{st} = 4926 mm^2</td></tr>
<tr><td>Steel stirrup spacing ⇒ s = 365 mm</td><td rowspan="3">Fracture strain
⇒ ε_{frpu} = 0.015 (assumed)
Fracture stress
⇒ f_{frpu} = 2060 MPa (approximated)</td></tr>
<tr><td>Cross sectional area of shear reinforcement ⇒ A_{sv} = 157.1 mm^2</td></tr>
<tr><td>Mean compressive strength of concrete f_{cm} = 31.9 MPa</td></tr>
<tr><td>Yield strength of stirrups $f_{sy.f}$ = 351.1MPa</td><td></td></tr>
</table>

E.2 Concrete and steel shear reinforcement contribution

E.2.1 Australian Code SAI (2001)

The shear strength of a reinforced concrete beam is given by

$$V_u = V_{uc} + V_{us} \qquad \text{(Eq. 8.2.2)}$$

where V_{uc} and V_{us} are the contributions from concrete and shear reinforcement given by

$$V_{uc} = \beta_1\beta_2\beta_3 b_v d_0 \left(\frac{A_{st} f'_c}{b_v d_0}\right)^{1/3} \qquad \text{(Eq. 8.2.7.1)}$$

$$V_{us} = (A_{sv} f_{sy.f} d_0 / s)\cot\theta_v \qquad \text{(Eq. 8.2.10)}$$

The ultimate shear strength is limited by web crushing given by

$$V_{u.max} = 0.2 f'_c b_v d_0 + P_v \qquad \text{(Eq. 8.2.6)}$$

1. Determination of shear strength limited by web crushing

$b_v = b_w = 225$ mm, $P_v = 0$ (Non prestressed member)

$$V_{u.max} = 0.2 f'_c b_v d_0 + P_v$$
$$= 0.2 \times 31.9 \times 225 \times 446 + 0 = 640.2 \times 10^3 \text{ N} = 640.2 \text{ kN}$$

2. Determination of contribution of concrete to the shear capacity V_{uc}

$$\beta_1 = 1.1(1.6 - d_0/1000) \geq 1.1$$
$$= 1.1(1.6 - 446/1000) = 1.2694$$

$\beta_2 = 1$ (No significant axial tension or compression)

$\beta_3 = 1$

$$V_{uc} = \beta_1\beta_2\beta_3 b_v d_0 \left(\frac{A_{st} f'_c}{b_v d_0}\right)^{1/3}$$

$$= 1.2694 \times 1 \times 1 \times 225 \times 446 \times \left(\frac{4926 \times 31.9}{225 \times 446}\right)^{1/3} = 147.9 \times 10^3 \text{ N} = 147.9 \text{ kN}$$

3. Determination of contribution of steel shear reinforcement to shear capacity V_{us}

$\theta_v = 45°$ (Conservative)

$$V_{us} = (A_{sv} f_{syf} d_0 / s)\cot\theta_v$$

$$= (157.1 \times 351.1 \times 446/365)\cot 45° = 67.4 \times 10^3 \text{ N} = 67.4 \text{ kN}$$

4. Shear strength of reinforced concrete T-beam V_u

$$V_u = V_{uc} + V_{us} = 147.9 + 67.4 = 215.3 \text{ kN}$$

E.2.2 American Code ACI Committee 318 (1999)

The shear strength of a reinforced concrete beam is given by

$$V_n = V_c + V_s \qquad \text{(Eq. 11-2)}$$

where V_c and V_s are the nominal shear strength provided by concrete and shear reinforcement given by

$$V_c = \left(\frac{\sqrt{f'_c}}{6}\right) b_w d \qquad \text{(Eq. 11-3)}$$

(Simplified approach)

or

$$V_c = \left(\sqrt{f'_c} + 120\rho_w \frac{V_u d}{M_u}\right)\frac{b_w d}{7} \left(< 0.3\sqrt{f'_c} b_w d\right) \qquad \text{(Eq. 11-5)}$$

(Detailed approach)

$$V_s = \frac{A_v f_y d}{s} \qquad \text{(Eq. 11-15)}$$

1. Determination of contribution of concrete to the shear capacity V_c

$$\rho_w = A_s / b_w d = 4926/(225 \times 418) = 0.05238$$

Ignoring self weight of beam, the moment at the shear span is given by

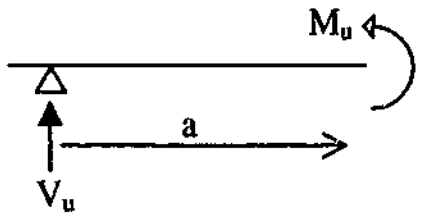

$$M_u = V_u a$$

$$\frac{1}{a} = \frac{V_u}{M_u}$$

$$\frac{d}{a} = \frac{V_u d}{M_u}$$

The minimum value of $\frac{V_u d}{M_u}$ occurs at the location of the load point at a = 1265mm

$$\frac{V_u d}{M_u} = \frac{418}{1265} = 0.33$$

⇒ Simplified approach

$$V_c = \left(\frac{\sqrt{f'_c}}{6}\right) b_w d = \left(\frac{\sqrt{31.9}}{6}\right) x\ 225\ x\ 418 = 88.5\ x\ 10^3 = 88.5\ kN$$

⇒ Detailed approach

$\rightarrow \frac{V_u d}{M_u} = 0.4935$ (Critical section occurs at distance d from loading point)

$$V_c = \left(\sqrt{f'_c} + 120\rho_w \frac{V_u d}{M_u}\right)\frac{b_w d}{7} (< 0.3\sqrt{f'_c} b_w d)$$

$$= \left(\sqrt{31.9} + 120\ x\ 0.05238\ x\ 0.4935\right)\frac{225\ x\ 418}{7} = 117.6\ x\ 10^3\ N = 117.6\ kN$$

Adopt value from detailed approach

V_c shall not be greated than $0.3\sqrt{f'_c} b_w d$

$$0.3\sqrt{f'_c} b_w d = 0.3\ x\ \sqrt{31.9}\ x\ 225\ x\ 418 = 159.4\ x\ 10^3\ N = 159.4\ kN$$

2. Determination of contribution of steel shear reinforcement to shear capacity V_s

$$V_s = \frac{A_v f_y d}{s} = \frac{157.1\ x\ 351.1\ x\ 418}{365} = 63.2\ x\ 10^3\ N = 63.2\ kN$$

3. Shear strength of reinforced concrete T-beam V_n

$$V_n = V_c + V_s = 117.6 + 63.2 = 180.8\ kN$$

E.2.3 Canadian Code CSA (1994)

The shear strength of a reinforced concrete beam is given by the minimum of

$$V_r = V_c + V_s \qquad \text{(Eq. 11-4)}$$

or

$$V_r = V_c + 0.8\lambda\phi_c\sqrt{f'_c}\,b_w d \qquad \text{(Eq. 11-5)}$$

where V_c and V_s are the shear strength provided by concrete and shear reinforcement given by

$$V_c = 0.2\phi_c\sqrt{f'_c}\,b_w d \qquad \text{(Eq. 11-6)}$$

(Satisfy requirement for minimum area of shear reinforcement given by

CSA-A23.3-94 (11-1) $\rightarrow A_v = 0.06\sqrt{f'_c}\,\dfrac{b_w s}{f_y}$)

$$V_s = \frac{\phi_s f_y A_v d}{s} \qquad \text{(Eq. 11-11)}$$

1. Determination of contribution of concrete to the shear capacity V_c

$\phi_c = 1.00$ (For comparison against experimental results)

$$V_c = 0.2\phi_c\sqrt{f'_c}\,b_w d = 0.2 \times 1.0 \times \sqrt{31.9} \times 225 \times 418 = 106.2 \times 10^3 \text{ N} = 106.2 \text{ kN}$$

2. Determination of contribution of steel shear reinforcement to shear capacity V_s

$\phi_s = 1.00$ (For comparison against experimental results)

$$V_s = \frac{\phi_s f_y A_v d}{s} = \frac{1.0 \times 351.1 \times 157.1 \times 418}{365} = 63.2 \times 10^3 \text{ N} = 63.2 \text{ kN}$$

3. Shear strength of reinforced concrete T-beam V_n

$\lambda = 1.00$, $\phi_c = 1.00$ (For comparison against experimental results)

$$V_r = V_c + V_s = 106.2 + 63.2 = 169.4 \text{ kN}$$

$$V_r = V_c + 0.8\lambda\phi_c\sqrt{f'_c}\,b_w d = 106.2 + 0.8 \times 1.00 \times 1.00 \times \sqrt{31.9} \times 225 \times 418$$

$$= \left(106.2 \times 10^3 + 425.0 \times 10^3\right)\text{N} = 531.2 \text{ kN}$$

$$V_r = \min(169.4, 531.2) = 169.4 \text{ kN}$$

E.2.4 European Code ENV 1992-1-1 (1991)

The shear strength of a reinforced concrete beam is given by

$$V_{Rd3} = V_{cd} + V_{wd} \qquad \text{(Eq. 4.22)}$$

where V_{cd} and V_{wd} are the contributions from concrete and shear reinforcement given by

$$V_{cd} = V_{Rd1} = [\tau_{Rd} k(1.2 + 40\rho_1) + |0.15|\sigma_{cp}]b_w d \qquad \text{(Eq. 4.18)}$$

$$V_{wd} = \frac{A_{sw}}{s} 0.9\, d\, f_{ywd} \qquad \text{(Eq. 4.23)}$$

The ultimate shear strength is limited by crushing at the compression struts given by

$$V_{Rd2} = (\frac{1}{2} \nu f_{cd}) b_w\, 0.9d(1 + \cot\alpha) \qquad \text{(Eq. 4.25)}$$

1. Determination of shear strength limited by crushing at the compression struts

$\cot\alpha = 0$ (Vertical stirrups were used)

$$\nu = 0.7 - \frac{f_{ck}}{200} > 0.5 \qquad \text{(Eq. 4.21)}$$

$$= 0.7 - \frac{31.9}{200} = 0.5405$$

$$V_{Rd2} = (\frac{1}{2} \nu f_{cd}) b_w\, 0.9d(1 + \cot\alpha)$$

$$= (\frac{1}{2} \text{x } 0.5405 \text{ x } 31.9) \text{ x } 225 \text{ x } 0.9 \text{ x } 418 \text{ x } (1+0)$$

$$= 729.7 \text{ x } 10^3 \text{ N} = 729.7 \text{ kN}$$

2. Determination of contribution of concrete to the shear capacity V_{cd}

$\tau_{Rd} = (0.25 f_{ctk0.05})/\gamma_c$

$f_{ctk0.05} = 2.076$ (Linearly interpolated from - Table 3.1)

$\gamma_c = 1.00$ (For comparison against experimental results)

$\tau_{Rd} = (0.25 \text{ x } 2.076)/1.00 = 0.519$

$$k = |1.6 - d| > 1 \qquad \text{(Clause 4.3.2.3)}$$

$$= |1.6 - 0.418| = 1.182$$

$$\rho_l = \frac{A_{sl}}{b_w d} < 0.02 \qquad \text{(Clause 4.3.2.3)}$$

$$= \frac{4926}{225 \times 418} = 0.0524$$

(For comparison against experiment, limit is ignored)

$\sigma_{cp} = 0$ (No axial loading or prestressing force)

$$V_{cd} = [\tau_{Rd} k(1.2 + 40\rho_l) + |0.15|\sigma_{cp}]b_w d$$
$$= [0.519 \times 1.182 \times (1.2 + 40 \times 0.0524) + 0] \times 225 \times 418$$
$$= 190.2 \times 10^3 \text{ N} = 190.2 \text{ kN}$$

3. Determination of contribution of steel shear reinforcement to shear capacity V_{wd}

$$V_{wd} = \frac{A_{sw}}{s} 0.9 d f_{ywd} = \frac{157.1}{365} \times 0.9 \times 418 \times 351.1 = 56.9 \times 10^3 \text{ N} = 56.9 \text{ kN}$$

4. Shear strength of re'nforced concrete T-beam V_n

$$V_{Rd3} = V_{cd} + V_{wd} = 190.2 + 56.9 = 247.1 \text{ kN}$$

E.2.5 Summary

The concrete and stirrup contribution to the shear strength using various design standards is summarised in Table E.2. The shear strength prediction using the European Code gave the closest result to the experiment.

Table E.2 - Existing shear strength of T-beams according to various design standards

Design standards	Shear strength			$V_{predicted} / V_{exp}$*
	V_c	V_s	$V_c + V_s$	
Australian code SAI (2001)	147.9	67.4	215.3	0.87
American code ACI Committee 318 (1999)	117.6	63.2	180.8	0.73
Canadian code CSA (1994)	106.2	63.2	169.4	0.69
European code ENV 1992-1-1 (1991)	190.2	56.9	247.1	1.00

* V_{exp} = 247.1 kN (Control beam)

E.3 FRP shear reinforcement contribution

E.3.1 Triantafillou and Antonopoulos (2000)

The contribution of the FRP to the shear strength of a reinforced concrete beam is given by

$$V_{fd} = 0.9\frac{\varepsilon_{fk,e}}{\gamma_f} E_f \rho_f b_w d(1+\cot\beta)\sin\beta \qquad \text{(Eq. 1)}$$

where $\varepsilon_{fk,e}$ is the characteristic value of effective FRP strain given by

$$\varepsilon_{fk,e} = \alpha\,\varepsilon_{f,e} \le \varepsilon_{max} \qquad \text{(Eq. 5)}$$

The effective FRP strain $\varepsilon_{f,e}$ is given by

$$\varepsilon_{f,e} = \min\left[\underbrace{0.65\left(\frac{f_c^{2/3}}{E_f\rho_f}\right)^{0.56} \times 10^{-3}}_{\text{Debonding}}\ ,\ \underbrace{0.17\left(\frac{f_c^{2/3}}{E_f\rho_f}\right)^{0.30}\varepsilon_{f,u}}_{\text{Fracture}}\right] \qquad \text{(Eq. 6b)}$$

The term $E_f\rho_f$ should not exceed $(E_f\rho_f)_{lim}$ given by

$$(E_F\rho_F)_{lim} = 0.018 f_{cm}^{2/3} \qquad \text{(Eq. 7)}$$

unless debonding can be prevented. In the present case, this limit is not considered since the CFRP laminates were well anchored.

1. Determination of characteristic value of effective FRP strain $\varepsilon_{Fk,e}$

$$\rho_{frp} = (2t_F/b_w)(w_f/s_f) = (2 \times 1.31/225)(41.71/s_f)$$
$$= 0.13307\,\%\ (s_f = 365\,mm)$$
$$= 0.16464\,\%\ (s_f = 295\,mm)$$
$$= 0.19824\,\%\ (s_f = 245\,mm)$$

$$\varepsilon_{fk,e} = \alpha\,\varepsilon_{F,e} \le \varepsilon_{max}$$

$$\varepsilon_{F,e} = \min\left[0.65\left(\frac{f_c^{2/3}}{E_f\rho_f}\right)^{0.56} \times 10^{-3}\ ,\ 0.17\left(\frac{f_c^{2/3}}{E_f\rho_f}\right)^{0.30}\varepsilon_{f,u}\right]$$

$$= \min\left[0.65\left(\frac{31.9^{2/3}}{137345 \times \rho_f}\right)^{0.56} \times 10^{-3}, 0.17\left(\frac{31.9^{2/3}}{137345 \times \rho_f}\right)^{0.30} \times 0.015\right]$$

$$= \min\begin{bmatrix} 0.000128 & , & 0.001068 \\ 0.000114 & , & 0.001002 \\ 0.000103 & , & 0.000948 \end{bmatrix}\begin{matrix}(s_f = 365\,mm)\\(s_f = 295\,mm)\\(s_f = 245\,mm)\end{matrix}$$

In the experiment, although debonding was observed, failure of the T-beams was caused by the separation of the overlap at the soffit of the beam. Failure did not occur due to debonding or fracture of the FRP laminates. For comparison against experimental results, $\varepsilon_{fk,e}$ is taken as $\varepsilon_{max} = 0.005$ for all of the strengthened beams.

$$\varepsilon_{fk,e} = 0.005$$

2. Determination of contribution of FRP shear reinforcement to shear capacity V_{Fd}

$\gamma_f = 1.00$ (For comparison against experimental results)

$$V_{Fd} = 0.9\frac{\varepsilon_{fk,e}}{\gamma_f} E_f \rho_f b_w d(1+\cot\beta)\sin\beta$$

$$= 0.9 \text{ x } \frac{0.005}{1.00} \text{x } 137345 \text{ x } \rho_F \text{ x } 225 \text{ x } 418 \text{ x } (1+0) \text{ x } \sin 90°$$

$$77.4 \text{ x } 10^3 \text{ N} \quad 77.4 \text{ kN } (s_f = 365 \text{ mm})$$

$$= 95.7 \text{ x } 10^3 \text{ N} = 95.7 \text{ kN } (s_f = 295 \text{ mm})$$

$$115.2 \text{ x } 10^3 \text{ N} \quad 115.2 \text{ kN } (s_f = 245 \text{ mm})$$

E.3.2 Neale (2001)

The contribution of the FRP to the shear strength of a reinforced concrete beam is given by

$$V_{frp} = \frac{\phi_{frp} E_{frp} \varepsilon_{frpe} A_{frp} d_{frp} (\sin\beta + \cos\beta)}{s_{frp}} \qquad \text{(Eq. 4-58)}$$

where ε_{frpe} is the FRP effective strain given by the minimum of

0.004 (above which aggregate interlock effect of concrete is lost)

and

$$\varepsilon_{frpe} = R\varepsilon_{frpu} \text{ (FRP fracture)} \qquad \text{(Eq. 4-60a)}$$

and

$$\varepsilon_{frpe} = \frac{\alpha\phi_{frp} k_1 k_2 L_e}{9525} \text{ (FRP debonding)} \qquad \text{(Eq. 4-62)}$$

$\alpha = 0.8$ (reduction coefficient for the effective strain)

The term R in Eq. 4-60a is given by

$$R = \alpha\lambda_1 \left[\frac{f'^{2/3}_c}{\rho_{frp} E_{frp}}\right]^{\lambda_2} \qquad \text{(Eq. 4-60b)}$$

$\lambda_1 = 1.35$
$\lambda_2 = 0.30$ (parameters for CFRP rupture)

$$\rho_{frp} = \frac{2t_{frp}w_{frp}}{b_w s_{frp}} \quad \text{(Eq. 4-61)}$$

The term L_e in Eq. 4-62 is the effective anchorage length given by

$$L_e = \frac{25350}{(t_{frp}E_{frp})^{0.58}} \quad \text{(Eq. 4-64)}$$

The parameters k_1 and k_2 account for the shear strength of the concrete and FRP configuration and are given by

$$k_1 = \left[\frac{f'_c}{27.65}\right]^{2/3} \quad \text{(Eq. 4-63a)}$$

$$k_2 = \frac{d_{frp} - n_e L_e}{d_{frp}} \quad \text{(Eq. 4-63b)}$$

1. Determination of FRP effective strain ε_{frpe} (FRP fracture)

$$\rho_{frp} = \frac{2t_{frp}w_{frp}}{b_w s_{frp}} = \frac{2 \times 1.31 \times 41.71}{225 \times s_{frp}} = 0.13307\,\% \; (s_{frp} = 365\,mm)$$
$$= 0.16464\,\% \; (s_{frp} = 295\,mm)$$
$$= 0.19824\,\% \; (s_{frp} = 245\,mm)$$

$$R = \alpha\lambda_1\left[\frac{f'^{2/3}_c}{\rho_{frp}E_{frp}}\right]^{\lambda_2} = 0.8 \times 1.35 \times \left[\frac{31.9^{2/3}}{\rho_{frp} \times 137345}\right]^{0.3} = 0.452\,(s_{frp} = 365\,mm)$$
$$= 0.424\,(s_{frp} = 295\,mm)$$
$$= 0.401\,(s_{frp} = 245\,mm)$$

$$\varepsilon_{frpe} = R\varepsilon_{frpu} = R \times 0.015 = 0.0068\,(s_{frp} = 365\,mm)$$
$$= 0.0064\,(s_{frp} = 295\,mm)$$
$$= 0.0060\,(s_{frp} = 245\,mm)$$

2. Determination of FRP effective strain ε_{frpe} (FRP debonding)

$\phi_{frp} = 1.00$ (For comparison against experimental results)

$n_e = 0$ (No free ends)

$d_{frp} = D = 490$ mm (Assumed to be totally wrapped since anchored very well)

$$L_e = \frac{25350}{(t_{frp}E_{frp})^{0.58}} = \frac{25350}{(1.31\times137345)^{0.58}} = 22.7$$

$$k_1 = \left[\frac{f'_c}{27.65}\right]^{2/3} = \left[\frac{31.9}{27.65}\right]^{2/3} = 1.1$$

$$k_2 = \frac{d_{frp} - n_e L_e}{d_{frp}} = \frac{490 - 0\times22.7}{490} = 1$$

$$\varepsilon_{frpe} = \frac{\alpha\phi_{frp}k_1k_2L_e}{9525} = \frac{0.8\times1.00\times1.1\times1\times22.7}{9525} = 0.0021$$

According to the calculations above, the effective strain due to debonding failure is fairly small. Since the FRP is anchored very well at both ends, we assume that the FRP shear reinforcement is wrapped around the entire section. For the case where the FRP shear reinforcement is wrapped around the section, we simply take $\varepsilon_{frpe} = 0.004$.

$$\varepsilon_{frpe} = \begin{pmatrix} \text{Agg.int.} & \text{Fracture} & \text{Debonding} \\ & 0.0068\,(s_{frp} = 365\,\text{mm}) & \\ 0.004 \quad , & 0.0064\,(s_{frp} = 295\,\text{mm}) \quad , & 0.004 \\ & 0.0060\,(s_{frp} = 245\,\text{mm}) & \end{pmatrix} = 0.004$$

2. Determination of contribution of FRP shear reinforcement to shear capacity V_{frp}

$\phi_{frp} = 1.00$ (For comparison against experimental results)

$$A_{frp} = 2w_{frp}t_{frp} = 2\,\text{x}\,41.71\,\text{x}\,1.31 = 109.28\text{mm}^2$$

$$V_{frp} = \frac{\phi_{frp}E_{frp}\varepsilon_{frpe}A_{frp}d_{frp}(\sin\beta + \cos\beta)}{s_{frp}}$$

$$= \frac{1.00\,\text{x}\,137345\,\text{x}\,0.004\,\text{x}\,109.28\,\text{x}\,490\,\text{x}\,(\sin 90° + \cos 90°)}{s_{frp}}$$

$$\begin{aligned} &80.6\,\text{x}\,10^3\ \text{N} \quad 80.6\,\text{kN}\,(s_{frp} = 365\,\text{mm}) \\ =\ &99.7\,\text{x}\,10^3\ \text{N} = 99.7\,\text{kN}\,(s_{frp} = 295\,\text{mm}) \\ &120.1\,\text{x}\,10^3\ \text{N} \quad 120.1\,\text{kN}\,(s_{frp} = 245\,\text{mm}) \end{aligned}$$

E.3.3 Chen and Teng (2003a, c)

The expressions reported hereafter were referenced from Teng et al. (2002), which in turn had been referenced from Chen and Teng (2003a, c). It should be noted that the expressions present hereafter are not design equations, which the researchers have also proposed through the introduction of safety and reduction factors. In the present study, design values are not required as we are comparing against actual experimental results.

The contribution of the FRP to the shear strength of a reinforced concrete beam is given by

$$V_{frp} = 2f_{frp,e}t_{frp}w_{frp}\frac{h_{frp,e}(\cot\theta+\cot\beta)\sin\beta}{s_{frp}} \qquad \text{(Eq. 4.7)}$$

where

$$h_{frp,e} = z_b - z_t \qquad \text{(Eq. 4.8)}$$

$$z_t = d_{frp,t} \qquad \text{(Eq. 4.9a)}$$

$$z_b = [d - (h - d_{frp})] - 0.1d \qquad \text{(Eq. 4.9b)}$$

$$f_{frp,e} = D_{frp}\sigma_{frp,max} \qquad \text{(Eq. 4.11)}$$

The average stress of FRP intersected by the shear crack at failure $f_{frp,e}$ in Eq. 4.11 depends on whether failure is governed by FRP rupture or debonding.

For FRP rupture

$$D_{frp} = \frac{1+\zeta}{2} \qquad \text{(Eq. 4.13)}$$

$$\zeta = \frac{z_t}{z_b} \qquad \text{(Eq. 4.14)}$$

$$\sigma_{frp,max} = \min\begin{cases} f_{frp} & \text{if } f_{frp}/E_{frp} \le \varepsilon_{max} \\ \varepsilon_{max}E_{frp} & \text{if } f_{frp}/E_{frp} > \varepsilon_{max} \end{cases} \qquad \text{(modification of Eq. 4.23)}$$

For FRP debonding

$$\sigma_{frp,max} = \min\begin{cases} f_{frp} \\ 0.427\beta_w\beta_L\sqrt{\dfrac{E_{frp}\sqrt{f'_c}}{t_{frp}}} \end{cases} \qquad \text{(Eq. 4.16)}$$

$$\beta_L = \begin{cases} 1 & \text{if } \lambda \geq 1 \\ \sin(\pi\lambda/2) & \text{if } \lambda < 1 \end{cases} \tag{4.17a}$$

$$\beta_w = \sqrt{\frac{2 - w_{frp}/(s_{frp}\sin\beta)}{1 + w_{frp}/(s_{frp}\sin\beta)}} \tag{4.17b}$$

$$\lambda = \frac{L_{max}}{L_e} \tag{4.18a}$$

$$L_{max} = \begin{cases} h_{frpe}/\sin\beta & \text{for U jackets} \\ h_{frpe}/(2\sin\beta) & \text{for side plates / wings} \end{cases} \tag{4.18b}$$

$$L_e = \sqrt{\frac{E_{frp}t_{frp}}{\sqrt{f'_c}}} \tag{4.18c}$$

$$D_{frp} = \begin{cases} \frac{2}{\pi\lambda}\frac{1-\cos(\pi/2)\lambda}{\sin(\pi/2)\lambda} & \text{if } \lambda \leq 1 \\ 1 - \frac{\pi - 2}{\pi\lambda} & \text{if } \lambda > 1 \end{cases} \tag{4.19}$$

1. Determination of f_{frpe} due to FRP fracture

$h = D = 490$ mm, $\varepsilon_{max} = 0.015$

$d_{frp} = 490$ mm (Assumed to be totally wrapped since anchored very well)

$z_t = d_{frp,t} = 0$ mm (CFRP is anchored in the flange)

$z_b = [d - (h - d_{frp})] - 0.1d = [418 - (490 - 490)] - 0.1 \times 418 = 376.2$ mm

$$\zeta = \frac{z_t}{z_b} = \frac{0}{376.2} = 0$$

$$D_{frp} = \frac{1+\zeta}{2} = \frac{1+0}{2} = 0.5$$

$f_{frp}/E_{frp} = 2060 / 137345 = 0.015 = \varepsilon_{max}$

$$\sigma_{frp,max} = \begin{cases} f_{frp} & \text{if } f_{frp}/E_{frp} \leq \varepsilon_{max} \\ \varepsilon_{max}E_{frp} & \text{if } f_{frp}/E_{frp} > \varepsilon_{max} \end{cases} = 2060 \text{ MPa}$$

$f_{frp,e} = D_{frp}\sigma_{frp,max} = 0.5 \times 2060 = 1030$ MPa

2. Determination of f_{frpe} due to FRP debonding

$h_{frp,e} = z_b - z_t = 376.2 - 0 = 376.2$ mm

$L_{max} = h_{frp,e} / \sin\beta = 376.2 / \sin 90° = 376.2$ mm

$$L_e = \sqrt{\frac{E_{frp} t_{frp}}{\sqrt{f'_c}}} = \sqrt{\frac{137345 \times 1.31}{\sqrt{31.9}}} = 178.5\,\text{mm} \qquad (4.18c)$$

$$\lambda = \frac{L_{max}}{L_e} = \frac{376.2}{178.5} = 2.1$$

$$D_{frp} = \begin{cases} \frac{2}{\pi\lambda}\frac{1-\cos(\pi/2)\lambda}{\sin(\pi/2)\lambda} & \text{if } \lambda \le 1 \\ 1 - \frac{\pi - 2}{\pi\lambda} & \text{if } \lambda > 1 \end{cases} = 1 - \frac{\pi-2}{\pi\lambda} = 1 - \frac{\pi-2}{\pi \times 2.1} = 0.828$$

$$\beta_L = \begin{cases} 1 & \text{if } \lambda \ge 1 \\ \sin(\pi\lambda/2) & \text{if } \lambda < 1 \end{cases} = 1$$

$$\beta_w = \sqrt{\frac{2 - w_{frp}/(s_{frp}\sin\beta)}{1 + w_{frp}/(s_{frp}\sin\beta)}} = \sqrt{\frac{2 - 41.71/(s_{frp} \times \sin 90°)}{1 + 41.71/(s_{frp} \times \sin 90°)}}$$

$$= \begin{cases} 1.301 & (s_{frp} = 365\,\text{mm}) \\ 1.276 & (s_{frp} = 295\,\text{mm}) \\ 1.250 & (s_{frp} = 245\,\text{mm}) \end{cases}$$

$$\sigma_{frp,max} = \min\left\{ f_{frp},\ 0.427\beta_w\beta_L\sqrt{\frac{E_{frp}\sqrt{f'_c}}{t_{frp}}} \right\} = \min\left\{ 2060,\ 0.427 \times \beta_w \times 1 \times \sqrt{\frac{137345 \times \sqrt{31.9}}{1.31}} \right\}$$

$$= \min\begin{cases} 2060 & \\ 427\ (s_{frp} = 365\,\text{mm}) & \\ 419\ (s_{frp} = 295\,\text{mm}) & \\ 411\ (s_{frp} = 245\,\text{mm}) & \end{cases} = \begin{cases} 427\,\text{MPa}\ (s_{frp} = 365\,\text{mm}) \\ 419\,\text{MPa}\ (s_{frp} = 295\,\text{mm}) \\ 411\,\text{MPa}\ (s_{frp} = 245\,\text{mm}) \end{cases}$$

$$f_{frp,e} = D_{frp}\sigma_{frp,max} = 0.828 \times \sigma_{frp,max} = \begin{cases} 354\,\text{MPa}\ (s_{frp} = 365\,\text{mm}) \\ 347\,\text{MPa}\ (s_{frp} = 295\,\text{mm}) \\ 340\,\text{MPa}\ (s_{frp} = 245\,\text{mm}) \end{cases}$$

3. Determination of contribution of FRP shear reinforcement to shear capacity V_{frp}

$$f_{frp,e} = \min(\text{Rupture, Debonding}) = \begin{cases} 354\,\text{MPa}\ (s_{frp} = 365\,\text{mm}) \\ 347\,\text{MPa}\ (s_{frp} = 295\,\text{mm}) \\ 340\,\text{MPa}\ (s_{frp} = 245\,\text{mm}) \end{cases}$$

$$V_{frp} = 2f_{frp,e}t_{frp}w_{frp}\frac{h_{frp,e}(\cot\theta+\cot\beta)\sin\beta}{s_{frp}}$$

$$= 2\times f_{frp,e}\times 1.31\times 41.71\times\frac{376.2\times(\cot 45°+\cot 90°)\sin 90°}{s_{frp}}$$

$$39.8\times10^3\ \text{N} \quad 39.8\,\text{kN}\ (s_{frp}=365\,\text{mm})$$
$$= 48.4\times10^3\ \text{N} = 48.4\,\text{kN}\ (s_{frp}=295\,\text{mm})$$
$$57.1\times10^3\ \text{N} \quad 57.1\,\text{kN}\ (s_{frp}=245\,\text{mm})$$

E.3.4 Summary

The FRP contribution to the shear strength using various proposed expressions is summarised in Table E.3. The shear strength prediction model by Neale (2001) gave the closest result to the experiment.

Table E.3 - FRP contribution to shear strength according to various design standards

Prediction model	Shear strength (kN)		$V_{predicted}$ / $V_{frp-exp}$*
	V_{frp}	$V_{frp-exp}$*	
Triantafillou and Antonopoulos (2000)	77.4	133.9	0.58 (S_{frp} = 0.75D)
	95.7	151.2	0.63 (S_{frp} = 0.60D)
	115.2	199.1	0.58 (S_{frp} = 0.50D)
Neale (2001)	80.6	133.9	0.60 (S_{frp} = 0.75D)
	99.7	151.2	0.66 (S_{frp} = 0.60D)
	120.1	199.1	0.60 (S_{frp} = 0.50D)
Chen and Teng (2003a, c)	39.8	133.9	0.30 (S_{frp} = 0.75D)
	48.4	151.2	0.32 (S_{frp} = 0.60D)
	57.1	199.1	0.29 (S_{frp} = 0.50D)

*Obtained by simply deducting shear capacity of the control beam from shear capacity of the strengthened beams

LIST OF PUBLICATIONS

Al-Mahaidi, R., Lee, K. and Taplin, G. (2001), Behavior and analysis of RC T-beams partially damaged in shear and repaired with CFRP laminates. Proceedings of the 21st Biennial Conference of the Concrete Institute of Australia - Concrete in the third millennium, Washington, DC, USA, American Society of Civil Engineers.

Lee, K. and Al-Mahaidi, R. (2003), Strength and failure mechanisms of reinforced concrete T-beams strengthened with CFRP plates. Proceedings of the 6th International Symposium on Fibre-Reinforced Polymer (FRP) Reinforcement for Concrete Structures (FRPRCS-6), Singapore (Accepted for publication).

Lee, K. and Al-Mahaidi, R. (2003), Shear strength and behaviour of RC T-Beams retrofitted with CFRP L-strips. Proceedings of the 21st Biennial Conference of the Concrete Institute of Australia - Concrete in the third millennium, Queensland, Australia (Accepted for publication).

Lee, K., Al-Mahaidi, R. and Taplin, G. (2000), Non-linear finite element modelling of shear-damaged concrete T-beams repaired with CFRP laminates. Proceedings of the ACUN-2 : International Composites Conference - Composites in the Transportation Industry, UNSW, Sydney, Australia, pp. 253-258.

Lee, K., Al-Mahaidi, R., Taplin, G. and Millar, D. (2002), Behaviour of reinforced concrete T-beams strengthened with prefabricated L-shaped CFRP plates. IABSE Symposium Melbourne: Towards a Better Built Environment - Innovation, Sustainability, Information Technology, Melbourne, Australia.